Geometrical and Substitutional Influences on the Electronic Structure and the Reactivity of First–Row Transition Metal–Radical Complexes

A Thesis in Chemistry
by

Samir Ghorai

A Dissertation Presented in Partial Fulfillment
of the Requirements for the Degree
Doctor of Philosophy

August 2014

Department of Chemistry
Indian Institute of Technology Guwahati
Guwahati–781039, Assam
India

To my family and friends

भारतीय प्रौद्योगिकी संस्थान गुवाहाटी
Indian Institute of Technology Guwahati

Chemistry can be a good or bad thing.

Chemistry is good when you make love with it.

Chemistry is bad when you make crack with it.

Adam Sandler

भारतीय प्रौद्योगिकी संस्थान गुवाहाटी
Indian Institute of Technology Guwahati

Indian Institute of Technology Guwahati

Department of Chemistry

DECLARATION

I do hereby declare that the research work embodied in this thesis entitled "***Geometrical and Substitutional Influences on the Electronic Structure and the Reactivity of First–Row Transition Metal–Radical Complexes***" has been carried out by me under the supervision of **Dr. Chandan Mukherjee** in the Department of Chemistry, Indian Institute of Technology Guwahati, Assam–781039, India.

In keeping with the general practice of reporting scientific observations, due acknowledgements have been made wherever the work described is based on the findings of other investigators.

IIT Guwahati Samir Ghorai

August, 2014

भारतीय प्रौद्योगिकी संस्थान गुवाहाटी
Indian Institute of Technology Guwahati

Dr. Chandan Mukherjee

Assistant Professor
Department of Chemistry
Indian Institute of Technology
Guwahati–781039
Assam, India

Ph: +91–361–258–2327

Fax: +91–361–258–2349

Email: cmukherjee@iitg.ernet.in

CERTIFICATE

This is to certify that the research work presented in this thesis entitled "***Geometrical and Substitutional Influences on the Electronic Structure and the Reactivity of First–Row Transition Metal–Radical Complexes***" is an authentic record of the results obtained from the research work carried out by **Mr. Samir Ghorai** (**Roll No. 11612213**) under my supervision in the Department of Chemistry, Indian Institute of technology Guwahati, India. This work is original and has not been submitted elsewhere for a degree or award.

IIT Guwahati

August, 2014

Dr. Chandan Mukherjee

(Thesis Supervisor)

भारतीय प्रौद्योगिकी संस्थान गुवाहाटी
Indian Institute of Technology Guwahati

Acknowledgements

I would like to admit that the submission of this thesis would not be possible at all had I not been bestowed with the benign association of the scientific elite of the Indian Institute of Technology Guwahati, India. I would like to acknowledge to everyone who extended their immense support, and help during my research period.

- *First of all, my deepest sense of appreciation goes to my supervisor* ***Dr. Chandan Mukherjee****, who introduced me into the bio–inorganic research field of coordination chemistry of transition metal–radical complexes. His constant guidance, spiritual inspiration and numerous scientific knowledge discussions always acted as catalyst during my research work. In the truest sense, He played the ideal role of the philosopher, the friend, and the guide to me.*
- *I am very much grateful to* ***Dr. Subhendu Sekhar Bag*** *(IIT Guwahati) to inspire me to choose my research field and constant support to start my research work at the beginning of my research life and sharing of his individual scientific knowledge during the research period.*
- *I am highly obliged to* ***Prof. Gopal Das*** *(IIT Guwahati) and* ***Prof. V. Manivannan*** *(IIT Guwahati) for their valuable time to share my research knowledge.*
- *Thanks to* ***Dr. Babulal Das****,* ***Dr. Himanshu Sekhar Jena****, and* ***Dr. Arghya Basu*** *for their support and elegant work with the X–ray crystallography.*
- *Thanks to* ***Prof. P. S. Anil Kumar*** *(IISC Bangalore),* ***Dr. Sanjit Konar*** *(IISER Bhopal),* ***Dr. Archana Tiwari*** *(Sikkim University) for measurements of SQUID.*
- *I indebted to* ***Dr. Tapan K. Paine*** *(IACS Kolkata) for the elemental analysis of my samples and performing of labeling experiment.*
- *Thanks to* ***Prof. Thorsten Glaser*** *(Universität Bielefeld) for the measurements of Mössbauer spectroscopy.*
- *I am gratified to my* ***parents*** *for their constant inspiration and encouragement.*
- *My elder* ***Brother*** *and elder* ***Sister*** *for their encouragement.*
- *My honest regards to* ***Prof. Manabendra Ray*** *(IIT Guwahati),* ***Dr. C. V. Sastri*** *(IIT Guwahati),* ***Dr. Chandan K. Jana*** *(IIT Guwahati),* ***Dr. Debapratim Das*** *(IIT Guwahati),* ***Dr. Sumana Dutta*** *(IIT Guwahati),* ***Dr. Pranab K. Mondal****,* ***Sri Dhrubajyoti Majumdar****,* ***Dr. Biplab Biswas****,* ***Dr. Shaishab Kumar Dinda*** *for their help and inspiration.*
- *I am highly indebted to the* ***UGC*** *for the doctoral fellowship.*

Last but not the least, my research–mates of this institute and of course my friends some of them are ***Mr. Mrinal Bhunia****,* ***Mr. Debashis Sahu****,* ***Mr. Santanu Sahu****,* ***Ms. Isita Bhakta****,* ***Ms. Chandani R. Das****,* ***Mr. Utpal Nath****,* ***Mr. Barun K. Dutta****,* ***Mr. Somnath Ghosh****,* ***Ms. Nirmali Prabha Das****,* ***Mrs. Bedika Phukan****,* ***Mr. Ganesh C. Paul****, and* ***Mr. Manas K. Mondal*** *for their well–wishes and aides, and their constant support in my weal and woe during my academic career in the Indian Institute of Technology Guwahati.*

Samir Ghorai

Present Address:

C/O: Dr. Chandan Mukherjee
Room No. T37, Brahmaputra Hostel
Department of Chemistry
Indian Institute of Technology Guwahati
Guwahati – 781039, Assam, India
Phone: +91 361 2583307
E mail: g.samir@iitg.ernet.in
sghorai.chem@gmail.com

Permanent Address:

Hazarichak,
Bara Kumarchak
Moyna
Purba Medinipur–721647
West Bengal, India
Mobile**:** +91 9957657517

Thesis Title:

"Geometrical and Substitutional Influences on the Electronic Structure and the Reactivity of First–Row Transition Metal–Radical Complexes"

Education:

2014 **Ph. D.** [Thesis submitted (August)]

2011 **Master of Science** (*in Inorganic Chemistry*)
Vidyasagar University, West Bengal, India

2006 **Bachelor of Science** *(Chemistry Hons.)*
Tamralipta Mahavidyalaya
Vidyasagar University, West Bengal, India

Honors/Awards:

1. Qualified CSIR–UGC combined test for 'National Eligibility Test for Lectureship (NET) and Junior Research Fellowship (JRF)–2010' under UGC scheme in Chemical Science.

List of Conferences/Symposiums:

1. Frontiers in Chemical Sciences (FICS)–2012, 2nd – 3rd December, Department of Chemistry, Indian Institute of Technology Guwahati.
2. 20th ISCB International Conference (ISCBC–2014), 1st – 4th March, Department of Chemistry, University of Delhi, Delhi, India.

This work was carried out between July 2011 and August 2014 at the ***Indian Institute of Technology Guwahati, Guwahati, Assam, 781039, India.***

Papers published:

1. "Ortho–Substituent Induced Triradical–Containing Tetranucelar Vanadium(IV) Cluster Formation via C–N Bond Breaking and C–O Bond Making", **Samir Ghorai**, and Chandan Mukherjee*, ***Chem. Commun.***, **2012**, 10180–10182.

2. "Solvatochromic fluorescent cyanophenoxazine: design, synthesis, photophysical properties and fluorescence light–up sensing of ct–DNA" Subhendu Sekhar Bag*, **Samir Ghorai**, Subhashis Jana, and Chandan Mukherjee*, ***RSC Adv.***, **2013**, *3*, 5374–5377.

3. "Effect of ligand substituent on the reactivity of Ni(II) complexes towards oxygen" **Samir Ghorai**, and Chandan Mukherjee*, ***Dalton. Trans.***, **2014**, *43*, 394–397.

4. "Effect of Ligand Substituent Coordination on the Geometry and the Electronic Structure of Cu(II)–Diradical Complexes" **Samir Ghorai**, Richa Rakshit, Soumava Biswas, and Chandan Mukherjee*, ***Inorg. Chem.***, **2014**, *53*, 3333–3337.

5. "Synthesis and Characterization of A Tetraradical–Containing Octanuclear Vanadium Cluster Formed *via* Ligand C–N bond Breaking and C–O bond Making" **Samir Ghorai**, and Chandan Mukherjee*, ***RSC Adv.***, **2014**, *4*, 24698–24703.

6. "Cu(II)–Mediated Transformation of a Tridentate Non–Innocent Ligand to a Tetradentate Salen–Type Innocent Ligand", **Samir Ghorai**, and Chandan Mukherjee*, ***Chem. Asian J.***, **2014**, ***DOI:10.1002/asia.201402868R1.***

Doctoral Committee:

Dr. Subhendu Sekhar Bag (chairman)

Prof. Gopal Das (member)

Prof. V. Manivannan (member)

Dr. Chandan Mukherjee (supervisor)

Abstract

भारतीय प्रौद्योगिकी संस्थान गुवाहाटी
Indian Institute of Technology Guwahati

Chapter I

General Introduction and Motivation

Widespread, naturally occurring enzymatic reactions are proceeded through a transient species consist of organic π–radical mainly, tyrosine radical containing metal complexes, known as metalloenzymes, e.g. GAOase, CuAOase, Ribonucleotide reductage, Cytochrome P450, etc. To have a look on such kinds of metal incorporate enzymes, bioinorganic chemists are interested and motivated to synthesize mimic complexes those are functionally same with metalloenzyme to understand the reaction mechanism of naturally occurring enzymatic reactions and to study structural aspects, as well as, the electronic properties of the active site of the enzyme. Organic moieties, showing redox non–innocent behavior are used full ligand in laboratory to synthesize radical–containing transition metal complexes. Substituents present at the ligand backbone that caused the structural distortion in the transition metal complexes and altered the reactivity.

Chapter II

Electron Withdrawing –CN as the –ortho Substituent to the Aniline Moiety of H_2AP^H Ligand and Its Effect to the First–Row Transition Metal Complexes

Substituent present in the ligand backbone is known to show a significant effect in the electrochemical behaviors of the corresponding metal–radical complexes. In the metal–radical complexes the electrochemical properties are mainly ligand oriented. Hence, the electron donating or withdrawing character of the substituent present in the ligand backbone should modulate the reactivity of metal–radical complexes. Knowing that a modification has been made to non–innocent ligands $\mathbf{H_2AP^H}$ by placing π–electron acceptance substituent like –CN group ($\mathbf{H_2L^{CN}}$) at the *–ortho* position of N–phenyl ring of the aniline moiety of $\mathbf{H_2AP^H}$ ligand. In addition to that, several other *–ortho* substituted ligands $\mathbf{H_2L^X}$ (X = –Me, –Et, –F, –Cl, –Br, and –I) were synthesized to investigate the role of substituent present at the ligand backbone, which alter the coordination environment and geometry of the transition metal complexes.

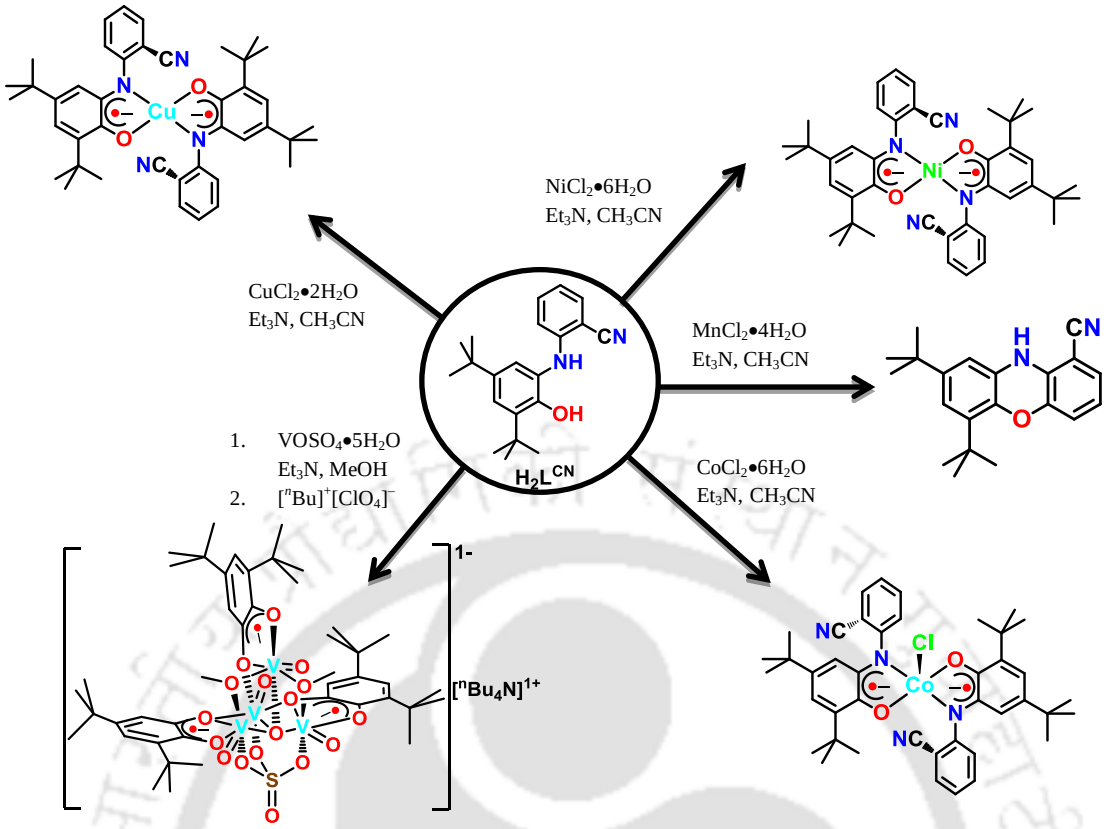

Scheme 1: *Ligand* $\boldsymbol{H_2L^{CN}}$ *and its different reactivity towards first–row transition metal complexes.*

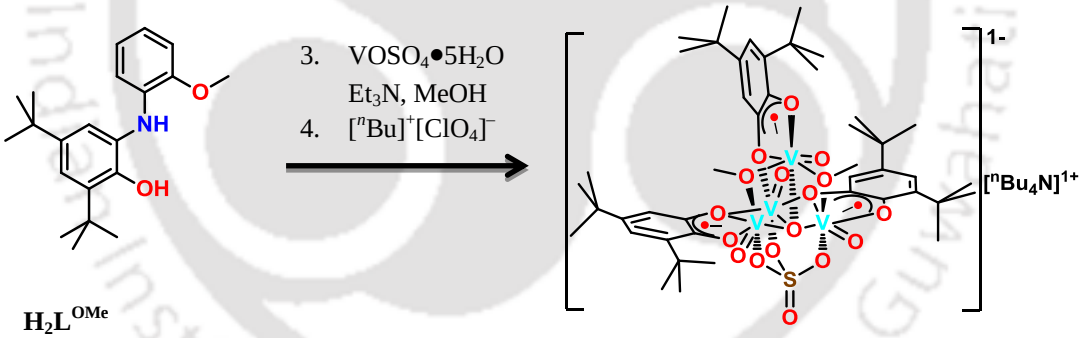

Scheme 2: *Ligand* $\boldsymbol{H_2L^{OMe}}$ *and its reaction towards* $VOSO_4 \bullet 5H_2O$.

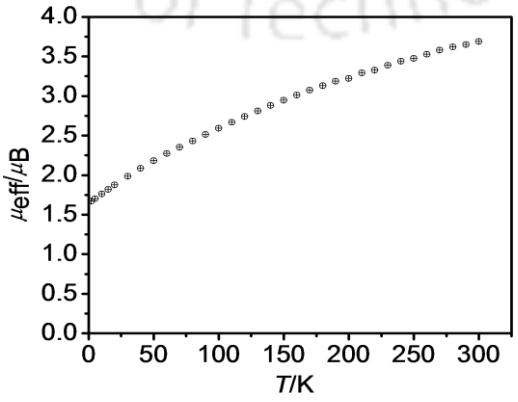

Figure 1: *μeff vs T plots for vanadium complex formed with ligand* $\boldsymbol{H_2L^X}$ *(X =* –CN, and –OMe*).*

Ligand $\mathbf{H_2L^{CN}}$ and $\mathbf{H_2L^{OMe}}$ (*o*–substituent having weak coordination property) reacted with $VOSO_4 \bullet 5H_2O$ in the presence of triethylamine provided a triradical–containing tetranuclear oxo–V(IV) cluster *via* ligand center C–N bond breaking and C–O bond making. Presence of weak coordinating substituent at the –*ortho* carbon atom to the aniline moiety of ligand 2–Anilino–4,6–di–*tert*–butylphenol [$\mathbf{H_2AP^H}$] was essential for the activation of vanadium center and thereafter ligand center C–N bond breaking and C–O bond making processes.

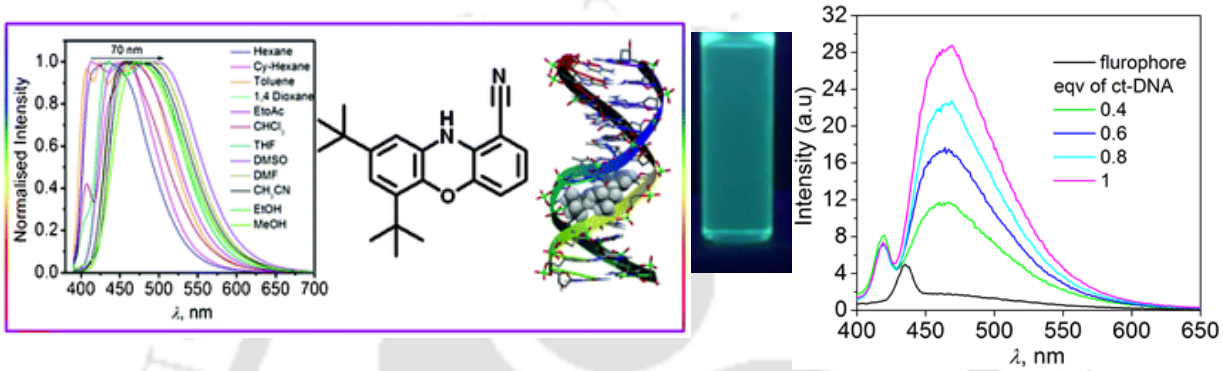

Figure 2: *Solvatochromic normalized emission spectrum of* ***phenoxazine*** *derivative and fluorescence titration probe of* ***phenoxazine*** *derivative with ct–DNA.*

The ligand $\mathbf{H_2L^{CN}}$ reacted with $MnCl_2 \bullet 4H_2O$ provides a highly fluorescent phenoxazine derivative. In this process, initially a Mn(III) complex coordinated to two π–radical anions was formed. This diradical species then acted as catalyst and oxidized the $\mathbf{H_2L^{CN}}$ ligand to its two–electron oxidized $\mathbf{L^{CNQ}}$ form, which upon cyclization provided the fluorescent compound. The fluorescent compound bound with ct–DNA and enhanced its fluorescent behavior. Hence, it behaved as a ct–DNA sensor.

The ligand provided diradical-containing diamagnetic square pyramidal Co(III) complex. The diamagnetic nature of the complex was accounted due to the strong antiferromagnetic coupling between the two radicals.

Complex $\mathbf{[CuL^{CN\bullet}{}_2]}$ was a three spin system [two radical and a Cu(II)] with an S = 1/2 ground state. A Cu(II)–centered X–Band EPR spectrum consolidated (↓↑↑) as the ground state electronic configuration owning a stronger antiferromagnetic coupling between the two radical (S_R = 1/2) centrers than that of the Cu(II) ($S_{Cu(II)}$ = 1/2) and a radical centre.

Chapter III

A Tridentate Ligand Combined of a Non–Innocent Core 2–Aminophenol and a Substrate Core Benzylamine and Its Corresponding Co(III), Ni(II), and Cu(II) Complexes: Synthesis, Characterization, and Reactivity

2–Anilino–4,6–di–*tert*–butylphenol is a non–innocent ligand and provides a diradical–containing Cu(II) complex. Incorporation of a $-CH_2NH_2$ group at the –*ortho* position to the aniline moiety of the ligand would provide a new that will be a combination of benzylamine, the substrate part, and 4,6–di–*tert*–butyl–2–aminophenol, the π–radical generating part and hence, the mechanism of AOs could be studied. The new non–innocent ligand will be represented in this thesis as $\mathbf{H_4L^{CH_2NH_2}}$.

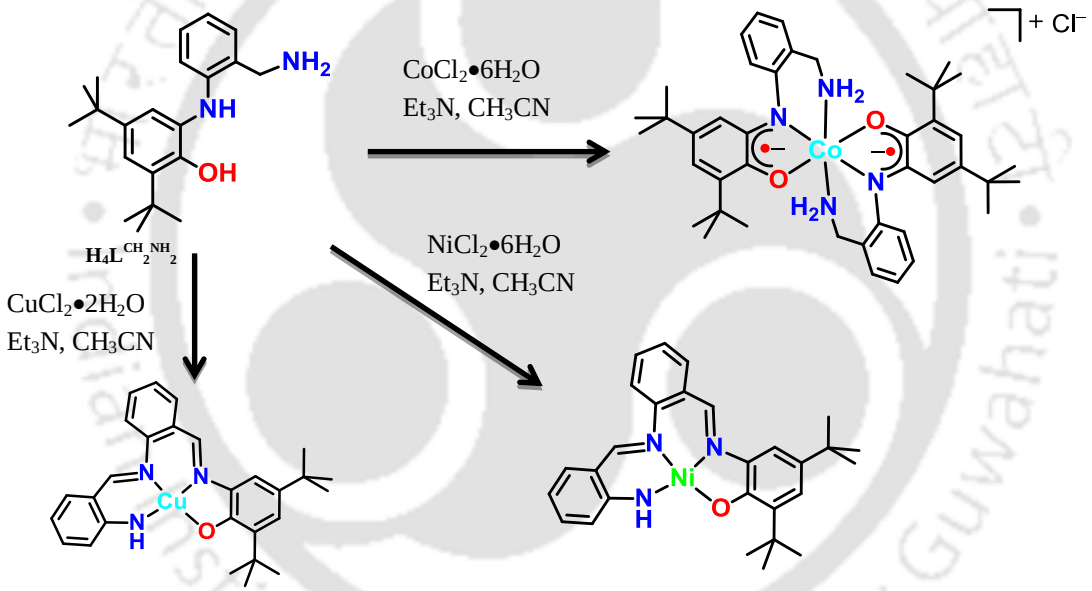

Scheme 3: Ligand $\mathbf{H_4L^{CH_2NH_2}}$ and its corresponding Co(III), Ni(II), and Cu(II) complexes.

The ligand $\mathbf{H_4L^{CH_2NH_2}}$ behaved as a non–innocent ligand and stabilized corresponding Co(III) complex in diradical–coordinated octahedral geometry. The complex was diamagnetic owing a strong antiferromagnetic coupling between two π–radicals. The angle between the two π–radical occupying C_6 planes was 55.6°. This deviation from the orthogonality was the main reason for the antiferromagnetic coupling.

The tridentate ligand $\mathbf{H_4L^{CH_2NH_2}}$ provided Ni(II) complex as complete ligand backbone modified salen–type complex *via* aryl migration and C=N hydrolysis.

The same ligand also provided a completely ligand backbone modified tetradentate salen–type Cu(II) complex *via* ligand center amine oxidation and C–N bond cleavage.

Chapter IV

An Innocent and A Non–Innocent Combined Tetradentate Ligand and Its Corresponding Fe(III), Ni(II), and Cu(II) complexes: Synthesis, Characterizaation, and Substituent dependent Reactivity

Four–coordinate salen complexes are not planar, rather, they have folded bowl or disc-shaped geometry. Because of this distortion, in salen complexes, the metal center is easily accessible and hence, salen complex are useful for various organic catalysis, for example epoxidation, sulfoxidation, etc.

Ligand–centered radical in a coordination complex is important in the sense that it can easily accept electron and donate electron. Therefore, the combination of radical generating non–innocent ligand with salen unit should provide unique ligand system where radical-coordinated metal complexes will have metal ion which will be situated above the ligand plane. Hence, the resulting complexes can be used as oxidation catalyst. In addition to that to study the effect of ligand center substituent, ligands $\mathbf{H_3L^{Mixed(H)}}$ and $\mathbf{H_3L^{Mixed(tBu)}}$ are synthesized.

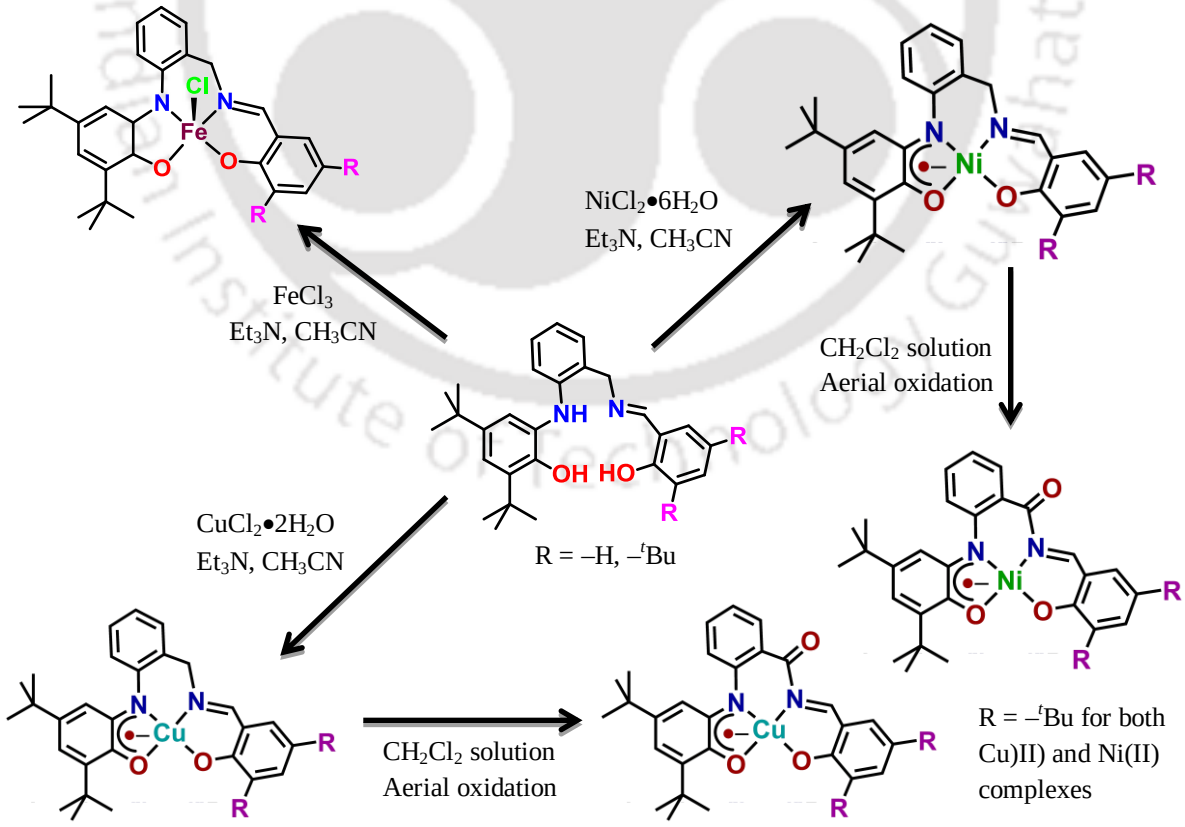

Scheme 4: *Ligand* $\boldsymbol{H_3L^{Mixed(H/tBu)}}$ *and its corresponding Fe(III), Ni(II), and Cu(II) complexes.*

The complexes shown in Scheme 4 have been synthesized using the ligands and presented. It was found that substituent do not show any effect on square pyramidal Fe(III) complexes, while, the corresponding Ni(II) and Cu(II) complexes show a substituent dependent aerial oxidation of the ligand backbone. The oxidation process was preceded through aerial oxygen activation and this activation process was favoured by the position of the metal ion above the ligand plane. Herein, the nature of the substituent played a crucial role in ligand folding and hence, the position of the metal ion with respect to the ligand plane.

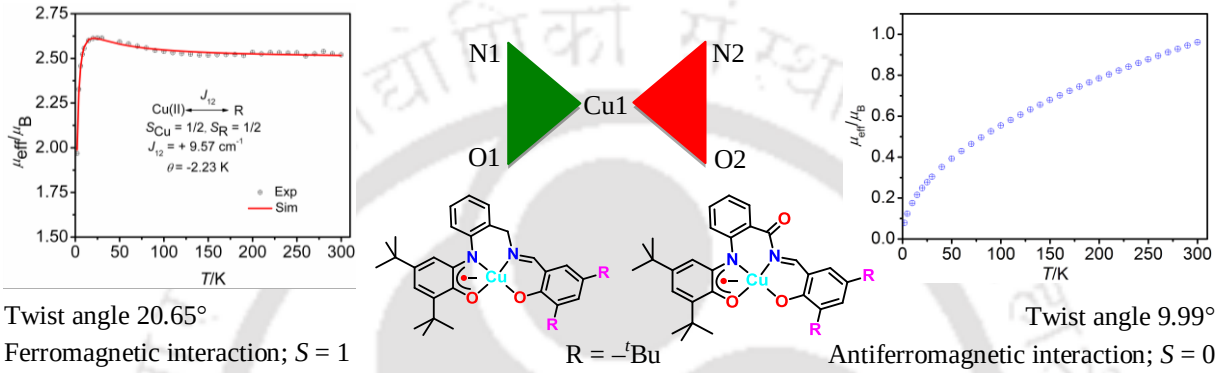

Figure 3: *Monoradical–containing distorted square planar Cu(II) complexes with mixed ligand and their anomalous magnetic behaviour to the twist angel.*

In addition to the substituent dependent reactivity, ligand folding–dependent coupling in between the paramagnetic centres have been observed **(Figure 3**).

Chapter V

Synthesis, Characterization, and Reactivity of Co(III) Complexes Isolated by Using H_2L^X (X = –Me, –Et, –F, –Cl, –Br, and –I) Ligands

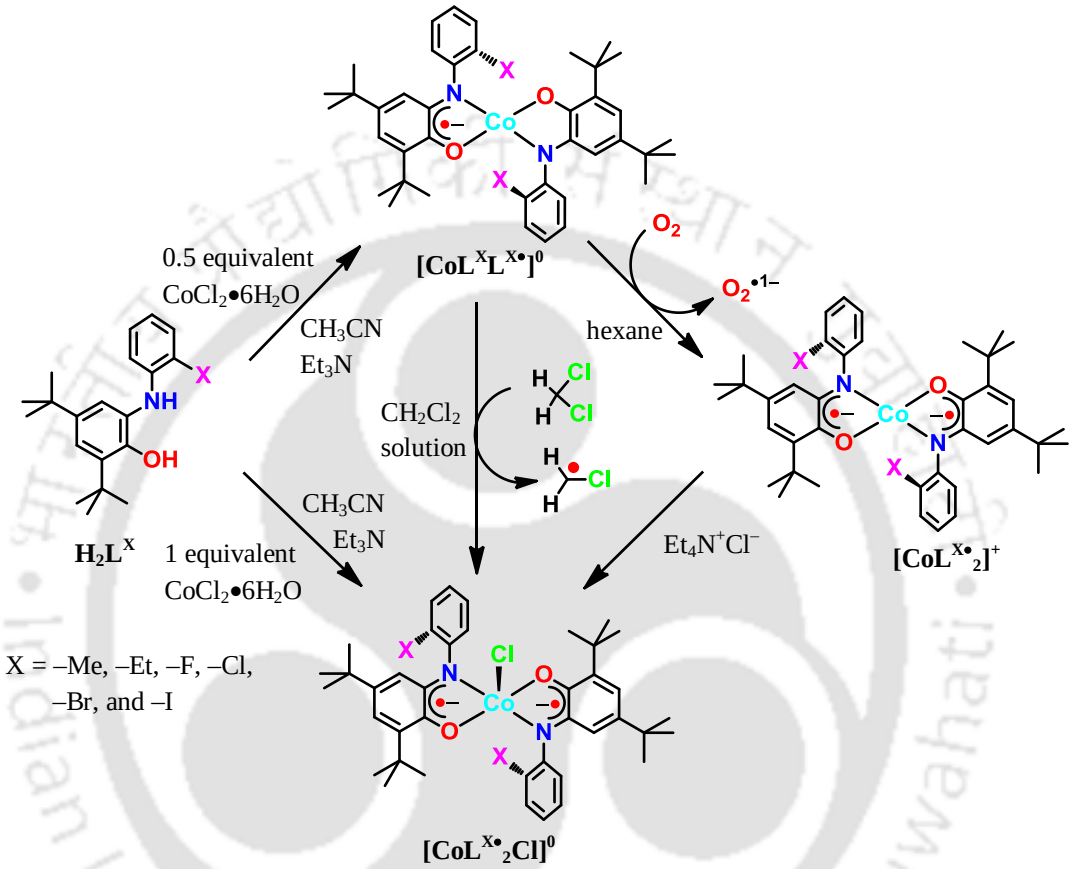

Scheme 5: *Ligand H_2L^X (X = –Me, –Et, –F, –Cl, –Br, and –I) and its corresponding Co(III) complexes.*

Placement of different substituents at *–ortho* position to the N–phenyl ring of H_2AP^H non–innocent ligand, the π–donor capacity of the ligand was enhanced, and thereafter, the non–innocent ligand $H_2L^{Me/Et/F/Cl/Br}$ yielded radical–containing square planar cobalt(III) complexes by varying the metal ion concentration and reaction period. Four coordinated square planar geometry were coordinatively unsaturated and transformed into five coordinated square pyramidal geometry *via* redox active electron transfer bond formation at the Co center.

Complex $[CoL^{Me}L^{Me•}]$ was unreacted towards excess $CoCl_2•6H_2O$ and also did not provide $[CoL^{Me•}{}_2Cl]$ with time that indicated monoradical–containing square planar Co(III) complex was thermodynamically controlled product. On the other hand, ligands $H_2L^{Cl/Br}$ (X

= –Cl, –Br) upon reacting with 0.5 equivalent of $CoCl_2 \bullet 6H_2O$ provided complex [**CoL^{X}L$^{X\bullet}$**] initially and finally [**CoL$^{X\bullet}{}_2$Cl**]. This indicated that [**CoL^{X}L$^{X\bullet}$**] was the kinetically controlled product, while, [**CoL$^{X\bullet}{}_2$Cl**] was the thermodynamically controlled product. It was found that [**CoL^{X}L$^{X\bullet}$**] reacted with molecular oxygen in the presence of Et_4NCl, transformed into [**CoL$^{X\bullet}{}_2$Cl**]. This evidenced that complex [**CoL^{X}L$^{X\bullet}$**] was first oxidized to form Co(III)–diradical species, [**CoL$^{X\bullet}{}_2$**], which then accept a Cl– ion from the reaction solution at the axial position and formed the corresponding neutral five–coordinate complex. Interestingly, it was found that all the four coordinated [**CoL^{X}L$^{X\bullet}$**]–type complexes reacted with CH_2Cl_2 in solution and provided the corresponding [**CoL$^{X\bullet}{}_2$Cl**]–type complexes.

CONTENTS

Chapter I

General Introduction and Motivation

Chapter II

Electron Withdrawing –CN as the –ortho Substituent to the Aniline Moiety of H_2AP^H Ligand and Its Effect to the First–Row Transition Metal Complexes

Chapter III

Synthesis, Characterization, and Reactivity of Co(III) Complexes Isolated by Using H_2L^X (X = –Me, –Et, –F, –Cl, –Br, and –I) Ligands

Chapter VI

Equipment and Experimental Section

Abbreviations:

Technical terms:

av. : average

B : magnetic field

LMCT : ligand–to–metal charge transfer

MLCT : metal–to–ligand charge transfer

LLCT : ligand–to–ligand charge transfer

LLIVCT : ligand–to–ligand intervalence charge transfer

D : zero–field splitting

deg. : degree (°)

e^- : electron

E : total energy

Exp : experimental

Sim : simulated

H : Hamiltonian

J : coupling constant (cm^{-1}) /or Hz

HS : high spin

LS : low spin

I : nuclear spin

SOMO : singly occupied molecular orbital

m/z : mass per charge

RT : room temperature (30 ℃)

S : electron spin

s : singlet

d = doublet

t = triplet

q = quartet

Units:

Å : angstrom (10^{-10} m)

cm : centimeter

emu : electromagnetic unit

G : gauss

h : hour

K : Kelvin

M : molar

m / min. : minute

mm : millimeter

nm : nanometer (10^{-9} m)

s : second

T : tesla

μ_B : bohr magnetron

B : magnetic field

° : degree

Symbols:

λ : wavelength (nm)

ε : extinction coefficient ($M^{-1}cm^{-1}$)

μ_{eff} : magnetic moment (μ_B)

δ : Isomer shift

ΔEQ : quadrupole splitting (mm/s)

X or * : multiplication

Solvents and reagents:

TBAP : tetrabutylammonium perchlorate

Cat.: catechol

SQ : semiquinone

ISQ : iminosemiquinone

IBQ : iminobenzoquinone

CH_2Cl_2 : dichloromethane

CCl_4 : carbontetrachloride

Et_2O : diethylether

Et_3N : triethylamine

EtOH : ethanol

KBr : potassium bromide

MeOH : methanol

CH_3CN : acetonitrile

THF : tetrahydrofural

EtOAc : ethylacetate

$Et_4N^+Cl^-$: tetraethylammonium chloride

Techniques:

EA : elemental analysis

EI : electron ionisation

EPR : electron paramagnetic resonance

NMR : nuclear magnetic resonance

ESI : electrospray ionisation

IR : infrared

MS: mass spectrometry

SQUID : superconducting quantum interface device

UV–vis/NIR : ultraviolet–visible/near infrared spectroscopy

Latin expressions:

ca. : around

et al. : and coworkers

e.g. : for example

i.e. : namely

tert– : tertiary

vs. : versus, against

via : through

Chapter I

General Introduction and Motivation

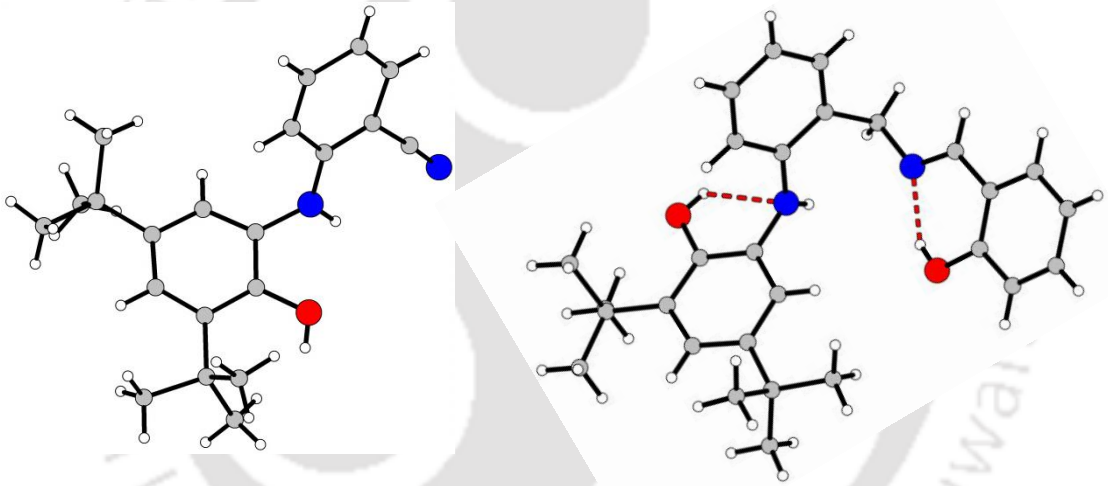

1.1: General Introduction and Motivation:

Bioinorganic chemistry is an area where the role of metal ions in various biological processes is studied. Enzymes that include metal ion are known as metalloenzymes and in most of the metalloenzymes the active site, where the enzymatic reactivity occurs, are the metal centers. Widespread occurrence of amino acid radicals, mainly tyrosine radical, in metalloenzymes and their involvements in several metalloenzymatic activities, for example; Galactose Oxidase,[1] Catechol Oxidase,[2] Photosystem I and Photosystem II,[3] organic cofactor formation in Amine Oxidases,[4] Cytochrome c Oxidase,[5] Cytochrome P450,[6] Rribonucleotide Reductase,[7] etc, have drawn considerable attention of chemists and biologists to the synthesis of radical–containing transition metal, mainly first–row transition metal, complexes. The main aim for the synthesis of radical–containing transition metal complexes is two–fold;

(i) understanding of metal–radical interactions in synthetic complexes and thereafter, their rationalization in metallloenzymatic activities, and

(ii) use of radical–containing transition metal complexes as biomimetic catalysts for industrial processes.

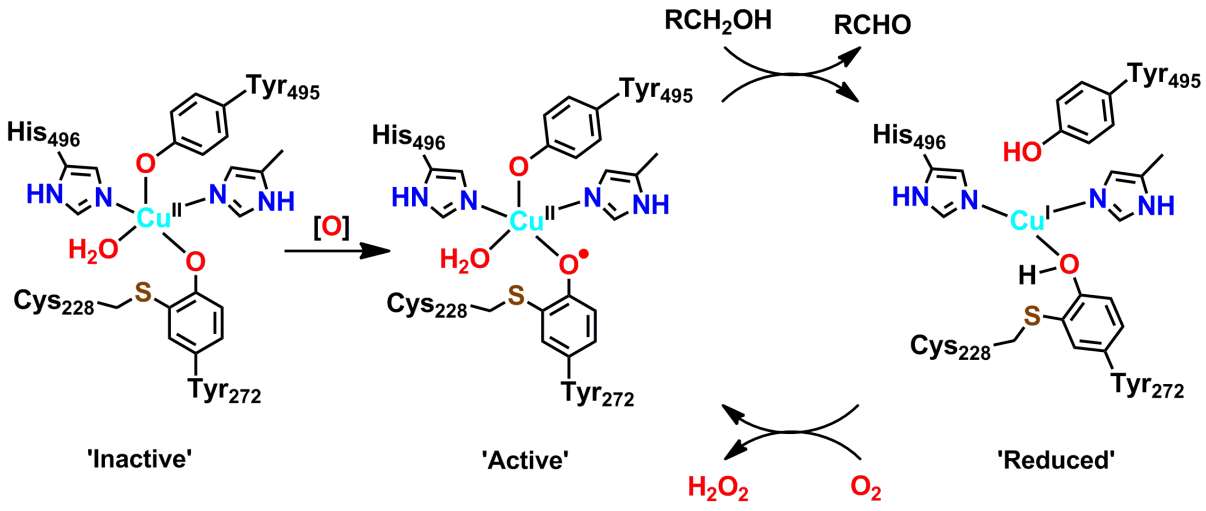

Scheme 1.1: *Schematic representation of active site, active form and catalytic reactivity of GOase.*[8]

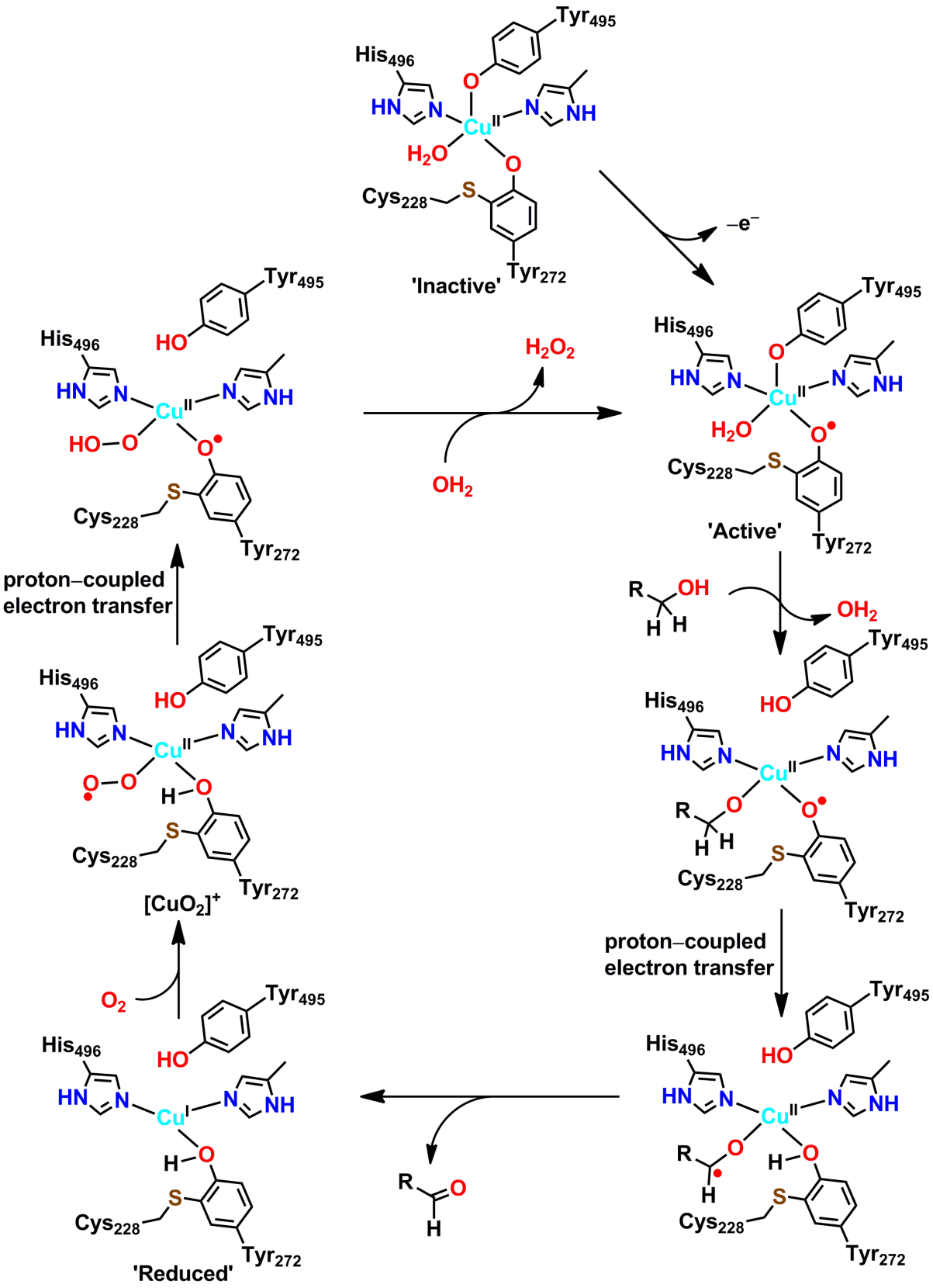

Scheme 1.2: *Proposed mechanism for GOase reactivity.*[9]

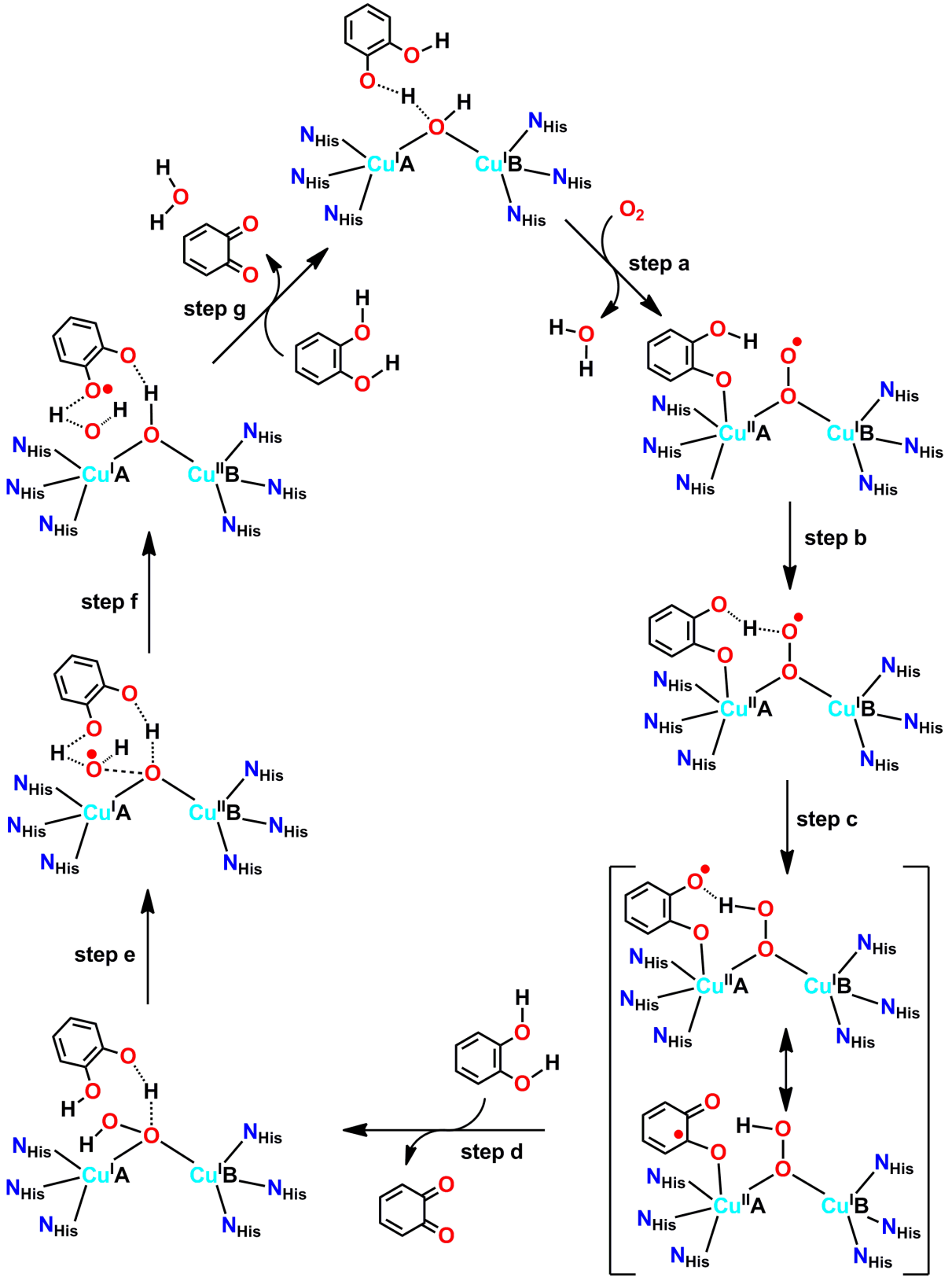

Scheme 1.3: *A mechanistic proposal for catechol oxidase reactivity.*[10]

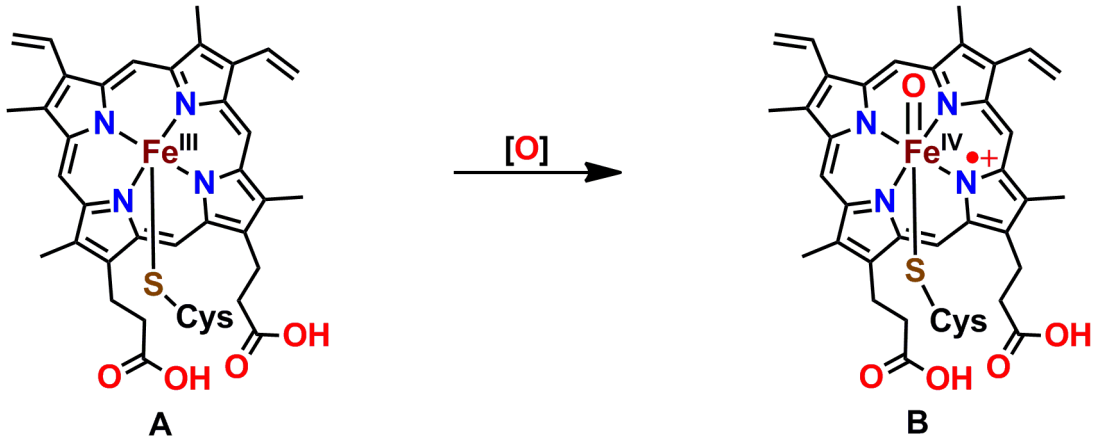

Scheme 1.4: *Iron(III) protoporphyrin IX with a cysteinate as the axial ligand (**A**), which is typical of cytochrome P450. The active oxygen species of these proteins and related heme enzymes is an oxoiron(IV)porphyrin cation radical (**B**).*[11]

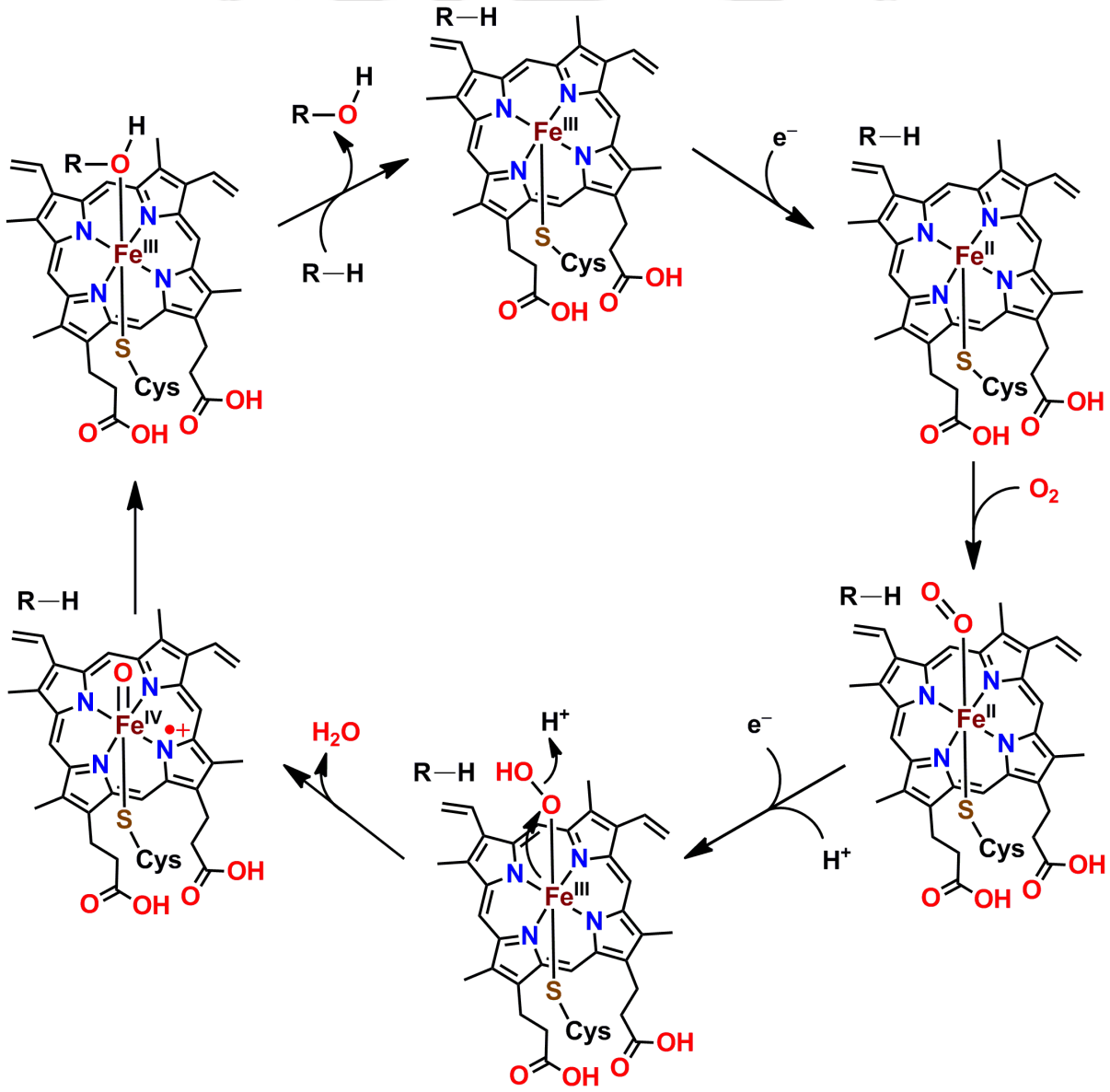

Scheme 1.5: *A consensus catalytic cycle for oxygen activation and transfer by cytochrome P450.*[11]

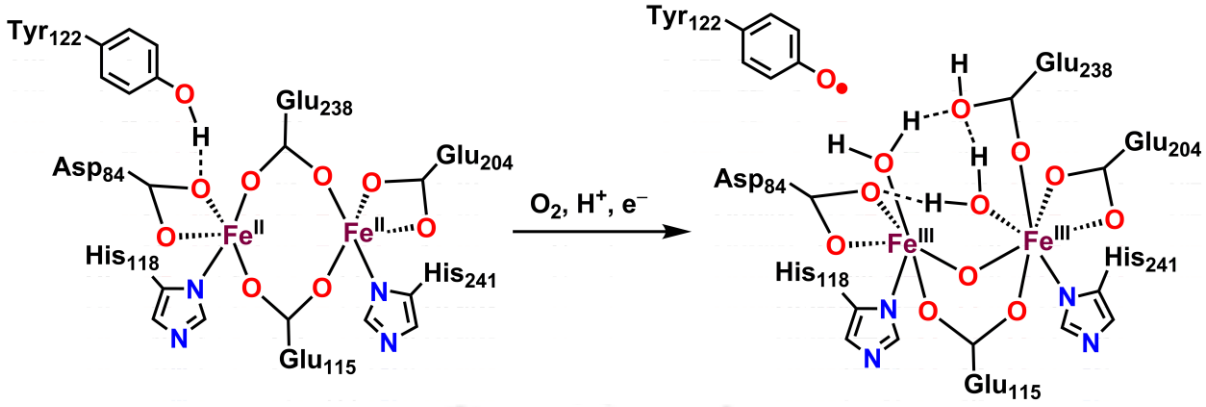

Scheme 1.6: *Generation of tyrosyl radical in the active site of ribonucleotide reductase.*[12]

Organic moieties capable of metal ion encapsulation are known as ligands. These ligands can be divided into two groups depending on the change of their oxidation state that occurs before and after metal ion encapsulation in the presence of oxygen. If there is no change in the ligand oxidation state after metal ion encapsulation, the ligand is called innocent ligand (IL), while, a change in the ligand oxidation state after metal ion encapsulation, designates the ligand as non–innocent ligand (NIL).[13] The innocent and non–innocent nature of a ligand depends on the metal ion to which it is coordinated. For instant, 2–anilino–4,6–di–*tert*–butylphenol (**H_2AP^R; R = H, Scheme 1.7**) behaves as a non–innocent ligand when it coordinates to copper(II), nickel(II), palladium(II), cobalt(III), iron(III), and manganese(IV) metal ions and provides the corresponding metal–radical complexes.[13*i*,14] On the contrary, the ligand does not show any change in its oxidation state in its corresponding vanadium(V) complex. This is possibly because of the energy required for the change in oxidation state of V is lower compared to the required energy for the oxidation of the ligand to its π–radical anion form.[15] Hence, oxidation potential tuning of ligand backbone is necessary for the synthesis of radical–containing various metal complexes.

One of the ways of tuning the oxidation potential of ligand in coordinated metal complexes is the attachment of various electron donating or withdrawing substituents in ligand backbone. For instance, Cu(II) complexes derived from 2–[3,5–di–substituted(R)–anilino]–4,6–di–*tert*–butylphenol (**H_2AP^R**) ligands (**Scheme 1.8**) show a clear trend in their first oxidation potential depending upon the substituents' nature. The first oxidation potential was higher when the substituent is electron withdrawing (**Figure 1.1**).[16]

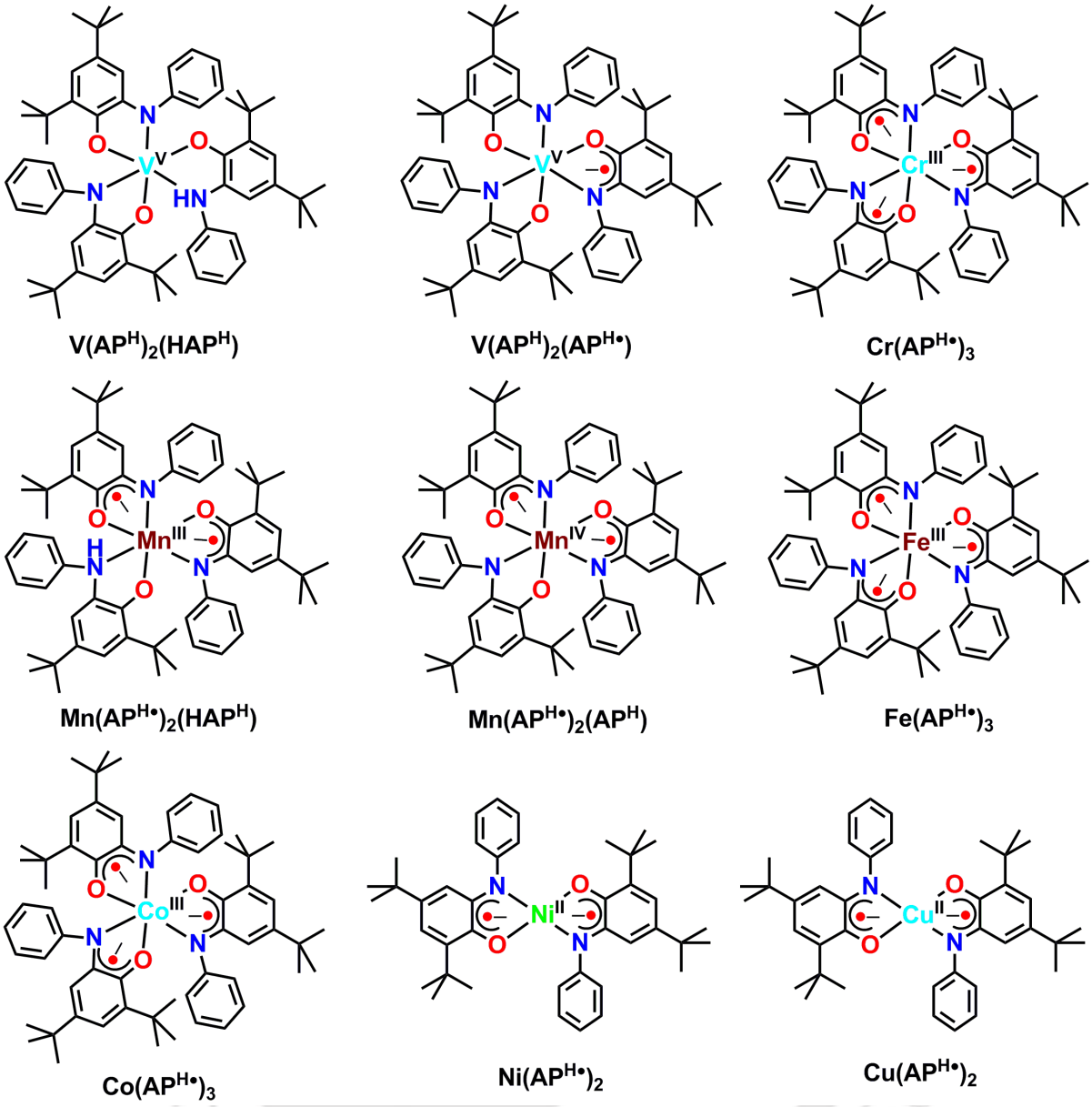

Scheme 1.7: *Schematic representation of ligand H_2AP^R (R = –H) and its first row transition metal complexes.*

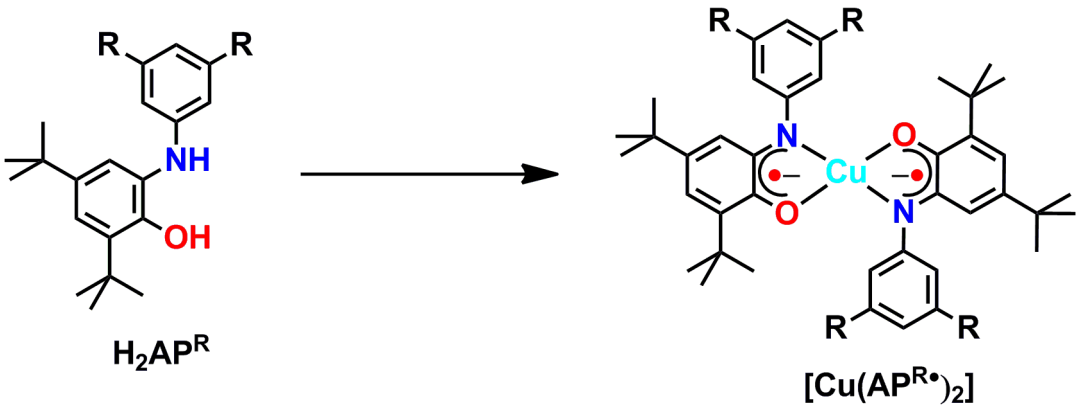

Scheme 1.8: *Schematic representation of ligand H_2AP^R and its di–radical containing Cu(II) complexes.*

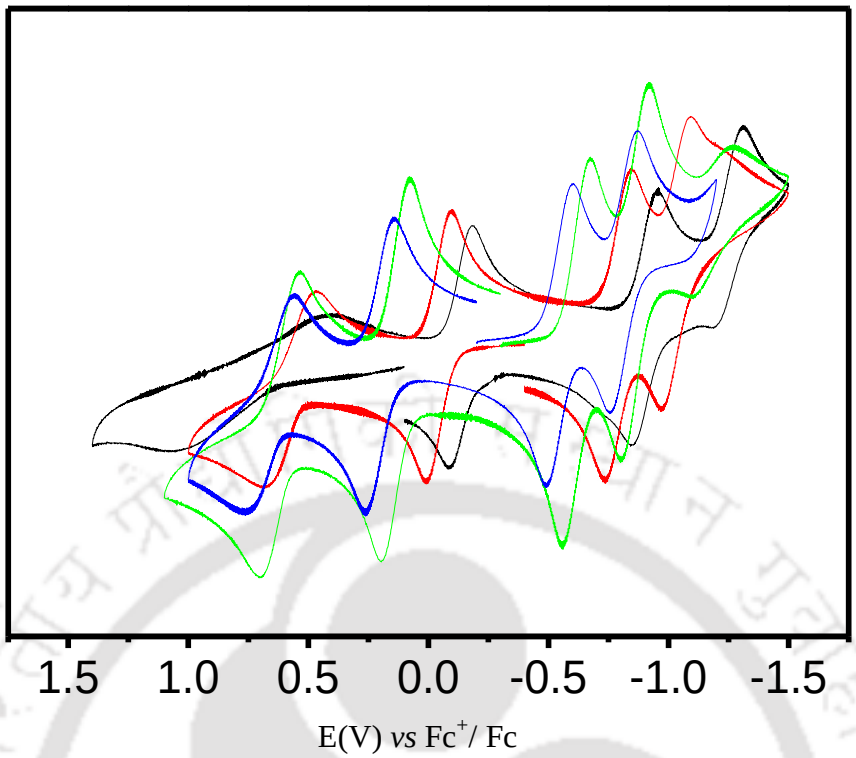

Figure 1.1: *Cyclic voltammograms for **1** (blue), **2** (green), **3** (red), and **4** (black).*

Table 1.1: *Redox potential values for Cu(II) complexes with* $\boldsymbol{H_2AP^R}$ *ligands.*

Complex	**Ox_1(V)**	**Ox_2(V)**	**Red_1(V)**	**Red_2(V)**
1(3,5–F)	–0.12	0.365	–0.99	–1.445
2(3,5–CF_3)	–0.06	0.41	–0.804	–1.07
3(3,5–OMe)	–0.30	0.318	–1.043	–1.289
4(3,5–^{t}Bu)	–0.393	0.47	–1.16	–1.51

In accordance to that, electron donating and withdrawing substituents have been attached at the –*ortho* position to the aniline moiety of 2–anilino–4,6–di–*tert*–butylphenol and presented in this thesis. The main reason of choosing the –*ortho* position is to achieve maximum electronic effect *via* mesomeric effect in addition to inductive effect. The organic moieties will be presented in this thesis as $\mathbf{H_2L^X}$; (X = –CN, –OMe, –Me, –Et, –F, –Cl, –Br, and –I, respectively), $\mathbf{H_3L^{COOH}}$,[17] **and** $\mathbf{H_4L^{CH_2NH_2}}$, respectively.

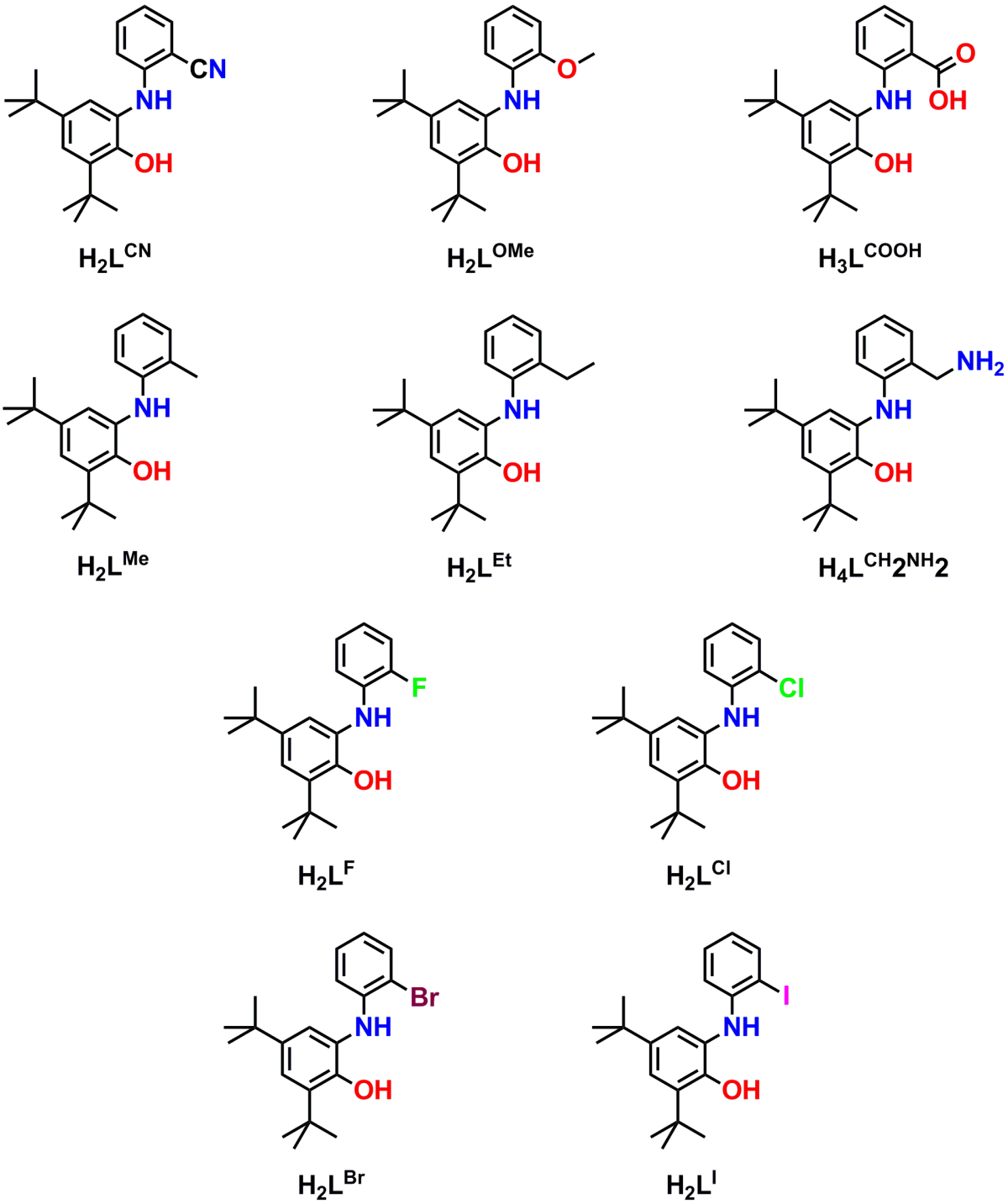

Scheme 1.9: *Representation of different –ortho substituted non–innocent ligands.*

Cu–containing Amine Oxidases (AOs) catalyzes oxidative deamination of primary amines to the corresponding aldehydes in the presences of water with concomitant production of one equivalent of ammonia and one equivalent of hydrogen peroxide.[4]

$$RCH_2NH_2 + H_2O + O_2 \longrightarrow RCHO + NH_3 + H_2O_2$$

The active site of the metalloenzye was comprised of a Cu(II) ion which is surrounded by three histidine units and closely located an organic cofactor (*e.g.* topa–quinone, dopa–quinone, lysyl tyrosine quinone, etc).[18] During the oxidation of amine the quinone moiety get reduced to aminophenol moiety. The reoxidation of the aminophenol to its initial quinone form is an aerial process. A univocal mechanism for this oxidation process is not known yet. However, it is well established that the Cu(II) center does not participate in the oxidative half reaction.[19,21] The main anomaly lies with the reductive half reaction, where the participation of Cu(II) center is yet to be well established univocally.

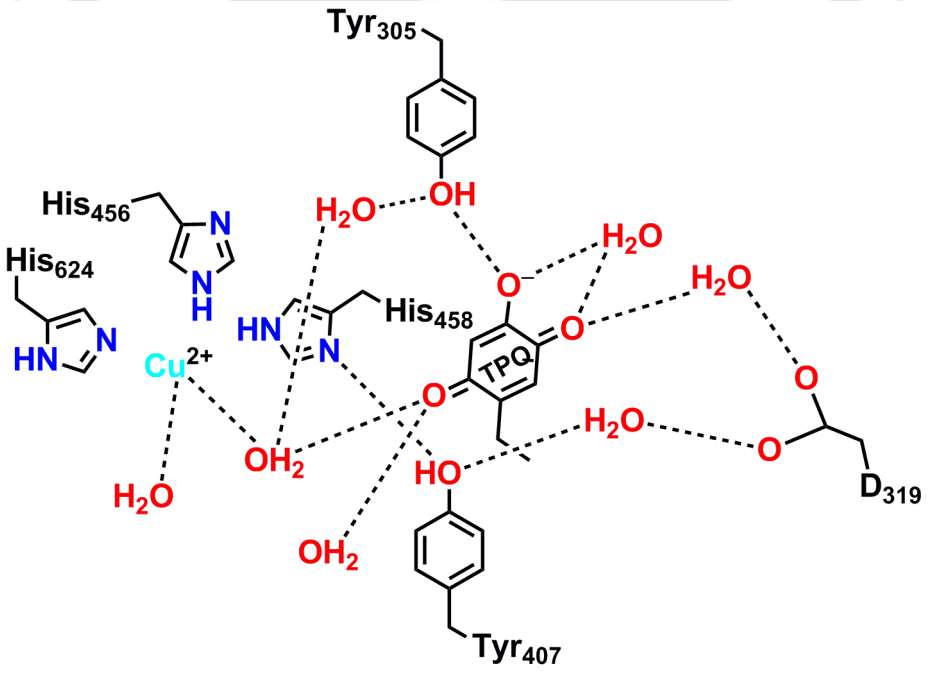

Scheme 1.10: *Schematic presentation of the key residues in the active site of HPAO, Hansenula polymorpha amine oxidase.*[20]

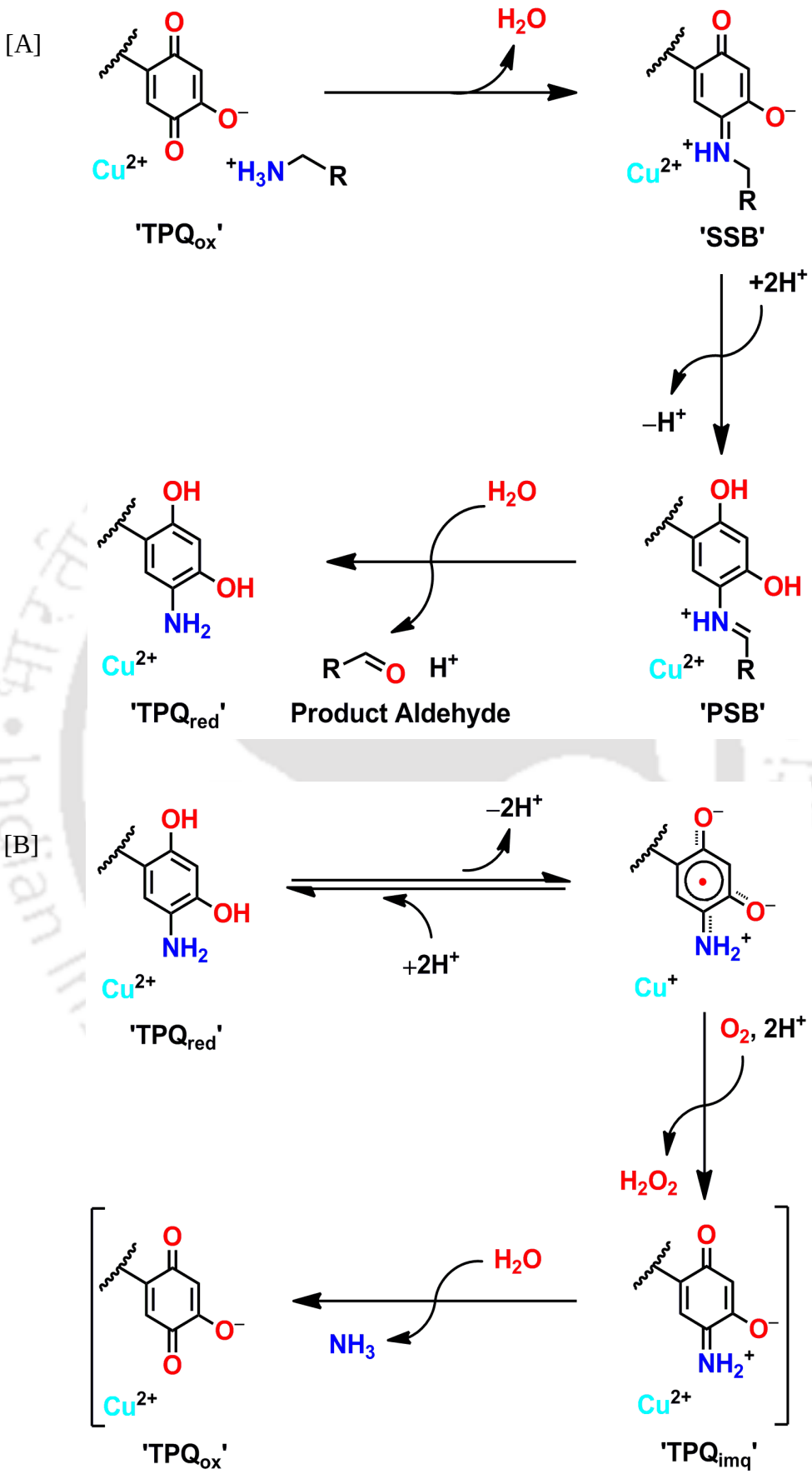

Scheme 1.11: *Proposed mechanism for the oxidative half reaction viz. direct involvement of oxygen [A]; and the reductive half reaction viz. the active site copper(II) [B].*[21]

2–Anilino–4,6–di–*tert*–butylphenol is a non–innocent ligand and provides a diradical–containing Cu(II) complex. Incorporation of a $–CH_2NH_2$ group at the *–ortho* position to the aniline moiety of the ligand would provide a new ligand that will be a combination of benzylamine, the substrate part, and 4,6–di–*tert*–butyl–2–aminophenol, the π–radical generating part and hence, the mechanism of AOs could be studied. The new non–innocent ligand will be represented in this thesis as **$H_4L^{CH_2NH_2}$ (Scheme 1.9).**

Four–coordinate salen complexes are non–planar, rather they have folded bowl or disc–shaped geometry.[22] Because of this distortion, in salen complexes, the metal center situates above the salen plane and therefore, is easily accessible. Due to this fact, salen complexes are useful organic catalysis for oxidation reactions, example of epoxidation, sulfoxidation, etc.[23]

Ligand–centered radical in a coordination complex is important because the radical centers can easily accept or donate electron. Therefore, the combination of radical generating non–innocent ligand with salen unit will provide unique ligand and the corresponding complexes might be useful as oxidation catalysts. Furthermore, mononuclear monoradical coordinated Cu(II) complexes are very important due to their structural resemblance to the GOase. In GOase the geometry of the active species is distorted square planar. Although, the unpaired electron present at p_z orbital of Tyr_{272} radical should couple ferromagnetically with the Cu(II) centered $d_{x^2-y^2}$ orbital, an antiferromagnetic coupling between the Tyr_{272} radical and the Cu(II) center appears in GOase due to this distortion. Hence, monoradical–coordinated Cu(II) complex with distorted square planar geometry would be ideal for the electronic structural study of GOase. As salen unit will provide distortion, the effect of distortion to the coupling fashion could also be investigated. In addition to that, to study the effect of ligand–centered substituent to the geometry and thereafter, geometry dependent reactivity, ligands **$H_3L^{Mixed(H)}$** and **$H_3L^{Mixed(tBu)}$** are synthesized (**Scheme 1.12**) by placing two *tert*–butyl substituent at the 3,5–positions of the salicylidene unit.

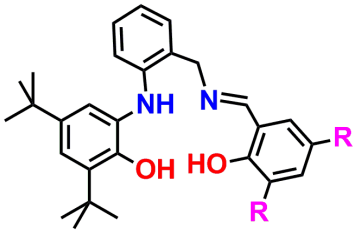

$H_3L^{Mixed(R)}$ **(R = –H, –^{t}Bu)**

Scheme 1.12: *Schematic representation of mixed ligands.*

References:

1. (*a*) N. Ito, S. E. V. Phillips, C. Stevens, Z. B. Ogel, M. J. McPherson, J. N. Keen, K. D. S. Yadav and P. F. Knowles, *Nature*, 1991, **350**, 87; (*b*) Y. Wang, J. L. DuBois, B. Hedman, K. O. Hodgson and T. D. P. Stack, *Science*, 1998, **279**, 537.

2. (*a*) E. I. Solomon, U. M. Sundaram and T. E. Machonkin, *Chem. Rev.*, 1996, **96**, 2563; (*b*) E. I. Solomon, M. J. Baldwin and M. D. Lowery, *Chem. Rev.*, 1992, **92**, 521; (*c*) I. A. Koval, P. Gamez, C. Belle, K. Selmeczib and J. Reedijk, *Chem. Soc. Rev.*, 2006, **35**, 814.

3. (*a*) J. Stubbe and W. A. van der Donk, *Chem. Rev.*, 1998, **98**, 705; (*b*) B. A. Barry and G. T. Babcock, *Proc. Natl. Acad. Sci. USA*, 1987, **84**, 7099.

4. (*a*) S. M. Janes, D. Mu, D. Wemmer, A. J. Smith, S. Kaur, D. Maltby, A. L. Burlingame and J. P. Klinman, *Science*, 1990, **248**, 981; (*b*) D. M. Dooley, M. A. McGuirl, D. E. Brown, P. N. Turowski, W. S. McIntire and P. F. Knowles, *Nature*, 1991, **349**, 262; (*c*) J. P. Klinman, *J. Biol. Chem.*, 1996, **271**, 27189.

5. M. T. T. Wong–Riley, H. L. Liang, J. T. Eells, B. Chance, M. M. Henry, E. Buchmann, M. Kane and H. T. Whelan, *J. Biol. Chem.*, 2005, **280**, 4761.

6. F. Peter Guengerich, *Chem. Res. Toxicol.*, 2008, **21**, 70.

7. (*a*) A. Gräslund and A. Ehrenberg, *Appl. Magn. Reson.*, 2007, **31**, 447; (*b*) M. A. S. Perez, P. A. Fernandes and M. J. Ramos, *J. Chem. Theory Comput.*, 2010, **6**, 2770; (*c*) T. P. Dang, A. J. Sobczak, A. M. Mebel, C. Chatgilialoglu and S. F. Wnuk, *Tetrahedron*, 2012, **68**, 5655; (*d*) E. C. Minnihan, D. G. Nocera and J. Stubbe, *Acc. Chem. Res.*, 2013, **46**, 2524; (*e*) J. Stubbe, D. G. Nocera, C. S. Yee and M. C. Y. Chang, *Chem. Rev.*, 2003, **103**, 2167.

8. J. A. Halfen, B. A. Jazdzewski, S. Mahapatra, L. M. Berreau, E. C. Wilkinson, L. Que, Jr. and W. B. Tolman, *J. Am. Chem. Soc.*, 1997, **119**, 8217.

9. (*a*) M. M. Whittaker, D. P. Ballou and J. W. Whittaker, *Biochemistry*, 1998, **37**, 8426; (*b*) F. Himo, L. A. Friksson, F. Maseras and P. E. M. Siegbahn, *J. Am. Chem. Soc.*, 2000, **122**, 8031; (*c*) L. Que, Jr. and W. B. Tolman, *Nature*, 2008, **455**, 333.

10. P. E. M. Siegbahn, *J. Biol. Inorg. Chem.*, 2004, **9**, 577.

11. (*a*) J. T. Groves, *PNAS*, 2003, **100**, 3569; (*b*) H. Isobe, K. Yamaguchi, M. Okumura and J. Shimada, *J. Phys. Chem. B*, 2012, **116**, 4713.
12. http://cancer-care-mesothelioma.blogspot.in/2009/01/structure-and-catalytic-cycle-of-rnr.html.
13. (*a*) C. K. Jørgensen, *Coord. Chem. Rev.*, 1966, **1**, 164; (*b*) S. Sproules and K. Wieghardt, *Coord. Chem. Revi.*, 2010, **254**, 1358; (*c*) C. G. Pierpont, *Coord. Chem. Rev.*, 2001, **219–221**, 415; (*d*) C. G. Pierpont, *Coord. Chem. Rev.*, 2001, **216–217**, 99; (*e*) S. Ye, B. Sarkar, C. Duboc, J. Fiedler and W. Kaim, *Inorg. Chem.*, 2005, **44**, 2843; (*f*) S. Ghumaan, B. Sarkar, S. Patra, J. van Slageren, J. Fiedler, W. Kaim and G. K. Lahiri, *Inorg. Chem.*, 2005, **44**, 3210; (*g*) A. Mederos, S. Dominguez, R. Hernandez–Molina, J. Sanchiz and F. Brito, *Coord. Chem. Rev.*, 1999, **193–195**, 913; (*h*) P. Chaudhuri, C. N. Verani, E. Bill, E. Bothe, T. Weyhermüller and K. Wieghardt, *J. Am. Chem. Soc.*, 2001, **123**, 2213; (*i*) H. Chun, C. N. Verani, P. Chaudhuri, E. Bothe, E. Bill, T. Weyhermüller and K. Wieghardt, *Inorg. Chem.*, 2001, **40**, 4157; (*j*) S. Kokatam, T. Weyhermüller, E. Bothe, P. Chaudhuri and K. Wieghardt, *Inorg. Chem.*, 2005, **44**, 3709.
14. H. Chun, P. Chaudhuri, T. Weyhermüller and K. Wieghardt, *Inorg. Chem.*, 2002, **41**, 790.
15. P. J. Chirik and K. Wieghardt, *Science*, 2010, **327**, 794.
16. C. Mukherjee, U. Pieper, E. Bothe, V. Bachler, E. Bill, T. Weyhermüller and P. Chaudhuri, *Inorg. Chem.*, 2008, **47**, 8943.
17. C. Mukherjee, T. Weyhermüller, E. Bothe and P. Chaudhuri, *C. R. Chim.*, 2007, **10**, 313.
18. (*a*) S. M. Janes, M. M. Palcic, C. H. Scaman, A. J. Smith, D. E. Brown, D. M. Dooley, M. Mure and J. P. Klinman, *Biochemistry*, 1992, **31**, 12147; (*b*) S. X. Wang, M. Mure, K. F. Medzihradszky, A. L. Burlingame, D. E. Brown, D. M. Dooley, A. J. Smith, H. M. Kagan and J. P. Klinman, *Science*, 1996, **273**, 1078; (*c*) A. P. Duff, A. E. Cohen, P. J. Ellis, J. A. Kuchar, D. B. Langley, E. M. Shepard, D. M. Dooley, H. C. Freeman and J. M. Guss, *Biochemistry*, 2003, **42**, 15148.
19. (*a*) M. Mure, *Acc. Chem. Res.*, 2004, **37**, 131; (*b*) M. Mure, S. A. Mills and J. P. Klinman, *Biochemistry*, 2002, **41**, 9269.
20. M. Mure, S. A. Mills and J. P. Klinman, *Biochemistry*, 2002, **41**, 9269.
21. J. P. Klinman, *J. Biol. Chem.*, 1996, **271**, 27189;
22. (*a*) S. Akine and T. Nabeshima, *Inorg. Chem.*, 2005, **44**, 1205; (*b*) A. V. Wiznycia, J. Desper and C. J. Levy, *Can. J. Chem.*, 2009, **87**, 224; (*c*) C. Mukherjee, A. Stmmler, H.

Bögge and T. Glaser, *Inorg. Chem*., 2009, **48**, 9476; (*d*) C. Mukherjee, A. Stmmler, H. Bögge and T. Glaser, *Chem–Eur. J*., 2010, 10137; (*e*) T. Glaser, M. Heidemeier, R. Föhlich, P. Hildebrandt, E. Bothe and E. Bill, *Inorg. Chem.*, 2005, **44**, 5467; (*f*) O. Rotthaus, O. Jarjayes, F. Thomas, C. Philouze, C. P. D. Valle, E. S. Aman and J. L. Pierre, *Chem. Eur. J.*, 2006, **12**, 2293.

23. (*a*) P. G. Cozzi, *Chem. Soc. Rev.*, 2004, **33**, 410l; (*b*) T. Kurahashi and H. Fuji, *Inorg. Chem.*, 2008, **47**, 7556; (*c*) P. Adão, J. Costa Pessoa, R. T. Henriques, M. L. Kuznetsov, F. Avecilla, M. R. Maurya, U. Kumar and I. Correia, *Inorg. Chem.*, 2009, **48**, 3542; (*d*) P. Adão, M. L. Kuznetsov, S. Barroso, A. M. Martins, F. Avecilla and J. C. Pessoa, *Inorg. Chem.*, 2012, **51**, 11430; (*e*) S. Barman, S. Patil, J. Desper, C. M. Aikens and C. J. Levy, *Eur. J. Inorg. Chem.*, 2013, **2013**, 5708.

Chapter II

*Electron Withdrawing –CN as the –ortho Substituent to the Aniline Moiety of H_2AP^H Ligand and Its Effect to the First–Row Transition Metal Complexes**

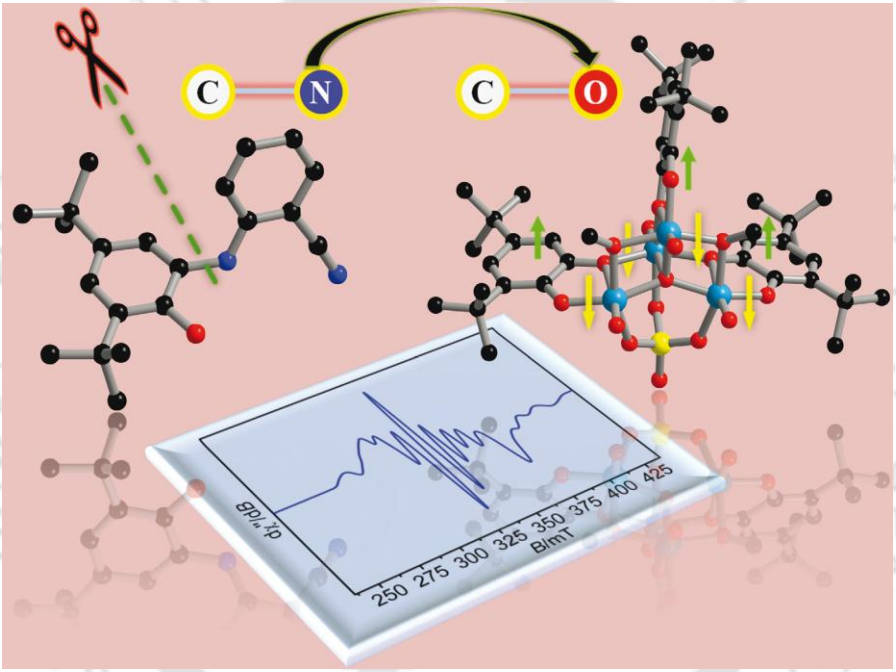

*some results have been published;

1. ***Chem. Commun.***, **2012**, 10180–10182.
2. ***RSC Adv.***, **2013**, *3*, 5374–5377.
3. ***RSC Adv.***, **2014**, *4*, 24698–24703.

2.1: Introduction:

o–catecholate, *o*–phenylenediimide, *o*–dithiolene and *o*–amidophenolate ligands are the key constituent to synthesize and stabilize radical–coordinated metal complexes.[1] These ligands belong to the non–innocent category owing to their versatile oxidation states upon coordination with transition metal ion in the presence of air (**Scheme 2.1**). For example *o*–catecholte system can exist in *o*–catecholate/*o*–semiquinonate/*o*–quinone form;[2] *o*–amidophenolate can survive in *o*–amidophenolate/*o*–iminosemiquinonate/*o*–iminobenzoquinone form.[3] Beside these ligands, $O_2/O_2^{\bullet 1-}/O_2^{2-}$; $NO^+/NO^{\bullet}/NO^{1-}$;[4] tyrosyl/tyrosinate redox systems,[5] the tetrapyrrole (porphyrinic) ligands,[6] the pterins,[7] and flavins,[8] *etc*, are also known as non–innocent ligand.

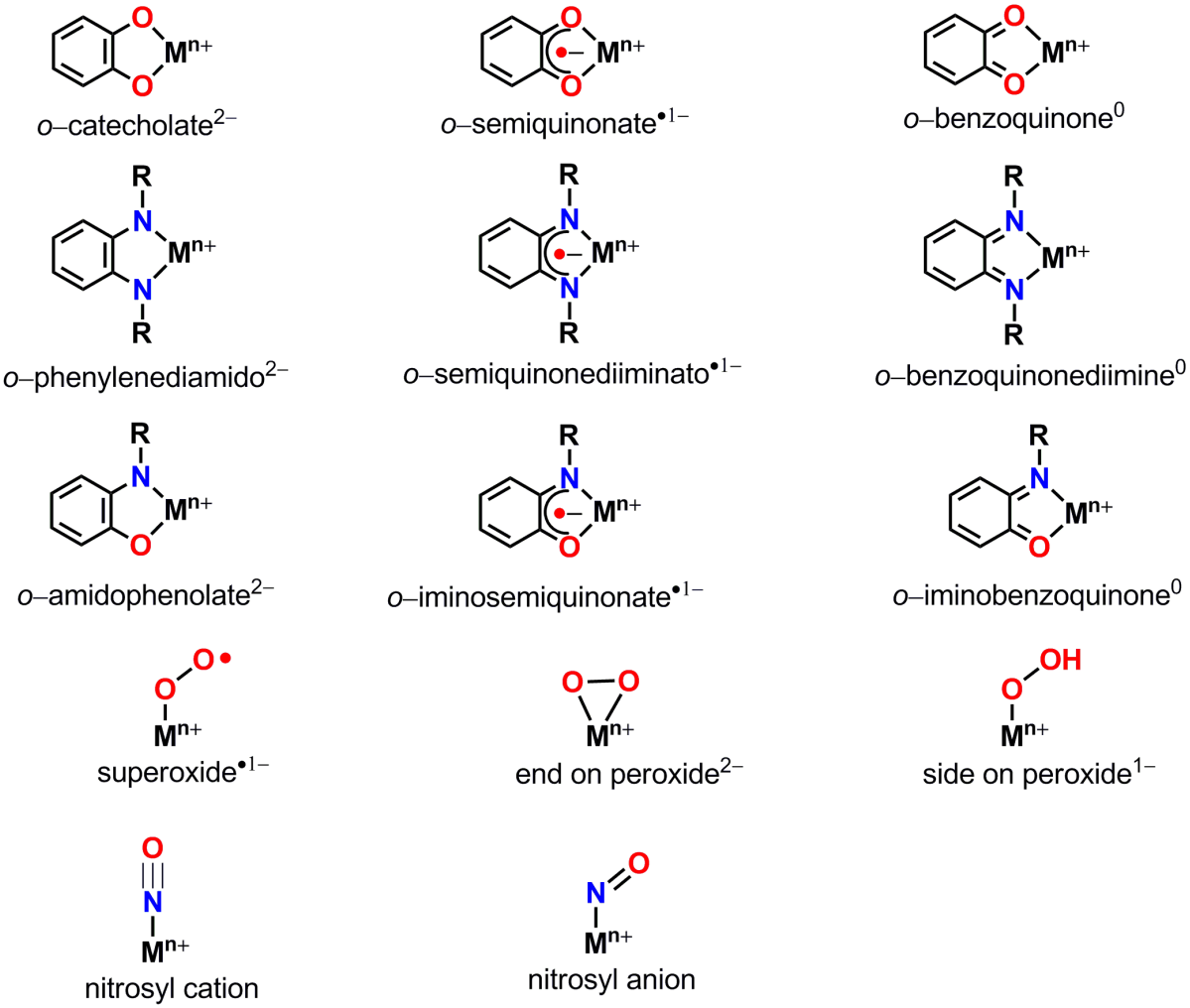

Scheme 2.1: *Various non–innocent ligands and their possible different oxidation states present in metal complexes.*

In some instance, the redox non–innocent properties widely depend upon the substituent presents in ligand backbones, *e.g.* phenol is an innocent ligand but electron rich substituted phenol can behave as non–innocent ligand.[9] Oxyquinolate (OQN) is an innocent ligand but by placing different substituent at the ligand backbone, the redox non–innocent behavior of the oxyquinolate derivative can be tuned in the presence of metal ion.[10]

Redox non–innocent behavior of ligands not only depends on substituents attached at the ligand backbone, it strongly depends on the nature of encapsulating transition metal ion in the complex form. The non–innocent nature of the dithiolene ligand in any complex is however, strongly dependent on the nature of the transition metal ion present in the complex. Thus, for the isoelectronic $[M^{II}(L^{2-})(L^{\bullet 1-})]^{1-}$ (M = Ni, Pd and Pt) or $[Au^{III}(L^{2-})(L^{\bullet 1-})]$ complexes involving a d^8 M(II) (M = Ni, Pd and Pt) or Au^{III} ion attached to both the dithiolato^{2-} and dithiobenzosemiquinoanto^{1-} forms of the ligand, the radical character (or the ligand character in the $2b_{2g}$ level) decreases in the order $[Au^{III}(L^{2-})(L^{\bullet 1-})] > [Pd^{II}(L^{2-})(L^{\bullet 1-})]^{1-} > [Pt^{II}(L^{2-})(L^{\bullet 1-})]^{1-} > [Ni^{II}(L^{2-})(L^{\bullet 1-})]^{1-}$.[11]

2–Anilino–4,6–di–*tert*–butylphenol [$\mathbf{H_2AP^H}$] is a non–innocent ligand and stabilizes several radical–containing transition–metal complexes, *e.g.* Cu(II), Ni(II), Co(III), Cr(III), Fe(III), etc.[12] However, its corresponding vanadium(V) complex is a mononuclear non–oxo V(V) with no coordinated π–radical anion. This could be because of the energy required for the change in oxidation state of V is lower compared to the energy required for the oxidation of the non–innocent ligand to its radical form.[13]

Several non–innocent ligands 2–[3,5–di–substituted(R)–anilino]–4,6–di–*tert*–butylphenol ($\mathbf{H_2AP^R}$, **Scheme 2.2**) and their corresponding Cu(II) complexes were synthesized by placing different substituents at the *m*,*m*′–positions to the aniline moiety of the parent ligand 2–anilino–4,6–di–*tert*–butylphenol.[14] The Cu(II) complexes derived from ligands show a clear trend in the ligand–based oxidation potentials with the electron–donating and –withdrawing capability of the attached substituents.[14] In this case, the geometric and electronic structural modulations of the corresponding Cu(II) complexes operate *via* σ–bonding interaction (σ–effect). Catalytic activity to oxidation of primary alcohol to aldehyde of these Cu complexes is also tuned by varying the nature of substituents.

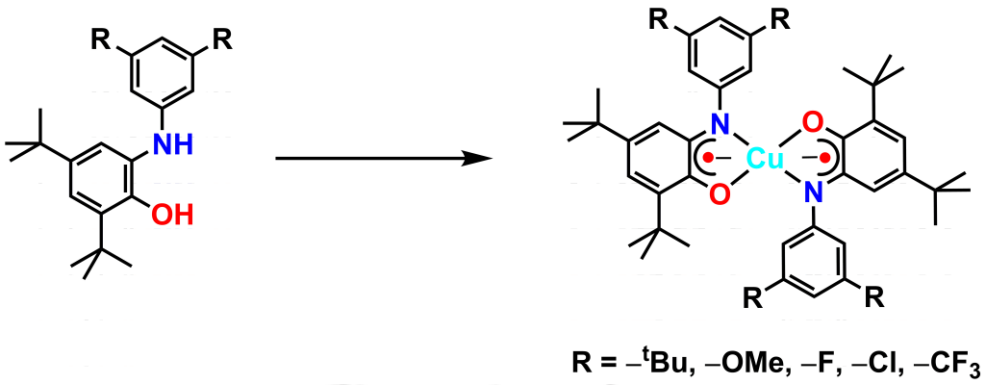

Scheme 2.2: ***H_2AP^R*** *ligands and theirs corresponding Cu(II) complexes.*

Knowing that (a) the π–effect is more pronounced compared to σ–effect, and (b) substituents have an effect on both electronic and geometric structure of the corresponding complexes, a modification has been made to the non–innocent ligand $\mathbf{H_2AP^H}$ by placing a π–electron acceptor substituent like cyanide group ($\mathbf{H_2L^{CN}}$, **Scheme 2.3**) at *–ortho* position of N–phenyl ring. In this chapter, the synthesis of ligand $\mathbf{H_2L^{CN}}$ and its different reactivity towards first row transition metal ion, *e.g.* V–, Mn–, Co–, Ni–, and Cu– ion and thereafter, corresponding product formation are reported.

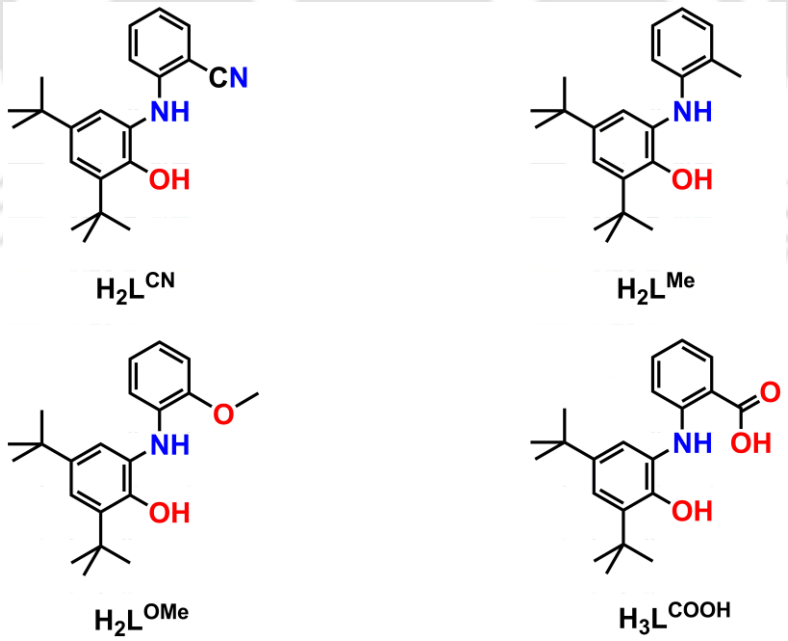

Scheme 2.3: *Different –ortho substituted non–innocent ligands.*

- **(a)** $[C_{44}H_{66}O_{17}S_1V_4]^-[^nBu_4N]^+ \bullet CH_3CN$; **(1•$CH_3CN$)**
- **(b)** $[C_{60}H_{92}O_{32}S_2V_8]^{2-}[^nBu_4N]^+$; **(2)**
- **(c)** $[C_{64}H_{96}N_4O_{16}V_4] \bullet CH_2Cl_2$; **(3•$CH_2Cl_2$)**
- **(d)** $[C_{21}H_{24}N_2O]$; **(4)**
- **(e)** $[C_{42}H_{54}ClMnN_2O_2]$; **(5)**
- **(f)** $[C_{42}H_{48}ClCoN_2O_2]$; **(6)**
- **(g)** $[C_{42}H_{48}N_2NiO_2]$; **(7)**
- **(h)** $[C_{42}H_{48}CuN_2O_2]$; **(8)**

2.2: Synthesis and Characterization of $C_{21}H_{26}N_2O$; H_2L^{CN}:

Ligand $\mathbf{H_2L^{CN}}$ was synthesized in good yield (72%) by the reaction between equimolar amounts of 3,5–di–*tert*–butylcatechol and 2–aminobenzonitrile in hexane in the presence of Et_3N under air.

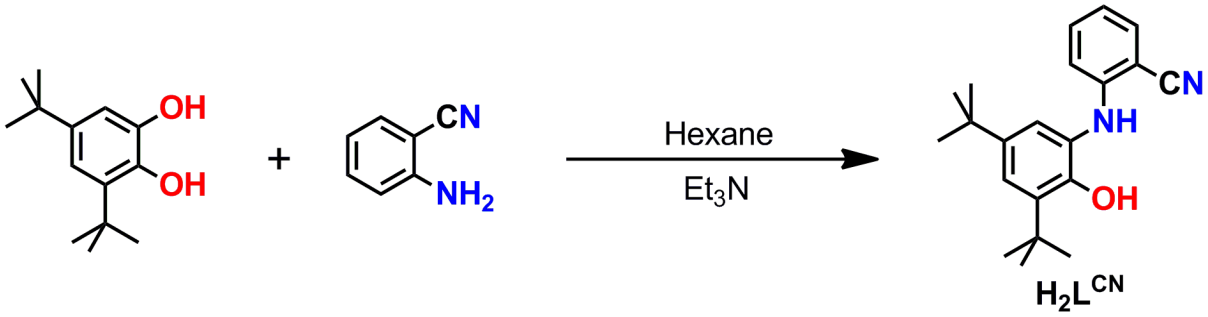

Scheme 2.4: *Synthetic route to the formation of ligand* $\boldsymbol{H_2L^{CN}}$.

Infrared (IR) spectrum of the ligand ($\mathbf{H_2L^{CN}}$) showed two sharp bands at 3421 cm^{-1} and 3354 cm^{-1} due to ν(O–H), and ν(N–H) stretching, respectively.[15] Aromatic C–H stretching bands appeared at 2977 and 3082 cm^{-1}. The asymmetric, symmetric and overtone bands of ν(C–H) stretching for *tert*–butyl groups appeared at 2950, 2864, 2904 cm^{-1}, respectively.[16] In addition to this, the bending ν(C–H) stretching frequency for the $–CH_3$ groups, which belonged to *tert*–butyl groups, appeared at 1482 and 1360 cm^{-1}. The stretching frequency for –CN group appeared as a sharp band at 2221 cm^{-1}.[17] The bending ν(N–H) appeared at 1600 cm^{-1}. The stretching bands at 1577, 1504, and 1458 cm^{-1} were attributed to the ν(C=C) stretches for phenyl system.[18] The phenolic ν(C–O) stretching band appeared at 1318 cm^{-1} and ν(C–N) stretching band appeared at 1218 cm^{-1}.[18]

^{1}H NMR spectrum (**Figure 2.1**) for the ligand displayed the resonance signals at 1.27 and 1.44 ppm that were singlet and appeared due to hydrogen atoms attached to two *tert*–butyl groups. Two singlet peaks appeared at 5.83 and 6.00 ppm were because of N–H and O–H protons, respectively. The aromatic six protons appeared in the region of 6.50–7.50 ppm. ^{13}C NMR spectrum (**Figure 2.2**) for the ligand showed the characteristic 17 peaks for 17 different kinds of carbon atoms.

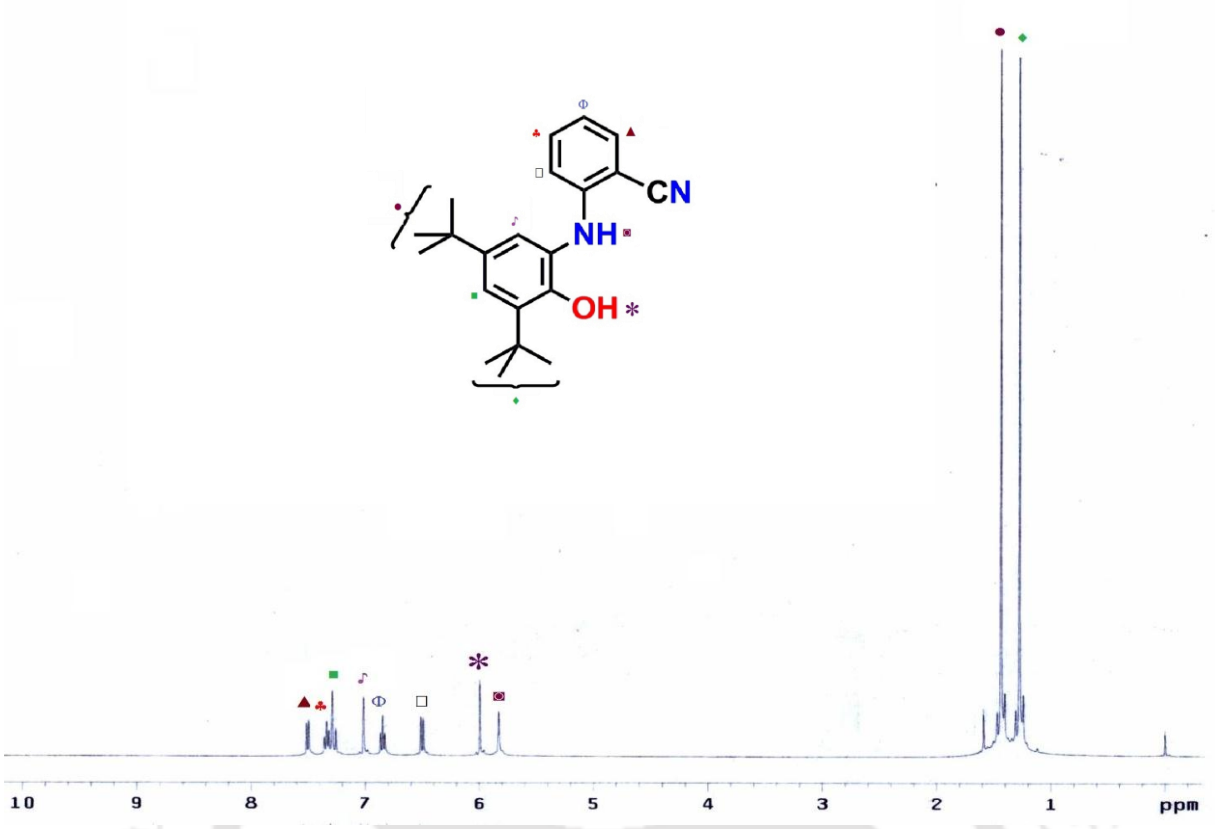

Figure 2.1: *^{1}H NMR spectrum of* $\boldsymbol{H_2L^{CN}}$.

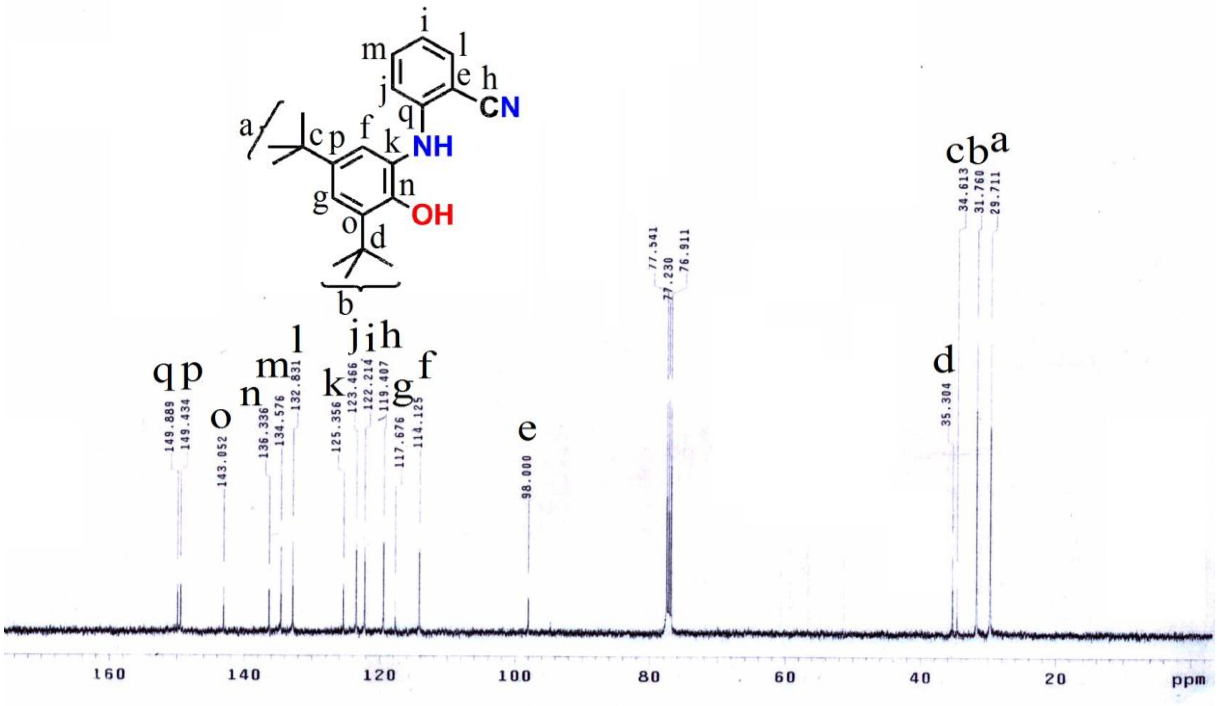

Figure 2.2: *^{13}C NMR spectrum of* $\boldsymbol{H_2L^{CN}}$.

Electrospray ionization mass spectrum (ESI–MS) of acetonitrile solution of $\mathbf{H_2L^{CN}}$ in positive mode showed a 100% molecular ion peak at *m/z* = 323.55 that corresponded to the

$[M + H]^+$ (M = molecular mass). Isotope distribution pattern examination of the observed mass peak showed the composition $\mathbf{C_{21}H_{26}N_2O}$ of ligand $\mathbf{H_2L^{CN}}$ (**Figure 2.3**).

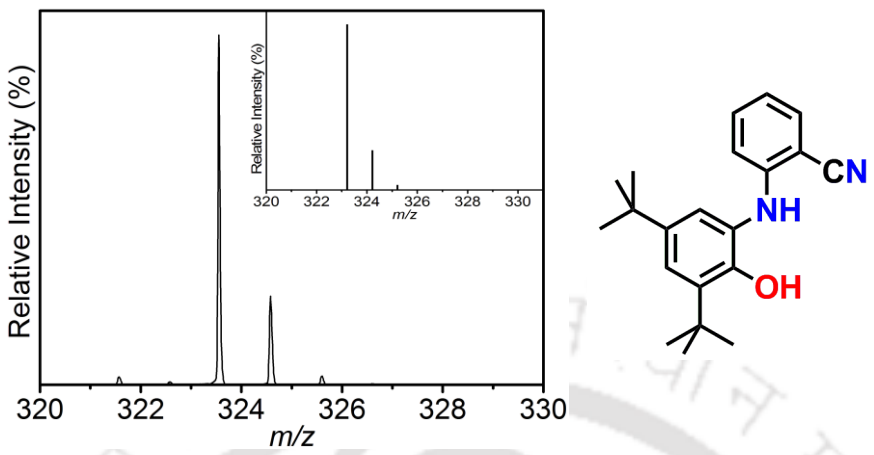

Figure 2.3: *ESI–mass spectrum of* $\boldsymbol{H_2L^{CN}}$*; experimental and isotope distribution pattern (inset).*

The synthesized ligand could behave as non–innocent and therefore, it might exist in different oxidation states in the presence of metal ions (preferably transition metal) and molecular oxygen. The possible oxidation states are shown below in **Scheme 2.5**.

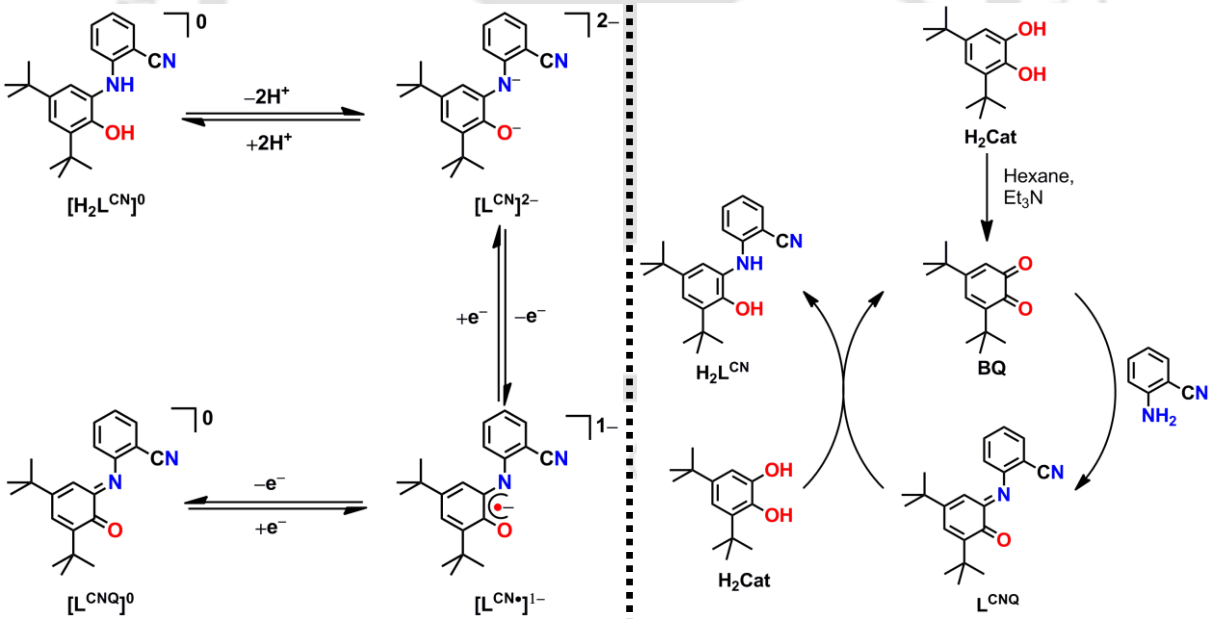

Scheme 2.5: *Possible oxidation states of* $\boldsymbol{H_2L^{CN}}$ *and proposed mechanism for the formation of ligand* $\boldsymbol{H_2L^{CN}}$.

Herein, it is important to note that *tert*–butyl substituents present at the 3– and 5–positions of the aminophenol moiety of the ligand play crucial role for the formation of the ligand by controlling steric factor. The synthesis of ligand followed the general mechanism as shown in **Scheme 2.5**. In general, to synthesize the ligand from 3,5–di–*tert*–butylcatechol

and substituted aniline derivative, aniline moiety selectively reacts with the less sterically hindered keto unit. In addition to steric controlling, the groups play vital role in stabilizing π–radical (unpaired electron) by means of +I effect.[19]

2.3a: Synthesis and Characterization of a Triradical–Containing Tetranuclear Oxo–V(IV) Cluster:

To a methanolic solution of $\mathbf{H_2L^{CN}}$ (1 equivalent), $VO(SO_4)\bullet 5H_2O$ (1 equivalent) and Et_3N (1 equivalent) were added and the resulting solution was refluxed for two hours. After that, the solution was stirred for another two hours at room temperature and then filtered and the filtrate was kept for slow solvent evaporation. This caused precipitation of a blue microcrystalline solid. The solid residue was filtered and thoroughly washed with methanol, and then, dried under vacuum. Thus, isolated blue solid was recrystallized from a 15:5:5 CH_2Cl_2:CH_3CN:MeOH solution in the presence of tetrabutylammonium perchlorate, which caused a precipitation of block shaped blue crystalline solid suitable for single crystal X–ray diffraction study.

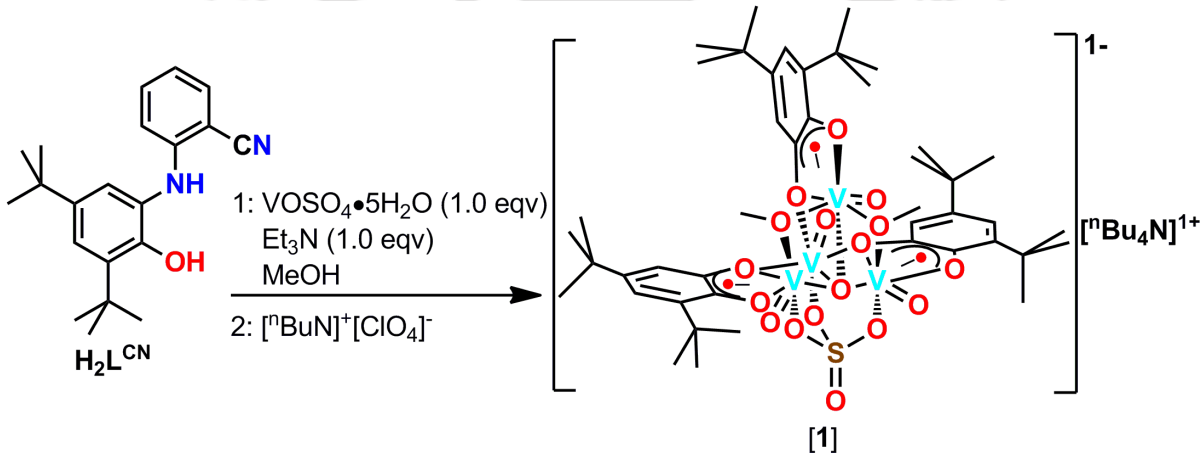

Scheme 2.6: *Synthesis route of* $[C_{44}H_{66}O_{17}S_1V_4]^-[^nBu_4N]^+$; ***(1)***.

In the IR spectrum of complex **1•CH$_3$CN**, the disappearance of ν(N–H), ν(O–H) stretching frequencies confirmed the ligation of the deprotonated binding sites to the metal center. Simultaneously, the disappearance of the band at 2221 cm^{-1} for –CN functional group, indicated the cleavage of the C–N bond and presence of 2961, 2913, 2873 cm^{-1} bands emphasized the coordination of the 3,5–di–*tert*–butylcatecholate moiety to the metal ion upon complex formation. Strong bands at 982 and 998 cm^{-1} indicated the presence of vanadyl (V=O) units in different coordination environments.[20] A sharp band at 1015 cm^{-1} appeared due to coordinated methoxy groups [ν(H_3C–O) stretch].[21] Bands at 1102, 1015, 689 and 657 cm^{-1} were attributed to ν(S=O) and ν(S–O) stretching of the coordinated μ_3–O_3SO unit.[22] The ν(V–O) stretching bands appeared in the 587–496 cm^{-1} region.[23]

Electrospray ionization mass (ESI–MS) spectrum in CH_3CN for complex **1•CH$_3$CN** (**Figure 2.4**) provided a 100% ion peak at *m/z* = 242.25 in the positive mode, while, in the negative mode, a 100% ion peak at *m/z* = 1101.92 was observed. The peak at *m/z* = 242.25 confirmed the presence of ^{n}**Bu$_4$N$^+$** in the complex. Simulated isotope pattern distributions indicated a **C$_{44}$H$_{66}$O$_{17}$S$_1$V$_4$** composition for the observed peak at *m/z* = 1101.92.

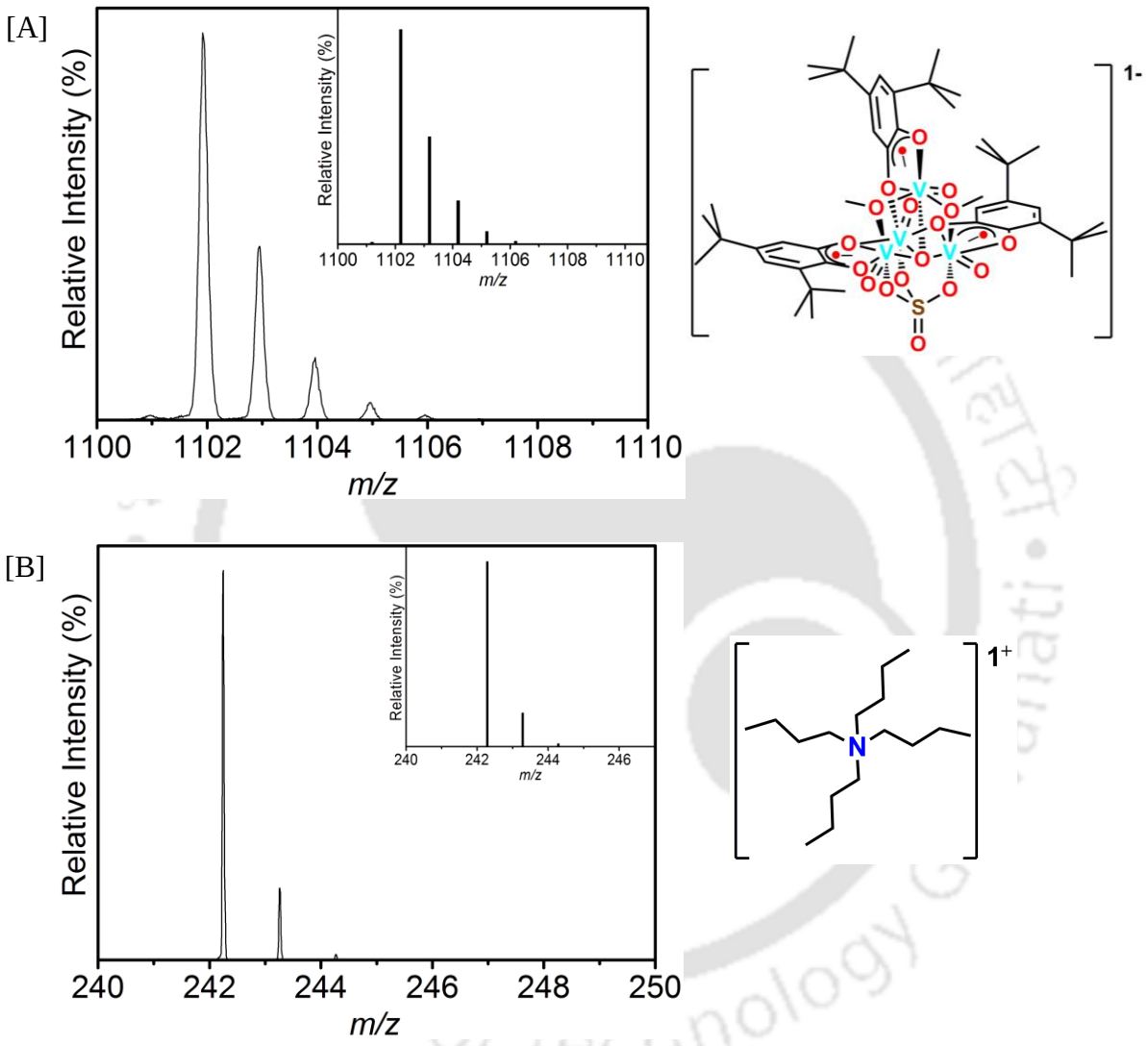

Figure 2.4: *[A] ESI–mass spectrum of **1•CH$_3$CN** in –ve mode, and [B] ESI–mass spectrum of **1•CH$_3$CN** in +ve mode; experimental and calculated isotope distribution pattern (inset).*

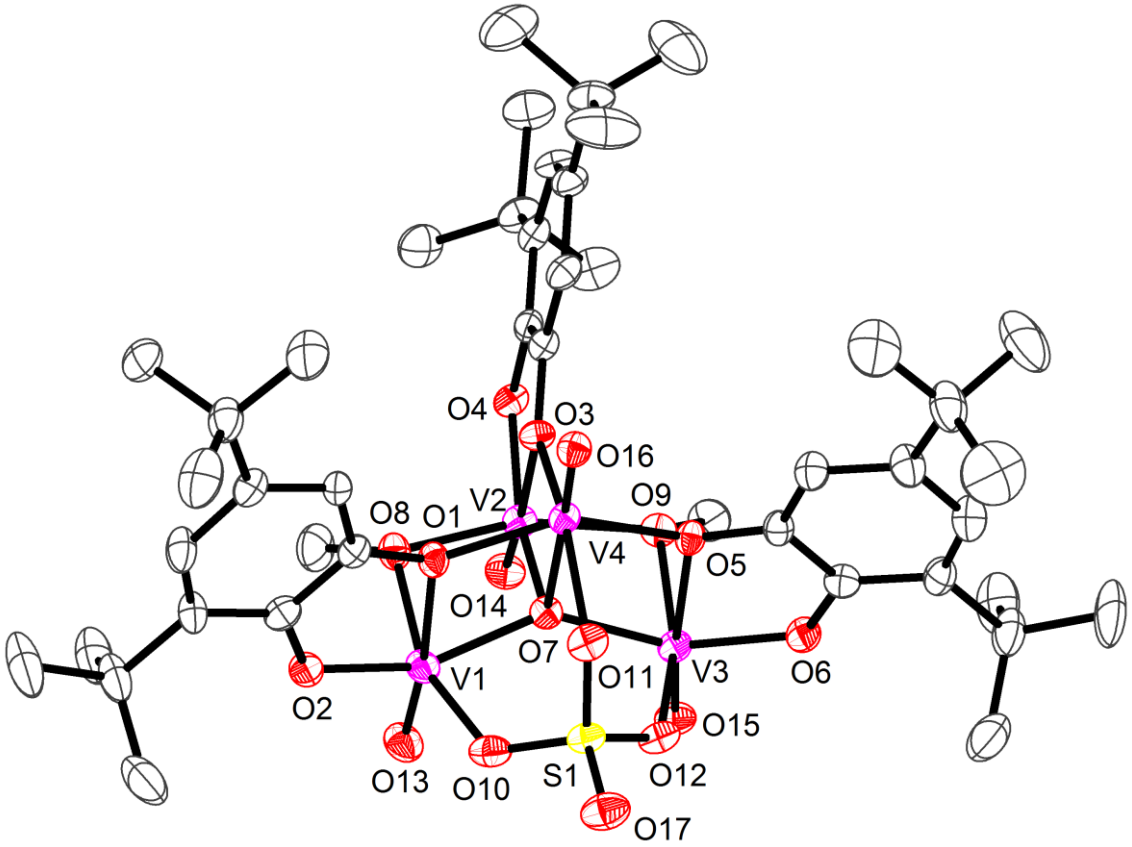

Figure 2.5: *The monoanionic tetranuclear V_4 cluster present in **1•CH$_3$CN**; thermal ellipsoids were drawn at the 50% probability level. Hydrogen atoms and solvent molecule were omitted for clarity.*

Complex **1•CH$_3$CN** crystallized in *P*bca space group. It composed of monoanionic cluster comprised of four vanadium ions and a counter cation $^{n}Bu_4N^{+}$. All the four vanadium (V1, V2, V3 and V4) atoms were in a distorted octahedral coordination environment ligated by six oxygen donors, and were connected to each other *via* a μ_4–O7 atom in almost tetrahedral fashion (**Figure 2.5**). The V1–O7, V2–O7, V3–O7 and V4–O7 bond distances were 1.937(3), 1.964(3), 1.946(3) and 2.408(3) Å, respectively. The V1–O13 = 1.583(3), V2–O14 = 1.584(3), V3–O15 = 1.584(3), and V4–O16 = 1.577(3) Å bond distances were shorter compared to other V–O bonds and were in accord with previously reported V(IV)=O units.[24] The shortest V4–O16 bond distance was because of the lowest *trans effect* as reflected by the highest V4–O7 bond distance compared to other V–O7 bonds. This feature allowed the V4 center to be also considered as in a square pyramidal geometry.

The V2 atom was connected to each V1 and V3 *via* two methoxy (–OMe) groups, while, a SO_4^{2-} group anchored V1, V3 and V4 centers as a μ_3–O_3SO bridging unit. V1, V2 and V3 atoms were each connected to a 3,5–di–*tert*–butylcatecholate moiety *via* O1 and O2; O3 and O4; O5 and O6 atoms, respectively. The V4 atom shared one oxygen atom (O1, O3 and O5) from each of the three 3,5–di–*tert*–butylcatecholate moieties as its coordinating sites.

The C–C bond distances of the phenyl rings were not all within the 1.400±0.010 Å range as observed for catecholate (Cat^{2-}) systems.[12,25] Rather alternate short and long C–C bond distances [*e.g.* C3–C4 = 1.371(6); C4–C5 = 1.421(6), C5–C6 = 1.381(7) Å], as previously reported for semiquinone π–radical ($SQ^{\bullet 1-}$) systems,[14,24*b*,25*c*,26] were observed. Additionally, the observed C–O_{Ph} (O_{Ph} corresponds to oxygen atom attached to phenyl rings) bond distances [C1–O1 = 1.316(5), C2–O2 = 1.322(5), C7–O3 = 1.333(5), C8–O4 = 1.346(5), C13–O5 = 1.329(5), C14–O6 = 1.331(5) Å], which were found in between that of Cat^{2-} (1.350–1.360 Å)[24*b*,25*b*,*c*,26*a*,*b*,*c*] and $SQ^{\bullet 1-}$ (1.298–1.326 Å)[26*c*,27] C–O_{Ph} bond distances, indicate the destruction of the aromaticity of the phenyl rings upon complexation. Hence, the presence of a π–radical delocalized between two phenolic oxygen atoms could be argued for the each 3,5–di–*tert*–butylcatecholate system.

The inconsistent V–O_{Ph} bond distances could not be considered for the assignment of the oxidation state of the V atoms [*e.g.* V1–O1 = 2.242(3) and V1–O2 = 1.862(3) Å]. However, the presence of three π–radical–containing catecholate moieties, almost same vanadyl bond distances, and the mononegative character of the V_4–cluster invoke the +IV oxidation state for all the V atoms (*vide infra*). Therefore, the monoanionic part of the complex is best described as a triradical–containing tetranuclear oxo–V(IV) cluster.

Table 2.1: *Selected bond distances (Å) and bond angels (°) for complex* ***1•CH$_3$CN****.*

C1–C2	1.424(6)	C7–C8	1.410(6)
C2–C3	1.414(6)	C8–C9	1.406(6)
C3–C4	1.371(6)	C9–C10	1.388(6)
C4–C5	1.421(6)	C10–C11	1.407(6)
C5–C6	1.381(7)	C11–C12	1.393(6)
C6–C1	1.395(6)	C12–C7	1.376(6)
C13–C14	1.412(6)	V1–O1	2.242(3)
C14–C15	1.417(6)	V1–O2	1.862(3)
C15–C16	1.377(6)	V1–O7	1.937(3)
C16–C17	1.407(6)	V1–O8	1.987(3)
C17–C18	1.388(6)	V1–O10	2.015(3)
C18–C13	1.387(6)	V1–O13	1.583(3)
V2–O3	2.244(3)	V3–O5	2.236(3)
V2–O4	1.839(3)	V3–O6	1.872(3)
V2–O7	1.964(3)	V3–O7	1.946(3)
V2–O8	1.992(3)	V3–O9	1.992(3)
V2–O9	1.969(3)	V3–O12	2.022(3)
V2–O14	1.584(3)	V3–O15	1.584(3)
V4–O1	1.968(3)	C1–O1	1.316(5)
V4–O3	1.983(3)	C2–O2	1.322(5)
V4–O5	1.968(3)	C7–O3	1.333(5)
V4–O7	2.408(3)	C8–O4	1.346(5)

V4–O11	2.037(3)	C13–O5	1.329(5)
V4–O16	1.577(3)	C14–O6	1.331(5)
V1–V2	3.041(1)	S1–O10	1.505(3)
V1–V3	3.672(1)	S1–O11	1.499(3)
V1–V4	3.364(1)	S1–O12	1.506(3)
V2–V3	3.040(1)	S1–O17	1.429(4)
V2–V4	3.464(1)		
V3–V4	3.364(1)		
C1–C2–O2	115.01(36)	C7–C8–O4	115.40(34)
C1–O1–V1	111.20(23)	C7–O3–V2	111.10(22)
C2–O2–V1	124.19(26)	C8–O4–V2	124.00(24)
C2–C1–O1	114.16(36)	C8–C7–O3	113.47(34)
O1–V1–O2	75.23(11)	O3–V2–O4	75.46(10)
O1–V1–O7	77.92(10)	O3–V2–O7	74.92(10)
O1–V1–O8	80.3(1)	O3–V2–O8	86.21(10)
O1–V1–O10	84.90(11)	O3–V2–O9	85.96(11)
O1–V1–O13	173.25(12)	O3–V2–O14	173.06(12)
O2–V1–O7	153.09(12)	O4–V2–O7	150.14(12)
O2–V1–O8	96.38(12)	O4–V2–O8	97.76(12)
O2–V1–O10	93.98(12)	O4–V2–O9	104.58(13)
O2–V1–O13	98.44(14)	O4–V2–O14	97.62(14)
O7–V1–O8	77.36(11)	O7–V2–O8	76.65(11)
O7–V1–O10	85.21(11)	O7–V2–O9	76.97(11)
O7–V1–O13	108.32(13)	O7–V2–O14	112.02(14)
O8–V1–O10	159.11(12)	O8–V2–O9	153.60(13)
O8–V1–O13	98.32(13)	O8–V2–O14	95.33(14)
O10–V1–O13	98.03(13)	O9–V2–O14	95.47(14)
V1–O1–V4	105.89(11)	V2–O3–V4	109.91(12)
C13–C14–O6	115.94(36)	O1–V4–O3	88.87(11)
C13–O5–V3	111.44(23)	O1–V4–O5	145.58(11)
C14–O6–V3	123.24(26)	O1–V4–O7	73.36(10)
C14–C13–O5	113.83(35)	O1–V4–O11	83.93(11)
O5–V3–O6	75.47(11)	O1–V4–O16	107.42(13)
O5–V3–O7	77.96(10)	O3–V4–O5	88.68(11)
O5–V3–O9	80.41(11)	O3–V4–O7	70.83(10)
O5–V3–O12	84.59(11)	O3–V4–O11	155.37(11)
O5–V3–O15	173.67(13)	O3–V4–O16	104.57(13)
O6–V3–O7	153.23(13)	O5–V4–O7	73.43(10)
O6–V3–O9	95.47(13)	O5–V4–O11	84.19(12)
O6–V3–O12	95.95(13)	O5–V4–O16	106.41(13)
O6–V3–O15	98.27(14)	O7–V4–O11	84.54(10)
O7–V3–O9	76.82(11)	O7–V4–O16	175.38(12)
O7–V3–O12	84.69(12)	O11–V4–O16	100.05(13)
O7–V3–O15	108.23(13)	V1–O7–V2	102.43(12)
O9–V3–O12	158.22(13)	V1–O7–V3	141.99(15)
O9–V3–O15	99.47(14)	V1–O7–V4	100.88(11)
O12–V3–O15	97.16(15)	V2–O7–V3	102.10(12)
V3–O5–V4	106.09(12)	V2–O7–V4	104.34(11)
		V3–O7–V4	100.62(11)

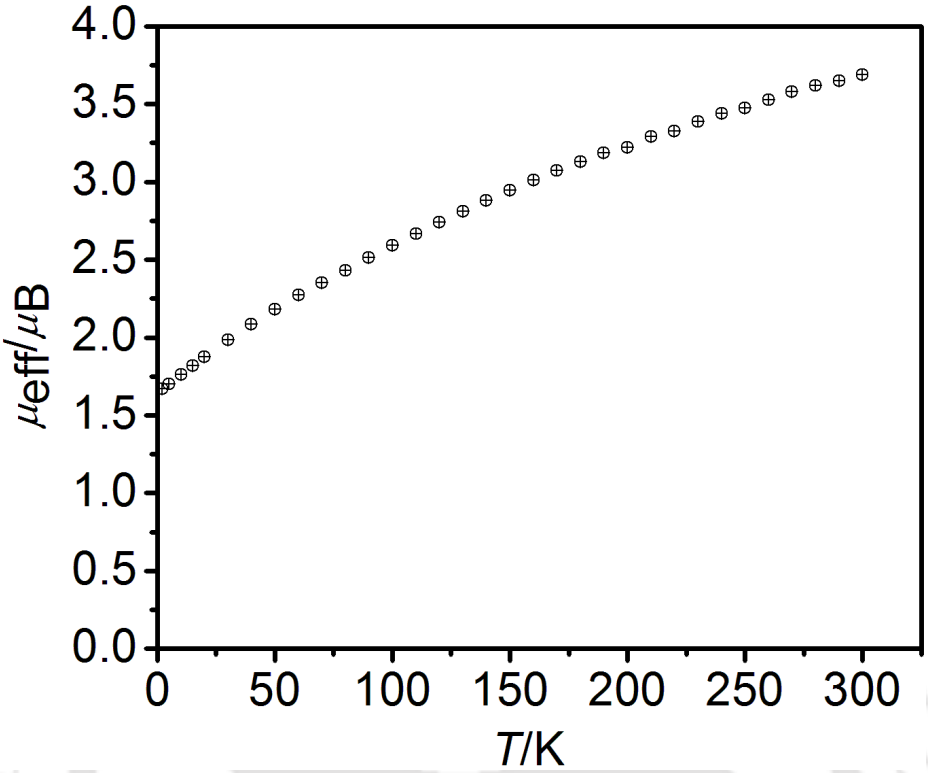

Figure 2.6: *A μ_{eff} vs T plots for **1•CH$_3$CN**; B = 0.1 T.*

Variable temperature (2–290 K) magnetic susceptibility measurements of solid sample using a SQUID magnetometer at 1 T indicated that complex **1•CH$_3$CN** was paramagnetic one with an S = ½ ground state. Complex **1•CH$_3$CN** showed μ_{eff} = 1.70 μ_B at 5 K and the value increased with increase in temperature and reached at 3.77 μ_B at 290 K (**Figure 2.6**). This feature indicated the existence of multi–paramagnetic centers in **1**. V1, V2 and V3 were each coordinated to ligand centered π–radical anions. The antiferromagnetic coupling between the paramagnetic V(IV) and π–radical provided a diamagnetic environment around the vanadium centers. V4, which was not coordinated to a π–radical anion, was then the paramagnetic center and carried the residual electron density at 5 K.

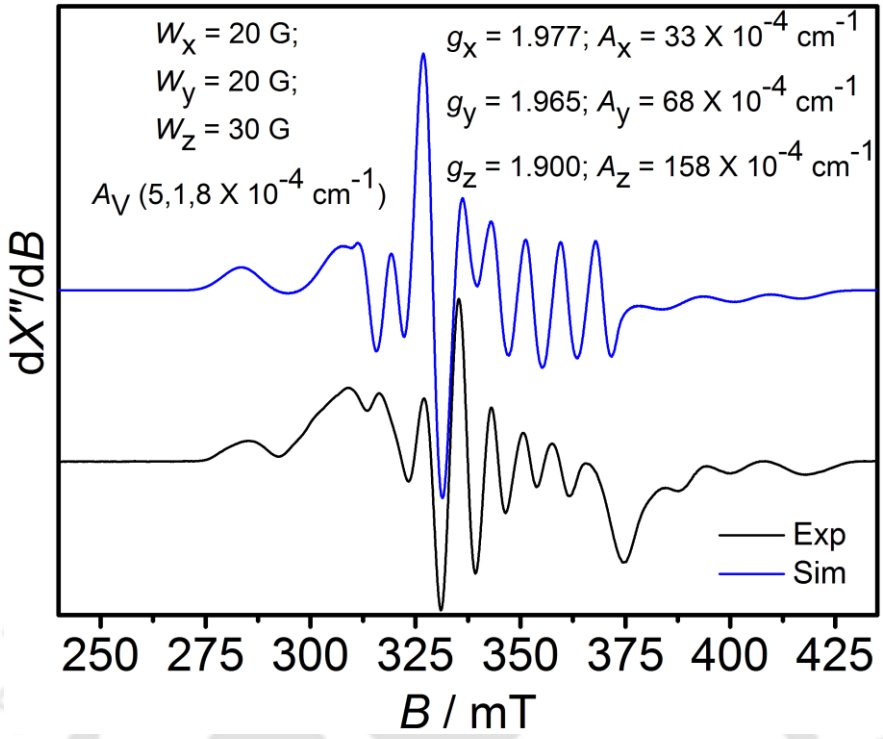

Figure 2.7: *X–band EPR spectrum of complex* ***1•CH₃CN*** *recorded at 25 °C in solid. Conditions: X–band microwave frequency (GHz), 9.450; modulation frequency (kHz), 100; modulation amplitude (G), 10.0; and microwave power, 0.998 [μW].*

Complex **1•CH₃CN** was EPR active and showed an eight–line anisotropic X–band EPR spectrum (^{51}V; I = 7/2). The best fit to the experimental data provided the parameters; g_x = 1.977, g_y = 1.965, g_z = 1.900, g_{av} = 1.978; A_{av} = 86.33×10^{-4} cm^{-1} (**Figure 2.7**).

2.3b: Effect of *–ortho* Substituent to the Formation of the Triradical–Containing Oxo–V(IV) Cluster:

To understand the effect of *–ortho* substituent at the aniline moiety of $\mathbf{H_2AP^H}$ ligand and exploring the probable mechanism for the C–N bond breaking and C–O bond making and consequently, the formation of triradical–containing tetranuclear oxo–vanadium(IV) cluster, another three different ligands have been synthesized by placing three different substituents, –OMe, –Me, and –COOH in place of –CN group. The corresponding ligands will be noted as $\mathbf{H_2L^{OMe}}$, $\mathbf{H_2L^{Me}}$, and $\mathbf{H_3L^{COOH}}$.[28] All three substituents were moderately bulky but they were only differed by their electronic properties as well as their coordination properties. –OMe group is π–electron donor in contrast to the –CN group, while both groups can weakly coordinate to the metal ions. On the contrary, –Me group shows only +I effect and no coordination property, while, –COOH group is an electron withdrawing group but strongly coordinate with the metal ions in its deprotonated form.

To note, it was found that, under the same reaction condition, ligand $\mathbf{H_2L^{OMe}}$ also provided complex $\mathbf{1{\bullet}CH_3CN}$. While, the ligand $\mathbf{H_2L^{Me}}$ could not provide complex $\mathbf{1{\bullet}CH_3CN}$. On the contrary, –COOH substituted $\mathbf{H_3L^{COOH}}$ ligand[28] produced a carboxylate–bridged tetranuclear oxo–vanadium(V) cluster $\mathbf{3{\bullet}CH_2Cl_2}$ (*vide infra*), no π–radical was observed in the coordinated ligand backbone. This indicated a weak interaction (coordination effect) between *–ortho* substituent and metal ion was essential for the formation of radical–containing vanadium cluster (complex **1**) *via* ligand centered C–N bond breaking and C–O bond forming.

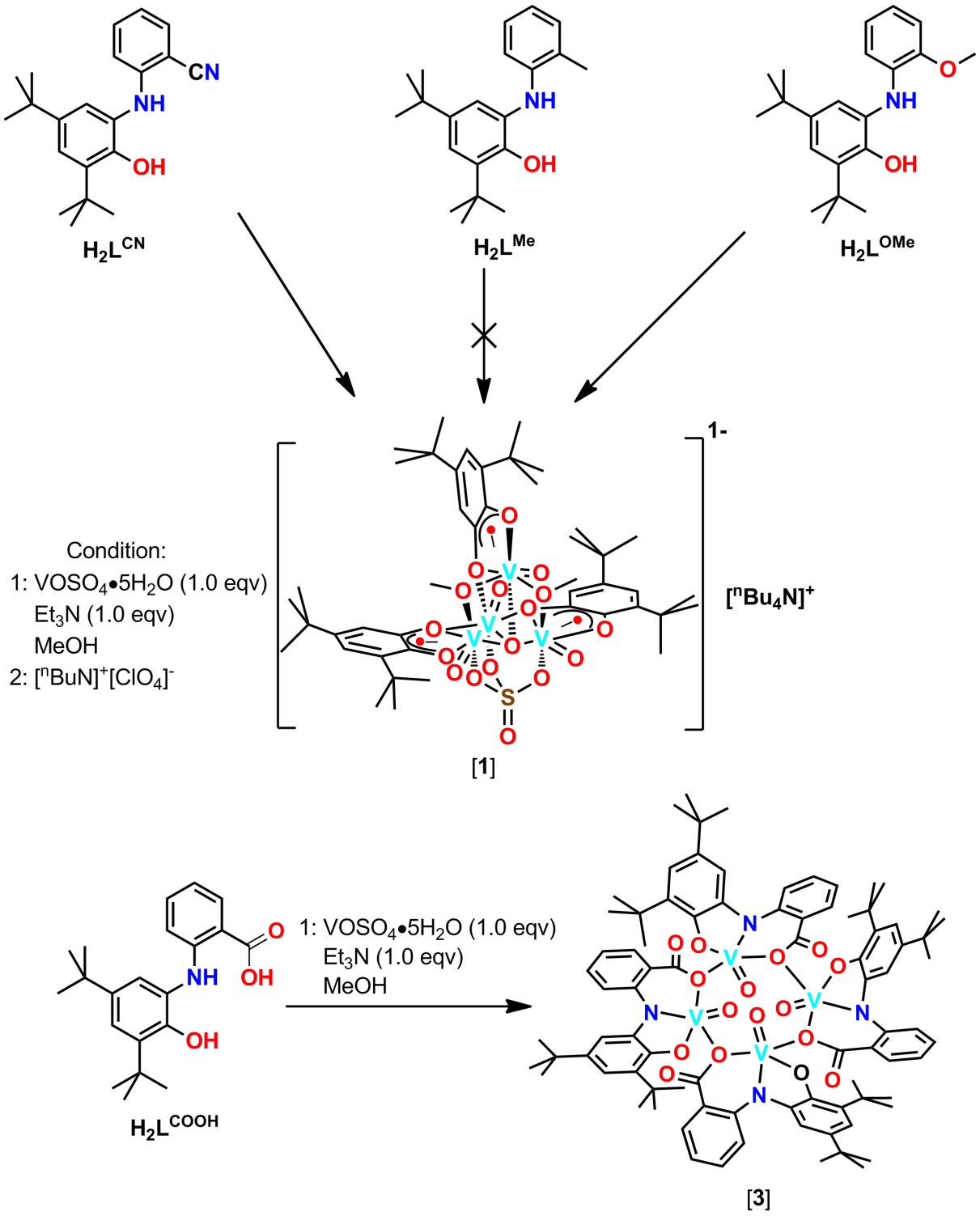

Scheme 2.7: *Substituent dependent reactivity towards $VOSO_4 \bullet 5H_2O$.*

2.3c: Synthesis and Characterization of a Tetraradical–Containing Octanuclear Vanadium Cluster:

The reaction between 1:3:3 H_2Sami^{OMe}:$VOSO_4 \bullet 5H_2O$:Et_3N in methanol under air provided a deep blue solid. The obtained solid upon recrystallization from a 3:1 CH_2Cl_2:MeOH solvent mixture in the presence of $^nBu_4NClO_4$, provided a deep blue crystalline solid that was suitable for single crystal X–ray diffraction measurement.

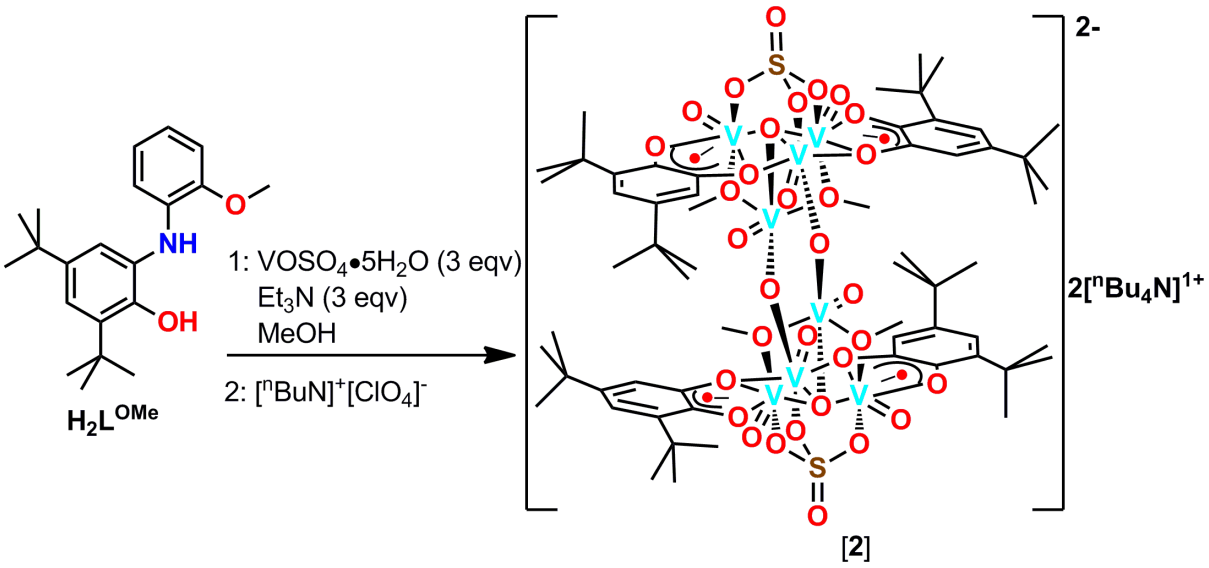

Scheme 2.8: *Synthesis route of complex* $\{[C_{60}H_{92}O_{32}S_2V_8]^{2-}([^nBu_4N]^+)_2\}$*; (2).*

In the infrared (IR) spectrum of **2**, ν(O–H), and ν(N–H) stretching bands vanished. The asymmetric, overtone, and symmetric ν(C–H) stretching bands for *tert*–butyl groups appeared at 2961, 2874, 2912 cm^{-1}, respectively. This indicated the presence of 3,5–di–*tert*–butylcatechol moiety in **2**. Strong bands at 987, and 1001 cm^{-1} indicated the presence of vanadyl (V=O) unit in the complex.[20] The band at 1014 cm^{-1} appeared due to the coordinated methoxide ν(H_3C–O) stretching. The ν(S=O), and ν(S–O) stretching bands for the coordinated μ_3–O_3SO units appeared at 1104, 1036, 691, and 660 cm^{-1}.[22] The ν(V–O) stretching bands appeared in the 573–421 cm^{-1} region. In order to understand the structural difference in terms of bonding–motif between the tetranuclear complex **1** and the octanuclear complex **2**, a comparative IR study has been done (**Figure 2.8**). It was observed that IR spectra for both the complexes were almost similar, except a new band at 783 cm^{-1} was present in the IR spectrum of complex **2** (**Figure 2.8**). This band position was in between of ν(V=O) and ν(V–O) stretching values and indicated the presence of V–O unit with partial double bond ν(V•••O) character in **2**. Indeed, V–O = 1.712 Å bond distance (*vide infra*), which was in between of V–O single bond and double band values, was present in **2**.

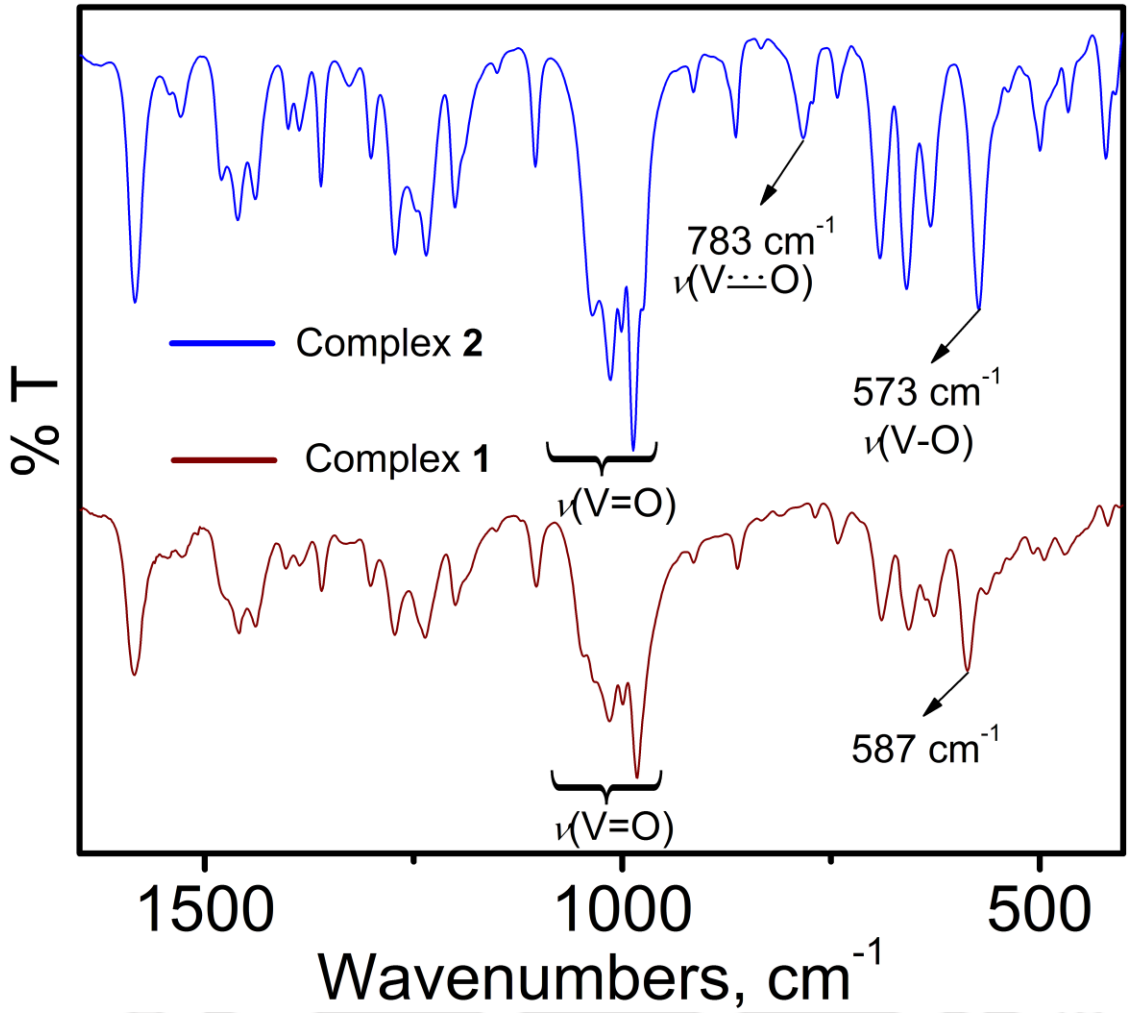

Figure 2.8: *IR spectra of* ***1•CH₃CN****, and* ***2*** *are presented in 1650–400 cm^{-1} range.*

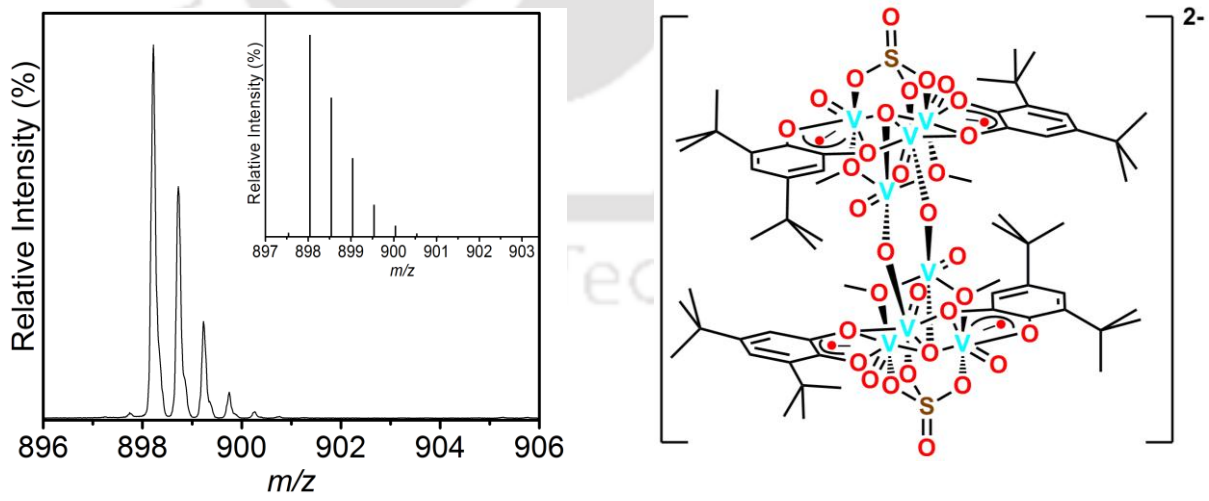

Figure 2.9: *ESI–mass spectrum of* ***2*** *in –ve mode; experimental and calculated isotope distribution pattern (inset).*

In the electrospray ionization mass (ESI–MS) spectrum of complex **2** in CH_3CN, a 100% ion peak in the positive mode appeared at *m*/*z* = 242.25, showing $\mathbf{C_{16}H_{36}N}$ as the

composition. This indicated the presence of ^{n}**Bu$_4$N$^+$** in complex **2**. A 100% mass peak at *m*/*z* = 898.21 appeared in the negative mode ESI–MS of **2**. Simulated isotope pattern distribution indicated **C$_{60}$H$_{92}$O$_{32}$S$_2$V$_8$** composition for the observed *m*/*z* = 898.21 peak and the dianionic character of the V_8 cluster (**Figure 2.9**).

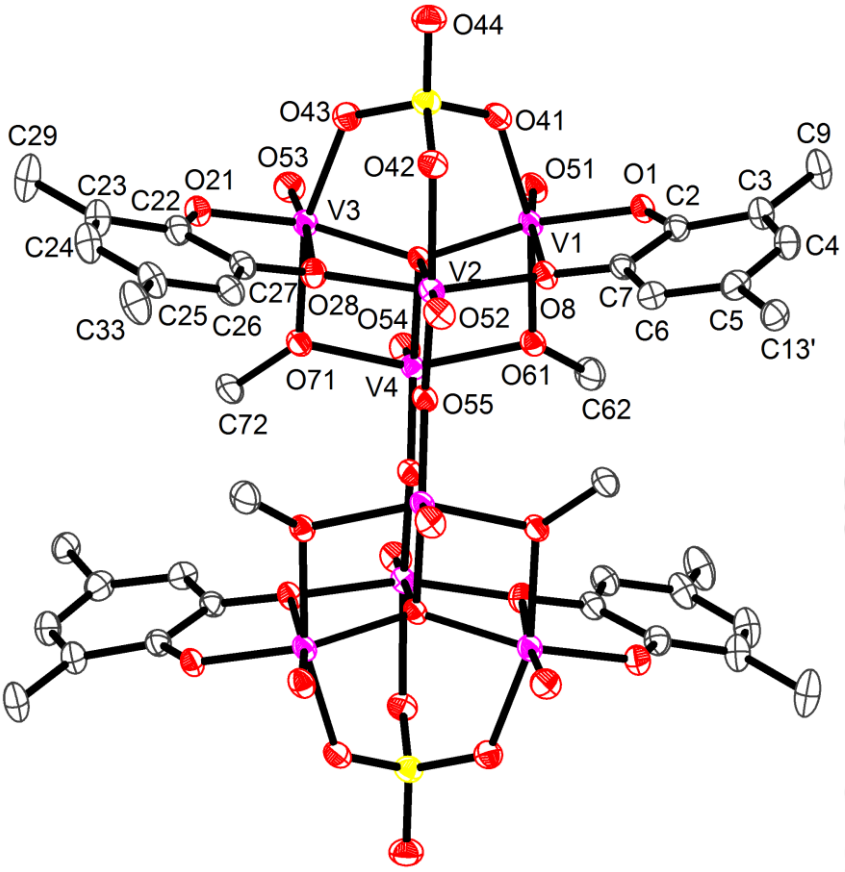

Figure 2.10: *The dianionic octanuclear V_8 cluster present in **2**; thermal ellipsoids were drawn at the 50% probability level. Methyl groups present in the tert–butyl groups, and hydrogen atoms were omitted for clarity.*

Single crystal X–ray diffraction measurement for **2** was performed at 100 K. The complex crystallized in the monoclinic space group $P2_1/n$ (no. 14). The molecular structure is presented in **Figure 2.10**. Selected bond distances, and bond angles are given in **Table 2.2**, and **Table 2.3**, respectively. Complex **2** is composed of a dianionic vanadium cluster containing eight vanadium (V) atoms and two $^{n}Bu_4N^+$ ions as counter cations. The eight vanadium centers were distributed equally between two identical tetranuclear vanadium clusters. Each tetranuclear cluster was reflected to the other by an imaginary point, known as inversion center, situated at the middle point of the line connecting two S atoms from the two SO_4^{2-} units. Hence, herein, only one cluster will be discussed.

All the four vanadium centers (V1, V2, V3, and V4) in a tetranuclear vanadium cluster were connected to each other by μ_4–O56 atom in almost tetrahedron fashion. The V1–

O56, V2–O56, V3–O56, and V4–O56 bond distances were 1.926(3), 2.4001(15), 1.940(3), and 2.023(2) Å, respectively. V1, V2 and V3 were anchored by the μ_3–O_3SO bridging unit and V4 was connected to both V1 and V3 through two individual methoxide (–OMe) bridges. Two tetranuclear vanadium clusters were connected to each other through two oxide (O^{2-}) bridges. The V2–O55 = 1.936(2) and V4–$O55^{i}$ = 1.712(2) Å (i represents the atom obtained by inversion center operation) bond distances indicated an uneven distribution of O^{2-} charge over the two V–O linkages and emphasized the existence of the V2 and V4 in completely localized +IV and +V oxidation states, respectively.[29]

V1, V2, and V3 atoms were in distorted octahedral geometry, while, V4 could be considered as in square pyramidal geometry due to the long V4–O56 = 2.0234(15) Å bond distance. The V1–O51 = 1.5984(16), V2–O52 = 1.5902(16), V3–O53 = 1.5945(16), and V4–O54 = 1.5944(16) Å bond distances were shorter with respect to other V–O bond distances (**Table 2.2**) and represented the vanadyl form of all the vanadium atoms. The coordination site of each V1 and V3 atoms was occupied by a 3,5–di–*tert*–butylcatecholate organic moiety. The V1–O1 = 1.8680(15), V3–O21 = 1.8787(16) Å bond distances were shorter compared to V1–O8 = 2.2321(15), V3–O28 = 2.2225(16) Å bond distances. This elongation reflected strong *trans effect* exerted by both V1–O51 and V3–O53 vanadyl units. The C–C bond distances of the coordinated 3,5–di–*tert*–butyl–containing phenyl rings were not within 1.390±0.01 Å range, as expected for a fully reduced 3,5–di–*tert*–butylcatecholate^{2-} (Cat^{2-}) form.[12,25*a*,30] Instead of that, three long [C22–C27 = 1.420(3), C22–C23 = 1.423(3), and C26–C27 = 1.394(3)] and three alternating short and long [C23–C24 = 1.380(4), C24–C25 = 1.426(4), and C25–C26 = 1.386(3)] bond distances, as previously reported for semiquinone π–radical ($SQ^{\bullet 1-}$) systems,[26*c*,27] were observed. These indicated a quinoid–type distortion in the phenyl ring. Additionally, observed O21–C22 = 1.322(3), and C27–O28 = 1.320 (3) Å bond distances, which were shorter than that of Cat^{2-} (1.350–1.360 Å),[24*b*,25*b*,*c*,26*a*,*b*,*c*] C–O_{Ph} (O_{Ph} corresponds to oxygen atom attached to phenyl rings) bond distance, emphasized the destruction of the aromaticity of the phenyl rings upon complexation. Hence, the presence of a π–radical delocalized between two phenolic oxygen atoms could be argued for the each coordinated 3,5–di–*tert*–butylcatecholate system. In summary, structural analysis indicated that each tetranulear vanadium cluster was composed of three V(IV) [V1, V2, and V3], and one V(V) [V4] atoms. Among them V1 and V3 were coordinated each to a π–radical.

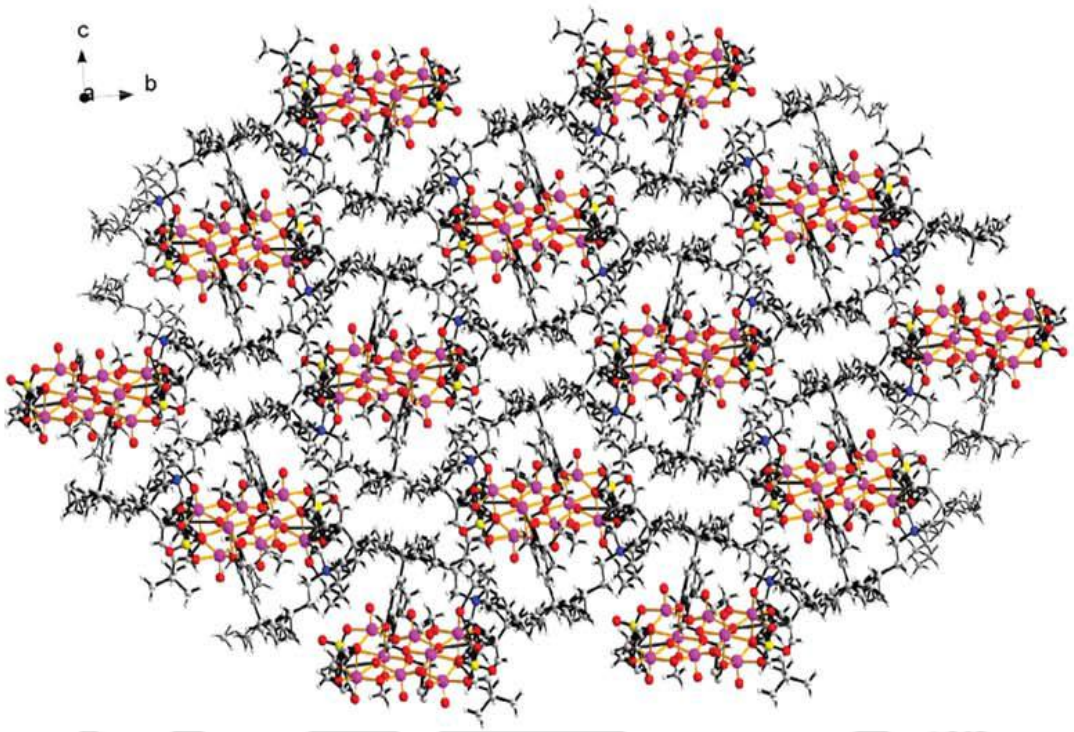

Figure 2.11: *Showing discrete V_8 clusters, which are separated from each other and are buried inside a hydrophobic pocket.*

Further investigation in the crystal structure of **2** revealed that each octanuclear vanadium (V_8) cluster was separated from each other and buried inside a hydrophobic pocket. The pockets ware made by two chain–like $^{n}Bu_4N^{+}$ ions and methyl groups from the *tert*–butyl groups that were attached to 3,5–di–*tert*–butylsemiquinone ($SQ^{\bullet 1-}$) moieties (**Figure 2.11**).

Table 2.2: *Selected bond distances (Å) for complex **2**.*

C2–C3	1.420(3)	C22–C23	1.423(3)
C3–C4	1.380(3)	C23–C24	1.380(4)
C4–C5	1.409(3)	C24–C25	1.426(4)
C5–C6	1.391(3)	C25–C26	1.386(3)
C6–C7	1.396(3)	C26–C27	1.394(3)
C2–C7	1.419(3)	C22–C27	1.420(3)
O1–C2	1.328(2)	O21–C22	1.322(3)
C7–O8	1.331(2)	C27–O28	1.320(3)
V1–O1	1.8680(15)	V3–O53	1.5945(16)
V1–O51	1.5984(16)	V3–O21	1.8787(16)
V1–O56	1.9256(15)	V3–O56	1.9402(15)
V1–O61	1.9879(16)	V3–O71	1.9745(16)
V1–O41	2.0179(17)	V3–O43	2.0208(16)
V1–O8	2.2321(15)	V3–O28	2.2225(16)
V2–O52	1.5902(16)	V4–O54	1.5944(16)
V2–O28	1.9673(16)	V4–O71	1.9556(16)
V2–O8	1.9708(15)	V4–O61	1.9820(15)
V2–O42	2.0504(16)	V4–O56	2.0234(15)
V2–O56	2.4001(15)	V4–V4^{i}	3.4533(6)

V1–V4	3.0681(5)	V3–V4	3.0443(6)
V2–V4	3.5996(7)	V2–V3	3.3666(7)
V2–V1	3.3485(5)	V1–V3	3.6496(6)

Table 2.3: *Selected bond angles (°) for complex* ***2****.*

O1–V1–O56	153.32(7)	V4–O55–V2^{i}	149.88(9)
O56–V1–O41	85.49(6)	V1–O56–V3	141.50(8)
O51–V1–O8	172.16(7)	V1–O56–V4	101.93(7)
O1–V1–O8	75.14(6)	V3–O56–V4	100.34(7)
O54–V4–O55	104.68(8)	V1–O56–V2	100.88(6)
O71–V3–O43	158.58(7)	V3–O56–V2	101.20(6)
O53–V3–O28	174.15(8)	O8–V2–O28	144.90(6)
O71–V4–O61	148.96(7)	O28–V2–O42	83.42(7)
O56–V3–O21	152.96(7)	O52–V2–O56	178.76(7)
O71–V4–O61	148.96(7)	O55^{i}–V2–O42	159.89(6)
V4–O56–V2	108.63(6)		

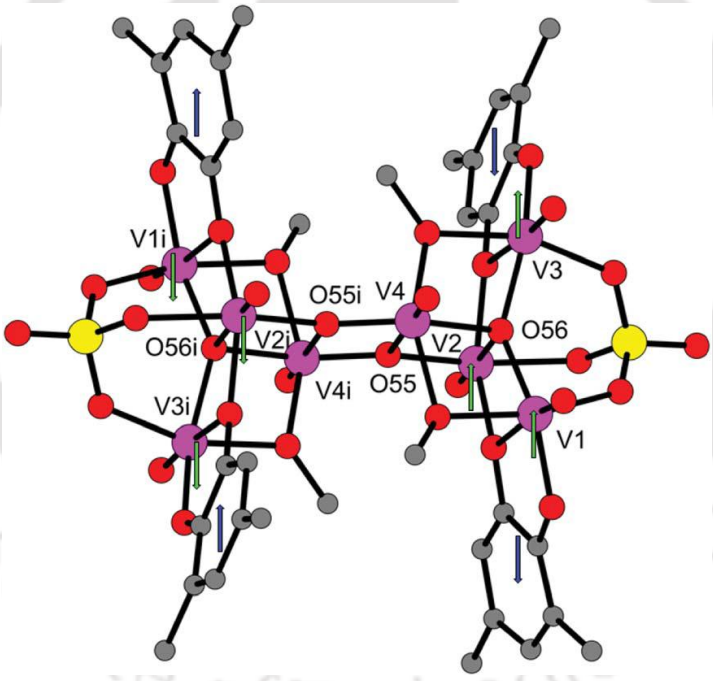

Figure 2.12: *The dianionic octanuclear V_8 cluster with the unpaired–spin alignments.*

The V_8 cluster was made of two identical V_4 clusters which were connected to each other by two oxide bridges, and one V_4 cluster was replicated to the other by means of an inversion center (*vide supra*). Each V_4 cluster was comprised of three paramagnetic V(IV) {$3d^1$, S = 1/2} centers and one diamagnetic V(V) {$3d^0$, S = 0} center. Among the three V(IV) {V1, V2, and V3} centers, two {V1, and V3} were coordinated each to a π–radical anion (S = ½) of semioquinone moiety, and the other one {V2} was connected to the diamagnetic V(V) {V4} center through oxide (O55 and O56) bridges (**Figure 2.12**).

The V_8 cluster was X–band EPR inactive at room temperature (25 °C). Variable–temperature magnetic susceptibility measurements indicated that the complex acquired a diamagnetic ground state and even at 300 K diamagnetic character retained. The coupling between a V(IV) $\{t_{2g}^1\}$ and the corresponding coordinated π–radical (p_z) was expected[31] and known to be antiferromagnetic, and therefore, a tetranuclear V_4 cluster, that contained a localized V(IV) paramagnetic center, was supposed to have S = ½ spin state. The diamagnetic character of the V_8 cluster confirmed an antiferromagnetic coupling between the two V_4 clusters. Herein, the antiferromagnetic coupling between the two V(IV) $\{d_{xy}^1\}$ centers, which were separated by 6.23 Å, was anticipated by the presence of the inversion center. Interestingly, this coupling progressed through two diamagnetic V(V) centers which were connected to the V(IV) centers by two oxide bridges having coupling favoring ~ 150 and ~ 109° V4–O55^i–V2^i, and V4–O56–V2 bond angles, respectively.

2.3d: Proposed Mechanism for the Formation of Complex 1, and 2:

To understand the formation of complex **1** and complex **2** *via* ligand centered C–N bond cleavage and C–O bond formation, ESI–MS and ^{1}H NMR analysis of the reaction solution were performed.

ESI–MS of the reaction solution after 2 h reflux and 15 min air–stirring showed a ion peak corresponding to a vanadyl moiety ligated to a deprotonated ligand $[L^{X}]^{n-}$ (X = –OMe, –CN), and a SO_4^{2-} ion (**Figure 2.13a**). Though the actual mechanism for the cluster formation is not completely clear, herein, it was proposed that at the initial stage both ligands form an identical SO_4^{2-} –ligated vanadyl complex (**Figure 2.14**). The substituent might then undergo a weak interaction with the vanadium center of another molecule owing their ambidentate (–CN)/bridging (–OMe) character, and consequently, favors cluster formation *via* C–N bond cleavage and C–O bond formation. This provided iminosemiquinonate coordinated complex formation (**Figure 2.13b**).

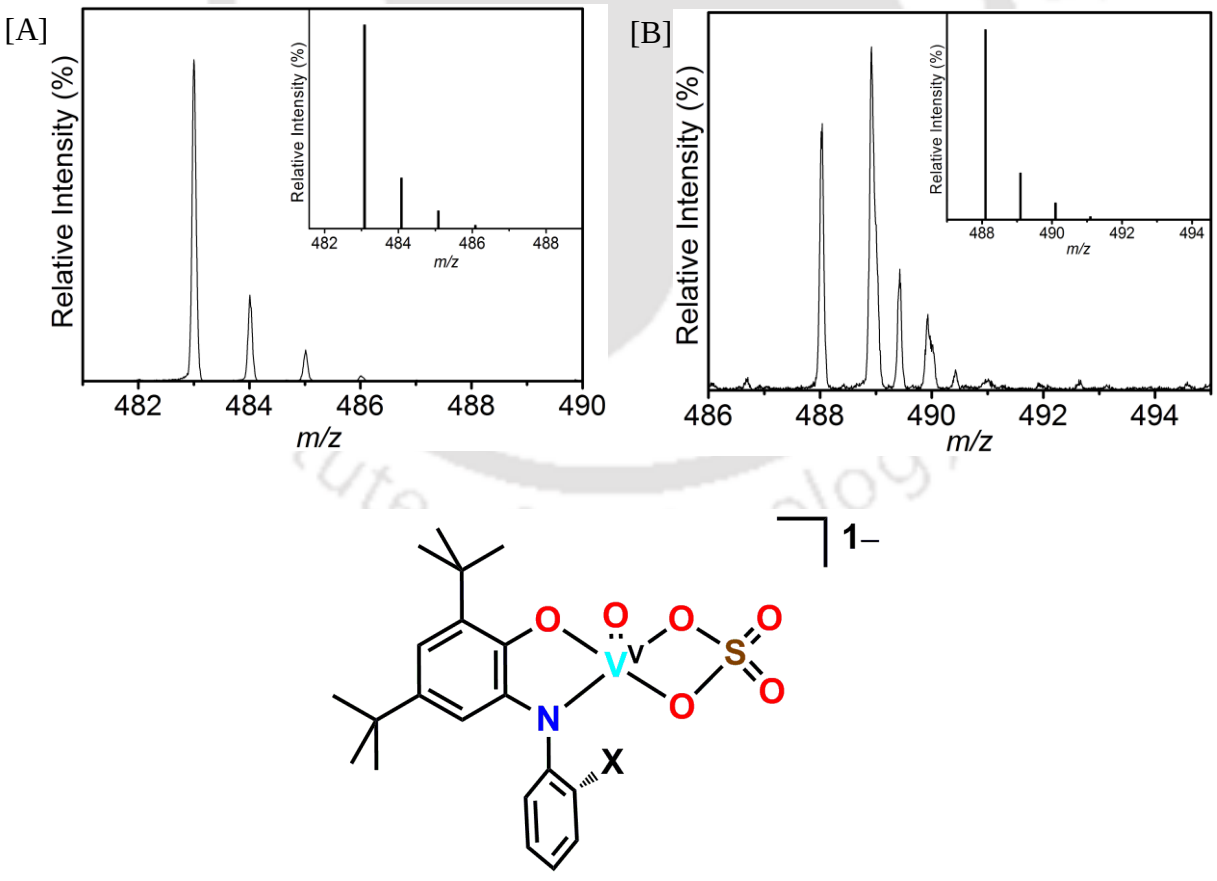

Figure 2.13a: *Experimental and simulated mass spectra (inset) appeared in ESI–MS negative mode. Showing the complex formed initially by the ligation of deprotonated ligand, SO_4^{2-} to vanadyl moiety; [A] corresponds to {[**$C_{21}H_{24}N_2O_6SV$**], (X = –CN)}, [B] corresponds to {[**$C_{21}H_{27}NO_7SV$**]}, (X = –OMe) have been shown.*

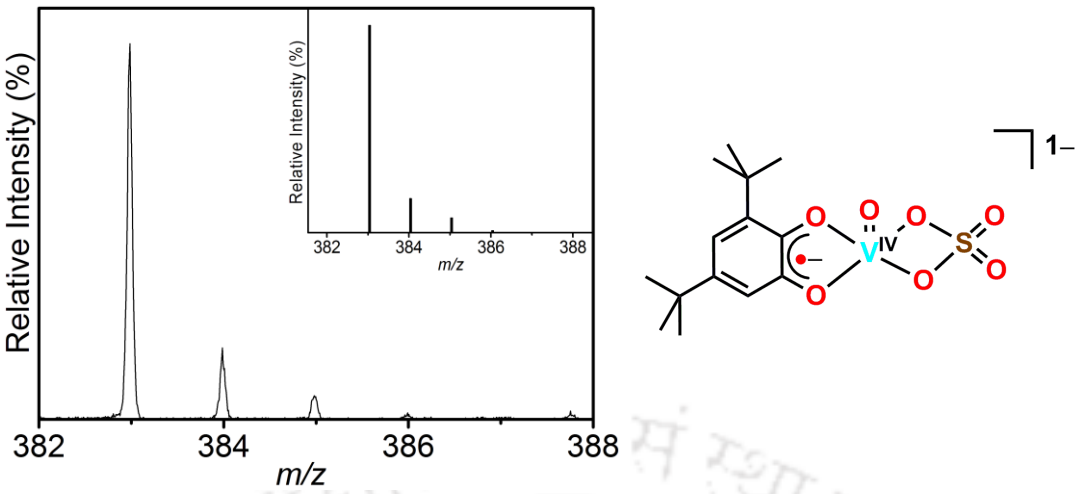

Figure 2.13b: *Experimental and simulated mass spectra (ESI–MS negative mode) for [**$C_{21}H_{20}O_7SV$**]; [**A**] species formed during the complex formation reaction.*

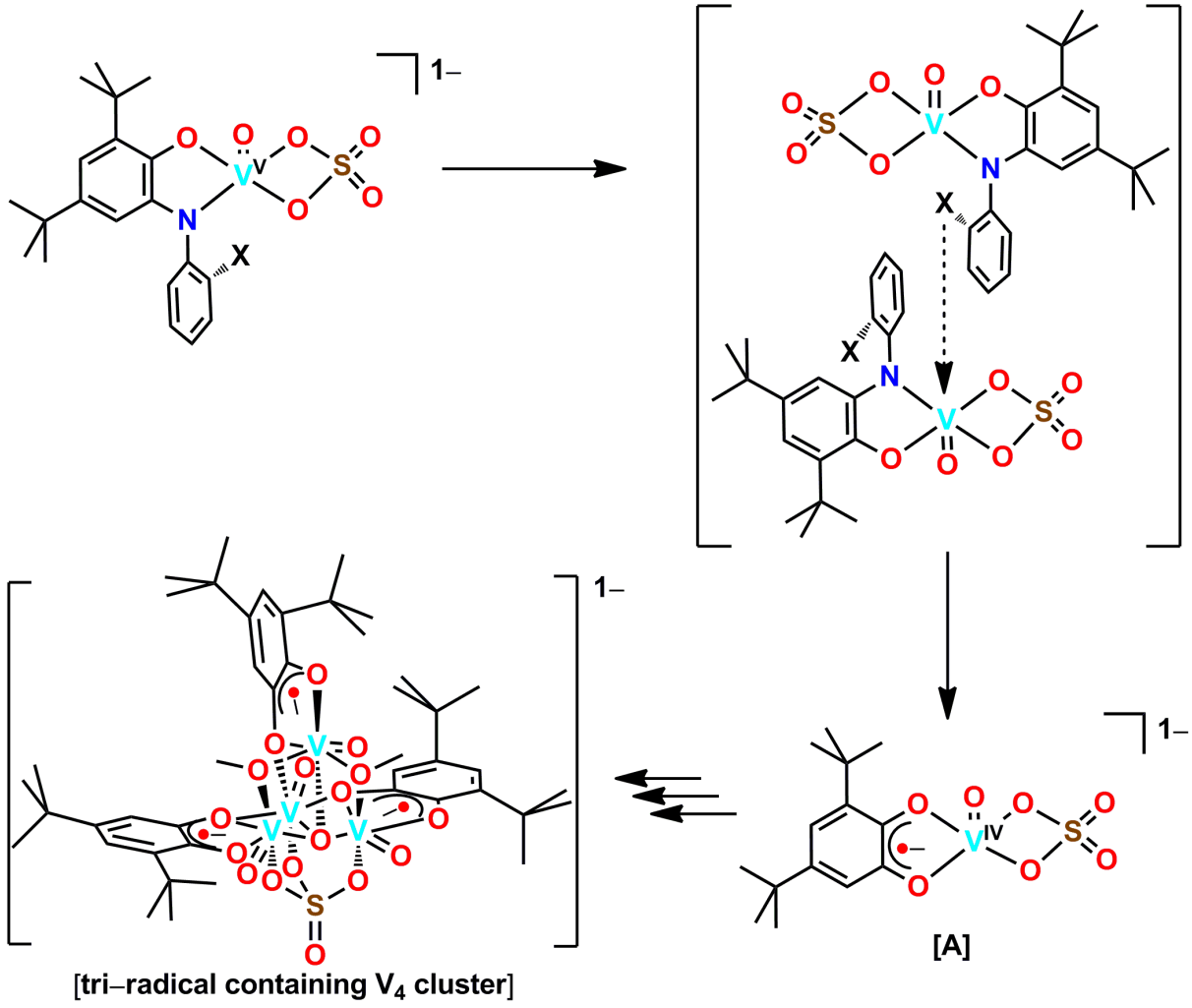

Figure 2.14: *Showing the complex formed initially by the ligation of deprotonated ligand, SO_4^{2-} to vanadyl moiety. The proposed intermolecular weak interaction owing ambident and/or weak–coordination character by X (–CN, –OMe). Intermediate [**A**] formed in the complex formation reaction using both ligands.*

Complex **2** was diamagnetic in nature. Hence, the process of ligand–centered C–N bond breaking and consequently C–O bond formation during the reaction of $VOSO_4 \bullet 5H_2O$ and $\mathbf{H_2L^{OMe}}$ in the presence of triethylamine was monitored in CD_3OD solution (**Scheme 2.9**).

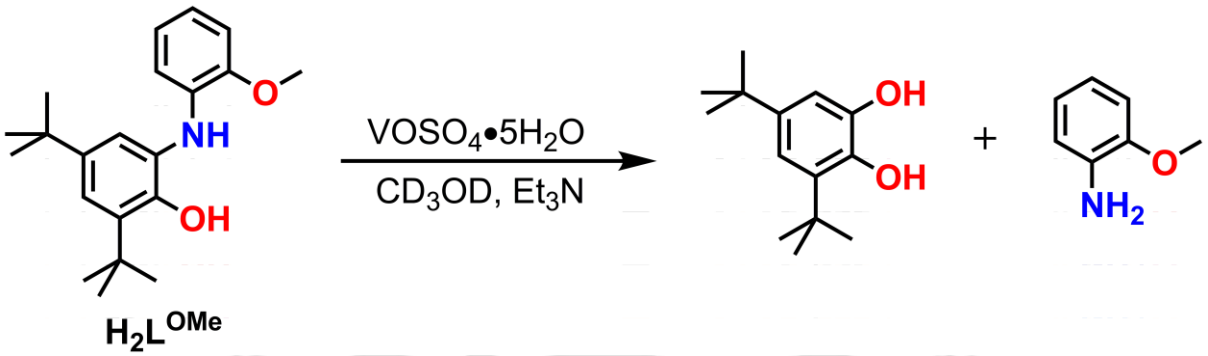

Scheme 2.9: *Ligand centered C–N bond breaking and C–O bond formation.*

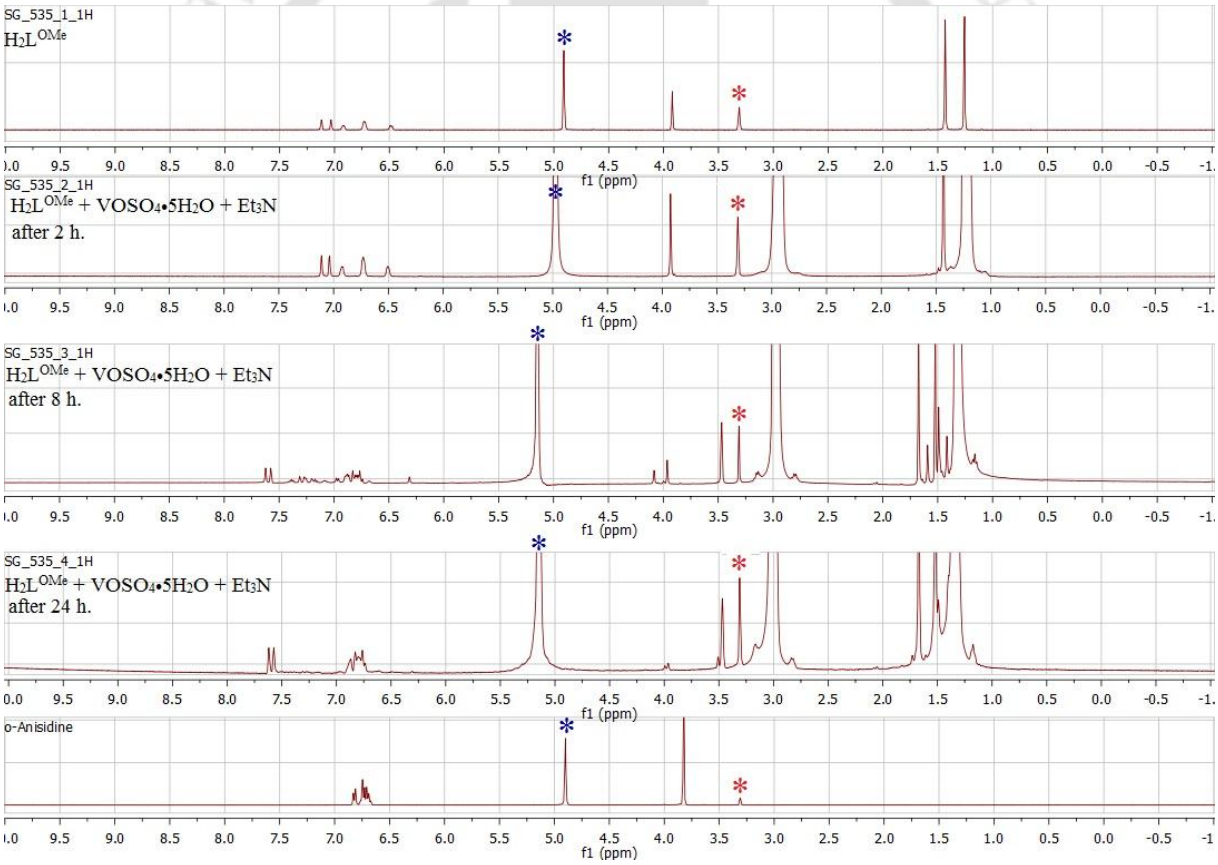

Figure 2.15: *^{1}H NMR spectra of free ligand, reaction solution at different time intervals and o–anisidine. Asterisks indicate solvent peaks.*

The ligand–centered C–N bond breaking would result *o*–anisidine and the C–O bond formation would provide vanadium–coordinated 3,5–di–*tert*–butyl–1,2–semiquinone units. In order to find out the formation of *o*–anisidine and vanadium–coordinated 3,5–di–*tert*–butyl–1,2–semiquinone units, ^{1}H NMR spectra of a CD_3OD solution obtained by adding the ligand

(3.5 mg),$VOSO_4 \bullet 5H_2O$ (7.0 mg), and Et_3N (0.04 mL) were recorded after 2 h (SG_535_2_1H), 8 h (SG_535_3_1H), and 24 h (SG_535_4_1H) of the reaction time. The ^1H NMR spectra were shown in **Figure 2.15**. The comparative studies of the spectra with the ^1H NMR spectrum of the free ligand (SG_535_1_1H) and the ^1H NMR spectrum of *o*–anisidine (*o*–anisidine), indicated the formation of *o*–anisidine (phenolic protons, SG_535_4_1H and *o*–anisidine) and the concentration of this species increases with time. Unfortunately, the methyl protons belong to the –OMe group of *o*–anisidine was not observed in the ^1H NMR spectrum of the reaction solution (SG_535_4_1H) at 3.82 ppm. The presence of peaks at 7.62, 757 ppm and at 1.67 and 1.52 ppm indicated the formation of vanadium–coordinated 3,5–di–*tert*–butyl–1,2–semiquinone unit. The low–field shift of the phenyl protons (7.05–7.20 ppm) compared to the free ligand (6.50–7.11 ppm) indicated the coordination of the free ligand to the metal center. These facts were further supported by the presence of six peaks for three sets of two *tert*–butyl groups (**set 1:** unreacted ligand; **set 2:** metal–coordinated ligand; **set 3:** metal–coordinated 3,5–di–*tert*–butyl–1,2–semiquinone). The appearance of the peak at 4.11 ppm was due to coordination of ligand–center –OMe group to the metal ion. The peak at 3.47 ppm could be due to methyl protons of the bridging –OMe groups present in complex **2**. However, peak–integration value did not match with the adequate number of the protons.

2:3d: Synthesis and Characterization of Complex 3•CH_2Cl_2:

Complex **3** was synthesized from $\mathbf{H_3L^{COOH}}$ ligand by its reaction with equimolar amounts $VOSO_4•5H_2O$ (1:1 equivalent) in methanol in the presence of triethylamine under air in very good yield.

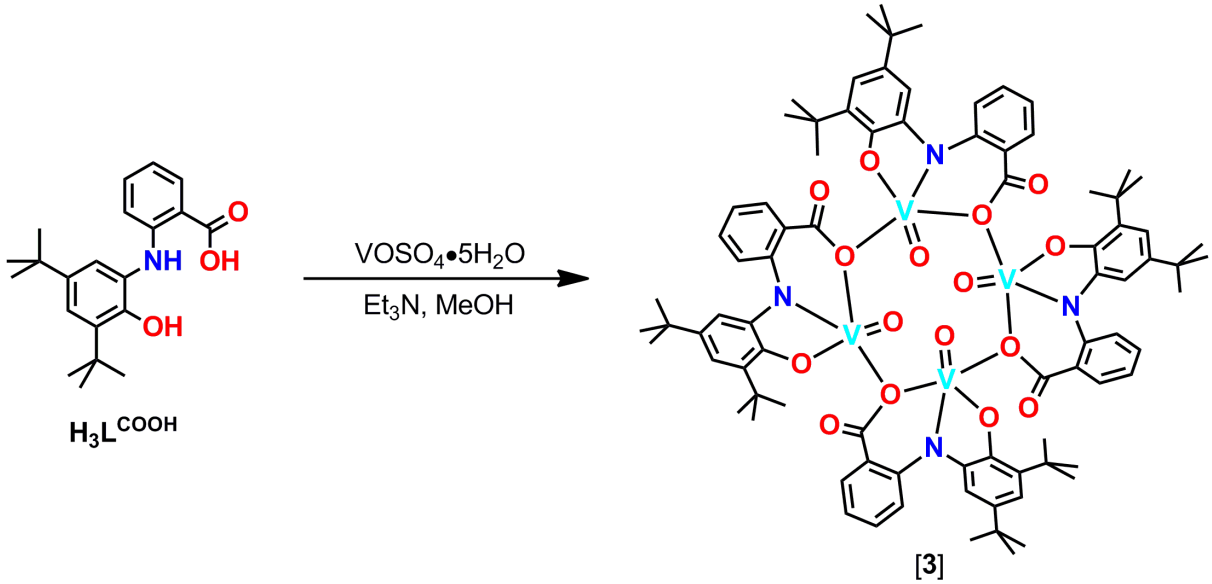

Scheme 2.10: *Synthetic route for [$C_{64}H_{96}N_4O_{16}V_4$]; (3).*

Infrared spectrum of **3•CH_2Cl_2** showed ν(C=O) stretching frequency for the $–COO^-$ functional group at 1573 cm^{-1}.[32] The ν(C=C) vibrational band appeared at 1520 cm^{-1}. The band at 1449 cm^{-1} was appeared due to ν(C–C–O) vibrational mode. A band corresponded to ν(V=O) stretch appeared at 1010 cm^{-1}.[33]

Complex **3•CH_2Cl_2** was diamagnetic as confirmed by ^{1}H NMR measurement. ^{1}H NMR spectrum of **3** was performed in $CDCl_3$ solvent and the resonance signals appeared at 1.12 (s, 36 H), 1.55 (s, 36 H), 6.65 (t, *J* = 7.2 Hz, 4H), 6.86 (s, 4H), 7.18 (d, *J* = 8.4 Hz, 4H), 7.26 (s, 4H), 7.47 (t, *J* = 8 Hz, 4H), 7.73 (d, *J* = 7.6 Hz, 4H) ppm, respectively.

ESI–mass spectrum of **3•CH_2Cl_2** was measured in acetonitrile in positive mode. A 100% molecular ion peak at *m/z* = 406.10; corresponded to $[M/4 + H]^+$, a 40% molecular ion peak at *m/z* = 811.21; corresponded to $[M/2 + H]^+$, and a 10% molecular ion peak at *m/z* = 1621.49; corresponded to $[M + H]^+$ were appeared; M = molecular weight of **3**. Isotope distribution pattern verification of the resulted mass peaks giving the composition of **3** was **$C_{84}H_{96}N_4O_{16}V_4$** (**Figure 2.16**).

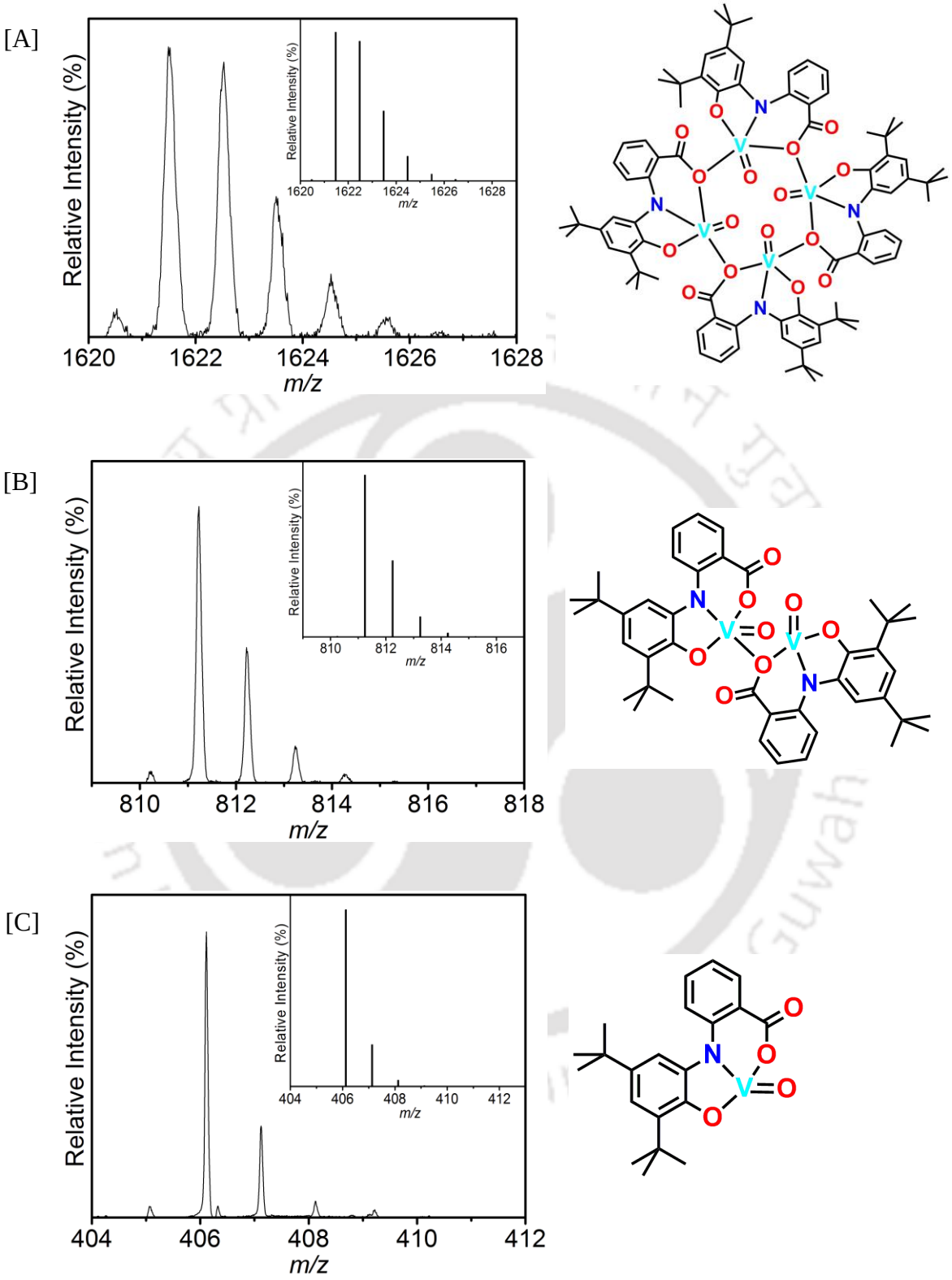

Figure 2.16: [A] *ESI–mass spectra of **3**; [A] corresponds to $[M + H]^+$; [B] corresponds to $[M/2 + H]^+$; and [C] corresponds to $[M/4 + H]^+$; experimental and simulated isotope distribution pattern (inset).*

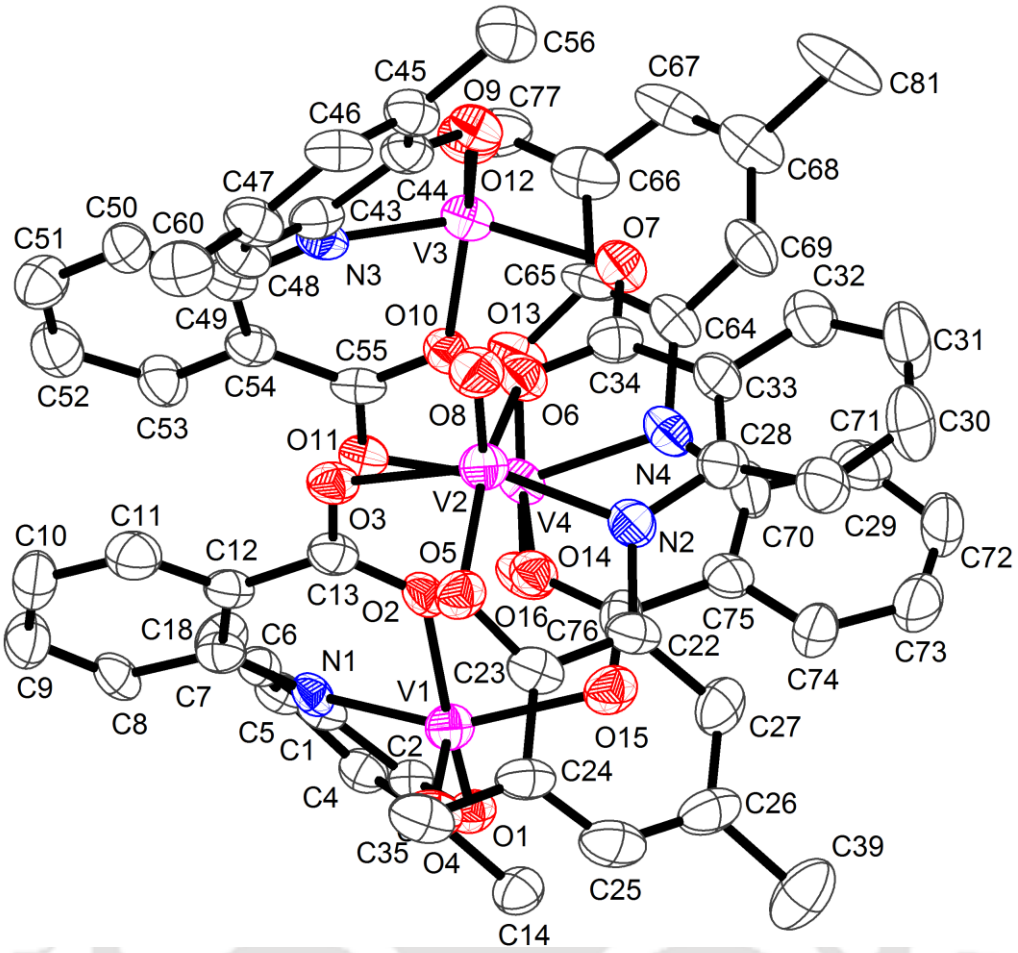

Figure 2.17a: *ORTEP representation of* ***3•CH$_2$Cl$_2$****. H atoms, solvent molecule and methyl groups attached to the tert–butyl groups were omitted for clarity.*

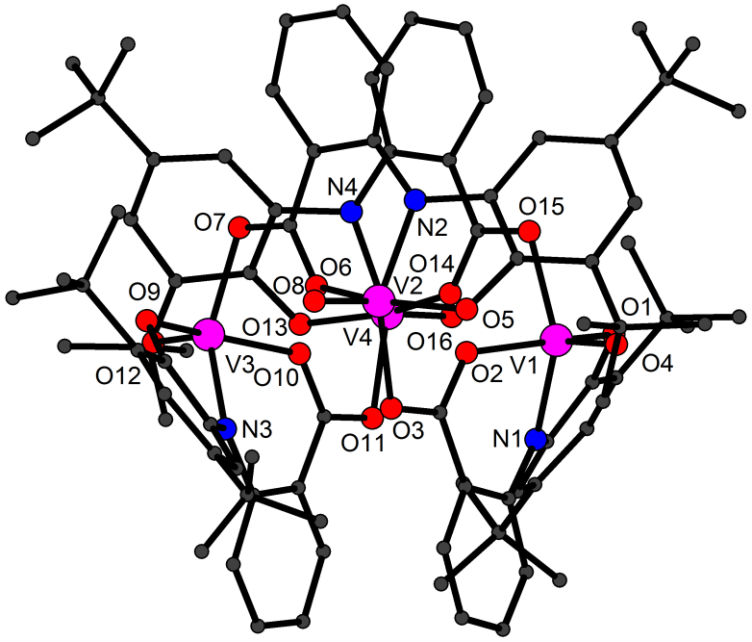

Figure 2.17b: *Ball and stick presentation of* ***3•CH$_2$Cl$_2$****. Selected atoms were labeled. H atoms and solvent molecule were omitted for clarity.*

Single crystal of complex **3•CH_2Cl_2**, suitable for X–ray diffraction study, was obtained by the slow evaporation of its dichloromethane–acetonitrile solvent mixture. Complex **3•CH_2Cl_2** was neutral and crystallized in the monoclinic space group $P12_1/n1$. All four vanadium atoms were in distorted square pyramidal environment in a NO4 coordination sphere. Each vanadyl unit was coordinated to a fully deprotonated tridentate ligand and each mononuclear unit connected to the other by a carboxylate bridging. The V1–O4, V2–O8, V3–O12, and V4–O16 bond distances were 1.591(6), 1.564(6), 1.582(7), and 1.572(6) Å, respectively, and were accord with the previously reported V(V)=O bond distances.[34] The V–N bond distances were reclined in range of 1.965±0.007 Å. The V–O_{Ph} bond lengths were in the range of 1.910±0.007 Å,[12] while, the V–O_{COO^-} bond distances were in the order of 2.002 Å,[35] which was slightly longer compared to the V–O_{Ph} bond distances because of the delocalization of the –ve charge over two oxygen atoms. The metal ligands bond distances, as described above, are good in agreement with their stable oxidation state of +V for the V atoms.

The average C_{Ph}–O_{Ph} bond lengths were 1.33 Å, while, the average C_{Ph}–N_{Ph} bond lengths were 1.38 Å and were in agreement with their single bond nature. In addition, no quinoid–type distortion was found in the *tert*–butyl groups–containing phenyl rings. The C–C bond distances in the phenyl rings were within the range of 1.400±0.025 Å.[36] Thus, the coordinating ligands exist in their fully reduced form *i.e.* each tridentate ligand possessed three –ve charges and oxo–unit bearing two –ve charges in the tetranuclear cluster. Hence, all the vanadium atoms in the neutral complex were in the +V oxidation state.

Table 2.4: *Selected bond distances (Å) and bond angels (°) for* ***3•CH_2Cl_2****.*

C1–N1	1.390(10)	C2–O1	1.314(10)
C22–N2	1.389(12)	C23–O5	1.342(12)
C43–N3	1.392(12)	C44–O9	1.305(11)
C64–N4	1.395(13)	C65–O13	1.342(11)
V1–O1	1.917(6)	V1–O2	2.021(7)
V1–O4	1.591(6)	V1–O15	2.056(7)
V1–N1	1.969(7)	V2–O5	1.901(7)
V2–O6	2.009(7)	V2–O8	1.564(6)
V2–O3	2.037(6)	V2–N2	1.972(8)
V3–O9	1.903(7)	V3–O10	1.987(6)
V3–O12	1.582(7)	V3–O7	2.038(7)
V3–N3	1.957(8)	V4–O13	1.911(6)
V4–O14	2.011(6)	V4–O16	1.572(6)
V4–O16	2.048(7)	V4–N4	1.970(8)

2.4a: Synthesis and Characterization of a Phenoxazine Derivative Using $MnCl_2 \bullet 4H_2O$ as a Catalyst to the Ligand H_2L^{CN}:

A colorless acetonitrile solution of ligand $\mathbf{H_2L^{CN}}$ became brown in color upon addition of $MnCl_2 \bullet 4H_2O$ and Et_3N. The resulting reaction mixture was refluxed for 8 h. After cooling to room temperature (30 °C), it was filtered and filtrate was kept in a beaker. A crystalline fluorescent compound, a phenoxazine derivative, was obtained in 69% yield.

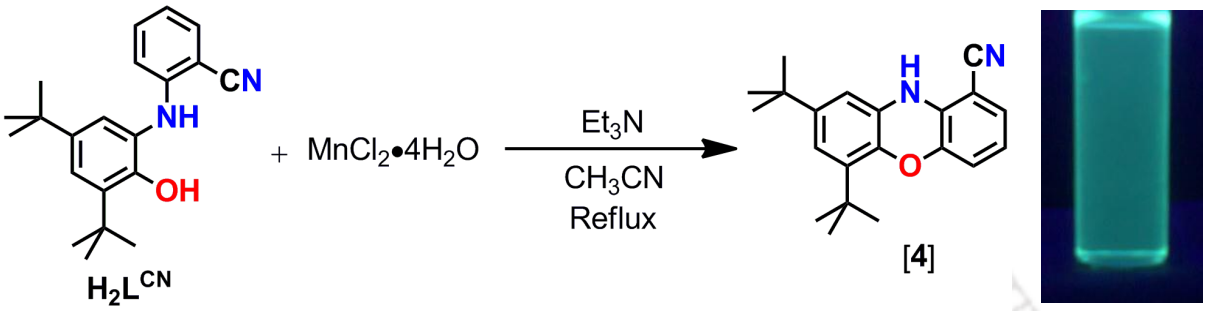

Scheme 2.11: *Synthetic route of phenoxazine derivative;* ***4****.*

In the IR spectrum, the compound showed strong peaks at 3318 and 2226 cm^{-1}, which were attributed to ν(N–H) and ν(C≡N) stretching frequencies. The bending ν(N–H) stretching frequency appeared at 1626 cm^{-1}. The ν(C–H) asymmetric, overtone, and symmetric stretching bands for the *tert*–butyl groups appeared at 2961, 2902, 2866 cm^{-1}, respectively, and corresponding bending vibration band appeared at 1484, 1361 cm^{-1}.

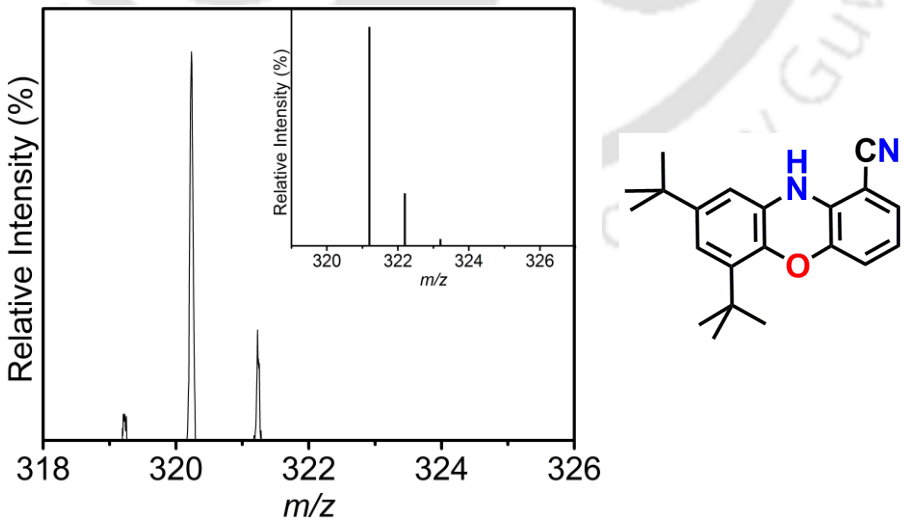

Figure 2.18: *ESI–mass spectrum of 4; experimental and simulated isotope distribution pattern (inset).*

ESI–MS (+ve) for compound **4** in acetonitrile showed a 100% molecular ion peak at *m/z* = 320.19; corresponded to $[M]^+$ (**Figure 2.18**). Isotope distribution pattern investigation

indicated $\mathbf{C_{20}H_{24}N_2O}$ as the composition of the observed mass and reconfirmed the formation of **4**.

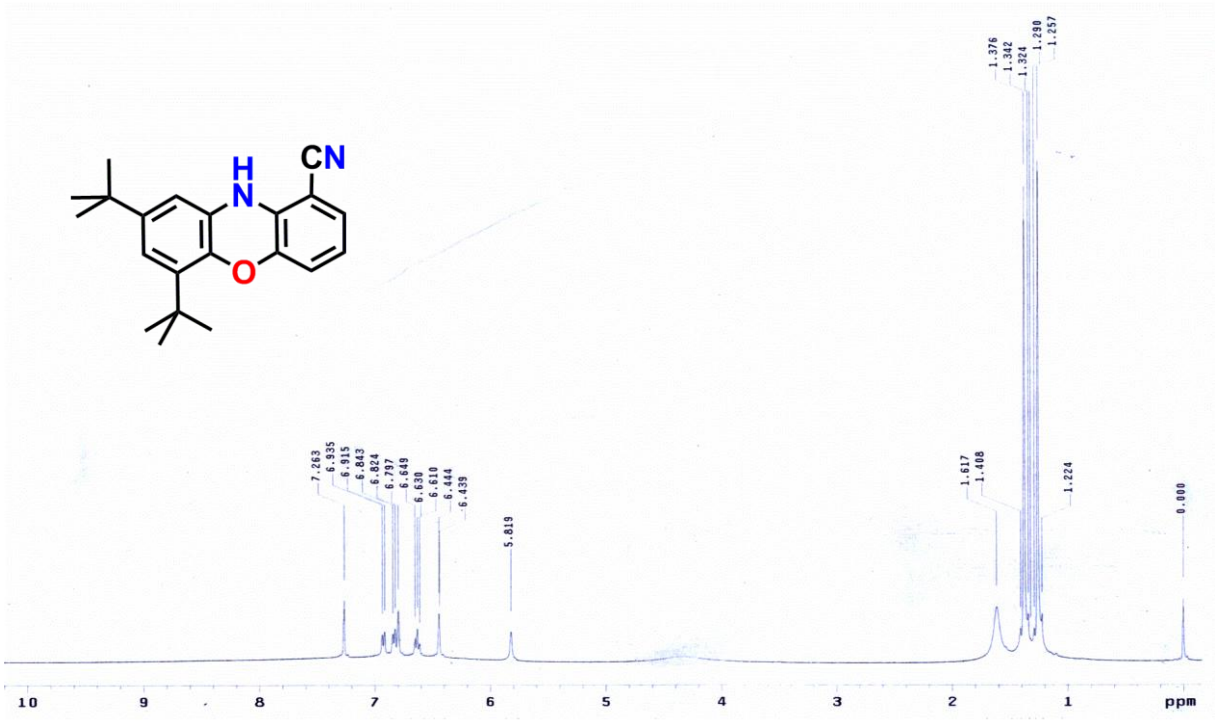

Figure 2.19: *^{1}H NMR spectrum of **4**.*

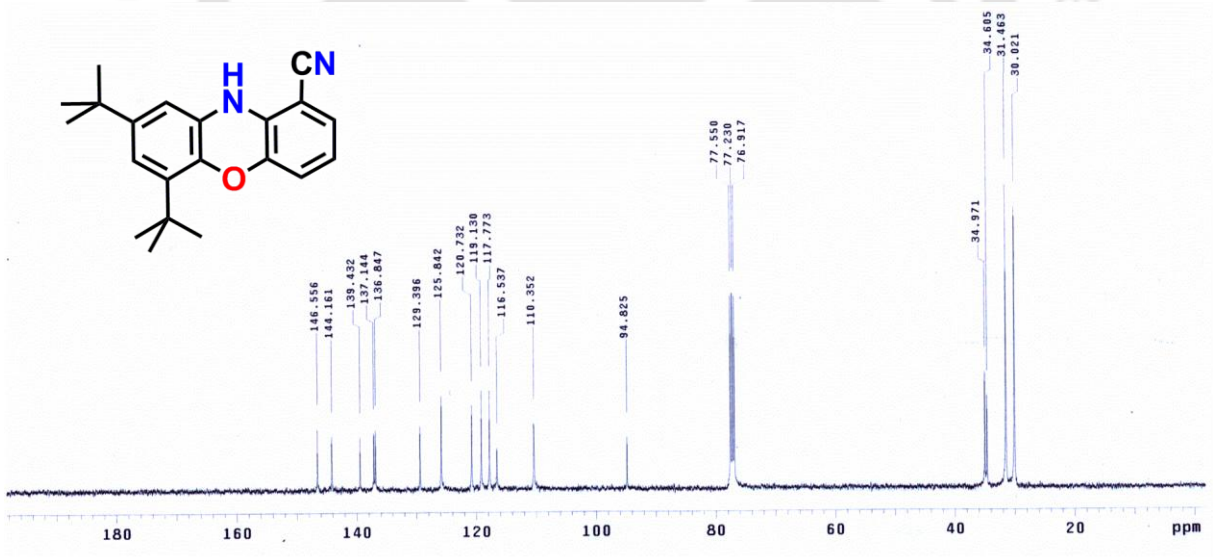

Figure 2.20: *^{13}C NMR spectrum of **4**.*

^{1}H NMR spectrum, the compound showed the resonance signals at δ 1.26 (s, 9H), 1.37 (s, 9H), 5.82 (s, 1H for N–H proton), 6.44 (d, J = 2 Hz, 1H), 6.63 (t, J = 7.8 Hz, 1H), 6.80 (s, 1H), 6.83 (d, J = 7.6 Hz, 1H), 6.92 (d, J = 8 Hz, 1H) ppm. ^{13}C NMR spectrum for the compound exhibited the characteristics 17 different resonance signals.

Compound **4** was also characterized by single crystal X–ray diffraction measurements at 296 K. The molecular structure of **4** is shown in **Figure 2.21**. Selective bond distances and bond angles are listed in **Table 2.5**.

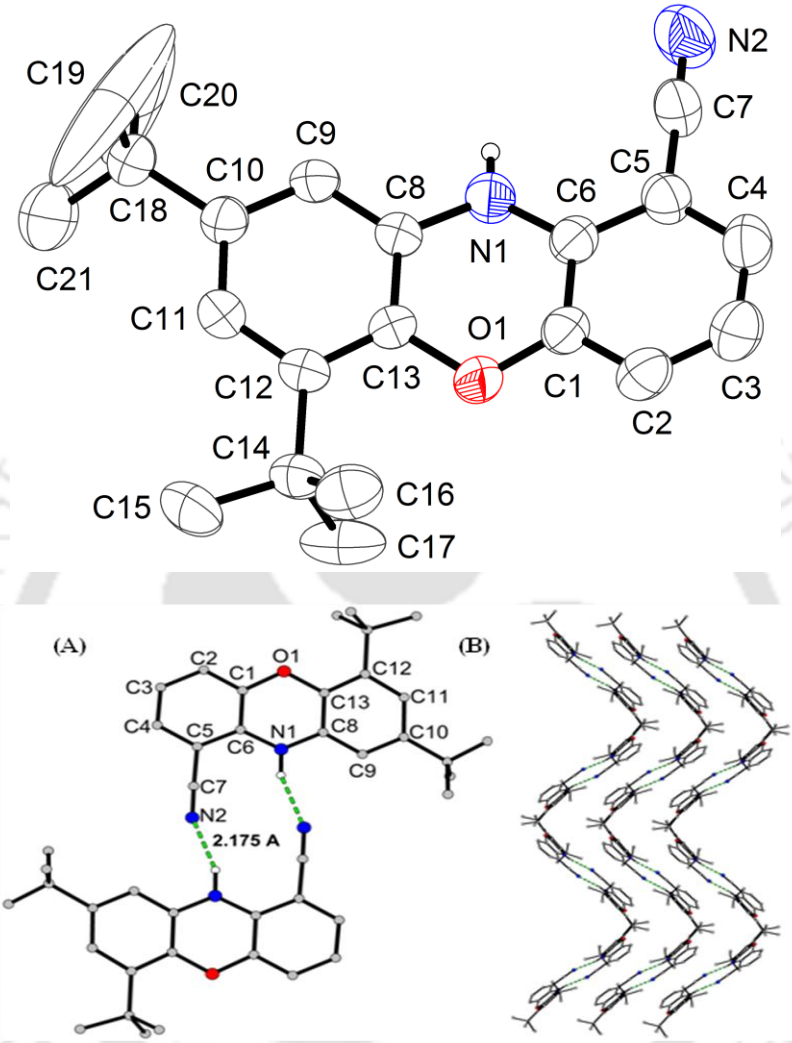

Figure 2.21: *Top: ORTEP representation of compound **4** at 50% thermal ellipsoid probability. H atoms except attached with N1 are omitted for clarity. Bottom: (A) showing H–bonds between two discrete molecules, and (B) molecular arrangement to result helix.*

Compound **4** was crystallized in the space group *C*12/*c*1. The two C_6 rings were fused by an amine nitrogen and an oxide oxygen units at 5 (N1) and 10 (O1) positions (**Figure 2.21A**). The angle between the two C_6 ring planes was ~ 13°. The C–C bond distances of the C_6 rings unambiguously indicated their phenyl form. Furthermore, C–N and C–O bond distances [C6–N1, 1.376(5); C8–N1, 1.401(5); C1–O1, 1.375(4); C13–O1, 1.394(5)] were in accord with their single bond character. Therefore, the compound was a well description of a phenoxazine derivative where one phenyl ring contained two *tert*–butyl groups at –*ortho* and –*para* positions and the second phenyl ring contained a cyanide group at –*meta* position compared to the bridging oxygen atom.

A detailed crystal structure study revealed that two adjacent molecules, connected to each other *via* two strong hydrogen bonds (2.175 Å), form a pair (**Figure 2.21B**). Each pair was almost perpendicular to the immediate pair. This resulted helical layers with 2.92 Å interlayer separations.

Table 2.5: *Selected bond distances (Å) and bond angels (°) for* ***4****.*

C1–C2	1.365(5)	C10–C11	1.391(4)
C2–C3	1.391(5)	C11–C12	1.397(5)
C3–C4	1.368(5)	C12–C13	1.385(4)
C4–C5	1.401(5)	C13–C8	1.390(4)
C5–C6	1.390(5)	N1–C6	1.378(5)
C6–C1	1.401(4)	N1–C8	1.401(4)
C5–C7	1.435(5)	N2–C7	1.141(5)
C8–C9	1.381(5)	O1–C1	1.374(4)
C9–C10	1.376(4)	O1–C13	1.392(4)
N1–C8–C13	119.03(28)	C1–C6–N1	118.28(28)
C8–C13–O1	119.24(26)	C6–N1–C8	119.68(28)
O1–C1–C6	120.26(28)		

2.4b: The Mechanistic Study:

To understand the reaction path, several reactions between $\mathbf{H_2L^{CN}}$ and $MnCl_2 \bullet 4H_2O$ have been carried out. Upon addition of 4 mole % of $MnCl_2 \bullet 4H_2O$ to an acetonitrile solution of the ligand in the presence Et_3N under air, the two–electron oxidized product iminobenzoquinone compound ($\mathbf{L^{CNQ}}$) was produced (**Scheme 2.12**). On the contrary, in the absence of metal salt under the same reaction condition, the ligand could not be oxidized. Thus, the $MnCl_2 \bullet 4H_2O$ (*i.e.* Mn^{2+}) behaved as a catalyst to oxidize the ligand. This oxidized product solely converted to the product phenoxazine molecule upon heating at reflux condition in acetonitrile. This might be because of the electron withdrawing group present at the N–substituted phenyl ring that facilitated the C–H activation and finally resulting the new C–O bond formation (**Scheme 2.12**).

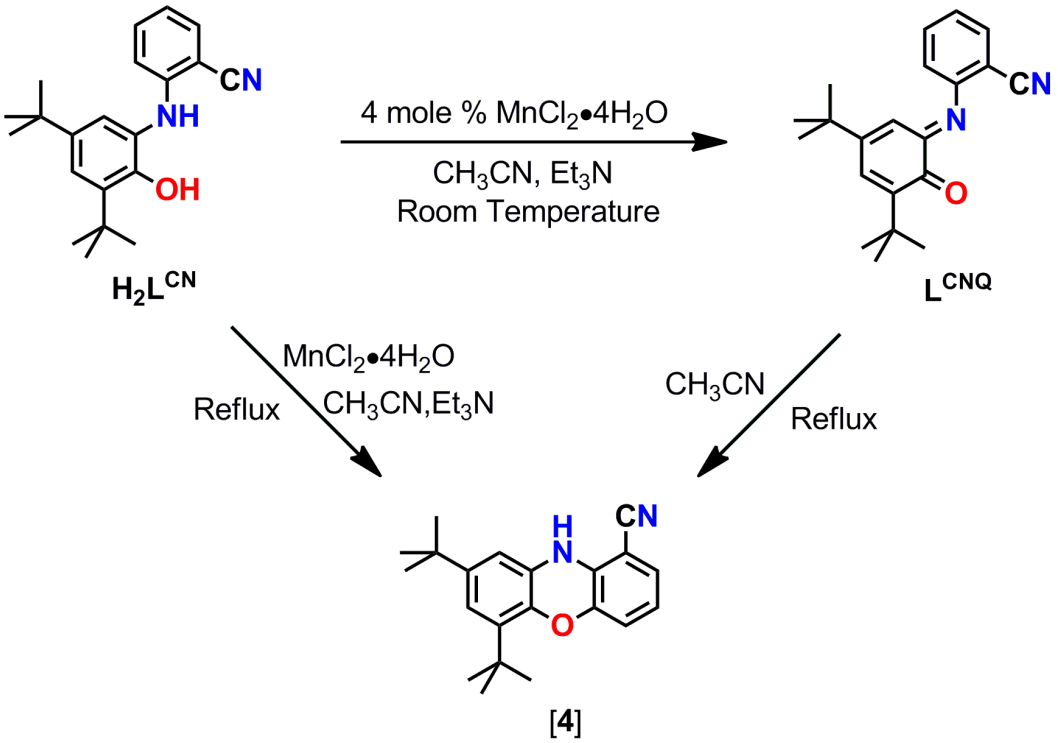

Scheme 2.12: *Systematic representation for the synthesis of* ***4****.*

To find out the intermediate for the phenoxazine formation, $\mathbf{H_2L^{Me}}$ ligand was allowed to react with $MnCl_2 \bullet 4H_2O$. Herein, $\mathbf{H_2L^{Me}}$ ligand was chosen because the size of methyl group and cyanide group will be almost same, moreover, due to less electrom pulling effect of methyl group, the informed complex could be stable under the reaction condition. Interestingly, $\mathbf{H_2L^{Me}}$ ligand provided diradical–containing neutral square pyramidal Mn(III) complex, [$\mathbf{MnL^{Me\bullet}{}_2Cl}$] (**5**) (*vide infra*). The formation of the square pyramidal Mn(III) complex from $\mathbf{H_2L^{Me}}$ ligand, indicated that, initially ligand $\mathbf{H_2L^{CN}}$ reacted with $MnCl_2 \bullet 4H_2O$

and possibly provided the same type Mn(III) complex. The one–electron oxidized iminosemiquinone (ISQ) ligand reoxidized to iminobenzoquinone (IBQ) through one–electron reduction of Mn(III) to Mn(II) that reoxidized to Mn(III) under air.[37] The iminobenzoquinone underwent cyclization *via* ligand C–H bond activation, and finally provided the phenoxazine chromophore. (**Scheme 2.13**)

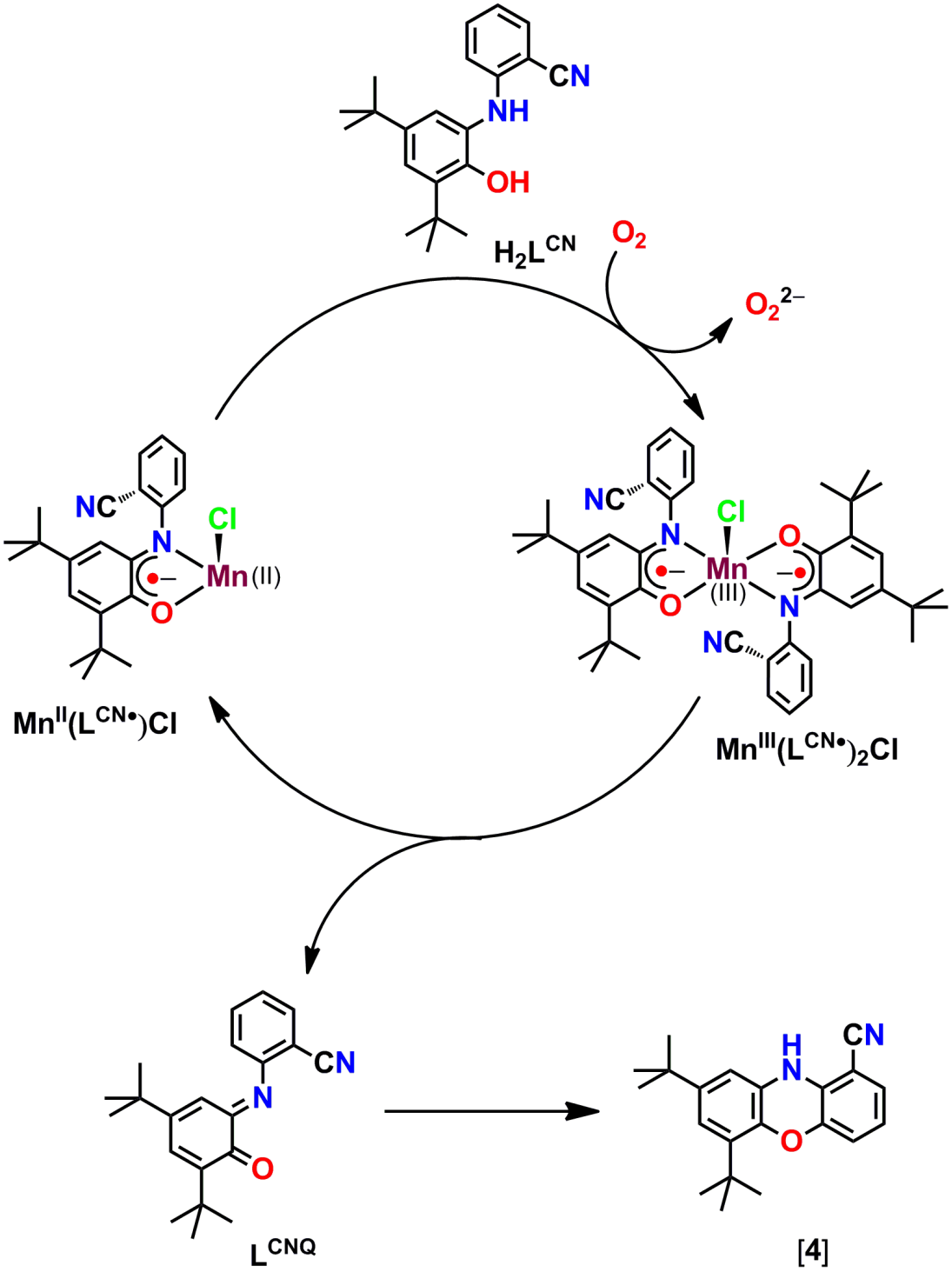

Scheme 2.13: *Mechanistic proposal for the formation of* ***4****.*

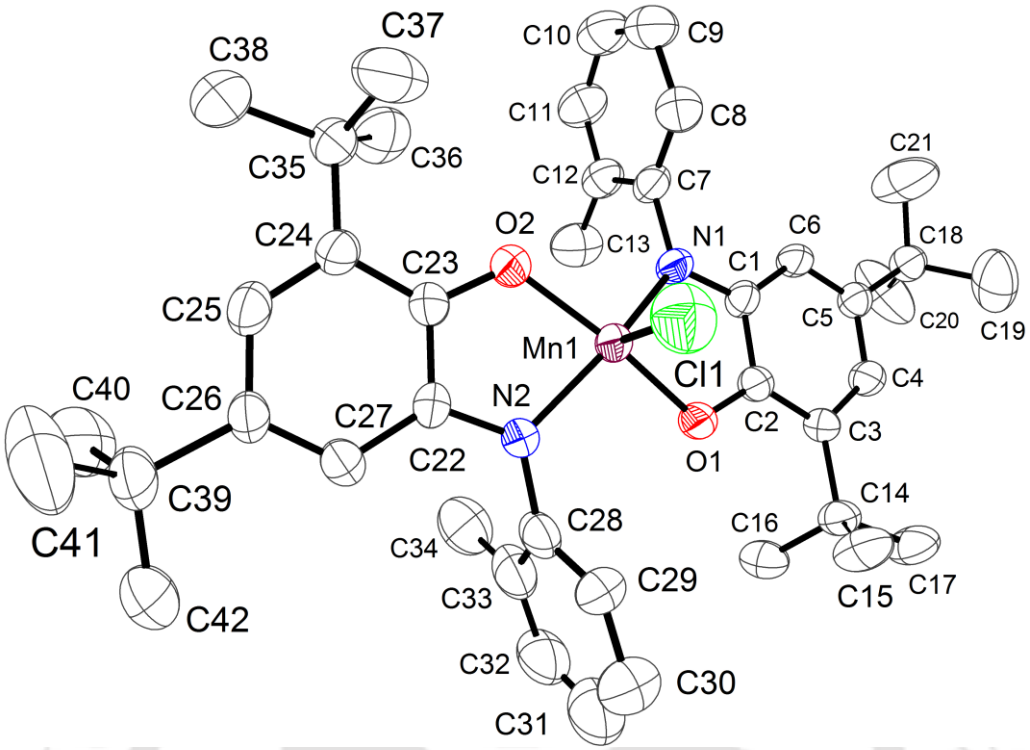

Figure 2.22: *ORTEP representation of [**MnL$^{Me•}_2$Cl**]; **5**. H atoms were omitted for clarity.*

X–ray quality single crystal of [**MnL$^{Me•}_2$Cl**] was gwon from a CH_2Cl_2:CH_3CN (3:1) solvent mixture by slow solvent evaporation method. The complex was crystallized in the tetragonal system, *P*43 space group. ORTEP diagram for the complex is shown in **Figure 2.22**. Selected bond distances and bond angles are given in **Table 2.6**. The five–coordiantion nature around the central Mn center revealed the square pyramidal geometry. Two deprotonated ligands coordianted with metal ion at the basal plane while the –Cl atom occupied the axial position. The central Mn atom was slightly (0.37 Å) lifted from the basal plane towards the apical –Cl atom. The Mn1–O1 = 1.887(2); Mn1–O2 = 1.881(3) Å and Mn1–N1 = 1.939(2) Å; Mn1–N2 = 1.945(3) Å, indicated the +III oxidation state of the Mn ion.[38] The C–C bond distances of the *tert*–butyl groups containing phenyl rings along with C_{Ph}–N_{Ph} and C_{Ph}–O_{Ph} bond distances (C_{Ph}, N_{Ph} and O_{Ph} represent carbon atoms belongs to phenyl rings, nitrogen atom, and oxygen atom attached to phenyl carbon atoms, respectively) indicated the one–electron oxidized π–radical anion ($ISQ^{•1–}$) form of the phenyl rings.[25*a*,39] The other C_6 rings were in their fully reduced phenyl form as confirmed by C–C bond distances (**Table 2.6**). Thus, single cyrstal X–ray structural study consolidated the complex as a diradiacl–containing neutral square pyramidal one where the central Mn ion is in +III oxidation state and two coordinating ligands were in their one–electron oxidized $ISQ^{•1–}$ form.

Table 2.6: *Selected bond distances (Å) and bond angels (°) of* ***5*** *are listed.*

Mn1–N1	1.939(3)	Mn1–N2	1.945(3)
Mn1–O1	1.887(2)	Mn1–O2	1.881(3)
N1–C1	1.348(4)	N2–C22	1.348(4)
N1–C7	1.430(4)	N2–C28	1.437(5)
C2–O1	1.313(4)	C23–O2	1.309(4)
C1–C2	1.437(5)	C22–C23	1.430(5)
C2–C3	1.411(5)	C23–C24	1.422(5)
C3–C4	1.396(5)	C24–C25	1.376(5)
C4–C5	1.416(5)	C25–C26	1.440(6)
C5–C6	1.369(5)	C26–C27	1.352(5)
C6–C1	1.413(5)	C27–C22	1.417(5)
C7–C8	1.376(6)	C28–C29	1.431(6)
C8–C9	1.394(6)	C29–C30	1.360(6)
C9–C10	1.384(7)	C30–C31	1.373(8)
C10–C11	1.360(7)	C31–C32	1.336(9)
C11–C12	1.393(6)	C32–C33	1.424(7)
C12–C7	1.393(6)	C33–C28	1.366(7)
C12–C13	1.485(6)	C33–C34	1.464(7)
Mn1–Cl1	2.2920(14)		
O1–Mn1–O2	163.03(14)	O1–Mn1–N1	81.61(11)
O1–Mn1–N2	94.51(11)	O2–Mn1–N1	94.02(11)
O2–Mn1–N2	81.57(11)	N2–Mn1–N1	151.81(14)
Cl1–Mn1–O1	98.32(10)	Cl1–Mn1–O2	98.65(10)
Cl1–Mn1–N1	105.53(11)	Cl1–Mn1–N2	102.67(11)

2.4c: Application of 4 as Biosensors:

Compound **4** showed a highly intense fluorescent property. Therefore, it was important to study its photophysical properties. The absorption spectra of **4** measured in the 250–700 nm range employing various solvent systems showed two absorption bands at ~ 309 and ~ 373 nm. The 373 nm band was assigned as an intramolecular charge transfer (ICT) band owing to the broad shape, intensity, and solvatochromicity (~ 16 nm) of the band (**Figure 2.23**).[40] The charge delocalization from the donor secondary amine (–NH–) to the acceptor cyanide (–CN) substituent was possibly responsible for the polar ground state and ICT nature of the molecule which caused a red shift of the absorption maxima.

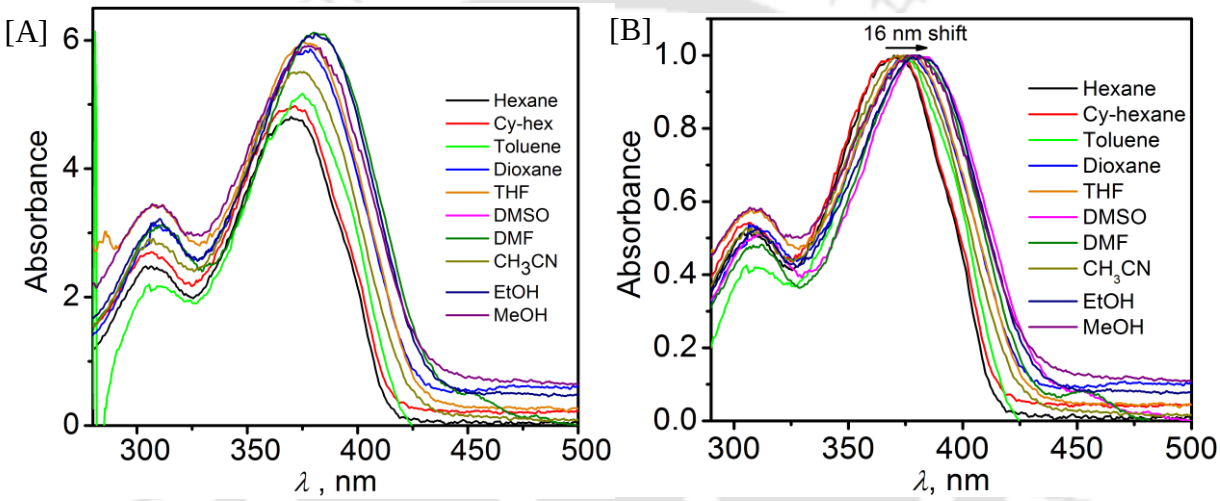

Figure 2.23: *[A] UV–vis, and [B] normalized UV–vis spectra of **4** in different solvents (10 μM, RT).*

A fluorescence photophysical study revealed that the effect of the solvent polarity on the emission maxima was more pronounced than that on the absorption maxima of **4** (**Figure 2.24**). The fluorescence spectra showed structureless broadband for the solvents chloroform, ethylacetate, MeOH, CH_3CN; while, structured band was found for the solvents, like cyclohexane, toluene, DMSO. An increase in solvent polarity has led to a large Stokes shift of the emission maxima for **4**.

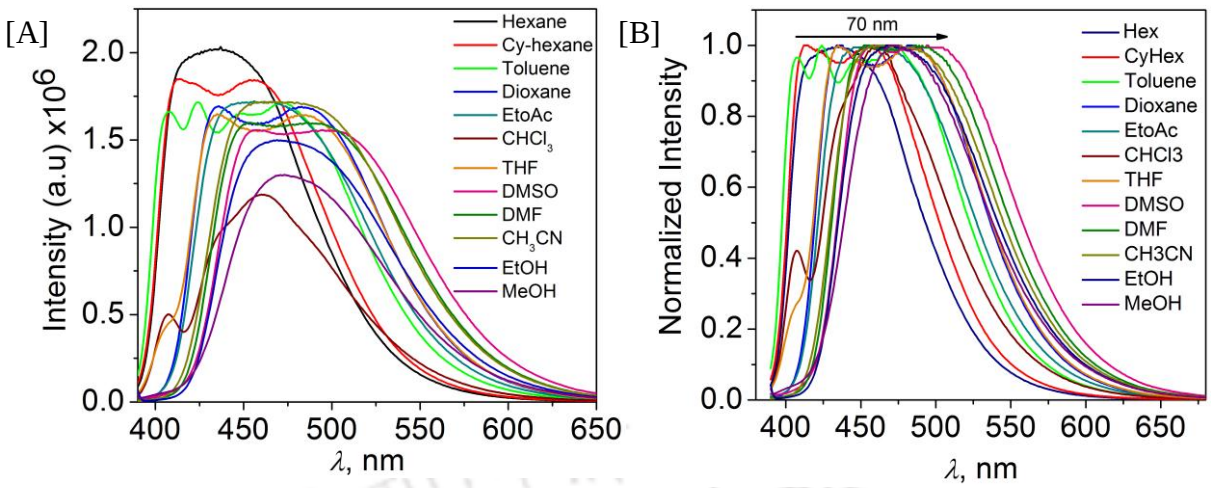

Figure 2.24: *[A] Fluorescence spectra, and [B] normalized fluorescence spectra of* ***4*** *in different solvents (10 μM, RT.;* λ_{ex} *= 370–380 nm).*

An encouraging solvatochromic fluorescence property shown by **4** and the importance of bezophenoxazine derivatives as labels for several biomolecules have motivated to examine and explore the possible sensing of biological microenvironment. As for an example Nile blue was found to interact with ct–DNA but with decrease in fluorescence.[41] Therefore, the interaction behaviors of the probe (**4**) with calf–thymus DNA (ct–DNA), an easily available biomolecule of wide applications, by spectroscopic means in aqueous phosphate buffer (*p*H 7.0) have been studied.[42] The absorption maxima of fluorophore **4** located at 375 nm, showed a negligible effect on the change in absorption maxima and intensity as ct–DNA was added gradually.

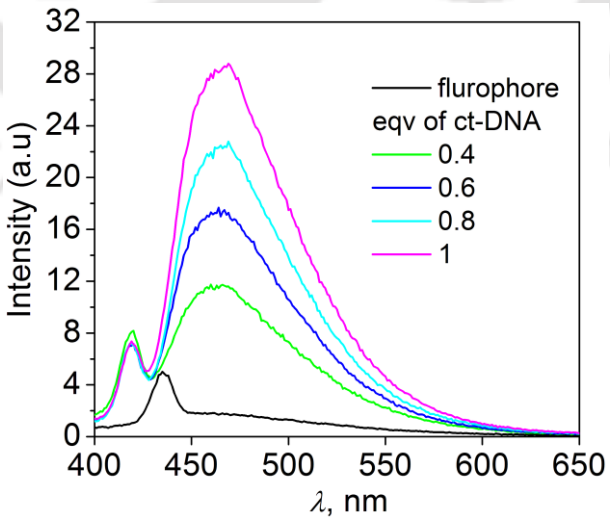

Figure 2.25: *The fluorescence titration of probe* ***4*** *with various concentration of ct–DNA ([probe] = 50 nM; phosphate buffer, pH 7.0, RT.,* λ_{ex} *= 345 nm).*

The fluorescence titration experiment showed that the emission intensity (λ_{em} = 470 nm) of the probe upon gradual addition of ct–DNA has been significantly enhanced upon

excitation at 345 nm (**Figure 2.25**). The emission became maximum at the 1:1 probe:ct–DNA concentration. This observation clearly indicated a well–defined binding of the probe with ct–DNA (**Figure 2.25**).[43] Beyond this ratio fluorescence quenching was observed that might be due to association of more DNA to the probe's surrounding and thus, probably and radiationless channel opens up.

2.5: Synthesis and Characterization of the Square Pyramidal Co(III) Complex [Co($L^{CN\bullet}_2$)Cl]; (6) Formed with H_2L^{CN} Ligand:

An acetonitrile solution containing 2:1 molar ratio of **H_2L^{CN}** and $CoCl_2 \bullet 6H_2O$ was stirred under air at room temperature in the presence of Et_3N that provided complex **[$CoL^{CN\bullet}_2Cl$]**; (**6**) in 71% yield.

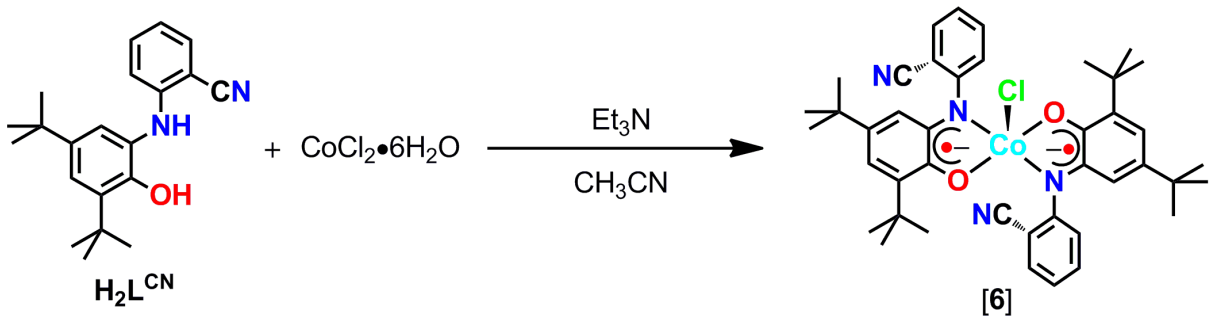

Scheme 14: *Showing the synthetic route to the formation of `[$CoL^{CN\bullet}_2Cl$]; (6).*

In the IR spectrum of the complex, no characteristic stretching bands for –OH, and –NH functional groups were found. This indicated the deprotonation of the groups occurred upon metal complex formation. The band for ν(C≡N) appeared at 2228 cm^{-1}, slightly higher in energy compared to the ligand, these could be for the lower conjugation towards C≡N group in the complex form. The band at 1590 cm^{-1} appeared for the ν(C=N), while, the peak at 1366 cm^{-1} indicated the ν(C⋯O) stretching frequency in the iminosemiquinone ($ISQ^{\bullet 1-}$) anion system.[44]

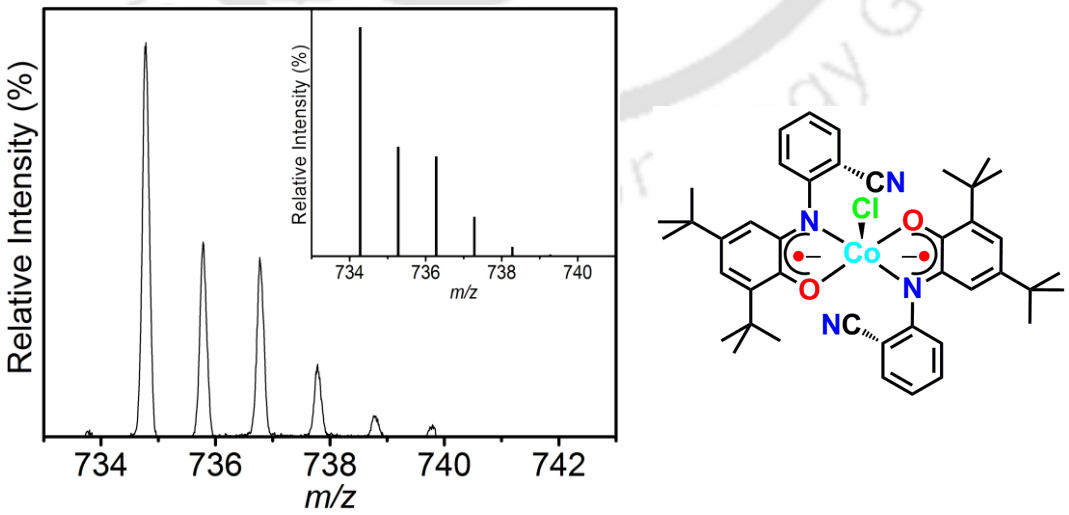

Figure 2.26a: *ESI–mass spectrum of [$CoL^{CN\bullet}_2Cl$] in +ve mode corresponded to $[M]^+$ molecular ion peak; experimental and calculated isotope distribution pattern (inset).*

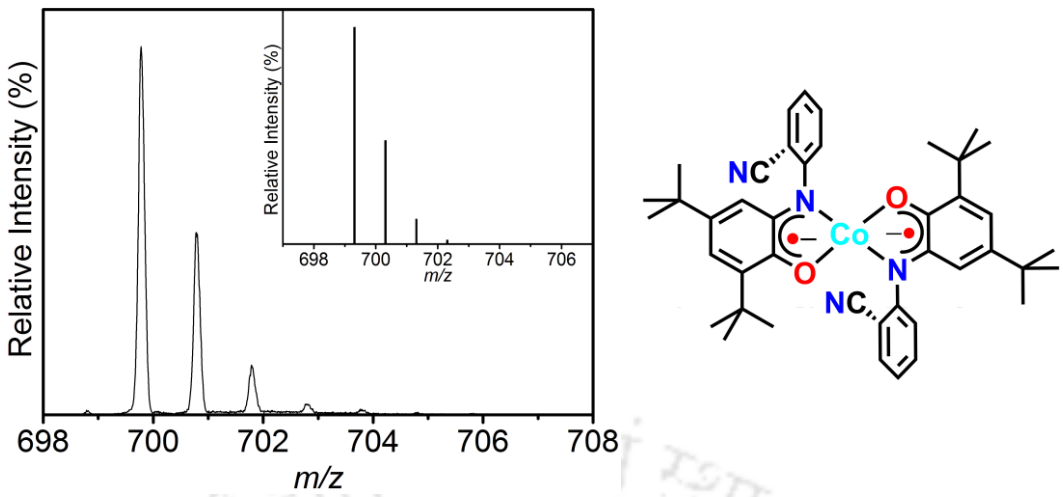

Figure 2.26b: *ESI–mass spectrum of [**CoL**$^{CN\bullet}_2$**Cl**] in +ve mode corresponded to [M – Cl]$^+$ molecular ion peak; experimental and calculated isotope distribution pattern (inset).*

Electrospray ionization (+ve) mass spectrum in acetonitrile for the complex exhibited a 30% molecular ion peak at *m/z* = 734.78 that corresponded to $[M]^+$ (**Figure 2.26a**), and the 100% molecular ion peak at *m/z* = 699.78 corresponded to $[M - Cl]^+$ (**Figure 2.26b**). Isotope distribution pattern indicated the peak at 734.78 corresponded to the composition $\mathbf{C_{42}H_{48}ClCoN_4O_2}$ and the peak at 699.78 for commensurate with the composition $\mathbf{C_{42}H_{48}CoN_4O_2}$.

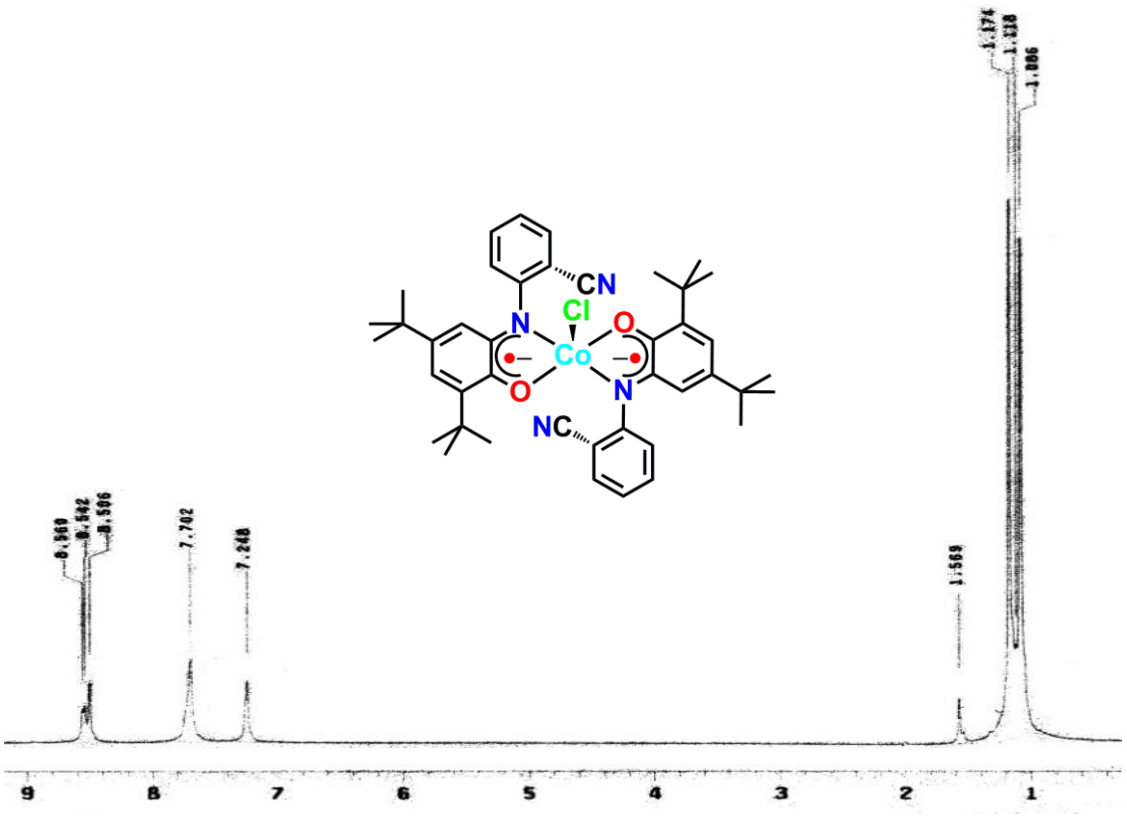

Figure 2.27: *^{1}H NMR spectrum of **6**.*

The complex was diamagnetic experiencing a strong antiferromagnetic coupling between the two π–radicals (*vide infra*). The diamagnetic nature of the complex **[Co(L$^{CN\bullet}$)$_2$Cl]** was also confirmed by ^{1}H NMR ($CDCl_3$, 399.85 MHz) measurement. ^{1}H NMR resonance signal appeared at δ 1.08 (s, 18H), 1.17 (s, 18H), 7.25 (s, 2H), 7.7 (s, 6H), 8.50–8.56 (m, 4H) ppm (**Figure 2.27**).

A blue color crystalline complex of [**CoL$^{CN\bullet}{}_2$Cl**], suitable for single crystal X–ray study was obtained by slow solvent evaporation of a CH_2Cl_2:CH_3CN (3:1) solvent mixture. Molecular structure is shown in **Figure 2.28**. Selected bond distances and bond angles are given in **Table 2.7**, and **Table 2.8**, respectively.

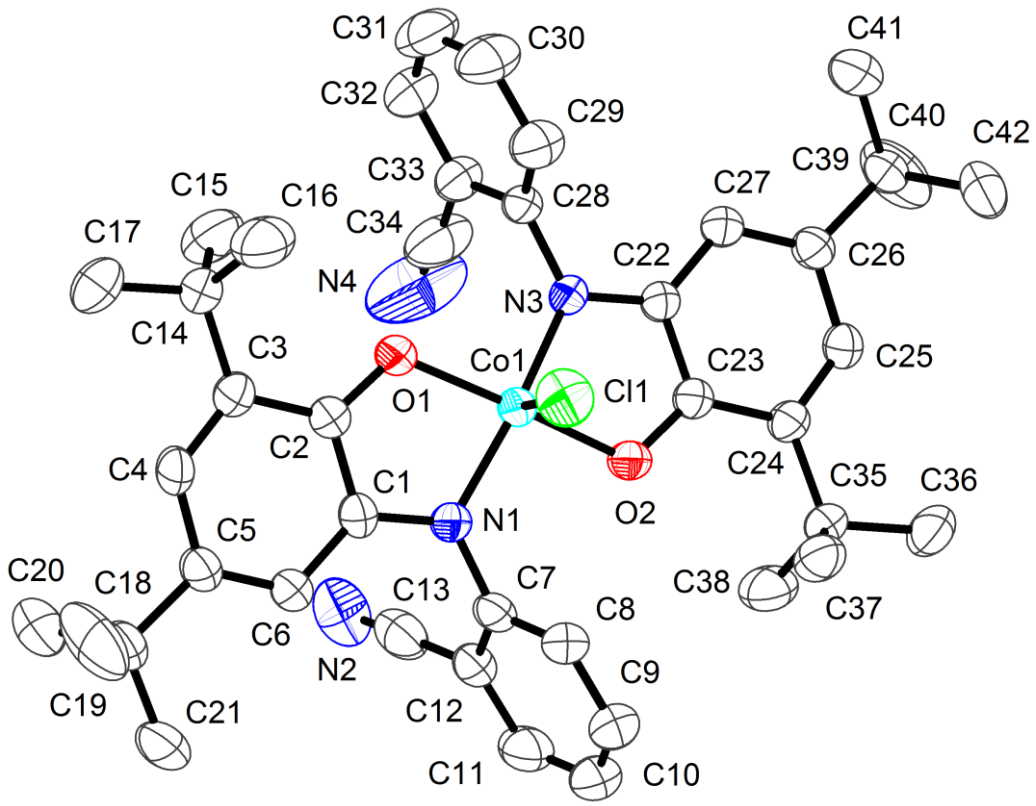

Figure 2.28: *ORTEP diagram of [**CoL$^{CN\bullet}{}_2$Cl**]; (**6**). H atoms were omitted for clarity.*

X–ray crystal structure showed that the central Co atom was coordinated to two deprotonated amidophenolate ligands at the basal position, while, a chloride ion occupied the apex position (*i.e.* fifth position) of the square pyramidal geometry. The central Co atom was situated ~ 0.26 Å above from the basal plane that was comprised of N1, O1, O2, and N3 atoms. The dihedral angle between the two planes passing through the atoms constituted the chelate rings (plane containing Co1, N1, C1, C2, O1 atoms and the plane containing Co1, N3, C22, C23, O2 atoms) was 17.34°. The average Co–O bond length was 1.87 Å and Co–N

bond length was 1.86 Å, while, the Co1–Cl1 bond distance was found as 2.25 Å. These bond distances were good in agreement with the low spin (LS) Co(III) complexes.[45] The average C_{Ph}–N_{Ph} and C_{Ph}–O_{Ph} bond distances (C_{Ph}, N_{Ph} and O_{Ph} represent carbon atoms belonged to phenyl rings, nitrogen atom, and oxygen atom attached to phenyl carbon atoms, respectively) were ~ 1.345 Å, and ~ 1.295 Å, respectively. These bond distances were in accord with their partial double bond values.[46] In addition, C–C bond distances in the *tert*–butyl groups–containing phenyl rings showed alternating four long and two short bond distances, *i.e.* a quinoid–type distortion. These structural parameters indicated that the coordinating ligand exist in its one–electron oxidized π–radical anion *i.e.* $ISQ^{\bullet 1-}$ form.[47] The other C–C bond distances (**Table 2.7**) of the other C_6 rings were in 1.39±0.01 Å and indicated their fully reduced phenyl form. Thus, from the X–ray single crystal measurement it was found that the complex was a diradical–coordinated neutral diamagnetic one.

Table 2.7: *Selected bond distances (Å) are listed for [**CoL$^{CN\bullet}_2$Cl**].*

Co1–N1	1.864(2)	Co1–N3	1.857(2)
Co1–O1	1.8677(19)	Co1–O2	1.8692(17)
N1–C1	1.343(4)	N3–C22	1.348(3)
N1–C7	1.425(4)	N3–C28	1.428(3)
C2–O1	1.294(3)	C23–O2	1.301(3)
C1–C2	1.443(4)	C22–C23	1.440(4)
C2–C3	1.432(4)	C23–C24	1.428(4)
C3–C4	1.363(4)	C24–C25	1.370(4)
C4–C5	1.438(4)	C25–C26	1.434(4)
C5–C6	1.353(4)	C26–C27	1.361(4)
C6–C1	1.415(4)	C27–C22	1.419(4)
C7–C8	1.391(5)	C28–C29	1.372(5)
C8–C9	1.383(4)	C29–C30	1.387(5)
C9–C10	1.367(6)	C30–C31	1.377(6)
C10–C11	1.381(6)	C31–C32	1.361(6)
C11–C12	1.406(4)	C32–C33	1.394(5)
C12–C7	1.390(5)	C33–C28	1.395(5)
C12–C13	1.446(6)	C33–C34	1.416(6)
C13–N2	1.143(5)	C34vN4	1.134(6)
Co1–Cl1	2.2521(11)		

Table 2.8: *Selected bond angels (°) are listed for [**CoL$^{CN\bullet}_2$Cl**].*

O1–Co1–O2	167.48(11)	O1–Co1–N1	83.41(9)
O1–Co1–N3	94.32(9)	O2–Co1–N1	94.48(9)
O2–Co1–N3	83.32(8)	N3–Co1–N1	159.47(13)
Cl1–Co1–O1	96.35(8)	Cl1–Co1–O2	96.17(8)
Cl1–Co1–N1	100.35(9)	Cl1–Co1–N3	100.18(9)

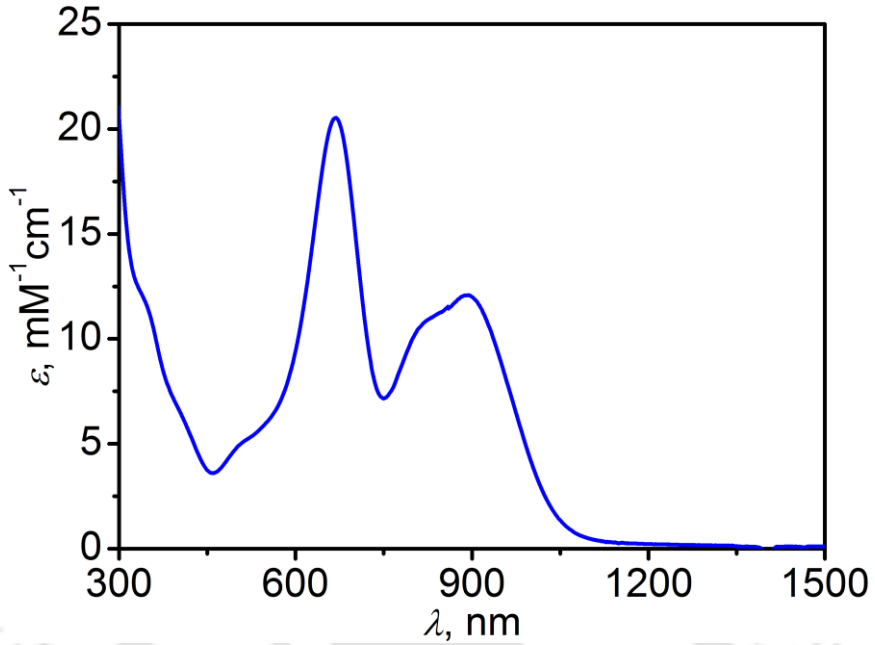

Figure 2.29: *UV–vis/NIR spectrum of [**CoL$^{CN\bullet}{}_2$Cl**].*

UV–vis/NIR spectrum of the neutral complex [**CoL$^{CN\bullet}{}_2$Cl**] is shown in **Figure 2.29**. The characteristic ligand–to–ligand charge transfer (LLCT) band appeared at λ_{max} = 892 nm (ε = 12050 $M^{-1}cm^{-1}$).[47a] A broad absorption maxima at 825 nm (10950 $M^{-1}cm^{-1}$) and a strong absorption band at λ_{max} = 668 nm (ε = 20500 $M^{-1}cm^{-1}$) were observed due to ligand–to–metal charge transfer (LMCT).[48]

2.6: Synthesis and Characterization of the Square Planar Ni(II) Complex [NiL$^{CN\bullet}_2$]; (7) Formed with Ligand H_2L^{CN}:

An acetonitrile solution containing **H_2L^{CN}** and $NiCl_2 \bullet 6H_2O$ in 2:1 ration was added Et_3N under aerial atmosphere. The resulting mixture was refluxed for 4 h. After cooling at room temperature (30 °C), it was stirred for another 1 h at the condition to get complex **[NiL$^{CN\bullet}_2$]** in 35% yield.

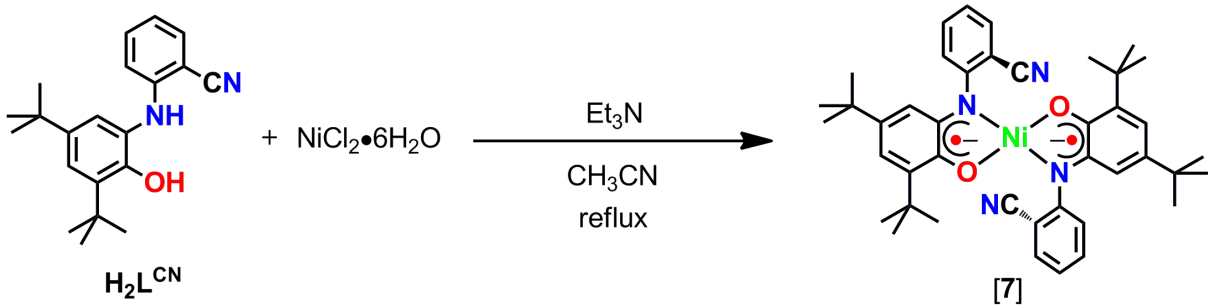

Scheme 2.15: *Synthetic route of [NiL$^{CN\bullet}_2$]; (7).*

IR spectrum of the complex showed no absorption bands for ν(O–H) and ν(N–H) bands, additionally, the presence of the *tert*–butyl and –CN stretching frequencies at 2955, 2906, 2867, and 2225 cm^{-1}, respectively, indicated that the ligand bound with Ni ion where O–H and N–H were deprotonated. The band at 1590 cm^{-1} appeared for the ν(C=N) stretching, in addition ν(C⋯O) stretching frequency appeared at 1440 cm^{-1}.[49]

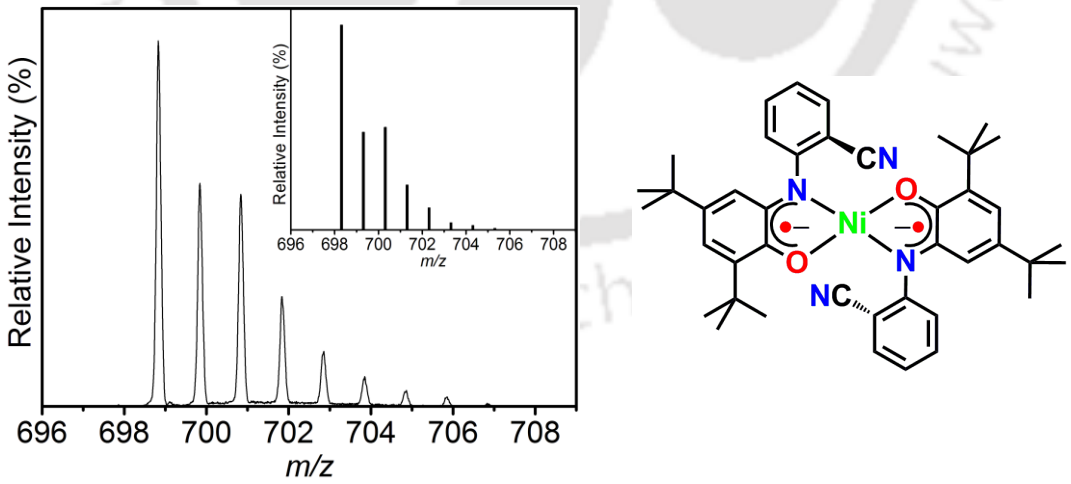

Figure 2.30: *ESI–mass spectrum of [NiL$^{CN\bullet}_2$] in +ve mode; experimental and simulated isotopic distribution pattern (inset).*

ESI–MS (+ve) for the complex in acetonitrile solution showed a 100% molecular ion peak at *m/z* = 698.82. Isotope distribution pattern indicated **$C_{42}H_{48}N_4NiO_2$** as the composition of the complex [**NiL$^{CN\bullet}_2$**]; (**7**) (**Figure 2.30**).

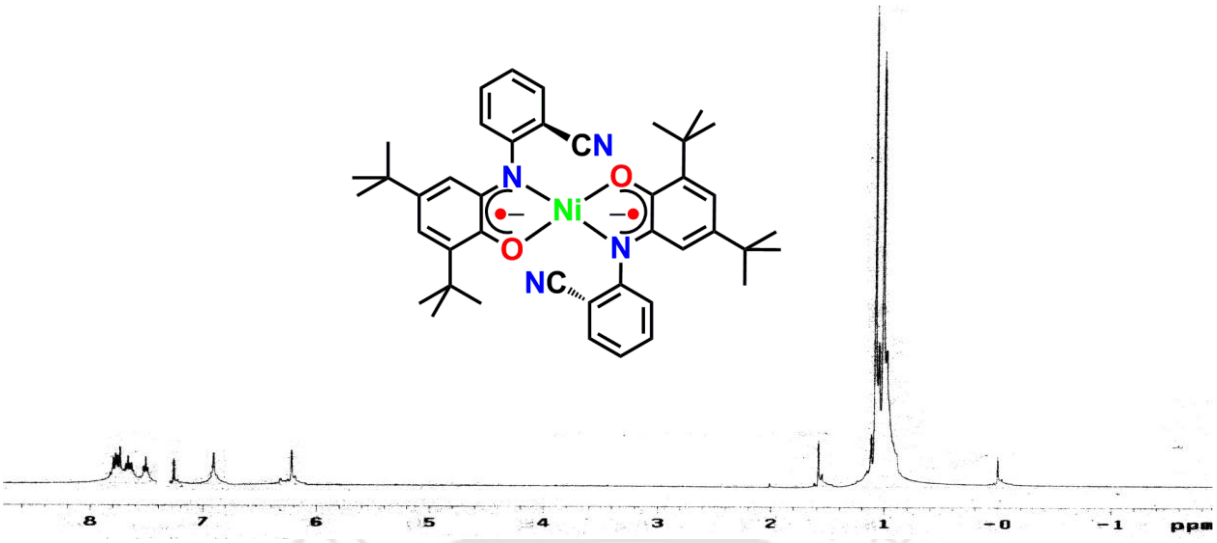

Figure 2.31: *^{1}H NMR spectrum of [**NiL**$^{CN\bullet}{}_2$]; (7).*

The complex [**NiL**$^{CN\bullet}{}_2$]; (**7**) was diamagnetic experiencing an antiferromagnetic coupling between two π–radicals (*vide infra*). The diamagnetic nature was confirmed by ^{1}H NMR ($CDCl_3$, 399.85 MHz) measurement (**Figure 2.31**). Isomeric shifting values for the ^{1}H NMR of the complex were δ 1.02 (s, 18H, –^{t}Bu), 1.09 (s, 18H, –^{t}Bu), 6.22 (s, 2H), 6.91 (s, 2H), 7.53 (t, J = 7.6 Hz, 2H), 7.62–7.71 (m, 2H)), 7.74–7.81 (m, 4H).

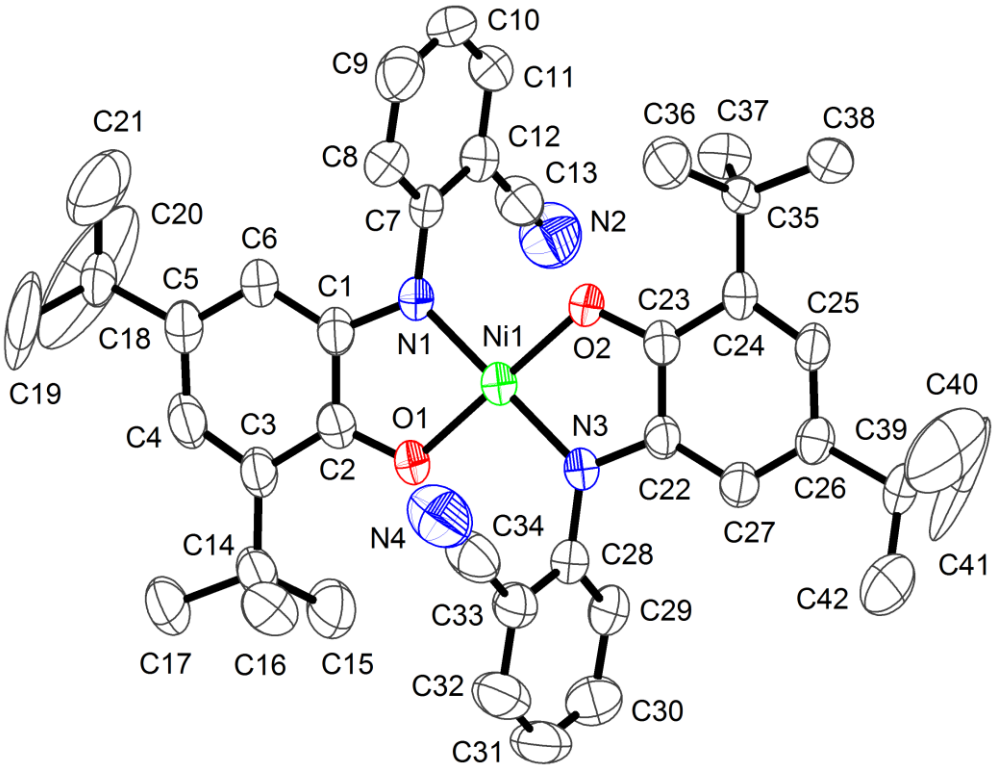

Figure 2.32: *ORTEP view of complex [**NiL**$^{CN\bullet}{}_2$]; (7) thermal ellipsoids were drawn at 50% probability level. H atoms were omitted for clarity.*

A green color needle shaped crystalline solid was obtained by slow solvent evaporation of CH_2Cl_2–CH_3CN (3:1) solvent mixture of the complex. X–ray single crystal diffraction measurements have been performed at 296 K. ORTEP view of complex **[NiL$^{CN\bullet}_2$]** is shown in **Figure 2.32**. Selected bond distances and bond angles are presented in **Table 2.9**, and **Table 2.10**, respectively.

The neutral complex crystallized in the monoclinic system, space group $P12_1/c1$, where each unit cell contained four individual molecules. Crystal structure exhibited the four coordination nature of the central Ni atom sitting in a N2O2 coordination sphere. Two deprotonated N, O donor chelate ligands bound with Ni atom in *trans* fashion. The N1–Ni1–1N3 and O1–Ni1–O2 bond angles were almost equal to 180° (τ_4 = 0°).[50] Thus, the geometry around the Ni atom was a square planar one. The bond distances at Ni1–O1, Ni1–O2, Ni1–N1, and Ni1–N3 were 1.834(3), 1.833(3), 1.837(4), and 1.836(4) Å, respectively, and were good in agreement with the +II oxidation state of the Ni atom.[30*a*,45*a*] The C1–N1, C22–N3, C2–O1, and C23–O2 bond distances were 1.361(5), 1.357(5), 1.317(5), and 1.312(5) Å, respectively. These bond distances indicated a partial double bond character of the coordinating units. In the *tert*–butyl groups–containing phenyl rings, an alternating four long and two short bond distances were observed (**Table 2.9**). These strongly indicated that the coordinating ligand exist in its one–electron oxidized π–radical anion form.[30*a*,45*a*] Thus, the complex should be a diradical–coordinated neutral square planar one.

Table 2.9: *Selected bond distances for complex [**NiL**$^{CN\bullet}_2$] are listed below.*

Ni1–N1	1.837(4	Ni1–N3	1.836(4)
Ni1–O1	1.834(3)	Ni1–O2	1.833(3)
N1–C1	1.361(5)	N3–C22	1.357(5)
N1–C7	1.416(5)	N3–C28	1.417(5)
C2–O1	1.317(5)	C23–O2	1.312(5)
C1–C2	1.428(6)	C22–C23	1.429(6)
C2–C3	1.418(6)	C23–C24	1.435(6)
C3–C4	1.367(6)	C24–C25	1.376(6)
C4–C5	1.427(6)	C25–C26	1.425(6)
C5–C6	1.365(6)	C26–C27	1.369(5)
C6–C1	1.407(6)	C27–C22	1.409(6)
C7–C8	1.373(6)	C28–C29	1.384(6)
C8–C9	1.379(6)	C29–C30	1.394(6)
C9–C10	1.364(7)	C30–C31	1.360(7)
C10–C11	1.358(7)	C31–C32	1.370(7)
C11–C12	1.386(7)	C32–C33	1.391(6)
C12–C7	1.386(6)	C33–C28	1.394(6)
C12–C13	1.441(8)	C33–C34	1.442(8)
C13–N2	1.152(7)	C34–N4	1.152(7)

Table 2.10: *Selected bond angles for [**NiL**$^{CN\bullet}_2$] are given below.*

O1–Ni1–O2	179.51(14)	O1–Ni1–N1	85.38(15)
O1–Ni1–N3	94.42(15)	O2–Ni1–N1	94.77(15)
O2–Ni1–N3	85.43(15)	N3–Ni1–N1	179.78(17)

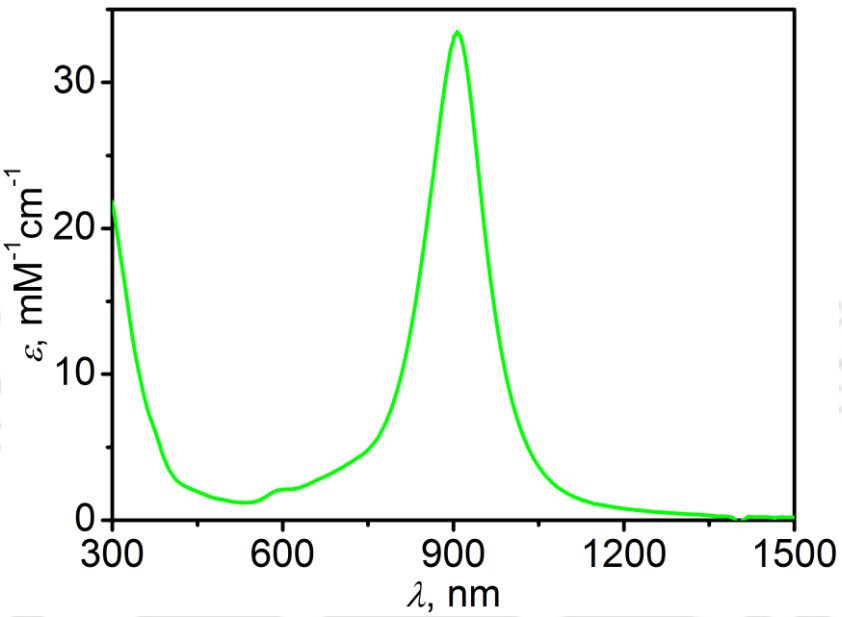

Figure 2.33: *UV–vis/NIR spectrum of [**NiL**$^{CN\bullet}_2$].*

Electronic absorption spectrum for the neutral complex **[NiL$^{CN\bullet}_2$]** was recorded in dichloromethane solution and presents in **Figure 2.33**. The spectrum showed a strong absorption band at λ_{max} = 902 nm for ligand–to–ligand charge transfer (LLCT) dominated in the spectrum.[30*a*,51]

2.7: Synthesis and Characterization of the Square Planar Cu(II) Complex, [CuL$^{CN\bullet}_2$]; (8) Formed with Ligand H_2L^{CN}:

Complex [**CuL$^{CN\bullet}_2$**] was synthesized in 58% yield by reacting 2:1 **H_2L^{CN}**:$CuCl_2\bullet 2H_2O$ in acetonitrile in the presence of Et_3N under air.

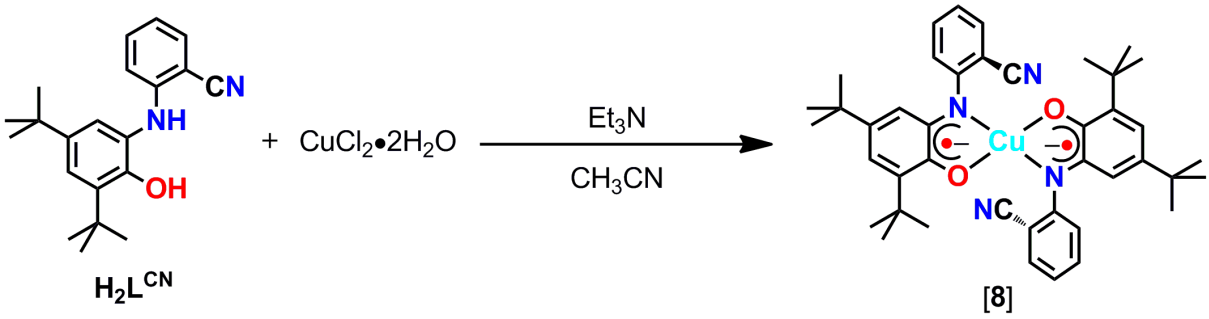

Scheme 2.16: *Synthetic route for [**CuL$^{CN\bullet}_2$**]; **8**.*

The IR spectrum of the complex showed the *tert*–butyl stretching frequencies along with the characteristic ν(C≡N) band at 2957, 2907, 2868 cm^{-1} and 2223 cm^{-1}, respectively. Furthermore, characteristic band for the ν(O–H) and ν(N–H) stretches which have been observed in the free ligand were not found in complex IR spectrum. These indicated the coordination of the units in their deprotonated O^- and N^- form in the corresponding copper complex. The sharp stretching frequencies at 1584 and 1479 cm^{-1} were attributed to the ν(C=N) and ν(C⋯O) of the iminosemiquinone ($ISQ^{\bullet 1-}$) anion form of the coordinated ligands.[52] The ν(C=C) stretching frequency in the C_6–aryl rings appeared at 1566 and 1518 cm^{-1}.

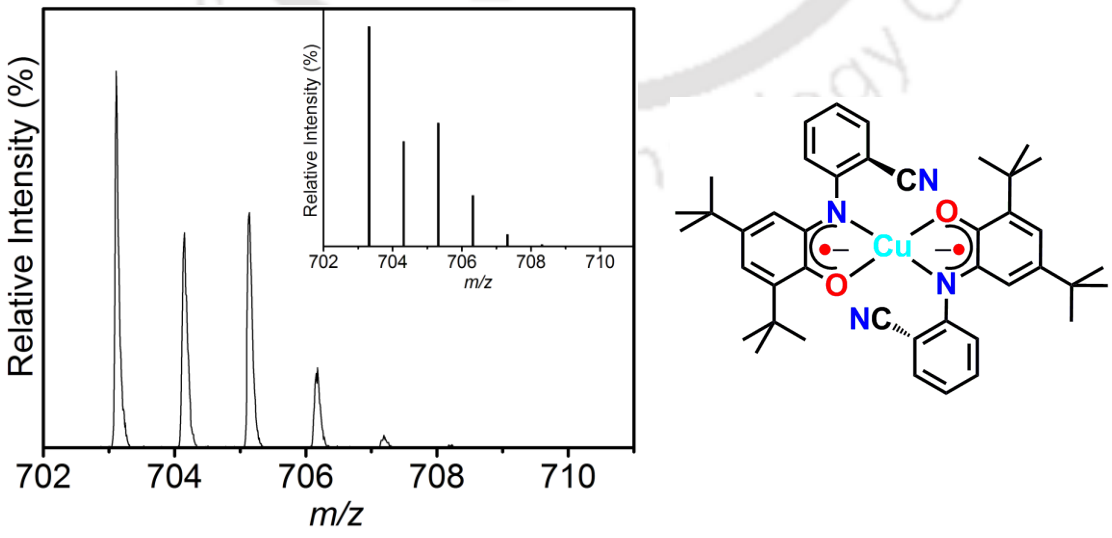

Figure 2.34: *ESI–mass spectrum of [**CuL$^{CN\bullet}_2$**]; (**8**) in +ve mode; experimental and simulated isotope distribution pattern (inset).*

The ESI–MS (+) in acetonitrile for the complex showed a 100% molecular ion peak at *m/z* = 703.12. Isotope distribution pattern indicated $\mathbf{C_{42}H_{48}CuN_4O_2}$ as the composition of the complex [$\mathbf{CuL^{CN\bullet}_2}$]; (**8**) (**Figure 2.34**).

X–ray quality single crystal of the complex was grown from a CH_2Cl_2:CH_3CN (3:1) solvent mixture by slow solvent evaporation technique. ORTEP diagram of the complex is shown in **Figure 2.35**. Selected bond distances and bond angles are presented in **Table 2.11**, and **Table 2.12**, respectively.

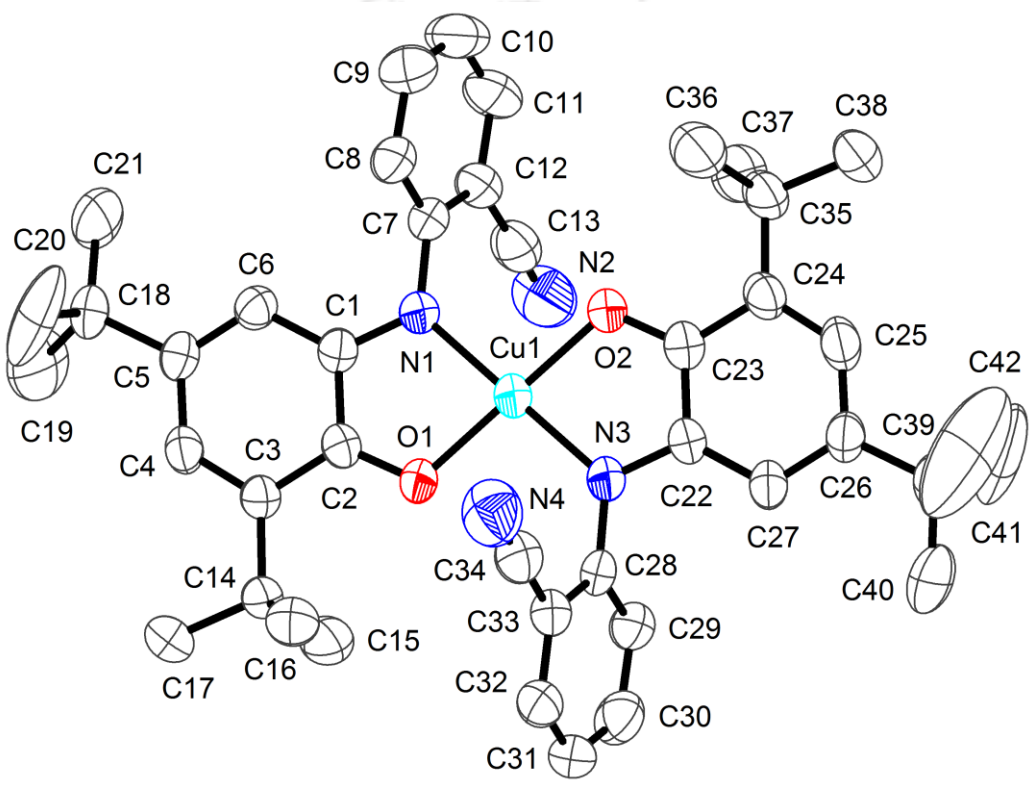

Figure 2.35: *ORTEP diagram of complex [**CuL$^{CN\bullet}_2$**]; (**8**) was shown at 50% probability level. H atoms were omitted for clarity.*

The neutral complex **[CuL$^{CN\bullet}_2$]** crystallized in monoclinic system, space group $P12_1/c1$. Four individual molecules constituted a unit cell. In each molecule, two bidentate (N,O donors) ligands formed two five–member chelate rings with Cu atom in a square planar geometry (τ_4 = 0.01),[53] where the coordinating N, O atoms and –CN group were situated *trans* to each other. The O1–Cu1–O2 and N1–Cu1–N3 bond angles were 178.75° and 179.44°, respectively. The average Cu–O and Cu–N bond distances were 1.914±0.002 Å and 1.929±0.005 Å, respectively. These bond distances were in solidarity with the +II oxidation state of the central Cu1 atom.[30a,54] The average C–N and C–O bond distances for the chelating unit in amidophenolate moiety were 1.350 Å and 1.297 Å, respectively. These bond

distances were corroborating neither with their respective single bond nor their respective double bond characters, rather, they existed in between their single bond and double bond characters. Furthermore, alternating four long bond distances and two short bond distances were observed in the *tert*–butyl groups–containing phenyl rings. The respective C3–C4, C5–C6, C24–C25 and C26–C27 bond distances were 1.371(6), 1.359(5), 1.374(6) and 1.366(6) Å, while, the other two C–C bond distances (**Table 2.11**) in the *tert*–butyl groups attached phenyl rings were in the range of 1.43±0.02 Å. The observed bond distances in the *tert*–butyl attached phenyl rings indicated a quinoid–type distortion and hence, the loss of aromaticity *i.e.* the coordinating ligands exist in their one–electron oxidized form ($ISQ^{\bullet 1-}$)[14,38,55] of the ligand was evidenced. Thus, the complex was a neutral diradical–containing square planar one.

Table 2.11: *Selected bond distances for complex [**CuL**$^{CN\bullet}_2$] are listed below.*

Cu1–N1	1.934(4)	Cu1–N3	1.924(4)
Cu1–O1	1.912(3)	Cu1–O2	1.916(3)
N1–C1	1.350(5)	N3–C22	1.350(5)
N1–C7	1.413(5)	N3–C28	1.413(6)
C2–O1	1.300(5)	C23–O2	1.294(5)
C1–C2	1.449(6)	C22–C23	1.447(6)
C2–C3	1.439(5)	C23–C24	1.426(6)
C3–C4	1.371(6)	C24–C25	1.374(6)
C4–C5	1.426(6)	C25–C26	1.417(6)
C5–C6	1.359(5)	C26–C27	1.366(6)
C6–C1	1.414(6)	C27–C22	1.418(6)
C7–C8	1.382(6)	C28–C29	1.370(6)
C8–C9	1.380(7)	C29–C30	1.387(7)
C9–C10	1.381(7)	C30–C31	1.384(7)
C10–C11	1.372(7)	C31–C32	1.359(7)
C11–C12	1.393(7)	C32–C33	1.375(6)
C12–C7	1.401(6)	C33–C28	1.405(6)
C12–C13	1.430(8)	C33–C34	1.430(8)
C13–N2	1.155(7)	C34–N4	1.153(7)

Table 2.12: *Selected bond angles for [**CuL**$^{CN\bullet}_2$] are given below.*

O1–Cu1–O2	178.75(14)	O1–Cu1–N1	83.59(13)
O1–Cu1–N3	96.33(14)	O2–Cu1–N1	96.77(14)
O2–Cu1–N3	83.32(14)	N3–Cu1–N1	179.44(16)

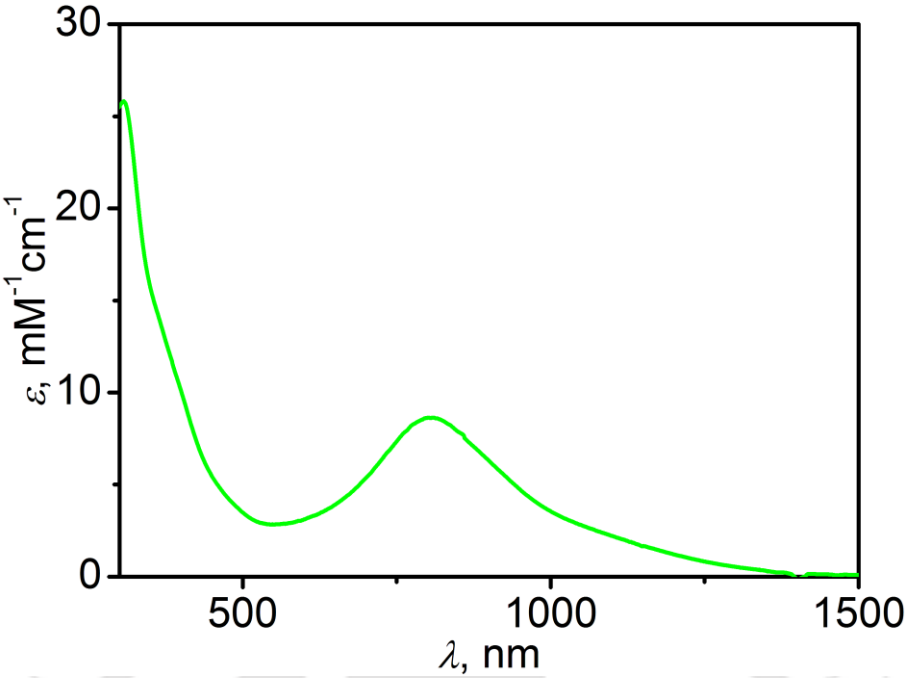

Figure 2.36: *UV–vis/NIR spectrum of complex [**CuL**$^{CN\bullet}{}_2$]; (**8**).*

UV–vis/NIR spectrum of the complex **[CuL$^{CN\bullet}{}_2$]** showed strong intra–ligand charge transfer (ILCT) absorption band at λ_{max} = 1015 nm (ε = 3300 $M^{-1}cm^{-1}$)[54] and a moderately sharp absorption band at λ_{max} = 803 nm (ε = 8650 $M^{-1}cm^{-1}$) due to the ligand–to–ligand charge transfer (LLCT).[14] The absorption band at λ_{max} = 360 nm (ε = 14500 $M^{-1}cm^{-1}$) was due to the ligand–to–metal charge transfer (LMCT).[54]

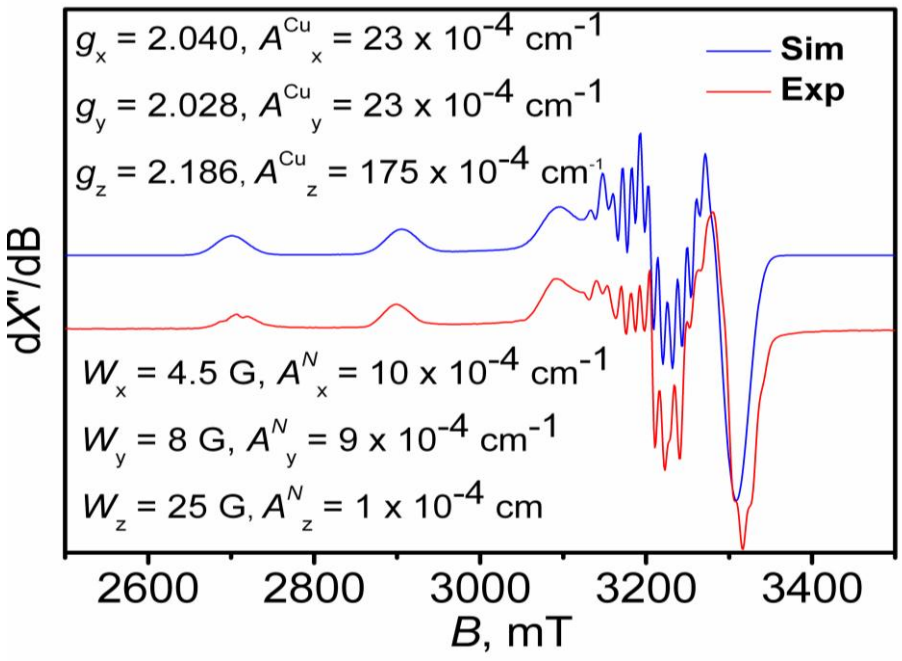

Figure 2.37: *X–band EPR spectrum of complex [**CuL**$^{CN\bullet}{}_2$]; (**8**).*

X–band EPR spectrum and simulation spectrum of the experimental results of complex is shown in **Figure 2.37**. Simulation of the experimental results provided following parameters; g_x = 2.040, g_y = 2.028, g_z = 2.186, W_x = 4.5 G, W_y = 8 G, W_z = 25 G, A_x = $23*10^{-4}$ cm^{-1}, A_y = $23*10^{-4}$ cm^{-1}, A_z = $175*10^{-4}$ cm^{-1}. From the spectrum pattern and simulation results, it was confirmed that the unpaired electron was residing on the Cu(II) center, and two ligand–center π–radicals were strongly antiferromagnetically coupled and higher in magnitude compared to a radical and Cu(II) ion (S = ½; $d_x2_{-y}2$).[14]

2.8: Conclusions:

1a. Ligand $\mathbf{H_2L^{CN}}$ and $\mathbf{H_2L^{OMe}}$ (*o*–substituent having weak coordination property) react with $VOSO_4 \bullet 5H_2O$ in the presence of triethylamine provided a triradical–containing tetranuclear oxo–V(IV) cluster *via* ligand centered C–N bond breaking and C–O bond making.

1b. Presence of weak coordinating substituent at the –*ortho* carbon atom to the aniline moiety of ligand 2–Anilino–4,6–di–*tert*–butylphenol [$\mathbf{H_2AP^H}$] was essential for the activation of vanadium center and thereafter ligand centered C–N bond breaking and C–O bond making processes.

2. By varying metal ion concentration and base concentration to the ligand $\mathbf{H_2L^{OMe}}$, a tetraradical–containing octanuclear mixed valence vanadium cluster was synthesized. Herein, it was found that in the presence of excess amount of vanadium salt and base triethylamine one of the semiquinone moieties oxidized to its two–electron oxidized quinone form. This quinone moiety being a week ligand was replaced by oxide units.

3a. The ligand $\mathbf{H_2L^{CN}}$ reacted with $MnCl_2 \bullet 4H_2O$ provides a highly fluorescent phenoxazine derivative. In this process, initially a Mn(III) complex coordinated to two π–radical anions was formed. This diradical–species then acted as catalyst and oxidized the $\mathbf{H_2L^{CN}}$ ligand to its two–electron oxidized $\mathbf{L^{CNQ}}$ form, which upon cyclization provided the fluorescent compound.

3b. The fluorescent compound bound with ct–DNA and enhanced its fluorescent behavior. Hence, it behaved as a ct–DNA sensor.

4. The ligand provided square pyramidal diradical–containing Co(III) complex and square planar Ni(II) and Cu(II) complexes. In all cases a strong antiferromagnetic coupling between the two radicals prevailed.

References:

1. (*a*) C. G. Pierpont and R. M. Buchanan, *Coord. Chem. Rev.*, 1981, **38**, 45; (*b*) C. G. Pierpont and C. W. Lange, *Progr. Inorg. Chem.*, 1994, **41**, 331; (*c*) K. D. Karlin and E. I. Stiefel, *Progr. Inorg. Chem.*, 2004, **52**; (*d*) A. L. Balch and R. H. Holm, *J. Am. Chem. Soc.*, 1966, **88**, 5201; (*e*) A. I. Poddel'sky, V. K. Cherkasov and G. A. Abakumov, *Coord. Chem. Rev.*, 2009, **253**, 291; (*f*) S. Sproules and K. Wieghardt, *Coord. Chem. Rev.*, 2010, **254**, 1358.

2. (*a*) T. Wada, J. T. Muckerman, E. Fujita and K. Tanaka, *Dalton Trans.*, 2011, **40**, 2225; (*b*) I. A. Koval, P. Gamez, C. Belle, K. Selmeczib and J. Reedijk, *Chem. Soc. Rev.*, 2006, **35**, 814; (*c*) S. Shekar and S. N. Brown, *Dalton Trans.*, 2014, **43**, 3601.

3. (*a*) V. K. Cherkasov, G. A. Abakumov, E. V. Grunova, A. I. Poddel'sky, G. K. Fukin, E. V. Baranov, Yu. A. Kurskii and L. G. Abakumova, *Chem. Eur. J.*, 2006, **12**, 3916; (*b*) P. Chaudhuri, M. Hess, K. Hildenbrand, E. Bill, T. Weyhermüller and K. Wieghardt, *Inorg. Chem.*, 1999, **38**, 2781; (*c*) G. Szigethy, D. W. Shaffer and A. F. Heyduk, *Inorg. Chem.*, 2012, **51**, 12606; (*d*) E. Bill, E. Bothe, P. Chaudhuri, K. Chlopek, D. Herebian, S. Kokatam, K. Ray, T. Weyhermüller, F. Neese and K. Wieghardt, *Chem. Eur. J.*, 2005, **11**, 204.

4. (*a*) J. A. McCleverty and M. D. Ward, *Proc. Indian Acad. Sci.* (*Chem. Sci.*), 2002, **114**, 291; (*b*) E. Broclawik, A. Stępniewski and M. Radoń, *J. Inorg. Biochem.*, 2014, **136**, 147.

5. (*a*) K. Range, I. Ayala, D. York and B. A. Barry, *J. Phys. Chem. B*, 2006, **110**, 10970; (*b*) W. L. Smith, T. E. Eling, R. J. Kulmacz, L. J. Marnett and A. Tsaii, *Biochemistry*, 1992, **31**, 3; (*c*) B. A. Barry and O. Einarsdóttir, *J. Phys. Chem. B*, 2005, **109**, 6972.

6. J. T. Groves, *PNAS*, 2003, **100**, 3569.

7. P. Basua and S. J.N. Burgmayer, *Coord. Chem. Rev.*, 2011, **255**, 1016.

8. A. Y. Lyubimov, K. Heard, H. Tang, N. S. Sampson and A. Vrielink, *Prot. Sci.*, 2007, **16**, 2647.

9. Y. Shimazaki, *Advances in Materials Physics and Chemistry*, 2013, **3**, 60.

10. H. C. Zhao, B.–L. Fu, D. Schweinfurth, J. P. Harney, B. Sarkar, M.–K. Tsai and J. Rochford, *Eur. J. Inorg. Chem.*, 2013, 4410.

11. K. Ray, T. Petrenko, K. Wieghardt and F. Neese, *Dalton Trans.*, 2007, 1552.

12. H. Chun, C. N. Verani, P. Chaudhuri, E. Bothe, E. Bill, T. Weyhermüller and K. Wieghardt, *Inorg. Chem.*, 2001, **40**, 4157.

13. P. J. Chirik and K. Wieghardt, *Science*, 2010, **327**, 794.

14. C. Mukherjee, U. Pieper, E. Bothe, V. Bachler, E. Bill, T. Weyhermüller and P. Chaudhuri, *Inorg. Chem.*, 2008, **47**, 8943.

15. (*a*) G. W. C. Silva, C. B. Yeamans, P. F. Weck, J. D. Hunn, G. S. Cerefice, A. P. Sattelberger and K. R. Czerwinski, *Inorg. Chem.*, 2012, **51**, 3332; (*b*) http://elearning2.uniroma1.it/pluginfile.php/60235/mod_resource/content/1/IR%20chart.pdf.

16. (*a*) D. L. Pavia, G. M. Lampman, G. S. Kriz and J. R. Vyvyan, *Introduction to Spectroscopy*, 4th edition. 31–34; (*b*) P. K. Kipkemboi, P. C. Kiprono and J. J. Sanga, *Bull. Chem. Soc. Ethiop.*, 2003, **17**, 211.

17. C. Addicott, P. V. Bernhardt and C. Wentrup. *ARKIVOC*, 2009 (vi) 30–37.

18. R. A. Meyers (Ed.) *Analytical Chemistry*, pp. 10815–10837.

19. P. Chaudhuri and K. Wieghardt, *Prog. Inorg. Chem.*, 2001, **50**, 151.

20. (*a*) M. R. Maurya, C. Haldar, A. Kumar, M. L. Kuznetsov, F. Avecilla and J. C. Pessoa, *Dalton Trans.*, 2013, **42**, 11941; (*b*) M. R. Maurya, *Coord. Chem. Rev.*, 2003, **237**, 163; (*c*) M. R. Maurya, M. Bisht, A. Kumar, M. L. Kuznetsov, F. Avecilla and J. C. Pessoa, *Dalton Trans.*, 2011, **40**, 6968.

21. (*a*) M. Hara, M. Kawamura, J. N. Kondo, K. Domen and K. Maruya, *J. Phys. Chem.*, 1996, **100**, 14462; (*b*) C. Y. Panicker, H. T. Varghese, K. R. Ambujakshan, S. Mathew, S. Ganguli, A. K. Nanda, C. V. Alsenoy and S. M. Yohannan, *Chem. Eur. J.*, 2010, **1**, 37.

22. (*a*) R. Farrmann, S. Boghosian, G. N. Papatheodorou, K. Nielsen, R. W. Berg and N. J. Bjerrum, *Inorg. Chem.*, 1989, **28**, 1849; (*b*) M. N. Bhattacharjee, M. K. Chaudhuri and N. S. Islam, *Inorg. Chem.*, 1989, **28**, 2420.

23. (*a*) C. Daniel and H. Hartl, *J. Am. Chem. Soc.*, 2005, **127**, 13978; (*b*) C. Rocchiccioli–Deltcheff, R. Thouvenot and M. Fouassier, *Inorg. Chem.*, 1982, **21**, 30.

24. (*a*) E. Carolina Sañudo, A. A. Smith, P. V. Mason, M. Helliwell, G. Arom and R. E. P. Winpenny, *Dalton Trans.*, 2006, 1981; (*b*) S. R. Cooper, Y. B. Koh and K. N. Raymond, *J. Am. Chem. Soc.*, 1982, **104**, 5092; (*c*) J. Selbin, *Chem. Rev.*, 1965, 65, 153; (*d*) J. Selbin, *Coord. Chem. Rev.*, 1966, **1**, 293.

25. (*a*) H. Chun, P. Chaudhuri, T. Weyhermüller and K. Wieghardt, *Inorg. Chem.*, 2002, **41**, 790; (*b*) C. Mukherjee. T. Weyhermüller, E. Bother and P. Chaudhuri, *Inorg. Chem.*, 2008, **47**, 11620.

26. (*a*) Y.–H. Chang, C.–L. Su, R.–R. Wu, J.–H. Liao, Y.–H. Liu and H.–F. Hsu, *J. Am. Chem. Soc.*, 2011, **133**, 5708; (*b*) M. E. Cass, Greene, D. L. Greene, R. M. Buchanan and C. G. Pierpont, *J. Am. Chem. Soc.*, 1983, **105**, 2680; (*c*) To review: S. N. Brown, *Inorg. Chem.*, 2012, **51**, 1251.

27. (*a*) A. M. Morris, C. G. Pierpont and R. G. Finke, *Inorg. Chem.*, 2009, **48**, 3496; (*b*) M. E. Cass, Greene, D. L. Greene, R. M. Buchanan and C. G. Pierpont, *J. Am. Chem. Soc.*, 1983, **105**, 2680.

28. C. Mukherjee, T. Weyhermüller, E. Bothe and P. Chaudhuri, *C. R. Chim.*, 2007, **10**, 313.

29. A. Müller, M. Penk and J. Döring, *Inorg. Chem.*, 1991, **30**, 4935.

30. (*a*) P. Chaudhuri, C. N. Verani, E. Bill, E. Bothe, T. Weyhermüller and K. Wieghardt, *J. Am. Chem. Soc.*, 2001, **123**, 2213; (*b*) H. Chun, E. Bill, T. Weyhermüller and K. Wieghardt, *Inorg. Chem.*, 2003, **42**, 5612.

31. O. Khan, *in Molecular Magnetism*, VCH, New York, 1993, pp. 199–200.

32. J. R. Anacona, J. Calvo and O. A. Almanza, *International Journal of Inorganic Chemistry*, 2013, **2013**, 7. Article ID 108740, doi:10.1155/2013/108740.

33. (*a*) R. Rulkens, J. L. Male, K. W. Terry, B. Olthof, A. Khodakov, A. T. Bell, E. Iglesia and T. D. Tilley, *Chem. Mater.*, 1999, **11**, 2966; (*b*) M. Sutradhar, G. Mukherjee, M. G. B. Drew and S. Ghosh, *Inorg. Chem.*, 2006, **45**, 5150.

34. (*a*) S. P. Rath, K. K. Rajak and A. Chakravorty, *Inorg. Chem.*, 1999, **38**, 4376; (*b*) J. A. Bonadies, W. M. Butler, V. L. Pecoraro and C. J. Carrano, *Inorg. Chem.*, 1987, **26**, 1218;

(*c*) C. Cordelle, D. Agustin, J.–C. Daran and R. Poli, *Inorg. Chim. Acta.*, 2010, **364**, 144; (*d*) G. Romanowski and T. Lis, *Inorg. Chim. Acta.*, 2013, **394**, 627.

35. (*a*) M. Mahroof–Tahir, A. D. Keramidas, R. B. Goldfarb, O. P. Anderson, M. M. Miller and D. C. Crans, *Inorg. Chem.*, 1997, **36**, 1657; (*b*) A. Kojima, K. Okazaki, S. Ooi and K. Saito, *Inorg. Chem.*, 1983, **22**, 1168.

36. Z. Chi, L. Zhu, X. Lu, H. Yu and B. Liu, *Z. Anorg. Allg. Chem.*, 2012, 1523.

37. (*a*) A. Jana, N. Aliaga–Alcalde, E. Ruiz and S. Mohanta, *Inorg. Chem.*, 2013, **52**, 7732; (*b*) S. K. Dey and A. Mukherjee, *ChemCatChem.*, 2013, **5**, 3533.

38. C. Mukherjee, T. Weyhermüller, K. Wieghardt and P. Chaudhuri, *Dalton Trans.*, 2006, 2169.

39. (*a*) G. A. Abakumov, A. I. Poddel'sky, M. P. Bubnov, G. K. Fukin, L. G. Abakumova, V. N. Ikorskii and V. K. Cherkasov, *Inorg. Chim. Acta.*, 2005, **358**, 3829.

40. (*a*) V. Wintgens, P. Valat, J. Kossanyi, A. Demeter, L. Biczok and T. Berces, *New J. Chem.*, 1996, **20**, 1149; (*b*) B. Ramachandram, G. Saroja, N. B. Sankaran and A. Samanta, *J. Phys. Chem. B*, 2000, **104**, 11824; (*c*) S. Saha and A. Samanta, *J. Phys. Chem. A*, 2002, **106**, 4763.

41. Q.Y. Chen, D.H. Li, Y. Zhao, H.H. Yang, Q.Z. Zhu and J.G. Xu, *Analyst*, 1999, **124**, 901.

42. (*a*) A. Granzhan and H. Ihmels, *Org. Lett.*, 2005, **7**, 5119; (*b*) F. Y. Wu, F. Y. Xie, Y. M. Wu and J. I. Hong, *J. Fluoresc.*, 2008, **18**, 175; (*c*) D. Sahoo, P. Bhattacharya and S. J. Chakravorti, *Phys. Chem. B.*, 2010, **114**, 2044.

43. (*a*) B. F. Ye, Z. J. Zhang and H. X. Ju, *Chin. J. Chem.*, 2005, **23**, 58; (*b*) B. K. Sahoo, K. S. Ghosh, R. Bera and S. Dasgupta, *Chem. Phys.*, 2008, **351**, 163; (*c*) R. Bera, B. K. Sahoo, K. S. Ghosh and S. Dasgupta, *Int. J. Biol. Macromol.*, 2008, **42**, 14; (*d*) R. Ghosh, S. Bhowmik, A. Bagchi, D. Das and S. Ghosh, *Eur. Biophys. J.*, 2010, **39**, 1243.

44. G. A. Abakumov, V. K. Cherkasov, M. P. Bubnov,a L. G. Abakumova, V. N. Ikorskii, G. V. Romanenko and A. I. Poddel´sky, *Russ. Chem. Bull., Int. Ed.*, 2006, **55**, 44.

45. (*a*) E. Bill, E. Bothe, P. Chaudhuri, K. Chlopek, D. Herebian, S. Kokatam, K. Ray, T. Weyhermüller, F. Neese and K. Wieghardt, *Chem. Eur. J.*, 2005, **11**, 204; (*b*) R. K.

Sherwood, C. L. Kent, B. O. Patrickb and W. S. McNeil, *Chem. Commun.*, 2010, **46**, 2456.

46. S. Kundu, S. Maity, A. N. Maity, S.–C. Keb and P. Ghosh, *Dalton Trans.*, 2013, **42**, 4586.

47. (*a*) C. N. Verani, S. Gallert, E. Bill, T.Weyhermüller, K. Wieghardt and P. Chaudhuri, *Chem. Commun.*, 1999, 1747; (*b*) D. Herebian, P. Ghosh, H. Chun, E. Bothe, T. Weyhermüller and K. Wieghardt, *Eur. J. Inorg. Chem.*, 2002, 1957.

48. A. I. Poddel'sky, V. K. Cherkasov, G. K. Fukin, M. P. Bubnov, L. G. Abakumova and G. A. Abakumov, *Inorg. Chim. Acta.*, 2004, **357**, 3632.

49. (*a*) G. Hastings and V. Sivakumar, *Biochemistry*, 2001, **40**, 3681; (*b*) J. Breton, J. Burie, C. Berthomieu, G. Berger and E. Nabedryk, *Biochemistry*, 1994, **33**, 4953.

50. P. Verma, J. Weir, L. Mirica and T. P. D. Stack, *Inorg. Chem.*, 2011, **50**, 9816.

51. (*a*) K. Ray, T. Weyhermüller, F. Neese and K. Wieghardt, *Inorg. Chem.*, 2005, **44**, 5345; (*b*) A. Mukherjee and R. N. Mukherjee, *Indian J. Chem.*, 2011, **504**, 484.

52. H. Suzuki, M.A. Nagasaka, M. Sugiura and T. Noguchi, *Biochemistry*, 2005, **44**, 11323.

53. S. Hong, L. M. R. Hill, A. K. Gupta, B. D. Naab, J. B. Gilroy, R. G. Hicksb, C. J. Cramera and W. B. Tolman, *Inorg. Chem.*, 2009, **48**, 4514.

54. S. Ye, B. Sarkar, F. Lissner, T. Schleid, J. van Slageren, J. Fiedler and W. Kaim, *Angew. Chem., Int. Ed.*, 2005, **44**, 2103.

55. (*a*) C. Mukherjee, T. Weyhermüller, E. Bothe, E. Rentschler and P. Chaudhuri, *Inorg. Chem.*, 2007, **46**, 9895; (*b*) C. Mukherjee, T. Weyhermüller, E. Bothe and P. Chaudhhuri, *Inorg. Chem.*, 2008, **47**, 2740; (*c*) P. Chaudhuri, E. Bill, R. Wagner, U. Pieper, B. Biswas and T. Weyhermüller, *Inorg. Chem.*, 2008, **47**, 5549.

भारतीय प्रौद्योगिकी संस्थान गुवाहाटी
Indian Institute of Technology Guwahati

Chapter III

*A Tridentate Ligand Combined of a Non–Innocent Core 2–Aminophenol and a Substrate Core Benzylamine and Its Corresponding Co(III), Ni(II), and Cu(II) Complexes: Synthesis, Characterization, and Reactivity**

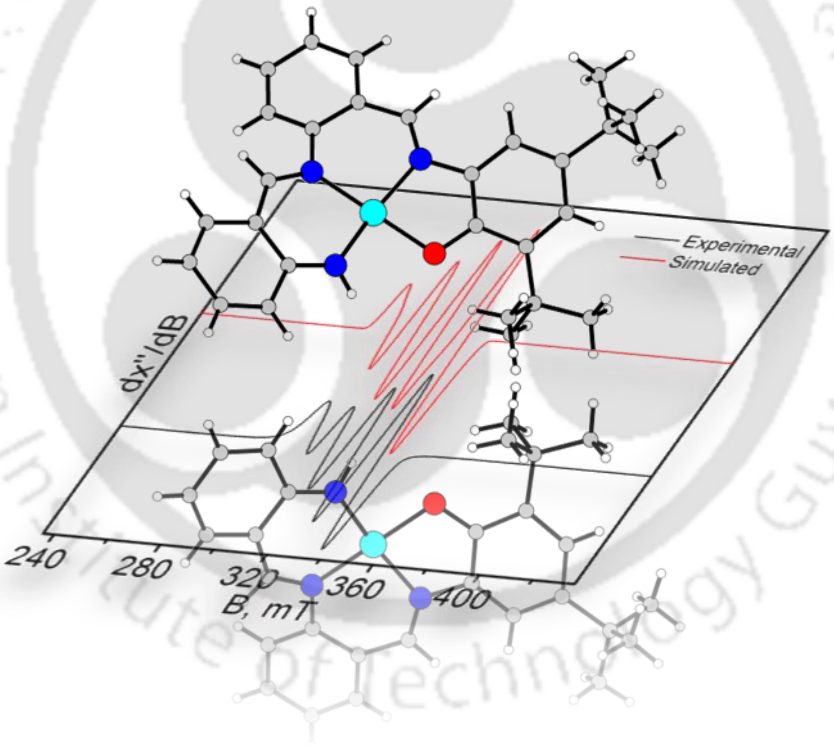

*some results have been published;

1. ***Chem. Asian J.*, 2014, *DOI:10.1002/asia.201402868R1.***

3.1: Introduction:

Organic moieties containing at least one π–radical and coordinated to a metal ion, especially transition metal ion, have achieved great importance to the synthesis of catalysts for metal complex–catalyzed organic small molecules oxidation reactions, for example, oxidation of primary alcohols to aldehydes, catechol to quinone, primary amines to aldehydes, etc.[1] The advantage of having π–radical in a molecule is the easy acceptance of electron from substrates. In this note, the syntheses of redox–active organic compounds, known as non–innocent ligands, and their corresponding transition metal complexes as catalysts have drawn considerable attention of chemists.[1,2] Enzymatic reactions are specific and selective[3] and therefore, the design of catalysts, *i.e.*, radical–containing transition metal complexes, is often influenced by the structure of either active site or radical–containing intermediate of metalloeznyzes.[1,2] Furthermore, aerial oxidation could also be performed using those catalysts.

Copper–containing Amine Oxidases (AOs)[4] catalyzes oxidation of primary amines to their corresponding aldehydes with concomitant production of one equivalent of ammonia and hydrogen peroxide. The active site of the primary amine oxidase contains a Cu(II) ion which is surrounded by three histidine imidazole units and a closely located topa quinone organic cofactor.[4] The topa quinone part accepts two electrons from an amine substrate and oxidizes amine to aldehyde in the presence of water. The reduced topa quinone, which undergoes to aminoquinol form, is reoxidized to its initial quinone form by molecular oxygen (air).[4d] Therefore, for the design of catalysts for the oxidation of primary amines to the corresponding aldehydes, Cu(II)–quinone complexes would be ideal. However, the synthesis of Cu(II) complex coordinated to a quinone moiety is a highly challenging task as Cu(II)–quinone complex will not be very stable due to weak coordination property of quinone moiety and will succumb to easy decomposition. Furthermore, reoxidation of catecholate^{2-} form, coordinated to a Cu(II) ion, to its two–electron oxidized *o*–quinone^{0} form by aerial oxygen would not be convenient. Therefore, Cu(II)–quinone complexes can rarely be used for the amine oxidation process. However, radical–containing Mn(IV) complex,[5] or *in situ* generated radical–Cu(II) complexes,[4c,6] as proposed, have previously used as catalysts for the oxidation of primary amines. In addition, Fe(III), Cu(I), and Cu(II) salts with additive organic radical, TEMPO, have used as catalysts for the aerial oxidation of primary, secondary amine and anilines.[7] It is to note that well defined π–radical–coordinated Cu(II) complex as functional model for primary amine oxidases is unknown. Hence, we have initially attempted

to understand the oxidation–mechanism of primary amines by employing a π–radical–containing Cu(II) complex for the betterment in designing of amine–oxidation catalysts.

2–Anilino–4,6–di–*tert*–butylphenol is a non–innocent ligand and provides a radical–containing Cu(II), Ni(II), Co(III) complexes. Incorporation of a $–CH_2NH_2$ group at the *–ortho* position to the aniline moiety of the ligand would provide a new non–innocent ligand $\mathbf{H_4L^{CH_2NH_2}}$ (**Scheme 3.1**). This ligand would be a combination of benzylamine, the substrate part, and 4,6–di–*tert*–butyl–2–aminophenol, the radical generating part (**Scheme 3.1**). The ligand $\mathbf{H_4L^{CH_2NH_2}}$ provided diradical–coordinated octahedral Co(III) complex; **9**, and a ligand backbone modified distorted square planar Ni(II); **10**, and Cu(II); **11**, complexes. Synthesis of Ni(II) complex under aerobic condition, the ligand should provide a diradical–coordinated square planar Ni(II) complex, that further underwent to aryl migration to generate the Ni(II) complex. Synthesis of Cu(II) complex under air employing the ligand should provide a π–radical–coordinated Cu(II) complex with aldehyde as the *–ortho* substituent due to the oxidation of $–CH_2NH_2$ group. Thereafter, the mechanistic study of the Cu(II) complex formation would get insight the primary amine oxidation process and consequently, would facilitate the design of π–radical–coordinated Cu(II) complexes as functional models for primary amine oxidation.

Furthermore, the formation of complexes **10**, and **11** where a complete modification of the new ligand propagated *via* a rearrangement in the position of 2,4–di–*tert*–butylphenol unit from the aniline part of the ligand to the benzylamine part. Therefore, to understand the modification as well as the rearrangement paths ligand $\mathbf{H_3L1}$ and $\mathbf{H_4L2}$ have also been synthesized (**Scheme 3.1**). The ligand $\mathbf{H_4L2}$ is the geometrical isomer of $\mathbf{H_4L^{CH_2NH_2}}$, while, $\mathbf{H_3L1}$ is the two–electron oxidized (amine to imine) form of $\mathbf{H_4L2}$. Interesting, both ligands $\mathbf{H_3L1}$, and $\mathbf{H_4L2}$ reacted with $CuCl_2 \bullet 2H_2O$ in the presence of Et_3N under air and provided complex **11** (**Scheme 3.1**). Similar type result was also obtained in case of Ni(II) complex.

In this chapter, Co, Ni, and Cu complexes using of $\mathbf{H_4L^{CH_2NH_2}}$, $\mathbf{H_3L1}$ and $\mathbf{H_4L2}$ ligands will be described. Furthermore, it has been noticed that ligand $\mathbf{H_3L1}$ reacted with salicylaldehyde only in the presence of Lewis acidic Zn(II) ion and provided fluorescent dinuclear complex. The synthesis and characterization of the complex is also described in this chapter.

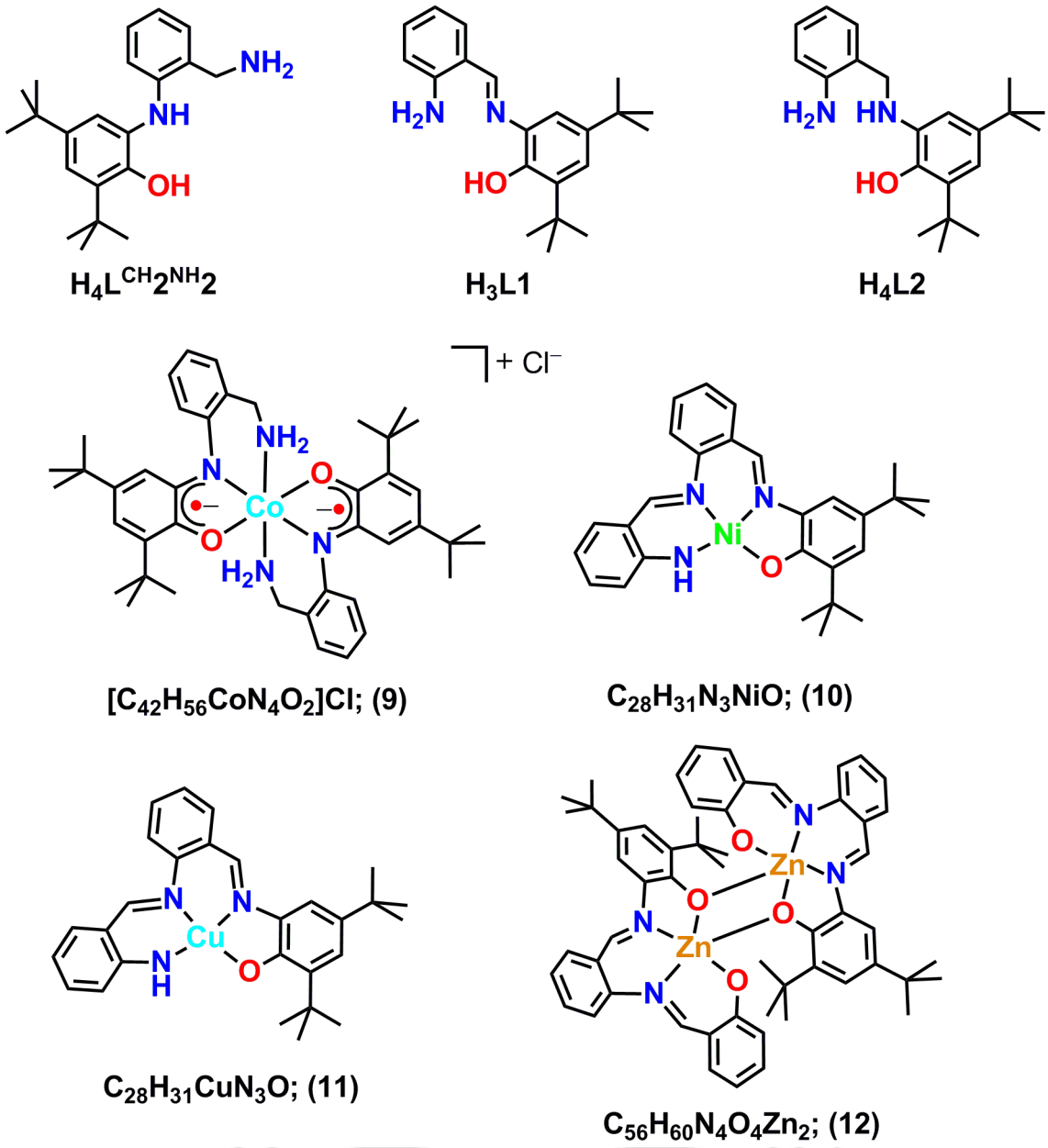

Scheme 3.1: *Different tridentate ligands and the metal complexes formed by using the ligands.*

- (a)**{[$C_{42}H_{56}CoN_4O_2$]Cl}•CH_3CN•H_2O**; (**9•CH_3CN•H_2O**)
- (b) **[$C_{28}H_{31}N_3NiO$]**; (**10**)
- (c) **[$C_{28}H_{31}CuN_3O$]**; (**11**)
- (d) **[$C_{56}H_{60}N_4O_4Zn_2$]**; (**12**)

3.2: Characterization of Tridentate Ligands:

The ligand $\mathbf{H_4L^{CH_2NH_2}}$ was synthesized from ligand $\mathbf{H_2L^{CN}}$ by reduction of –CN group using $LiAlH_4$ in dry THF in good yield (70%) (**Scheme 3.2**). The condensation of 2–aminobenzylamine with an equivalent amount of 3,5–di–*tert*–butyl–1,2–benzoquinone in absolute ethanol provided ligand $\mathbf{H_3L1}$ (yield: 35%). Reduction of $\mathbf{H_3L1}$ by $NaBH_4$ yielded 40% $\mathbf{H_4L2}$ (**Scheme 3.2**).

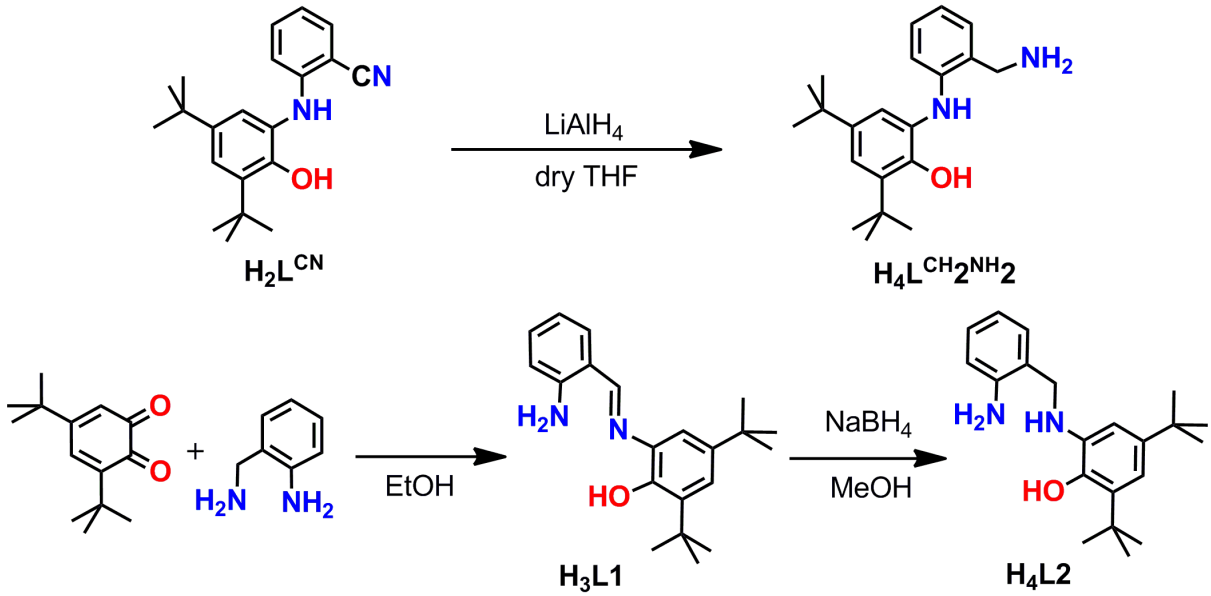

Scheme 3.2: *Synthetic route for different tridentate ligands.*

Infrared (IR) spectrum of $\mathbf{H_2L^{CN}}$ showed two distinct bands at 3421 and 3354 cm^{-1} due to ν(O–H) and ν(N–H) vibrational stretches. The characteristic –CN stretching band was found at 2221 cm^{-1}. In the reduced form of $\mathbf{H_2L^{CN}}$ *i.e.* in ligand $\mathbf{H_4L^{CH_2NH_2}}$, no band for –CN group appeared, additionally, two new bands arose at 3293 and 3195 cm^{-1} due to the generation of $–NH_2$ functional group. In the spectrum of $\mathbf{H_3L1}$, band at 3476 cm^{-1} appeared for ν(O–H). The bands at 3423 and 3323 cm^{-1} were due to respective asymmetric and symmetric ν(N–H) stretches of aniline $–NH_2$ group. The band at 1617 cm^{-1} appeared for ν(C=N) stretch and confirmed the condensation process. The ligand $\mathbf{H_4L2}$ showed ν(O–H) stretch at 3450 cm^{-1} and the bands at 3361, 3320 cm^{-1} were due to respective asymmetric and symmetric ν(N–H) stretches of aniline $–NH_2$ functional group. The appearance of a new band at 3240 cm^{-1} was due to ν(N–H) stretching of the secondary amine and confirmed the reduction of imine to amine. The absence of 1617 cm^{-1} band in the IR spectrum of $\mathbf{H_4L2}$ further confirmed the reduction of imine to amine. The asymmetric, overtone, and symmetric

ν(C–H) stretches for the *tert*–butyl groups appeared nearly at the same region, 2957–2863 cm^{-1}, respectively, for **$H_4L^{CH_2NH_2}$**, **H_3L1**, and **H_4L2**.

[A]

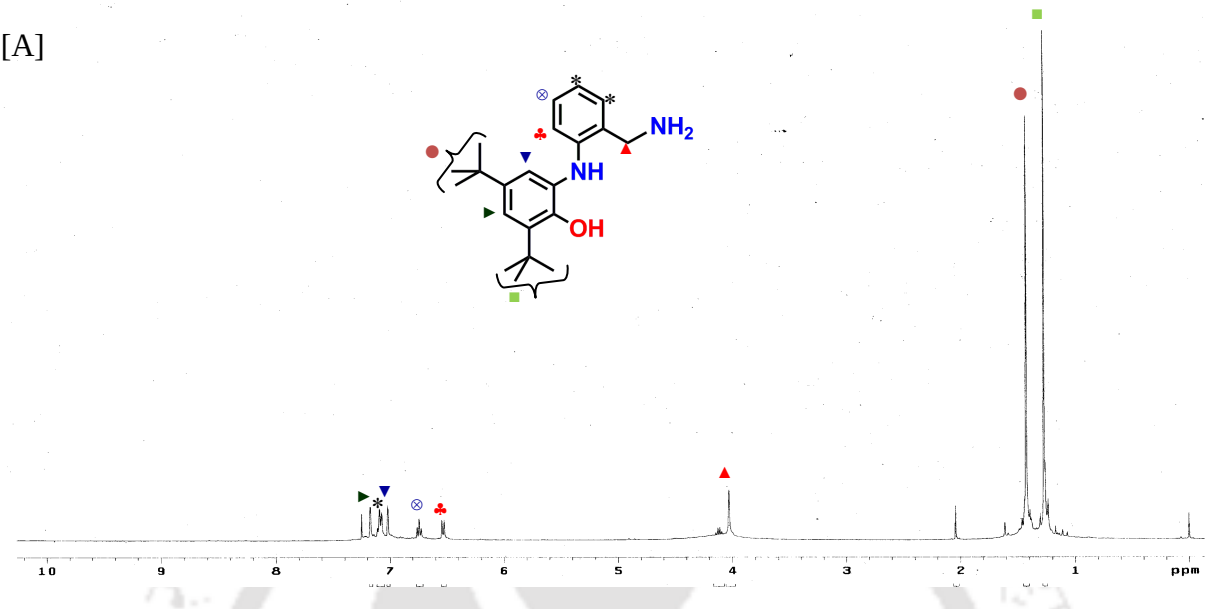

[B]

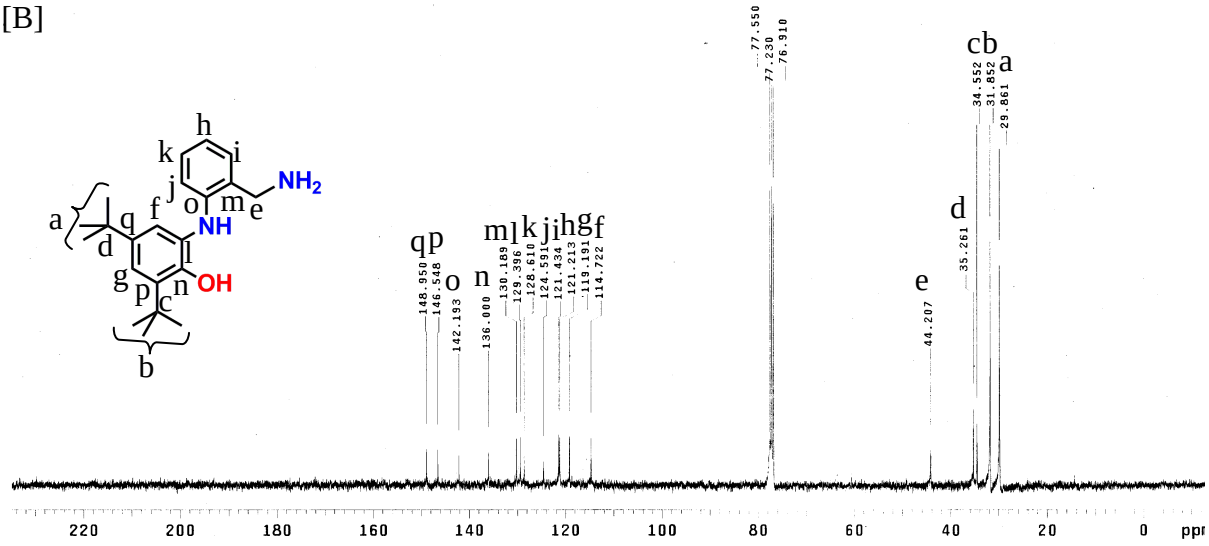

[C]

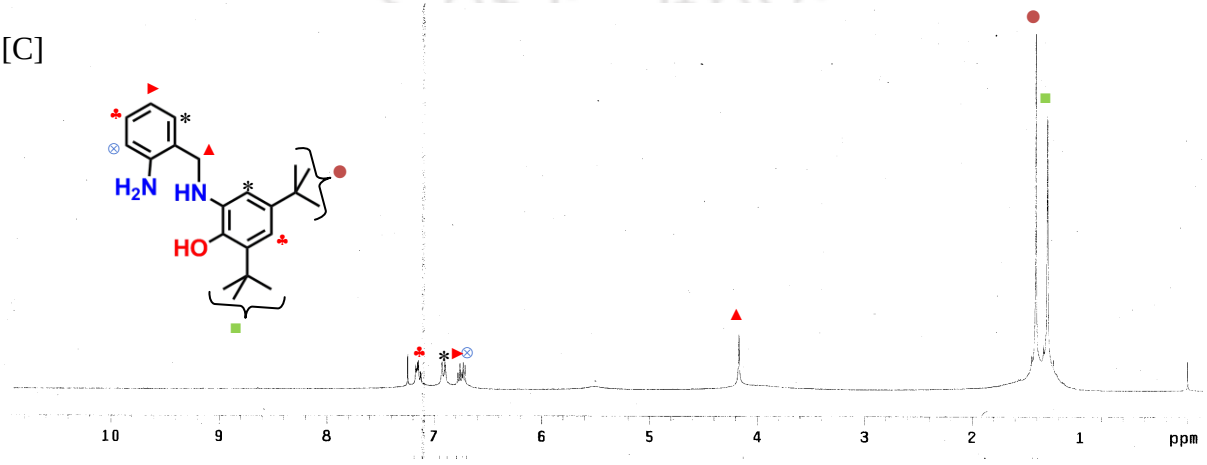

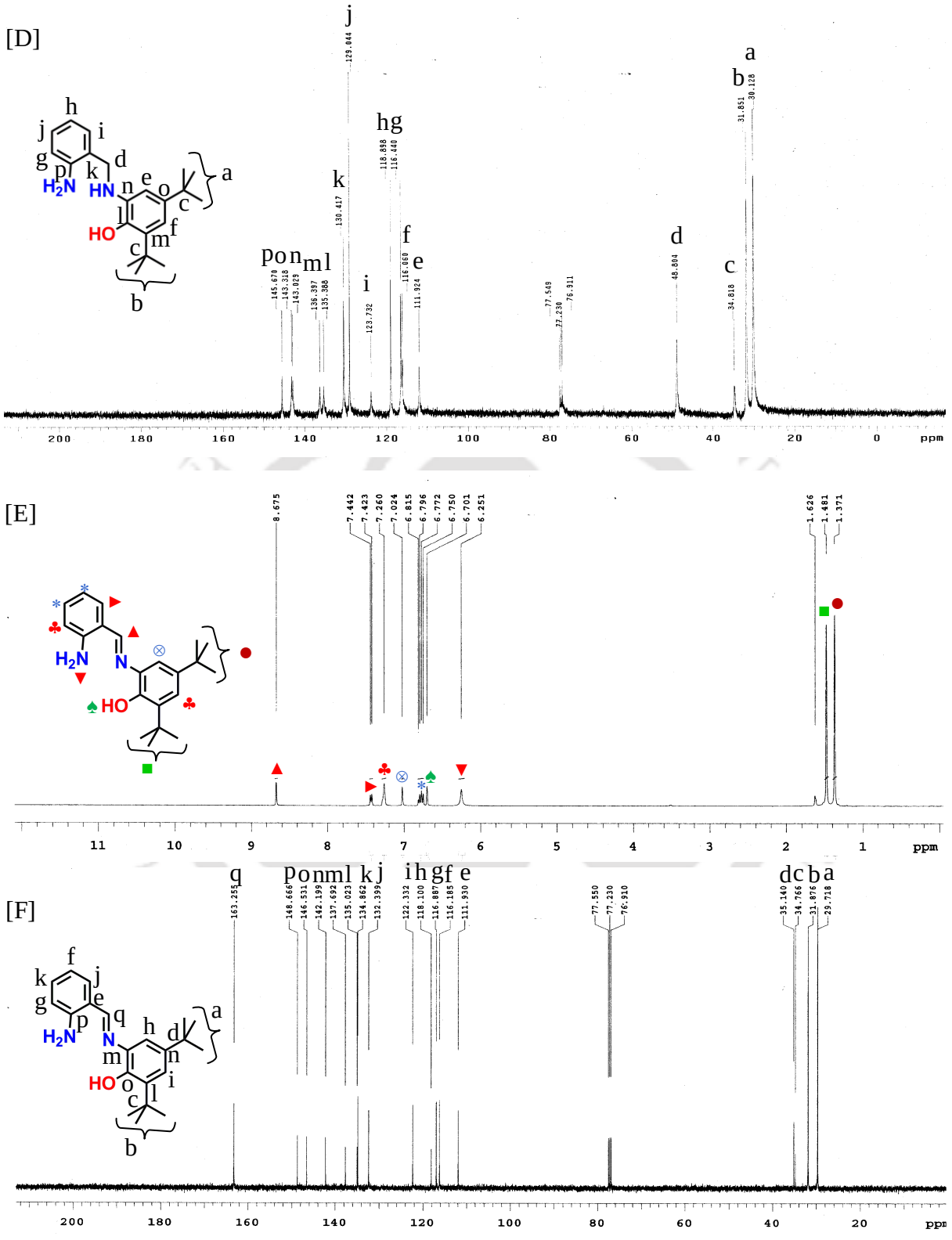

Figure 3.1: *[A] ^{1}H NMR spectrum of* ***H$_4$L^{CH_2NH_2}****; [B] ^{13}C NMR spectrum of* ***H$_4$L^{CH_2NH_2}****; [C] ^{1}H NMR spectrum of* ***H$_4$L2****; [D] ^{13}C NMR spectrum of* ***H$_4$L2*** *; [E] ^{1}H NMR spectrum of* ***H$_3$L1****; [F] ^{13}C NMR spectrum of* ***H$_3$L1****.*

All the ligands were further characterized by NMR spectroscopic method. In the ^{1}H NMR spectrum ligand $\mathbf{H_4L^{CH_2NH_2}}$ showed the resonance signals at δ 1.27 (s, 9H), 1.43 (s, 9H), 4.03 (s, 2H), 6.54 (d, J = 8.4 Hz, 1H), 6.75 (t, J = 7.2 Hz, 1H), 7.02 (d, J = 2.4 Hz, 1H), 7.08 (d, J = 7.2 Hz, 2H), 7.17 (d, J = 2.4 Hz, 1H), 7.25 (s, 1H) ppm. ^{13}C NMR spectrum of ligand $\mathbf{H_4L^{CH_2NH_2}}$ showed 17 kinds of carbon signals at δ 29.9 (3C), 31.9 (3C), 35.3, 44.2, 114.7, 119.2, 121.2, 121.4, 124.6, 128.6, 129.4, 130.2, 136.0, 142.2, 146.6, 148.9 ppm. ^{1}H NMR signals for ligand **H_3L1** appeared at δ 1.37 (s, 9H), 1.48 (s, 9H), 6.25 (s, 2H, –NH_2), 6.70 (s, 1H, –OH), 6.75–6.82 (m, 2H), 7.02 (s, 1H), 7.26 (s, 2H), 7.43 (d, J = 7.6 Hz, 1 H), 8.68 (s, 1H) ppm. Akin to ligand $\mathbf{H_4L^{CH_2NH_2}}$, ^{13}C NMR measurement of the ligand **H_3L1** revealed 17 different kinds of carbon signals at δ 29.7, 31.9, 34.8, 35.1, 111.9, 116.2, 116.9, 118.1, 122.3, 132.4, 134.9, 135.0, 137.7, 142.2, 146.5, 148.7, 163.3 ppm. The ligand **H_4L2** showed the ^{1}H NMR isomer shifts at δ 1.31 (s, 9H); 1.41 (s, 9H); 4.17 (s, 2H); 6.72 (d, J = 8 Hz, 1H); 6.76 (t, J = 7.4 Hz, 1H); 6.91 (d, J = 9.6 Hz, 2H); 7.12–7.17 (m, 2H) ppm. In ^{13}C NMR spectrum isomer shifts appeared at δ 30.1, 31.9, 34.8, 48.8, 111.9, 116.1, 116.4, 118.9, 123.7, 129.0, 130.4, 135.4, 136.4, 143.0, 143.3, 145.7 ppm.

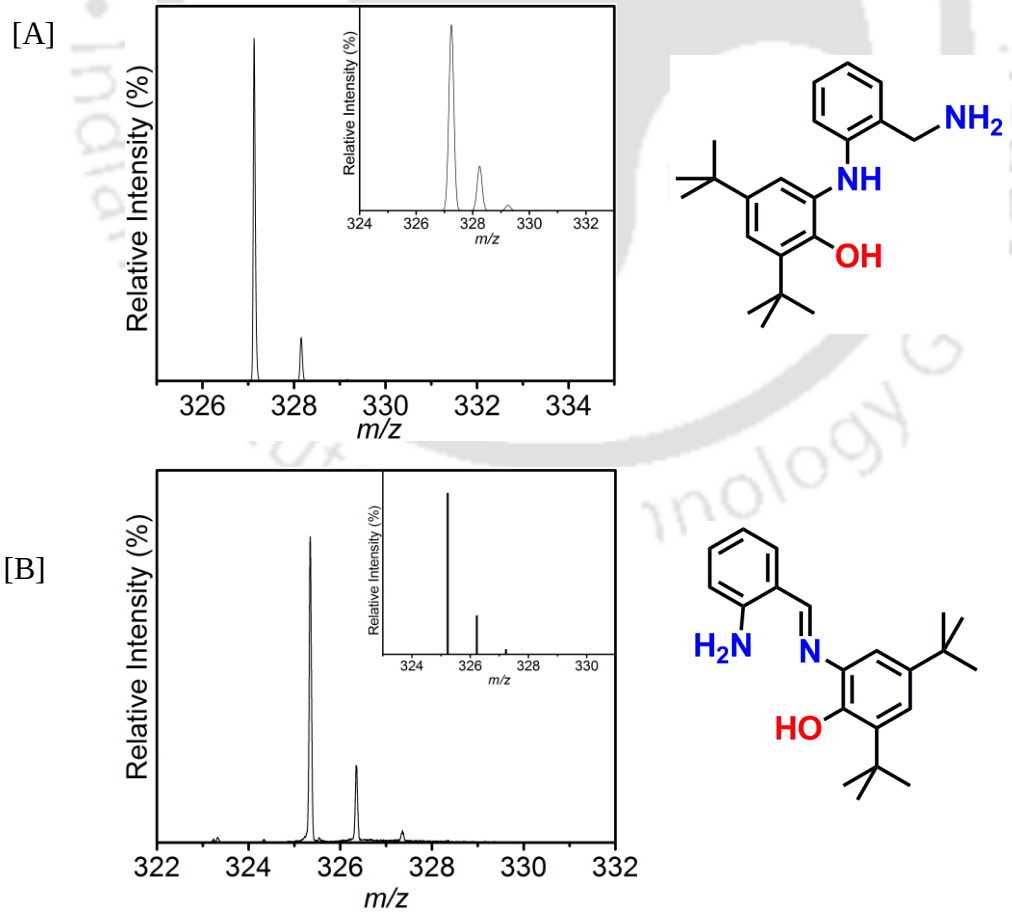

Figure 3.2: *Experimental ESI–mass spectrum and simulated isotope distribution pattern (inset); [A] ligand* ***$H_4L^{CH_2NH_2}$****, and [B] ligand* ***H_3L1****.*

The electrospray ionization mass (ESI–MS) spectra of $\mathbf{H_4L^{CH_2NH_2}}$, **H_3L1**, and **H_4L2** ligands were measured in positive mode in CH_3CN solution. Mass peaks (100%) corresponding to the $[M + H]^+$; M = molecular mass, were appeared for $\mathbf{H_4L^{CH_2NH_2}}$ (*m/z* = 327.12), **H_3L1** (*m/z* = 325.23), **H_4L2** (*m/z* = 327.20), and their respective composition was $\mathbf{C_{21}H_{30}N_2O}$, $\mathbf{C_{21}H_{28}N_2O}$, and $\mathbf{C_{21}H_{30}N_2O}$ as found by isotope distribution pattern examinations.

3.3: Synthesis and Characterization of Co(III) Complex (9) Formed With Ligand $H_4L^{CH_2NH_2}$:

The reaction between 1:1 $CoCl_2 \bullet 6H_2O$ and $\mathbf{H_4L^{CH_2NH_2}}$ in CH_3CN in the presence of Et_3N under aerobic condition caused the precipitation of complex **9** (**Scheme 3.3**). The complex was recrystallized from a 3:1 CH_2Cl_2:CH_3CN solvent mixture, which provided X–ray quality reddish brown single crystal.

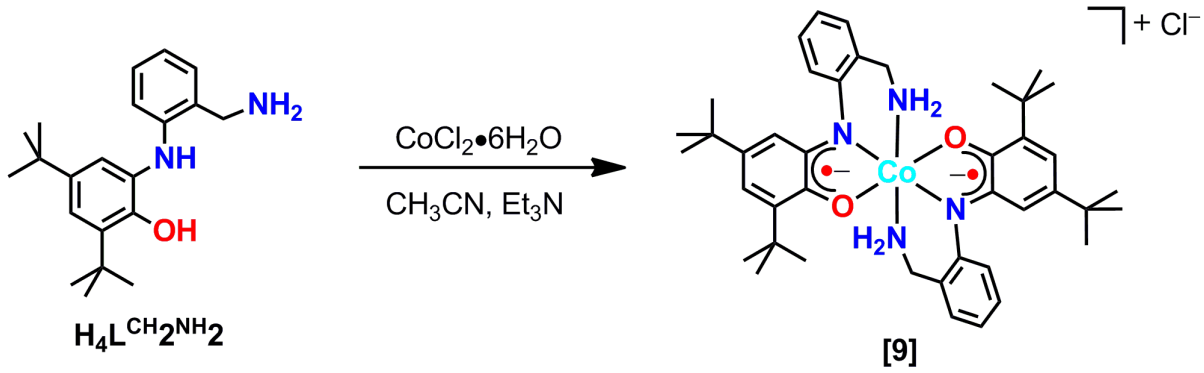

Scheme 3.3: *Synthetic route for complex **9**.*

In the infrared (IR) spectrum of complex **9•CH₃CN•H₂O**, the stretching band appeared at 3619 cm^{-1} was attributed to the lattice water, and the bands at 3456, 3399, 3227, and 3115 cm^{-1} were ascribed for the ν(N–H) stretches of two coordinated $–NH_2$ groups that were situated at different environments because of the weak interaction with Cl^- counter anion. The symmetric, asymmetric, and overtone ν(C–H) stretches for the *tert*–butyl groups appeared in the region of 2952–2867 cm^{-1}. A moderate intense band appeared at 1432 cm^{-1} for ν(C···O)[8] and a low intense band for ν(C···N) at 1583 cm^{-1}, while, the ν(C–N) band appeared at 1179 cm^{-1}. The band at 1112 cm^{-1} stands for C–C stretch (skeletal vibration).[9]

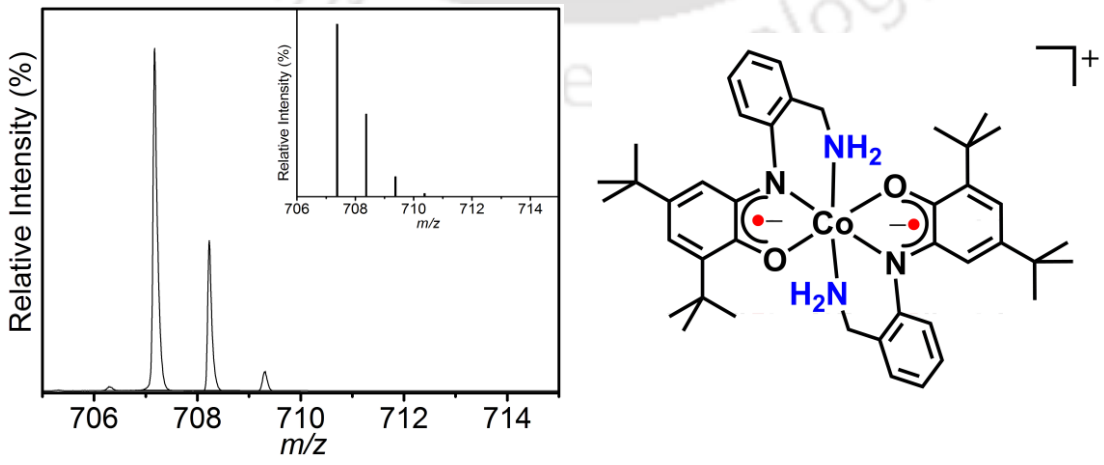

Figure 3.3: *ESI–mass spectrum for **9•CH₃CN•H₂O** in +ve mode; experimental and simulated isotopic distribution pattern (inset).*

The electrospray ionization mass spectrum (ESI–MS) of complex **9•CH_3CN•H_2O** in CH_3CN showed a 100% ion peak at *m/z* = 707.17 in positive mode for M^+; (M = molecular mass). Isotope distribution pattern examination confirmed the **$C_{42}H_{56}CoN_4O_2$** composition for the molecular ion peak and thus for complex **9** (**Figure 3.3**).

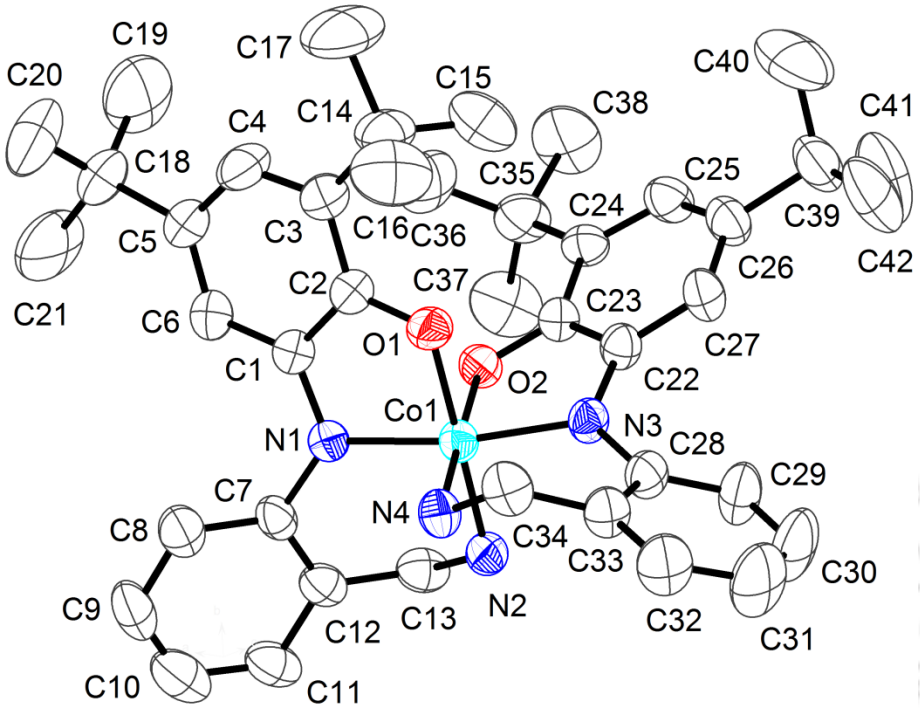

Figure 3.4: *ORTEP representation of* ***9•CH_3CN•H_2O****. Thermal ellipsoids were drawn at 50% probability level. H atoms, counter anion, and solvent molecules (H_2O, and CH_3CN) were omitted for clarity.*

Single crystal X–ray examination of the complex revealed that the complex was crystallized in the monoclinic space group $P12_1/c1$. ORTEP diagram of cationic complex core of **9** is presented in **Figure 3.4**. Selected bond distances, and bond angels are summarized in **Table 3.1**.

Complex **9** was composed of a cationic complex core $[\mathbf{Co(H_2L^{CH_2NH_2\bullet})_2}]^+$ and a counter chloride anion. The monopositive complex core was six–coordinate with a distorted octahedral geometry around the central Co atom. Amide, phenolate, and benzylamine donor set from two ligands were spanned meridionally around the Co coordination sphere. Structural rigidity of tridentate ligand possibly facilitated the coordination of the ligand to the metal ion in meridional fashion .[10] The Co–O1 and Co–O2 bond distances were 1.901±0.002 Å and Co–N bonds distances were 1.928±0.031 Å, respectively and were in accord with the low spin Co(III) complexes.[11] An alternate short and long C–C bond distances were observed for *tert*–butyl containing C_6 aryl rings. This confirmed a quinoid–type distortion in

the C_6 aryl rings and hence, the non–innocent behavior of the ligand. Thus, the distance at C3–C4, C5–C6, C24–C25, C26–C27 were of 1.370±0.010 Å, significantly shorter compared to the other C–C bonds which were at 1.425±0.010 Å. Furthermore, the C_{Ph}–O and C_{Ph}–N (C_{Ph} = *tert*–butyl containing aryl ring) bond distances were 1.305±0.005 and 1.360±0.004 Å, respectively. These bond distances were in accord with their partial double bond character and reconfirmed the delocalized iminosemiquinonate ($ISQ^{\bullet 1-}$) electronic structure of the coordinating ligands.[8,12] On the contrary, expected C–C bond distances 1.380±0.020 Å were found in the other two phenyl rings.

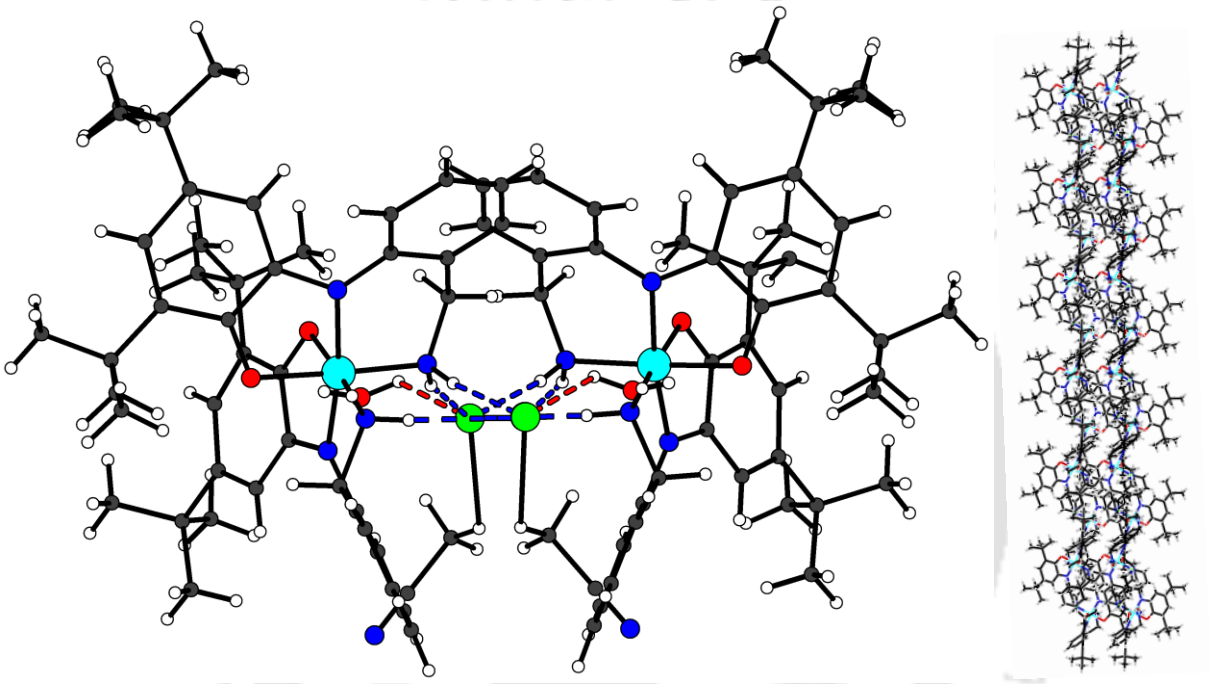

Figure 3.5: *(Left) H–bonding and molecular packing in* ***9•CH$_3$CN•H$_2$O*** *and (right) double strand helical structure.*

Crystal structure investigation revealed that the counter anion Cl^- acted as an intermolecular bridging unit through weak H–bond interactions. The H–bonded molecular packing of **9•CH$_3$CN•H$_2$O** as well as double–strand helical structure are shown in **Figure 3.5**. Selected bond distances and bond angels are listed in **Table 3.1**.

Table 3.1: *Selected bond distances (Å), and bond angels (°) for complex* ***9•CH$_3$CN•H$_2$O****.*

C1–C2	1.433(5)	C22–C23	1.435(5)
C2–C3	1.422(5)	C23–C24	1.428(5)
C3–C4	1.380(5)	C24–C25	1.383(5)
C4–C5	1.417(5)	C25–C26	1.417(5)
C5–C6	1.360(5)	C26–C27	1.366(5)
C6–C1	1.416(5)	C27–C22	1.415(5)
C7–C8	1.399(5)	C28–C29	1.391(5)

C8–C9	1.397(5)	C29–C30	1.375(5)
C9–C10	1.373(6)	C30–C31	1.363(6)
C10–C11	1.360(6)	C31–C32	1.375(6)
C11–C12	1.397(5)	C32–C33	1.383(5)
C12–C7	1.401(5)	C33–C28	1.404(5)
C12–C13	1.494(5)	C33–C34	1.493(5)
C1–N1	1.363(4)	C22–N3	1.357(4)
C7–N1	1.401(4)	C28–N3	1.403(4)
C13–N2	1.476(4)	C34–N4	1.487(4)
C2–O1	1.311(4)	Co1–N1	1.906(3)
C23–O2	1.301(4)	Co1–N2	1.935(3)
Co1–O1	1.899(2)	Co1–N3	1.897(3)
Co1–O2	1.903(2)	Co1–N4	1.959(3)
Cl1…H4B(N4)	2.422(1)	Cl1…H2A(N2)	2.377(1)
Cl1…H2B(N2)	2.381(1)	Cl1…H5B(O5)	2.820(81)
O1–Co1–O2	87.97(10)	O2–Co1–N4	177.17(11)
O1–Co1–N1	84.52(11)	N1–Co1–N2	94.32(11)
O1–Co1–N2	177.62(11)	N1–Co1–N3	170.57(12)
O1–Co1–N3	89.58(11)	N1–Co1–N4	93.90(11)
O1–Co1–N4	89.88(11)	N2–Co1–N3	91.30(11)
O2–Co1–N1	87.72(11)	N2–Co1–N4	92.27(12)
O2–Co1–N2	89.91(11)	N3–Co1–N4	93.43(12)
O2–Co1–N3	84.72(11)		

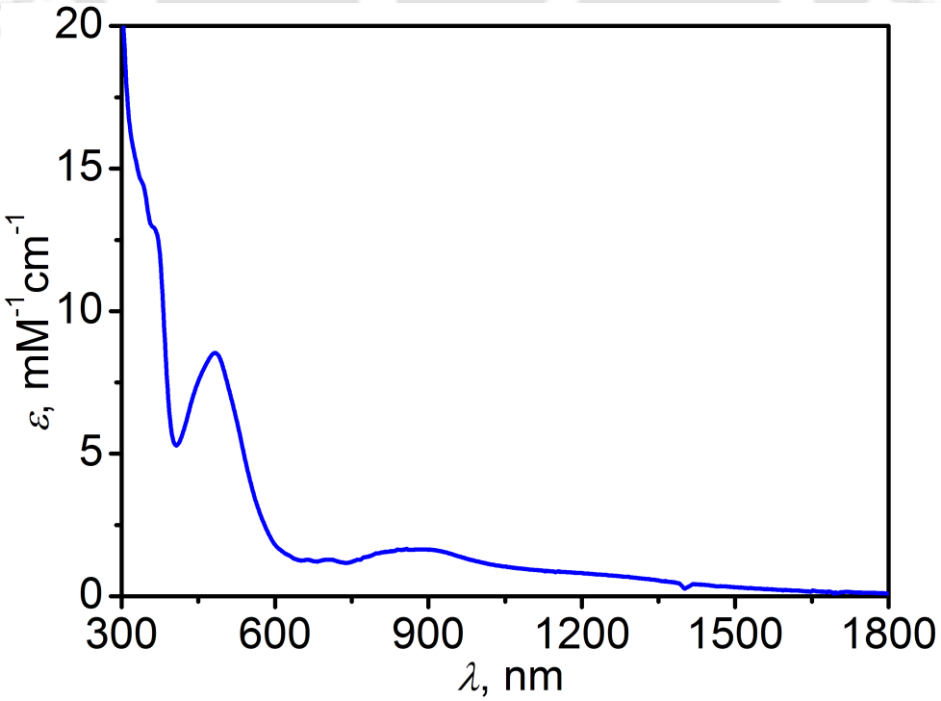

Figure 3.6: *UV–vis/NIR spectrum of* ***9•CH₃CN•H₂O*** *measured at room temperature (RT) in dichloromethane solution in 300–1800 nm range.*

Electronic absorption spectrum of **9•CH_3CN•H_2O** is shown in **Figure 3.6**. The complex **9** showed near infrared (NIR) absorption at λ_{max} = 1182 nm (ε = 850 $M^{-1}cm^{-1}$). This absorption band can be characterized as mixed (LMCT)/(LLCT) transition.[13] A broad absorption maxima at λ_{max} = 875 nm (ε = 1700 $M^{-1}cm^{-1}$) was appeared due to the ligand–to–ligand charge transfer (LLCT),[13] while, the ligand–to–metal charge transfer (LMCT) band was appeared at λ_{max} = 480 nm (ε = 8550 $M^{-1}cm^{-1}$).[13,14]

3.4: Synthesis and Characterization of the Ni(II) Complex (10) Formed with *in situ* Generated Salen–Type Ligand:

The reaction between equimolar amounts of ligand $\mathbf{H_4L^{CH_2NH_2}}$ and $NiCl_2 \bullet 6H_2O$ in acetonitrile in the presence of triethylamine and air provided complex **10** (**Scheme 3.4**). Interestingly, under the same reaction condition, ligand $\mathbf{H_3L1}$ and $\mathbf{H_4L2}$ also provided complex **10**.

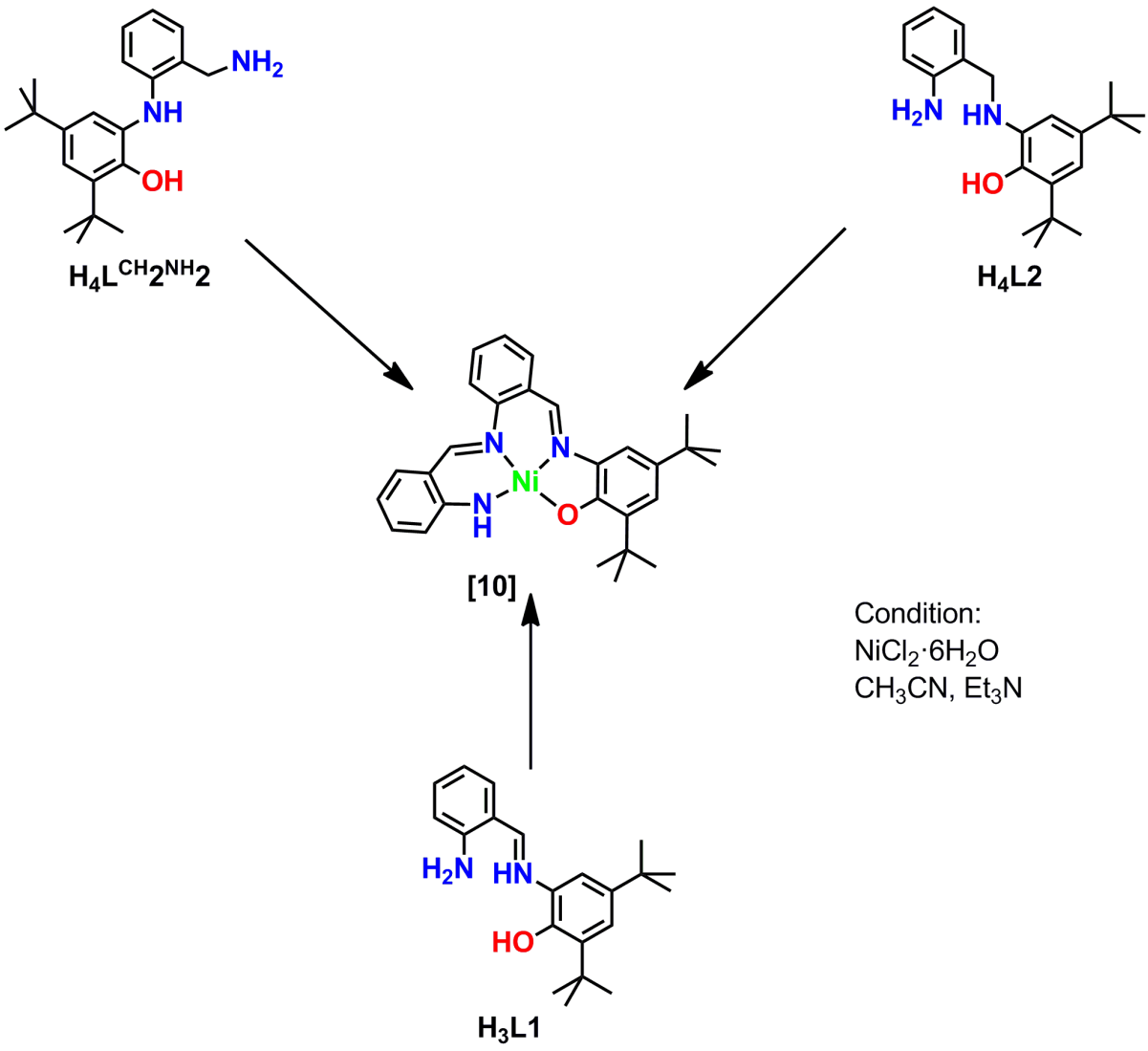

Scheme 3.4: *Synthetic route for complex **10**.*

IR spectrum of complex **10** showed a small intense sharp band at 3346 cm^{-1} due to asymmetric ν(N–H) stretching. The asymmetric, symmetric, and bending overtone bands for ν(C–H) stretches of *tert*–butyl groups were found at 2945, 2860, and 2900 cm^{-1}, while the corresponding bending vibrational band arose at 1476 cm^{-1}. Two bands appeared at 1617, and 1599 cm^{-1} for two different ν(C=N) stretching units.[15] The phenolate ν(C–O) band

appeared at 1264 cm^{-1},[15] while the band at 1154 cm^{-1} was appeared due to the ν(C–N) stretch.[16]

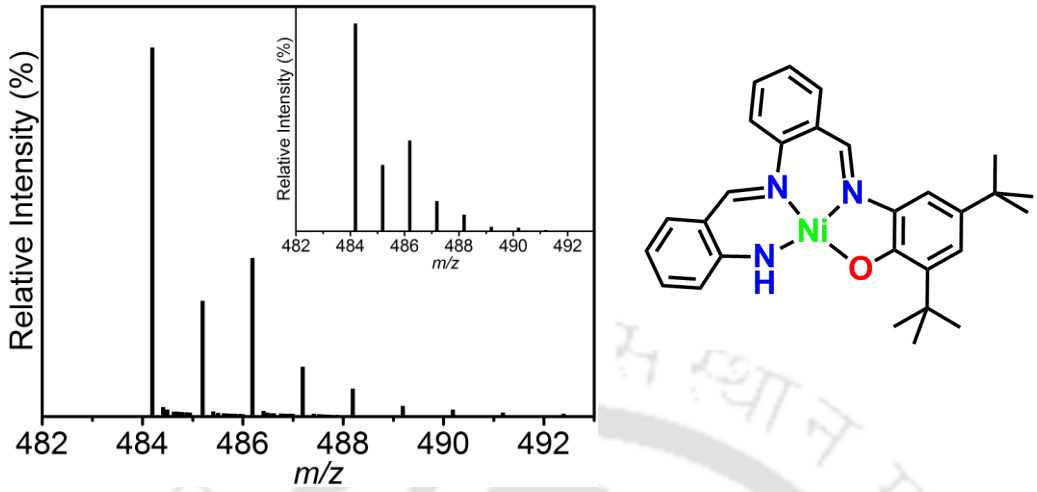

Figure 3.7: *ESI–mass spectrum of **10** with experimental and simulated isotopic distribution pattern (inset).*

Electrospray ionization mass spectrum (ESI–MS) of complex **10** was examined in acetonitrile solution in positive mode. In the spectrum a 100% molecular ion peak appeared at *m/z* = 484.20 that corresponded to $[M + H]^+$; where M = molecular mass (**Figure 3.7**). The composition of the observed mass and hence the complex was $\mathbf{C_{28}H_{31}N_3NiO}$ as confirmed by isotope pattern distribution examination.

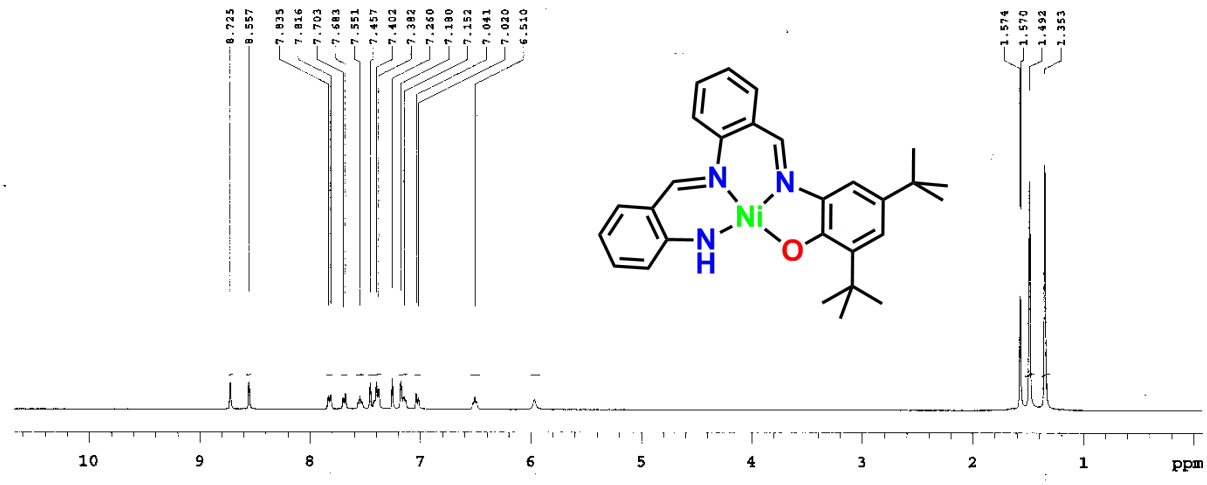

Figure 3.8: *^{1}H NMR spectrum of **10**.*

^{1}H NMR spectrum of **10** was measured in $CDCl_3$ solvent and is shown in **Figure 3.8**. Complex showed the normal isomer shifting value at δ 1.35 (s, 9H), 1.49 (s, 9H), 5.97 (s, 1H), 6.51 (t, *J* = 7.2 Hz, 1H), 7.03 (d, *J* = 8.4 Hz, 1H), 7.15 (t, *J* = 6.8 Hz, 1H), 7.18 (s, 1H), 7.40 (t, *J* = 7.6 Hz, 2H), 7.46 (s, 1H), 7.55 (t, *J* = 7.8 Hz, 1H), 7.69 (d, *J* = 8.0 Hz, 1H), 7.82

(d, *J* = 7.6 Hz, 1H), 8.56 (s, 1H), 8.73 (s, 1H) ppm and strongly suggested its diamagnetic nature.

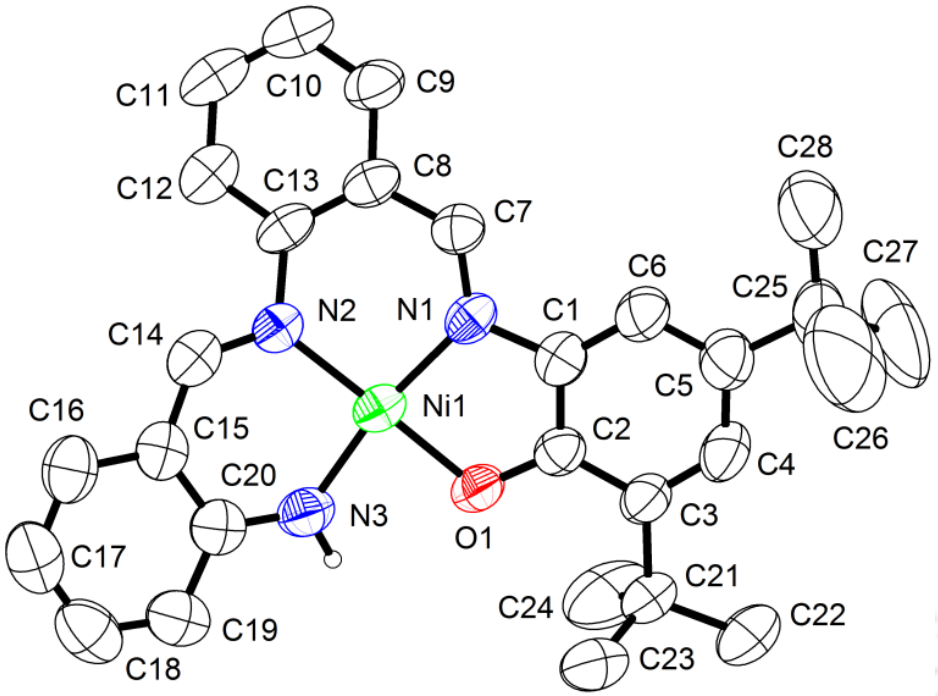

Figure 3.9: *ORTEP representation **10**. Thermal ellipsoids were drawn at 50% probability level. H atoms (except the one attached to N3 atom) were omitted for clarity.*

The molecular structure of complex **10** was analyzed by X–ray single crystal diffraction measurement at 298 K. The complex crystallized in the monoclinic system, *C*12/*c*1 space group. The molecular structure is shown in **Figure 3.9** and the selected bond distances and bond angles are given in **Table 3.2**.

In the neutral complex **10** the central Ni1 atom was four–coordinate with a slightly distorted square planar geometry (τ = 0.11).[17] The dihedral angle between N2–N1–N3 and N1–Ni1–O1 planes was 8.3° and indicated a small twist around the Ni atom in the molecule. An asymmetric environment around Ni1 atom was reflected by the Ni1–O1 = 1.858(2), Ni1–N1 = 1.867(3), Ni1–N2 = 1.876(3), and Ni1–N3 = 1.830(3) Å bond distances. The difference in the bond distances was due to the different nature (hybridization) of the coordinating atoms. The C–C bond distances of the *tert*–butyl groups containing C_6 phenyl ring were almost all within 1.39±0.02 Å range and were in accord with the phenyl C=C bond distances.[18] Furthermore, both C1–N1 = 1.417(5), O1–C2 = 1.321(4) Å bond distances implied their single bond character. These bond distances along with the double bond characterizing N1–C7 = 1.301(4) Å bond confirmed an iminophenolate form of the *tert*–butyl

groups containing phenyl ring where the phenolate^{1-} charge was located on phenolate oxygen atom. The C–C bond distances in the C_6 ring comprised of C15–to–C20 atoms showed a substantial elongation in C15–C16 = 1.422(6), C20–C15 = 1.426(5), and C19–C20 = 1.424(6) Å bond distances compared to the C16–C17 = 1.357(6), C17–C18 = 1.398(6), C18–C19 = 1.365(6) Å and indicated a quinoid–type distortion in the C_6 ring. This distortion was due to the delocalization of amide^{1-} charge over the iminosalicylidene moiety as evidenced by short N3–C20 = 1.327(5), and C14–C15 = 1.408(5) Å bond distances compared to their corresponding single band characterizing values[19] followed by an elongated C14–N2 = 1.324(5) Å bond distance compared to its double bond characterizing value (1.28 Å).[20] This type of alternative shortening and elongation is common in salen complexes where the ligand is found to be in its fully reduced form.[19] Hence, from the X–ray structural analysis it was evidenced that the neutral asymmetric complex **10** was Ni(II) salen–type with two imine N1 and N2 atoms, one amide N3 atom, and one phenolate O1 atom in its coordination environment.

Table 3.2: *Selected bond distances (Å), and bond angels (°) for complex **10**.*

C1–C2	1.402(5)	C16–C17	1.357(6)
C2–C3	1.412(5)	C17–C18	1.398(6)
C3–C4	1.373(6)	C18–C19	1.365(6)
C4–C5	1.421(6)	C19–C20	1.424(6)
C5–C6	1.372(5)	C20–C15	1.426(5)
C6–C1	1.392(6)	C1–N1	1.417(5)
C7–C8	1.418(5)	N1–C7	1.301(4)
C8–C9	1.408(5)	C13–N2	1.434(5)
C9–C10	1.355(6)	N2–C14	1.324(5)
C10–C11	1.382(7)	C20–N3	1.327(5)
C11–C12	1.389(6)	C2–O1	1.321(4)
C12–C13	1.387(5)	Ni1–O1	1.858(2)
C13–C8	1.403(6)	Ni1–N1	1.867(3)
C14–C15	1.408(5)	Ni1–N2	1.876(3)
C15–C16	1.422(6)	Ni1–N3	1.830(3)
O1–Ni1–N1	85.76(12)	C13–N2–C14	115.1(3)
N1–Ni1–N2	95.67(13)	N2–C14–C15	127.9(4)
N2–Ni1–N3	93.54(14)	C14–C15–C20	122.0(4)
N3–Ni1–O1	85.46(13)	C15–C20–N3	119.6(4)
O1–Ni1–N2	176.61(13)	N1–Ni–N3	168.20(14)
O1–C2–C1	117.1(4)	Ni1–O1–C2	112.9(2)
C2–C1–N1	111.7(4)	Ni1–N1–C1	111.3(2)
C1–N1–C7	121.8(3)	Ni1–N1–C7	126.8(3)
N1–C7–C8	124.3(4)	Ni1–N2–C13	122.3(3)
C7–C8–C13	124.8(3)	Ni1–N2–C14	122.6(3)
C8–C13–N2	121.1(4)	Ni1–N3–C20	131.2(3)

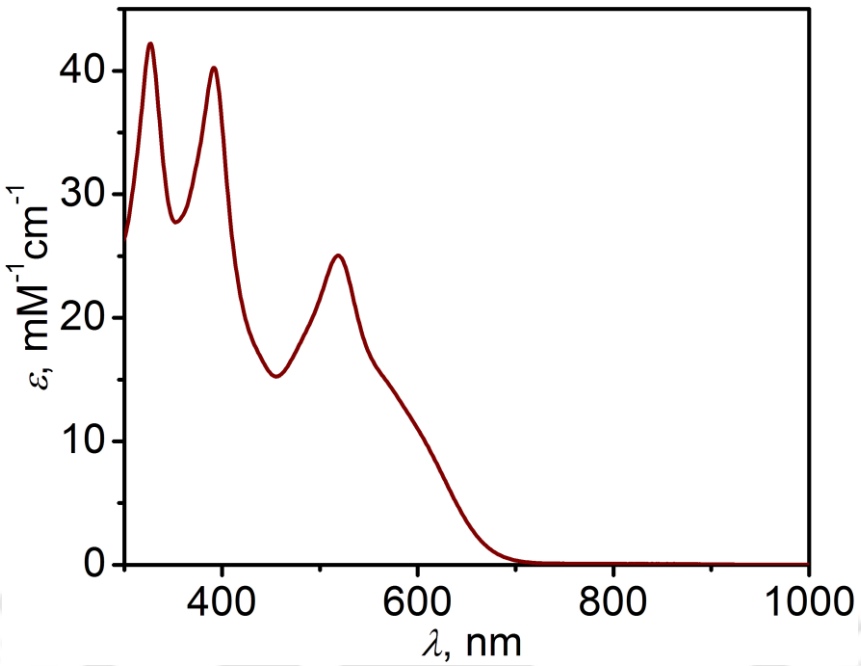

Figure 3.10: *UV–vis/NIR spectrum of **10** measured at room temperature in dichloromethane solution in 300–1000 nm range.*

The electronic absorption spectrum of complex **10** is shown in **Figure 3.10**. All the observed bands appeared in the UV–vis region and bands were high in intensity. This indicated that the bands were appearing because of charge transfer. The absorption maxima at λ_{max} = 518 nm (ε = 25100 $M^{-1}cm^{-1}$) appeared due to metal–to–ligand charge transfer (MLCT),[21] while, the band at λ_{max} = 326 nm (ε = 42050 $M^{-1}cm^{-1}$) was due to the ligand–to–metal charge transfer (LMCT).[22] A ligand–to–ligand charge transfer (LLCT) band owing to $\pi \rightarrow \pi^*$ transition was appeared at λ_{max} = 390 nm (ε = 40200 $M^{-1}cm^{-1}$).[21b]

A plausible reaction mechanism for the formation of complex **10** from the initially used ligand $\mathbf{H_4L^{CH_2NH_2}}$ *via* the *in situ* generation of ligand **H_3L1** and **H_4L2** and their corresponding Ni(II) complexes is presented in **Scheme 3.5**.

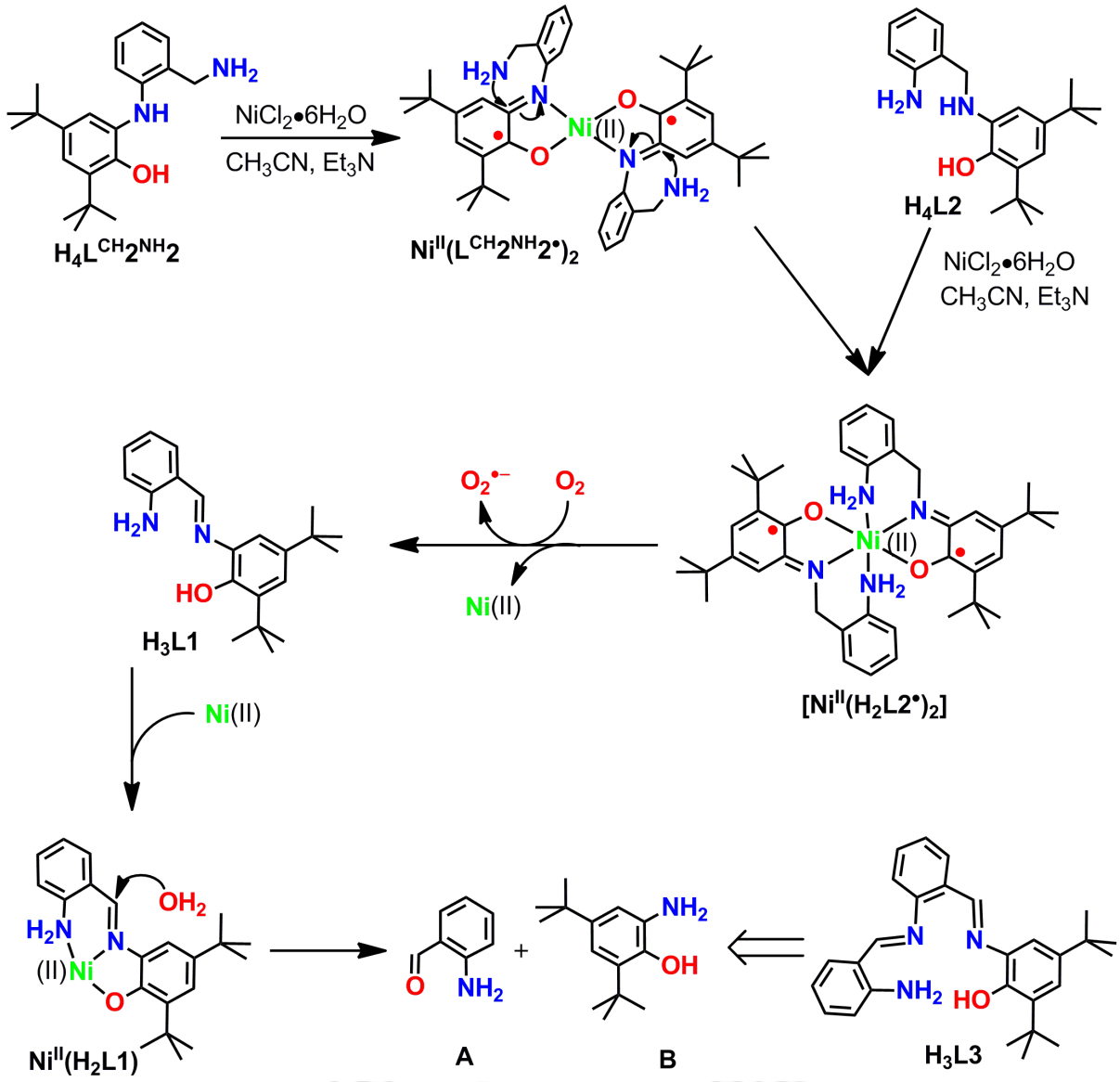

Scheme 3.5: *Showing mechanistic proposals for the formation of* ***H_3L3*** *from ligand* ***H_4L2****, and ligand* $\boldsymbol{H_4L^{CH_2NH_2}}$.

Ligand $\mathbf{H_4L^{CH_2NH_2}}$ initially reacted with $NiCl_2\bullet 6H_2O$ in the presence of triethylamine and provided a diradical–coordinated square planar Ni(II) complex, $[\mathbf{Ni^{II}(H_2L^{CH_2NH_2\bullet})_2}]$. Mass spectrometric analysis (**Figure 3.11**) of the reaction solution (CH_3CN) that obtained after immediate mixing of the reactants ($\mathbf{H_4L^{CH_2NH_2}}$, $NiCl_2\bullet 6H_2O$, and Et_3N) under air showed a mass peak at *m/z* = 706.39, which correspond to $[\mathbf{Ni^{II}(H_2L^{CH_2NH_2\bullet})_2}]$ species and supported its formation. The N atom from free amine group of benzylamine then attacked at

the imine carbon atom present in [$\mathbf{Ni^{II}(H_2L^{CH_2NH_2^{\bullet}})_2}$] species. This resulted an aryl migrated diradical–coordinated octahedral Ni(II) complex [$\mathbf{Ni^{II}(H_2L2^{\bullet})_2}$] formation and a complete modification of the initially used ligand backbone. [$\mathbf{Ni^{II}(H_2L2^{\bullet})_2}$] underwent further two–electron aerial oxidation and provided two equivalents of organic ligand $\mathbf{H_3L1}$, which upon coordination with Ni(II) ion provided [$\mathbf{Ni^{II}H_2L1}$] species. This species then succumbed to ligand imine hydrolysis and provided 2–aminobenzaldehyde (**A**) and 4,6–di–*tert*–butyl–2–aminophenol (**B**). The coordination of imine N atom to Lewis acidic Ni(II) center activated the imine carbon atom by increasing its electrophilicity and hence, the hydrolysis was occurred favorably.

To consolidate the formation of new ligands $\mathbf{H_3L1}$ and $\mathbf{H_4L2}$, and its corresponding Ni(II) complex as intermediate to the formation of complex **10**, both ligand $\mathbf{H_3L1}$ and $\mathbf{H_4L2}$ were synthesized (Experimental section). In accordance with the proposal, complex **10** was isolated by employing both ligands under the same reaction condition. Hence, their formation was confirmed.

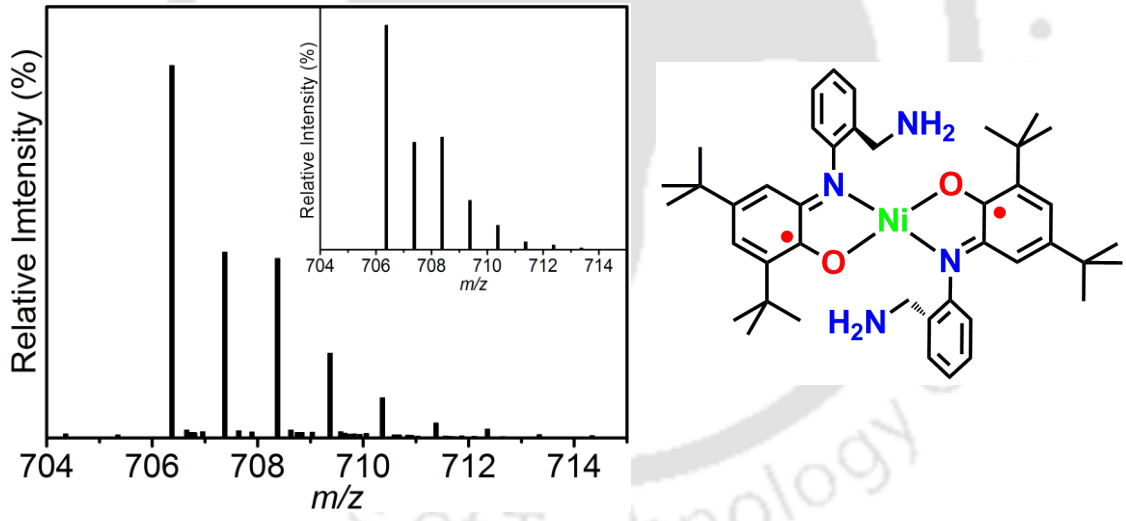

Figure 3.11: *ESI–mass spectrum of* [$\mathbf{Ni^{II}(H_2L^{CH_2NH_2^{\bullet}})_2}$] *with experimental and simulated isotopic distribution pattern (inset).*

3.5: Synthesis and Characterization of the Cu(II) Complex (11) Formed with *in situ* Generated Salen–Type Ligand:

Complex **11** was synthesized by the reaction of $CuCl_2 \bullet 2H_2O$ and ligand $\mathbf{H_4L^{CH_2NH_2}}$ in 1:1 molar ratio in acetonitrile in the presence of Et_3N under air (**Scheme 3.6**). Under the same reaction condition, ligand $\mathbf{H_3L1}$ and $\mathbf{H_4L2}$ also provided the same complex **11**.

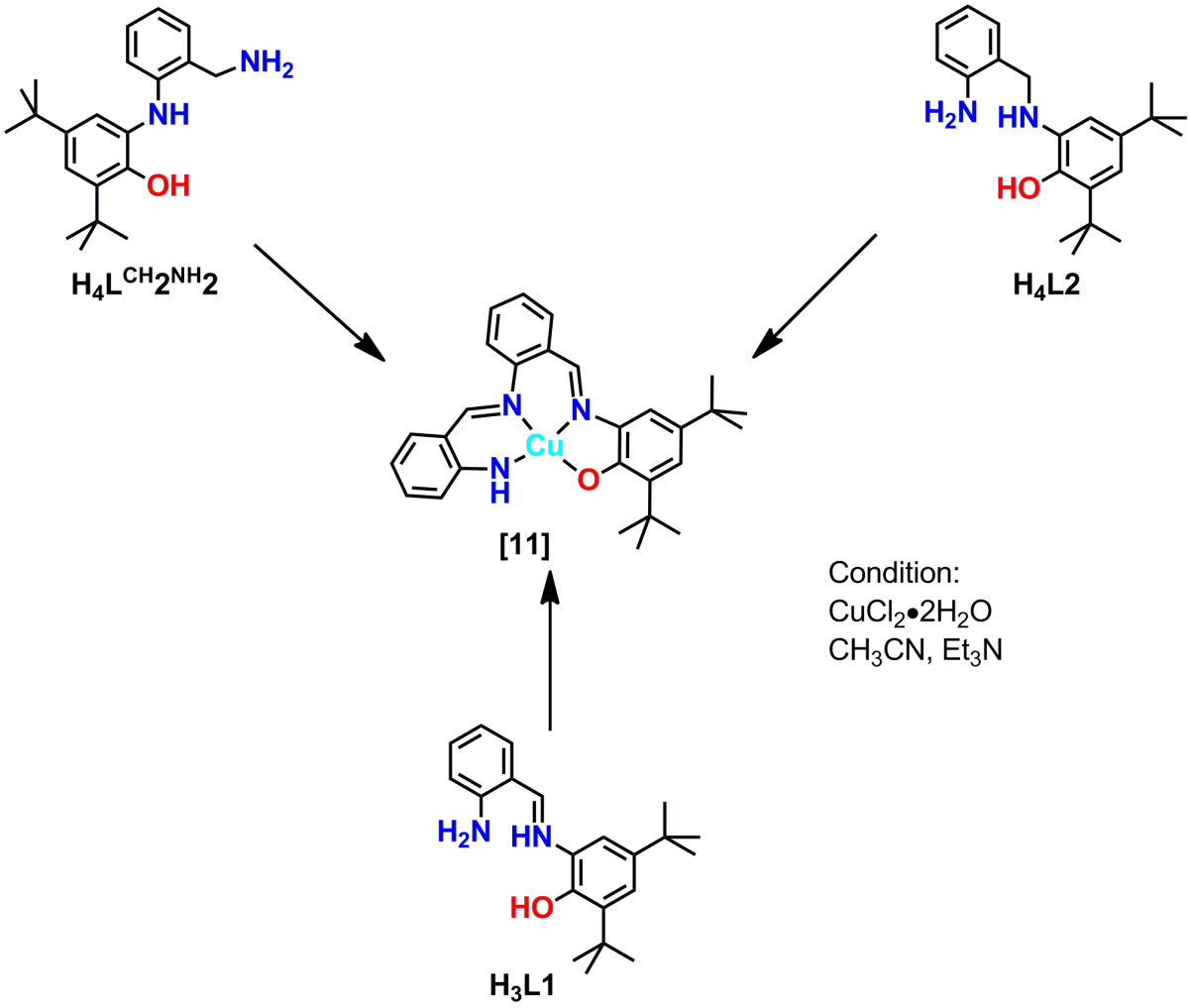

Scheme 3.6: *Synthetic route for complex **11**.*

In the infrared spectrum of complex **11**, the ν(N–H) stretching band appeared at 3350 cm^{-1}. No band for phenolic proton indicated the ligation of deprotonated phenolate moiety. The characteristic bands for the presence of the *tert*–butyl groups appeared at 2950, 2902, and 2863 cm^{-1} and the phenolic ν(C–O) stretching band appeared at 1272 cm^{-1}.[15] These confirmed the presence of 2,4–di–*tert*–butylphenolate moiety in the coordinating ligand. The 1616 cm^{-1} vibration band appeared due the presence of ν(C=N) unit in the ligand backbone of **11**.

The electrospray ionization mass (ESI–MS) spectrum for complex **11** was measured in CH_3CN solution in positive mode. A 100% molecular ion peak appeared at *m/z* = 489.17 ($[M + H]^+$; M = molecular mass), indicated the formation of **11**. The isotope distribution pattern confirmed **$C_{28}H_{31}CuN_3O$** as its composition (**Figure 3.12**).

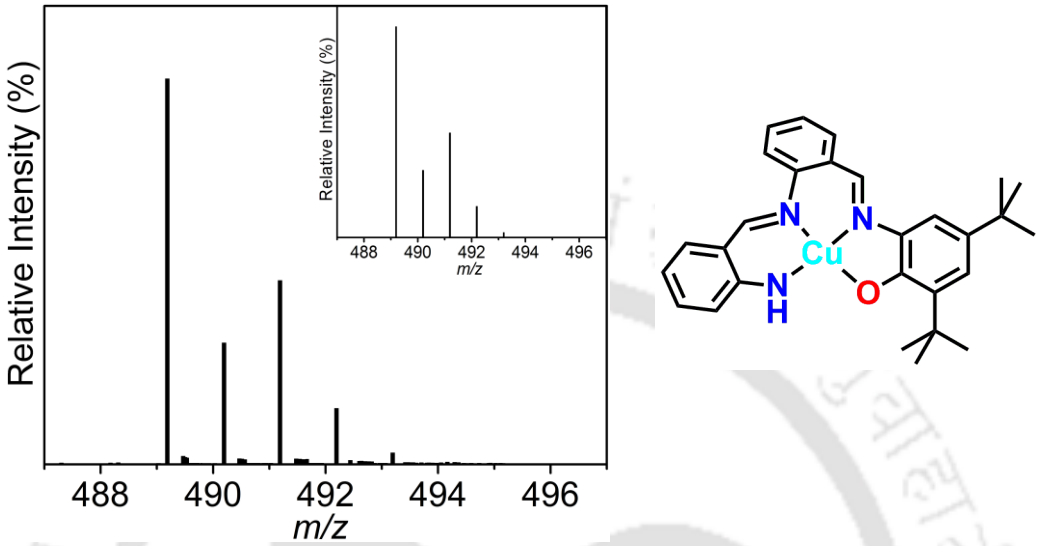

Figure 3.12: *ESI–mass spectrum of **11** with experimental and simulated isotopic distribution pattern (inset).*

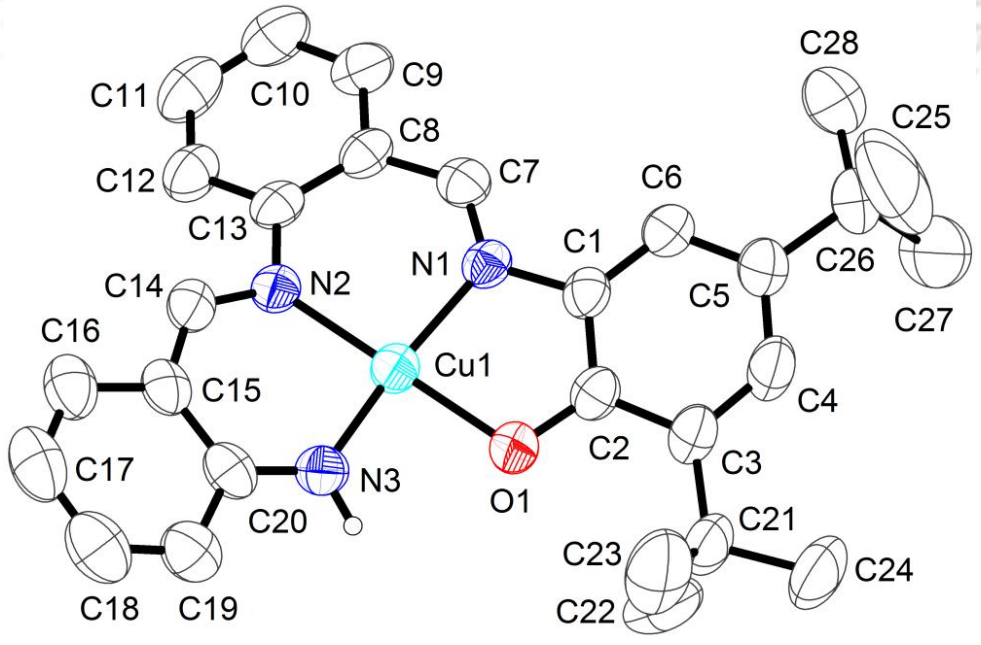

Figure 3.13: *ORTEP representation of **11**; thermal ellipsoids were drawn at 50% probability. H atoms (except the one attached to N3 atom) were omitted for clarity.*

Complex **11** was structurally characterized by single crystal X–ray diffraction measurements at 296 K. Molecular structure in ORTEP format is shown in **Figure 3.13**. Selected bond distances and bond angles data are presented in **Table 3.3**. Complex **11**

crystallized in the monoclinic space group *C*12/*c*1 (no. 15). Notably, X–ray crystal structure of complex **11** showed a new ligand backbone that was completely different from the original ligand $\mathbf{H_4L^{CH_2NH_2}}$.

The central Cu1 atom in the neutral complex **11** was four–coordinate with a distorted square planar geometry [τ_4 = 0.13; O1–Cu1–N2 = 173.82(10), N1–Cu1–N3 = 167.85 (11)]. The ligand backbone was asymmetric and the coordination sites were comprised of three N atoms and one O atom. The Cu1–N1 = 1.939(2), Cu1–N2 = 1.965(2), Cu1–N3 = 1.881(2), and Cu1–O1 = 1.932(2) Å bond distances clearly indicated an asymmetric environment around Cu1 center and the bond distances were in accord with the +II oxidation state of Cu1 atom.[2a-g] The dihedral angle between the planes containing N1, Cu1, and O1 atoms and N2, Cu1, and N3 atoms was ~ 12º. This demonstrated a small twist around the Cu(II) centre. The ligand backbone was majorly constituted of three C_6 rings. The C–C bond distances (**Table 3.3**) of the C_6 rings comprised of C1–to–C6 and C8–to–C13 carbons were in accord with phenyl C–C bond distance and indicated the phenyl form of the rings. On the contrary, the C–C bond distances in the C_6 ring comprised of C15–to–C20 atoms showed a substantial elongation in C15–C16 = 1.421(4), C20–C15 = 1.430(4), C19–C20 = 1.423(4) Å bond distances from 1.39±0.01 Å as expected for phenyl C=C bond distances. Moreover, short C16–C17 = 1.350(5), and C18–C19 = 1.360(5) Å bond distances confirmed a quinoid–type distortion in the C_6 ring. Furthermore, the shortening in N3–C20, C14–C15 bond distances and elongation in N2–C14 bond distance compared to imine bond distance (1.28 Å) indicated the delocalization of amide^{1-} charge over the 2–amidobenzylidene moiety. The C1–O1 = 1.318(3), and C1–N1 = 1.420(4) Å bond distances supported the imidophenolate^{1-} form of the *tert*–butyl groups–containing C_6 ring. The N1–C7 = 1.280(4), and C7–C8 = 1.439(4) Å bond distances were in accord with the double bond and single bond character, respectively. Hence, from the X–ray structural analysis it was confirmed that the neutral asymmetric complex **11** was Cu(II) salen–type with two imine N atoms, one amide N atom, and one phenolate O atom in its coordination environment.

Table 3.3: *Selected bond distances (Å), and bond angels (°) for complex **11**.*

C1–C2	1.391(4)	C16–C17	1.350(5)
C2–C3	1.431(4)	C17–C18	1.392(5)
C3–C4	1.381(4)	C18–C19	1.360(5)
C4–C5	1.396(5)	C19–C20	1.423(4)
C5–C6	1.378(4)	C20–C15	1.430(4)
C6–C1	1.386(4)	C1–N1	1.420(4)
C7–C8	1.439(4)	N1–C7	1.280(4)

C8–C9	1.395(4)	C13–N2	1.423(4)
C9–C10	1.368(5)	N2–C14	1.327(4)
C10–C11	1.375(5)	C20–N3	1.320(4)
C11–C12	1.375(5)	C2–O1	1.318(3)
C12–C13	1.392(4)	Cu1–O1	1.932(2)
C13–C8	1.410(4)	Cu1–N1	1.939(2)
C14–C15	1.399(4)	Cu1–N2	1.965(2)
C15–C16	1.421(4)	Cu1–N3	1.881(2)
O1–Cu1–N3	83.84(10)	C13–N2–C14	116.46(25)
N1–Cu1–N2	94.27(10)	N2–C14–C15	128.30(29)
N2–Cu1–N3	93.16(10)	C14–C15–C20	124.00(32)
N3–Cu1–O1	89.72(10)	C15–C20–N3	120.42(30)
O1–C2–C1	119.25(28)	Cu1–O1–C2	111.98(18)
C2–C1–N1	112.53(27)	Cu1–N1–C1	111.07(18)
C1–N1–C7	122.84(28)	Cu1–N1–C7	125.81(21)
N1–C7–C8	126.29(31)	Cu1–N2–C13	122.50(19)
C7–C8–C13	125.63(28)	Cu1–N2–C14	120.80(2)
C8–C13–N2	121.35(27)	C13–N2–C14	116.46(25)

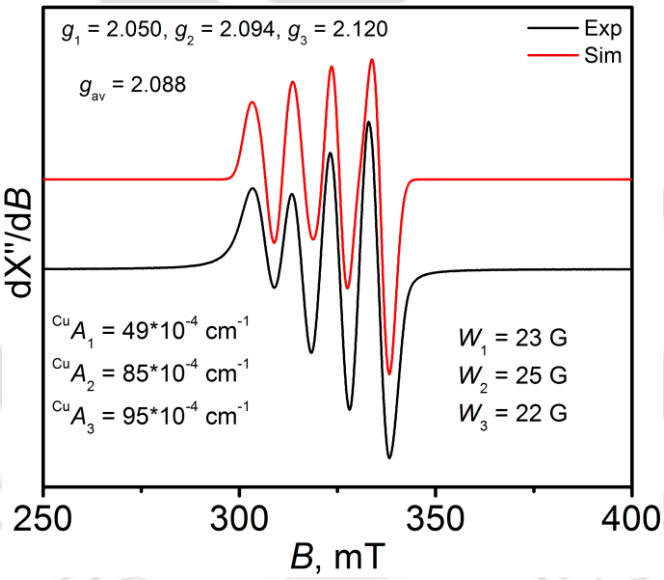

Figure 3.14: *X–band EPR spectrum of **11**, black: experimental and red: simulated. Conditions: X–band microwave frequency (GHz), 9.440; modulation frequency (kHz), 100; modulation amplitude (G), 10.0.*

X–band EPR spectrum measurement of complex **11** was performed in a dichloromethane solution at room temperature (**Figure 3.14**). Complex **11** was paramagnetic and showed a four–line EPR signal [^{Cu}I = 3/2]. The experimental as well as simulated EPR spectra of complex **11** are shown in **Figure 3.14**. Simulation to the experimental result provided the following parameters; g_1 = 2.050, g_2 = 2.094, g_3 = 2.120, g_{av} = 2.088, $^{Cu}(A_1, A_2, A_3)$ = (49, 85, 95) × 10^{-4} cm^{-1}. These parameter clearly indicated a distorted square planar geometry with an asymmetric coordination environment around the Cu(II) centre.[23] Using the

relation, $g_{av} = 1/3(g_{||} + 2g_{\perp})$, it was found that $g_{||} = 2.120$ and $g_{\perp} = 2.072$. The $g_{||} > g_{\perp}$ indicated that the unpaired electron resided on $d_{x^2-y^2}$ magnetic orbital in **11**.[23]

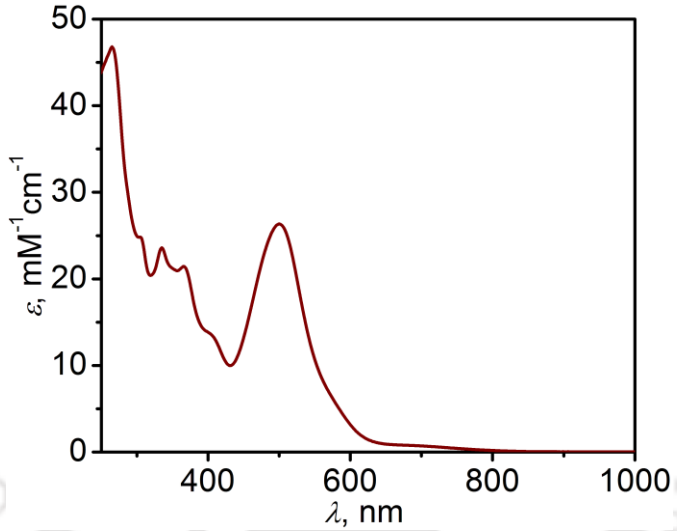

Figure 3.15: *UV–vis/NIR spectrum of complex **11** measured at RT in dichloromethane up to 250–1000 nm range.*

Electronic absorption (UV–vis/NIR) spectrum for complex **11** was recorded in the range of 250–1000 nm range in dichloromethane solution at room temperature. The spectrum (**Figure 3.15**) was comprised of a low intense absorption band at ~ 662 nm (ε = 950 $M^{-1}cm^{-1}$), and three highly intense bands at ~ 500 nm (ε = 26400 $M^{-1}cm^{-1}$), ~ 400 nm (ε = 13700 $M^{-1}cm^{-1}$), ~ 365 nm (ε = 21400 $M^{-1}cm^{-1}$). The extinction coefficient of these bands indicated that the absorption band at ~ 662 nm appeared due to *d–d* transition of Cu(II) centre,[1j] while, the other three bands were due to charge transfer. The band at ~ 500 nm was attributed to metal–to–ligand (MLCT) charge transfer, while, the high energy band at ~ 365 nm was due to phenolate–to–Cu(II) (LMCT) charge transfer.[24a] The band at 400 nm was appeared due to π→π* transition (LLCT) of the two imine moieties present in **11**.[24]

Ligand $\mathbf{H_4L^{CH_2NH_2}}$ and **H_4L2** are geometrical isomers (**Scheme 3.1**) and ligand **H_3L1** is the two–electron oxidized (amine to imine) form of **H_4L2**. Each ligand provided complex **11** under the same reaction condition (**Scheme 3.6**). This feature indicated; i) that at the initial stage of the reaction ligand $\mathbf{H_4L^{CH_2NH_2}}$ was converted to either **H_4L2** or **H_3L1** under the reaction condition, and/or ii) all the ligands generated the same reactants to have **H_3L3** under the same reaction condition in the reaction medium. A retro–synthetic route to **H_3L3** implied the formation of **A** and **B** in the reaction medium (**Scheme 3.7**) and indicated the possible formation of the species in the reaction medium.

To rationalize the formation of **H_3L3** and thereafter **11** *via* the *in situ* generation of **A** and **B** from ligand **H_4L2** and **H_3L1** in the presence of Cu(II) ion, Et_3N and air, ESI–MS measurement of the reaction solution has been performed. Mass spectrum analyses clearly showed the formation of $[\mathbf{Cu^{II}(H_2L2^{\bullet})}]^+$ (*m/z* = 387.28), $[\mathbf{H_3L1} + H]^+$ (*m/z* = 325.34), $[\mathbf{A} + H]^+$ (*m/z* = 122.02), and $[\mathbf{B}+H]^+$ (*m/z* = 222.26) in the reaction mixture (**Scheme 3.7; [A]**. For mass spectra: **Figure 3.16**). Thus, the formation of **A** and **B** from **H_4L2** proceeded *via* the initial oxidation of the organic moiety to **H_3L1** and after that the hydrolysis of imine bond (**Scheme 3.7; [A]**) occurred. This hydrolysis was favored due to the coordination of Lewis acidic Cu(II) ion to the ligand, which enhanced the nucleophilic attack of H_2O to the imine carbon atom (**Scheme 3.7; [A]**).

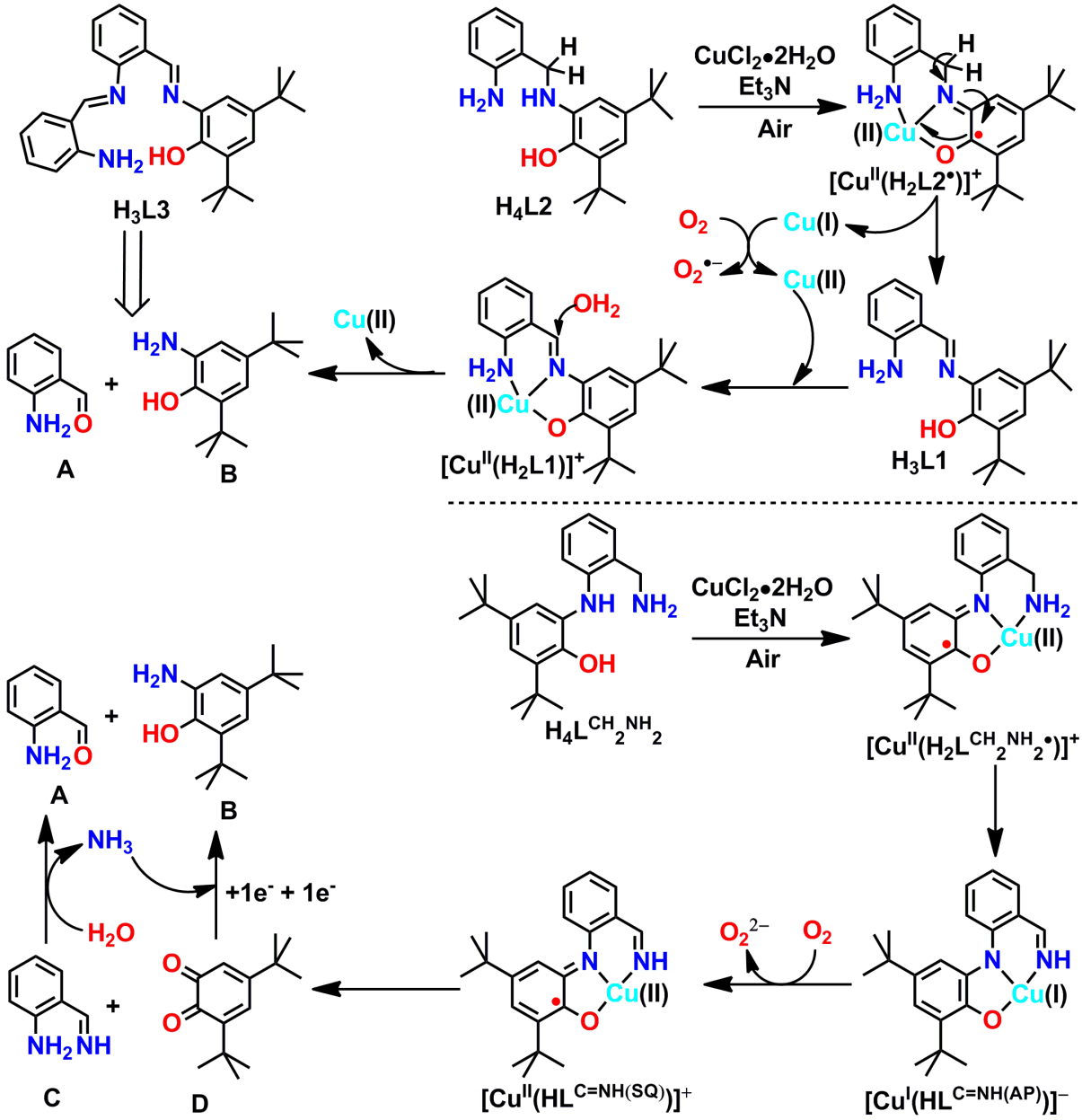

Scheme 3.7. *A mechanistic proposals for the formation of* ***H_3L3*** *from* ***H_4L2****, and* ***$H_4L^{CH_2NH_2}$*** *ligands.*

In order to find out the role of air, we have allowed ligand $\mathbf{H_4L^{CH_2NH_2}}$, $CuCl_2 \bullet 2H_2O$, and Et_3N to react in the absence of air. Complex **11** was not generated under the reaction condition. When, the above reaction was repeated in the presence of air but in the absence of Et_3N, to slow down the rate of the reaction by prolonging the N–H, O–H deprotonation and imine hydrolysis processes, monoradical–containing $[\mathbf{Cu^{II}(H_2L^{CH_2NH_2\bullet})}]^+$ (*m/z* = 387.28; **Figure 3.16**) and $[\mathbf{Cu^{II}(HL^{C=NH(SQ)})}]^+$ (*m/z* = 385.24; **Figure 3.16**) species along with **A**, **B**, and $\mathbf{H_3L3}$ were formed as evidenced by ESI–MS spectrum analyses. The generation of **A**, **B**, and ligand $\mathbf{H_3L3}$ clearly indicated the ligand centre amine oxidation, C–N bond cleavage, and C–O bond formation processes and the generation processes were proceeded *via* $[\mathbf{Cu^{II}(H_2L^{CH_2NH_2\bullet})}]^+$ and $[\mathbf{Cu^{II}(HL^{C=NH(SQ)})}]^+$ species. A mechanistic proposal for the formation of $\mathbf{H_3L3}$ form $\mathbf{H_4L^{CH_2NH_2}}$ is summarized in **Scheme 3.7**. Herein, in it important to note that the reaction in the presence of Et_3N under air produced a large amount of ammonia gas, instantaneously. The gas was characterized by using Nessler reagent. The formation of ammonia gas was attributed to hydrolysis of the imine (**C**) to aldehyde (**A**) {$[\mathbf{A} + H]^+$; *m/z* = 122.02}. This generated ammonia reacted with *in situ* generated 3,5–di–*tert*–butyl–1,2–benzoquinone and formed 3,5–di–*tert*–butyl–1,2–iminobenzoquinone ($[M + H]^+$ = *m/z* = 220.25; M = molecular mass}) which then underwent a two–electron reduction in the reaction medium and transformed to **B** {$[\mathbf{B} + H]^+$; *m/z* = 222.26}.

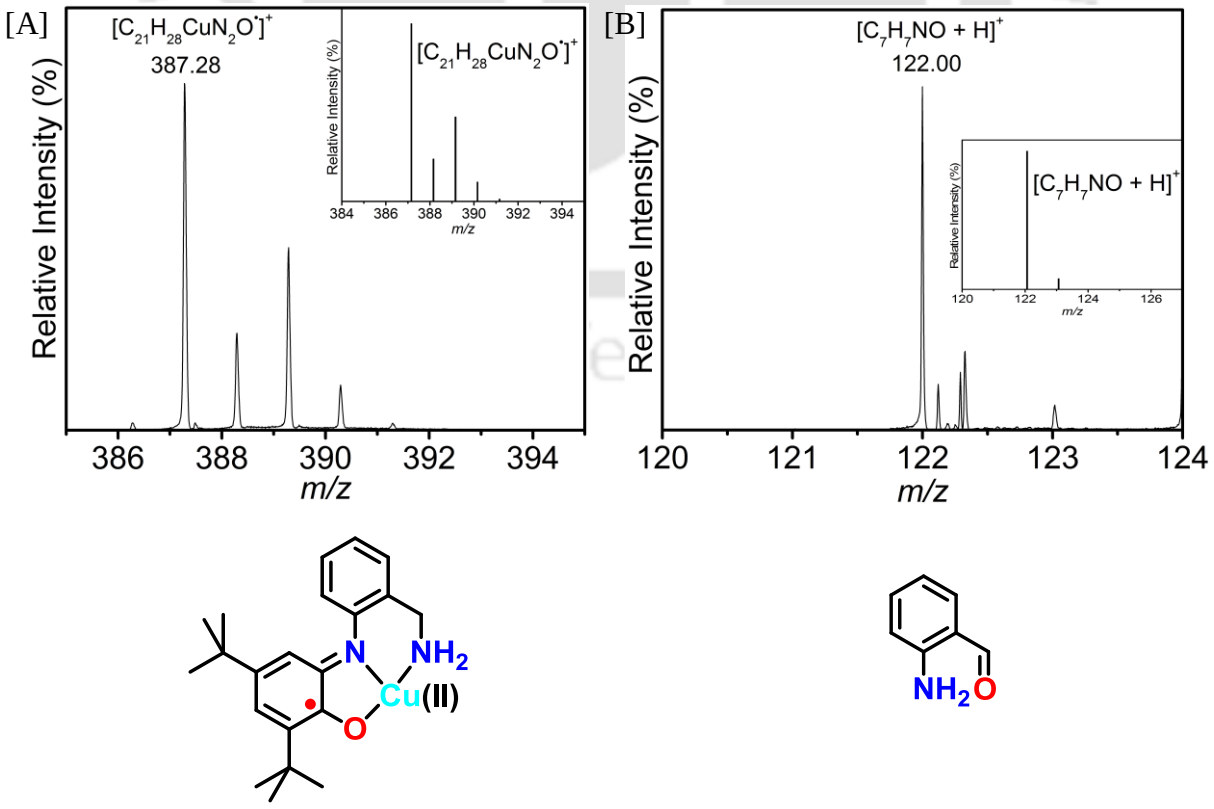

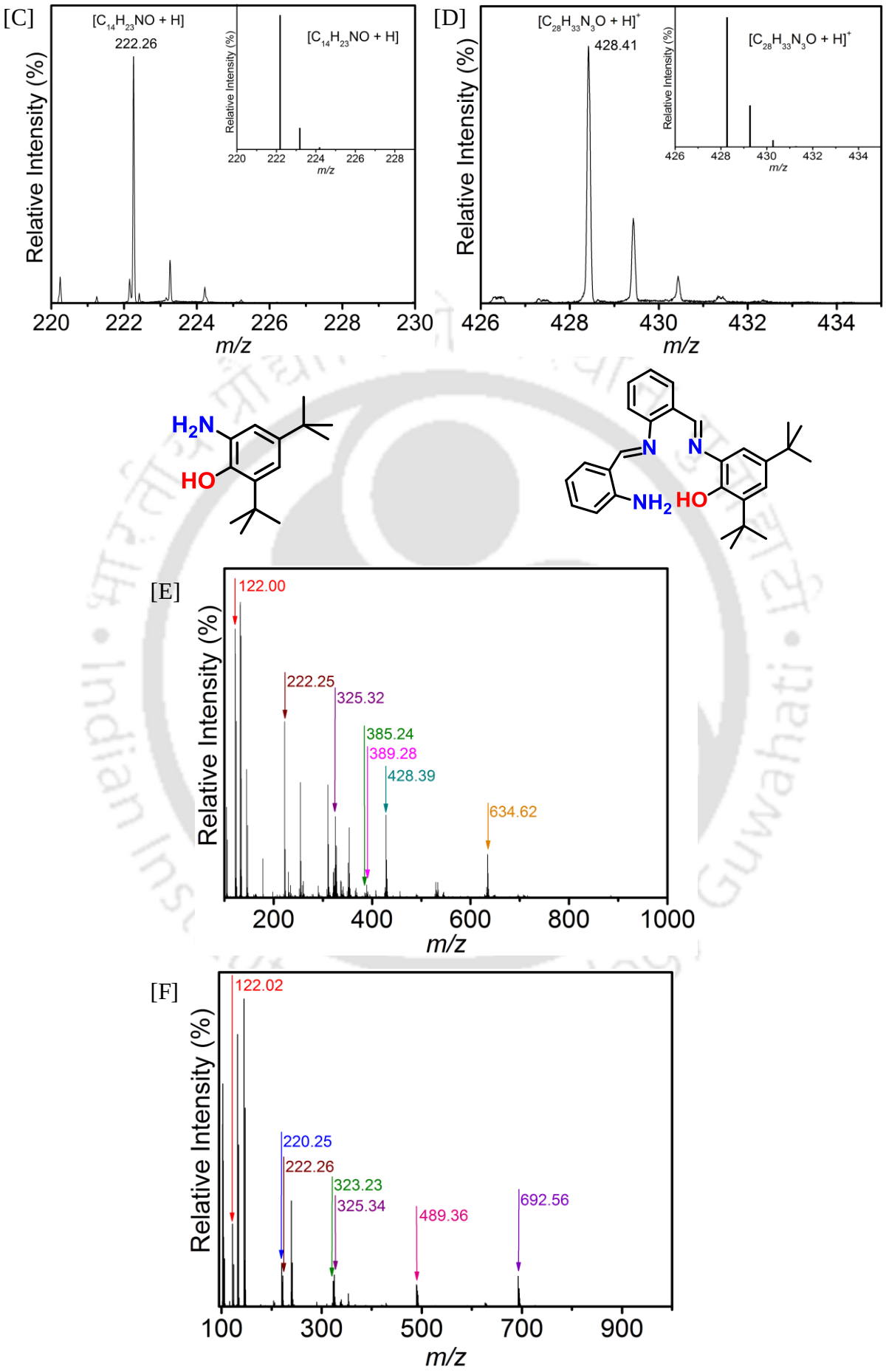
[C]
[C14H23NO + H]
222.26
Relative Intensity (%)
m/z
[D]
[C28H33N3O + H]+
428.41
[E]
122.00
222.25
325.32
385.24
389.28
428.39
634.62
[F]
122.02
220.25
222.26
323.23
325.34
489.36
692.56

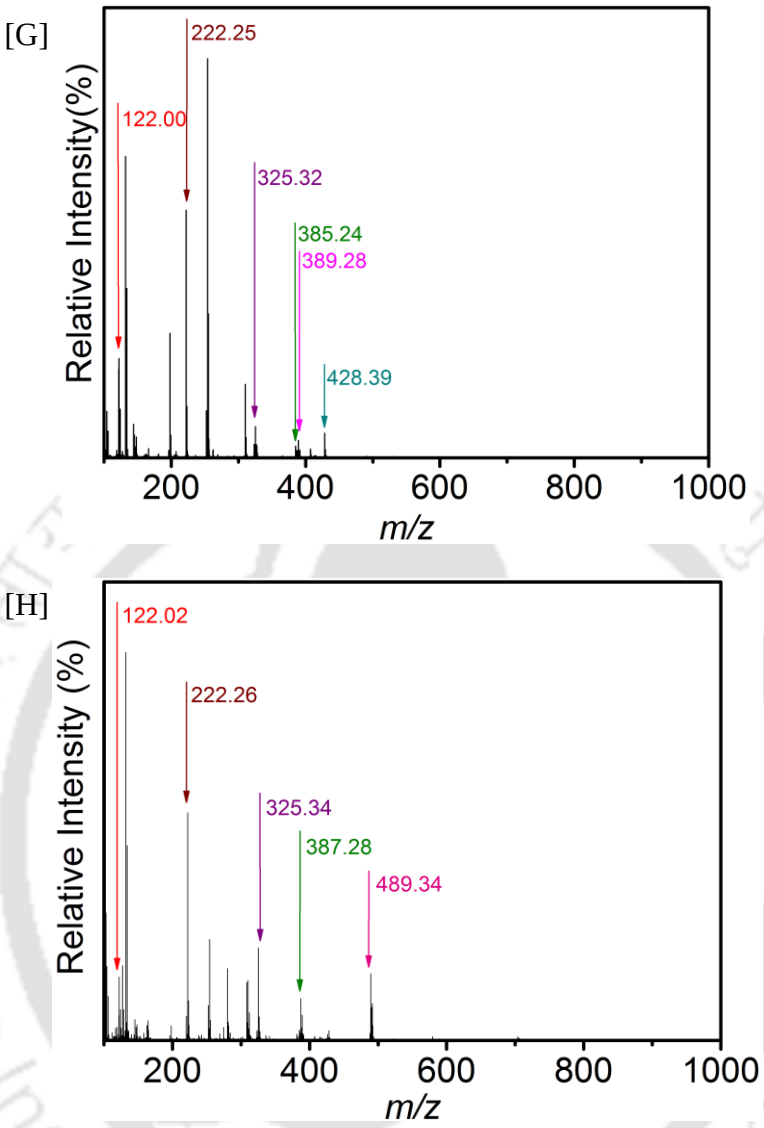

Figure 3.16: *[A] experimental and simulated (inset)ESI–mass spectrum for* $\mathbf{Cu^{II}(H_2L^{CH_2NH_2^{\bullet}})}$*; [B] experimental and simulated (inset) ESI–mass spectrum for* ***A****; [C] experimental and simulated (inset) mass spectrum for* ***B****; [D] experimental and simulated (inset) ESI–mass spectrum for* $\mathbf{H_3L3}$*; [E] experimental ESI–mass spectrum of a reaction mixture containing* $\mathbf{H_4L^{CH_2NH_2}}$ *and* $CuCl_2{\bullet}2H_2O$ *in absence of triethylamine; [F] experimental ESI–mass spectrum of a reaction mixture containing* $\mathbf{H_4L^{CH_2NH_2}}$ *and* $CuCl_2{\bullet}2H_2O$ *in the presence of triethylamine; [G] experimental mass spectrum of a reaction mixture containing* $\mathbf{H_4L2}$ *and* $CuCl_2{\bullet}2H_2O$ *in absence of triethylamine; [H] experimental ESI–mass spectrum of a reaction mixture containing* $\mathbf{H_4L2}$ *and* $CuCl_2{\bullet}2H_2O$ *in the presence of triethylamine.*

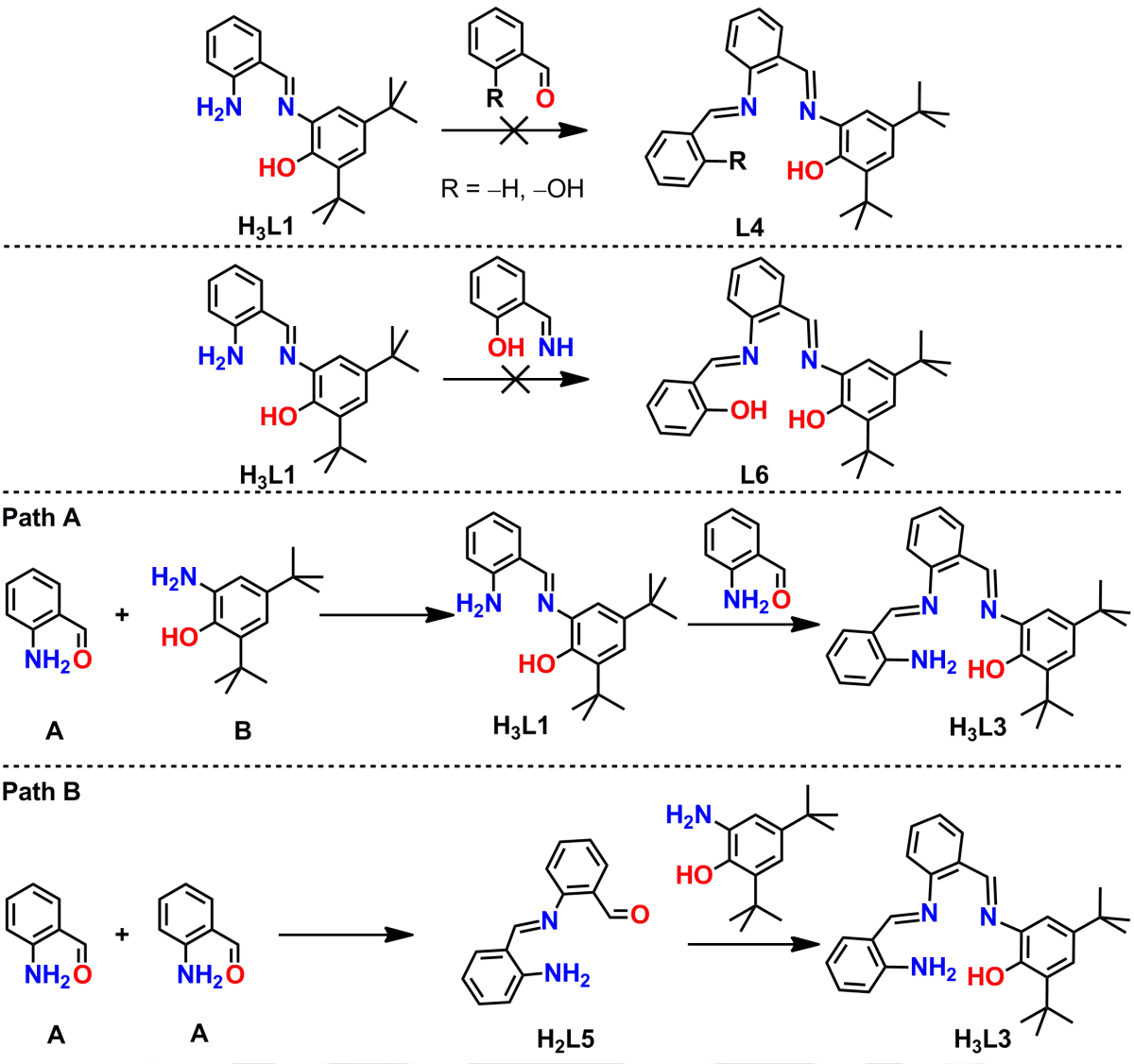

Scheme 3.8: *The formation route to* ***H_3L3****.*

The formation of **H_3L3** could propagate through either Path A or Path B (**Scheme 3.8**). To distinguish between the two paths, **H_3L1** was allowed to react with benzaldehyde or salicyladehyde. Noteworthy, 2–Aminobenzaldehyde was avoided as it polymerizes by self–condensation. It was observed that no condensation between **H_3L1** and benzaldehyde or salicyladehyde proceeded. This fact indicated the low nucleophilicity of amine group due to the conjugation of amine lone–pair electron with the imine moiety attached to the *–ortho* position. I discarded the reaction between **H_3L1** with 2–aminobenzaldehyde, owing to its high reactivity to self–condensation reaction, and thereafter, polymerization reaction. Hence, the Path A was not followed to the formation of **H_3L3**, rather, Path B was followed favorably.

3.6: Ligand H_3L1 and Its Selective Reactivity with Salicylaldehyde in the Presence of $Zn(OAc)_2 \bullet 2H_2O$: A Fluorescent Active Dinuclear Zn(II) Complex (12) Formation and Its Characterization:

Ligand **H_3L1** alone does not react with salicylaldehyde, even in the presence of triethylamine. This could be because of less availability of aniline lone–pair (low nucleophilicity), which is in conjugation with the adjacent imine unit. Notably, it was found that when the ligand and salicylaldehyde were treated with $Zn(OAc)_2 \bullet 2H_2O$ in the presence of triethylamine, it produced a dinuclear zinc complex (**12**) with a tetradentate ligand (**H_2L4**) comprised of ONNO donor atoms. The new ligand was formed by the 1:1 condensation of ligand **H_3L1** and salicylaldehyde. Herein, the condensation occurred due to the reason that Zn^{2+} ion initially coordinated with a moderately soft ligand salicylaldehyde and enhanced the electrophilicity of aldehyde group (**Scheme 3.9**). Though, the nucleophilic character of the aniline unit is less, yet it reacted with salicylaldehyde because of the enhancement of electrophilic character of aldehyde unit.

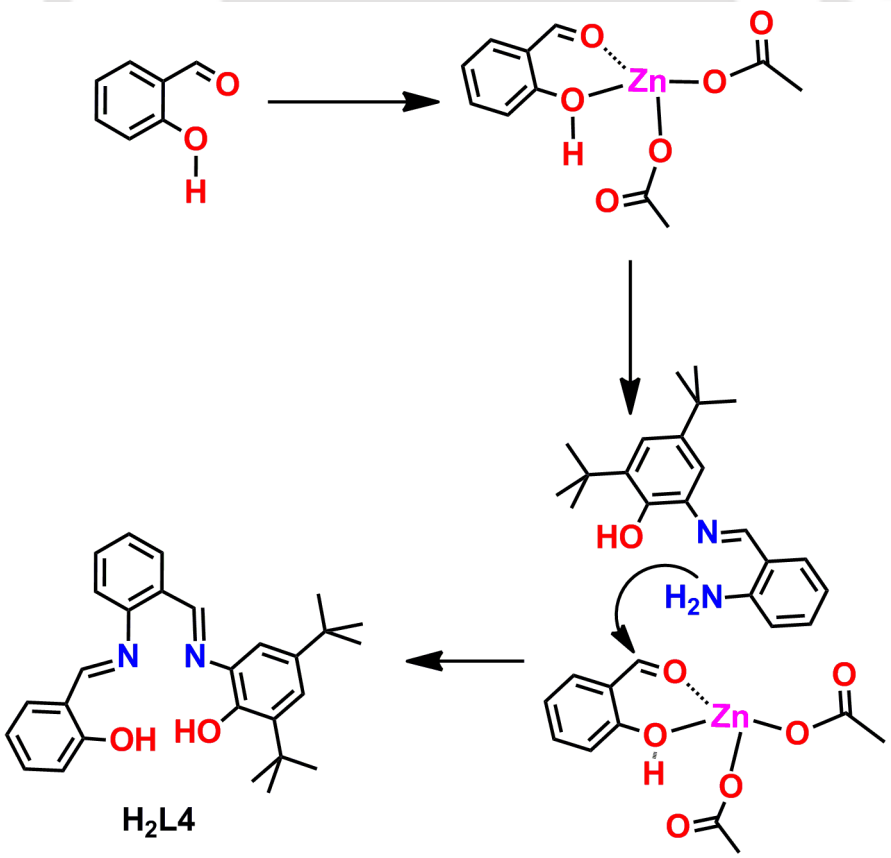

Scheme 3.9: *A possible route to formation of **H_2L4** ligand.*

The complex **12** was prepared by treatment of 1 equivalent salicylaldehyde to the ligand **H_3L1** in the presence of 1 equivalent of $Zn(OAc)_2 \bullet 2H_2O$ and triethylamine in acetonitrile under air (**Scheme 3.10**).

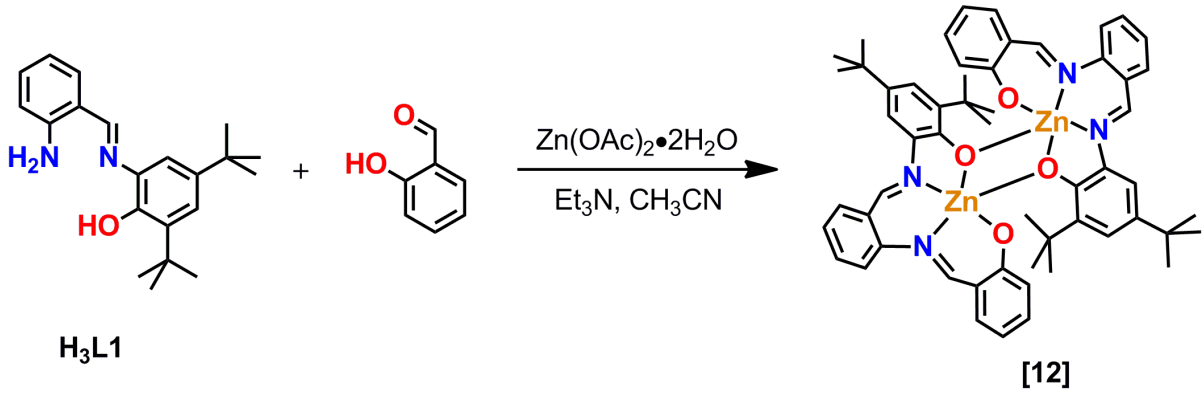

Scheme 3.10: *Synthetic route for complex **12**.*

In the IR spectrum of complex **12**, no stretching frequency for ν(N–H), or ν(O–H) was observed. This implied ligation of the generated ligand to the Zn ion occurred in the course of the reaction and alcohol, and amine groups were in their deprotonated form. The asymmetric, symmetric, and overtone ν(C–H) bands for *tert*–butyl group in complex **12** were appeared at 2955, 2862, and 2900 cm^{-1} and further indicated the coordination of ligand with metal ion. Interestingly, in complex **12**, two different ν(C=N) stretches appeared at 1610, and 1589 cm^{-1}.[24] The multiple bands at 1246 to 1276 cm^{-1} were appeared for the phenolate ν(C–O) stretches, while, ν(C–N) band appeared at 1146 cm^{-1}.

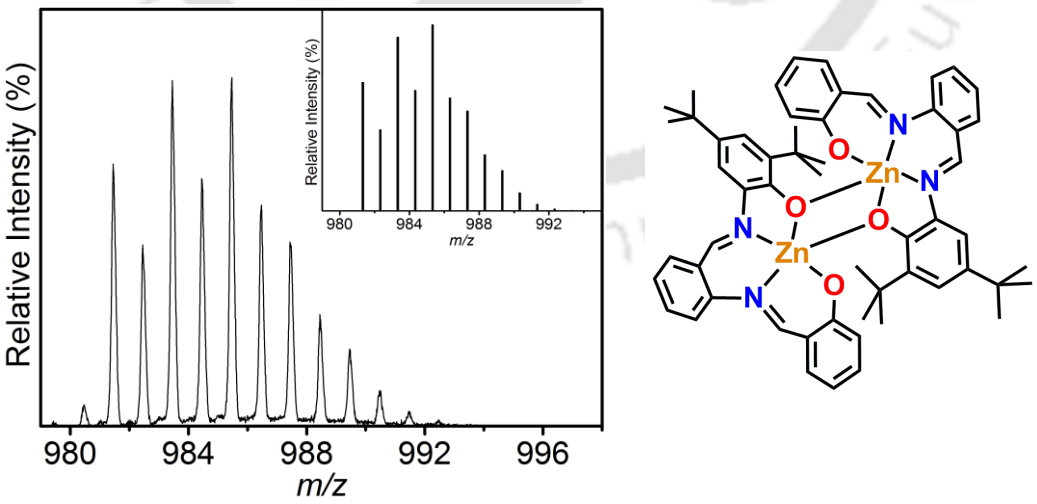

Figure 3.17: *ESI–mass spectrum of **12** with experimental and simulated isotopic distribution pattern (inset).*

Electrospray ionization mass spectrum (ESI–MS) for **12** was measured in acetonitrile solution in positive mode. Mass spectrum analysis of complex **12** exhibited a 100%

molecular ion peak at *m/z* = 985.47; which corresponded to $[M + H]^+$, M = molecular mass. Isotope distribution pattern examination showed that the observed mass spectrum has the composition $\mathbf{C_{56}H_{61}N_4O_4Zn_2}$. Therefore, the composition of **12** was $\mathbf{C_{56}H_{60}N_4O_4Zn_2}$.

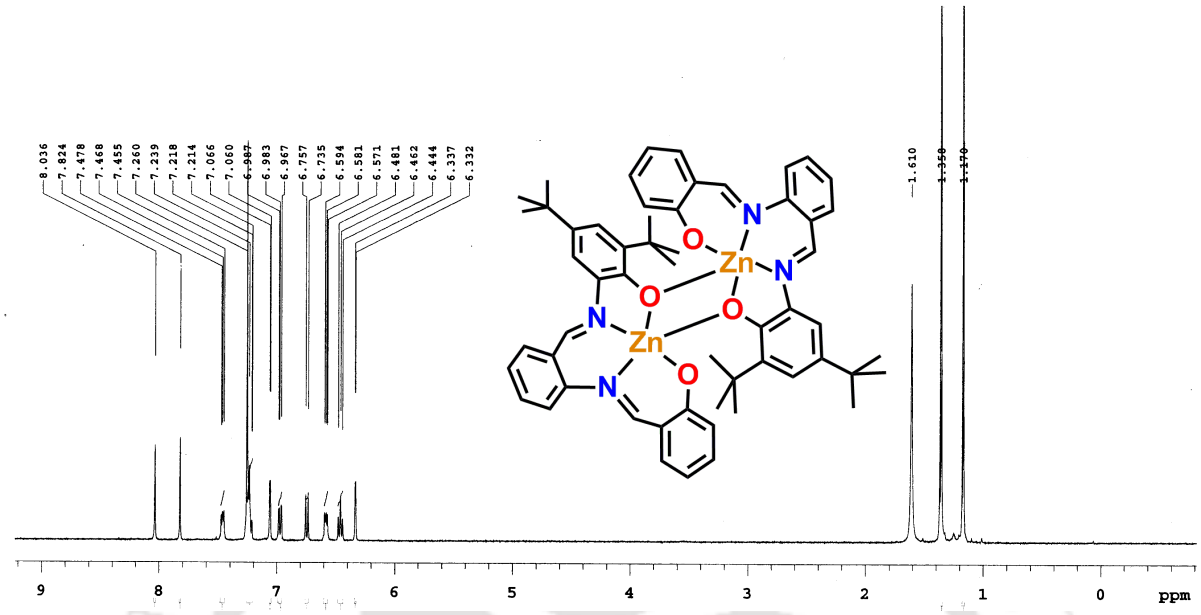

Figure 3.18: *^{1}H NMR spectrum for **12**.*

Complex **12** was diamagnetic and ^{1}H NMR signals ($CDCl_3$) appeared at δ 1.17 (s, 18H), 1.36 (s, 18H), 6.33 (d, *J* = 2 Hz, 2H), 6.46 (t, *J* = 7.4 Hz, 2H), 6.58 (t, *J* = 4.6 Hz, 2H), 6.75 (d, *J* = 8 Hz, 2H), 6.98 (dd, *J* = 8 Hz, and 1.6 Hz, 2H), 7.06 (d, *J* = 2.4 Hz, 2H), 7.24 (m, 6H), 7.47 (t, *J* = 4.6 Hz, 2H), 7.82 (s, 2H), 8.04 (s, 2H) ppm, respectively.

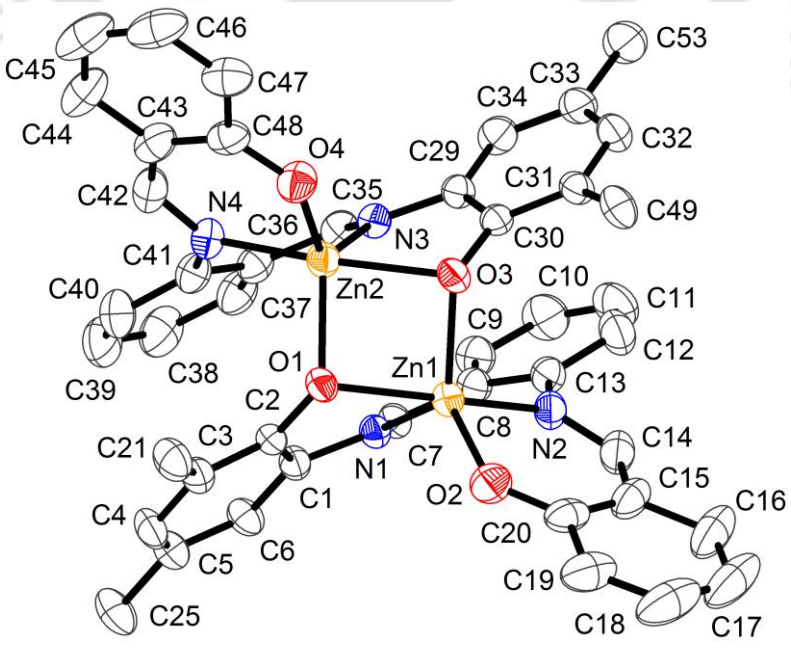

Figure 3.19: *ORTEP representation of **12**; thermal ellipsoids were drawn at the 50% probability level. Methyl groups present in the tert–butyl groups, and hydrogen atoms were omitted for clarity.*

X–ray diffraction measurement for complex **12** was performed at 298 K. Complex **12** crystallized in the monoclinic space group $P12_1/n1$. ORTEP representation of complex **12** is shown in **Figure 3.19**. Selected bond distances and angles are summarized in **Table 3.4**.

The molecular structure analysis showed the formation of a neutral dinuclear Zn complex where both the Zn centers were in distorted trigonal bipyramidal geometry [τ_5 = 0.64 (Zn1); 0.61 (Zn2), parenthesis indicates the Zn centre][26] and were connected to each other *via* two strong phenolate bridges [Zn1–O3 = 2.035(2), and Zn2–O1 = 2.020(2) Å]. For Zn1 center, the equatorial plane was constituted by N1, O2 and O3 atoms and the axial positions were occupied O1 and N2 atoms. In the other unit, Zn2 was surrounded by N3, O4, and O1 atoms at the equatorial positions, while, N4, and O3 atoms were at the axial coordination sites. Two units were almost identical and hence, only one unit will be discussed here. The Zn1–N1, Zn1–O2, and Zn1–O3 bond distances were 2.108(3), 1.911(2), and 2.035(2) Å, respectively, while, the axial bonds, Zn1–O1 and Zn1–N2, were 2.124(2), 2.083(3) Å, respectively. These bond distances were in agreement with the +II oxidation state of the Zn atom.[26,27]

All the C–C bond distances of the *tert*–butyl containing C_6 aryl ring, which constituted by C8–C9–C10–C11–C12–C13 atoms, were nearly equal and were within 1.40±0.01 Å range. Albeit, a slightly quinoid–type distortion was observed in the iminosalicylaldene unit, that was comprised of N2–C14–C15–C16–C17–C18–C19–C20–O2 atoms. The C15–C16, C16–C17, C17–C18, C18–C19, C19–C20, and C20–15 bond distances were 1.418(5), 1.349(7), 1.403(7), 1.362(6), 1.418(5), and 1.419(5) Å, respectively. The two imine as well as two phenolate bonds were not same. *i.e.* N1–C7 = 1.278(4) Å and N2–C14 = 1.300(4) Å, and C2–O1 = 1.346(3) and C20–O2 = 1.304(4) Å. These features clearly indicated that due to higher electron density within the C_6 ring with *tert*–butyl substituent the delocalization of phenolate^{1-} charge was less compared to the C_6 iminosalicylaldene aryl ring unit having no *tert*–butyl substituent. To note, this type of phenolate^{1-} charge delocalization in salen complexes is common and the coordinating ligands in the complexes, as reported, are in their fully reduced form mononegative form.[19] Hence, in the dinuclear neutral complex **12**, ligands were in their dinegative form and two Zn ion were in their +II oxidation state.

Table 3.4: *Selected bond distances (Å,)and bond angels (°) for complex **12**.*

Zn1–O1	2.124(2)	Zn2–O1	2.020(2)
Zn1–O2	1.911(2)	Zn2–O3	2.101(2)
Zn1–O3	2.035(2)	Zn2–O4	1.931(2)

Zn1–N1	2.108(3)	Zn2–N3	2.125(3)
Zn1–N2	2.083(3)	Zn2–N4	2.082(3)
C1–C2	1.404(5)	C29–C30	1.412(4)
C2–C3	1.412(4)	C30–C31	1.403(4)
C3–C4	1.389(5)	C31–C32	1.393(5)
C4–C5	1.391(5)	C32–C33	1.394(5)
C5–C6	1.385(4)	C33–C34	1.385(5)
C6–C1	1.391(4)	C34–C29	1.386(4)
C1–N1	1.423(4)	C29–N3	1.418(4)
N1–C7	1.278(4)	N3–C35	1.275(4)
C7–C8	1.459(4)	C35–C36	1.465(5)
C8–C9	1.394(5)	C36–C37	1.388(5)
C9–C10	1.380(5)	C37–C38	1.386(5)
C10–C11	1.377(6)	C38–C39	1.376(6)
C11–C12	1.371(6)	C39–C40	1.378(5)
C12–C13	1.393(5)	C40–C41	1.395(5)
C13–C8	1.413(5)	C41–C36	1.402(5)
C13–N2	1.419(4)	C41–N4	1.421(4)
N2–C14	1.300(4)	N4–C42	1.293(4)
C14–C15	1.428(5)	C42–C43	1.432(5)
C15–C16	1.418(5)	C43–C44	1.417(5)
C16–C17	1.349(7)	C44–C45	1.360(6)
C17–C18	1.403(7)	C45–C46	1.380(6)
C18–C19	1.362(6)	C46–C47	1.369(5)
C19–C20	1.418(5)	C47–C48	1.427(5)
C20–C15	1.419(5)	C48–C43	1.417(5)
C20–O2	1.304(4)	C48–O4	1.301(4)
O1–Zn1–N1	76.35(9)	O2–Zn1–N2	93.06(11)
O1–Zn1–O2	102.20(9)	O2–Zn1–O3	119.25(10)
O1–Zn1–O3	81.73(8)	O2–Zn1–N1	121.52(10)
O1–Zn1–N2	159.95(10)	N1–Zn1–N2	84.63(10)
N1–Zn1–O3	118.27(9)	O3–Zn1–N2	102.21(9)
O1–Zn2–O3	82.66(8)	O1–Zn2–O4	118.67(10)
O1–Zn2–N3	117.17(9)	O1–Zn2–N4	103.47(9)
O3–Zn2–N3	76.41(9)	O3–Zn2–N4	159.96(10)
O3–Zn2–O4	101.38(9)	N3–Zn2–O4	123.27(10)
N3–Zn2–N4	83.90(10)	O4–Zn2–N4	92.44(10)
Zn1–O1–Zn2	91.83(8)	Zn1–O3–Zn2	92.05(8)
Zn1–O3–C30	120.04(19)	Zn2–O3–C30	110.45(18)
Zn2–O1–C2	122.87(19)	Zn1–O1–C2	109.38(18)

Complex **12** showed moderate fluorescent property. Generally, Zn complexes are four coordinate. Due to having high Lewis acidity, coordination number increases and consequently, Zn complexes show charge transfer fluorescence property compared to the low coordination–number Zn complexes.[28] The difference in energy in Zn complexes caused by the coordination environment is the main reason for fluorescence in higher

coordination–numbered Zn complexes.[29] As the complex **12** contained two Zn atoms whose were in five–coordination environment, complex **12** showed the chelation enhancement fluorescence (CHEF) property.[30]

Electronic absorption spectroscopic investigation of **12** in the 275–675 nm region employing various solvent systems showed mainly three bands in non–coordinating solvent systems at ~ 428, ~ 350, and ~ 310 nm, while, in coordinating solvent systems an additional band at ~ 515 nm appeared. The absorption bands at 310–350 nm rage was appeared which might be associated with the π→π* transition originated mainly due to the azomethine (imine π→π*) chromophore.[31] Ligand–to–metal charge transfer (LMCT) band arose at ~ 428 nm.[31b] Interestingly, in coordinating solvent systems a new band at ~ 515 nm was appeared due to formation of dinuclear solvated six–coordinated Zn complex.

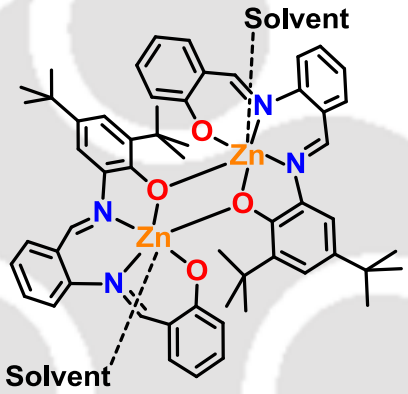

Scheme 3.11: *Schematic representation of plausible six–coordinate dinuclear Zn(II) complex.*

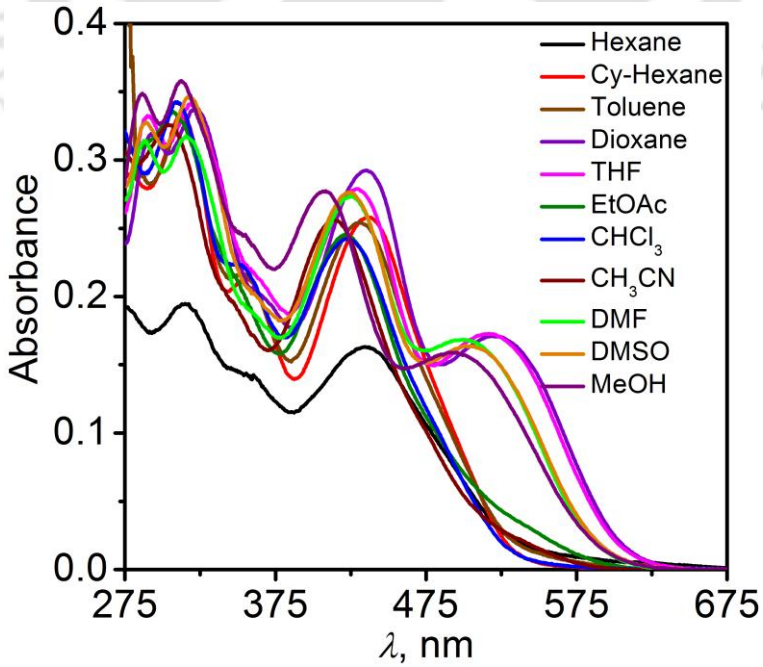

Figure 3.20: *UV–vis spectra at RT in different solvent (C = 10 μM).*

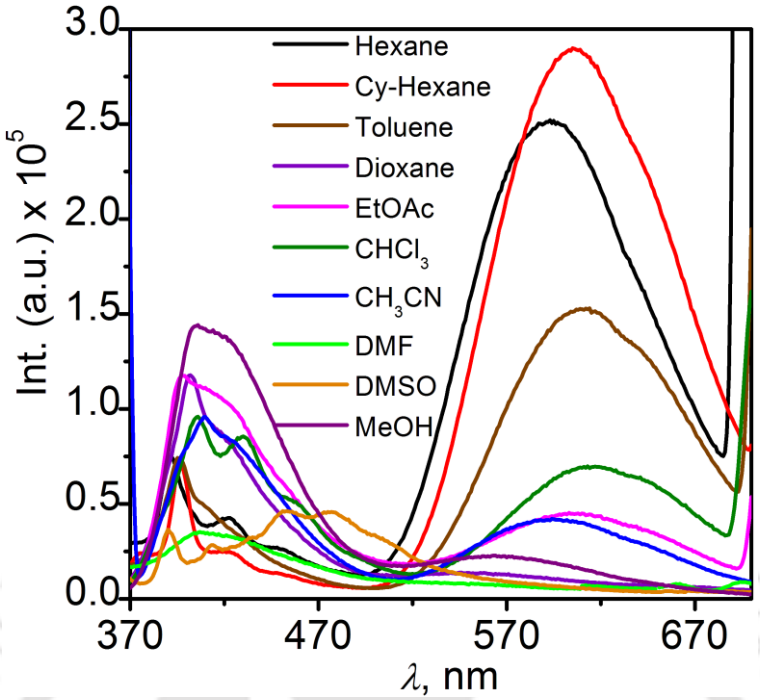

Figure 3.21: *Emmisions spectra at λ = 350 nm (C = 10 μM).*

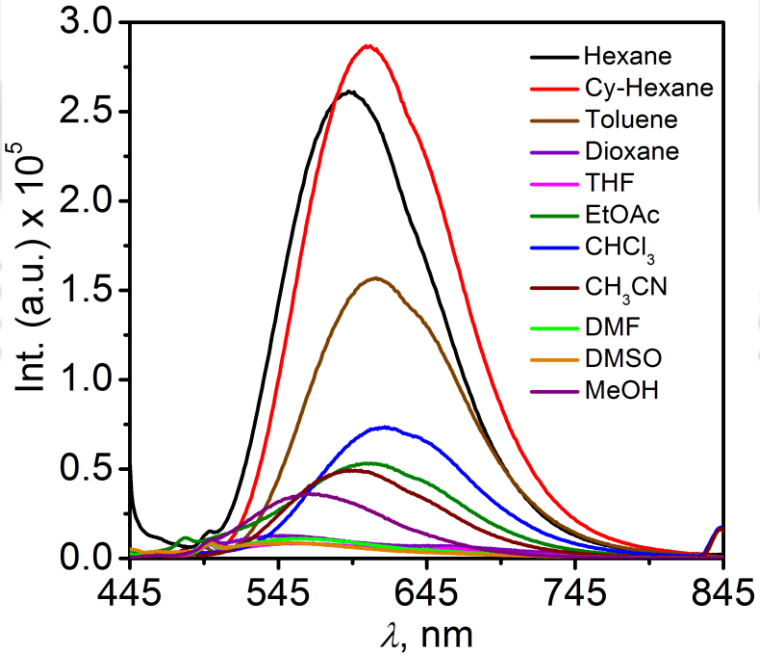

Figure 3.22: *Emission spectra at λ = 428 nm (C = 10 μM).*

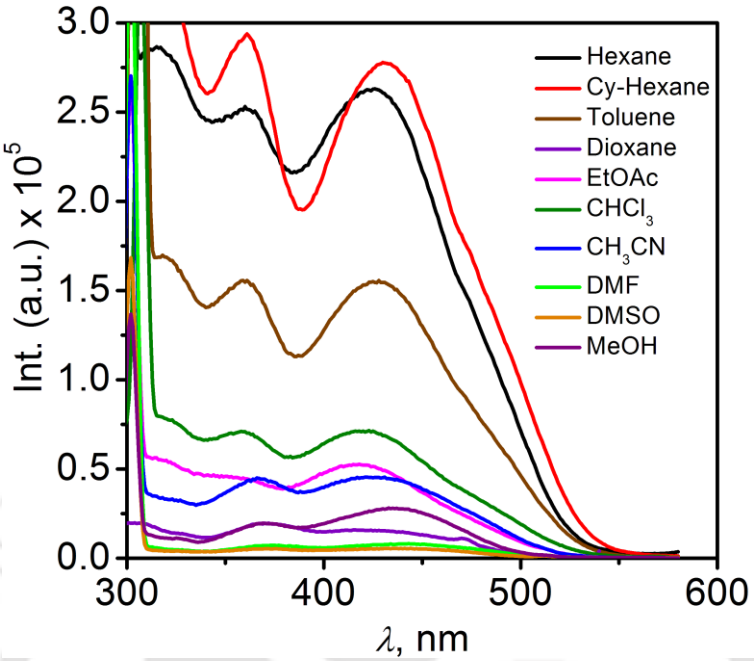

Figure 3.23: *Excitation spectra λ = 600 nm (C = 10 μM).*

Photophysical study of **12** in different solvent systems showed emission fluorescent upon excitation at λ_{ex} = 350 nm (**Figure 3.20**). The emission fluorescent spectral intensity was maxima in non–coordinating solvent systems, while, in coordinating solvent systems, the fluorescent property was quenched due to electron transfer. A similar type of spectral appeared upon excitation of **12** at λ_{ex} = 428 (**Figure 3.21**).

3.7: Conclusions:

1. The ligand $\mathbf{H_4L^{CH_2NH_2}}$ behaved as a non–innocent ligand and stabilized corresponding Co(III) complex in diradical–coordinated octahedral geometry. The complex was diamagnetic owing a strong antiferromagnetic coupling between two π–radicals. The angle between the two π–radical occupying C_6 planes was 55.6°. This deviation from the orthogonality was the main reason for the antiferromagnetic coupling.

2. The tridentate ligand $\mathbf{H_4L^{CH_2NH_2}}$ provided Ni(II) complex as complete ligand backbone modified salen–type complex *via* aryl migration and C=N hydrolysis.

3. The same ligand also provided a completely ligand backbone modified tetradentate salen–type Cu(II) complex *via* ligand center amine oxidation and C–N bond cleavage.

4. The tridentate ligand **H_3L1** reacts with salicylaldehyde selectively, in the presence of $Zn(OAc)_2 \bullet 2H_2O$ and triethylamine, produced a fluorescence active phenolate bridged dinuclear Zn(II) complex.

References:

1. (*a*) Y. Wang, J. L. Dubois, B. Hedman, K. O. Hodgson and T. D. P. Stack, *Science*, 1998, **279**, 537; (*b*) P. Chaudhuri, M. Hess, J. Müller, K. Hildenbrand, E. Bill, T. Weyhermüller and K. Wieghardt, *J. Am. Chem. Soc.*, 1999, **121**, 9599; (*c*) T. K. Paine, T. Weyhermüller, K. Wieghardt and P. Chaudhuri, *Dalton Trans.*, 2004, 2092; (*d*) P. Chaudhuri, M. Hess, T. Weyhermüller and K. Wieghardt, *Angew. Chem., Int. Ed.*, 1999, **38**, 1095; (*e*) P. Chaudhuri, M. Hess, U. Flörke and K. Wieghardt, *Angew. Chem., Int. Ed.*, 1998, **37**, 2217; (*f*) F. Thomas, G. Gellon, I. Gautier–Luneau, E. Saint–Aman and J.–L. Pierre, *Angew. Chem., Int. Ed.*, 2002, **41**, 3047; (*g*) P. Chaudhuri, K. Wieghardt, T. Weyhermüller, T. K. Paine, S. Mukherjee and C. Mukherjee, *Biol. Chem.*, 2005, **386**, 1023; (*h*) S. Mukherjee, T. Weyhermüller, E. Bothe, K. Wieghardt and P. Chaudhuri, *Dalton Trans.*, 2004, 3842; (*i*) C. Mukherjee, T. Weyhermüller, E. Bothe and P. Chaudhuri, *C. R. Chim.*, 2007, **10**, 313; (*j*) C. Mukherjee, U. Pieper, E. Bothe, V. Bachler, E. Bill, T. Weyhermüller and P. Chaudhuri, *Inorg. Chem.*, 2008, **47**, 8943 and references therein; (*k*) C. Mukherjee, T. Weyhermüller, E. Bothe and P. Chaudhuri, *Inorg. Chem.*, 2008, **47**, 11620; (*l*) Y. Wang and T. D. P. Stack, *J. Am. Chem. Soc.*, 1996, **118**, 13097; (*m*) F. Thomas, *Eur. J. Inorg. Chem.*, 2007, 2379; (*n*) S. Itoh, M. Taki and S. Fukuzumi, *Coord. Chem. Rev.*, 2000, **198**, 3; (*o*) S. E. Allen, R. R. Walvoord, R. P. Salinas and M. C. Kozlowski, *Chem. Rev.*, 2013, **113**, 6234.

2. (*a*) P. Chaudhuri and K. Wieghardt, *Prog. Inorg. Chem.*, 2001, **50**, 151; (*b*) Jr. L. Que and W. B. Tolman, *Nature*, 2008, **455**, 333; (*c*) G. A. Abakumov, V. K. Cherkasov, V. I. Nevodchikov, V. A. Kuropatov, G. T. Yee and C. G. Pierpont, *Inorg. Chem.*, 2001, **40**, 2434; (*d*) S. Ye, B. Sarkar, F. Lissner, T. Schleid, J. van Slageren, J. Fiedler and W. Kaim, *Angew. Chem., Int. Ed.*, 2005, **44**, 2103; (*e*) C. Benelli, A. Dei, D. Gatteschi and L. Pardi, *Inorg. Chem.*, 1990, **29**, 3409; (*f*) C. G. Pierpont, *Coord. Chem. Rev.*, 2001, **99**, 216.

3. *Principles of Bioinorganic Chemistry*, by S. J. Lippard, University Science Book, 1994.

4. (*a*) J. P. Klinman, *J. Biol. Chem.*, 1996, **271**, 27189; (*b*) M. Mure, *Acc. Chem. Res.*, 2004, **37**, 131; (*c*) J. P. Klinman, *Biochim. Biophys. Acta.*, 2003, **1647**, 131; (*d*) M. Mure, S. A. Mills and J. P. Klinman, *Biochemistry*, 2002, **41**, 9269; (*e*) S. M. Janes, D. Mu, D. Wemmer, A. J. Smith, S. Kaur, D. Maltby, A. L. Burlingame and J. P. Klinman, *Science*, 1990, **248**, 981; (*f*) D. M. Dooley, R. A. Scott, P. F. Knowles, C. M. Colangelo, M. A.

McGuirl and D. E. Brown, *J. Am. Chem. Soc.*, 1998, **120**, 2599; (*g*) D. M. Dooley, M. A. McGuirl, D. E. Brown, P. N. Turowski, W. S. McIntire and P. F. Knowles, *Nature*, 1991, **349**, 262.

5. C. Mukherjee, T. Weyhermüller, E. Bother and P. Chaudhuri, *C. R. Chimie.*, 2007, **10**, 313.

6. (*a*) *Metal Ions in Biological Systems*, ed. H. Sigel and A. Sigel, Marcel–Dekker, New York, 1994, vol. 30; (*b*) J. Stubbe and W. A. van der Donk, *Chem. Rev.*, 1998, **98**, 705; (*c*) J. P. Klinman, *Chem. Rev.*, 1996, **96**, 2541; (*d*) M. M. Palcic and J. P. Klinman, *Biochemistry*, 1983, **22**, 5957; (*e*) J. M. Murray, C. G. Saysell, C. M. Wilmot, W. S. Tambyrajan, J. Jaeger, P. F. Knowles, S. E. V. Phillips and M. J. McPherson, *Biochemistry*, 1999, **38**, 8217.

7. (*a*) B. Huang, H. Tian, S. Lin, M. Xie, X. Yu and Q. Xu, *Tetrahedron Lett.*, 2013, **54**, 2861; (*b*) T. Sonobe, K. Oisaki and M. Kanai, *Chem. Sci.*, 2012, **3**, 3249; (*c*) R. D. Patil and S. Adimurthy, *Adv. Synth. Catal.*, 2011, **353**, 1695; (*d*) E. Zhang, H. Tian, S. Xu, X. Yu and Q. Xu, *Org. Lett.*, 2013, **15**, 2704.

8. C. N. Verani, S. Gallert, E.Bill, T. Weyhermüller, K. Wieghardt and P. Chaudhuri, *Chem. Commun.*, 1999, 1747.

9. J. Coates, *Encyclopedia of Analytical Chemistry* R.A. Meyers (Ed.) 2000, pp. 10815–10837.

10. C. Imbert, H. P. Hratchian, M. Lanznaster, M. J. Heeg, L. M. Hryhorczuk, B. R. McGarvey, H. B. Schlegel and C. N. Verani, *Inorg. Chem.*, 2005, **44**, 7414.

11. (*a*) R. M. Haak, M. M. Belmonte, E. C. Escudero–Adàn, J. Benet–Buchholz*a* and A. W. Kleij, *Dalton Trans.*, 2010, **39**, 593; (*b*) C. W. Lange, B. J. Conklin and C. G. Pierpont, *Inorg. Chem.*, 1994, **33**, 1276.

12. (*a*) D. Herebian, P. Ghosh, H. Chun, E. Bothe, T. Weyhermüller and K. Wieghardt, *Eur. J. Inorg. Chem.* **2002**, 1957; (*b*) C. Mukherjee, T. Weyhermüller, E. Bothe and P. Chaudhuri, *Inorg. Chem.*, 2008, **47**, 2740; (*c*) G. Szigethy, D. W. Shaffer and A. F. Heyduk, *Inorg. Chem.*, 2012, **51**, 12606.

13. A. Kumar Das, R. Hübner, B. Sarkar, J. Fiedler, S. Záliš, G. K. Lahiri and W. Kaim, *Dalton Trans.*, 2012, **41**, 8913.

14. S. Ye, B. Sarkar, C. Duboc, J. Fiedler and W. Kaim, *Inorg. Chem.*, 2005, **44**, 2843.

15. M. Asadi, K. A. Jamshid and A. H. Kyanfar, *Inorg. Chim. Acta.*, 2007, **360**, 1725.

16. (*a*) M. S. Braiman, D. M. Briercheck and K. M. Kriger, *J. Phys. Chem. B*, 1999, **103**, 4744; (*b*) http://www.biomaterial.com.br/FTIR.pdf.

17. (*a*) S. Blanchard, F. Neese, E. Bothe, E. Bill, T. Weyhermüller and K. Wieghardt, *Inorg. Chem.*, 2005, **44**, 3636; (*b*) H. Ohtsu and K. Tanaka, *Inorg. Chem.*, 2004, **43**, 3024.

18. (*a*) A. I. Poddel'sky, N. N. Vavilina, N. V. Somov, V. K. Cherkasov and G. A. Abakumov, *J. Organomet. Chem.*, 2009, **694**, 3462; (*b*) A. I. Poddel'sky, V. K. Cherkasov, G. A. Abakumov, *Coord. Chem. Rev.*, 2009, **253**, 291; (*c*) C. Mukherjee, T. Weyhermüller, K. Wieghardt and P. Chaudhuri, *Dalton Trans.*, 2006, 2169.

19. (*a*) C. Mukherjee, A. Stmmler, H. Bögge and T. Glaser, *Inorg. Chem.*, 2009, **48**, 9476; (*b*) C. Mukherjee, A. Stmmler, H. Bögge and T. Glaser, *Chem.–Eur. J.*, 2010, 10137; (*c*) T. Glaser, M. Heidemeier, R. Föhlich, P. Hildebrandt, E. Bothe and E. Bill, *Inorg. Chem.*, 2005, **44**, 5467; (*d*) O. Rotthaus, O. Jarjayes, F. Thomas, C. Philouze, C. P. D. Valle, E. S. Aman and J. L. Pierre, *Chem.–Eur. J.*, 2006, **12**, 2293.

20. (*a*) M. Asadi, K. A. Jamshid and A. H. Kyanfar, *Inorg. Chim. Acta.*, 2007, **360**, 1725; (*b*) L. Benisvy, R. Kannappan, Y.–F. Song, S. Milikisyants, M. Huber, I. Mutikainen, U. Turpeinen, P. Gamez, L. Bernasconi, E. J. Baerends, F. Hartl and J. Reedijk, *Eur. J. Inorg. Chem.* 2007, 637.

21. (*a*) M. Barwiolek, E. Szlyk, A. Surdykowski and A. Wojtczak, *Dalton Trans.*, 2013, **42**, 11476; (*b*) A. Akbari and Z. Alinia, *Computational Research*, 2013, **1**, 19.

22. (*a*) A. Patti, S. Pedotti, F. P. Ballistreri and G. T. Sfrazzetto, *Molecules*, 2009, **14**, 4312; (*b*) M. Barwiolek, E. Szlyk, T. M. Muzioł and T. Lis, *Dalton Trans.*, 2011, **40**, 11012.

23. (*a*) B. J. Hathaway and A. A. G. Tomlinson, *Coord. Chem. Rev.*, 1970, **5**, 1; (*b*) T. G. Brown and B. M. Hoffman, *Mol. Phys.*, 1980, **39**, 1073.

24. (*a*) T. Glaser, M. Heidemeier, J. B. H. Strautmann, H. Bögge, A. Stammler, E. Krickemeyer, R. Huenerbein, S. Grimme, E. Bothe and E. Bill, *Chem. Eur. J.*, 2007, **13**, 9191 and references therein; (*b*) A. Kochem, G. Gellon, N. Lectone, B. Baptiste, C. Philouze, A. Jarjayes, M. Orio and F. Thomas, *Chem. Eur. J.*, 2013, **19**, 16707 and

references therein; (*c*) A. Kochem, F. Thomas, O. Jarjayes, G. Gellon, C. Philouze, T. Weyhermüller, F. Neese and M. van Gastel, *Inorg. Chem.*, 2013, **52**, 14428 and references therein.

25. F. Firdaust, K. Fatma, A. U. Khan and M. Shakir, *J. Serb. Chem. Soc.*, 2009, **74**, 939.

26. S. Ponsico, H. Gulyas, M. Martínez–Belmonte, E. C. Escudero–Adán, Z. Freixa and P. W. N. M. van Leeuwen, *Dalton Trans.*, 2011, **40**, 10686.

27. (*a*) H. S. Jena and V. Manivannan, *Inorg. Chim. Acta.*, 2012, **394**, 210; (*b*) S. Shita, J. Chakrabortya, B. Samantaa, G. M. Rosairb and S. Mitra, *Z. Naturforsch.*, 2009, **64b**, 403; (*c*) H.–Q. Chen, K. Zhang, C. Jin and W. Huang, *Dalton Trans.*, 2014, **43**, 8486.

28. (*a*) P. Roy, K. Dhara, M. Manassero, J. Ratha and P. Banerjee, *Inorg. Chem.*, 2007, **46**, 6405; (*b*) S. Majumder, L. Mandal and S. Mohanta, *Inorg. Chem.*, 2012, **51**, 8739; (*c*) H. Sekhar Jena, *RSC Adv.*, 2014, **4**, 3028; (*d*) X. Xu, Y. Liao, G. Yu, H. You, C. Di, Z. Su, D. Ma, Q. Wang, S. Li, S. Wang, J. Ye and Y. Liu, *Chem. Mater.*, 2007, **19**, 1740.

29. L. Yi, L.–N. Zhu, B. Ding, P. Cheng, D.–Z. Liao, S.–P. Yan and Z.–H. Jiang, *Inorg. Chem. Commun.*, 2003, **6**, 1209.

30. G. Consiglio, S. Failla, P. Finocchiaro, I. P. Oliveri and S. D. Bella, *Inorg. Chem.*, 2012, **51**, 8409.

31. (*a*) L. A. Saghatforoush, A. Aminkhani, S. Ershad, G. Karimnezhad, S. Ghammamy and R. Kabiri, *Molecules*, 2008, **13**, 804; (*b*) N. Ananthi, U. Balakrishnan, S. Velmathi, K. B. Manjunath and G. Umesh, *Optics and Photonics Journal*, 2012, **2**, 40.

भारतीय प्रौद्योगिकी संस्थान गुवाहाटी
Indian Institute of Technology Guwahati

Chapter IV

*An Innocent and A Non–Innocent Combined Tetradentate Ligand and Its Corresponding Fe(III), Ni(II), and Cu(II) complexes: Synthesis, Characterizaation, and Substituent dependent Reactivity**

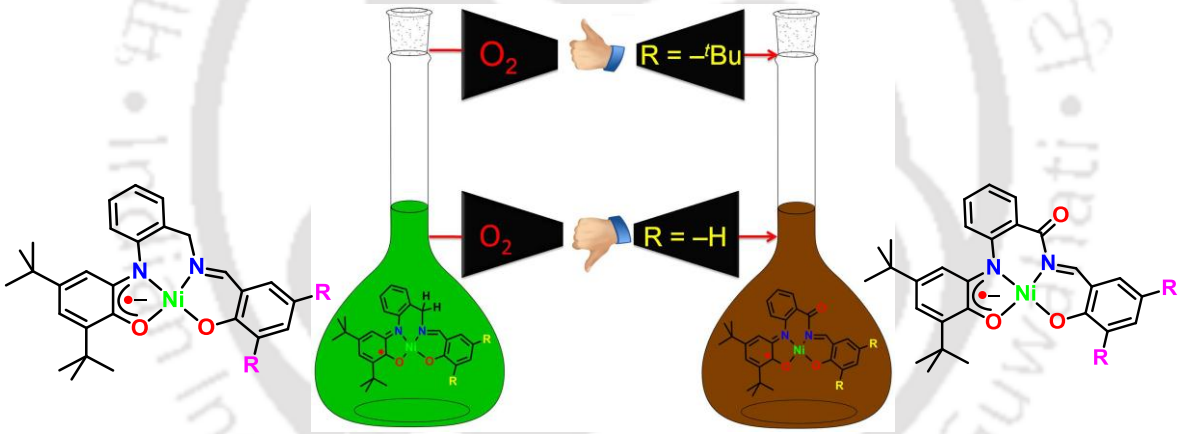

*some results have been published;

1. ***Dalton. Trans.***, **2014**, *43*, 394–397.

4.1: Introduction:

Now a days, it is known that various enzymatic reactions proceed through the formation of coordinated organic phenolate π–radical that arises by one–electron oxidation of tyrosine residue of amino acid to the metal ion in metalloproteins.[1] Hence, the synthesis of radical–containing complexes and the study of transition metal–radical interactions[2] have drawn great attention to chemists. Fe–containing metalloenzymes such as Escherichia coli ribonucleotide reductase, which contains two subunits; protein B1 and protein B2.[3] The active site of protein B2 contains a non–heme iron complex coordinated to a tyrosine radical, which is regenerated during the reduction process of ribose to deoxy–ribose sugar, and found for the enzyme activity.[3,4] The electronic interactions between the organic π–radical and iron center widely depend on structural distortion. Hence, it is interesting to synthesize and structurally characterize radical–coordinated Fe complexes as structural as well as functional models of metalloenzymes. Although, a large number of non–heme iron complexes where the central iron atom directly coordinated with π–radicals are reported,[5] but the non–heme iron complex with a tetradentate mixed ligand to provide monoradical–coordinated Fe complexes are rare.[5*f*]

Tetradentate ligands coordinated with a Fe(III) ion are known to acquire a distorted square pyramidal geometry having an axially bound halogen atom. Structural distortion as well as the reactivity of the Fe(III) complexes can be tuned by introducing different substituent at the ligand backbone. As for an example, a Fe–porphyrin complex where hemoglobin acts as an oxygen carrier metalloenzyme in biology, however, it may act as an oxygen activation catalyst just by protein fine–tuning of the structure around the heme.[6] Generally, ligand exists at the equatorial position of square pyramidal complexes form a strong metal–ligand bond, while, the axial ligand forms a weak coordinate bond with metal center. However, it has been well established using various model systems and hemoproteins that the electronic structure and function of the Fe(III)–heme complexes strongly depend on the ligands coordinated to the axial sites of the metal ion.[7] A distorted square pyramidal Fe(III) complex, where the central Fe(III) can stabilize as $S = {}^{5}/_{2}$ (HS); or, $S = ½$ (LS) ground state. Depending upon the structural distortion and displacement of metal center from the basal plane Fe(III) can show another interesting unknown ground state; $S = {}^{3}/_{2}$ (intermediate spin state).[5*a*,8]

Polynuclear metal complexes having different oxidation states of the metal ion are typically known as mixed valence compounds. Mixed valence compounds have useful importance to study of electron transfer process which is most fundamental reaction in physics, chemistry, and biology.[9] A mononuclear transition metal complex having redox active metal center and is connected with two redox active ligands generates a mixed valence complex, L–M–$L^{\bullet+}$, upon one–electron oxidation at ligand center. In this system, electron transfer takes place from electron rich species L to the electron deficient species $L^{\bullet+}$ through redox active transition metal.[10] Thus, the mixed valence assemblies containing multiple–redox centers has significant implication in understanding the long range electron transfer process in biology and building molecular conducting devices.

In some instances mixed valence complexes are effective catalysts and reactive towards aerial oxygen to form metal–superoxo / peroxo intermediate during oxidation of various species by activating molecular oxygen.[11] Metal–oxo units have been proposed as active intermediates for several enzymatic and biomimetic C–H bond activation reactions.[12] Since then, transition metal mediated dioxygen activation as well as characterization of metal–oxo intermediates have drawn considerable attention of both chemists and biologists. So, it's important to investigate the interaction and activation of molecular oxygen by transition metal complexes. Cu(II) and Ni(II) peptide complexes can activate molecular oxygen where Cu(III)–superoxo and Ni(III)–superoxo were consider as an intermediate peptide complex.[13]

Both the steric effect and electronic effect play the crucial role to activate the molecular oxygen by the metal complexes. Some cases, the presence of the donor substituent at the ligand backbone increase the electron density at the metal center and consequently, the electron rich metal center activates the molecular oxygen to form a reactive intermediate metal–superoxo / or metal–oxo species.[11,12]

To understand the effect of substituent at the ligand backbone, the steric effect as well as the electronic effect towards metal complexes, two new asymmetric tetradentate mixed ligands (with and without substituent as *tert*–butyl in the salicylidene unit) and their metal complexes have been synthesized. Tetradentate ligand will be presented here as mixed ligand, since it is composed of both redox active aminophenol (change in its oxidation state is favored in the presence of metal ion and molecular oxygen) and redox inactive salicylidene (change in its oxidation state is not favored in the presence of metal ion and oxygen)

compartments connected *via* benzyl linker. Both the ligands differ from each other by the presence of *tert*–butyl group at 3,5–position of the salicylidene unit.

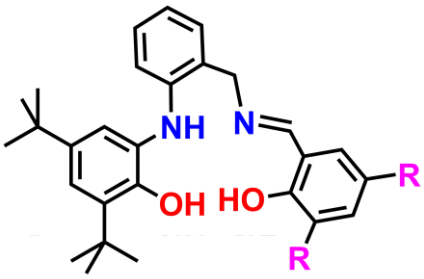

$[H_3L^{Mixed(R)}]$ R = –H, –^{t}Bu

This chapter describes the synthesis and characterization of Fe(III), Ni(II), and Cu(II) metal complexes formed with these mixed ligands. Furthermore, substituent dependent reactivity towards aerial oxygen through metal–superoxo, and metal–peroxo intermediate formation is discussed.

- (a) [**Fe($L^{Mixed(H)}$)Cl**], (**13**)
  (b) [**Fe($L^{Mixed(tBu)}$)Cl**], (**14**)
- (a) [**Ni$L^{Mixed(H)}$**], (**15**)
  (b) [**Ni$L^{Mixed(tBu)}$**], (**16**)
  (c) [**Ni$L^{Mixed(tBu),\ oxidized}$**], (**16a**)
- (a) [**Cu$L^{Mixed(H)}$**], (**17**)
  (b) [**Cu$L^{Mixed(tBu)}$**], (**18**)
  (c) [**Cu$L^{Mixed(tBu),\ oxidized}$**], (**18a**)

4.2: Synthesis and Characterization of Mixed Ligands:

The ligand $\mathbf{H_3L^{Mixed(H)}}$ was synthesized by the condensation reaction between equimolar amounts of $\mathbf{H_4L^{CH_2NH_2}}$ and salicyaldehyde in ethanol. Whereas, the ligand $\mathbf{H_3L^{Mixed(tBu)}}$ was synthesized by refluxing equimolar amounts of $\mathbf{H_4L^{CH_2NH_2}}$ and 3,5–di–*tert*–butylsalicyaldehyde in acetonitrile and used for metallation reactions directly.

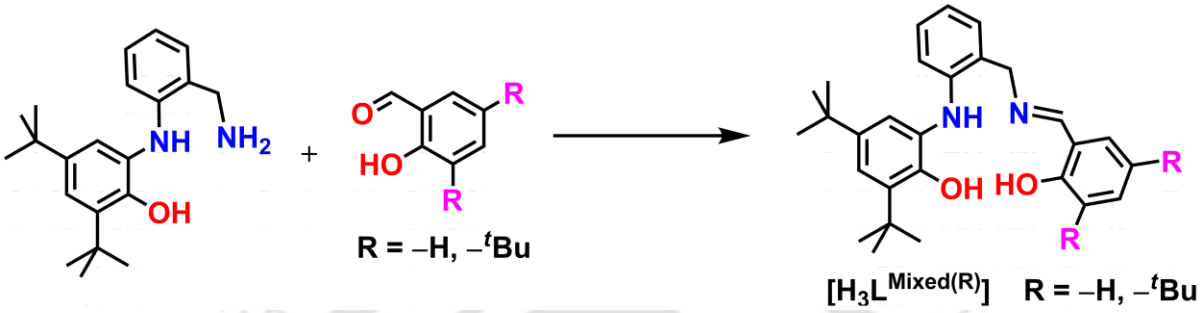

Scheme 4.1: *Synthetic route of Mixed ligands.*

Infrared (IR) spectrum of ligand $\mathbf{H_3L^{Mixed(H)}}$ showed the ν(O–H) stretch at 3463 cm^{-1} and ν(N–H) stretch at 3365 cm^{-1}. The IR bands at 2962–2865 cm^{-1} were appeared for the ν(C–H) stretches of *tert*–butyl groups. The sharp band at 1631 cm^{-1} was characteristic stretching frequency for ν(C=N) vibration. The bending ν(N–H) band appeared at 1607 cm^{-1}. In addition, the bending ν(C–H) bands appeared at 1462 cm^{-1}, 1361 cm^{-1}. The IR bands at 1214, and 1193 cm^{-1} were attributed for the phenolate ν(C–O) stretches, while the ν(C–N) band appeared at 1151 cm^{-1}.

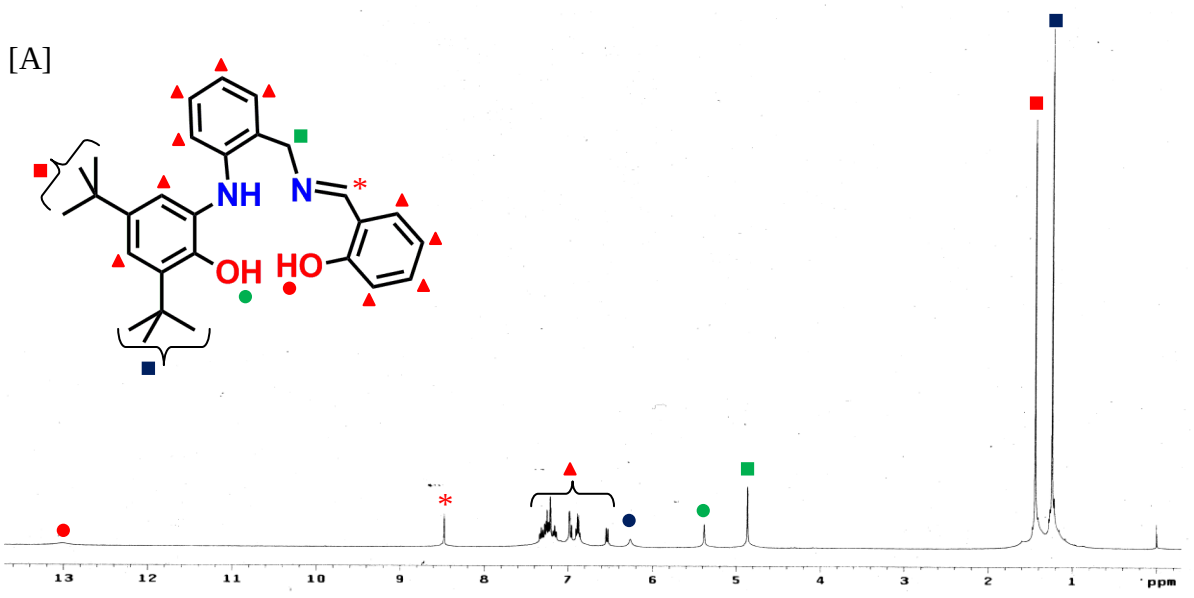

Figure 4.1A: *^{1}H NMR spectrum of $H_3L^{Mixed(H)}$.*

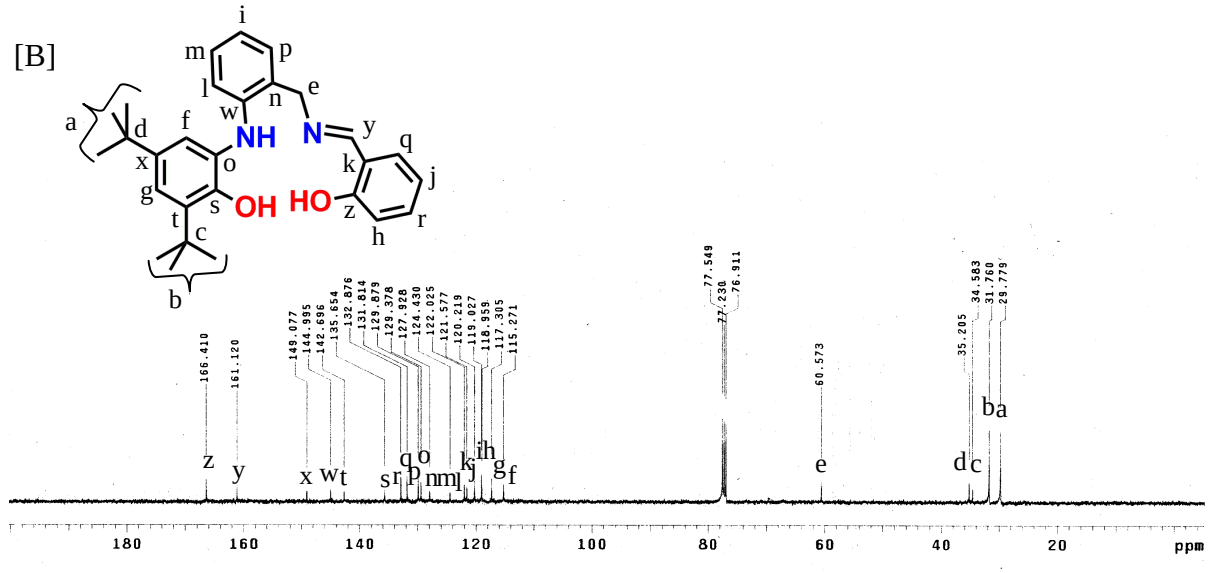

Figure 4.1B: *^{13}C NMR spectrum of* $\boldsymbol{H_3L^{Mixed(H)}}$.

^{1}H NMR spectrum of $\mathbf{H_3L^{Mixed(H)}}$ ligand was measured in $CDCl_3$ solvent and showed (**Figured 4.1A**) proton NMR signals at δ 1.25 (s, 9H), 1.44 (s, 9H), 4.87 (s, 2H), 5.38 (s, 1H), 6.27 (s, 1H), 6.54 (d, J = 8 Hz, 1H), 6.88 (m, 2H), 6.96 (s, 1H), 6.98 (d, J = 2.4 Hz, 1H), 7.16 (t, J = 7.2 Hz, 1H), 7.21–7.28 (m, 3H), 7.32 (t, J = 7.6 Hz, 1H), 8.48 (s, 1H), 13.02 (s, 1H) ppm. ^{13}C NMR spectrum of the ligand showed (**Figure 4.1B**) resonance signals at δ 29.8, 31.8, 34.6, 35.2, 60.6, 115.3, 117.3, 118.95, 119, 120.2, 121.6, 122, 124.4, 127.9, 129.4, 129.9, 131.8, 132.9, 135.7, 142.7, 145, 149.1, 161.1, 166.4 ppm.

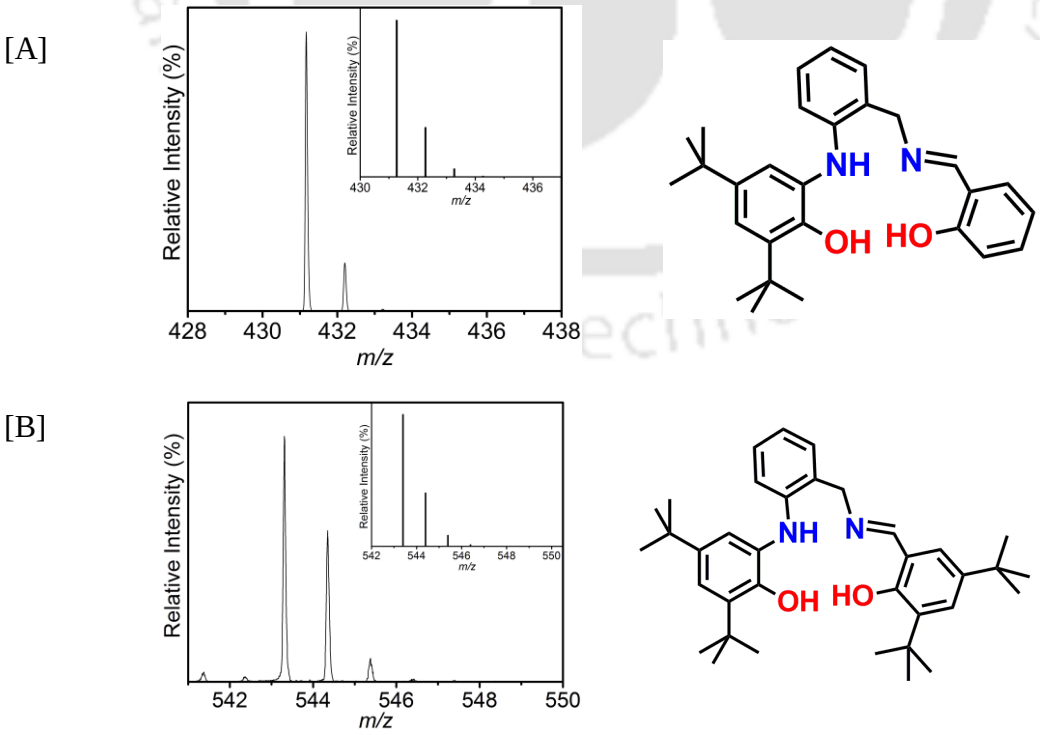

Figure 4.2: *[A] ESI–mass spectrum of the* $\boldsymbol{H_3L^{Mixed(H}}$*, and [B] ESI mass spectrum of* $\boldsymbol{H_3L^{Mixed(tBu)}}$*; experimental and simulated isotope distribution pattern (inset).*

Electrospray ionization mass spectrum (ESI–MS) of ligand $\mathbf{H_3L^{Mixed(H)}}$ was measured in CH_3CN in positive mode (+ve) and showed a 100% molecular ion peak at *m/z* = 431.17 (corresponded to $[M + H]^+$; M = molecular mass) and isotope distribution pattern examination confirmed $\mathbf{C_{28}H_{34}N_2O_2}$ composition of the observed mass. ESI–mass spectrum of *in situ* generated $\mathbf{H_3L^{Mixed(tBu)}}$ in CH_3CN in positive mode showed a 100% molecular ion peak at *m/z* = 543.40, which corresponded to $[M + H]^+$; M = molecular mass. Isotope distribution pattern examination of the corresponding mass revealed the composition of $\mathbf{H_3L^{Mixed(tBu)}}$ as $\mathbf{C_{36}H_{50}N_2O_2}$.

The mixed ligand can exist in several oxidation states and are shown in **Scheme 4.2**.

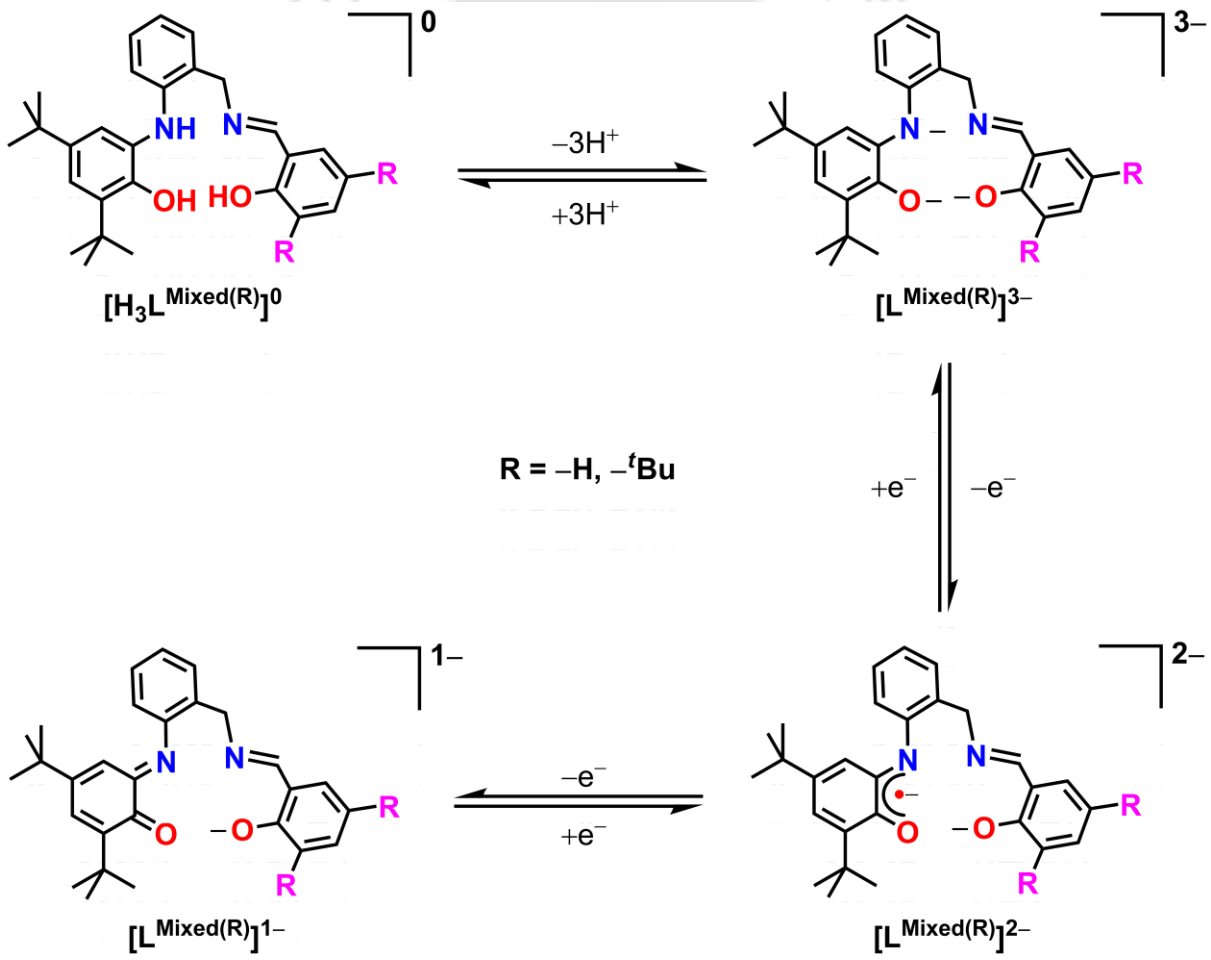

Scheme 4.2: *Different oxidation state of ligand* $\boldsymbol{H_3L^{Mixed(R)}}$, *(R = –H, –*^{t}*Bu).*

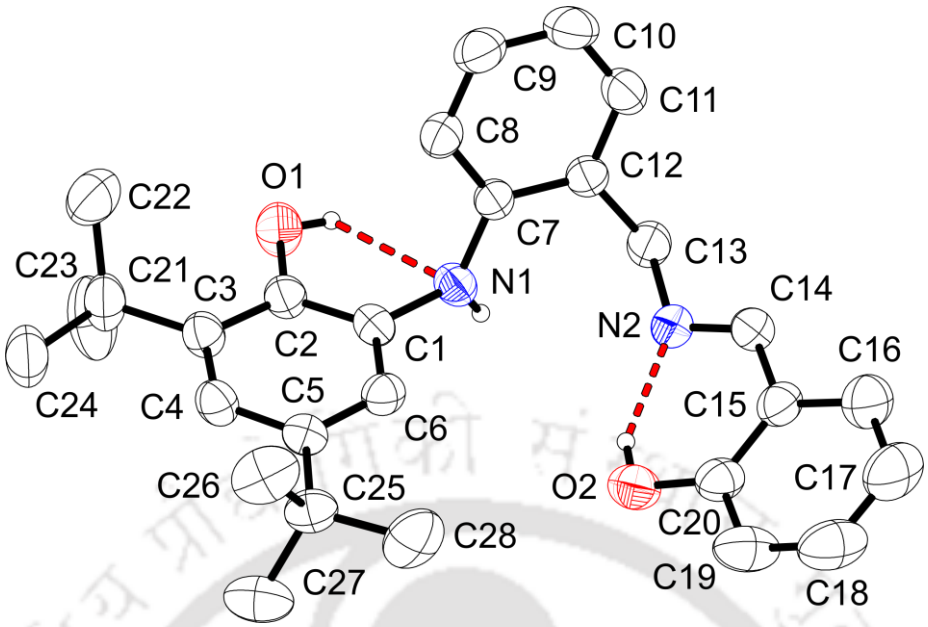

Figure 4.3: *ORTEP representation of* $\boldsymbol{H_3L^{Mixed(H)}}$ *was drawn at 50% thermal probability level. Hydrogen atoms except attached with O1, N1, and O2 were omitted for clarity.*

Single crystal X–ray diffraction measurements for ligand $\mathbf{H_3L^{Mixed(H)}}$ was performed at 296(2) K. Ligand $\mathbf{H_3L^{Mixed(H)}}$ crystallized in the triclinic space group *P*–1. The asymmetric ligand was comprised of three different kinds of C_6 aryl rings. The C–C bond distances of C_6 aryl rings can be taken into consideration for assigning the oxidation state of the ligand. In the fully reduced form the C–C bond distances in C_6 aryl ring appear within the 1.39±0.01 Å range.[5f,14] In case of one–electron oxidized iminosemiquinonate ($ISQ^{\bullet 1-}$) or two–electron oxidized iminobenzoquinone (IBQ) form (**Scheme 4.2**) of the ligand a discrete alternative short and long C–C bond distances, *i.e.* quinoid–type distortion, in C_6 aryl ring is expected.[5f,14a,b] Furthermore, in the $ISQ^{\bullet 1-}$ form the C_{Ph}–N_{Ph} and C_{Ph}–O_{Ph} (C_{Ph}, N_{Ph}, and O_{Ph} stand for the phenyl carbon atom, N, and O atom attach to phenyl ring, respectively) bond distances are 1.35±0.01 and 1.30±0.01 Å.[5f,14a,b] These are in between of single bond and double bond character, and refer to the π–radical form of the organic moiety. In ligand $\mathbf{H_3L^{Mixed(H)}}$, the C–C bond distances of the 3,5–di–*tert*–butyl–containing aminophenol unit were in 1.380(5)–1.400(5) Å range (**Table 4.1**). The C1–N1 = 1.435(5) and C2–O1 = 1.375(5) Å bond distances along with the C–C bond distances indicated the fully reduced form of the aryl ring. C14–N2 = 1.275(4) Å showed its double bond character and C20–O2 = 1.355(3) Å was in accord with the phenolic C–O bond distance.[14c–f] The C–C bond distances of other two C_6 rings were found in the range of 1.366(4)–1.402(4) Å with no quinoid–type

distortion. Hence, the ligand was in its fully reduced form where the benzyl group was bridging between an aminophenol and a salicylidene units.

Table 4.1: *Selected bond distances (Å) for* $H_3L^{Mixed(H)}$.

C1–C2	1.389(2)	C11–C12	1.380(2)
C2–C3	1.400(2)	C12–C7	1.404(2)
C3–C4	1.389(2)	C12–C13	1.513(2)
C4–C5	1.396(2)	C13–N2	1.470(2)
C5–C6	1.380(2)	C14–N2	1.275(2)
C6–C1	1.390(2)	C14–C15	1.447(2)
C2–O1	1.3749(19)	C15–C16	1.402(3)
C1–N1	1.434(2)	C16–C17	1.376(3)
N1–C7	1.403(2)	C17–C18	1.375(3)
C7–C8	1.392(2)	C18–C19	1.365(3)
C8–C9	1.379(3)	C19–C20	1.384(3)
C9–C10	1.369(3)	C20–C15	1.396(3)
C10–C11	1.387(3)	C20–O2	1.355(2)
H(O1)⋯N1	2.2736(18)	H(O2)⋯N2	1.8800(12)

4.3: Synthesis and Characterization of Square Pyramidal Fe(III) Complexes Formed with Mixed Ligands:

Complex [$\mathbf{FeL^{Mixed(H)}Cl}$]; (**13**) was synthesize from ligand $\mathbf{H_3L^{Mixed(H)}}$ by reacting with $FeCl_3$ in the presence of Et_3N under air. Treatment of 1 equivalent of anhydrous $FeCl_3$ to the *in situ* generated $\mathbf{H_3L^{Mixed(tBu)}}$ ligand in presence of Et_3N under air at room temperature (30 °C) provided [$\mathbf{FeL^{Mixed(tBu)}Cl}$]; (**14**) as green precipitate. Both complexes were recrystallized from a 3:1 CH_2Cl_2:CH_3CN solvent mixture.

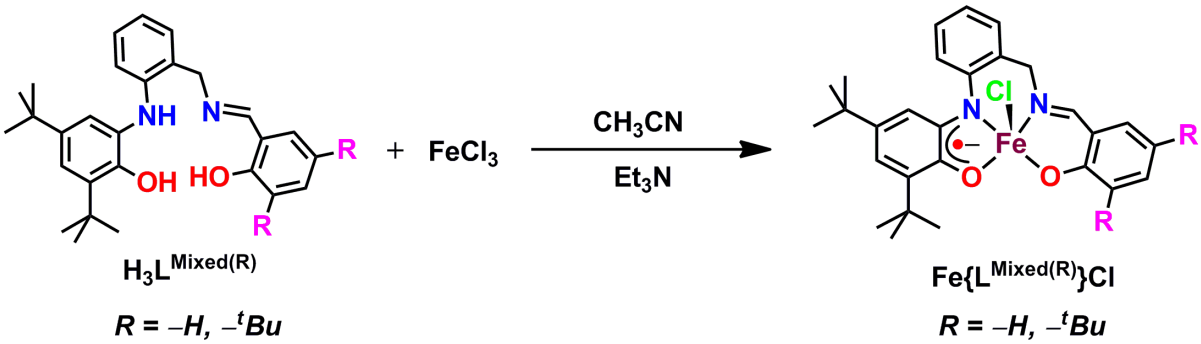

Scheme 4.3: *Synthetic route of Fe(III) complexes [**13**, and **14**] with Mixed ligands.*

Both **13** and **14** complexes were characterized by IR spectroscopic method. Infrared (IR) spectra of **13**, and **14** showed the ν(C–H) stretching frequencies for *tert*–butyl nearly at same region, 2958–2865 cm^{-1}. The characteristic ν(C=N) stretch appeared at 1612 cm^{-1}. The band at 1443 cm^{-1} for **13**, and 1434 cm^{-1} for **14**, was appeared for ν(C⋯O) stretch.[5f]

[A]

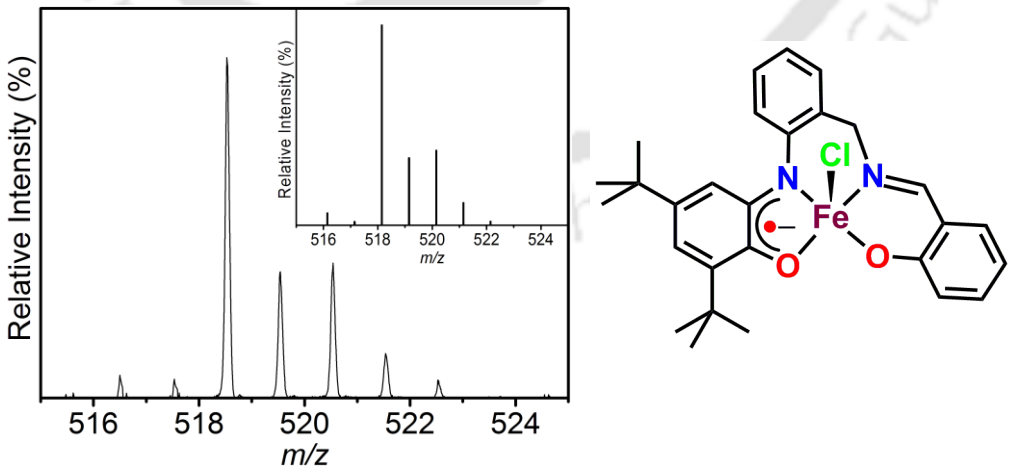

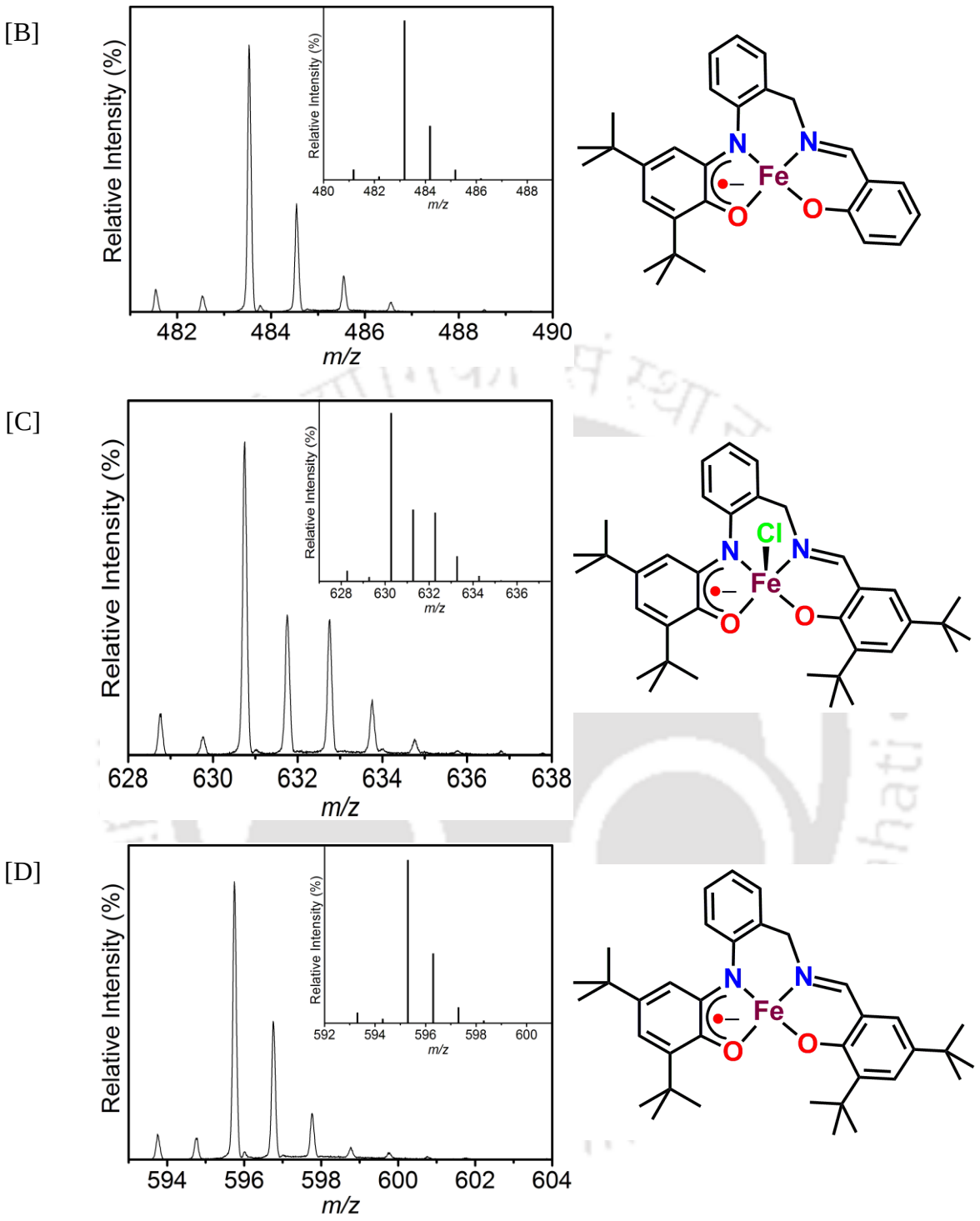

Figure 4.4: *[A] and [B] ESI–mass spectrum of **13**; [C] and [D] ESI–mass spectrum of **14**; experimental and simulated (inset).*

Electrospray ionization mass spectra (ESI–MS) of **13**, and **14** were measured in CH_3CN in positive mode. Complex **13**, and complex **14** showed a ~ 30% molecular ion peak at *m/z* = 518.53[**13**], 630.72[**14**]; corresponded to $[M]^+$ (M = molecular mass) and a 100% molecular ion peak at *m/z* = 483.53[**13**], 595.72[**14**]; corresponded to $[M - Cl]^+$, respectively.

Isotope distribution pattern examinations of the experimental results revealed the composition $\mathbf{C_{28}H_{31}ClFeN_2O_2}$ for **13** and $\mathbf{C_{36}H_{47}ClFeN_2O_2}$ for **14** (**Figure 4.4**).

The Single crystal X–ray diffraction measurements for **13** and **14** were performed at room temperature (296 K). ORTEP views of the molecular structure with atom labeling scheme for complex **FeL$^{Mixed(H)}$Cl**; (**13**), and **FeL$^{Mixed(tBu)}$Cl**; (**14**) are shown in **Figure 4.5**. Selected bond distances and bond angles are given in the **Table 4.2**.

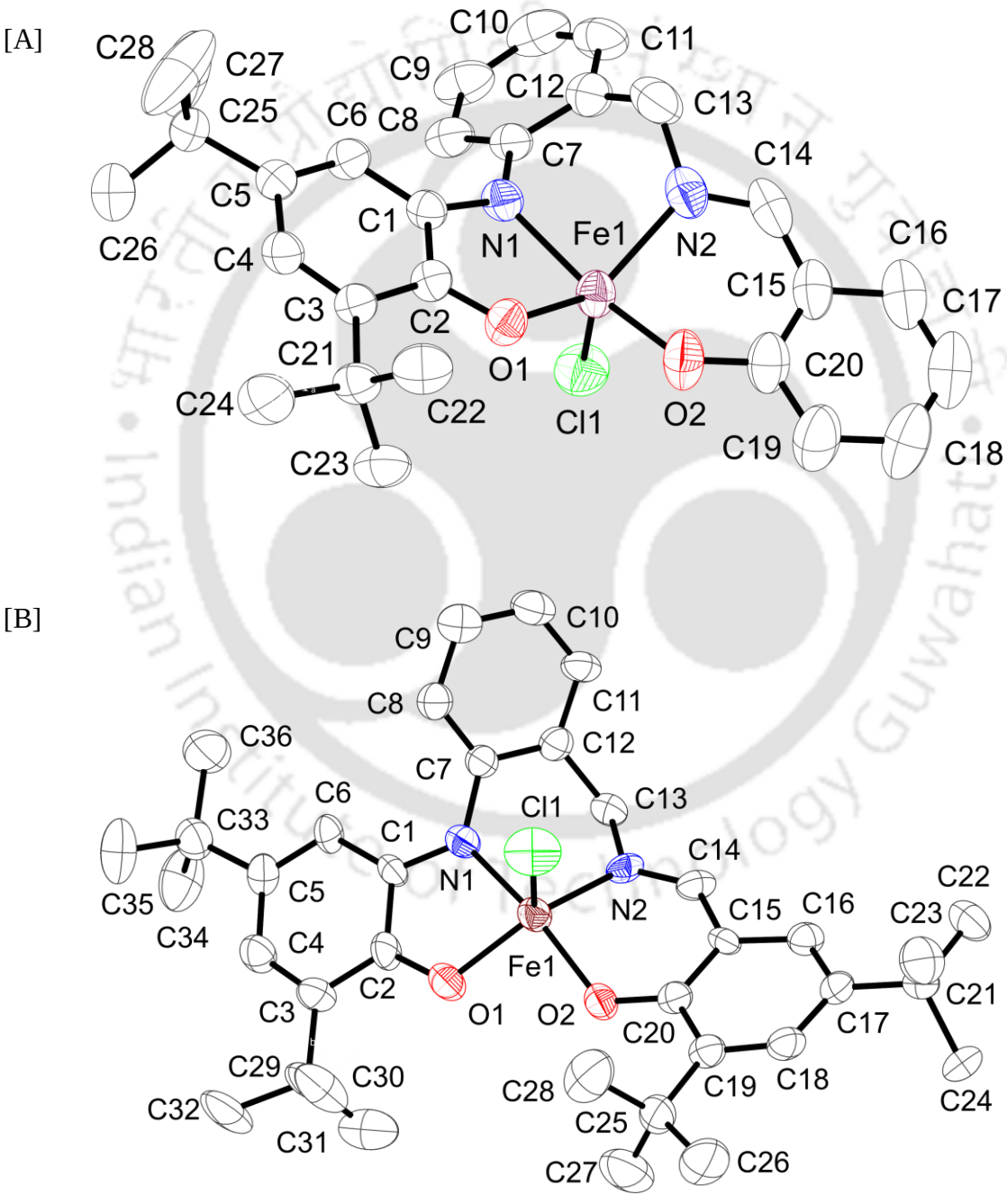

Figure 4.5: *ORTEP representation of [A]* ***FeL$^{Mixed(H)}$Cl; (13)****, and [B]* ***FeL$^{Mixed(tBu)}$Cl; (14)****. Hydrogen atoms were omitted for clarity.*

X–ray diffraction examination of the complexes revealed that complex **13** crystallized in the monoclinic space group $P12_1/n1$, while, complex **14** crystallized in the triclinic system space group *P*–1. From the molecular structure it has been found that both complexes were five–coordinate where the central Fe atom was surrounded by N–H, O–H deprotonated mixed ligand at the basal position, and a chlorine atom bound axially. The central Fe atom was situated towards the apical chloride atom from the basal plane at 0.557 Å [**13**]; and at 0.584 Å [**14**], respectively (parenthesis represents the complex). The average dihedral angles between the basal plane and the individual plane passing through 3,5–di–*tert*–butylamidophenolate, salicylidene unit, and aminobenzylamine linker are shown in **Table 4.2**. The N1–Fe1–O2 bond angle was 160.81(12)° [**13**]; 157.75(14)° [**14**] and the O1–Fe1–N2 bond angle was 134.56(12)° [**13**]; 133.97(13)° [**14**], respectively, and deviated significantly from the linearity. Therefore, the coordination nature around Fe center was distorted square pyramidal (τ_5 = 0.44 [**13**]; 0.40 [**14**], respectively).[5e] The Fe1–N1 bond distance was 2.050(3) [**13**]; 2.037(3) [**14**] Å while, Fe1–N2 bond distance was 2.082(3) [**13**]; 2.076(3) [**14**] Å respectively.[5,6,8] The Fe1–O1 and Fe1–O2 bond distances were 1.946(2) [**13**]; 1.936(3) [**14**] Å and 1.897(3) [**13**]; 1.904(3) [**14**] Å, respectively.[5,6,8] Above mentioned bond distances strongly suggested high spin (HS) and +III state of Fe atom in these complexes.[5,6] All the C–C bond distances in all C_6–aryl rings were not same and were not falling in the range of 1.39±0.01 Å, as it would be in case of fully reduced phenyl form. Alternating short and long C–C bond distances pattern were observed in *tert*–butyl groups–containing amidophenolate unit in both **13**, and **14**. The bond distances at C1–C2, C2–C3, C3–C4, C4–C5, C5–C6, C6–C1 were {1.443(5) [**13**]; 1.438(5) [**14**] Å}, {1.426(5) [**13**]; 1.439(5) [**14**] Å}, {1.369(5) [**13**]; 1.373(6) [**14**] Å}, {1.433(5) [**13**]; 1.421(6) [**14**] Å}, {1.362(5) [**13**]; 1.354(5) [**14**] Å}, and {1.421(5) [**13**]; 1.426(5) [**14**] Å}, respectively.[5] In addition, C1–N1 bond distance was 1.343(4) [**13**]; 1.337(4) [**14**] Å and C2–O1 bond distance was 1.303(4) [**13**]; 1.302(4) [**14**] Å. Both the bond distances (C1–N1 and C2–O1) neither represented their single bond character nor corresponded with their double bond character, rather, in between. Hence, it could be argued that the coordinating amidophenolate unit existed in its one–electron oxidized iminosemiquinonate form ($ISQ^{\bullet 1-}$). Furthermore, C–C bond distances in the salen unit were also not in the range of 1.39±0.01 Å, rather, a quinoid–type distortion was also found in the salen unit. The bond distances at C15–C16, C16–C17, C17–C18, C18–C19, C19–C20, C20–C15 were {1.411(6) [**13**]; 1.421(5) [**14**] Å}, {1.367(7) [**13**]; 1.368(5) [**14**] Å}, {1.364(7) [**13**]; 1.416(5) [**14**] Å}, {1.395(6) [**13**]; 1.388(6) [**14**] Å}, {1.385(6) [**13**]; 1.420(5) [**14**] Å}, and {1.412(6) [**13**]; 1.424(5) [**14**] Å}, respectively. Additionally, the shortening of C20–O2, and

C14–C15 bond distances and the elongation of N2–C14 bond distance were observed. Herein, these features indicated the delocalization of phenolate^{1-} charge over the O2–C20–C15–C14–N2 unit (**Table 4.2**) and supported by previous reports[14c–f] where salen–phenolate unit has been found in their fully reduced form.

Table 4.2: *Selected bond distances (Å) and bond angles (°) are shown for the complexes **13** and **14**.*

	13	**14**
Fe1–N1	2.050(3)	2.037(3)
Fe1–N2	2.082(3)	2.076(3)
Fe1–O1	1.946(2)	1.936(3)
Fe1–O2	1.897(3)	1.904(3)
Fe1–Cl1	2.2232(12)	2.2129(15)
C2–O1	1.303(4)	1.302(4)
C1–N1	1.343(4)	1.337(4)
C1–C2	1.443(5)	1.438(5)
C2–C3	1.426(5)	1.439(5)
C3–C4	1.369(5)	1.373(6)
C4–C5	1.433(5)	1.421(6)
C5–C6	1.362(5)	1.354(5)
C6–C1	1.421(5)	1.426(5)
C20–O2	1.323(5)	1.320(4)
C14–N2	1.292(5)	1.272(5)
C14–C15	1.431(6)	1.446(5)
C15–C16	1.411(6)	1.421(5)
C16–C17	1.367(7)	1.368(5)
C17–C18	1.364(7)	1.416(5)
C18–C19	1.395(6)	1.388(6)
C19–C20	1.385(6)	1.420(5)
C20–C15	1.412(6)	1.424(5)
O1–Fe1–N1	78.30(10)	78.17(12)
N1–Fe1–N2	85.59(13)	86.43(12)
N2–Fe1–O2	88.60(13)	86.82(11)
O2–Fe1–O1	93.05(11)	91.50(12)
O1–Fe1–N2	134.56(12)	133.97(13)
N1–Fe1–O2	160.81(12)	157.75(14)
Cl1–Fe1–O1	113.36(8)	117.21(11)
Cl1–Fe1–N1	97.74(9)	97.88(10)
Cl1–Fe1–N2	110.73(9)	107.67(9)
Cl1–Fe1–O2	101.41(10)	104.36(10)
Fe1–O1–C2	117.7(2)	117.9(2)
Fe1–N1–C1	115.0(2)	115.7(2)
Fe1–N1–C7	120.9(2)	120.9(2)
Fe1–N2–C13	120.5(3)	120.7(2)
Fe1–N2–C14	121.2(3)	121.7(2)
Fe1–O2–C20	126.5(3)	125.2(2)

Table 4.3: *Comparative structural studies between complex **13** and complex **14**.*

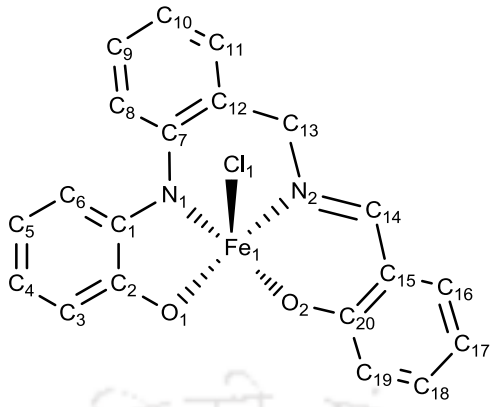

Plane A: O1–N1–N2–O2

Plane B: O1–C2–C3–C4–C5–C6–C1–N1

Plane C: N1–C7–C8–C9–C10–C11–C12–C13–N2

Plane D: N2–C14–C15–C16–C17–C18–C19–C20–O2

Distance (Å)	**13**	**14**
Plane A and **Fe1**	0.5574(6)	0.5844(5)

Dihedral angle (°)	**13**	**14**
Plane A and **Plane B**	–15.570(72)	–21.131(67)
Plane A and **Plane C**	+27.721(75)	+25.708(78)
Plane A and **Plane D**	+12.329(79)	+16.042(75)

(–) indicated below the basal plane A; (+) indicated above the basal plane B

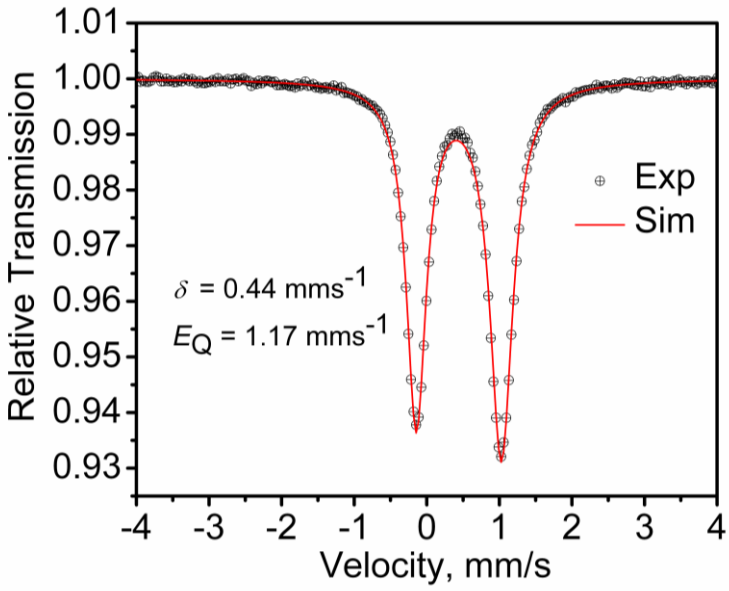

Figure 4.6: *Mössbauer spectrum of **14** at 80 K and at zero–field.*

It has been observed that both complexes were having almost same molecular geometry; therefore, zero–field Mössbauer measurement only on solid sample of **14** was performed. The zero–field Mössbauer spectrum of solid sample **14** with its computer simulation is shown in **Figure 4.6**. Simulation to the experimental results provides the isomer shift value δ = 0.44 mms^{-1} and quadrupole splitting $|\Delta E_Q|$ = 1.912 mms^{-1}. The large value of isomer shift value and low quadruple splitting value are strongly suggested for the presence of high spin ferric ion in the neutral monoradical–coordinated complex.[5a,f,g,15]

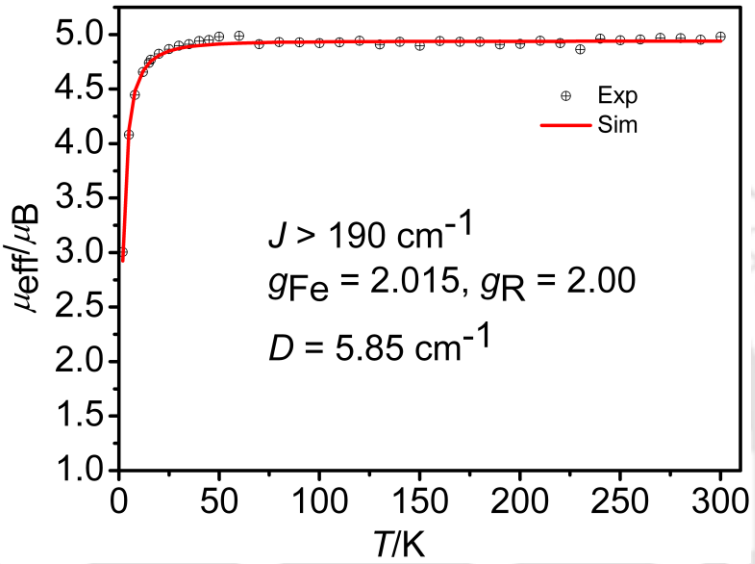

Figure 4.7: μ_{eff} *vs T* plots for **14**.

Temperature dependent magnetic susceptibility measurement on solid sample of **14** was examined in the temperature range of 2–290 K using SQUID magnetometer at external field 0.5 T. The μ_{eff} *vs T* plot for complex **14** is shown in **Figure 4.7**. From the μ_{eff} *vs T* plot, a constant magnetic moment μ_{eff} = 4.85 μ_B in temperature range 10–290 K was found. Below 10 K there was a stiff decrease in μ_{eff} value which was due to zero–field splitting and/or intermolecular antiferromagnetic interactions. The μ_{eff} value in 10–290 K temperature range was consistent with a strongly antiferromagnetically coupled high spin (HS) Fe(III) center ($3d^5$ electronic configuration; S = $^5/_2$) and a ligand center π–radical (S = ½).[5a,c,15b,c] The experimental resulted was simulated using the following parameters; $g_{Fe(III)}$ = 2.015, g_R = 2.00, J > 190 cm^{-1}, D = 5.85 cm^{-1}.

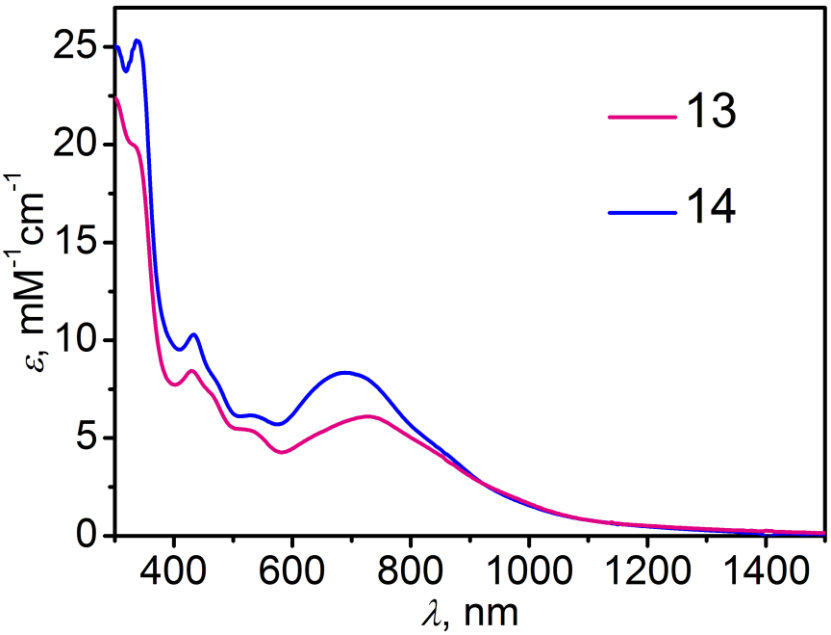

Figure 4.8: *UV–vis/NIR spectra for **13**, and **14** are shown from 300 nm to 1500 nm range.*

Electronic absorption spectra for **13**, and **14** were recorded in CH_2Cl_2 at ambient temperature and are shown in **Figure 4.8**. Both complexes showed a broad absorption band at λ_{max} = 950 nm (ε = 2250 $M^{-1}cm^{-1}$) which could be due to intervalence ligand(phenolate) –to–ligand(iminosemiquinone) charge transfer. The intraligand charge transfer due to the presence of center π–radical appeared at λ_{max} = 730 nm (ε = 6850 $M^{-1}cm^{-1}$) for **13**, and λ_{max} = 690 nm (ε = 8350 $M^{-1}cm^{-1}$) for complex **14**.[5c,f,16] Absorption band at λ_{max} = 530 nm was attributed for the ligand(phenolate)–to–metal charge transfer (LMCT) (ε = 5400 $M^{-1}cm^{-1}$ for **13**, and ε = 6200 $M^{-1}cm^{-1}$ for **14**).[5c,f,16]

4.4a: Square Planar Ni(II) Complexes Synthesized by Using Mixed Ligands; Synthesis, Characterization, and Reactivity Studies:

Reaction between $\mathbf{H_3L^{Mixed(H)}}$ and $NiCl_2{\bullet}6H_2O$ in methanol under air in the presence of triethylamine provided complex $\mathbf{NiL^{Mixed(H)}}$, (**15**). Whereas, the complex **16** was synthesized from the *in situ* generated mixed ligand $\mathbf{H_3L^{Mixed(tBu)}}$ by adding 1 equivalent of $NiCl_2{\bullet}6H_2O$ in the presence of triethylamine under air. Interestingly, a remarkable substituent dependent reactivity of the Ni complexes with molecular oxygen has been observed. Complex **16** underwent aerial oxidation in solution to produce complex **16a**. Non–participation of ligand centered π–radical to Ni–oxygen/dioxygen intermediate was also observed and reported here.

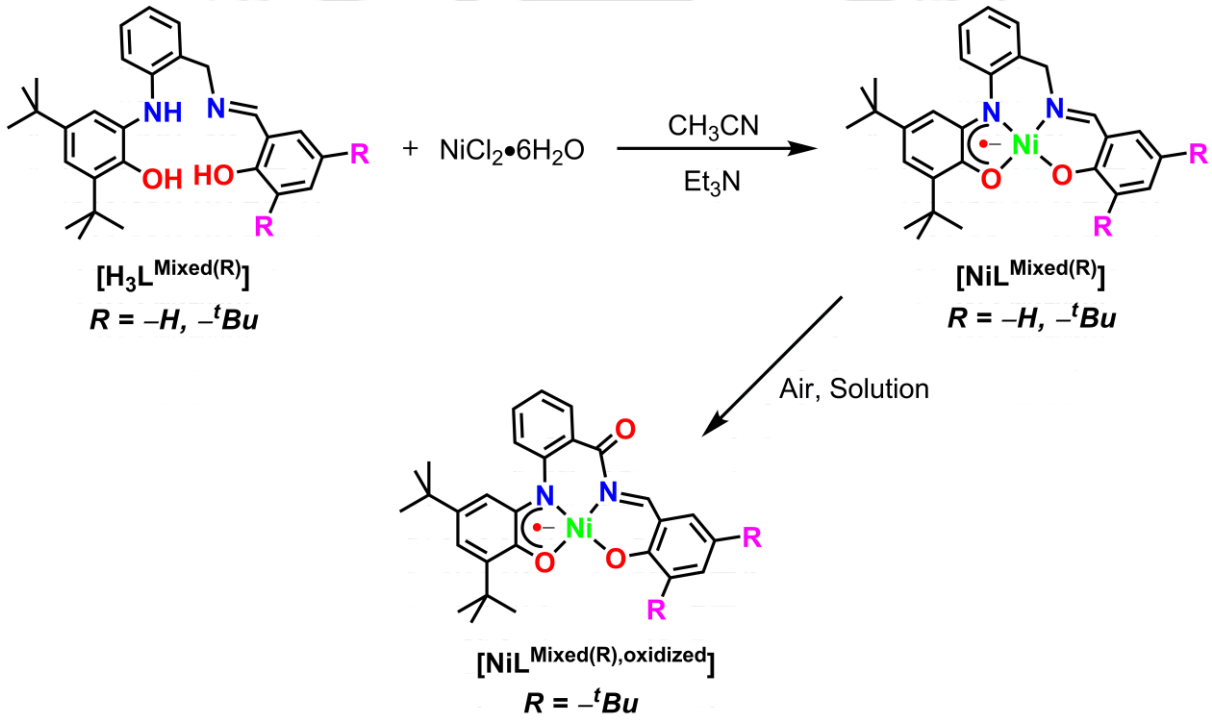

Scheme 4.4: *Synthetic route of Ni(II) complexes [**15**, **16**, and **16a**] with Mixed ligands.*

IR spectra of the complexes showed stretching frequencies for the *tert*–butyl groups at 2960–2862 cm^{-1} range. A small splitting in the ν(C–H) stretching corresponds to *tert*–butyl groups was observed in complexes **16**, and **16a**. This indicated their different environment possibly due to H–bonding. The band at 1612[**15**], 1611[**16**], and 1620[**16a**] cm^{-1} was attributed to the ν(C=N) stretching frequency. The band at 1452 cm^{-1} [**15**], 1438 cm^{-1} [**16**], and 1431 cm^{-1} [**16a**] was appeared due to ν(C⋯O) vibration mode.[17] While, in complex **16a**, an additional band appeared at 1661 cm^{-1} due to the ν(C=O) stretching frequency.[18]

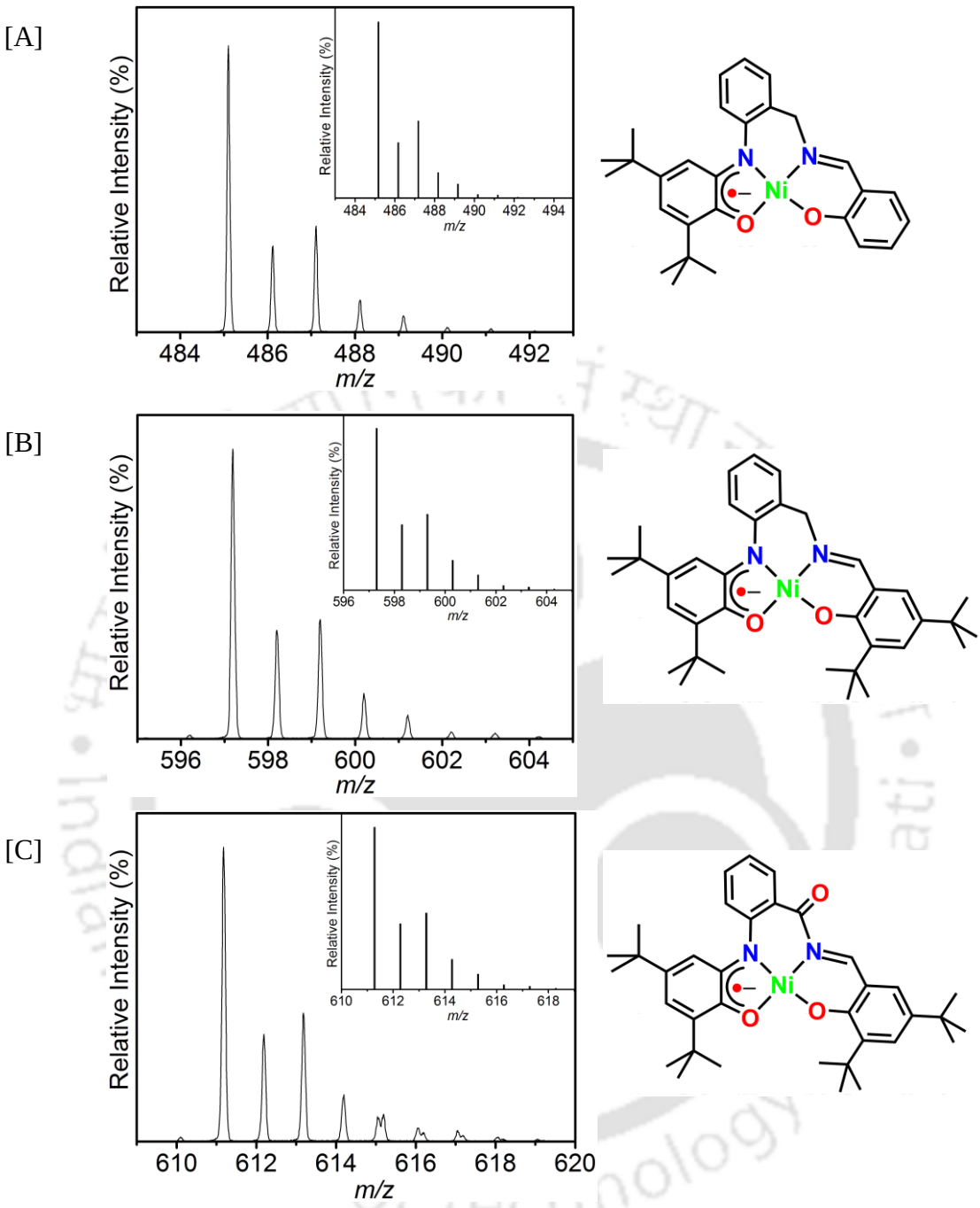

Figure 4.9: *ESI–Mass spectra of the [A]* ***15****, [B]* ***16****, and [C]* ***16a****; experimental and simulated isotope distribution pattern (inset).*

ESI–MS in CH_3CN in positive mode, complex **15**, **16**, and **16a** showed a 100% molecular ion peak at *m/z* = 485.10[**15**], 597.30[**16**], and 611.30[**16a**]; corresponded to $[M]^+$ (M = molecular mass), respectively. Isotope distribution pattern examinations of the resulted mass peaks revealed composition $\mathbf{C_{28}H_{31}N_2NiO_2}$ corresponded to the mass peak 485.30; $\mathbf{C_{36}H_{47}N_2NiO_2}$ corresponded to the mass peak 597.30; and $\mathbf{C_{36}H_{45}N_2NiO_3}$ corresponded to the mass peak 611.30 (**Figure 4.9**).

All the complexes were neutral. Complex **15**, and complex **16** crystallized in the monoclinic space group $P2_1/a$, and $C2_1/c1$, respectively, while, complex **16a** crystallized in the orthorhombic space group $P2_12_12_1$. The molecular structures are shown in **Figure 4.10**. Selected bond distances and bond angles are given in **Table 4.4**.

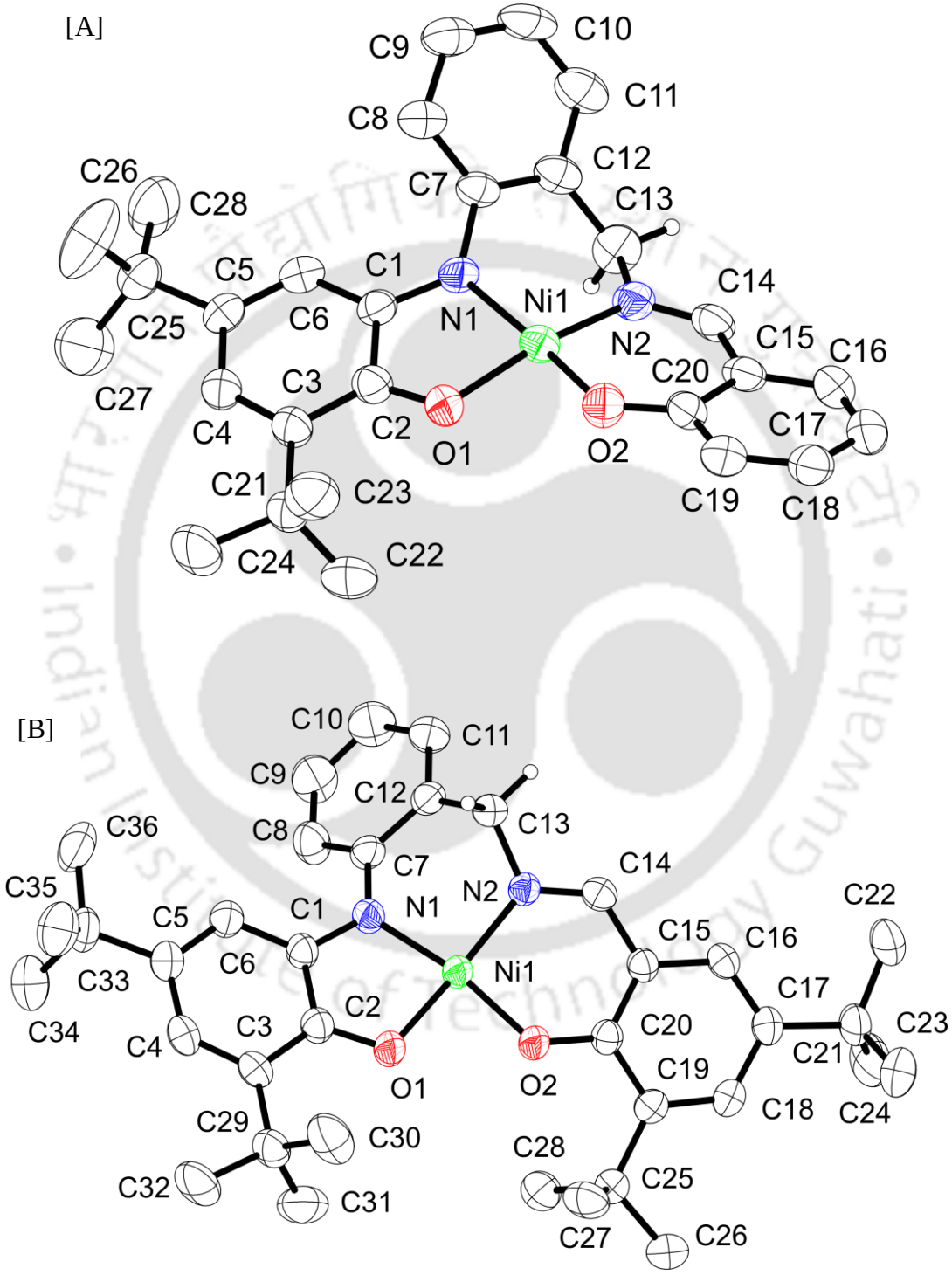

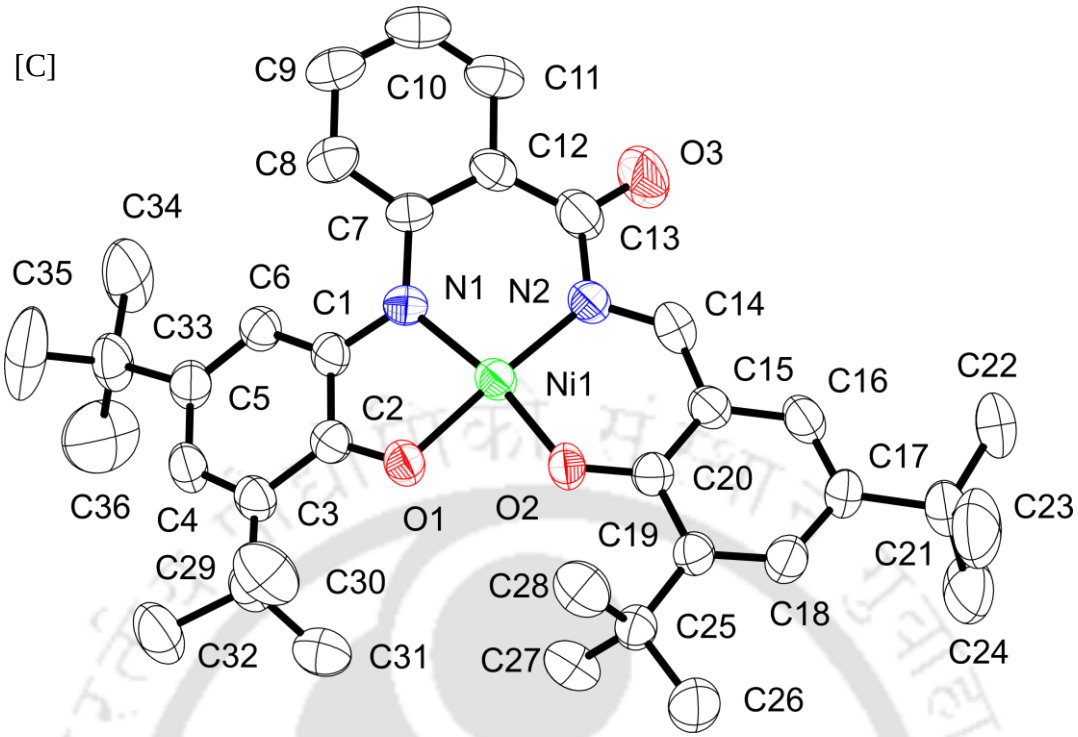

Figure 4.10: *ORTEP representation of [A]* ***NiL$^{Mixed(H)}$****; (**15**), [B]* ***NiL$^{Mixed(tBu)}$****; (**16**), [C]* ***NiL$^{Mixed(tBu)oxidized}$****; (**16a**). Hydrogen atoms except attached with C13 atom in complexes **15**, and **16** are omitted for clarity.*

In the complexes all the C–C bond distances of the *tert*–butyl–containing C_6 aryl rings (amidophenolate unit) were not falling within 1.39±01 Å, rather a quinoid–type distortion was observed (**Table 4.4**). Furthermore, C1–N1 = 1.364(6) [**15**], 1.371(4) [**16**], 1.380(5) [**16a**] Å and C2–O1 = 1.293(8) [**15**], 1.310(3) [**16**], 1.305(5) [**16a**] Å (parenthesis corresponds to the respective complex) bond distances were in between of their single bond and double bond range. There were shortening in C20–O2 and C14–C15 bonds and elongation in C14–N2 bond on going from free ligand to **15** or **16** (**Table 4.4**). These bond distance changes were mainly due to delocalization of phenolate^{1-} charge over the O2–O20–C15–C14–N2 unit. These shortening and elongation in **16a** were more pronounced due to increase of delocalization of the charge over the molecule *via* the newly formed amide unit. This type of shortening and elongation are common in salen complexes where the salicylidene unit is in its fully reduced form.[14c–f] Hence, in the complexes the amidophenolate part of the ligand was found to be in its one–electron oxidized ISQ$^{\bullet 1-}$ form and no oxidation in the salen unit was observed.

In the complexes the central Ni1 atom was coordinated by two N and two O atoms. The Ni1–O1, Ni1–N1 and Ni1–N2 bond distances were almost equal for the complexes and found within the 1.86±0.01 Å range. These bond distances were in accord with the +II

oxidation state of the Ni center.[5f,14b,e,f] Interestingly, the Ni1–O2 bond distance was ~ 0.02 Å shorter in **16** compare to **15**, indicated higher covalency of the bond that caused by the presence of electron donating *tert*–butyl substituent at the 3,5–positions of the parent salicylidene unit. This covalency difference seemed to be responsible for the reactivity difference between **15** and **16** under air. A higher electron density to Ni(II) center *via* PhO^- in **16** might facilitate the required stabilization of Ni to its higher oxidation state[19] and hence, the oxygenation reaction.

Table 4.4: *Selected bond distances (Å) and bond angles (°) are shown for the complexes **15**, **16**, and **16a**.*

	15	**16**	**16a**
Ni1–N1	1.870(4)	1.8596(17)	1.862(4)
Ni1–N2	1.860(4)	1.8494(18)	1.864(3)
Ni1–O1	1.856(4)	1.8599(15)	1.869(3)
Ni1–O2	1.840(4)	1.8183(14)	1.834(3)
C2–O1	1.293(6)	1.310(3)	1.305(5)
C1–N1	1.363(6)	1.371(3)	1.380(5)
C1–C2	1.447(7)	1.426(3)	1.429(6)
C2–C3	1.413(7)	1.430(3)	1.423(6)
C3–C4	1.370(7)	1.369(3)	1.375(6)
C4–C5	1.417(7)	1.415(3)	1.430(6)
C5–C6	1.363(7)	1.372(3)	1.357(6)
C6–C1	1.410(7)	1.415(3)	1.415(6)
N1–C7	1.404(6)	1.397(3)	1.390(6)
C7–C8	1.408(7)	1.402(3)	1.390(6)
C8–C9	1.376(7)	1.370(4)	1.365(7)
C9–C10	1.373(9)	1.379(4)	1.391(7)
C10–C11	1.374(8)	1.384(4)	1.357(7)
C11–C12	1.385(7)	1.381(3)	1.394(7)
C12–C7	1.390(7)	1.403(3)	1.414(6)
C12–C13	1.500(7)	1.502(3)	1.455(7)
C13–N2	1.486(6)	1.485(3)	1.431(6)
C13–O3			1.226(5)
C14–N2	1.286(6)	1.302(3)	1.336(5)
C14–C15	1.436(7)	1.437(3)	1.393(6)
C15–C16	1.406(7)	1.414(3)	1.422(6)
C16–C17	1.373(8)	1.364(3)	1.349(6)
C17–C18	1.373(8)	1.411(3)	1.418(6)
C18–C19	1.358(8)	1.386(3)	1.383(6)
C19–C20	1.418(7)	1.425(3)	1.447(6)
C20–C15	1.423(7)	1.408(3)	1.422(6)
C20–O2	1.296(6)	1.318(2)	1.284(5)
O1–Ni1–N1	84.84(17)	85.20(7)	84.98(15)
N1–Ni1–N2	94.69(19)	94.97(8)	95.60(16)
N2–Ni1–O2	95.80(19)	94.74(7)	95.30(14)
O2–Ni1–O1	87.17(16)	86.55(7)	84.19(13)
O1–Ni1–N2	165.83(18)	169.34(7)	173.36(16)

N1–Ni1–O2	166.19(18)	168.04(7)	169.10(14)
Ni1–O1–C2	114.5(3)	112.87(14)	112.6(3)
Ni1–N1–C1	112.4(3)	112.83(14)	110.9(3)
Ni1–N1–C7	121.6(3)	123.44(14)	125.8(3)
Ni1–N2–C13	118.3(4)	116.71(13)	125.3(3)
Ni1–N2–C14	125.2(4)	125.31(16)	121.8(3)
Ni1–O2–C20	127.3(4)	127.39(13)	129.7(3)

A detailed solid–state structural comparison was done and the parameters are given in **Table 4.5**. The Ni atom in **15** was observed almost planar to the both **P** and **R** planes, while, that in **16** was 0.30 and 0.34 Å below and above from the respective planes. Furthermore, it was found that the position of the central Ni atom from the plane passing through the salicylidene unit was differed remarkably (0.01 Å towards the benzyl carbon atom for **15** and 0.30 Å opposite to the benzyl carbon atom for **16**). These positional differences of Ni(II) center seemed to facilitate oxygen adduct to the metal center.

Table 4.5: *A comparative structural study between complex **15** and complex **16**.*

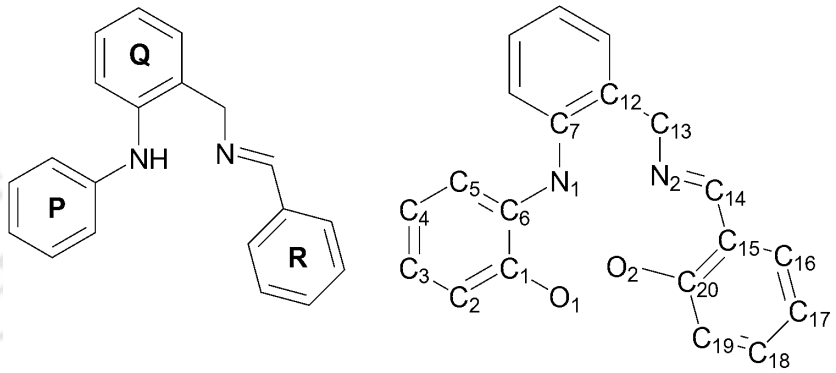

Comparing factors*	Complex **15**	Complex **16**
Angle between **P** and **Q** planes	43.9	46.3
Angle between **Q** and **R** planes	54.2	58.2
Angle between **P** and **R** planes	26.6	23.6
Angle between **N1–C7–C12–C13** and **C13–N2–C14–C15–C16–C17–C18–C19–C20–O2** planes	49.6	54.9
Angle between **N1–C7–C12–C13** and **N2–C14–C15–C16–C17–C18–C19–C20–O2** planes	49.5	54.7
Distance of **Ni1** atom from plane **P**	–0.072	–0.304
Distance of **Ni1** atom from plane **Q**	1.310	1.079
Distance of **Ni1** atom from plane **R**	0.044	0.339
Distance of **N1** atom from **Ni1–C7–C12–N2** plane	–0.475	–0.352
Distance of benzyl **C13** atom from **Ni1–C7–C12–N2** plane	0.609	0.662

Distance of **Ni1** atom from **O1–C2–C3–C4–C5–C6– C1–N1** plane	–0.154	–0.251
Distance of Ni1 atom from **N2–C14–C15–C16–C17–C18–C19–C20–O2** plane (salen plane)	–0.012	0.300

** Here –ve sign indicates the position towards benzyl C13 atom. The angles are in deg (°) and distances are in Å.*

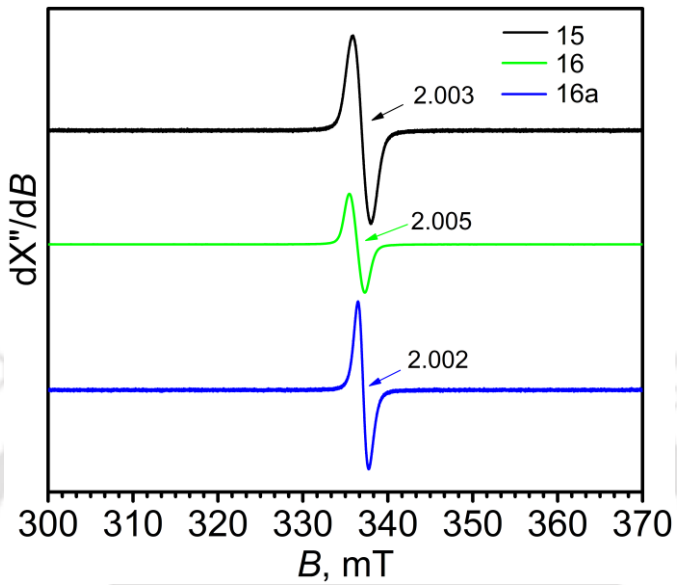

Figure 4.11: *X–band EPR spectra of **15**, **16**, and **16a** (X–band microwave frequency (MHz), 9452.247[**15**], 9442.441 [**16**], 9451.240 [**16a**]; modulation frequency (kHz), 100 [**15**, **16**, & **16a**]; modulation amplitude (G), 1.0 [**15**], 2.0 [**16**], 1.0 [**16a**]; and microwave power, 0.998000 mW) [**15**, **16**, & **16a**].*

The X–band EPR spectra of **15**, **16**, and **16a** (**Figure 4.11**) displayed isotopic resonance signals at g = 2.003 (**15**), g = 2.005 (**16**) and g = 2.002 (**16a**) (parentheses indicate the complex). Thus, the neutral complexes can be best described as Ni(II)–mono(iminosemiquinonate) complexes, *i.e.* Ni(II) coordinated to a π–radical anion.

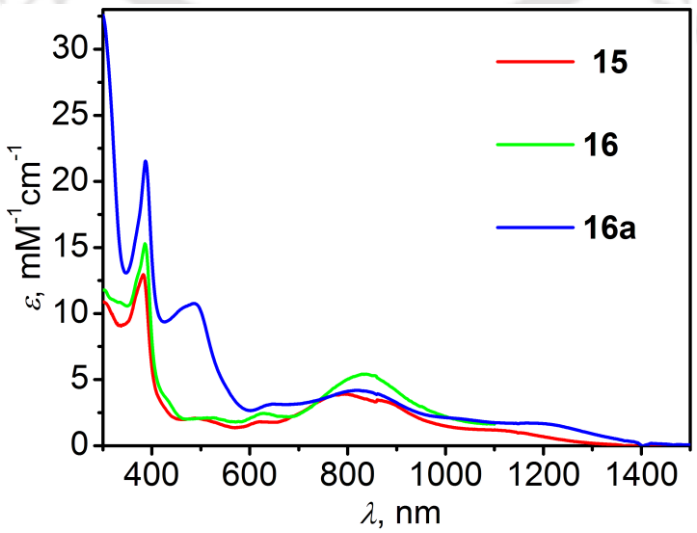

Figure 4.12: *UV–vis/NIR spectra of **15**, **16**, and **16a** are shown at 1500–300 nm range.*

Figure 4.12 represents the UV–vis/NIR spectra of **15**, **16**, and **16a**. Complexes **15**, **16**, and **16a** showed the intervalence charge transfer (IVCT) from the electron rich salen unit to the electron deficient iminosemiquinonate unit at λ_{max} (ε = $M^{-1}cm^{-1}$) = 1100 nm (1300) for **15**; 1180 nm (1800) for **16**; and 1200 nm (1900) for **16a**, respectively.[20] Ligand centered π–radical band was appeared at λ_{max} (ε = $M^{-1}cm^{-1}$) = 790 nm (4100) for **15**; 835 nm (5500) for **16**; and 810 nm (4300) for **16a**, respectively,[5f,21] while the band at λ_{max} = 485 nm (ε = 10800 $M^{-1}cm^{-1}$) for **16a** was arisen owing to charge transfer transition for the amide N–C=O unit.[22]

4.4b: Reactivity and kinetic Studies:

A CH_2Cl_2 solution of **16** was continuously purged with oxygen gas and time–dependent UV–vis/NIR spectra were simultaneously recorded (**Figure 4.13**). A gradual and regular increase in the absorption band (dotted lines) at ~ 652 nm was observed until 70 min. Noticeably, the band at ~ 835 nm, known as a marker of π–radical character,[5f] showed little change in absorption (ε = 5000 $M^{-1}cm^{-1}$). This confirmed no reaction and/or participation of the ligand centered π–radical [**16**, ~ 835 nm (ε, 5500 $M^{-1}cm^{-1}$)]. The generation of the band at ~ 652 nm was related to the formation of diamagnetic species (28%) as evidenced by the decrease of the EPR signal (**Figure 4.14**). After 70 min, the band at ~ 652 nm gradually decreased with the increase of the product marking band at ~ 485 nm. This increase was related to the increase of the EPR signal (**Figure 4.14**).

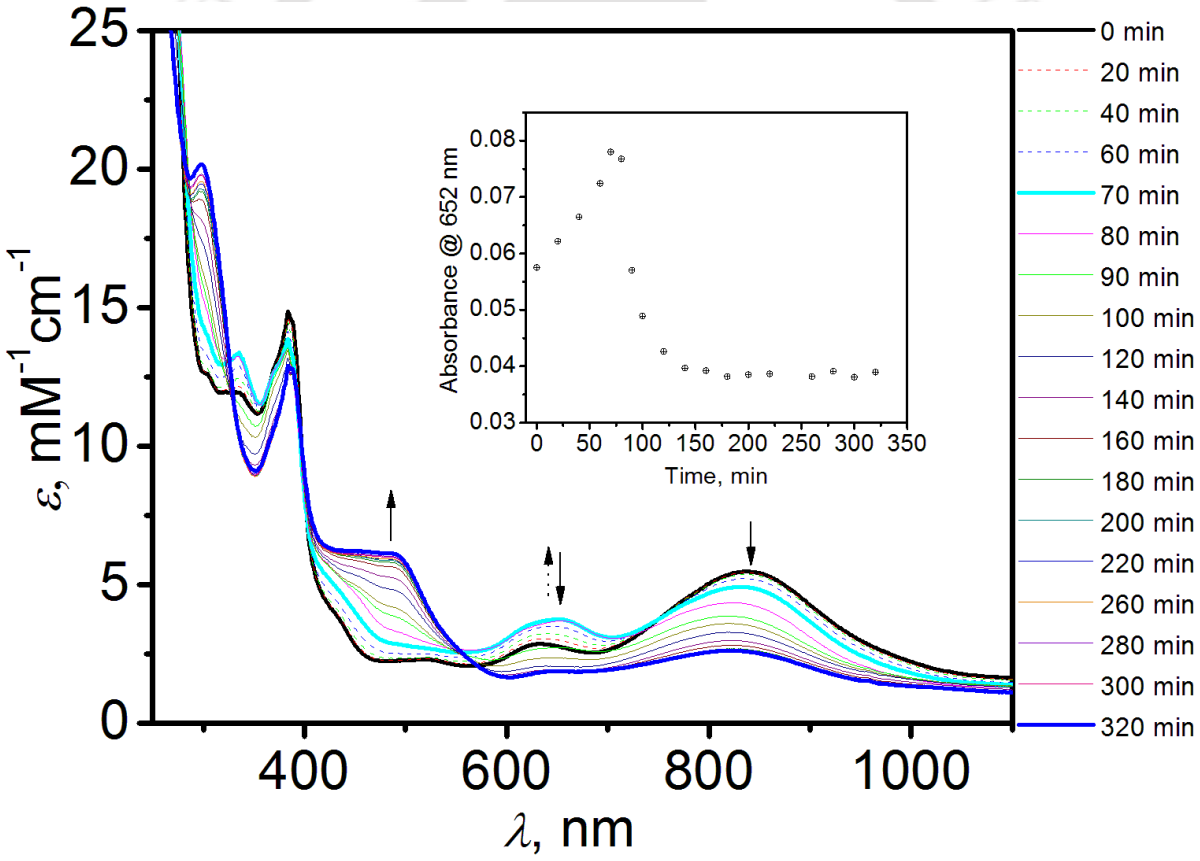

Figure 4.13: *Time–dependent UV–vis/NIR spectral changes of **16** at RT in CH_2Cl_2 in the presence of molecular oxygen.*

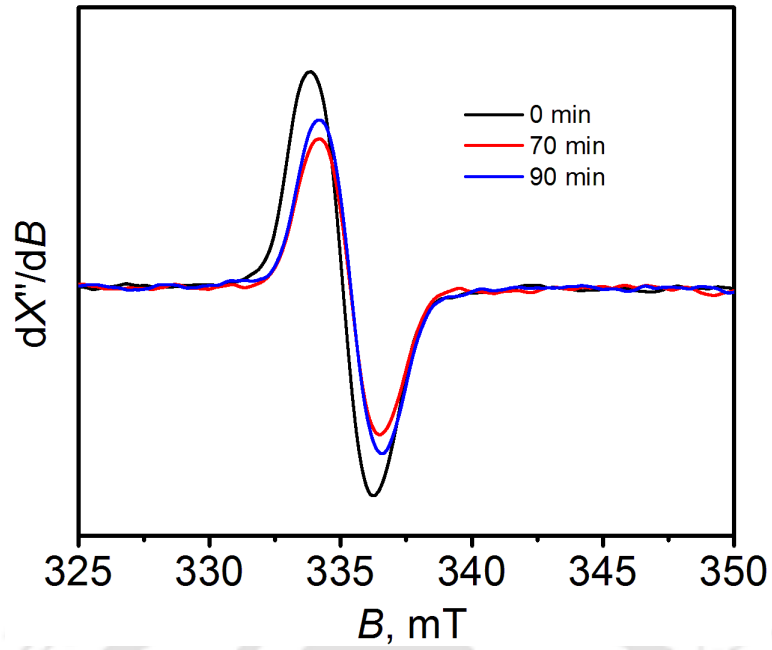

Figure 4.14: *Showing change in X–Band EPR signals intensity during oxygen gas purging to the CH_2Cl_2 solution of* ***16****.*

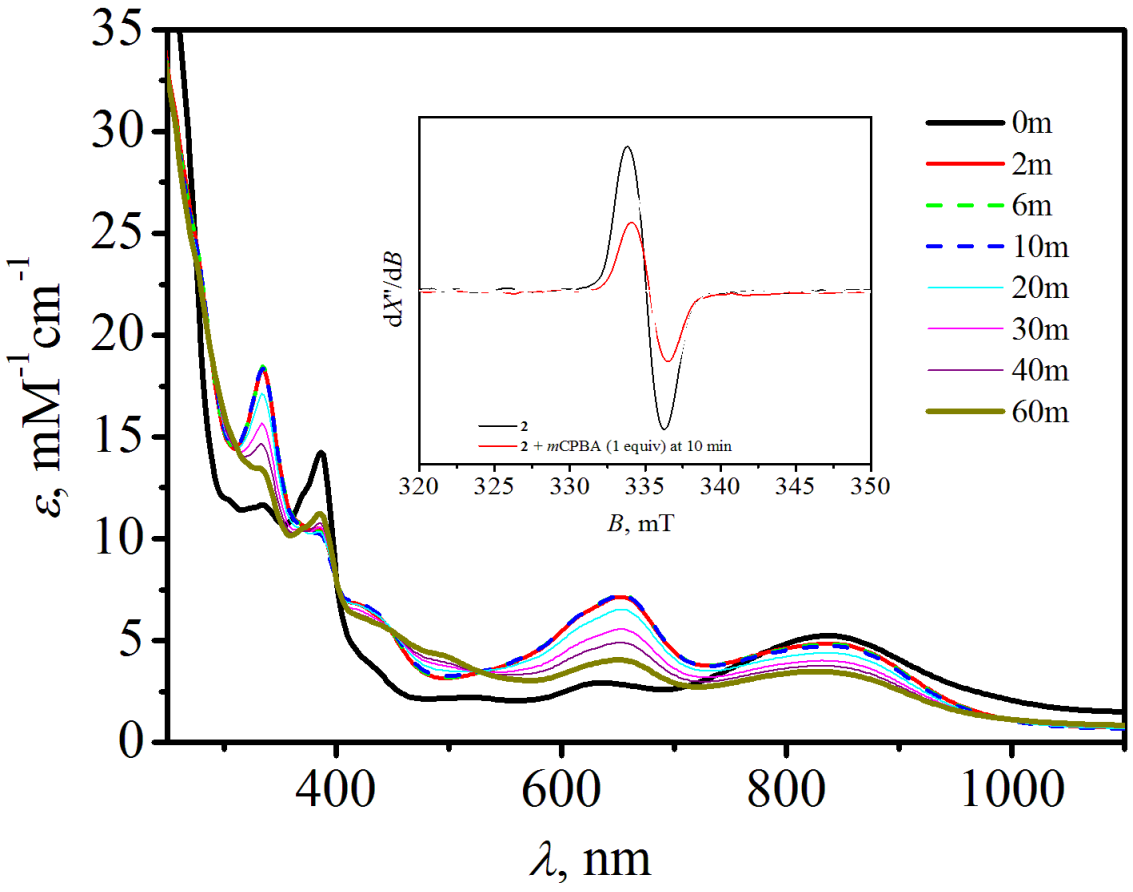

Figure 4.15: *Time–dependent absorption changes upon addition of mCPBA (1 equiv.) to* ***16****. Inset showing change in X–band EPR signal.*

Ni(II) or Ni(III)–superoxo, –peroxo, –hydroperoxo, –oxide, and –hydroxo species do not give rise to a strong absorption band at ~ 652 nm.[23] Moreover, the addition of *m*CPBA (1 equiv.) to the CH_2Cl_2 solution of **16** gave rise to similar changes in the UV–vis/NIR spectral features (**Figure 4.15**) as air did. Therefore, the species showing absorption at ~ 652 nm were not the corresponding –superoxo, –peroxo, or –hydroperoxo species. Herein, the band at ~ 652 nm was attributed to the generation of a diamagnetic species **X2**, having a delocalizing radical[24] at the benzyl position (**Scheme 4.5**).

[A]

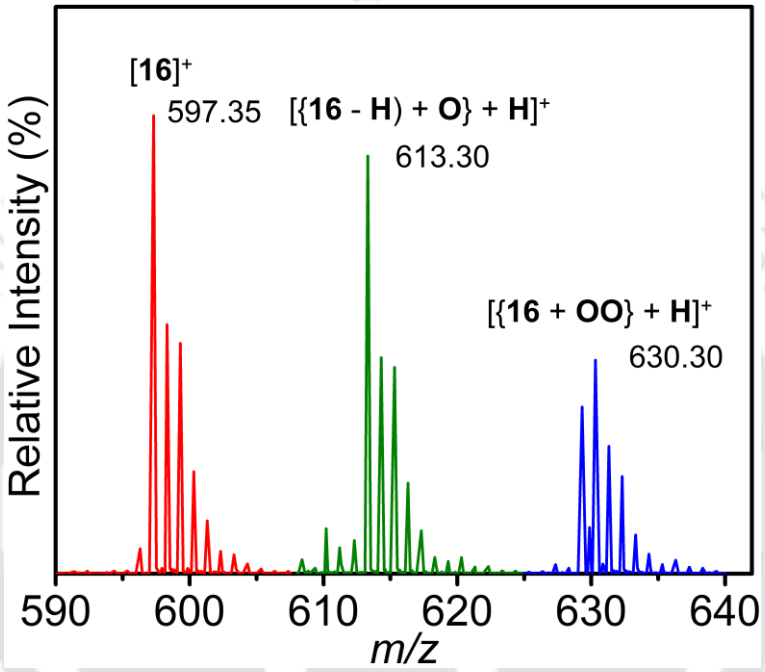

[B]

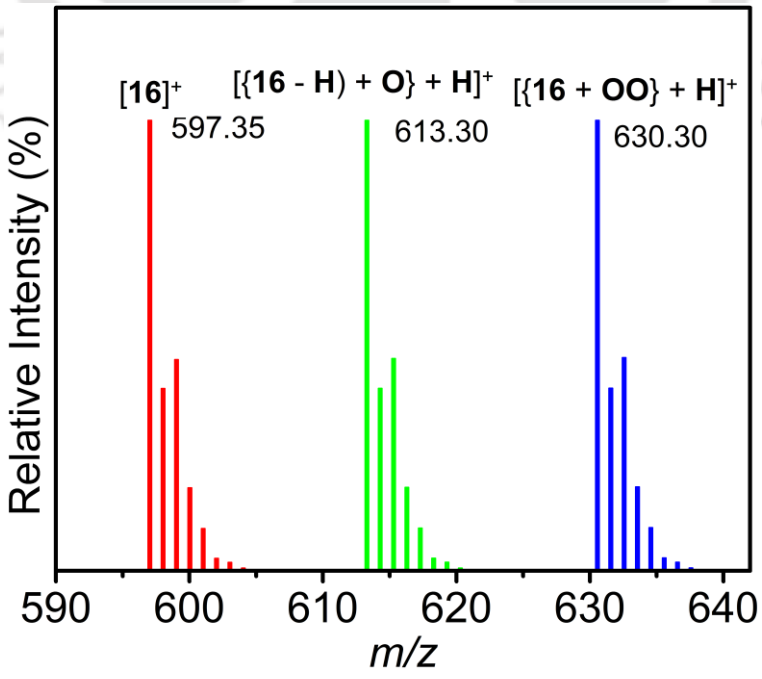

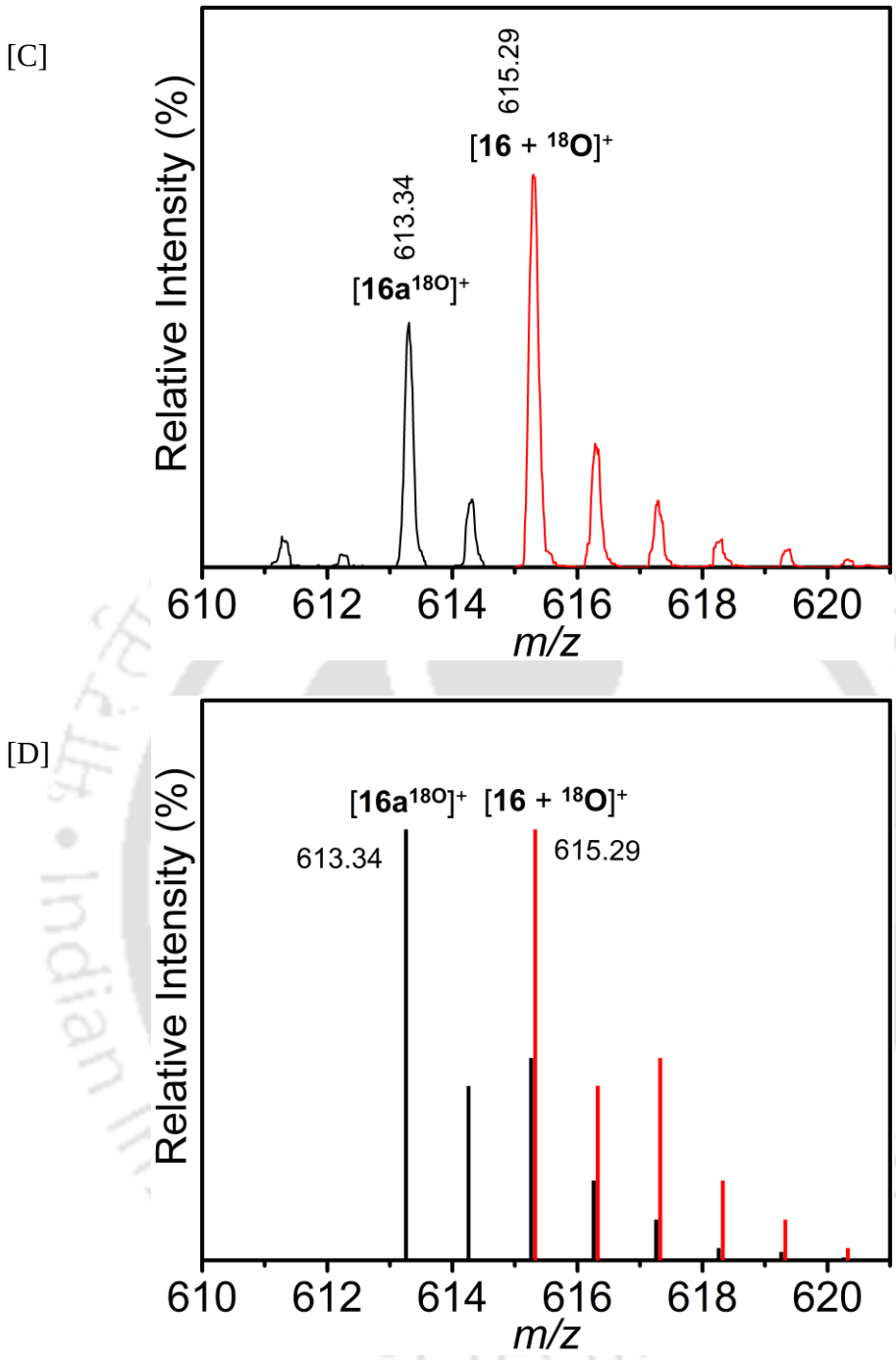

Figure 4.16: *[A] Experimental and [B] simulated mass spectra for m/z = 613.27; [**$C_{36}H_{47}N_2NiO_2$** + **O**], and m/z = 631.26; [**{$C_{36}H_{47}N_2NiO_2$** + **OOH}** + **H**] have been shown. [C] Experimental and [D] simulated mass spectra of labelling experiment using $^{18}O_2$ showed m/z = 613.34 for [**$C_{36}H_{45}N_2Ni^{16}O_2{}^{18}O$**], and m/z = 615.29 for [**$C_{36}H_{47}N_2NiO_2$** + **^{18}O**], indicating the formation of **16a** with ^{18}O and Ni–monooxygen [(**16** + O)]$^+$ species, respectively, and confirming the incorporation of molecular oxygen in to **16** for the formation of **16a**.*

The ESI (positive mode) mass spectrum of the reaction mixture (**16** + molecular oxygen) at 75 min showed peaks at *m/z* = 613.30 and *m/z* = 630.30, in addition to the molecular mass peaks for **16** and **16a** (**Figure 4.16**). The *m/z* = 613.27 peak and its isotope distribution pattern correspond to a [{(**16** – H) + O} + H]$^+$ species, i.e. [**X2** + H]$^+$, while the *m/z* = 630.26 peak represents a [{**16** + OO} + H]$^+$ unit, *i.e.* [**X1** + H]$^+$, a dioxygen–**16** adduct

(**Figure 4.16**). When the reaction was carried out with $^{18}O_2$, the reaction solution exhibited ion peaks at *m/z* = 615.29 and 613.34. These peaks corresponded to [**16** + ^{18}O]$^+$ and [**16a** (with one ^{18}O)] species with the expected isotope distribution pattern (**Figure 4.16**). This labeling experiment confirmed the incorporation of one oxygen atom from molecular oxygen into **16a**, in addition to the transient intermediate (**Figure 4.16**). Considering the above experimental (UV–vis/NIR, X–band EPR, MS) observations, the oxidation process seemed to proceed *via* the route presented in **Scheme 4.5**.

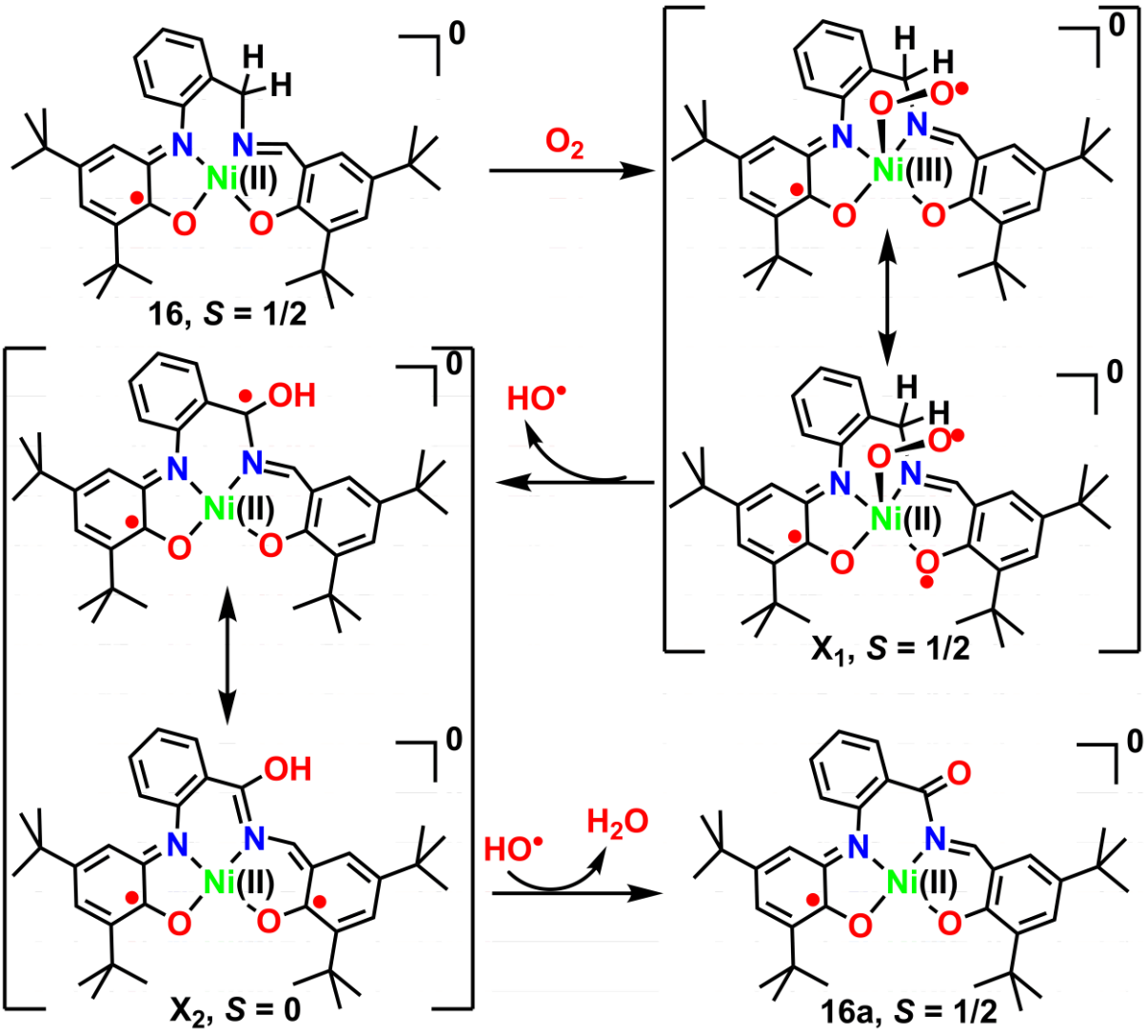

Scheme 4.5: *A mechanistic proposal for the aerial oxidation of **16** to **16a**.*

4.5: Synthesis and Characterization of Monoradical–Containing Distorted Square Planar Cu(II) Complexes with Mixed Ligands:

Square planar Cu(II) complexes [**CuL**$^{\mathbf{Mixed(H)}}$]; (**17**), and [**CuL**$^{\mathbf{Mixed(}t\mathbf{Bu)}}$]; (**18**) of the mixed ligands were synthesized by the reaction of equimolar amounts of $CuCl_2 \bullet 2H_2O$ and **H$_3$L**$^{\mathbf{Mixed(H)}}$ or by the addition of 1 equivalent amount of $CuCl_2 \bullet 2H_2O$ to the *in situ* generated ligand **H$_3$L**$^{\mathbf{Mixed(tBu)}}$ in the presence of triethylamine under air. Interestingly, **18** under air in solution converted to [**CuL**$^{\mathbf{Mixed(}t\mathbf{Bu),\ oxidized}}$]; (**18a**). The rate of reaction was very slow and hence, it took about 7 days for 20% conversion of **18** to **18a**.

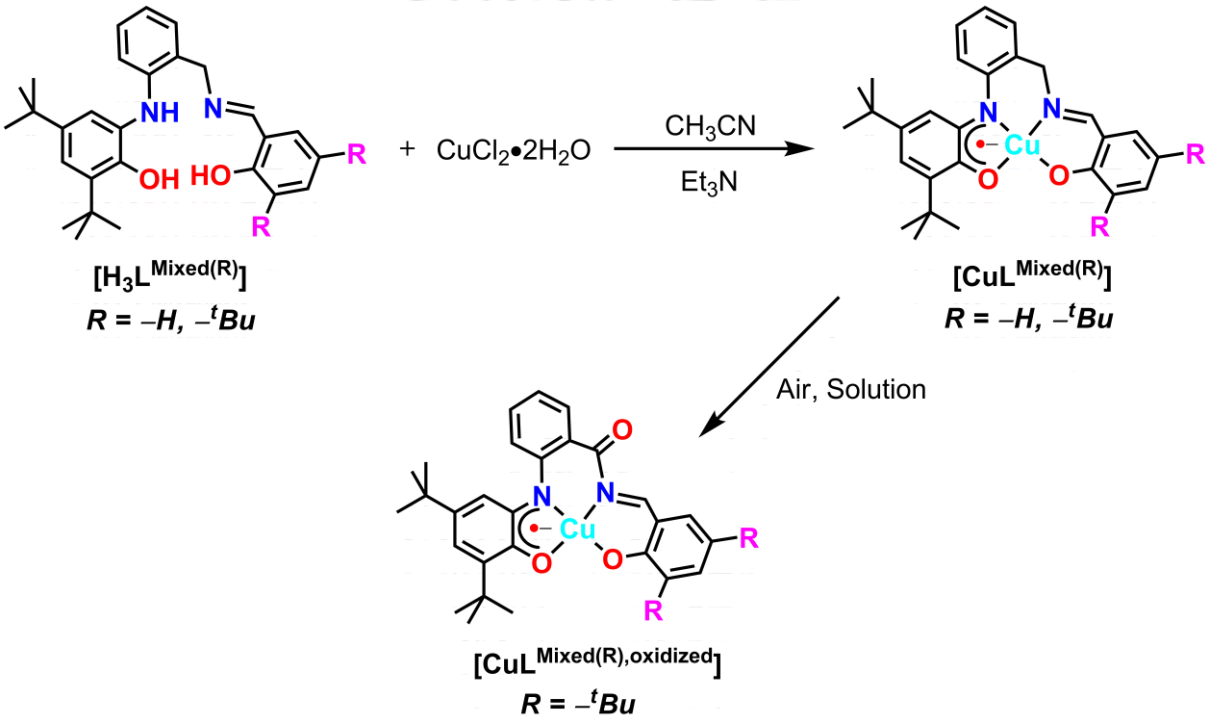

Scheme 4.6: *Synthetic route of Cu(II) complexes [**17**, **18**, and **18a**] with Mixed ligands.*

Infrared (IR) spectra of **17**, **18**, and **18a** showed no band corresponds to ν(O–H), and ν(N–H) stretches. The band corresponds to asymmetric, symmetric, and bending overtone mode of ν(C–H) stretches were appeared at 2960–2862 cm^{-1}, region. The ν(C=N) band appeared at 1626, 1619, and 1621 cm^{-1} for **17**, **18**, and **18a**, respectively. While, **18a** showed a sharp band at 1657 cm^{-1}, due to ν(C=O) stretch. The band at 1450 cm^{-1} for **17**, 1438 cm^{-1} for **18**, and **18a** was arose due to ν(C⋯O) stretch.[25]

Electrospray ionization mass spectra (ESI–MS) of **17**, **18**, and **18a** in CH_3CN in positive mode showed a 100% molecular ion peak (corresponded to M^+, M = molecular mass) at *m/z* = 490.36, for **17**; *m/z* = 602.53, for **18**, and *m/z* = 616.54, for **18a**, respectively

(**Figure 4.17**). Isotope distribution pattern examination revealed the compositions $C_{28}H_{31}CuN_2O_2$ for **17**, $C_{36}H_{47}CuN_2O_2$ for **18**, and $C_{36}H_{45}CuN_2O_3$ for **18a**, respectively.

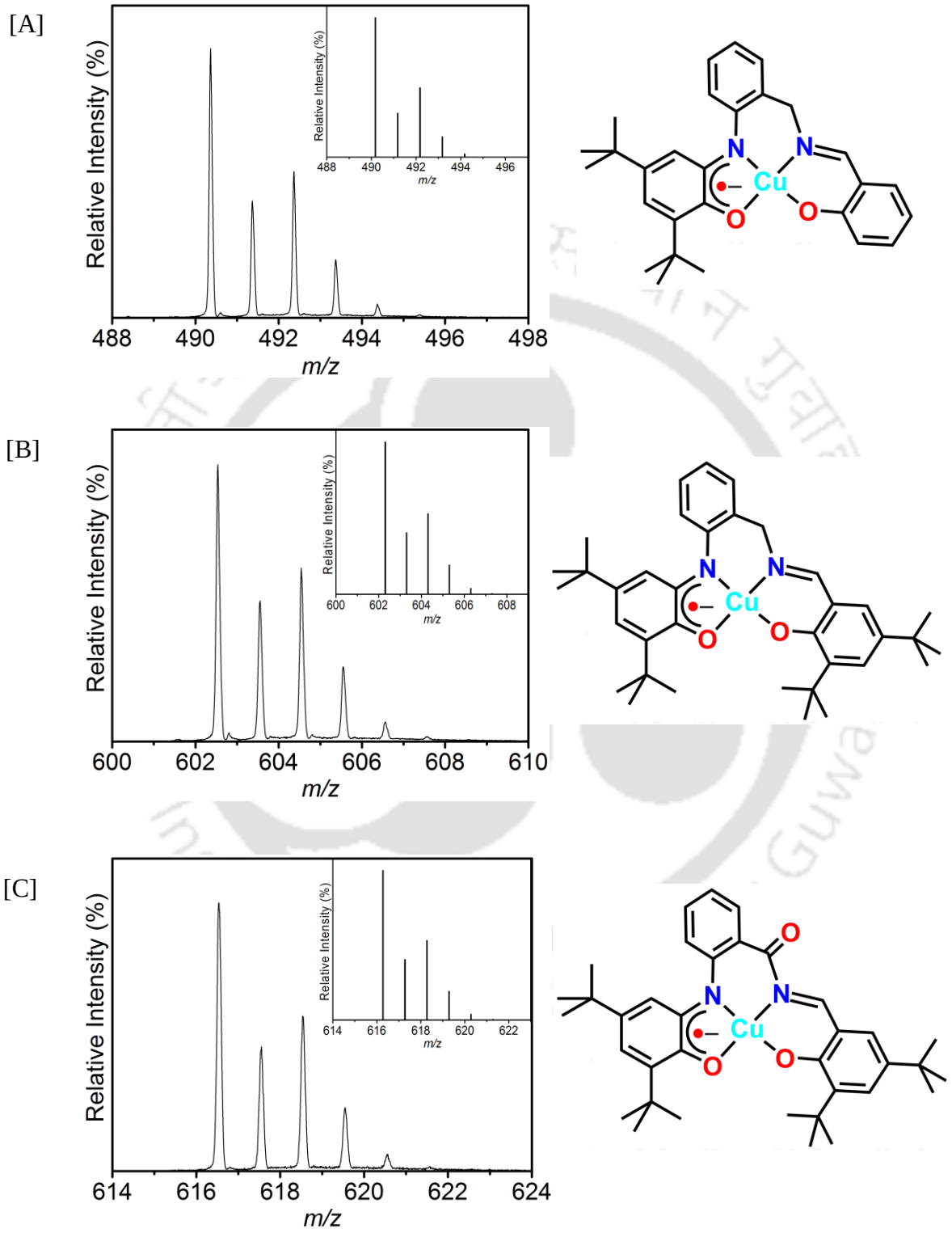

Figure 4.17: *ESI–mass spectra of [A]* ***CuL$^{Mixed(H)}$****; (**17**), [B]* ***CuL$^{Mixed(tBu)}$****; (**18**), and [C]* ***CuL$^{Mixed(tBu),\ oxidized}$****; (**18a**); experimental and calculated isotope distribution pattern (inset).*

Single crystal X–ray molecular structure of complexes **18** and **18a** are shown in **Figure 4.18**. Complex **18** crystalized in the monoclinic space group *C*12/*c*1, while, complex **18a** crystalized in the orthorhombic space group $P2_12_12_1$.

[A]

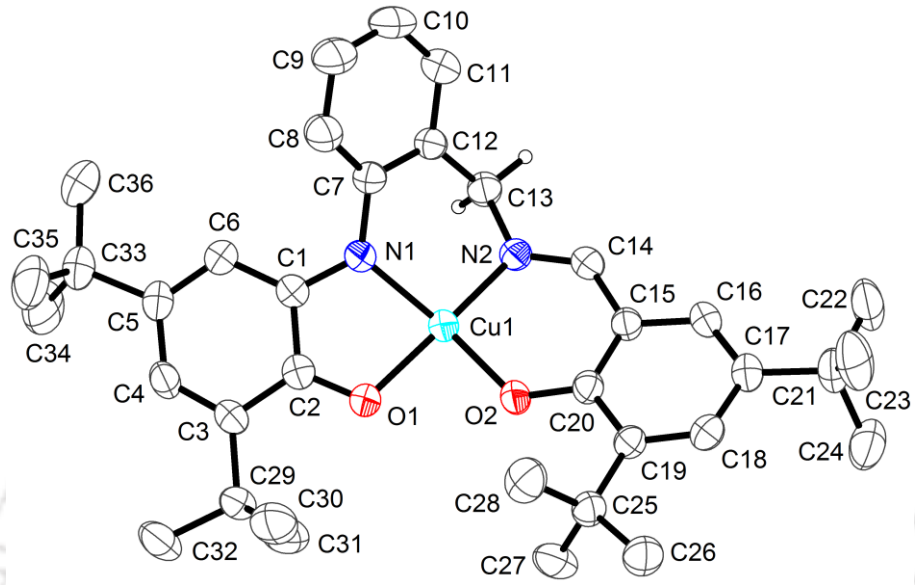

[B]

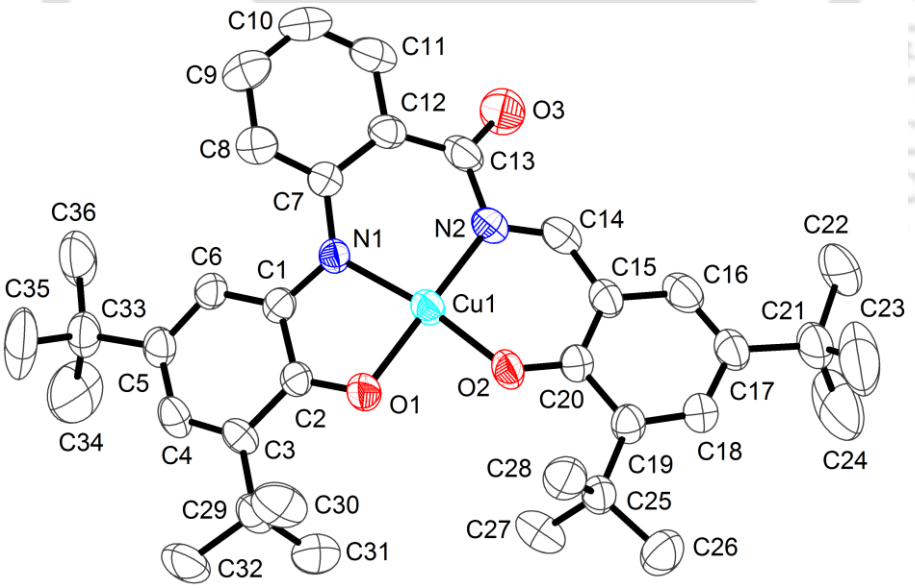

Figure 4.18: *ORTEP representation of [A]* ***CuL$^{Mixed(tBu)}$*** *; **(18)**, and [B]* ***CuL$^{Mixed(tBu),\ oxidized}$*** *; **(18a)** were drawn at 50% probability thermal ellipsoid.*

From the molecular structure of complex **18** and complex **18a**, it was found that the central Cu1 atom was coordinated with N2O2 donor set form the mixed ligand. Complex **18** and complex **18a** were differed from each other only at the C13 position where a benzyl

group in **18** was oxidized to carbonyl group in **18a**. Cu1–O1 and Cu1–O2 bond distances were 1.9265(15) [**18**]; 1.928(4) [**18a**] and 1.8577(14) [**18**]; 1.877(4) [**18a**] Å, respectively. While, the Cu1–N1 and Cu1–N2 bond distances were in the range of 1.925±0.005 Å. Notably, the Cu1–O2 bond distances were shorter compared to the Cu1–O1 bond distances, because of having higher covalent character that appeared due to presence of two *tert*–butyl groups at the 3, 5–positions. However, the above mentioned metal–ligand bond distances were in accord with the +II oxidation state of the center Cu atom.[26] The angle between N1–Cu1–O2 and N2–Cu1–O1 were 165.02(7)° [**18**]; 169.60(18)° [**18a**] and 163.85(8)° [**18**]; 169.97(18)° [**18a**] (parenthesis represent the complex), respectively. Structural distortion parameter, τ_4, for the complex **18** and **18a** were 0.22 and 0.14, respectively. Therefore, the structural distortion from the planar geometry to the non–planar geometry was more pronounced in **18** compared to **18a**.

Interestingly, all the C–C bond distances in the C_6 aryl rings were not same and were in the range of 1.39±0.01 Å. Alternating short and long C–C bond distances *i.e.* a quinoid–type distortion was observed in the *tert*–butyl groups–containing amidophenolate units. The bond distances at C1–C2, C2–C3, C3–C4, C4–C5, C5–C6, and C6–C1 were 1.443(3), 1.438(3), 1.360(3), 1.423(3), 1.363(3), and 1.419(3) Å for complex **18**, while, those were 1.421(8), 1.440(7), 1.368(8), 1.402(8), 1.372(8), 1.423(8) Å for complex **18a**, respectively. Furthermore, C2–O1 and C1–N1 bond length were 1.289(3) [**18**]; 1.288(7) [**18a**] Å and 1.354(5) [**18**]; 1.367(7) [**18a**] Å, respectively. These bond distances were neither commensurating with their respective single bond character nor double bond character. *i.e.* the coordinating amidophenolate units were present in their one–electron oxidized iminosemiquinonate ($ISQ^{\bullet 1-}$) form. To note, an alternate short and long bond distances were also found in the salicylidene unit in both complexes, because of delocalization of phenolate^{1-} charge over phenolate to imine unit.[14c–f] This type of distortion was found more pronounced in the complex **18a** compared to **18** because of higher conjugation of the phenolate^{1-} charge up to newly formed C=O bond at C13 position. This type of distortion in the salen unit is common in the metal complexes, where the salicylidene unit exist in the fully reduced form. Thus, the deprotonated mixed ligands were bearing dinegative charges and it provided the neutral Cu(II) complexes.

Table 4.6: *Selected bond distances (Å), and bond angels (°) for* ***18****, and* ***18a****.*

	18	**18a**
Cu1–N1	1.9312(17)	1.934(4)
Cu1–N2	1.9205(17)	1.935(5)
Cu1–O1	1.9265(15)	1.928(4)
Cu1–O2	1.8577(14)	1.877(4)
C2–O1	1.289(2)	1.299(6)
C1–N1	1.354(2)	1.350(7)
C1–C2	1.443(3)	1.421(8)
C2–C3	1.438(3)	1.440(7)
C3–C4	1.360(3)	1.368(8)
C4–C5	1.423(3)	1.402(8)
C5–C6	1.363(3)	1.372(8)
C6–C1	1.419(3)	1.423(8)
N1–C7	1.404(3)	1.384(7)
C7–C8	1.399(3)	1.401(8)
C8–C9	1.378(3)	1.348(8)
C9–C10	1.380(3)	1.388(9)
C10–C11	1.386(3)	1.357(9)
C11–C12	1.385(3)	1.395(8)
C12–C7	1.404(3)	1.436(8)
C12–C13	1.510(3)	1.466(9)
C13–O3		1.212(7)
C13–N2	1.475(2)	1.425(7)
C20–O2	1.312(2)	1.281(6)
C14–N2	1.290(2)	1.307(7)
C14–C15	1.446(3)	1.414(8)
C15–C16	1.407(3)	1.422(8)
C16–C17	1.372(3)	1.373(9)
C17–C18	1.409(3)	1.400(8)
C18–C19	1.385(3)	1.358(8)
C19–C20	1.423(3)	1.454(8)
C20–C15	1.425(3)	1.426(8)
O1–Cu1–N1	83.25(7)	83.20(18)
N1–Cu1–N2	95.36(7)	95.3(2)
N2–Cu1–O2	94.21(7)	94.75(19)
O2–Cu1–O1	90.68(6)	87.17(17)
O1–Cu1–N2	163.85(7)	170.3(2)
N1–Cu1–O2	165.01(7)	169.72(18)
Cu1–O1–C2	113.17(14)	111.6(4)
Cu1–N1–C1	112.87(13)	110.6(4)
Cu1–N1–C7	122.87(14)	125.3(4)
Cu1–N2–C13	115.89(13)	125.0(4)
Cu1–N2–C14	124.63(15)	120.4(4)
Cu1–O2–C20	127.76(13)	128.9(4)

Table 4.7: *A comparative study of solid state structure of* ***18****, and* ***18a****:*

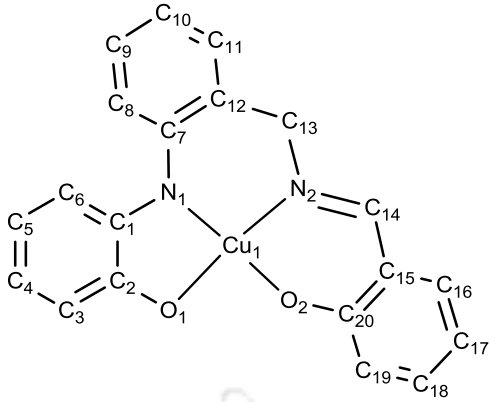

Plane A: C1–C2–C3–C4–C5–C6
Plane B: N1–C1–C2–O1
Plane C: Cu1–O1–N1
Plane D: Cu1–N2–O2
Plane E: N1–Cu1–N2
Plane F: N2–C14–C15–C20–O2
Plane G: Cu1–N2–C14–C15–C20–O2

Dihedral angel between	Complex 18	Complex 18a
Plane A and **Plane D**	**20.15**	**23.24**
Plane B and **Plane C**	**6.32**	**16.46**
Plane D and **Plane E**	**11.55**	**1.95**
Plane C and **Plane D**	**20.65**	**9.99**
Plane A and **Plane F**	**19.10**	**34.93**
Plane A and **Plane G**	**19.73**	**28.26**

[A]

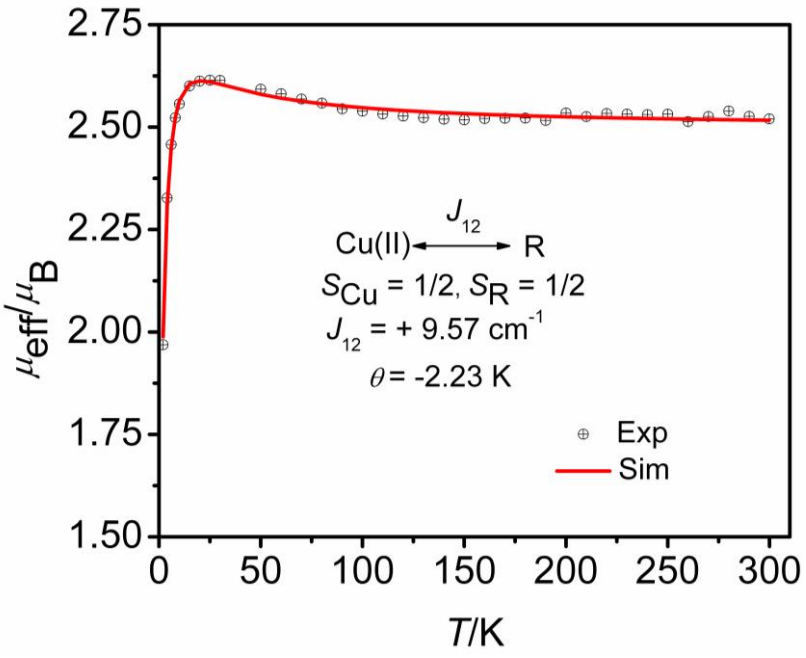

[B]

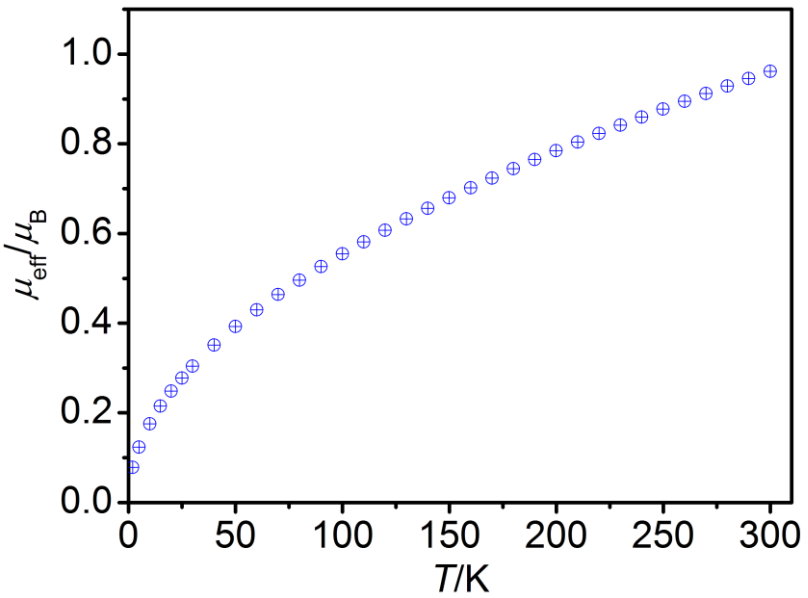

Figure 4.19: *[A] μ_{eff} vs T plots for complex **18**; [B] μ_{eff} vs T plots for complex **18a**.*

Variable–temperature magnetic susceptibility measurement of **18** and **18a** in solid state were performed in the temperature range 2–300 K at an external magnetic field 0.1 T using a SQUID magnetometer. **Figure 4.19[A]** represents the measured as well as the simulated μ_{eff} *vs T* plots for complex **18**, on the other hand **Figure 4.19[B]** represents the μ_{eff} *vs T* plots for complex **18a**. Complex **18** showed μ_{eff} = 2.52 μ_B, at 300 K, which was close to non–interacting a Cu(II) and a π–radical system. Upon cooling, μ_{eff} value increases to μ_{eff} = 2.58 μ_B at 20 K and then decreased. Increase in μ_{eff} with decrease in temperature indicated a ferromagnetic coupling between the two spins.[27] Further decrease in μ_{eff} was due to intermolecular antiferromagnetic coupling. The experimental result was simulated using the following parameters; $g_{Cu(II)}$ = 2.06, g_R = 2.00, J = +9.57 cm^{-1}, and θ = –2.23 K. On the other hand, complex **18a** showed a diamgentic ground state (S = 0) where two spin were strongly antiferromagnetically coupled to each other. The μ_{eff} value at 300 K was below 1.00 μ_B and at 2 K was closed to zero.

Planar Cu(II) semiquinone complexes show a ferromagnetic ground state because of orthogonalty of two interacting spin systems, where a the unpaired electron of Cu(II) resides on $d_{x^2-y^2}$ magnetic orbital and the π–radical of the semiquinone system locates on p_z magnetic orbital.[28] The distortion from the planar geometry means the loss of orthogonalty between two spin states and that leads to the antiferromagnetic interaction between same, and consequently, stabilizes a diamagnetic ground state (S = 0). Although, it is reported and theoretically proved that a distorted square planar Cu(II) semiquinone complex shows a

ferromagnetic ground state below the twist angel ~ 20° (twist angle refers the angel between the two biting planes around the Cu(II) center). [27a] However, above the twist angle value the complex shows an antiferromagnetically coupled ground state (S = 0).[27a] The twist angel in complexes **18**, and 1**8a** were ~ 20.65° and ~ 9.99°, respectively. Therefore, both complexes, according to the report, should show a ferromagnetic ground state (S = 1). In fact, complex **18** showed a ferromagnetic ground state, while, complex **18a** showed an antiferromagnetic ground state. Hence, to interpret this discriminating results the dihedral angle between the Cu(II) plane comprised of N2–to–O2 atoms (plane **F**) and the plane passing through the C_6–aryl ring (plane **A**) where the π–radical was residing need to be considered (**Table 4.7**). In **18** the dihedral angle was ~ 19°, while in **18a** the angle was ~ 35°. Because of the higher deviation an antiferromagnetic coupling was observed.

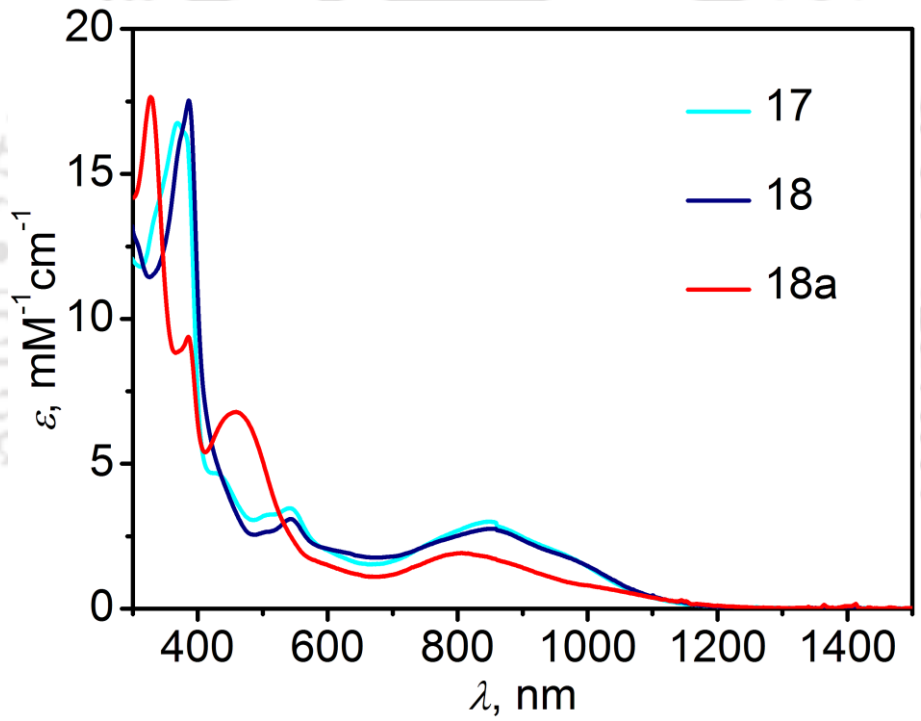

Figure 4.20: *UV–vis/NIR spectra for **17**, **18**, and **18a** were measured in dichloromethane solution at ambient temperature in 300–1500 nm range.*

The electronic absorption spectra for complexes **17**, **18**, and **18a** are shown in **Figure 4.20**. Complex **17**, and **18** showed a broad absorption band at λ_{max} = 970 nm (ε = 1800 $M^{-1}cm^{-1}$) due to the intervalence ligand(phenolate)–to–ligand(iminosemiquinone) charge transfer (IVCT). While, in **18a**, that band appeared around λ_{max} = 1000 nm (ε = 800 $M^{-1}cm^{-1}$). The intra–ligand charge transfer due to presence of π–radical appeared at λ_{max} = 845 nm (ε = 2900 $M^{-1}cm^{-1}$) for both **17** and **18**.[21a,26a] Absorption at λ_{max} = 540 nm (ε = 3400 $M^{-1}cm^{-1}$) for **17** and λ_{max} = 540 nm (ε = 3050 $M^{-1}cm^{-1}$) for **18** was due to

ligand(phenolate)–to–metal[Cu(II)] charge transfers.[5f,26c] Complex **18a** showed absorption maxima at λ_{max} = 800 nm (ε = 1950 $M^{-1}cm^{-1}$) due to ligand center π–radical (intra ligand charge transfer), while, the band at λ_{max} = 460 nm (ε = 6800 $M^{-1}cm^{-1}$) appeared due to charge transfer transition for amide N–C=O unit.[22]

4.6: Conclusions:

1. Tetradentate N,O donors ligands reacted with transition metal ion provided a π–radical–coordinated Fe(III), Ni(II), and Cu(II) compounds.

2. Substituent dependent reactivity was prominent for Ni(II) and Cu(II) complexes, while, the effect of substituent was not observed for Fe(III) complexes.

3. Although, the geometry of the Fe(III) complexes were in between of square planar and square pyramidal, no admixing were observed.

4. Between Ni(II) and Cu(II) complexes, Ni(II) complex (**16**) showed higher reactivity to aerial oxygen compared to Cu(II) complex (**18**).

5. A ferromagnetic coupling was observed in complex **18**, while, an antiferromagnetic coupling between the paramagnetic Cu(II) and the radical center was found in complex **18a**. It was found that a subtle change in dihedral angel in the ligand backbone affected the coupling fashion.

References:

1. (*a*) P. Vermaa, R. C. Pratta, T. Storrb, E. C. Wasingerc and T. D. P. Stacka, *PNAS*, 2011, **108**, 46; (*b*) G. Avigad, D. Amaral, C. Asensio and B. L. Horecker, *J. Biol. Chem.*, 1962, **237**, 2736; (*c*) M. M. Whittaker, V. L. DeVitos, S. A. Asher and J. W. Whittaker, *J. Biol. Chem.*, 1989, **264**, 7104; (*d*) J. Heinecke and P. C. Ford, *Coord. Chem. Rev.*, 2010, **254**, 235; (*e*) J. L. Vey, J. Yang, M. Li, W. E. Broderick, J. B. Broderick and C. L. Drennan, *PNAS*, 2008, **105**, 16137.

2. (*a*) L. D. Wickramasinghe, M. M. Perera, L. Li, G. Mao, Z. Zhou and C. N. Verani, *Angew. Chem., Int. Ed.*, 2013, **52**, 1; (*b*) B. Adam, E. Bill, E. Bothe, B. Goerdt, G. Haselhorst, K. Hildenbrand, A. Sokolowski, S. Steenken, T. Weyhermiiller and K. Wieghardt, *Chem. Eur. J.*, 1997, **3**, 2; (*c*) Y. Shimazaki, *AMPC*, 2013, **3**, 60; (*d*) B. Chakraborty, S. Bhunya, A. Paul and T. K. Paine, *Inorg. Chem.*, 2014, **53**, 4899; (*e*) D. Herebian, P. Ghosh, H. Chun, E. Bothe, T. Weyhermüller and K. Wieghardt, *Eur. J. Inorg. Chem.*, 2002, 1957; (*f*) C. Mukherjee, T. Weyhermiiller, E. Bothe and P. Chaudhuri, *C. R. Chimie*, 2007, **10**, 313.

3. (*a*) T. Barlow, R. Eliasson, A. Platz, P. Reichardt and B.–M. Sjöberg, *Biochemistry*, 1983, **80**, 1492; (*b*) R. Eliasson, H. Jornvall and P. Reichard, *Biochemistry*, 1986, **83**, 2373; (*c*) U. Uhlin and H. Eklund, *Nature*, 1994, **370**, 533; (*d*) M. R. Seyedsayamdost, T. Argirević, E. C. Minnihan, J. Stubbe and M. Bennati, *J. Am. Chem. Soc.*, 2009, **131**, 15729; (*e*) M. Bennati, J. H. Robblee, V. Mugnaini, J. Stubbe, J. H. Freed and P. Borbat, *J. Am. Chem. Soc.*, 2005, **127**, 15014.

4. (*a*) P. E. M. Siegbahn, L. Eriksson, F. Himo and M. Pavlov, *J. Phys. Chem. B*, 1998, **102**, 10622; (*b*) M. Ekberg, M. Sahlin, M. Eriksson and B.–M. Sjöberg, *J. Biol. Chem.*, 1996, **271**, 20655; (*c*) S. Y. Reece, J. M. Hodgkiss, J. Stubbe and D. G. Nocera, *Philos. Trans. R. Soc., B*, 2006, **361**, 1351; (*d*) J. Stubbe, D. Nocera, C. S. Yee and M. C. Y. Chang, *Chem. Rev.*, 2003, **103**, 2167; (*e*) M. R. Seyedsayamdost and J. Stubbe, *J. Am. Chem. Soc.*, 2006, **128**, 2522; (*f*) S. J. Jovanovic, S. Steenken, M. Tosic, B. Marjanovic and M. G. Simic, *J. Am. Chem. Soc.*, 1994, **116**, 4846.

5. (*a*) H. Chun, T. Weyhermüller, E. Bill and K. Wieghardt, *Angew. Chem., Int. Ed.*, 2001, **40**, 2489; (*b*) M. D. Snodin, L. Ould–Moussa, U. Wallmann, S. Lecomte, V. Bachler, E. Bill, H. Hummel, T. Weyhermüller, P. Hildebrandt and K. Wieghardt, *Chem. Eur. J.*,

1999, **5**, 2554; (*c*) H. Chun, C. N. Verani, P. Chaudhuri, E. Bothe, E. Bill, T. Weyhermüller and K. Wieghardt, *Inorg. Chem.*, 2001, **40**, 4157; (*d*) C. L. Simpson, S. R. Boone and C. G. Pierpont, *Inorg. Chem.*, 1989, **28**, 4379; (*e*) M. M. Bittner, S. V. Lindeman and A. T. Fiedler, *J. Am. Chem. Soc.*, 2012, **134**, 5460; (*f*) C. Mukherjee, T. Weyhermüller, E. Bothe and P. Chaudhuri, *Inorg. Chem.*, 2008, **47**, 11620; (*g*) A. Rajput, A. K. Sharma, S. K. Barman, D. Koley, M. Steinert and R. Mukherjee, *Inorg. Chem.*, 2014, **53**, 36.

6. (*a*) W. R. Scheidt, D. K. Geiger, R. G. Hayes and G. Lang, *J. Am. Chem. Soc.*, 1983, **105**, 2625; (*b*) F. A. Walker, B. H. Huynh, W. R. Scheidt and S. R. Osvath, *J. Am. Chem. Soc.*, 1986, **108**, 5288.

7. (*a*) W. R. Scheidt and C. A. Reed, *Chem. Rev.*, 1981, **81**, 543; (*b*) D. Sakow, D. Baabe, B. Böker, O. Burghaus, M. Funk, C. Kleeberg, D. Menzel, C. Pietzonka and M. Bröring, *Chem. Eur. J.*, 2014, **20**, 2913.

8. (*a*) H. Keutel, I. Käpplinger, E.–G. Jäger, M. Grodzicki, V. Schünemann and A. X. Trautwein, *Inorg. Chem.*, 1999, **38**, 2320; (*b*) E.–G. Jäger and H. Keutel, *Inorg. Chem.*, 1997, **36**, 3512; (*c*) R. Cheng, P. Chen, P. Gau, C. Chen and S. Peng, *J. Am. Chem. Soc.*, 1997, **119**, 2563; (*d*) P. Leeladee, G. N. L. Jameson, M. A. Siegler, D. Kumar, S. P. de Visser and D. P. Goldberg, *Inorg. Chem.*, 2013, **52**, 4668; (*e*) S. Sinnecker, N. Svensen, E. W. Barr, S. Ye, J. M. Bollinger, Jr. F. Neese and C. Krebs, *J. Am. Chem. Soc.*, 2007, **129**, 6168; (*f*) R. Boča, I. Nemec, I. Šalitroš, J. Pavlik, R. Herchel and F. Renz, *Pure Appl. Chem.*, 2009, **81**, 1357;

9. (*a*) S. F. Nelsen, *Chem. –Eur. J.*, 2000, **6**, 581; (*b*) H. Nishihara, *Bull. Chem. Soc. Jpn.*, 2001, **74**, 19; (*c*) K. D. Demadis, C. M. Hartshorn and T. Meyer, *J. Chem. Rev.*, 2001, **101**, 2655; (*d*) B. S. Brunschwig, C. Creutz and N. Sutin, *Chem. Soc. Rev.*, 2002, **31**, 168; (*e*) E. Evangelio and D. Ruiz-Molina, *Eur. J. Inorg. Chem.*, 2005, 2957; (*f*) D. M. D'Alessandro and F. R. Keene, *Chem. Soc. Rev.*, 2006, **35**, 424; (*g*) D. M. D'Alessandro and F. R. Keene, *Chem. Rev.*, 2006, **106**, 2270; (*h*) M. H. Chisholm and N. Patmore, *J. Acc. Chem. Res.*, 2007, **40**, 19; (*i*) W. Kaim and G. K. Lahiri, *Angew. Chem., Int. Ed.*, 2007, **46**, 1778; (*j*) S. D. Glover, J. C. Goeltz, B. J. Lear and C. P. Kubiak, *Eur. J. Inorg. Chem.*, 2009, 585.

10. T. Storr, E. C. Wasinger, R. C. Pratt and T. D. P. Stack, *Angew. Chem., Int. Ed.*, 2007, **46**, 5198.

11. (*a*) C. Tejel, M. A. Ciriano, M. P. del Río, F. J. van den Bruele, D. G. H. Hetterscheid, N. T. i Spithas and B. de Bruin, *J. Am. Chem. Soc.*, 2008, **130**, 5844; (*b*) X. Zhang, M. Tong and X. Chen, *Angew. Chem., Int. Ed.*, 2002, **41**, 1029.

12. (*a*) M. Ghosh, K. K. Singh, C. Panda, A. Weitz, Michael P. Hendrich, T. J. Collins, B. B. Dhar and S. S. Gupta, *J. Am. Chem. Soc.*, 2014, **136**, 9524; (*b*) S. R. Bell and J. T. Groves, *J. Am. Chem. Soc.*, 2009, **131**, 9640; (*c*) S. Fukuzumi, Y. Morimoto, H. Kotani, P. e. Naumov, Y.–M. Lee and W. Nam, *Nat. Chem.*, 2010, **2**, 756; (*d*) L. Que, *Acc. Chem. Res.*, 2007, **40**, 493; (*e*) J.–U. Rohde, J.–H. In, M. H. Lim, W. W. Brennessel, M. R. Bukowski, A. Stubna, E. Münck, W. Nam and L. Que, *Science*, 2003, **299**, 1037; (*f*) P.–C. Huang, P. Gandeepan and C.–H. Cheng, *Chem. Commun.*, 2013, **49**, 8540; (*g*) P. Gandeepan, K. Parthasarathy and C.–H. Cheng, *J. Am. Chem. Soc.*, 2010, **132**, 8569; (*h*) J. Karthikeyan and C.–H. Cheng, *Angew. Chem., Int. Ed.*, 2011, **50**, 9880; (*i*) J. Jayakumar, K. Parthasarathy and C.–H. Cheng, *Angew. Chem., Int. Ed.*, 2012, **51**, 197; (*j*) B. S. Mandimutsira, J. L. Yamarik, T. C. Brunold, W. Gu, S. P. Cramer and C. G. Riordan, *J. Am. Chem. Soc.*, 2001, **123**, 9194; (*k*) C. C. Cheng, J. Gulia, S. E. Rokita and C. J. Burrows, *J. Mol. Catal. A*, 1996, **113**, 379; (*l*) E. Szajna, A. M. Arif and L. M. Berreau, *J. Am. Chem. Soc.*, 2005, **127**, 17186.

13. (*a*) W. Bal, M. I. Djuran, D. W. Margerum, T. Edward, J. Gray, M. A. Mazid, R. T. Tom, E. Nieboer and P. J. Sadler, *J. Chem. Soc., Chem. Commun.*, 1994, 1889; (*b*) M. Suzuki, *Acc. Chem. Res.*, 2007, **40**, 609; (*c*) C. N. Sudhamani, H. S. B. Naik, D. Girija and T. Aravinda, *International Research Journal of Pure & Applied Chemistry*, 2011, **1**, 42; (*d*) M. Prudent and H. H. Girault, *J. Am. Soc. Mass Spectrom*, 2008, **19**, 560; (*e*) M. Bruschi, L. Bertini, V. Bonačić-Koutecký, L. D. Gioia, R. Mitric, G. Zampella and P. Fantucci, *J. Phys. Chem. B*, 2012, **116**, 6250.

14. (*a*) A. L. Smith, K. I. Hardcastle and J. D. Soper, *J. Am. Chem. Soc.*, 2010, **132**, 14358; (*b*) C. Mukherjee, T. Weyhermüller, E. Bothe and P. Chaudhuri, *Inorg. Chem.*, 2008, **47**, 2740; (*c*) C. Mukherjee, A. Stmmler, H. Bögge and T. Glaser, *Inorg. Chem.*, 2009, **48**, 9476; (*d*) C. Mukherjee, A. Stmmler, H. Bögge and T. Glaser, *Chem.–Eur. J.*, 2010, 10137; (*e*) T. Glaser, M. Heidemeier, R. Föhlich, P. Hildebrandt, E. Bothe and E. Bill, *Inorg. Chem.*, 2005, **44**, 5467; (*f*) O. Rotthaus, O. Jarjayes, F. Thomas, C. Philouze, C. P. D. Valle, E. S. Aman and J. L. Pierre, *Chem.–Eur. J.*, 2006, **12**, 2293.

15. (*a*) *Mössbauer Spectroscopy*; D. P. E. Dickson and Eds. F. J. Berry, Cambridge University Press: Cambridge, 1986; (*b*) G. R. A. Wyllie, O. Q. Murro, C. E. Schulz and W. R. Scheidt, *Polyhedron*, 2007, **26**, 4664; (*c*) K. S. Min, T. Weyhermüller and K. Wieghardt, *Dalton trans.*, 2004, 178.

16. H. Chun, E. Bill, E. Bothe, T. Weyhermüller and K. Wieghardt, *Inorg. Chem.*, 2002, **41**, 5091.

17. (*a*) G. Hastings and V. Sivakumar, *Biochemistry*, 2001, **40**, 3681; (*b*) J. Breton, J. Burie, C. Berthomieu, G. Berger and E. Nabedryk, *Biochemistry*, 1994, **33**, 4953.

18. (*a*) R. A. Meyers (Ed.), *Encyclopedia of Analytical Chemistry*, pp. 10815–10837; (*b*) M. G. A. Elwahed, *J. Serb. Chem. Soc.*, 2003, **68**, 463.

19. (*a*) S. Yao and M. Driess, *Acc. Chem. Res.*, 2012, **45**, 276; (*b*) S. Otsuka, A. Nakamura and Y. Tatsuno, *J. Am. Chem. Soc.*, 1969, **91**, 6994; (*c*) S. Sripothongnak, N. Barone and C. J. Ziegler, *Chem. Commun.*, 2009, 4584.

20. T. Kurahashi and H. Fujii, *J. Am. Chem. Soc.*, 2011, **133**, 8307.

21. (*a*) M. Franks, A. Gadzhieva, L. Ghandhi, D. Murrell, A. J. Blake, E. S. Davies, W. Lewis, F. Moro, J. McMaster and M. Schröder, *Inorg. Chem.*, 2013, **52**, 660; (*b*) L. Benisvy, R. Kannappan, Y.–F. Song, S. Milikisyants, M. Huber, I. Mutikainen, U. Turpeinen, P. Gamez, L. Bernasconi, E. J. Baerends, F. Hartl and J. Reedijk, *Eur. J. Inorg. Chem.*, 2007, 637.

22. (*a*) A. K. Singh and R. Mukherjee, *Dalton Trans.*, 2005, 2886; (*b*) A. K. Singh and R. Mukherjee, *Inorg. Chem.*, 1999, **38**, 1388; (*c*) G. Zou and G. L. Boyer, *BioMetals*, 2005, **18**, 63.

23. (*a*) T. D. Manuel and J.–U. Rohde, *J. Am. Chem. Soc.*, 2009, **131**, 15582; (*b*) F. F. Pfaff, F. Heims, S. Kundu and K. Ray, *Chem. Commun.*, 2012, 3730; (*c*) A. Company, S. Yao, K. Ray and M. Driess, *Chem.–Eur. J.*, 2010, **16**, 9669; (*d*) J. Cho, R. Sarangi, J. Annaraj, S. Y. Kim, M. Kubo, T. Ogura, E. I. Solomon and W. Nam, *Nat. Chem.*, 2009, **1**, 568; (*e*) B. Bag, M. Mondal, G. Rosair and S. Mitra, *Chem. Commun.*, 2000, 1729.

24. (*a*) J. Seth, V. Palaniappan and D. F. Bocian, *Inorg. Chem.*, 1995, **34**, 2201; (*b*) D. Chang, T. Malinski, A. Ulman and K. M. Kadish, *Inorg. Chem.*, 1984, **23**, 817.

25. H. Suzuki, M–aki. Nagasaka, M. Sugiura and T. Noguchi, *Biochemistry*, 2005, **44**, 11323.

26. (*a*) P. Chaudhuri, C. N. Verani, E. Bill, E. Bothe, T. Weyhermüller and K. Wieghardt, *J. Am. Chem. Soc.*, 2001, **123**, 2213; (*b*) S. Ye, B. Sarkar, F. Lissner, T. Schleid, J. van Slageren, J. Fiedler and W. Kaim, *Angew. Chem., Int. Ed.*, 2005, **44**, 2103; (*c*) C. Mukherjee, U. Pieper, E. Bothe, V. Bachler, E. Bill, T. Weyhermüller and P. Chaudhuri, *Inorg. Chem.*, 2008, **47**, 8943.

27. (*a*) P. Verma, J. Weir, L. Mirica and T. D. P. Stack, *Inorg. Chem.*, 2011, **50**, 9816; (*b*) Y. Ma, D.–Z. Gao, W. Zhang, K. Yoshimura, D.–Z. Liao, Z.–H. Jiang and S.–P. Yan, *Inorg. Chim. Acta.*, 2006, 359, 4655; (*c*) H.–H. Lin, H.–H. Wei, G.–H. Lee and Y. Wang, *Polyhedron*, 2001, **20**, 3057; (*d*) I. Dasna, S. Golhen, L. Ouahab and N. Daro, *New J. Chem.*, 2001, **25**, 1572; (*e*) Z. Liu, Z. Lu, D. Zhang, Z. Jiang, L. Li, C. Liu and D. Zhu, *Inorg. Chem.*, 2004, **43**, 6620.

28. (*a*) A. Dei, D. Gatteschi, L. Pardi and U. Russo, *Inorg. Chem.*, 1991, **50**, 9816; (*b*) C. G. Pierpont and A. S. Attia, *Collect. Czech. Chem. Commun.*, 2001, **66**, 33; (*c*) O. Kahn, R. Pris, J. Rieedjik and J. S. Thompson, *Inorg. Chem.*, 1987, **26**, 3557; (*d*) C. G. Pierpont and C. W. Lange, *Prog. Inorg. Chem.*, 1994, **41**, 331; (*e*) C. Benelli, A. Dei, D. Gatteschi and L. Pardi, *Inorg. Chem.*, 1990, **29**, 3409; (*f*) J. Müller, T. Weyhermüller, E. Bill, P. Hildebrandt, L. Ould–Moussa, T. Glaser and K. Wieghardt, *Angew. Chem., Int. Ed.*, 1998, **37**, 616.

Chapter V

Synthesis, Characterization, and Reactivity of Co(III) Complexes Isolated by Using H_2L^X (X = –Me, –Et, –F, –Cl, –Br, and –I) Ligands

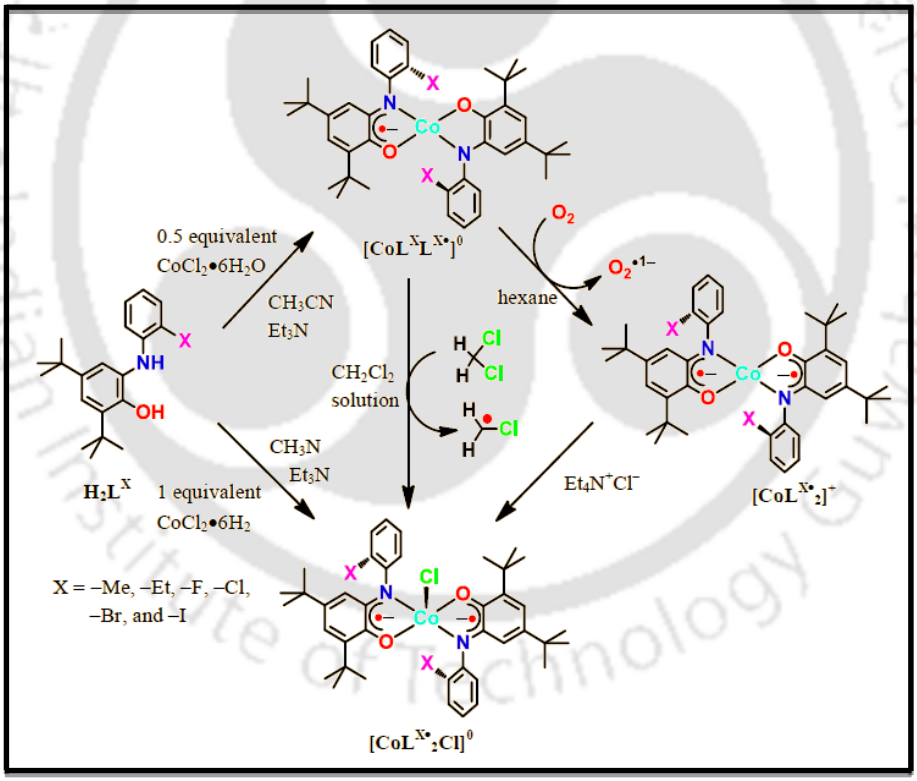

5.1: Introduction:

In square planar cobalt complexes the central metal ion is coordinatively unsaturated. This ease the access of substrate to the metal center and because of this fact coordinatively unsaturated cobalt complexes have shown high catalytic efficiency towards olefin–epoxidation,[1] C–H activation,[2] C–C bond formation[3] than those of coordinaively saturated complexes. In this regard, the synthesis of coordinatively unsaturated cobalt complex has achieved great importance. However, the synthesis of coordinatively unsaturated four coordinate cobalt complex is of great challenge because of having high axial Lewis acidity. In this note, strong σ–donating ligands have been employed to synthesize four–coordinated square planar Co(III) complexes by reducing the axial Lewis acidity of the cobalt (Co) center. Mono–anionic square planar $[(n\text{–}C_4H_9)_4N]^{1+}[Co^{III}(S_2C_6X_2Y_2)_2]^{1-}$; (X = Y = –H, $–CH_3$, –Cl; X = –H, Y = $–CH_3$) complexes were first reported by M. J. Baker–Hawkes in 1966.[4]

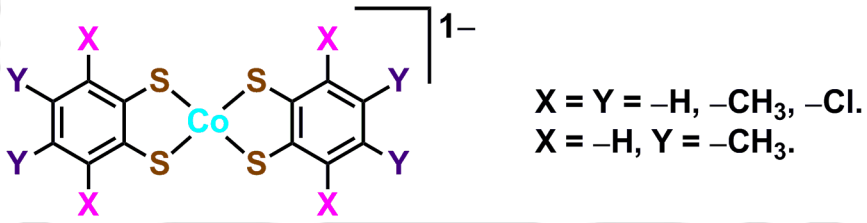

Scheme 5.1: *Mono–anionic square planar Co(III) complexes.*[4]

Later on, in 1988, Brewer *et al.* were the first to report a neutral square planar Co(III) complex with the alkoxide–containing polyanionic chelating (PAC) ligands having strong donor capacity[5] in comparison to the related phenoxido–containing PAC ligands have weaker donor capacity, and the cobalt(III) complexes exhibit a greater axial Lewis acidity, that favor the common octahedral coordination geometry.[6]

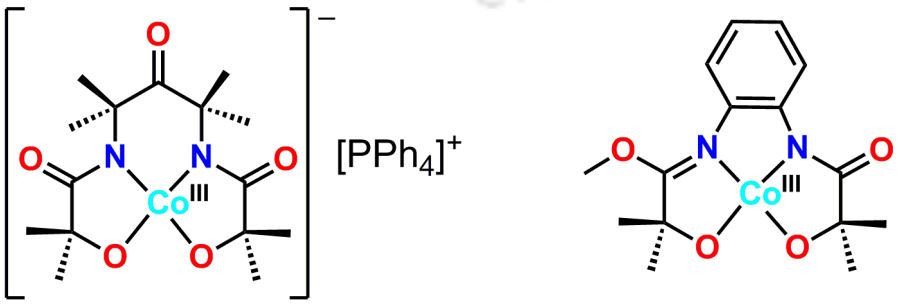

Scheme 5.2: *Mono–anionic, and neutral square planar Co(III) complexes.*[5]

So the most important aspect for the synthesis and the stabilization of square planar Co–complexes is the donor capacity as well as donating nature of the ligands. A ligand fragment possesses four strongly σ–donating anions, which reduced the axial Lewis acidity of the central cobalt ion, facilitate the formation of square planar geometry. Although, an increment in ligand σ–donating capability stabilizes cobalt ion in its square planar geometry, the affinity of the metal center toward the substrate decreases and hence, the catalytic efficiency of the metal complexes diminishes. In this note, the synthesis and study of cobalt–radical complexes have drawn a considerable attention. Herein, the importance of the presence of radical(s) lies with the easy acceptance of electron(s).

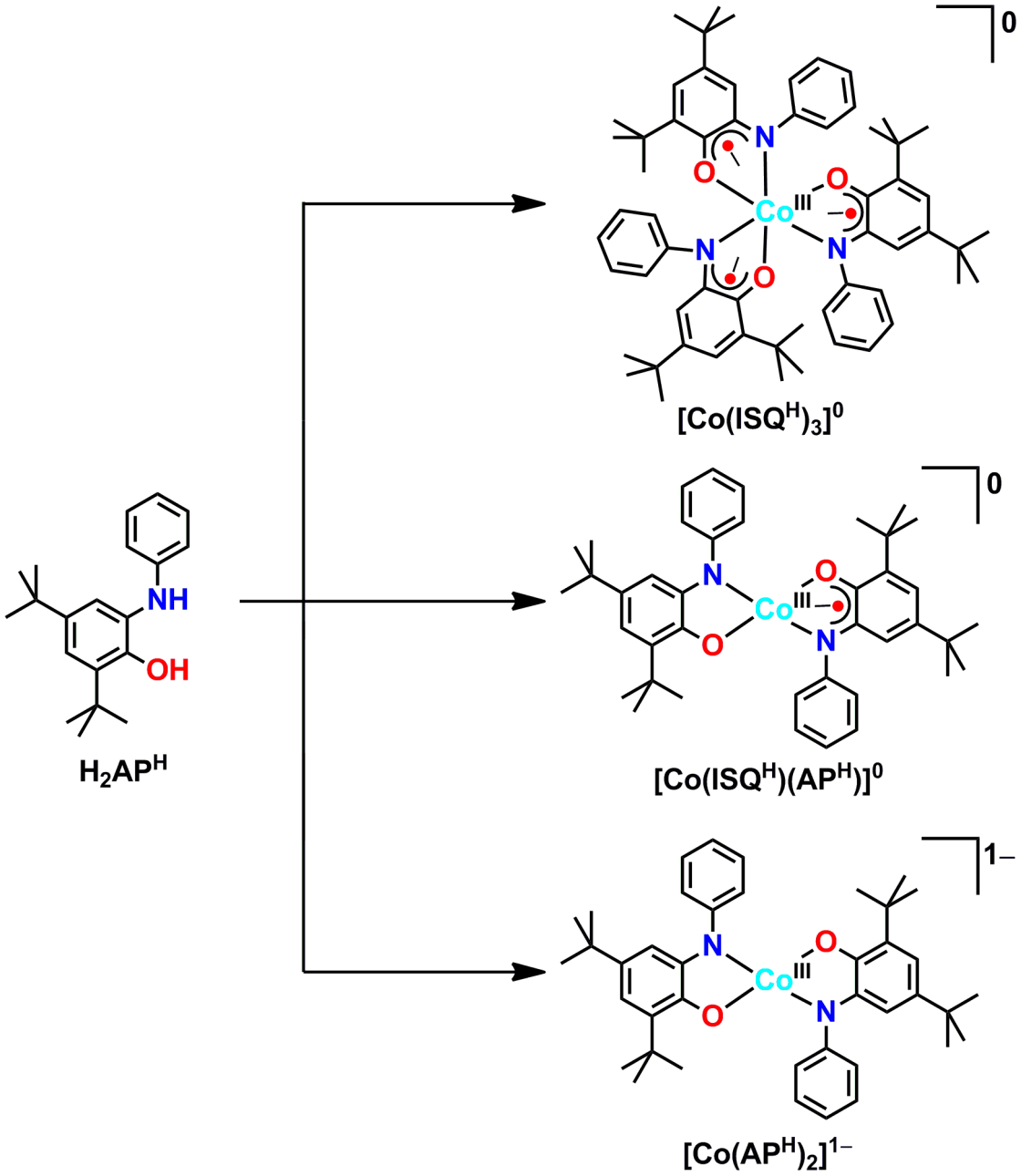

Scheme 5.3: *Ligand* $\boldsymbol{H_2AP^H}$ *and its Co(III) complexes.*

Chaudhuri and *et al.* in 1999 were reported the triradical–containing octahedral cobalt(III) complex [**Co(ISQ^{H})$_3$**] using a σ–donor strong field non–innocent ligand as **H$_2$AP^{H}** (without substituent).[7] Interestingly, by changing the metal to ligand ratio, a neutral square planar complex [**Co(ISQ)^{H}(AP^{H})**] and mono–anionic square planar complex [**Co(AP^{H})$_2$**]$^{-}$ were synthesized by A. L. Smith *et al.* in 2010.[8] In 2011, they showed the amidophenolate ligand as electron supplier for bond forming redox reaction to form metal–carbon bond at the Co center and used these type metal complexes as catalyst in cross coupling reaction.[9] Furthermore, introducing of bulky substituents *e.g.* –Me, –iPr, which capable of strong σ–donation, at the *–o,o′* position to the N–Phenyl rings of **H$_2$AP^{H}** ligand (non–innocent ligand), square planar radical–containing cobalt complexes have been stabilized.[10] Herein, as claimed, the steric hindrance exerted by the substituent present at *–o,o′* position played an additional role to stabilize the square planar geometry. However, it was observed that a less sterically hindered –CF_3 substituent present at the *–ortho* position of N–phenyl ring in **H$_2$AP^{CF_3}** ligand also stabilize a monoradical–containing square planar Co(III) complex.[11] This clearly provide anomaly in the system. Hence, to find out the effect of *–ortho* substituent and also the role of metal ion concentration to the formation of various radical–containing coordinatively unsaturated cobalt complexes, the following **H$_2$L^{X}** (X = –Me, –Et, –F, –Cl, –Br, and –I) ligands and their corresponding cobalt complexes have been synthesized and presented here.

- (a) [**CoL^{Me}L$^{Me•}$**]; (**19**)
  (b) [**CoL$^{Me•}{}_2$Cl**]; (**19a**)
- (a) [**CoL^{Et}L$^{Et•}$**]; (**20**)
  (b) [**CoL$^{Et•}{}_2$Cl**]; (**20a**)
- (a) [**CoL^{F}L$^{F•}$**]; (**21**)
  (b) [**CoL$^{F•}{}_2$Cl**]; (**21a**)
- (a) [**CoL^{Cl}L$^{Cl•}$**]; (**22**)
  (b) [**CoL$^{Cl•}{}_2$Cl**]; (**22a**)
- (a) [**CoL^{Br}L$^{Br•}$**]; (**23**)
  (b) [**CoL$^{Br•}{}_2$Cl**]; (**23a**)
- (a) [**CoL$^{I•}{}_2$Cl**]; (**24**)

5.2: Synthesis and Characterization of bidentate H_2L^X (X = –Me, –Et, –F, –Cl, –Br, and –I) Ligands:

All $\mathbf{H_2L^X}$ (X = –Me, –Et, –F, –Cl, –Br, and –I) ligands were synthesized in very good yield by reacting equimolar amounts of 3,5–di–*tert*–butylcatechol and *o*–toluidine, or *o*–ethylaniline, or *o*–haloaniline in hexane in the presence of triethylamine (**Scheme 5.4**).

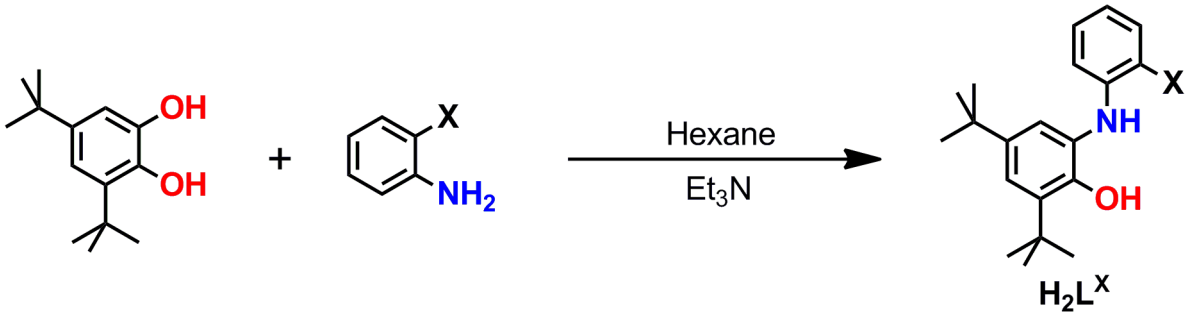

Scheme 5.4: *Synthetic route for* $\boldsymbol{H_2L^X}$ *ligands (X = –Me, –Et, –F, –Cl, –Br, and –I).*

All the ligands were well characterized by FTIR spectroscopy, NMR spectroscopy as well as by mass spectrometry techniques.

In the IR spectrum of ligand $\mathbf{H_2L^F}$, the band at 3432 cm^{-1} was appeared for the ν(O–H) vibration, while, the asymmetric, bending overtone, and bending modes for ν(N–H) stretch appeared at 3382 cm^{-1}, 3356 cm^{-1} and 1619 cm^{-1}. The other ligands showed the ν(O–H) stretching frequency above 3400 cm^{-1} and the ν(N–H) stretching frequency nearly at 3350 cm^{-1}. The aromatic ν(C–H) stretches for the ligands appeared at 3055 cm^{-1}. Asymmetric, symmetric, and bending overtone bands for aliphatic ν(C–H) stretches due to presence of *tert*–butyl methyl groups appeared at ~ 2953–2906 cm^{-1}, while, the corresponding bending vibrational modes appeared around ~ 1480 cm^{-1} and ~ 1364 cm^{-1}.

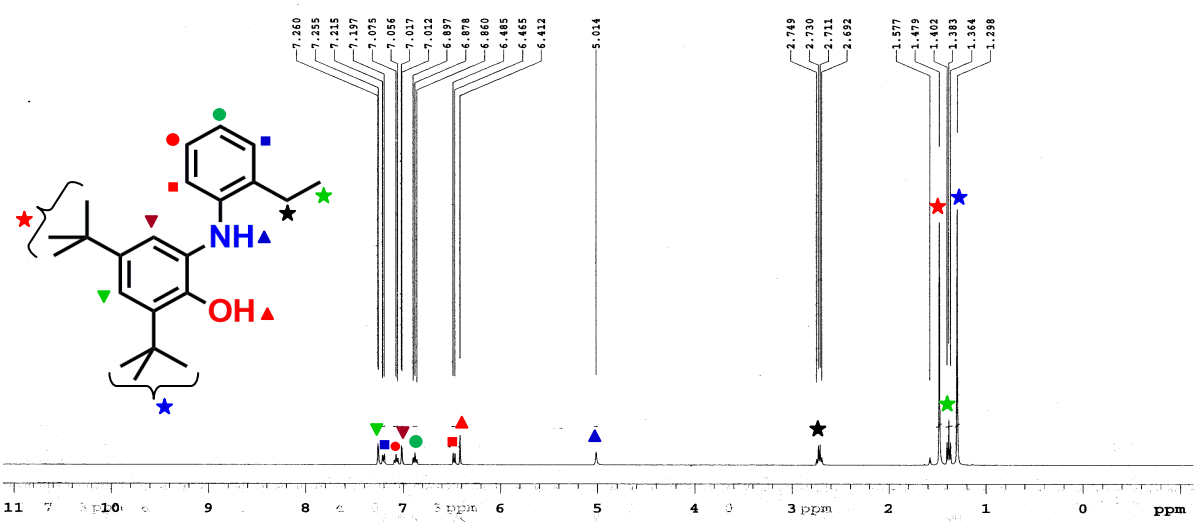

Figure 5.1: *^{1}H NMR spectrum for* $\boldsymbol{H_2L^{Et}}$.

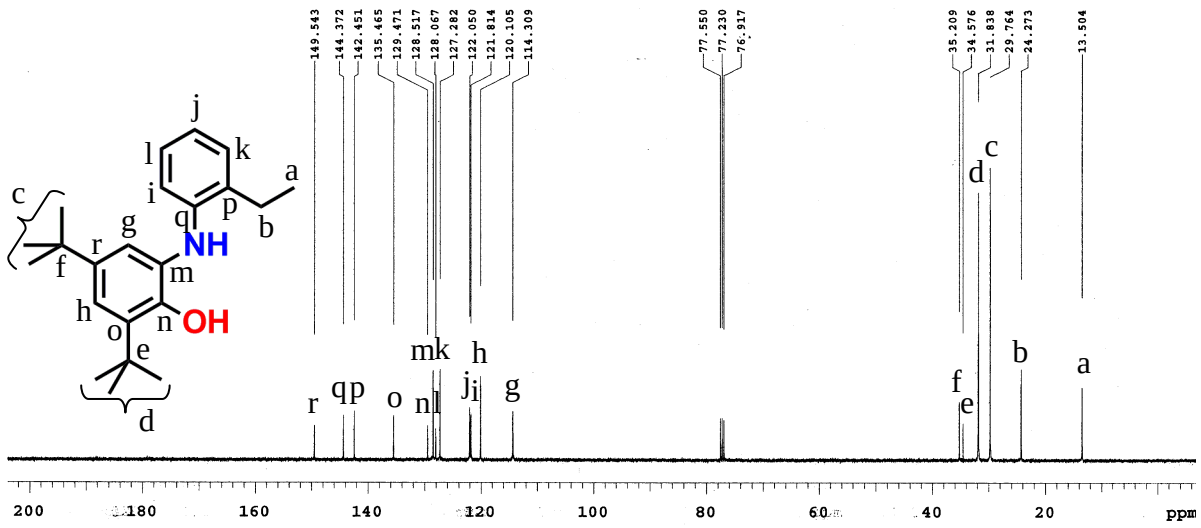

Figure 5.2: *^{13}C NMR spectrum for ligand* $\boldsymbol{H_2L^{Et}}$.

^{1}H NMR spectra of the ligands were measured in $CDCl_3$ solvent. All ligands showed peaks for six aromatic protons in the range of 6.00–8.00 ppm. Both –NH and –OH protons of all the ligands appeared in the range of 5.00–6.00 ppm, while, the *tert*–butyl protons appeared at 1.44 and 1.27 ppm. In case of $\mathbf{H_2L^{Me}}$, –Me protons appeared at 2.32 ppm. On the other hand, in ligand $\mathbf{H_2L^{Et}}$ the methylene and methyl protons were found to be appeared at 2.72 and 1.38 ppm, respectively. ^{13}C NMR spectra of the ligands revealed the characteristic 16 (X = –F, –Cl, –Br, and –I); 17 (X = –Me); and 18 (X = –Et) distinguish peaks in their expected position, respectively.

Electrospray ionization mass spectra (ESI–MS) of all the ligands were measured in acetonitrile solution in positive mode. A 100% molecular peak corresponded to the $[M + H]^+$ (M = molecular mass) was appeared for each ligand; at *m/z* = 312.58 for $\mathbf{H_2L^{Me}}$; 326.26 for $\mathbf{H_2L^{Et}}$; 316.21 for $\mathbf{H_2L^{F}}$; 332.18 for $\mathbf{H_2L^{Cl}}$; 376.12 for $\mathbf{H_2L^{Br}}$; and 424.11 for $\mathbf{H_2L^{I}}$. Isotope distribution pattern examinations of the observed mass peaks revealed the composition of $\mathbf{C_{21}H_{29}NO}$ for $\mathbf{H_2L^{Me}}$; $\mathbf{C_{22}H_{31}NO}$ for $\mathbf{H_2L^{Et}}$; $\mathbf{C_{20}H_{26}FNO}$ for $\mathbf{H_2L^{F}}$; $\mathbf{C_{20}H_{26}ClNO}$ for $\mathbf{H_2L^{Cl}}$; $\mathbf{C_{20}H_{26}BrNO}$ for $\mathbf{H_2L^{Br}}$; and $\mathbf{C_{20}H_{26}INO}$ for $\mathbf{H_2L^{I}}$, respectively.

All the ligands were potentially non–innocent and they could exist in several oxidation states as shown in **Scheme 5.5**.

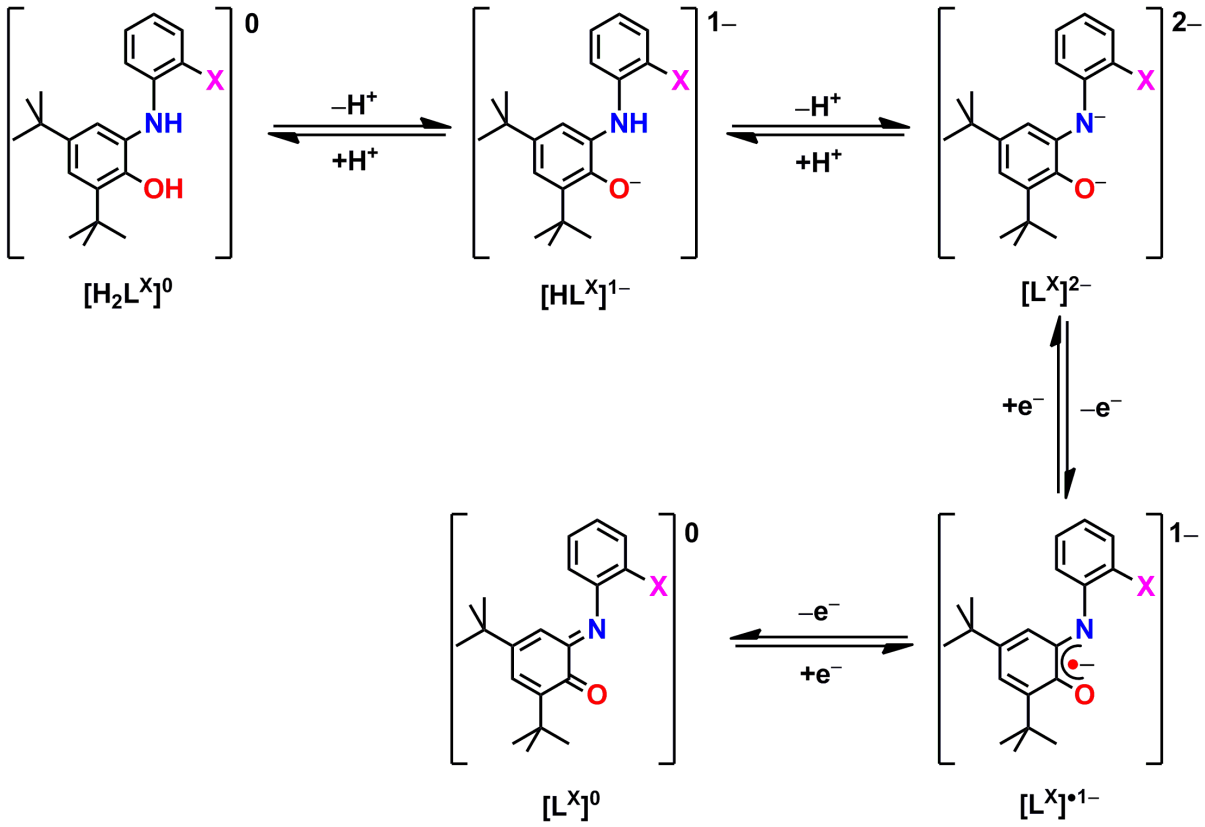

Scheme 5.5: *Different oxidation states of* H_2L^X *ligand.*

5.3: Synthesis and Characterization of Co(III) complexes with H_2L^X (X = –Me, and –Et) Ligands:

Treatment of $CoCl_2 \bullet 6H_2O$ (0.5 equivalent) to $\mathbf{H_2L^X}$ ligand (X = –Me, and –Et) in acetonitrile in the presence of triethylamine under air produced corresponding square planar cobalt complexes **19**, and **20** (general formula [$\mathbf{CoL^XL^{X\bullet}}$]), which were recrystallized from a ether–acetonitrile solvent mixture. Both complexes were reactive to chlorine species generated *in situ* in their dichloromethane solution and transformed to complexes **19a**, and **20a** having a general formula of [$\mathbf{CoL^{X\bullet}{}_2Cl}$], respectively (**Scheme 5.6**). Complex **20a** can also be synthesized using 1 equivalent of $CoCl_2 \bullet 6H_2O$ to ligand $\mathbf{H_2L^{Et}}$ in acetonitrile in the presence of triethylamine. Interestingly, use of 1 equivalent of $CoCl_2 \bullet 6H_2O$ to the ligand $\mathbf{H_2L^{Me}}$ complex **19a** could not be obtained.

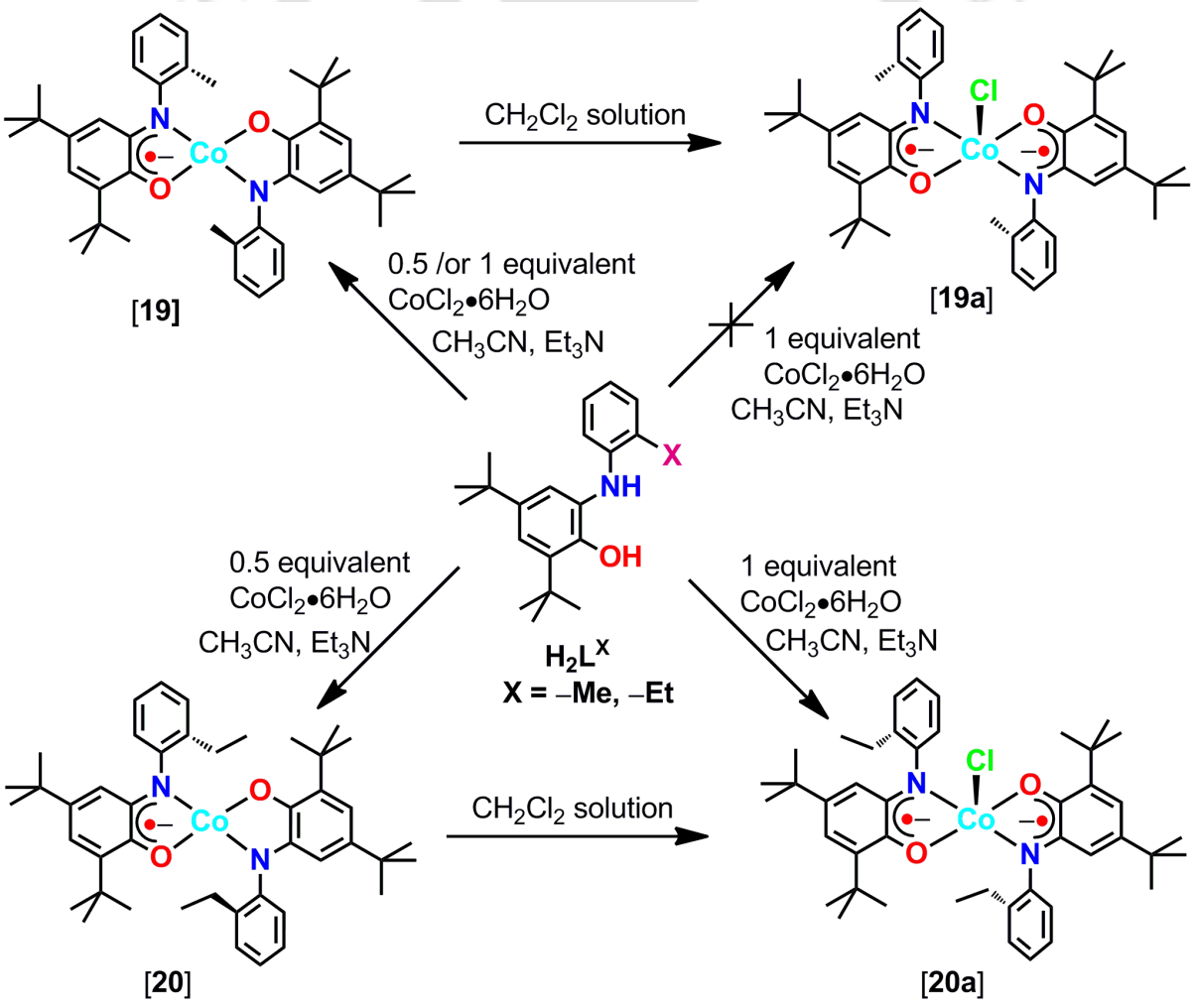

Scheme 5.6: *Schematic representation for the formation of Co(III) complexes with* $\boldsymbol{H_2L^X}$ *(X = –Me, –Et) ligands.*

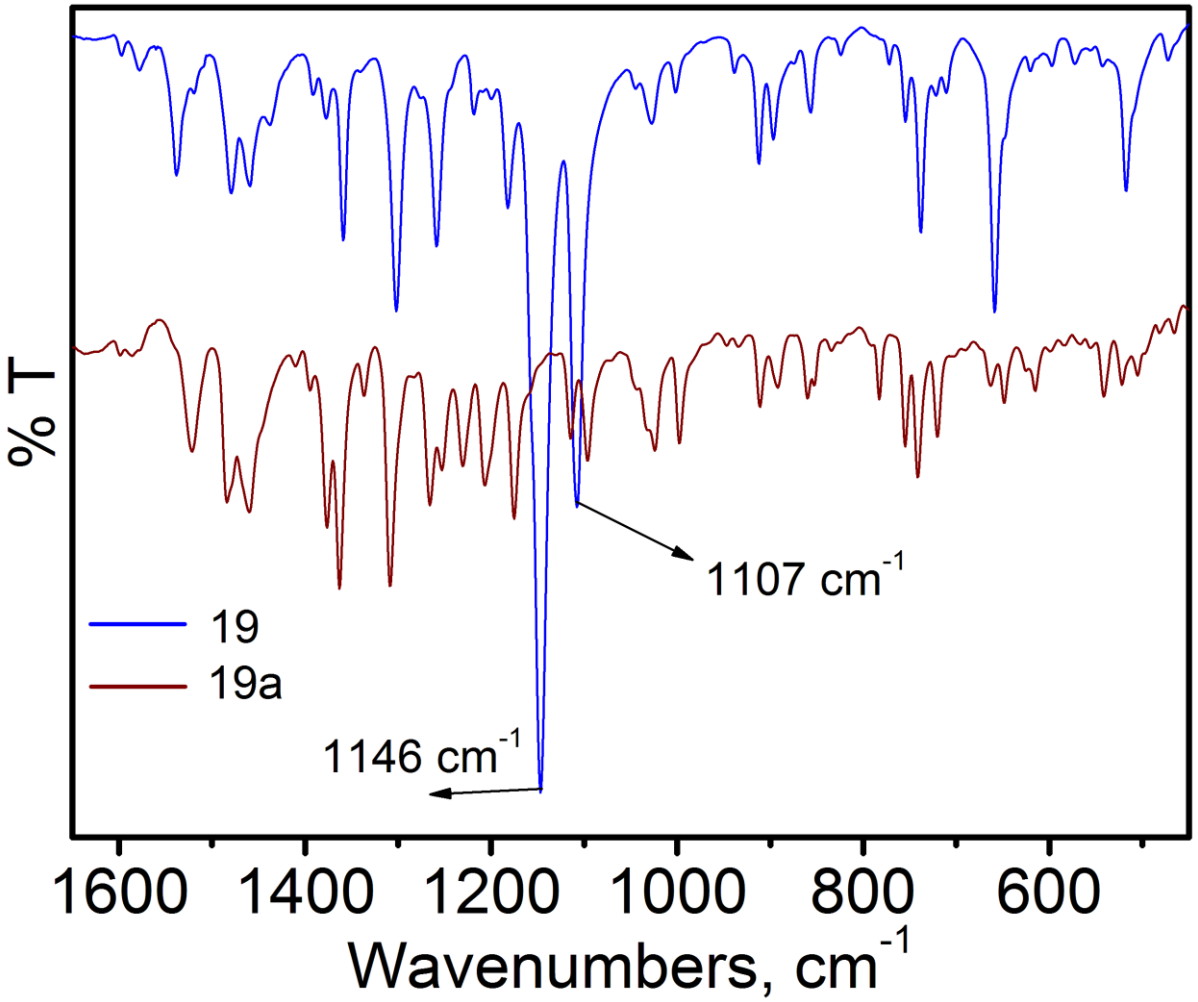

Figure 5.3: *Infrared spectral difference between square planar Co(III) complex (**19**) vs square pyramidal Co(III) complex (**19a**) is shown in 1650–450 cm^{-1} range.*

In the IR spectra of the complexes disappearances of ν(O–H), and ν(N–H) stretching frequencies were observed. The ν(C–H) stretching frequencies for the *tert*–butyl groups were found at 2956–2862 cm^{-1}. The bands at 1478, 1358 cm^{-1} for **19** and 1460, 1360 cm^{-1} for **20**, were appeared due to the bending ν(C–H) stretch. The ν(C–O) vibrational mode for **19**, and **20** appeared at ~ 1301, 1258 cm^{-1} and 1302, 1259 cm^{-1}, respectively. Two intense sharp bands at 1146, 1107 cm^{-1} for **19** and 1141, 1106 cm^{-1} for **20**, respectively, were observed and attributed to phenyl skeleton ν(C–C) stretch in a one–electron oxidized (radical–center) delocalized system. In the IR spectra of **19a**, and **20a** the band at 1363 cm^{-1} [**19a**], and 1362 cm^{-1} [**20a**] were appeared for ν(C⋯O) stretch.[12] Interestingly, the bands at ~ 1146 and ~ 1106 cm^{-1} were vanished in both complexes (**Figure 5.3**).

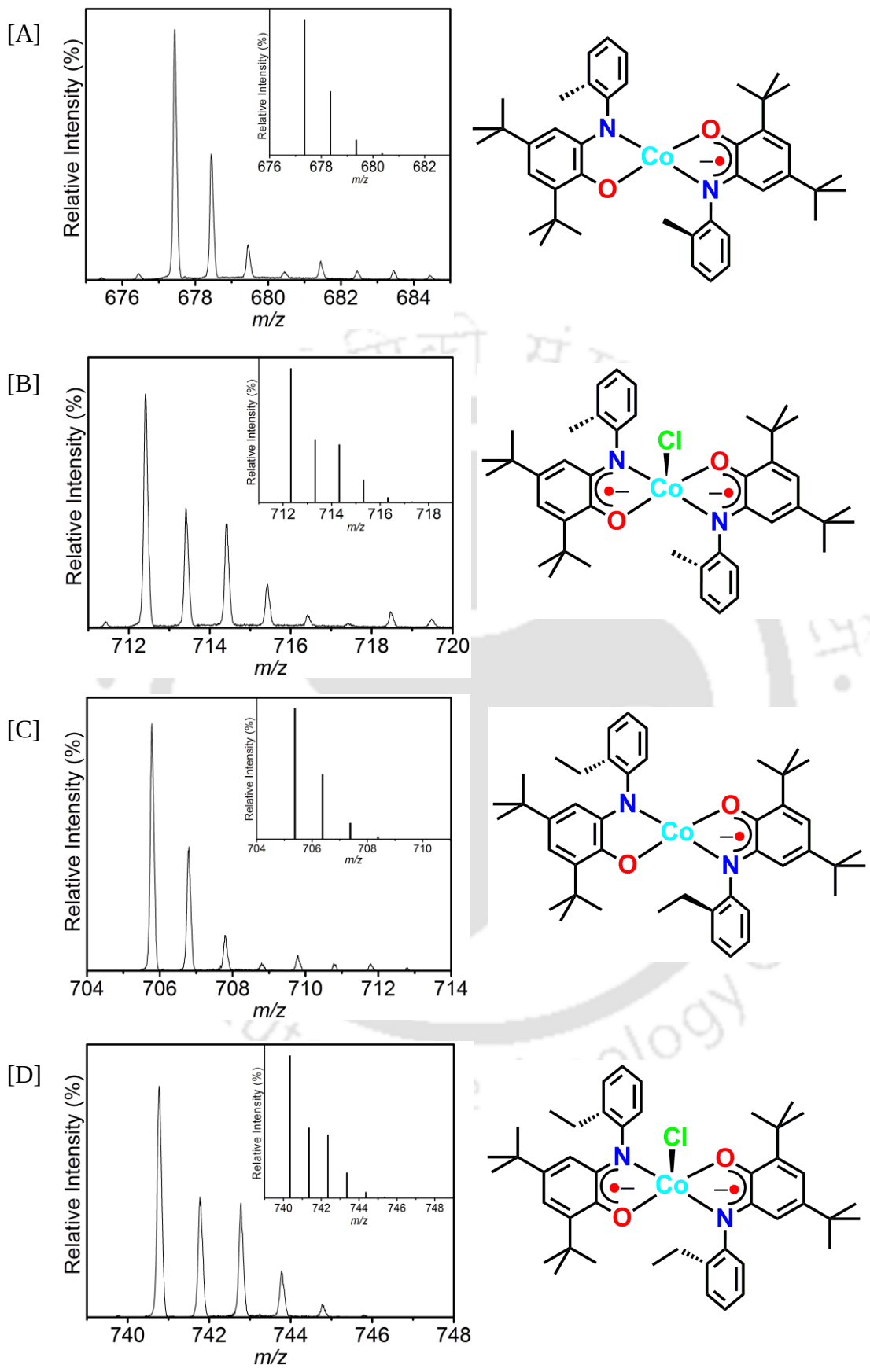

Figure 5.4: *ESI–mass spectra of [A] for **19**, [B] for **19a**, [C] for **20**, and [D] for **20a**; experimental and simulated isotope distribution pattern (inset).*

Electrospray ionization mass spectra (ESI–MS) were measured in acetonitrile in positive mode. A 100% molecular ion peak at *m/z* = 677.44 appeared in both **19** (corresponded to $[M]^+$), and **19a** (corresponded to $[M - Cl]^+$); M = molecular mass. Additionally, **19a** showed a 30% molecular ion peak at *m/z* = 712.41 (corresponded to $[M]^+$). Similarly, a 100% molecular ion peak at *m/z* = 705.78 was found for both **20** (corresponded to $[M]^+$), and **20a** (corresponded to $[M - Cl]^+$). Additionally, a 25% molecular ion at *m/z* = 740.77 (corresponded to $[M]^+$), was appeared for **20a**. Isotope distribution pattern examinations of the observed mass peaks revealed the composition of $\mathbf{C_{42}H_{54}CoN_2O_2}$, for **19**; $\mathbf{C_{42}H_{54}ClCoN_2O_2}$, for **19a**; $\mathbf{C_{44}H_{58}CoN_2O_2}$, for **20**; and $\mathbf{C_{44}H_{58}ClCoN_2O_2}$, for **20a**.

Molecular structure of **19** is shown in **Figure 5.5**. The neutral complex **19** crystallized in *P*–1 space group. Selective bond distances and bond angels are given in **Table 5.1**.

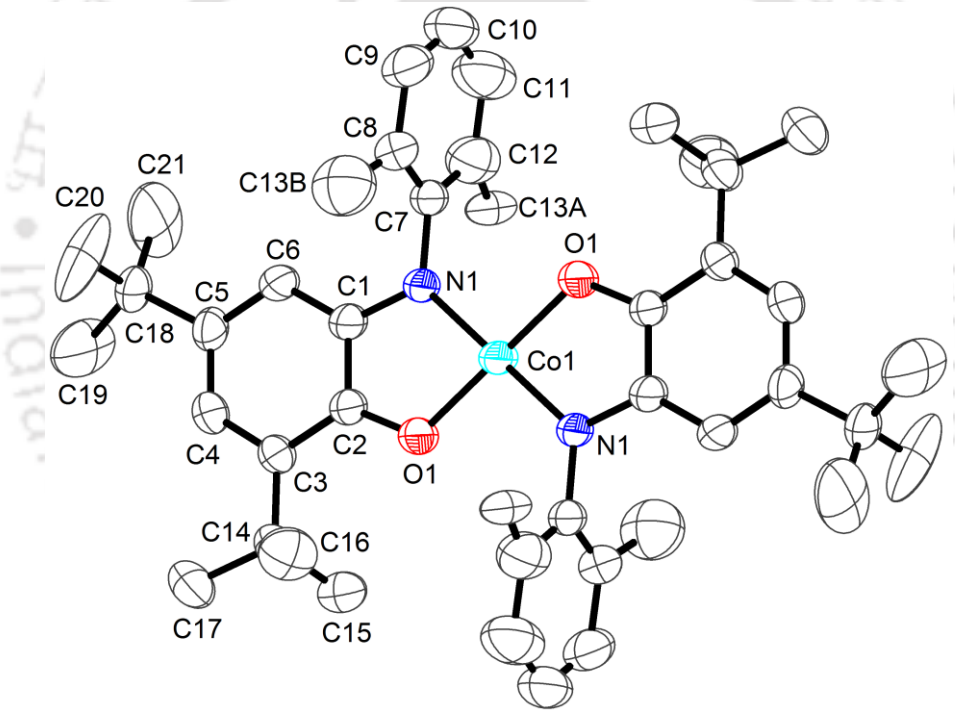

Figure 5.5: *ORTEP diagram of complex **19**. Hydrogen atoms are omitted for structural clarity.*

In the neutral complex **19**, the central Co1 atom was surrounded by two N atoms and two O atoms of the two deprotonated ligands. Two deprotonated bidentate ligands were spanned *trans* to each other around the central Co1 atom. The Co1–O1 = 1.832(4) Å and Co1–N1 = 1.836(5) Å bond distances suggest the +III oxidation state of the center metal ion.[8,11,13] This implied that coordinating ligands were not in their identical oxidation state. That means that one of the two ligands should be present in its fully reduced amidophenolate^{2-} form, and the other should be present in its one–electron oxidized iminosemiquinonate$^{\bullet 1-}$ form. Herein, it is interesting to note that the molecular structure of

complex **19** showed the identical structural parameters for both coordinating ligands. The bond distances for the amidophenolate ring were not consistence with the fully reduced form (bond distances should be 1.390±0.001 Å)[14] as well as for the one–electron oxidized form (two bond length should be 1.370±0.002 Å and four bond length should be 1.440±0.002 Å) also.[15] *i.e.* both the ligand were in between the single electron oxidized iminosemiquinonate$^{\bullet 1-}$ form and fully reduced amidophenolate^{2-} form. This was due to a complete delocalized system where the extra electron in the amidophenolate ligand was delocalized to the one–electron oxidized iminosemiquinonate$^{\bullet 1-}$ ligand.[8a,11]

Table 5.1: *Selected bond distances (Å) and bond angels (°) for complex **19**.*

Co1–N1	1.836(5)	Co1–O1	1.832(4)
C1–N1	1.371(7)	N1–C7	1.430(5)
C2–O1	1.327(6)	C1–C2	1.421(8)
C2–C3	1.410(7)	C3–C4	1.393(7)
C4–C5	1.407(8)	C5–C6	1.372(8)
C6–C1	1.403(7)		
O1–Co1–N1	85.84(19)	O1–Co1–N1^{i}	94.16(19)
O1–Co1–O1^{i}	180.000(2)	N1–Co1–N1^{i}	180.000(2)
C1–N1–Co1	113.6(4)	N1–C1–C2	111.7(5)
C1–C2–O1	115.4(5)	C2–O1–Co1	113.4(3)

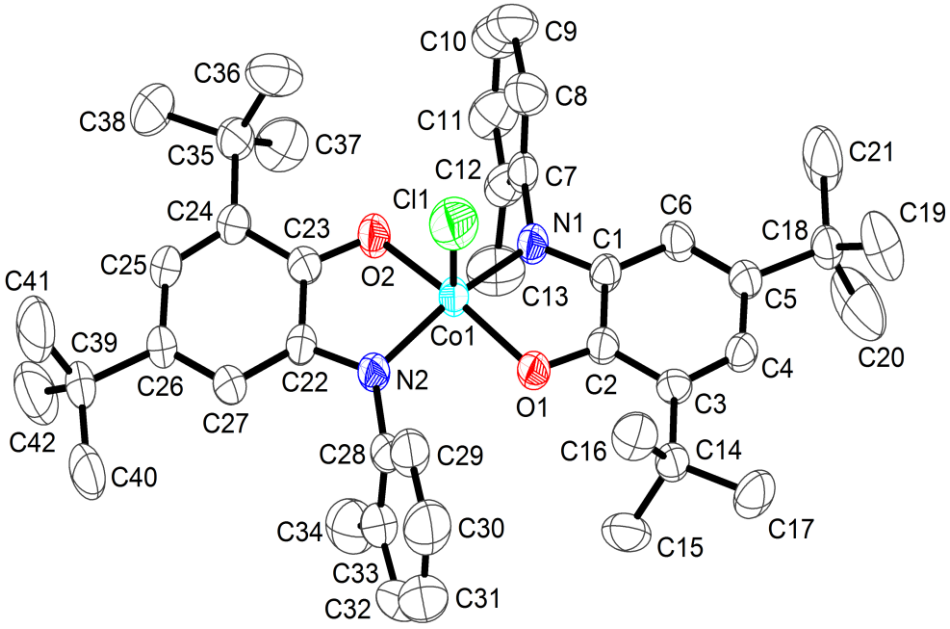

Figure 5.6a: *ORTEP diagram of complex **19a**. Hydrogen atoms were omitted for clarity.*

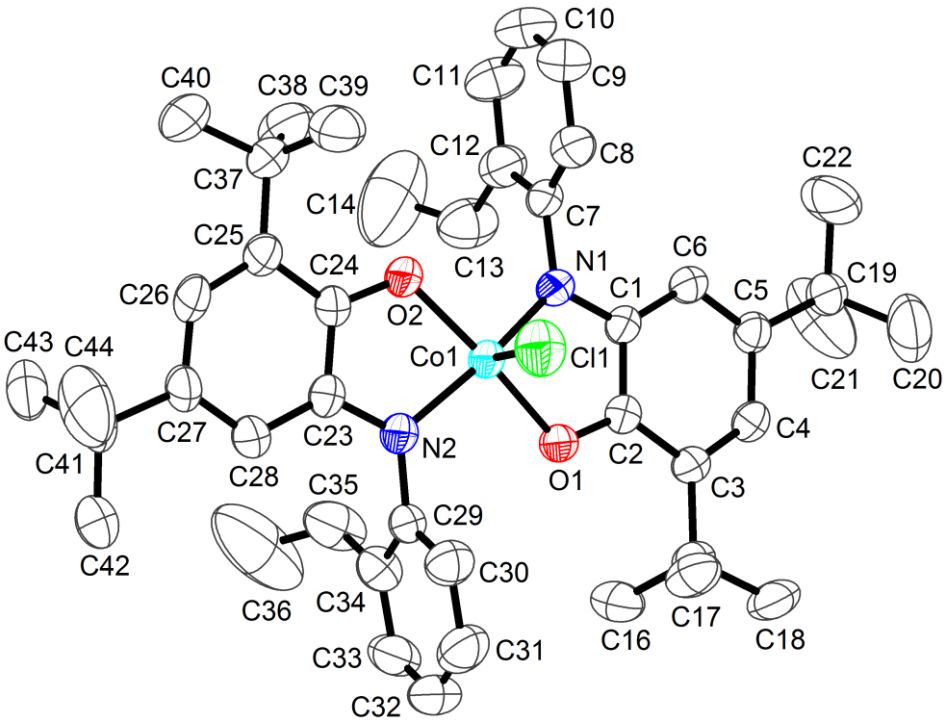

Figure 5.6b: *ORTEP diagram of complex **20a**. Hydrogen atoms were omitted for clarity.*

Molecular structure of **19a**, and **20a** are shown in **Figure 5.6a/b**. Both complexes crystallized in tetragonal system *P*43 space group. Both complexes are identical in geometry, and therefore, the molecular structure of **19a** is discussed here.

In the molecular structure of **19a**, two deprotonated ligands were connected with Co1 atom at the basal plane, while, a chloride ion attached with Co1 atom at the axial position. The five–coordinated metal ion was buried in a distorted square pyramidal geometry. The Co1–O1, Co1–O2, Co1–N1, Co1–N2, and Co1–Cl1 bond distances were 1.872(2), 1.868(2), 1.852(3), 1.858(3), and 2.2753(15) Å, respectively. These bond distances were good in agreement with the +III oxidation state of central Co atom.[7,11,16] The *tert*–butyl groups–containing phenyl rings showed an alternate short and long C–C bond distances. *i.e.* the C1–C2, C2–C3, C3–C4, C4–C5, C5–C6, and C6–C1 bond distances were 1.446(4), 1.434(4), 1.370(5), 1.437(5), 1.350(5), and 1.414(4) Å, respectively. Furthermore, C1–N1, and C2–O1 bond distances of 1.345(4), and 1.291(4) Å, respectively,[15,17] were neither their respective single bond character (C–N = 1.40 Å; C–O = 1.35 Å),[13a,15d,18] nor their respective double in character (C=N = 1.30 Å; C=O = 1.24 Å).[18d,19] Similar type bond distances were also found in another coordinating ligand (**Table 5.2**). This clearly indicated the π–radical coordination nature of the ligands. Therefore, **19a** was a neutral diradical–containing square pyramidal Co(III) complex.

Table 5.2: *Selected bond distances (Å) and angels (°) for complex* ***19a****, and* ***20a****.*

	19a	**20a**
Co1–O1	1.872(2)	1.8815(15)
Co1–O2	1.868(2)	1.8742(17)
Co1–N1	1.852(3)	1.8544(19)
Co1–N2	1.858(3)	1.859(2)
Co1–Cl1	2.2753(15)	2.2560(10)
C1–N1	1.345(4)	1.348(3)
N1–C7	1.436(4)	1.431(3)
C2–O1	1.291(4)	1.298(3)
C1–C2	1.446(4)	1.439(3)
C2–C3	1.434(4)	1.437(3)
C3–C4	1.370(5)	1.367(3)
C4–C5	1.437(5)	1.431(4)
C5–C6	1.350(5)	1.361(3)
C6–C1	1.414(4)	1.419(3)
C7–C8	1.365(6)	1.370(4)
C8–C9	1.396(6)	1.379(4)
C9–C10	1.370(7)	1.366(5)
C10–C11	1.369(8)	1.375(5)
C11–C12	1.404(6)	1.388(4)
C12–C7	1.377(6)	1.387(4)
O1–Co1–O2	167.75(14)	165.68(9)
N1–Co1–N2	158.11(17)	158.28(10)
O1–Co1–N1	83.60(10)	83.56(7)
O2–Co1–N2	83.50(11)	83.69(8)
Cl1–Co1–O1	95.85(10)	98.93(7)
Cl1–Co1–N1	101.65(13)	102.63(8)
Cl1–Co1–O2	96.40(11)	95.39(7)
Cl1–Co1–N2	100.24(12)	99.07(8)

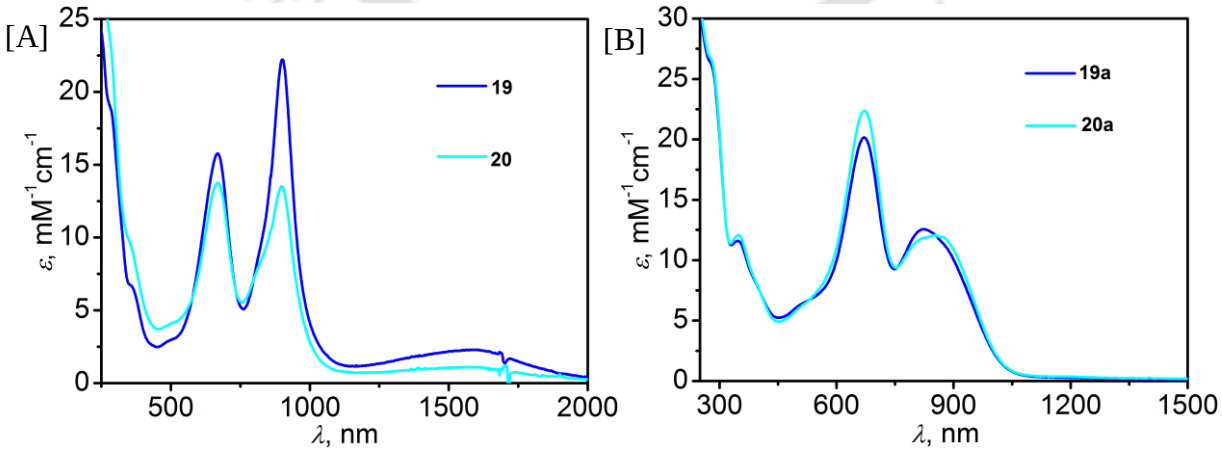

Figure 5.7: *UV–vis/NIR spectra of [A]* ***19*** *and* ***20*** *are shown in 2000–250 nm region; [B]* ***19a*** *and* ***20a*** *are shown in 1500–250 nm region.*

Electronic absorption spectra of **19** and **20** were measured in dichloromethane solvent at ambient temperature. Both complexes **19**, and **20** showed similar type of absorption spectra and the absorption bands were appeared at λ_{max} = 1600 nm; λ_{max} = 900 nm; and λ_{max} = 666 nm. The extinction coefficient of the corresponding observed bands are summarized in **Table 5.3**. The absorption maxima at 1600 nm as the ligand–to–ligand intervalence charge transfer (LLIVCT),[11,20] while, the band at 900 nm and 666 nm was arose due to the ligand–to–metal charge transfer (LMCT).[10,11] Complexes **19a**, and **20a** showed no absorption band above 1050 nm. Both complexes **19a**, and **20a** showed a broad absorption band from 868 to 820 nm and a moderately sharp absorption band 670 nm. All three absorption bands were appeared due to the charge transfer. The absorption bands at 868 nm and 670 nm were considered as ligand–to–metal charge transfers (LMCT), while the band at 820 nm was appeared due to ligand–to–ligand charge transfer (LLCT).[7,10,20*e*,*g*]

Table 5.3: *UV–vis/NIR spectral data for **19**, **19a**, **20**, and **20a**.*

Complex	λ_{max}, nm (ε, $M^{-1}cm^{-1}$)
19	1600(2800); 900(22200); 666(15800)
19a	868(11500); 820(12550); 670(20200)
20	1600(1100); 900(13500); 666(13750)
20a	868(12000); 820(11750); 670(22300)

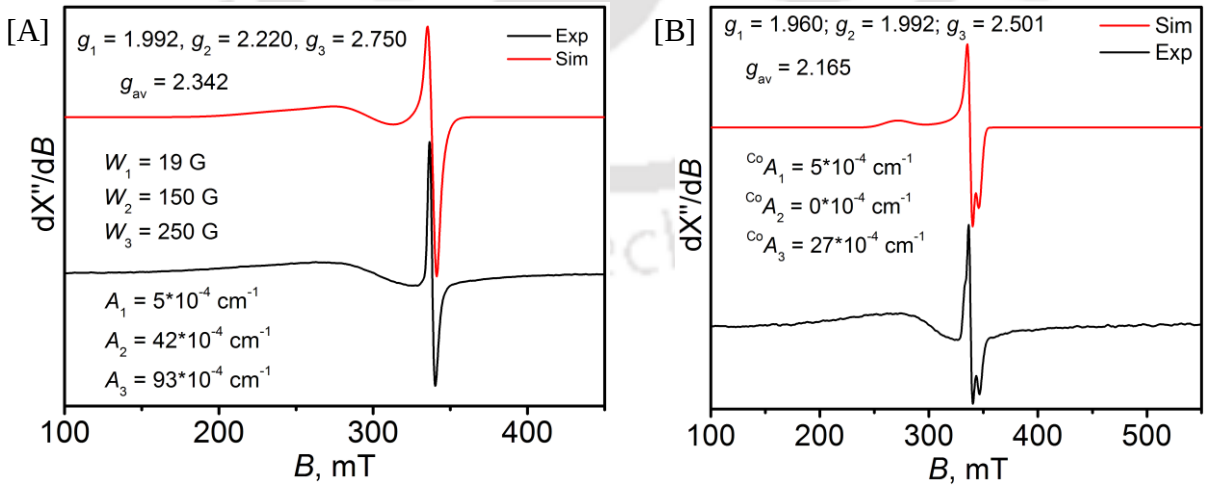

Figure 5.8: *X–band EPR spectra of complex **19**, and **20** recorded at 30 °C in CH_2Cl_2 solution. Conditions: X–band microwave frequency (GHz), 9.437 [**19**], 9.439 [**20**]; modulation frequency (kHz), 100 [**19**, and **20**]; modulation amplitude (G), 20.0 [**19**], 30.0 [**20**]; and microwave power (mW), 0.998 [**19**, and **20**].*

Figure 5.8 represents the X–band EPR spectrum of **19**, and **20**. Both cases axial–type signals were observed. The experimental EPR spectra were simulated by using the following parameters; g_1 = 1.992 [**19**], 1.960 [**20**]; g_2 = 2.220 [**19**], 1.992 [**20**]; g_3 = 2.750 [**19**], 2.501 [**20**]; g_{av} = 2.342 [**19**], 2.165 [**20**]. $^{Co}(A_1, A_2, A_3) = (5, 42, 93) \times 10^{-4}$ cm^{-1} for **19**, and $^{Co}(A_1, A_2, A_3) = (5, 0, 27) \times 10^{-4}$ cm^{-1} for **20**. The resulted (g_1, g_2, g_3) and g_{av} (2.342 [**19**]; 2.165 [**20**]) values for both complexes were highly anisotropic in nature and indicated that the singly occupied molecular orbital (SOMO) has predominantly metal character (g_{av} > 2.00 due to spin–orbit coupling). This suggested that the unpaired electron resides on the metal–centered *d* orbital. In a square planar system, Co(III) ion possesses an S_{Co}= 1 local spin state.[21] Strong antiferromagnetic interaction between π–radical and the metal center provided an *S* = ½ ground state in which the resultant spin resided on metal–centered *d* orbital.[10,11]

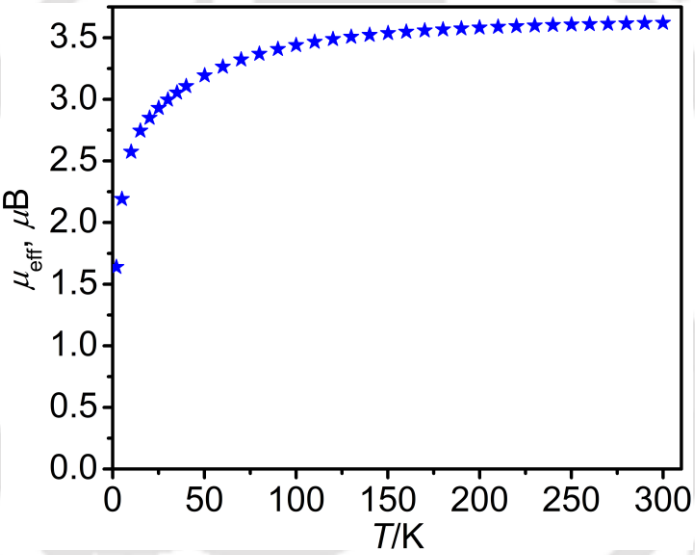

Figure 5.9: μ_{eff} *vs T* plot of **19**.

Both complexes **19**, and **20** were monoradical–containing square planar geometry and their spectral data suggested their identical electronic properties. Therefore, variable temperature magnetic moment of complex **19** was measured and discuss here. Variable temperature magnetic moment measurement of the solid sample of **19** showed μ_{eff} = 1.70 μ_B at 5 K which was indicative of an *S* = ½ ground state (**Figure 5.9**). The value increased with increased in temperature and at room temperature (300 K), μ_{eff} = 3.60 μ_B. This increased in magnetic moment with temperature indicated the increase in thermal population of unpaired electron in the thermally excited state *S* = $^3/_2$.[10,11]

5.4: Synthesis and Characterization of Co(III) complexes with H_2L^X (X = –F, –Cl, –Br, and –I) Ligand:

Complex **21**, **22**, **23**, and **24** were synthesized from the ligand $\mathbf{H_2L^X}$ using 0.5 equivalent of $CoCl_2 \bullet 6H_2O$ in acetonitrile in the presence of triethylamine. Complex **21**, **22**, and **23** were reactive in dichloromethane solution and underwent to the complex **21a**, **22a**, and **23a** (**Scheme 5.7**). Complex **21a**, **22a**, and **23a** can be synthesized in good yield by the equimolar reaction between $\mathbf{H_2L^X}$ and $CoCl_2 \bullet 6H_2O$ in acetonitrile under air in the presence of triethylamine.

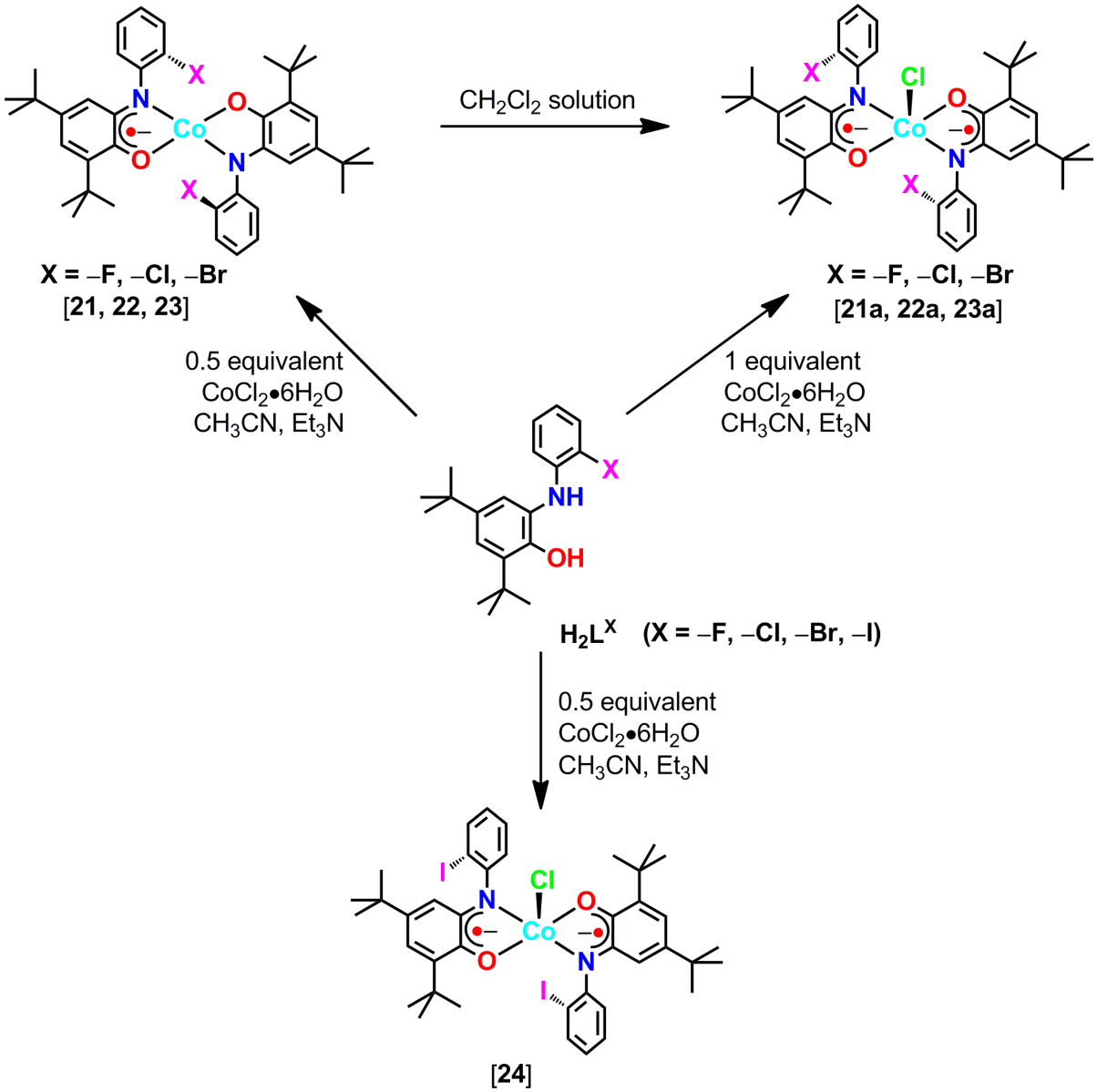

Scheme 5.7: *Schematic representation of the formation of Co(III) complexes with* $\boldsymbol{H_2L^X}$ *(X = –F, –Cl, –Br, and –I) ligands.*

In the IR spectra of **21**, **21a**, **22**, **22a**, **23**, **23a**, and **24**, no band correspond to ν(O–H), and ν(N–H) stretches were appeared, additionally, the present of *tert*–butyl groups ν(C–H) stretching frequencies in the range of 2957–2866 cm^{-1} indicated a deprtonated ligand coordinated with metal ion. IR spectra of complexes **21**, **22**, and **23** were almost similar, on the other hand, IR spectra of **21a**, **22a**, **23a**, and **24** were almost identical but quite different than those of **21**, **22**, **23**, respectively. In the IR spectra of **21**, **22**, and **23**, the band at ~ 1583 cm^{-1} was considered as ν(C=N) stretch, while, the band at 1465–1454 cm^{-1} and 1360–1358 cm^{-1} were appeared due to the bending mode of ν(C–H) stretch. The ν(C⋯O) band was arose at 1309–1305 cm^{-1}, while the ν(C–O) stretch was appeared at 1247–1259 cm^{-1}. Interestingly, all three complexes (**21**, **22**, **23**) showed two sharp bands at 1144–1103 cm^{-1}.[22]

In the IR spectra of **21a**, **22a**, **23a**, and **24**, the band at ~ 1585 cm^{-1} was appeared due to ν(C=N) stretch. The ν(C⋯O) band was appeared at the region of 1380–1360 cm^{-1}. Notably, two sharp bands those were arisen at 1144–1103 cm^{-1} in complexes **21**, **22**, and **23**, were absent in the IR spectra of **21a**, **22a**, and **23a** indicated the change in geometrical nature.

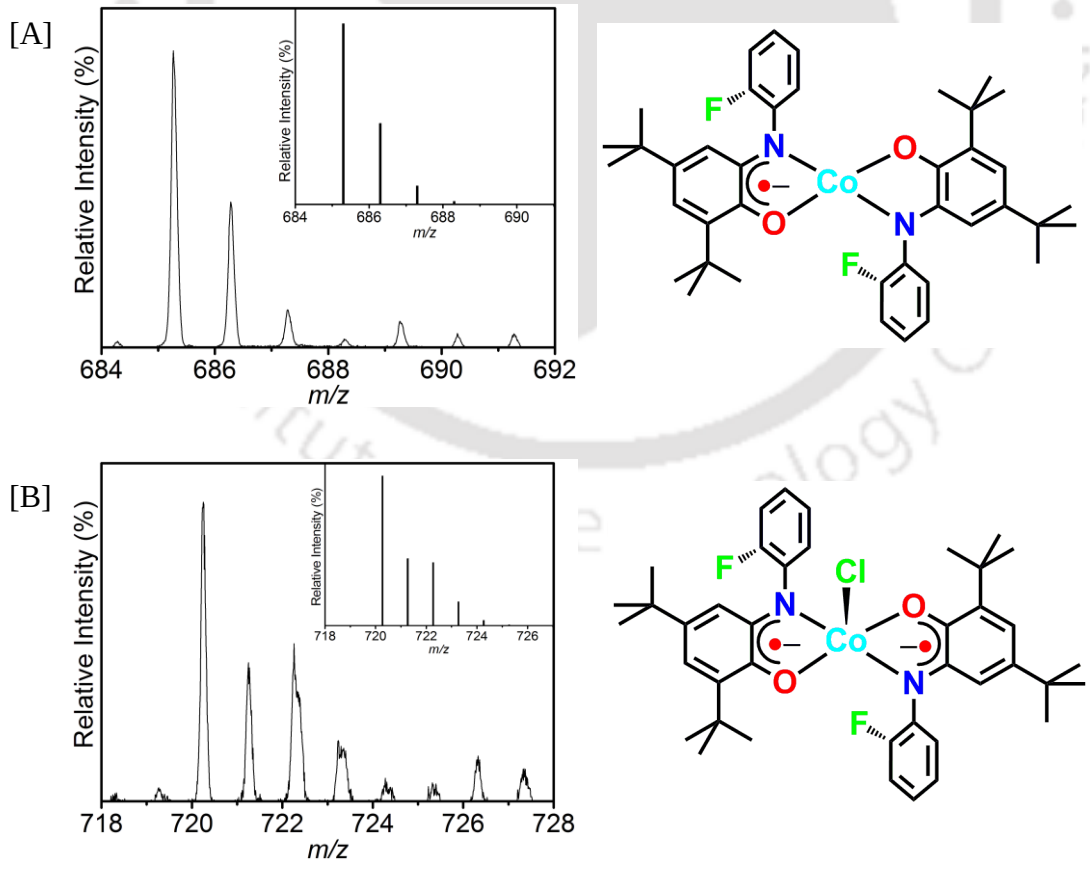

Figure 5.10: *ESI–mass spectra [A] for **20**, and [B] for **20a**; experimental and simulated isotope distribution pattern (inset).*

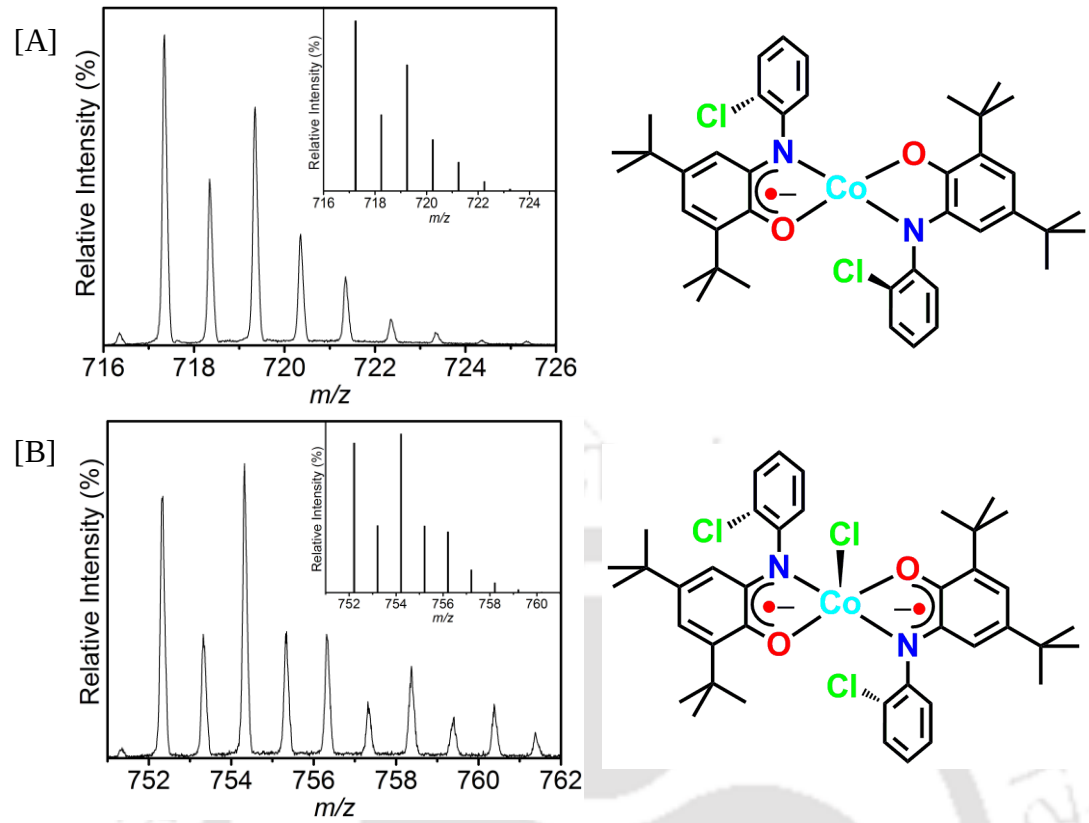

Figure 5.11: *ESI–mass spectra [A] for **21**, and [B] for **21a**; experimental and simulated isotope distribution pattern (inset).*

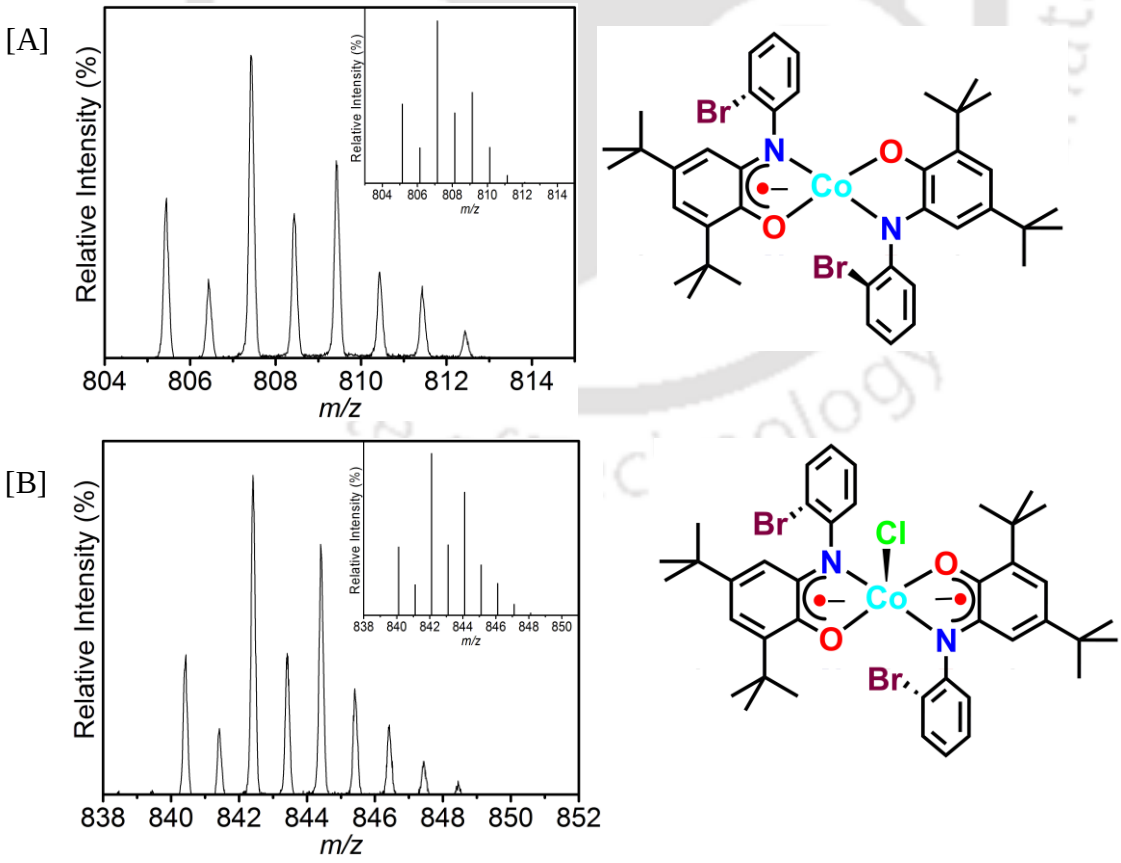

Figure 5.12: *ESI–mass spectra [A] for **22**, and [B] for **22a**; experimental and simulated isotope distribution pattern (inset).*

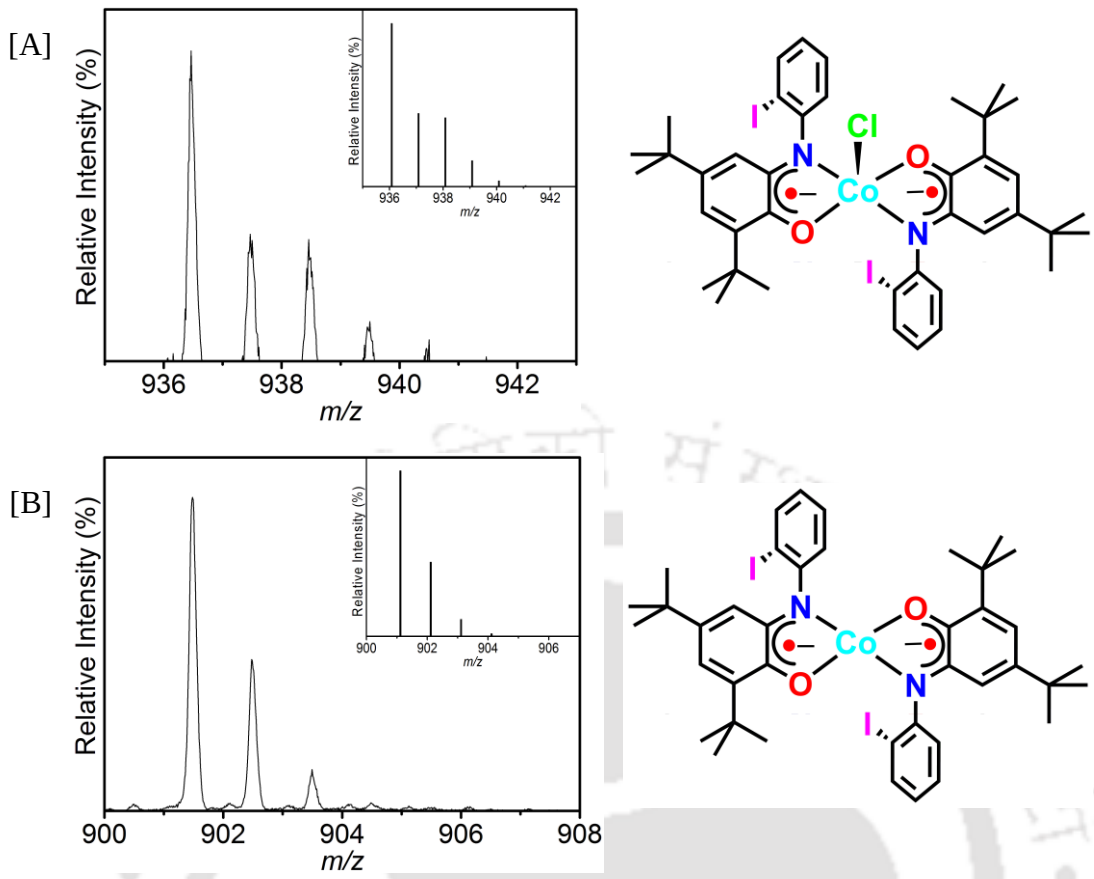

Figure 5.13: *ESI–mass spectra of* ***23*** *[A] corresponds to* $[M]^+$*, and [B] corresponds to* $[M - Cl]^+$*; M = molecular mass; experimental and simulated isotope distribution pattern (inset).*

Electrospray ionization mass spectra (+ve mode) of the complexes were measured in acetonitrile solution. A 100% molecular ion peak at *m/z* = 685.27 for **21**, and **21a** (**Figure 5.10A**); 717.52 for **22**, and **22a** (**Figure 5.11A**); 807.42 for **23**, and **23a** (**Figure 5.12A**); 901.48 for **24** (**Figure 5.13B**) were observed. Additionally, **21a** showed a 10% molecular ion peak at *m/z* = 720.26 (**Figure 5.10B**); **22a** showed a 30% molecular ion peak at *m/z* = 754.32 (**Figure 5.11B**); **23a** showed a 30% molecular ion peak at *m/z* = 842.41 (**Figure 5.12B**); and **24** showed a 10% molecular ion peak at *m/z* = 936.46 (**Figure 5.13A**), respectively. Isotope distribution pattern examination of the observed mass peaks revealed the composition $\mathbf{C_{40}H_{48}CoF_2N_2O_2}$ for **21**, $\mathbf{C_{40}H_{48}ClCoF_2N_2O_2}$ for **21a**, $\mathbf{C_{40}H_{48}Cl_2CoN_2O_2}$ for **22**; $\mathbf{C_{40}H_{48}Cl_3CoN_2O_2}$ for **22a**; $\mathbf{C_{40}H_{48}Br_2CoN_2O_2}$ for **23**; $C_{40}H_{48}Br_2ClCoN_2O_2$ for **23a**; and $\mathbf{C_{40}H_{48}ClCoI_2N_2O_2}$ for **24**.

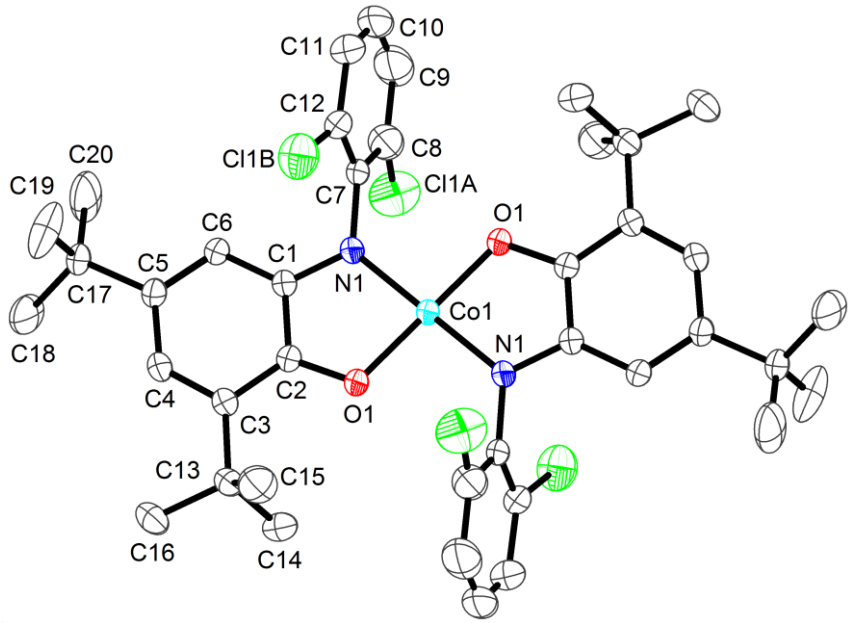

Figure 5.14: *ORTEP view of **22** was drawn at 30% thermal probability level. H atoms were omitted for clarity.*

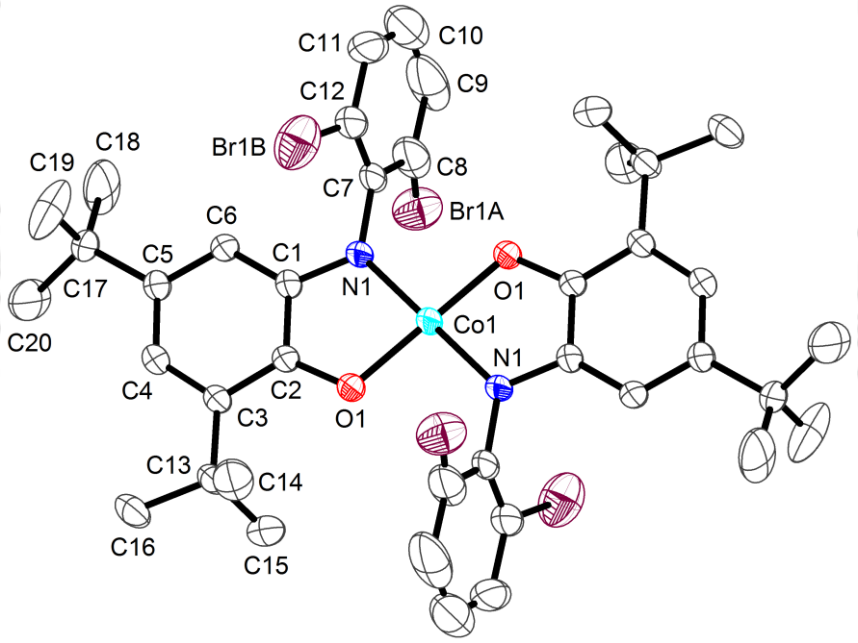

Figure 5.15: *ORTEP view of **23** was drawn at 30% thermal probability level. H atoms were omitted for clarity.*

Complex **22** and **23** were crystallized in triclinic system, in *P*–1 space group, where the central cobalt atom was lounged at the inversion center of the complexes. ORTEP diagrams of complexes **22** and **23** are shown in **Figure 5.14**, and **Figure 5.15**, respectively. Selected bond distances and bond angels are listed in **Table 5.4**. The geometry around the four–coordinated metal center was perfect square planar with two five–membered chelate rings made by coordinated amidophenolate ligands and Co atom. No solvent molecule was

present at the axial position. Substituent as well as the donor atoms in both complexes were oriented *trans* to each other. The Co1–O1 and Co1–N1 bond distances were 1.828(2)[**22**]; 1.829(3)[**23**] Å and 1.832(3)[**22**]; 1.830(4)[**23**] Å, respectively, and were good in agreement with the +III oxidation state of central Co atom.[7,11,16] This implied that the two coordinating ligands must be in different oxidation states in order to maintain the neutrality of the complex. The C2–O1 bond distance was 1.327(4) [**22**]; 1.330(5) [**23**] Å; and C1–N1 bond distance was 1.369(4) [**22**]; 1.369(6) [**23**] Å, respectively. The mentioned C2–O1 and C1–N1 bond distances were slightly shorter than their corresponding single bond distance in amidophenolate form (C–O, 1.35–1.36 Å; C–N, 1.39–1.40 Å),[13*a*,15*d*,18] and also slightly longer from their respective partial double bond length in iminosemiquinonate form (C–O, 1.30 Å; C–N, 1.35 Å).[15,17] The C–C bond distances in the *tert*–butyl containing phenyl rings in both complexes were not fall within the expected 1.39±0.1 Å range as found for fully reduced phenyl ring system. An alternating short and long C–C bond distances {e.g. C1–C2 = 1.417(4) [**22**], 1.411(7) [**23**]; C2–C3 = 1.406(4) [**22**], 1.410(6) [**23**]; C3–C4 = 1.387(4) [**22**], 1.385(7) [**23**]; C4–C5 = 1.413(4) [**22**], 1.406(7) [**23**]; C5–C6 = 1.365(4) [**22**], 1.375(7) [**23**]; C6–C1 = 1.399(4) [**22**], 1.396(7) [**23**]} were observed. These bond distances were quite different from the observed O,N–coordinated iminosemiquinonate systems. So, from the crystal structure, it was concluded that coordinating two ligands were neither in the one–electron oxidized ($ISQ^{\bullet 1-}$) form, nor in the fully reduced amidophenolate ($[AP]^{2-}$) form. Here, one ligand was present in fully reduced ($[AP]^{2-}$) form and other one should be in one–electron oxidized iminosemiquinonate ($ISQ^{\bullet 1-}$) form but they were quite delocalized over both sides.

Table 5.4: *Selected bond distances (Å) for complex **22** and **23**.*

	22	**23**
Co1–O1	1.828(2)	1.828(3)
Co1–N1	1.832(3)	1.837(3)
O1–C2	1.327(4)	1.330(6)
N1–C1	1.369(4)	1.371(6)
N1–C7	1.437(4)	1.418(5)
C1–C2	1.417(4)	1.411(7)
C2–C3	1.406(4)	1.410(6)
C3–C4	1.387(4)	1.385(7)
C4–C5	1.413(4)	1.406(7)
C5–C6	1.365(4)	1.375(7)
C6–C1	1.399(4)	1.396(7)
C7–C8	1.361(6)	1.3900
C8–C9	1.399(7)	1.3900
C9–C10	1.359(9)	1.3900

C10–C11	1.323(9)	1.3900
C11–C12	1.381(6)	1.3900
C12–C7	1.411(7)	1.3900
C12–X1B*	1.561(6)	1.727(6)
C8–X1A*	1.412(6)	1.299(6)
O1–Co1–N1	85.33(10)	85.67(16)
O1–Co1–N1^{i}	94.67(10)	94.33(16)
C1–N1–Co1	114.3(2)	113.6(3)
N1–C1–C2	111.3(3)	111.7(4)
C1–C2–O1	115.2(3)	115.5(4)
C2–O1–Co1	113.9(2)	113.5(3)

*X = –Cl for **22**, and X = –Br for **23**.

All three complexes **22a**, **23a**, and **24** have very similar structure where a central cobalt atom was five–coordinate in a square pyramidal geometry. Complex **22a**, and **23a** crystallized in tetragonal system, space group *P*43, while **24** crystallized in orthorhombic system, space group *P*ca2$_1$. **Figure 5.16**, **Figure 5.17**, and **Figure 5.18** represent the ORTEP diagrams for complexes **22a**, **23a**, and **24**, respectively. Selected bond distances and bond angels for **22a**, **23a**, and **24** are summarized in **Table 5.5**. Here, the X–ray crystal structure of complex **24** is described.

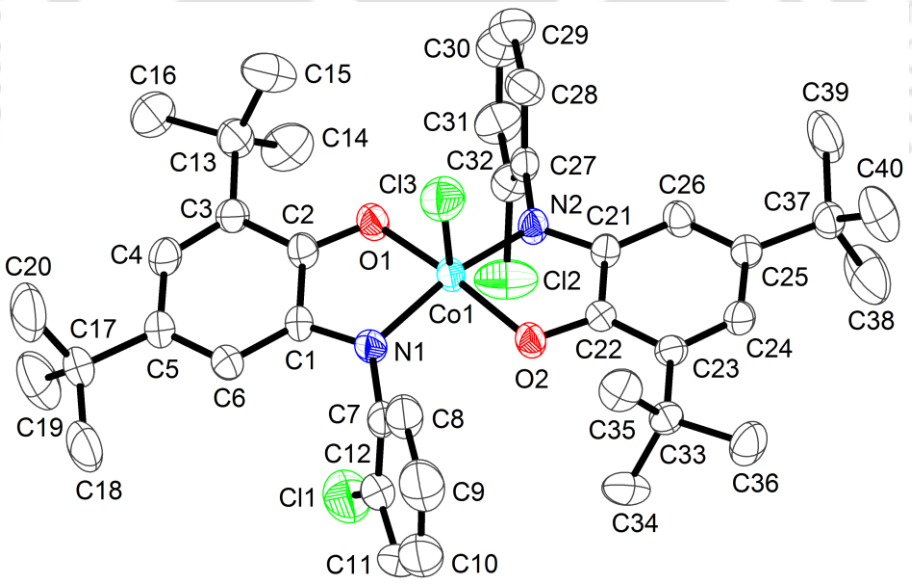

Figure 5.16: *Molecular structure of **22a** was drawn at 50% thermal probability level. H atoms were omitted for structural clarity.*

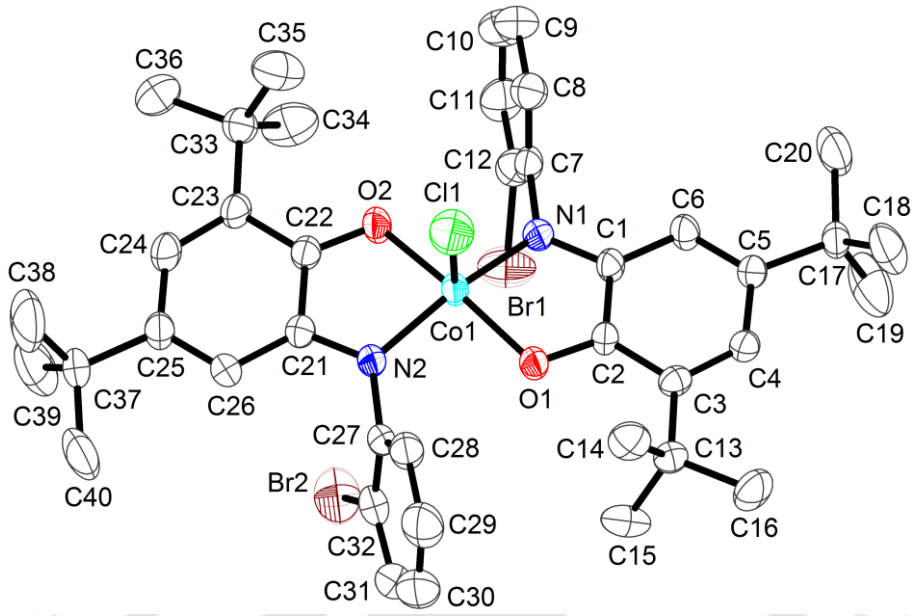

Figure 5.17: *Molecular structure of **23a** was drawn at 50% thermal probability level. H atoms were omitted for structural clarity.*

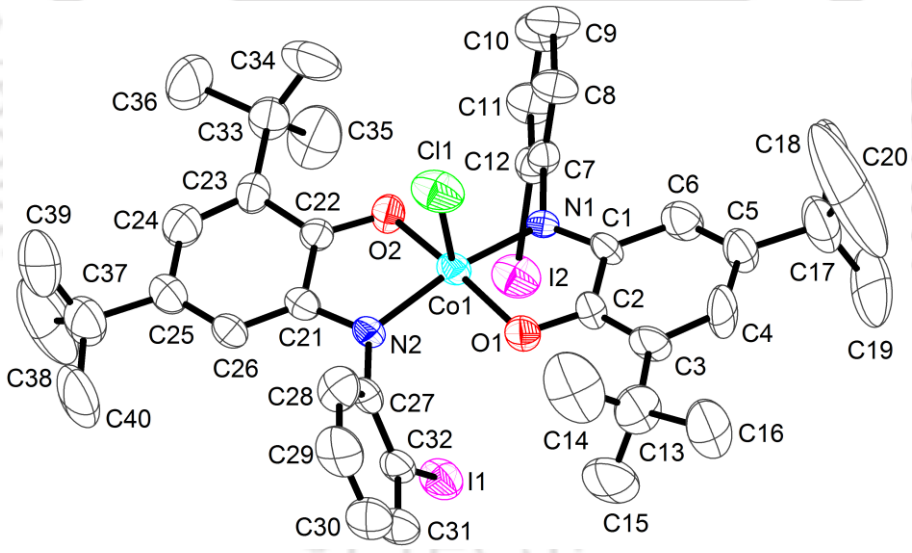

Figure 5.18: *Molecular structure of **24** was drawn at 50% thermal probability level. H atoms were omitted for structural clarity.*

In the neutral complex, central Co1 atom was surrounded by two deprotonated amidophenolate ligands at the basal plane and a chloride ion at the axial position. Two –iodo groups were situated *cis* to each other, while, *trans* to the axially bound chlorine atom. The central cobalt atom was slightly above from the basal plane and situated towards the apical chloride atom at 0.20 Å. This strongly suggested a distorted square pyramidal geometry

around the metal center. The *tert*–butyl groups–containing phenyl rings were comprised of four long and two short bond distances (**Table 5.5**) and ensured a quinoid–type distortion. Additionally, the C1–N1, C21–N2, C2–O1, and C22–O2 bond distances were 1.347(6), 1.353(7), 1.266(6), and 1.306(6) Å, those were of their partially double bond in nature. These types of irregular bond distances were common in one–electron oxidized form of the coordinating ligands *i.e.* iminosemiquinonate$^{\bullet 1-}$ form. The average Co–N and Co–O bond distances were of 1.870 Å and 1.862 Å, and were in accord with the +III oxidation state of the cobalt center. Thus, the complex was a diradical–containing neutral square pyramidal Co(III).

Table 5.5: *Selected bond distances (Å) and angels (°) for complexes **22a**, **23a**, and **24**.*

	22a	**23a**	**24**
Co1–O1	1.874(2)	1.873(3)	1.858(3)
Co1–O2	1.878(2)	1.872(3)	1.866(3)
Co1–N1	1.862(3)	1.860(3)	1.858(4)
Co1–N2	1.855(3)	1.863(3)	1.873(4)
Co1–Cl	2.2562(13)	2.2557(15)	2.2448(11)
O1–C2	1.294(4)	1.295(4)	1.266(6)
N1–C1	1.352(4)	1.348(5)	1.347(6)
N1–C7	1.427(4)	1.428(5)	1.461(7)
C1–C2	1.430(5)	1.431(5)	1.420(7)
C2–C3	1.433(5)	1.433(5)	1.414(6)
C3–C4	1.365(5)	1.371(5)	1.392(7)
C4–C5	1.430(5)	1.433(5)	1.466(8)
C5–C6	1.372(5)	1.364(5)	1.341(7)
C6–C1	1.410(5)	1.418(5)	1.416(7)
C7–C8	1.393(6)	1.376(6)	1.356(7)
C8–C9	1.379(6)	1.378(7)	1.379(8)
C9–C10	1.349(8)	1.375(8)	1.423(8)
C10–C11	1.381(9)	1.378(8)	1.389(8)
C11–C12	1.395(6)	1.380(7)	1.358(7)
C12–C7	1.388(6)	1.375(6)	1.395(7)
C12–X1*	1.730(5)	1.895(5)	2.125(5)
O1–Co1–O2	167.94(12)	167.55(14)	170.33(13)
N1–Co1–N2	158.57(15)	158.88(17)	164.84(13)
O1–Co1–N1	83.40(11)	83.17(13)	82.75(17)
O2–Co1–N2	83.23(10)	83.15(13)	84.45(18)
Cl–Co1–O1	96.25(9)	96.26(10)	94.84(12)
Cl–Co1–N1	100.42(11)	101.01(13)	97.23(13)
Cl–Co1–O2	95.81(9)	96.19(11)	94.79(12)
Cl–Co1–N2	101.00(11)	100.11(12)	97.90(13)

*X = –Cl, –Br, and –I for **22a**, **23a**, and **24**, respectively.

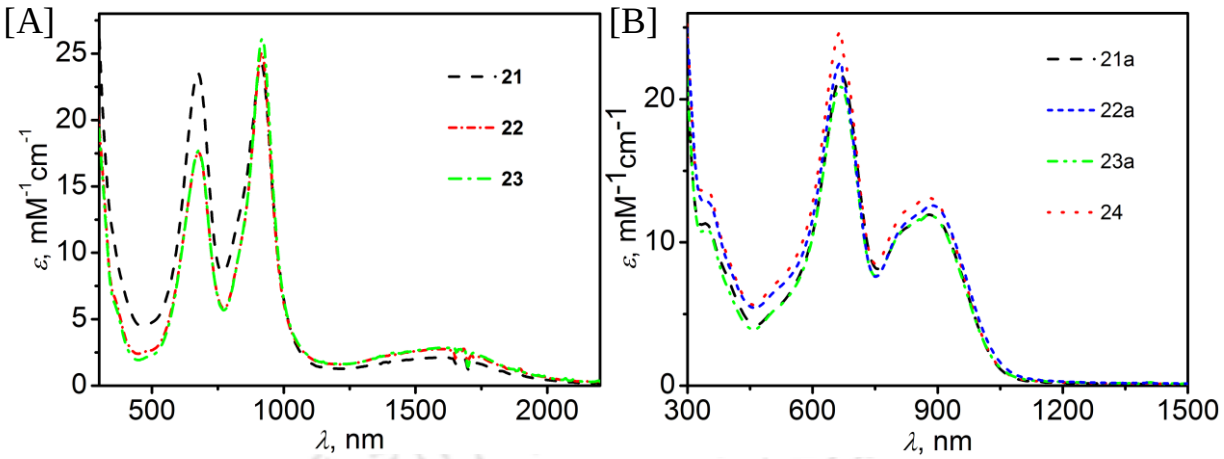

Figure 5.19: *UV–vis/NIR spectra of **21**, **22**, and **23** are shown in [A]; **21a**, **22a**, **23a**, and **24** are shown in [B].*

Electronic absorption spectra for all the complexes were measured in dichloromethane at room temperature. **Figure 5.19[A]** represents the UV–vis/NIR spectra of **21**, **22**, and **23**, while, the UV–vis spectra of other complexes are shown in **Figure 5.19[B]**. Complexes **21**, **22**, and **23** showed a broad absorption band at λ_{max} = 1600 nm (ε = 2150 [**21**]; 2800 [**22**, and **23**] $M^{-1}cm^{-1}$); and two sharp absorption bands at λ_{max} = 920 nm (ε = 24200 [**21**]; 25100 [**22**]; 26100 [**23**] $M^{-1}cm^{-1}$); and λ_{max} = 675 nm (ε = 23400 [**21**], 17700 [**22** & **23**] $M^{-1}cm^{-1}$). The first two are for the ligand–to–ligand intervalence charge transfer (LLIVCT),[11,20] while the band at 675 nm was appeared due to the ligand–to–metal charge transfers (LMCT).[10,11]

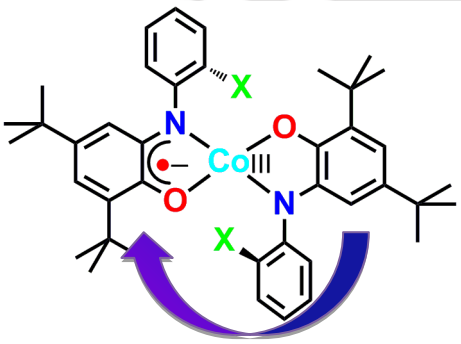

Thus, the d^6 Co(III) square planar complexes **21**, **22** and **23** belong to Class III mixed–valence in nature[11,23] where the charge transfer occurs from the electron rich amidophenolate^{2-} unit to electron deficient iminosemiqunonate$^{\bullet 1-}$ unit in the complexes. Delocalized nature of the coordinated ligands was reasonably justified by X–ray crystal structure too.

On the other hand, complexes **21a**, **22a**, **23a**, and **24** showed an intense broad absorption maxima at λ_{max} = 825–885 nm and an intense sharp absorption maxima at λ_{max} = 666 nm. Extinction coefficient values are summarized in **Table 5.6**. All the absorption bands were appeared due to the charge transfer. The absorption maxima at 885 nm and 666 nm were considered as ligand–to–metal charge transfer (LMCT) band,[10,11] while, the band at 825 nm was appeared due to ligand–to–ligand charge transfer (LLCT).[7,10,20e,g]

Table 5.6: *Electronic absorption data of **21**, **21a**, **22**, **22a**, **23**, **23a**, and **24**:*

Complex	λ_{max}, nm (ε, $M^{-1}cm^{-1}$)
21	1600(2150); 920(2400); 675(23400)
21a	885(11800); 825(11100); 666(21600)
22	1600(2800); 920(25100); 675(17700)
22a	885(12550); 825(11450); 666(22500)
23	1600(2800); 920(26100); 675(17700)
23a	885(11800); 825(11100); 666(20750)
24	885(13100); 825(12300); 666(24650)

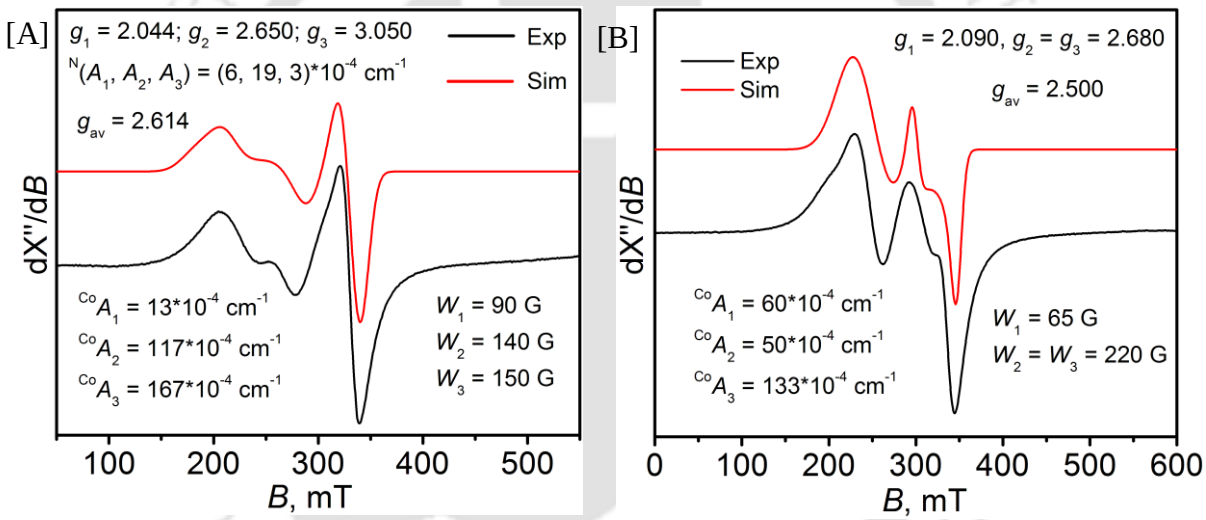

Figure 5.20: *X–band EPR spectra of complex **22** [A], and **23** [B] recorded at 30 °C in CH_2Cl_2 solution. Conditions: X–band microwave frequency (GHz), 9.449 [**22**], 9.449 [**23**]; modulation frequency (kHz), 100 [**22**, and **23**]; modulation amplitude (G), 100.0 [**22**], 20.0 [**22**]; and microwave power (mW), 0.998 [**21**, and **22**]..*

X–band EPR spectra of complexes **22** and **23** were measured at room temperature in the solid state. In both cases axial–type signals were observed. Experimental spectra were simulated to estimate the g tensor and hyperfine splitting constant on Co nuclei (^{59}Co, $I = {}^{7}/_{2}$). Both experimental and simulated spectra are shown in **Figure 5.20**. Experimental results were well simulated with the following parameters: g_1 = 2.044[**22**], 2.09[**23**]; g_2 = 2.65[**22**], 2.68[**23**]; g_3 = 3.05[**22**], 2.68[**23**]. $^{Co}(A_1, A_2, A_3)$ = (13, 117, 167)*10^{-4} cm^{-1} and $^{N}(A_1, A_2, A_3)$ = (6, 19, 3)*10^{-4} cm^{-1} for complex **22**. $^{Co}(A_1, A_2, A_3)$ = (60, 50, 133)*10^{-4} cm^{-1} for complex **23**. The average g value for the complexes **22** and **23** were 2.614 and 2.500, respectively. These indicated a high spin–orbit coupling and the presence of an unpaired electron on

Co(III) centre.[10,11] In the square planar Co(III) complex, the metal center possesses two unpaired electrons those were residing in d_{z2} and d_{xy} magnetic orbitals.[21] Ligand center p_z orbital coupled antiferromagnetically with the d_{z2} orbital, hence the rest electron resides on the d_{xy} magnetic orbital that led the cobalt (metal) center EPR.

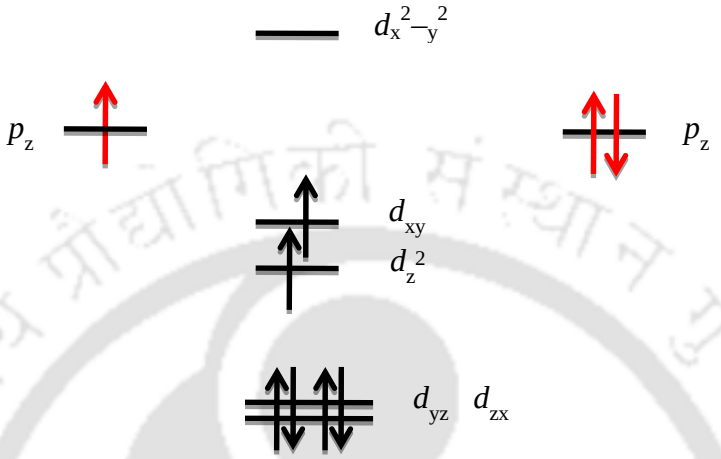

Figure 5.21: *d–orbital splitting of low spin Co^{3+} ion in square planar geometry, and ligand p_z orbital.*

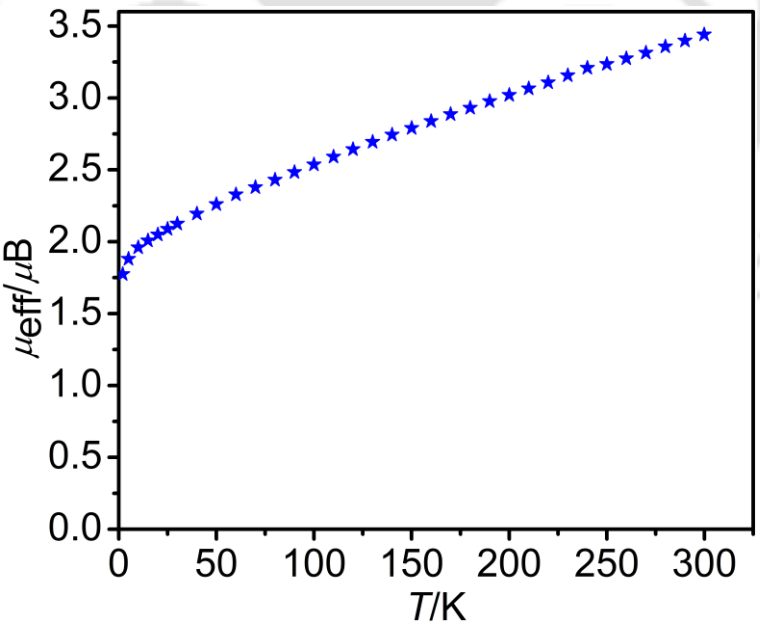

Figure 5.22: *μ_{eff} vs T plot of **23**.*

Variable temperature (2–300 K) magnetic moment measurement of the solid sample of **23** was performed using SQUID magnetometer at an external magnetic field 1 T. Complex **23** showed μ_{eff} = 1.75 μ_B at 5 K, while, the value increased with increase in temperature and

reached at μ_{eff} = 3.47 μ_B at 300 K (**Figure 5.22**). The resulted magnetic moment value at 5 K strongly implied that S = ½ ground state. While, the value increased with increase in temperature owing to the increase in population of unpaired electron in the thermally stable excited state $S = {}^3/_2$ which was the combination of S_{Co} = 1, and S_{rad} = ½.

5.5: Reactivity study:

In this chapter, it has already been mentioned that ligand $\mathbf{H_2L^X}$ (X = –Me, –Et, –F, –Cl, –Br) provided monoradical–containing square planar as well as diradical–containing square pyramidal Co(III) complexes. Ligand $\mathbf{H_2L^{Me}}$ reacted with $CoCl_2 \bullet 6H_2O$ always provided monoradical–containing square planar Co(III) complex. By increasing the reaction period, even using of excess metal salt to the ligand $\mathbf{H_2L^{Me}}$ did not alter the product. On the other hand, ligands $\mathbf{H_2L^{Et/F/Cl/Br}}$ provided monoradical–containing square planar Co(III) as well as diradical–containing square pyramidal Co(III) complexes, depending upon the reaction period and metal ion concentration. When ligand was exposed to react with 0.5 equivalent of $CoCl_2 \bullet 6H_2O$ for 5 minutes at room temperature, a monoradical–containing square planar Co(III) complex was isolated. Interestingly, when the reaction was carried out using same equivalent of $CoCl_2 \bullet 6H_2O$ to the ligand $\mathbf{H_2L^{Et/F/Cl/Br}}$ with increase the reaction period up to 40 minutes, diradical–containing square pyramidal Co(III) complex was produced. This indicated that monoradical–containing square planar Co(III) complexes were kinetically controlled products, while, diradical–containing square pyramidal Co(III) complexes were thermodynamically controlled products. Interestingly, it was found that 1:1 treatment of $CoCl_2 \bullet 6H_2O$ to ligands ($\mathbf{H_2L^X}$, X = –F, –Cl, –Br) also yielded a diradical–containing square pyramidal Co(III) complexes, even shortening the reaction period to 5 minutes. Notably, ligand $\mathbf{H_2L^I}$ provided only diradical–containing square pyramidal Co(III) complex being indifferent to the reaction time and metal ion concentration (**Table 5.7**).

Table 5.7: *Reaction conditions and different products are summarized below. Equivalency refers the concentration with respect to the specifically shown ligand.*

	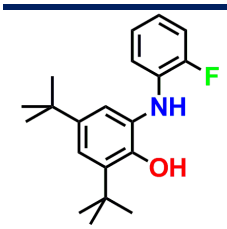	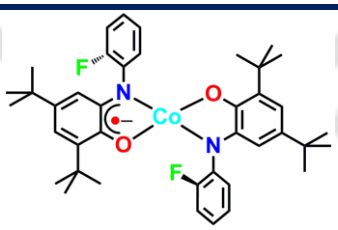	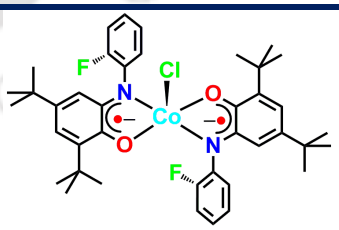
		[**21**]	[**21a**]
Condition 1: 0.5 equivalent $CoCl_2 \bullet 6H_2O$		5 minutes	40 minutes
Condition 2: 1 equivalent $CoCl_2 \bullet 6H_2O$			10 minutes

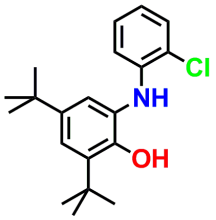	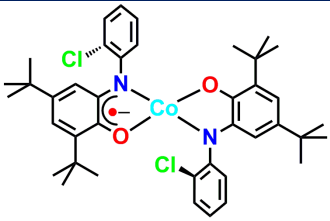	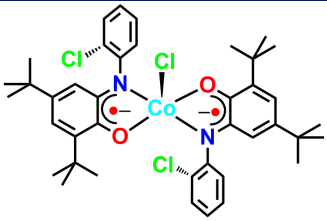
	[**22**]	[**22a**]
Condition 1: 0.5 equivalent $CoCl_2 \bullet 6H_2O$	5 minutes	40 minutes
Condition 2: 1 equivalent $CoCl_2 \bullet 6H_2O$		5 minutes
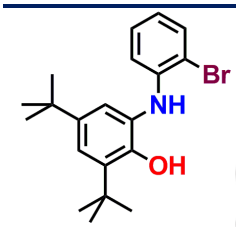	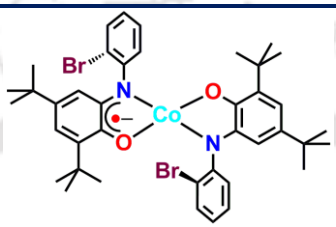	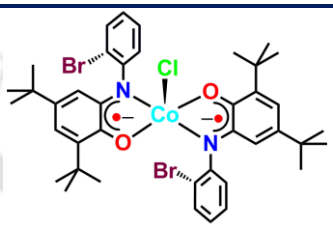
	[**23**]	[**23a**]
Condition 1: 0.5 equivalent $CoCl_2 \bullet 6H_2O$	5 minutes	40 minutes
Condition 2: 1 equivalent $CoCl_2 \bullet 6H_2O$		5 minutes
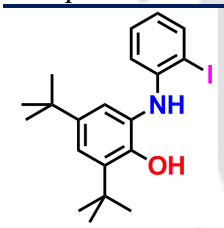		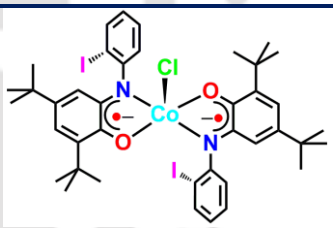
		[**24**]
Condition 1: 0.5 equivalent $CoCl_2 \bullet 6H_2O$		5 minutes

Ligands $\mathbf{H_2L^{F/Cl/Br}}$ yielded time–dependent different products when the ligands were treated with 0.5 equivalent of $CoCl_2 \bullet 6H_2O$ under air. It has been established that monoradical–containing square planar Co(III) complex reacts with radical species,[8a] here it then would be Cl^- to have the diradical–containing square pyramidal Co(III) complex with Cl^- as axial ligand. However, in the reaction medium, the availability or generation of $Cl^\bullet$ was very unlikely. The formation of diradical–containing square pyramidal, as reported, is associated with the initial formation of square planar Co(III) diradical species. Hence, to have the diradical–containing square planar Co(III) complex an aerial oxidation of monoradical–containing Co(III) complex was necessary. Therefore, to investigate the possible role of air,

for the possible transformation of square planar geometry to square pyramidal geometry of the synthesized square planar Co(III) complexes, complexes **22**, and **23** were continuously purged with molecular oxygen in the presence of tetraethylammonium chloride in hexane, individually. The reaction was monitored by UV–vis/NIR spectroscopic method.

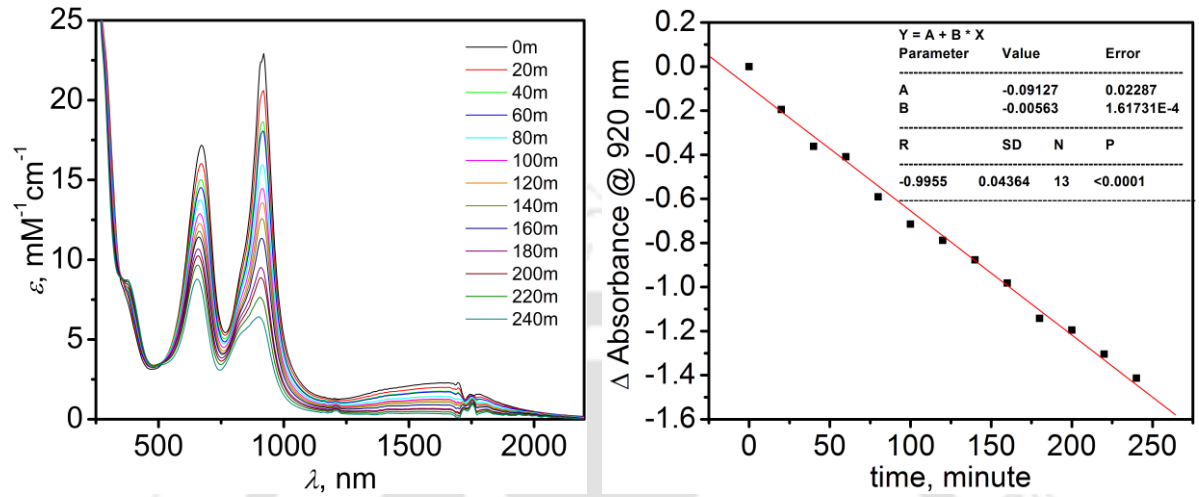

Figure 5.23: *[A] UV–vis/NIR spectral changes of **22** in hexane in the presence of molecular oxygen and $Et_4N^+Cl^-$; and [B] rate of decrease of the absorption maxima at λ_{max} = 920 nm.*

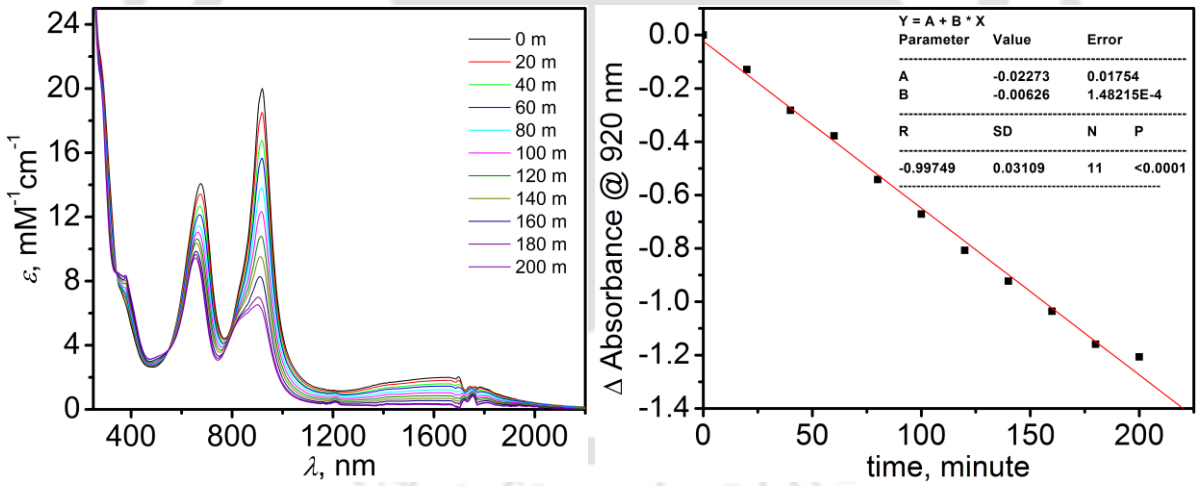

Figure 5.24: *UV–vis/NIR spectral changes of **23** in hexane in the presence of molecular oxygen and $Et_4N^+Cl^-$ [A]; and rate of decrease of the absorption maxima at λ_{max} = 920 nm [B].*

From the **Figure 5.23** and **Figure 5.24**, it is found that complexes **22**, and **23** showed a gradual decreased in intervalence charge transfer band originated due to the charge transfer from electron rich amidophenolate^{2-} unit to electron deficient iminosemiquinonate$^{\bullet 1-}$ unit. This was because of the oxidation of fully reduced ligand center (amidophenolate^{2-}) to its one electron oxidized form iminosemiquinonate$^{\bullet 1-}$ form. Thereafter, complexes **22**, and **23** were converted to **22a**, and **23a** by taking a chloride ion at the axial position, respectively.

5.6: Reactivities Toward Solvent, Benzyl Bromide, and 2–nitrobenzyl Bromide:

Complexes **19**, **20**, **21**, **22**, and **23** were coordinatively unsaturated *i.e.* square planar in nature. All were reactive and transformed to the most stable square pyramidal geometry by abstracting a chloride atom from solvent dichloromethane while it recrystallized from dichloromethane. The five–coordination geometry acquired by one–electron transfer from fully reduced amidophenolate ligand to Cl atom from dichloromethane through Co center, as a result of redox active electron transfer Co–Cl bond was formed at the axial position.[8,9] Conversion of **19** to **19a** was also monitored by time dependent electronic absorption spectral changes while a toluene solution of complex **19** was treated with CCl_4 are shown in **Figure 5.25**. From the absorption spectra, it was found that the absorption maxima at λ_{max} = 1600 nm and λ_{max} = 900 nm were gradually decreased with time. Simultaneously, the absorption maxima at λ_{max} = 666 nm was increased slightly with time. Decreased in absorption maxima at λ_{max} = 1600 nm and λ_{max} = 900 nm meant decreased in ligand–to–ligand inter valence charge transfer (LLIVCT) band associated between mixed oxidation state of the coordinated ligand. This clearly indicated the oxidation of fully reduced amidophenolate^{2-} unit to one–electron oxidized iminosemiquinonate$^{\bullet 1-}$ form proceeded *via* electron transfer from electron rich amidophenolate to chlorine atom of dichloromethane through metal center. To note, similar kind of time dependent spectral change has also observed upon addition of benzyl bromide to a toluene solution of **19** (**Figure 5.26**).

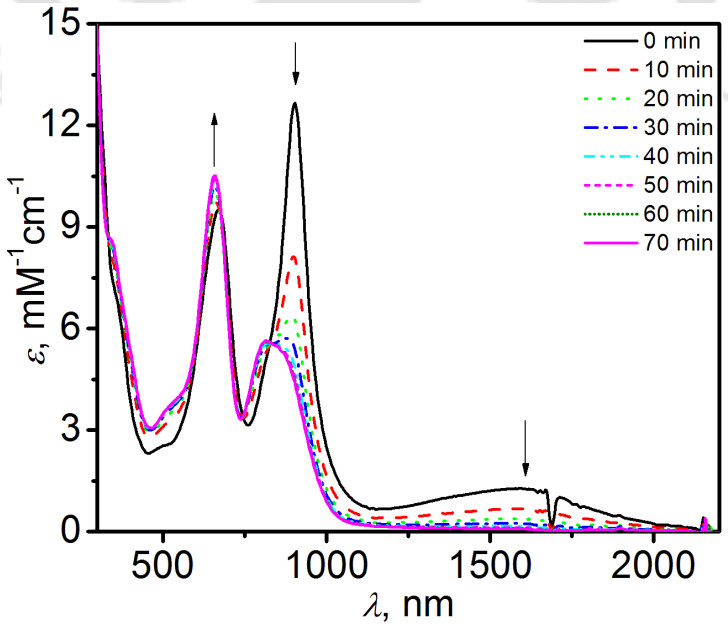

Figure 5.25: *Time dependent UV–vis/NIR spectral changes upon addition of CCl_4 to a toluene solution of complex **19**.*

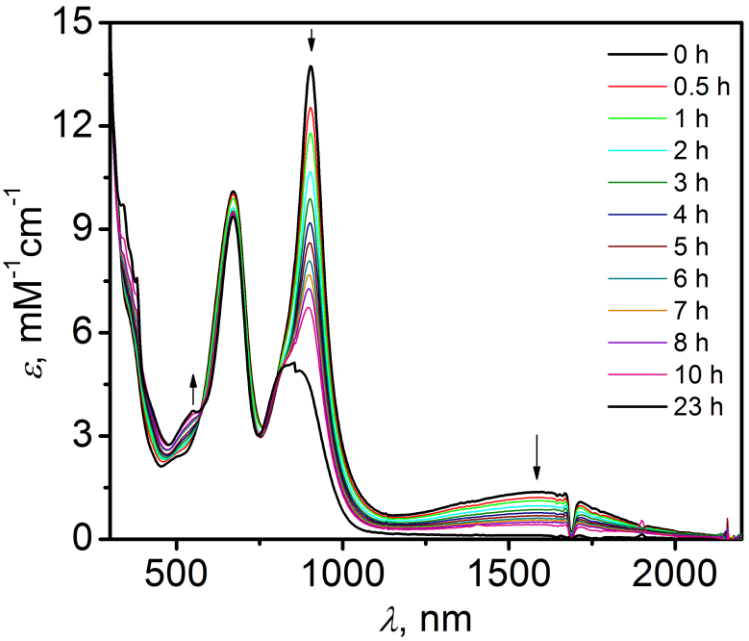

Figure 5.26: *Time dependent UV–vis/NIR spectral changes upon addition of benzyl bromide to a toluene solution of complex **19**.*

Plausible mechanism for the Co–Br bond formation at axial position during the transformation of **19** to **19b** is shown in **Scheme 5.8**.

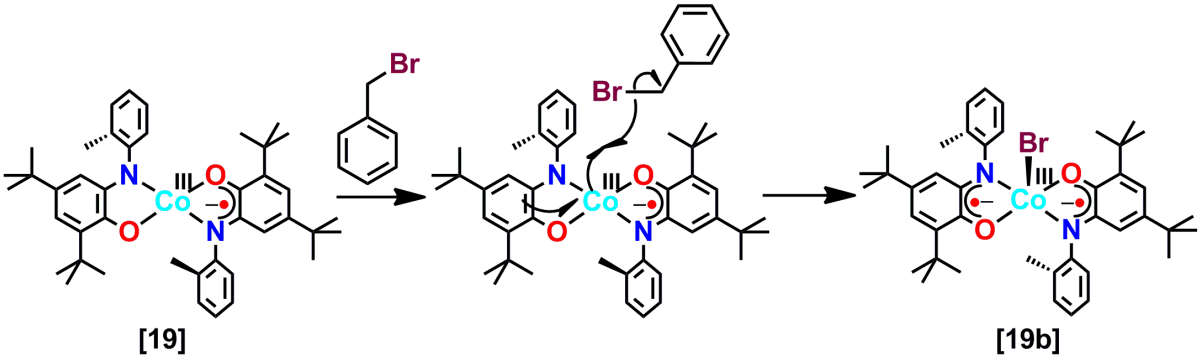

Scheme 5.8: *A mechanistic path for the formation of Co–Br bond of **19**.*

To intervene further, 2–nitrobenzyl bromide was taken as the substrate and it was found that the substrate was oxidized to 2–nitrobenzaldehyde upon treatment of 1 equivalent 2–nitrobenzyl bromide to an ethereal solution of complex **19** under air. Complex **19**, itself produced complex **19b**. Product formation (yield = 60%) was confirmed by the ^{1}H NMR spectroscopy.* Plausible mechanism for the formation of 2–nitrobenzaldehyde is shown in **Scheme 5.9**.

*http://sdbs.db.aist.go.jp/sdbs/cgi-bin/direct_frame_top.cgi

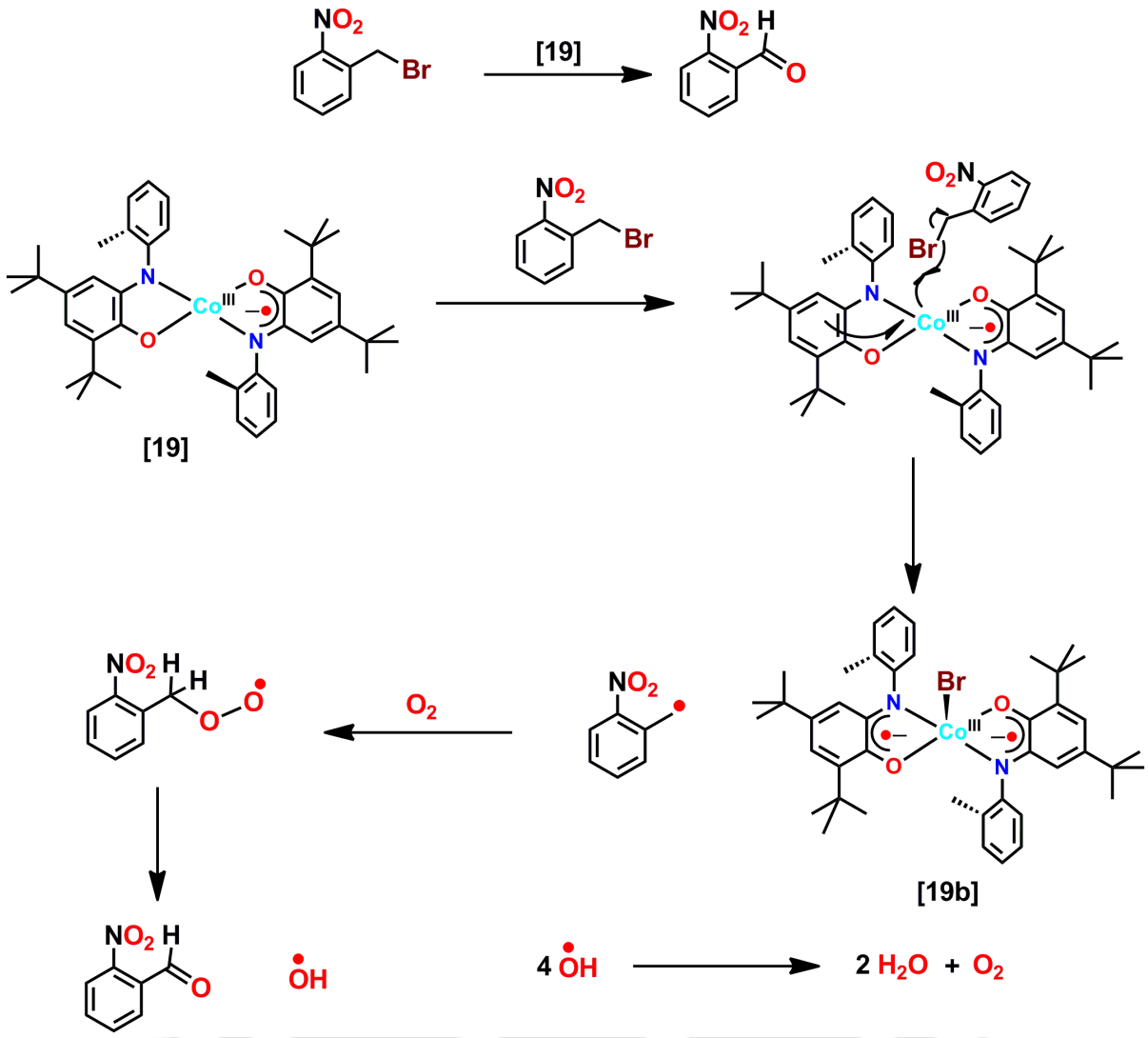

Scheme 5.9: *Propose mechanism for the oxidation of 2–nitrobenzyl bromide to 2–nitrobenzaldehyde.*

5.7: Conclusions:

1. Placement of different substituents at *–ortho* position to the N–phenyl ring of $\mathbf{H_2AP^H}$ non–innocent ligand, the σ–donor capacity of the ligand was enhanced, and thereafter, the non–innocent ligand $\mathbf{H_2L^{Me/Et/F/Cl/Br/I}}$ yielded radical–containing square planar cobalt complexes.
2. Square planar cobalt(III) complexes showed characteristic two sharp IR stretching bands at ~ 1145 cm^{-1}, and ~ 1100 cm^{-1}, respectively, due to phenyl ν(C–C) stretching of a one–electron oxidized, delocalized system.
3. Square planar Co(III) complexes belong to the Class III mixed valence in category.
4. Four coordinated square planar geometry were coordinatively unsaturated and transformed into five coordinated square pyramidal geometry *via* redox active electron transfer bond formation at the Co center.
5. Complex **19**, $\mathbf{[CoL^{Me}L^{Me\bullet}]}$ an effective oxidation initiator for the oxidation 2–nitrobenzylbromide to 2–nitrobenzaldehyde.
6. Complex $\mathbf{[CoL^{Me}L^{Me\bullet}]}$ was unreacted towards excess $CoCl_2\bullet 6H_2O$ that indicated mono–radical containing square planar Co(III) complexes were kinetically controlled. On the other hand, $\mathbf{[CoL^{X}L^{X\bullet}]}$ (X = –Cl, –Br) reacted with molecular oxygen in the presence of Et_4NCl, transformed into $\mathbf{[CoL^{X\bullet}{}_2Cl]}$, that indicated complex $\mathbf{[CoL^{X}L^{X\bullet}]}$ was first oxidized to form Co(III)–diradical species $\mathbf{[CoL^{X\bullet}{}_2]}$, which then took a Cl^- ion from the reaction solution at the axial position and formed the corresponding neutral five–coordinate complexes.
7. Thermodynamically controlled and kinetically controlled product obtained from $\mathbf{H_2L^X}$ (X = –Et, –F, –Cl, and –Br) ligands would be tuned by varying the metal ion concentration to the ligand.

References:

1. (*a*) S. Ozaki, H. Mimura, N. Yasuhara, M. Masui, Y. Yamagata, K. Tomita and T. J. Collins, *J. Chem. Soc., Perkin Trans.*, 1990, **2**, 353; (*b*) K.–J. Kim, S.–W. Park and S. S. Yoon, *J. Korean Chem. Soc.*, 2000, **44**, 286; (*c*) T. J. Collins, S. Ozaki and T. G. Richmond, *J. Chem. Soc., Chem. Comm.*, 1987, 803; (*d*) E. N. Jacobsen, *Acc. Chem. Res.*, 2000, **33**, 421.

2. (*a*) X. Zhou, A. I. Day, A. J. Edwards, A. C. Willis and W. G. Jackson, *Inorg. Chem.*, 2005, **44**, 452; (*b)* Z. Mo, D. Chen, X. Leng and L. Deng, *Organometallics*, 2012, **31**, 7040; (*c*) S. S. Rozenel, R. Padilla and J. Arnold, *Inorg. Chem.*, 2013, **52**, 11544.

3. (*a*) J. Kim, J. A. Ashenhurst and M. Movassaghi, *Science*, 2009, **324**, 238; (*b*) C. C. H. Atienza, C. Milsmann, S. P. Semproni, Z. R. Turner and P. J. Chirik, *Inorg. Chem.*, 2013, **52**, 5403; (*c*) T. R. Dugan, E. Bill, K. C. MacLeod, G. J. Christian, R. E. Cowley, W. W. Brennessel, S. Ye, F. Neese and P. L. Holland, *J. Am. Chem. Soc.*, 2012, **134**, 20352; (*d*) J. M. Darmon, S. C. E. Stieber, K. T. Sylvester, I. Fernández, E. Lobkovsky, S. P. Semproni, E. Bill, K. Wieghardt, S. DeBeer and P. J. Chirik, *J. Am. Chem. Soc.*, 2012, **134** , 17125; (*e*) E. B. Hulley, P. T. Wolczanski and E. B. Lobkovsky, *J. Am. Chem. Soc.*, 2011, 133, 18058; (*f*) J. Bachman and D. G. Nocera, *J. Am. Chem. Soc.*, 2005, **127**, 4730; (*g*) J. Bachmann, J. M. Hodgkiss, E. R. Young and D. G. Nocera, *Inorg. Chem.*, 2007, **46**, 607; (*h*) K. Wakabayashi, H. Yorimitsu and K. Oshima, *J. Am. Chem. Soc.*, 2001, **123**, 5374; (*i*) G. Cahiez and A. Moyeux, *Chem. Rev.*, 2010, **110**, 1435.

4. M. J. Baker–Hawkes, E. Billig and H. B. Gray, *J. Am. Chem. Soc.*, 1966, **88**, 4870.

5. J. C. Brewer, T. J. Collins, M. R. Smith and B. D. Santarsiero, *J .Am. Chem. Soc.*, 1988, **110**, 423.

6. F. C. Anson, T. J. Collins, T. G. Richmond, B. D. Santarsiero, J. E. Toth and B. G. R. T. Treco, *J. Am. Chem. Soc.*, 1987, **109**, 2914.

7. C. N. Verani, S. Gallert, E. Bill, T. Weyhermüller, K. Wieghardt and P. Chaudhuri, *Chem. Commun.*, 1999, 1747.

8. (*a*) A. L. Smith, L. A. Clapp, K. I. Hardcastle and J. D. Soper, *Polyhedron*, 2010, **29**, 164; (*b*) D. Herebian, P. Ghosh, H. Chun, E. Bothe, T. Weyhermüller and K. Wieghardt, *Eur. J. Inorg. Chem.*, 2002, 1957.

9. A. L. Smith, K. I. Hardcastle and J. D. Soper, *J. Am. Chem. Soc.*, 2010, **132**, 14358.

10. A. I. Poddel'sky, V. K. Cherkasov, G. K. Fukin, M. P. Bubnov, L. G. Abakumova and G. A. Abakumov, *Inor. Chim. Acta.*, 2004, **357**, 3632.

11. E. Bill, E. Bothe, P. Chaudhuri, K. Chlopek, D. Herebian, S. Kokatam, K. Ray, T. Weyhermüller, F. Neese and K. Wieghardt, *Chem. Eur. J.*, 2005, **11**, 204.

12. A. V. Piskunov, A. V. Lado, G. A. Abakumov, V. K. Cherkasov, O. V. Kuznetsova, G. K. Fukin, and E. V. Baranov, *Russ.Chem.Bull., Int.Ed.*, 2007, 56, 2007.

13. (*a*) A. I. Poddel'sky, V. K. Cherkasov and G. A. Abakumov, *Coord. Chem. Rev.*, 2009, **253**, 291; (*b*) J. Luo, N. P. Rath and L. M. Mirica, *Inorg. Chem.*, 2011, **50**, 6152; (*c*) C. G. Pierpont, *Coord. Chem. Rev.*, 2001, **99**, 216; (*d*) F. L.S. Bustamante, F. S. Miranda, F. A.V. Castro, J. A.L.C. Resende, M. D. Pereira and M. Lanznaster, *J. Inorg. Biochem.*, 2014, **132**, 37; (*e*) S. R. Garaeva, A. A. Medzhidov, O. Beukgunger, A. Aydin, B. Yalcin and M. G. Abbasov, *Russ. J. Coord. Chem.*, 2012, **38**, 140; (*f*) M. M. Sow, O. Diouf, M. Gaye, A. S. Sall, P. Pérez–Lourido, L. Valencia–Matarranz, G. Castro, A. Caneschi and L. Sorace, *Inorg. Chim. Acta.*, 2013, **406**, 171.

14. H. Chun, C. N. Verani, P. Chaudhuri, E. Bothe, E. Bill, T. Weyhermüller and K. Wieghardt, *Inorg. Chem.*, 2001, **40**, 4157.

15. (*a*) D. L. J. Broere, B. de Bruin, J. N. H. Reek, M. Lutz, S. Dechert and J. I. van der Vlugt, *J. Am. Chem. Soc., in press.* dx.doi.org/10.1021/ja502164f; (*b*) C. Mukherjee, T. Weyhermüller, K. Wieghardt and P. Chaudhuri, *Dalton Trans.*, 2006, 2169; (*c*) M. E. Cass, Greene, D. L. Greene, R. M. Buchanan and C. G. Pierpont, *J. Am. Chem. Soc.*, 1983, **105**, 2680; (*d*) To review: S. N. Brown, *Inorg. Chem.*, 2012, **51**, 1251; (*e*) H. Chun, P. Chaudhuri, T. Weyhermüller and K. Wieghardt, *Inorg. Chem.*, 2002, **41**, 790; (*f*) C. Mukherjee. T. Weyhermüller, E. Bother and P. Chaudhuri, *Inorg. Chem.*, 2008, **47**, 11620.

16. R. K. Sherwood, C. L. Kent, B. O. Patrickb and W. S. McNeil, *Chem. Commun.*, 2010, **46**, 2456.

17. (*a*) A. M. Morris, C. G. Pierpont and R. G. Finke, *Inorg. Chem.*, 2009, **48**, 3496; (*b*) S. Mukherjee, T. Weyhermüller, E. Bothe, K. Wieghardt and P. Chaudhuri, *Dalton Trans.*, 2004 , 3842.

18. (*a*) K. C. Gross and P. G. Seybold, *Int. J. Quantum Chem.*, 2000, **80**, 1107; (*b*) A. I. Poddel'sky, Y. A. Kurskii, A. V. Piskunov, N. V. Somov, V. K. Cherkasov and G. A. Abakumov, *Appl. Organometal. Chem.*, 2011, **25**, 180; (*c*) A. V. Piskunov, I. V. Ershova, G. K. Fukin and A. S. Shavyrin, *Inorg. Chem. Commun.*, 2013, **38**, 127; (*d*) N. Deibel, D. Schweinfurth, S. Hohloch, M. Delor, I. V. Sazanovich, M. Towrie, J. A. Weinstein and B. Sarkar, *Inorg. Chem.*, 2014, **53**, 1021.

19. (*a*) C. Mukherjee, T. Weyhermüller, E. Bothe and P. Chaudhuri, *Inorg. Chem.*, 2008, **47**, 2740; (*b*) K. S. Min, T. Weyhermüller and K. Wieghardt, *Dalton Trans.*, 2003, 1126.

20. (*a*) T. Kurahashi and H. Fujii, *J. Am. Chem. Soc.*, 2011, **133**, 8307; (*b*) A. Rajput, A. K. Sharma, S. K. Barman, D. Koley, M. Steinert and R. Mukherjee, *Inorg. Chem.*, 2014, **53**, 36; (*c*) W. Kaim, *Inorg. Chem.*, 2011, **50**, 9752; (*d*) C. G. Pierpont, *Inorg. Chem.*, 2011, **50**, 9766; (*e*) M. M. Khusniyarov, K. Harms, O. Burghaus, J. Sundermeyer, B. Sarkar, W. Kaim, J. van Slageren, C. Duboc and J. Fiedler, *Dalton Trans.*, 2008, 1355; (*f*) T. Storr, E. C. Wasinger, R. C. Pratt and T. D. P. Stack, *Angew. Chem., Int. Ed.*, 2007, **46**, 5198; (*g*) S. Kokatam, T. Weyhermüller, E. Bothe, P. Chaudhuri and K. Wieghardt, *Inorg. Chem.*, 2005, **44**, 3709.

21. (*a*) E. Vinck, D. M. Murphy, I. A. Fallis, R. R. Strevens and S. V. Doorslaer, *Inorg. Chem.*, 2010, **49**, 2083; (*b*) A. Zombeck, R. S. Drago, B. B. Corden and J. H. Gaul, *J. Am. Chem. Soc.*, 1981, **103**, 7580; (*c*) H. Arora, C. Philouze, O. Jarjayes and F. Thomas, *Dalton Trans.*, 2010, **39**, 10088; (*d*) C.–H. Cho, T.–Y. Chien, J.–H. Chen, S.–S. Wangb and J.–Y. Tung, *Dalton Trans.*, 2010, **39**, 2609; (*e*) K. M. Kadish, V. A. Adamian, E. V. Caemelbecke, E. Gueletii, S.Will, C. Erben and E. Vogel, *J. Am. Chem. Soc.*, 1998, **120**, 11986; (*f*) K. Ray, A. Begum, T. Weyhermüller, S. Piligkos, J. V. Slageren, F. Neese and K. Wieghardt, *J. Am. Chem. Soc.*, 2005, **127**, 4403.

22. B. Chakraborty, S. Bhunya, A. Paul and T. K. Paine, *Inorg. Chem.*, 2014, **53**, 4899.

23. M. B. Robin and P. Day, *Adv. Inorg. Chem. Radiochem.*, 1967, **10**, 247.

Chapter VI

Equipment and Experimental Section

6.1: Methods and Equipments:

All the chemicals and solvents were obtained from commercial sources and were used as supplied, unless noted otherwise. Solvents were obtained from Merck (India). THF was dried before used. UV–vis/NIR and Kinetics were performed in HPLC grade CH_2Cl_2. Mass spectra were taken in HPLC grade CH_3CN solvent.

Infrared Spectroscopy

IR spectra were recorded (4000–400 cm^{-1}) on 'Perkin Elmer Instrument' at normal temperature making KBr pellet grinding the sample with KBr (IR Grade).

NMR Spectroscopy

^1H, ^{13}C NMR spectra were recorded on '*Varian Mercury plus 400 MHz*' (at 298 K). Chemical shifts, δ (in ppm), are reported relative to TMS (δ (^1H) 0.0 ppm, δ (^{13}C) 0.0 ppm) which was used as the inner reference. Otherwise the solvents residual proton resonance and carbon resonance ($CHCl_3$, δ (^1H) 7.26 ppm, δ (^{13}C) 77.0 ppm.

Mass Spectroscopy

Mass spectral data were obtained from either QTOF–MS Spectrometer ('Waters, Model: Q–Tof Premier') or 'Agilent Accurate–Mass Q–TOF LC/MS 6520', and peaks are given in *m/z* (% of basis peak).

Elemental Analysis

The determination of the C, H, N was performed on 'FLASH EA 1112 series' CHN analyzer at SAIF Mumbai and on 'Perkin–Elmer 2400 series II' CHN analyzer at IACS Kolkata.

UV–vis/NIR Spectroscopy

UV–vis/NIR spectra were recorded on 'Perkin Elmer, Lamda 750, UV/VIS/NIR spectrometer' preparing a known concentration of the samples in HPLC Grade CH_2Cl_2 at room temperature using cuvette of 1 cm width.

Magnetic Susceptibility Measurements

The measurements of the temperature or field dependent magnetization of the sample were performed in the range 2 to 295 K at 1, 4 or 7 T on a '*Quantum Design* SQUID Magnetometer MPMS'. The samples were encapsulated in gelatin capsules and the response functions were measured four times for each given temperature, yielding a total of 32 measured points. The resulting volume magnetization from the samples had its diamagnetic contribution compensated and was recalculated as volume susceptibility. Diamagnetic contributions were estimated for each compound by using Pascal's constants. The experimental results were fitted with the programme JULX (Dr. Echard Bill, Max–Planck–Institut für Chemische Energiekonversion). calculating through full–matrix diagonalzation of the Spin–Hamiltonian. The following Hamiltonian–operators were used:

The calculation of static molar magnetic susceptibilities is based on the usual spin Hamiltonian approach for up to **four spins** with local multiplicities up to $S = {}^5/_2$:

$H = H_{ex} + H_{ZFS} + H_{Zee}$ where

$Hex = -2 \sum_{i=1}^{ns-1} \sum_{j=i+1}^{ns} J_{ij} \vec{S_i} \cdot \vec{S_j}$ is the exchange Hamiltonian, and

$H_{ZFS} = \sum_{i=1}^{ns} D_i[S^2_{z,i} - 1/3\ S_i(S_i + 1) + E_i/D_i(S^2_{x,i} - S^2_{y,i})]$ account for zero–field splitting

$H_{Zee} = \sum_{i=1}^{ns} g\beta \vec{S_i} \cdot \vec{B}$ is the Zeeman interaction.

J_{ij} are the exchange *coupling constants* of spins i and j, ns is the number of spins (max. four), D_i , E/D_i and g_i are the local axial and rhombic zero field splitting parameters and g–values (isotropic average).

EPR Spectroscopy

First derivative X–Band EPR spectra of powdered or frozen solution samples were measured with a 'JEOL JES–FA200 Spectrometer'. Spin–Hamiltonian simulations of the

EPR spectra were performed with a program which was developed from the $S = {}^5/_2$ routines of Gaffney and Silverstone and which specifically makes use of the resonance search procedure based on a Newton–Raphson algorithm as described therein.

^{57}Fe–Mössbauer Spectroscopy

^{57}Fe–Mössbauer spectra were measured with an '*Oxford Instruments'* Mössbauer spectrometer in the constant acceleration mode. ^{57} Co/Rh was used as the radiation source. The minimum experimental linewidths were 0.24 mm/s. The temperature of the sample was controlled by an '*Oxford Instruments* Variox Cryostat'. Isomer shifts were determined relative to α–iron at 300 K. The measurements were carried out at 80 K and 100 K with solid samples containing the isotope ^{57}Fe.

Crystallography

X−ray crystallographic data were collected using either a 'Bruker SMART APEX−II CCD diffractometer', equipped with a fine focus 1.75 kW sealed tube Mo−Ka radiation (l = 0.71073 Å) at 296(2) K, with increasing w (width of 0.3° per frame) at a scan speed of 3 s/frame or a 'Super Nova, Single source at offset, Eos diffractometer'. Structure was solved with the Superflip, structure solution program using Charge Flipping and refined by direct methods using 'SHELXS–97' and with full–matrix least squares on F^2 using 'SHELXL–97', or with the Superflip structure solution program using Charge Flipping and refined with the olex2.refine refinement package using Gauss−Newton minimisation. All then non−hydrogen atoms were refined anisotropically.

6.2: Experimental Section:

Synthesis of $[C_{21}H_{26}N_2O]$; H_2L^{CN}:

To a suspension of 3,5–di–*tert*–butylcatechol (2.22 g, 10 mmol) and 2–aminobenzonitrile (1.18 g , 10 mmol) in hexane (40 mL), triethylamine (0.05 mL) was added and the suspension was refluxed for two days. During the time a homogeneous yellow color solution appeared that turned to red upon stirring at room temperature (30 °C) under air for four days. After that, the reaction mixture was kept at 4 °C for overnight. This caused precipitation of unreacted 2–aminobenzonitrile. The solution was decanted and was kept for precipitation. The precipitate was then recrystallized thrice from a 5:1 CH_2Cl_2–EtOH solvent mixture. A colorless crystalline solid appeared. Washed with EtOH and then dried under air.

Yield: 2.320 g, 72%.

FTIR (KBr pellet, cm^{-1}): 3421, 3354, 2950, 2904, 2864, 2221, 1600, 1577, 1504, 1481, 1458, 1444, 1419, 1360, 1318, 1308, 1290, 1217, 1197, 1163, 976, 759.

^{1}H NMR ($CDCl_3$, 399.85 MHz): δ 1.27 (s, 9H), 1.44 (s, 9H), 5.83 (s, N–H), 6.00 (s, 1H), 6.50 (d, J = 8.8 Hz, 1H), 6.85 (t, J = 7.6 Hz, 1H), 7.01 (s, 1H), 7.28 (s, 1H), 7.34 (t, J = 8.0 Hz, 1H), 7.50 (d, J = 7.6 Hz, 1H) ppm.

^{13}C NMR ($CDCl_3$, 100.55 MHz): δ 29.7, 31.76, 34.6, 35.3, 98.0, 114.1, 117.7, 119.4, 122.2, 123.5, 125.4, 132.8, 134.6, 136.3, 143.1, 149.4, 149. 9 ppm.

ESI–MS (CH_3CN) *m/z* for $[C_{21}H_{26}N_2O + H]^+$: Calcd, 323.21; Found, 323.55.

UV–vis (CH_2Cl_2) λ_{max}, nm (ε, $M^{-1}cm^{-1}$): 396 (450), 320 (4750), 283 (4850), 248 (8800).

Anal. Calcd for $C_{21}H_{26}N_2O$: C, 78.22; H, 8.12; N, 8.69. Found: C, 78.53; H, 8.34; N, 9.08.

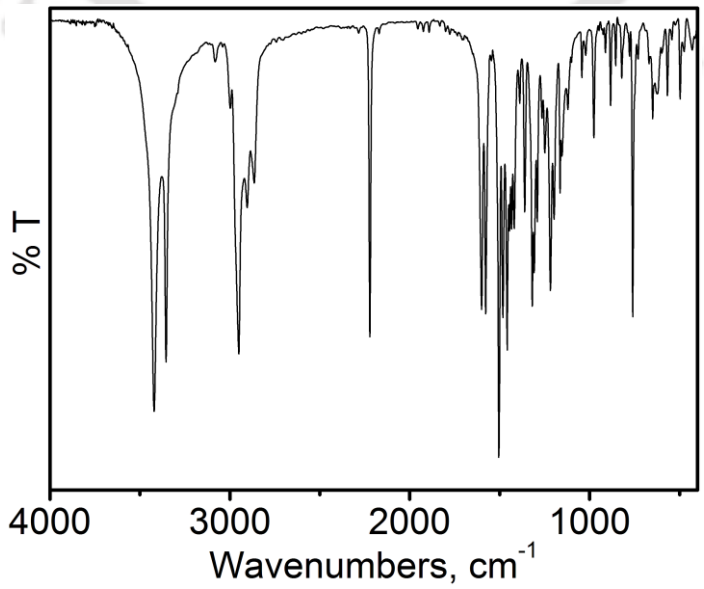

Figure 6.1: *Infrared spectrum of* H_2L^{CN}.

Synthesis of $[C_{21}H_{29}NO_2]$; H_2L^{OMe}:

A mixture of 3,5–di–*tert*–butylcatechol (2.22 g, 10 mmol), *o*–anisidine (1.23 g, 10 mmol), and Et_3N (0.1 mL) in hexane (35 mL) was refluxed for 24 h. After that, the resulting red solution was stirred at room temperature (30 °C) for another 24 h. The solution was then kept at 4 °C for overnight. A white precipitate was appeared, which was then filtered and recrystallized from a CH_2Cl_2:MeOH (5:1) solvent mixture.

Yield: 2.025 g, 62 %.

FTIR (KBr pellet, cm^{-1}): 3482, 3395, 3005, 2957, 2901, 2868, 1595, 1511, 1487, 1451, 1425, 1391, 1360, 1331, 1304, 1249, 1220, 1200, 1177, 1151, 1119, 1109, 1045, 1020, 974, 877, 824, 754, 742, 651, 575.

^{1}H NMR ($CDCl_3$, 399.85 MHz): δ 1.26 (s, 9H), 1.45 (s, 9H), 3.93 (s, 3H), 5.56 (s, N–H), 6.44 (m, 2H), 6.76–6.82 (m, 2H), 6.86–6.88 (m, 1H), 7.01 (d, J = 1.2 Hz, 1H), 7.21 (m, J = 2.2 Hz, 1H) ppm.

^{13}C NMR ($CDCl_3$, 100.55 MHz): δ 29.8, 31.8, 34.6, 35.2, 55.7, 110.1, 113.6, 119.3, 121.5, 121.8, 121.9, 127.8, 135.3, 136.7, 142.2, 147.8, 149.9 ppm.

ESI–MS (CH_3CN) *m/z* for $[C_{21}H_{29}NO_2 + H]^+$: Calcd, 328.47; Found, 328.59.

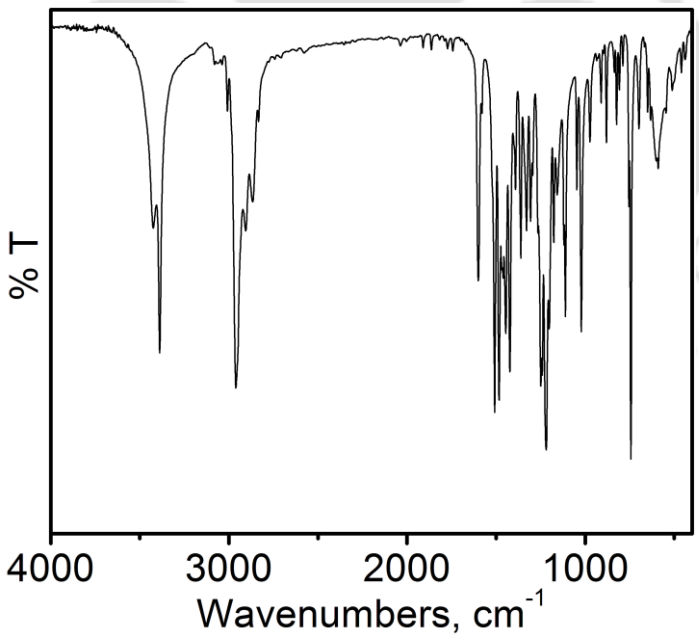

Figure 6.2: *Infrared spectrum of* H_2L^{OMe}.

Synthesis of $[C_{21}H_{29}NO]$; H_2L^{Me}:

This compound was synthesized in a manner analogous to that for $\mathbf{H_2L^{OMe}}$.

FTIR (KBr pellet, cm^{-1}): 3409, 3369, 3030, 2961, 2901, 2867, 1607, 1597, 1586, 1498, 1480, 1419, 1391, 1361, 1308, 1261, 1253, 1238, 1226, 1202, 1158, 1116, 1109, 1050, 972, 882, 823, 808, 795, 747, 712.

^{1}H NMR ($CDCl_3$, 399.85 MHz): δ 1.27 (s, 9H), 1.44 (s, 9H), 2.32 (s, 3H), 4.88 (s, N–H), 6.36 (s, O–H), 6.42 (d, *J* = 8 Hz, 1H), 6.80 (t, *J* = 7 Hz, 1H), 6.99 (d, *J* = 2 Hz, 1H), 7.04 (t, *J* = 7.2 Hz, 1H), 7.14 (d, *J* = 7.2 Hz, 1H), 7.23 (t, J = 2 Hz, 1H) ppm.

^{13}C NMR ($CDCl_3$, 100.55 MHz): δ 17.8, 29.8, 31.9, 34.6, 35.2, 113.9, 119.9, 121.9, 122.1, 123.8, 127.4, 127.9, 130.7, 135.5, 142.4, 144.9, 149.5 ppm.

ESI–MS (CH_3CN) *m/z* for $[C_{21}H_{29}NO + H]^+$: Calcd, 312.47; Found, 312.58.

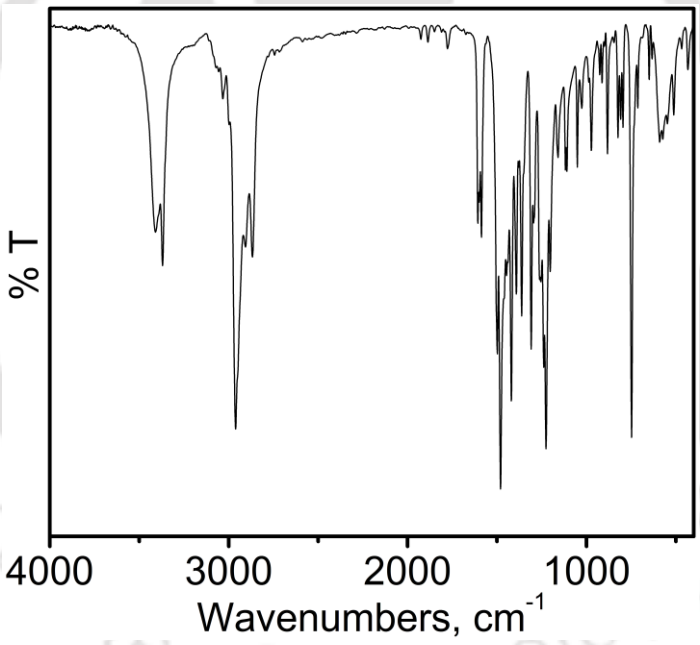

Figure 6.3: *IR spectrum of* $\boldsymbol{H_2L^{Me}}$.

Synthesis of ligand $[C_{21}H_{30}N_2O]$; $H_4L^{CH_2NH_2}$:

To a solution of $\mathbf{H_2L^{CN}}$ (1.290 g, 4 mmol) in dry THF (5 mL), $LiAlH_4$ (0.76 g, 20 mmol) was added and the reaction mixture was allowed to stir at room temperature (30 °C) for 16 h under argon. After that, the reaction was quenched by using ice cold water (30 mL). The resulting solution was filtered through a Celite pad and the pad was rinsed with ethyl acetate (50 mL). The filtrate was extracted with ethyl acetate (100 mL), washed thrice with brine. The combined organic part was dried over anhydrous Na_2SO_4. Solvent was removed under reduced pressure and super dried under high vacuum to have amorphous solid. Addition of hexane (10 mL) to the solid and followed by slow evaporation provided the ligand $\mathbf{H_4L^{CH_2NH_2}}$ as white solid.

Yield: 0.913 g (70%).

FTIR (KBr pellet, cm^{-1}): 3395, 3357, 3293, 3195, 3042, 2957, 2906, 2867, 2616, 1605, 1586, 1502, 1481, 1459, 1423, 1390, 1362, 1310, 1224, 1200, 1158, 1116, 1047, 1020, 977, 750, 653.

^{1}H NMR (399.85 MHz, $CDCl_3$): δ 1.27 (s, 9H), 1.43 (s, 9H), 4.03 (s, 2H), 6.54 (d, J = 8.4 Hz, 1H), 6.75 (t, J = 7.2 Hz, 1H), 7.02 (d, J = 2.4 Hz, 1H), 7.08 (d, J = 7.2 Hz, 2H), 7.17 (d, J = 2.4 Hz, 1H), 7.25 (s, 1H) ppm.

^{13}C NMR (100.55 MHz, $CDCl_3$): δ 29.9 (3C), 31.9 (3C), 35.3, 44.2, 114.7, 119.2, 121.2, 121.4, 124.6, 128.6, 129.4, 130.2, 136.0, 142.2, 146.6, 148.9 ppm.

ESI–MS (CH_3CN) *m/z* for $[C_{21}H_{30}N_2O + H]^+$: Calcd, 327.24; Found, 327.12.

Anal. Calcd for $C_{21}H_{30}N_2O\bullet0.35C_6H_{12}\bullet0.5H_2O$: C, 76.02; H, 9.72; N, 7.68. Found: C, 75.75; H, 9.97; N, 7.70.

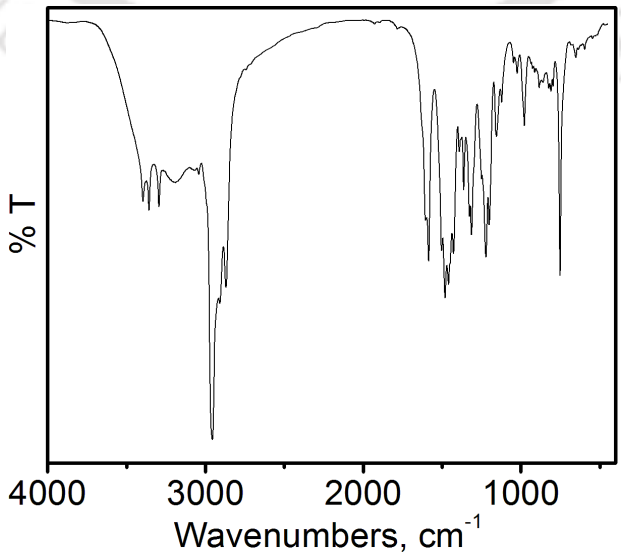

Figure 6.4: *Infrared spectrum of $H_4L^{CH_2NH_2}$ ligand.*

Synthesis of $[C_{21}H_{28}N_2O]$; H_3L1:

To an ethanolic solution (15 mL) of 2–aminobenzylamine (0.611 g, 5 mmol), 3,5–di–*tert*–butyl benzoquinone (1.110 g, 5 mmol) was added and the resulting mixture was stirred vigorously for 4 h at room temperature (30 °C) under inert (argon) atmosphere. A yellow color precipitate was appeared, filtered through Buchner funnel and washed with ethanol.

Yield: 0.567 g, 35%.

FTIR (KBr pellet, cm^{-1}): 3476, 3423, 3323, 2955, 2902, 2865, 1617, 1593, 1556, 1476, 1457, 1414, 1378, 1362, 1246, 1229, 1231, 1199, 1155, 960, 867, 754, 559, 530.

^{1}H NMR ($CDCl_3$, 399.85 MHz): δ 1.37 (s, 9H), 1.48 (s, 9H), 6.25 (s, 2H, $–NH_2$), 6.70 (s, 1H, –OH), 6.75–6.82 (m, 2H), 7.02 (s, 1H), 7.26 (s, 2H), 7.43 (d, J = 7.6 Hz, 1 H), 8.68 (s, 1H) ppm.

^{13}C NMR ($CDCl_3$, 100.75 MHz): δ 29.7, 31.9, 34.8, 35.1, 111.9, 116.2, 116.9, 118.1, 122.3, 132.4, 134.9, 135.0, 137.7, 142.2, 146.5, 148.7, 163.3 ppm.

ESI–MS (CH_3CN) *m/z* for $[C_{21}H_{28}N_2O + H]^+$: Calcd, 325.23; Found, 325.23.

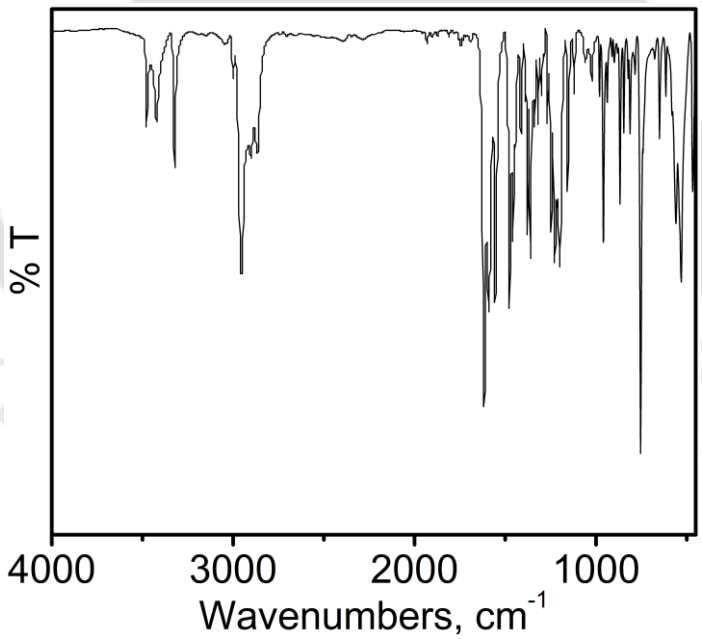

Figure 6.5: *Infrared spectrum of* ***H_3L1*** *ligand.*

Synthesis of $[C_{21}H_{30}N_2O]$; H_4L2:

To an ethanolic solution (15 mL) of 2–aminobenzylamine (0.619 g, 5 mmol), 3,5–di–*tert*–butyl–1,2–benzoquinone (1.110 g, 5 mmol) was added and the solution was stirred vigorously for 4 h at room temperature under argon atmosphere. A yellow color precipitate was appeared. Solvent was then removed under vacuum and methanol (15 mL) was added to the residue. This resulting solution was then treated with $NaBH_4$ until the yellow color of the solution disappeared and stirred further for 3 h at room temperature. The reaction mixture was quenched by cold water and extracted by dichloromethane (50 mL × 3). The combine organic layer then washed by water (50 mL × 4) and brine solution (20 mL × 2). After that, the organic layer was dried over anhydrous Na_2SO_4 and evaporation of solvent left a white solid. The solid was further purified by recrystallizing from hexane.

Yield: 0.652 g, 40%.

FTIR (KBr pellet, cm^{-1}): 3450, 3361, 3320, 3240, 2956, 2903, 2863, 1611, 1587, 1496, 1463, 1449, 1425, 1390, 1361, 1326, 1306, 1263, 1242, 1225, 1203, 1154, 1119, 1080, 1037, 962, 948, 924, 854, 768, 656, 532, 457.

^{1}H NMR ($CDCl_3$, 399.85 MHz): δ 1.31 (s, 9H), 1.41 (s, 9H), 4.17 (s, 2H), 6.72 (d, J = 8 Hz, 1H), 6.76 (t, J = 7.4 Hz, 1H), 6.91 (d, J = 9.6 Hz, 2H), 7.12–7.17 (m, 2H) ppm.

^{13}C NMR ($CDCl_3$, 100.75 MHz): δ 30.1, 31.9, 34.8, 48.8, 111.9, 116.1, 116.4, 118.9, 123.7, 129.0, 130.4, 135.4, 136.4, 143.0, 143.3, 145.7 ppm.

ESI–MS (CH_3CN) *m/z* for $[C_{21}H_{30}N_2O + H]^+$: Calcd, 327.24; Found, 327.20.

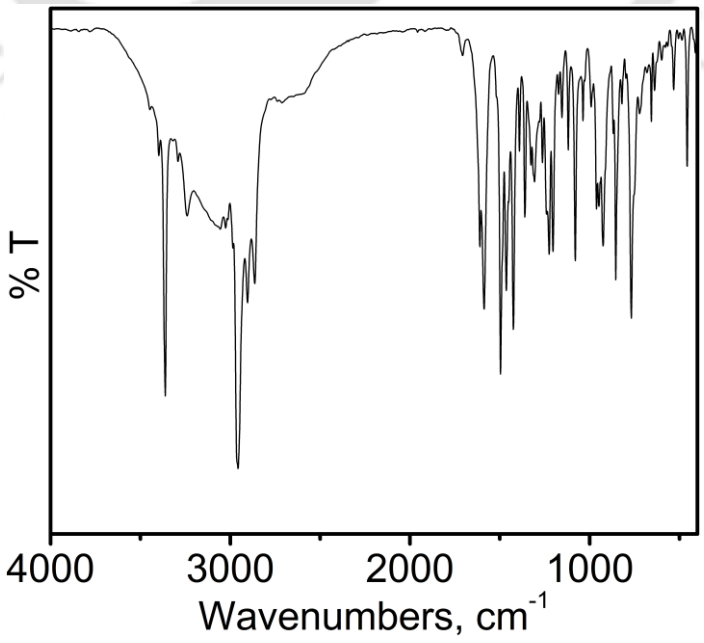

Figure 6.6: *Infrared spectrum of* ***H_4L2*** *ligand.*

Synthesis of $[C_{28}H_{34}N_2O_2]$; $H_3L^{Mixed(H)}$:

To an ethanolic (5 mL) solution of $H_4L^{CH_2NH_2}$ (0.815 g, 2.5 mmol), salicyaldehyde (0.305 g, 2.5 mmol) in EtOH (5 mL) was added dropwise. The reaction mixture was then stirred at room temperature for 5 h. A yellow precipitation occurred during the course. The precipitate was filtered, washed with EtOH (15 mL) dried under air.

Yield: 0.753 g, (70%).

FTIR (KBr pellet, cm^{-1}): 3463, 3365, 2999, 2962, 2906, 2865, 1631, 1607, 1586, 1509, 1485, 1462, 1427, 1387, 1361, 1320, 1294, 1267, 1240, 1214, 1193, 1151, 1123, 1036, 1012, 987, 976, 924, 883, 827, 781, 757, 746, 651, 604, 461.

^{1}H NMR ($CDCl_3$, 399.85 MHz): δ 1.25 (s, 9H), 1.44 (s, 9H), 4.87 (s, 2H), 5.38 (s, 1H), 6.27 (s, 1H), 6.54 (d, J = 8 Hz, 1H), 6.88 (m, 2H), 6.96 (s, 1H), 6.98 (d, J = 2.4 Hz, 1H), 7.16 (td, J = 7.2 Hz, 1H), 7.28–7.21 (m, 3H), 7.32 (td, J = 7.6 Hz, 1H), 8.48 (s, 1H), 13.02 (s, 1H) ppm.

^{13}C NMR ($CDCl_3$, 100.55 MHz): δ 29.8, 31.8, 34.6, 35.2, 60.6, 115.3, 117.3, 118.95, 119.0, 120.2, 121.6, 122, 124.4, 127.9, 129.4, 129.9, 131.8, 132.9, 135.7, 142.7, 145, 149.1, 161.1, 166.4 ppm.

ESI–MS (CH_3CN) *m/z* for $[C_{28}H_{34}N_2O_2 + H]^+$: Calcd, 431.27; Found, 431.17.

Anal. Calcd for $H_3L^{Mixed(H)}$: C, 78.09; H, 7.96; N, 6.51. Found: C, 78.21; H, 8.10; N, 6.44.

UV–vis/NIR (CH_2Cl_2) λ_{max}, nm (ε, $M^{-1}cm^{-1}$): 280(11200), 340(1050)^{sh}.

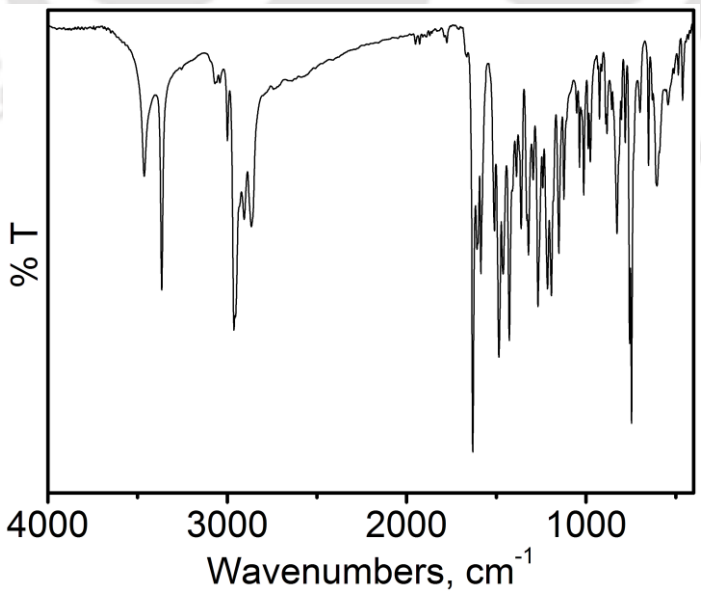

Figure 6.7: *IR spectrum of* $H_3L^{Mixed(H)}$ *ligand.*

Synthesis of $[C_{22}H_{31}NO]$, H_2L^{Et}:

This compound was synthesized in a manner analogous to that for $\mathbf{H_2L^{OMe}}$.

Yield: 60%.

FTIR (KBr pellet, cm^{-1}): 3449, 3390, 2999, 2963, 2932, 2869, 1604, 1583, 1500, 1480, 1449, 1420, 1391, 1362, 1311, 1303, 1234, 1219, 1202, 1159, 1121, 881, 825, 753, 688, 580.

^{1}H NMR ($CDCl_3$, 399.85 MHz): δ 1.30 (s, 9H), 1.38 (t, J = 7.6 Hz, 3H), 1.48 (s, 9H), 2.72 (q, J = 7.6 Hz, 2H), 5.01 (s, 1H), 6.41 (s, 1H), 6.47 (d, J = 8 Hz, 1H), 6.88 (t, J = 7.4 Hz, 1H), 7.01 (d, J = 2 Hz, 1H), 7.07 (t, J = 7.6 Hz, 1H), 7.20 (d, J = 7.2 Hz, 1H), 7.26 (d, J = 2 Hz, 1H) ppm.

^{13}C NMR ($CDCl_3$, 100.55 MHz): δ 13.5, 24.3, 29.8, 31.8, 34.6, 35.2, 114.3, 120.1, 121.8, 122.1, 127.3, 128.1, 128.5, 129.5, 135.5, 142.5, 144.4, 149.5 ppm.

ESI–MS (CH_3CN) *m/z* for $[C_{22}H_{31}NO + H]^+$: Calcd, 326.25; Found, 326.25.

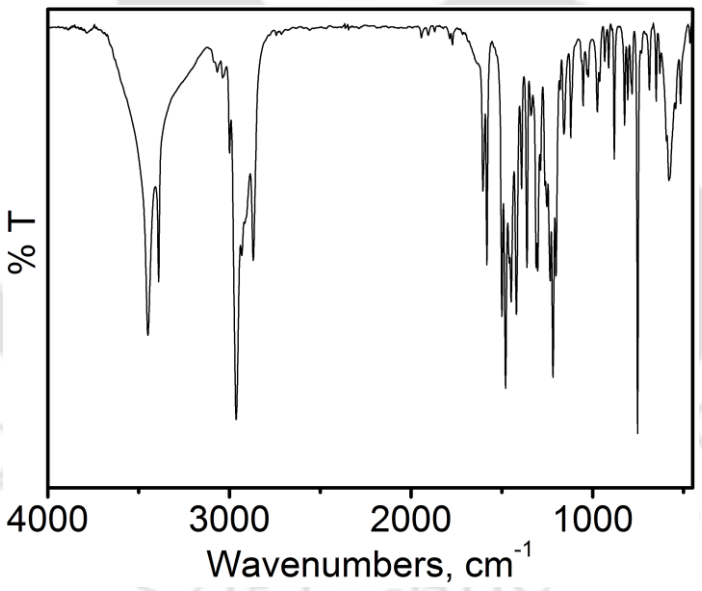

Figure 6.8: *IR spectrum of* $\boldsymbol{H_2L^{Et}}$ *ligand.*

Synthesis of $[C_{20}H_{26}FNO]$; H_2L^F:

To a suspention of 3,5–di–*tert*–butylcatechol (2.22 g, 10 mmol) in hexane (15 mL), 2–fluoroaniline (1.11 g, 10 mmol) and Et_3N (0.05 mL) were added sequentially. Then the resulting reaction mixture was stirred for 24 h at room temperature (30 °C). During this time a white precipitate was obtained. The solvent was removed and the residue was recrystallized from methanol. It afforded colorless crystals that then dried under vacuum.

Yield: 1.640 g, 52%.

FTIR (KBr pellet, cm^{-1}): 3432, 3382, 3356, 2963, 2909, 2868, 1619, 1507, 1483, 1424, 1319, 1117, 881, 743.

^{1}H NMR ($CDCl_3$, 399.85 MHz): δ 1.27 (s, 9H), 1.44 (s, 9H), 5.25 (br s, 1H), 6.35 (s, 1H), 6.49–6.53 (m, 1H), 6.75–6.81 (m, 1H), 6.94 (t, J = 7.6 Hz, 1H), 7.02–7.03 (m, 1H), 7.05–7.10 (m, 1H), 7.23–7.24 (m, 1H) ppm.

^{13}C NMR ($CDCl_3$, 150.91 MHz): δ 29.7, 31.8, 34.6, 35.2, 115.1, 115.7, 119.7, 121.8, 122.6, 124.9, 126.8, 135.7, 142.6, 149.7, 151.7, 153.3 ppm.

ESI–MS (CH_3CN) *m/z* for $[C_{20}H_{26}NOF + H]^+$: Calcd, 316.2071; Found, 316.2051.

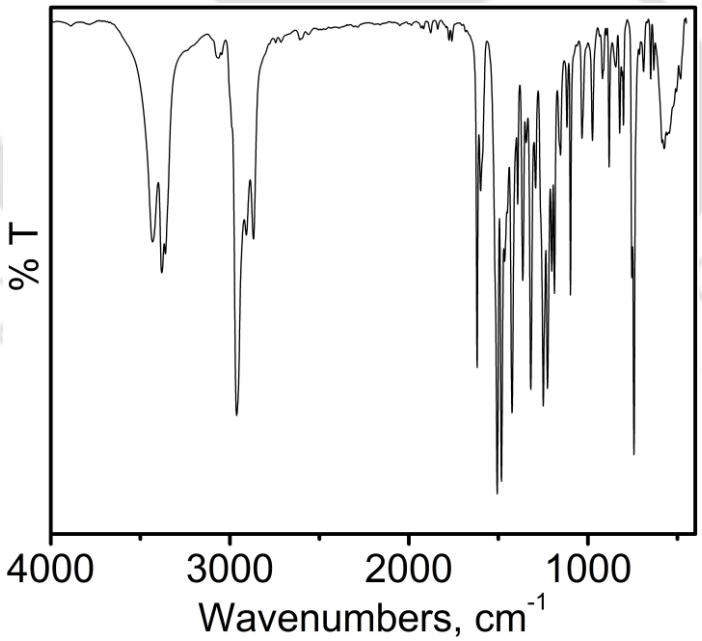

Figure 6.9: *IR spectrum of* H_2L^F.

Synthesis of $[C_{20}H_{26}ClNO]$; H_2L^{Cl}:

To a stirred solution of 3,5–di–*tert*–butylcatechol (1.14 g, 5.12 mmol) and 2–chloroaniline (0.65, 5.12 mmol) in hexane (15 mL), Et_3N (0.05 mL) was added and allowed to stir for 24 h at room temperature (30 °C). During this period a white precipitate appeared. The solid was filtered and washed with hexane (10 mL) and then dried under vacuum.

Yield: 0.766 g, 46%.

FTIR (KBr pellet, cm^{-1}): 3449, 3356, 2961, 2904, 2867, 1590, 1496, 1476, 1417, 1390, 1308, 1216, 1197, 1151, 1034, 970, 824, 808, 748, 678.

^{1}H NMR ($CDCl_3$, 399.85 MHz): δ 1.27 (s, 9H), 1.44 (s, 9H), 5.60 (br s, 1H), 6.28 (s, 1H), 6.47 (d, J = 8.0, 1H), 6.76–6.79 (m, 1H), 7.00–7.01 (m, 1H), 7.06 (t, J = 8.0 Hz, 2H), 7.34 (d, J = 8 Hz, 1H) ppm.

^{13}C NMR ($CDCl_3$, 150.91 MHz): δ 29.8, 31.8, 34.6, 35.3, 114.9, 120.1, 120.6, 122.2, 122.8, 126.7, 128.1, 129.5, 135.8, 142.7, 143.3, 149.8 ppm.

ESI–MS (CH_3CN) *m/z* for $[C_{20}H_{26}ClNO + H]^+$: Calcd, 332.1776; Found, 332.1787.

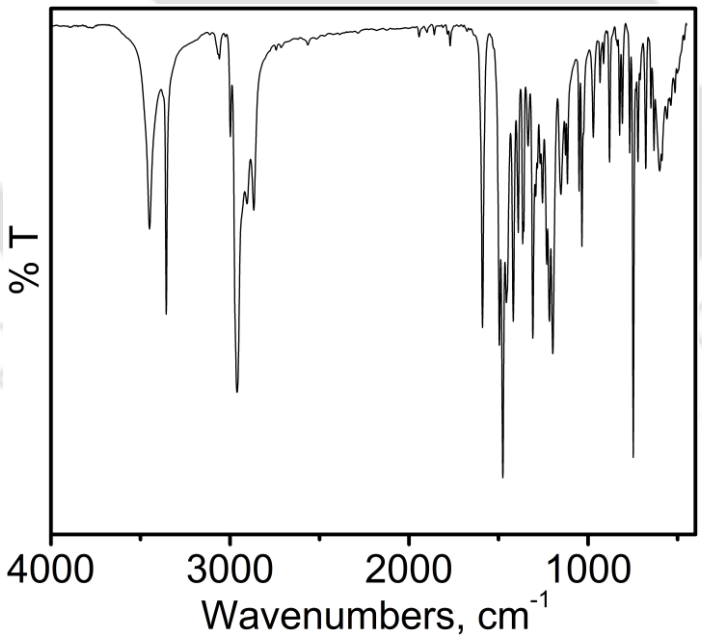

Figure 6.10: *IR spectrum of* H_2L^{Cl}.

Synthesis of $[C_{20}H_{26}BrNO]$; H_2L^{Br}:

A solution mixture containing 3,5–di–*tert*–butylcatechol (1.01 g, 4.58 mmol), 2–bromoaniline (0.78 g, 4.38 mmol), and Et_3N (0.05 mL) in hexane (15 mL) was stirred for 24 h at room temperature (30 °C). The solvent was removed and the residue was recrystallized from methanol. It afforded colorless crystals, which then dried under vacuum.

Yield: 0.898 mg, 52 %.

FTIR (KBr pellet, cm^{-1}): 3344, 3345, 2959, 2909, 2866, 1585, 1474, 1416, 1390, 1307, 1196, 1151, 1021, 969, 880, 824, 748, 714, 649.

^{1}H NMR ($CDCl_3$, 399.85 MHz): δ 1.27 (s, 9H), 1.44 (s, 9H), 5.59 (br s, 1H), 6.26 (s, 1H), 6.45 (dd, J = 8.8 Hz and 1.6 Hz, 1H), 6.70 (td, J = 8.4 Hz and 1.6 Hz, 1H), 7.00 (d, J = 2.8 Hz, 1H), 7.09 (td, J = 1.2 Hz, J = 8.2 Hz, 1H), 7.26 (d, J = 2.4 Hz, 1H), 7.50 (dd, J = 1.6 Hz, J = 4.8 Hz, 1H) ppm.

^{13}C NMR ($CDCl_3$, 150.91 MHz): δ 29.7, 31.8, 34.6, 35.3, 111.0, 115.0, 120.6, 122.3, 122.9, 126.8, 128.8, 132.7, 135.8, 142.7, 144.4, 149.7 ppm.

ESI–MS (CH_3CN) *m/z* for $[C_{20}H_{26}NOBr + H]^+$: Calcd, 376.1270; Found, 376.1187.

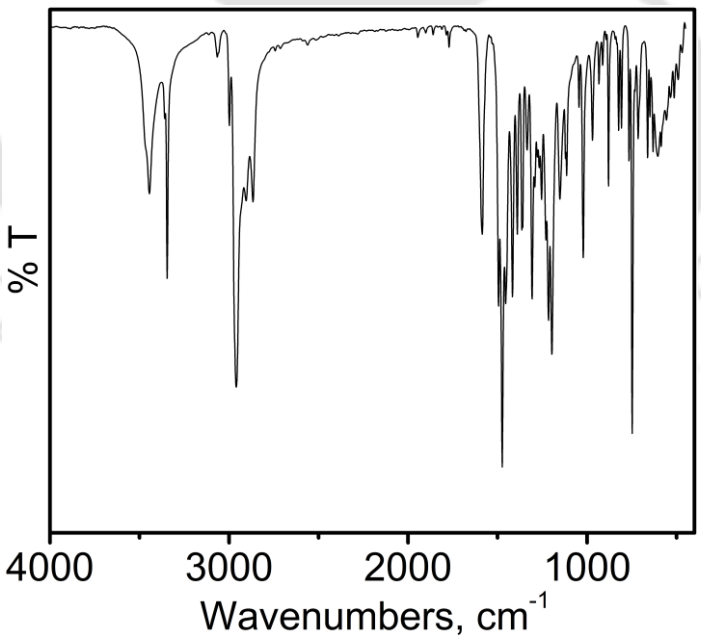

Figure 6.11: *IR spectrum of* H_2L^{Br}.

Synthesis of $[C_{20}H_{26}INO]$; H_2L^I:

To a solution of 3,5–di–*tert*–butylcatechol (1.11 g, 5 mmol) and 2–iodoaniline (1.09 g, 5 mmol) in hexane (15 mL), Et_3N (0.05 mL) was added and stirred for 24 h at room temperature (30 °C). A brown precipitate was obtained, filtered and washed with hexane giving a white solid. The filtrate was kept aside and after 48 h crystals appeared, filtered and washed with minimum amount of hexane (3 mL) and dried under vacuum.

Yield: 1.03 g, 49%.

FTIR (KBr pellet, cm^{-1}): 3440, 3333, 2958, 2901, 2864, 1582, 1471, 1449, 1416, 1359, 1305, 1232, 1198, 1006, 968, 879, 808, 822, 751,709, 650.

^{1}H NMR ($CDCl_3$, 399.85 MHz): δ 1.27 (s, 9H), 1.44 (s, 9H), 5.45 (br s, 1H), 6.26 (s, 1H), 6.40 (d, J = 8 Hz, 1H), 6.58 (t, J = 7.6 Hz, 1H), 6.99–7.00 (m, 1H), 7.13 (t, J = 7.6 Hz, 1H), 7.74(d, J = 7.6 Hz, 1H) ppm.

^{13}C NMR ($CDCl_3$, 150.91 MHz): δ 29.7, 31.8, 34.6, 35.3, 86.5, 114.4, 121.4, 122.3, 122.9, 127.2, 129.7, 135.8, 139.2, 142.7, 146.8, 149.6 ppm.

ESI–MS (CH_3CN) *m/z* for $[C_{20}H_{26}NOI + H]^+$: Calcd, 424.1132; Found, 424.1135.

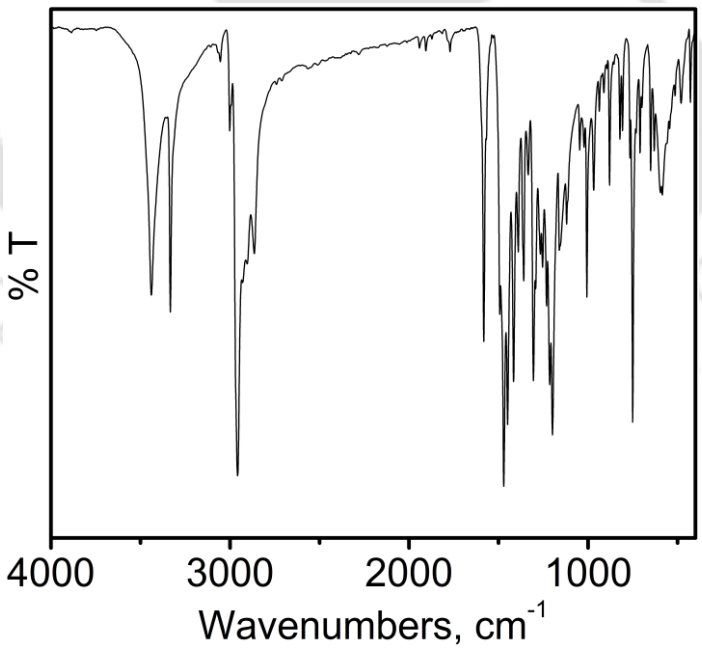

Figure 6.12: *IR spectrum of* H_2L^I.

Synthesis of $[(C_{60}H_{102}NSO_{17}V_4)\bullet CH_3CN]$; $1\bullet CH_3CN$:

To a methanolic solution (30 mL) of $\mathbf{H_2L^{CN}}$ (0.497 g, 1.54 mmol), $VO(SO_4)\bullet 5H_2O$ (0.394 g, 1.56 mmol) and Et_3N (0.2 mL) were added and the resulting solution was refluxed for two hours. After that, the solution was stirred for another two hours at room temperature and then filtered and the filtrate was kept for slow evaporation. This caused precipitation of blue microcrystalline solid. Filtered and the solid residue was thoroughly washed with methanol, and then, dried under vacuum.

Yield: 0.265 g.

To 15:5:5 CH_2Cl_2:CH_3CN:MeOH solution of the blue solid (0.050 g), tetrabutylammonium perchlorate (0.060 g, 0.175 mmol) was added. Slow evaporation of the solution caused precipitation of block shaped blue crystalline solid suitable for single crystal X–ray diffraction study.

Yield: 0.048 g, 47% [with respect to $VO(SO_4)\bullet 5H_2O$].

FTIR (KBr pellet, cm^{-1}): 2961, 2913, 2873, 1584, 1459, 1438, 1272, 1236, 1102, 1046, 1015, 998, 982, 689, 657, 627, 587.

ESI–MS (CH_3CN) *m/z* for $[C_{44}H_{66}O_{17}SV_4]^-$: Calcd, 1102.18; Found, 1101.92.

ESI–MS (CH_3CN) *m/z* for $[C_{16}H_{36}N]^+$: Calcd, 242.28; Found, 242.25.

Anal. Calcd for $C_{44}H_{66}O_{17}SV_4\bullet 1CH_3CN\bullet 1H_2O$: C, 53.03; H, 7.68; N, 2.0. Found: C, 53.01; H, 7.75; N, 2.36.

UV–vis/NIR (CH_2Cl_2) λ_{max}, nm (ε, $M^{-1}cm^{-1}$): 734(16500), 566(14950).

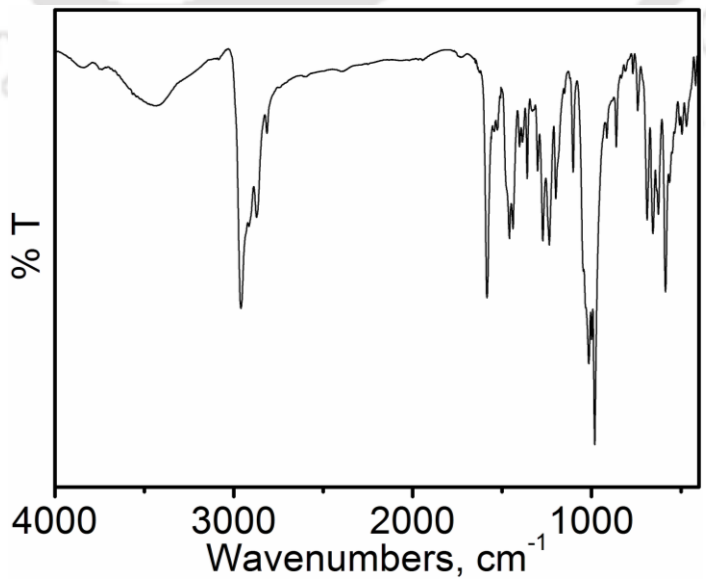

Figure 6.13: *IR spectrum of* ***1•CH₃CN****.*

Synthesis of $[C_{92}H_{164}N_2O_{32}S_2V_8]$; 2:

H_2L^{OMe} (0.164 g, 0.5 mmol), $VOSO_4 \bullet 5H_2O$ (0.380 g, 1.5 mmol) and Et_3N (0.15 mL) were added sequentially in methanol (7 mL). The reaction mixture was stirred under air at room temperature (30 °C) for 2 h and 40 min. During this period a blue precipitate was appeared. The precipitate was filtered and washed with minimum volume of methanol (5 mL). The blue precipitate was then recrystallized from a CH_2Cl_2–MeOH (3:1) solvent mixture after adding tetrabutylammonium perchlorate (0.015 g). A block shape crystalline compound appeared in 4 days. The crystalline solid was then thoroughly washed further with methanol (20 mL) to get complex **2**.

Yield: 0.040 g, 15%.

FTIR (KBr pellet, cm^{-1}): 2961, 2912, 2874, 1584, 1529, 1480, 1460, 1440, 1400, 1387, 1361, 1301, 1272, 1235, 1200, 1104, 1036, 1014, 1001, 987, 915, 864, 783, 742, 691, 660, 630, 573, 500, 466, 420.

ESI–MS (CH_3CN) for $[C_{60}H_{92}O_{32}S_2V_8]^{2-}$: Calcd, 898.04; Found, 898.21.

ESI–MS (CH_3CN) for $[C_{16}H_{36}N]^+$: Calcd, 242.28; Found, 242.25.

UV–vis/NIR (CH_2Cl_2) λ_{max}, nm (ε, $M^{-1}cm^{-1}$): 777(32250), 576(22650).

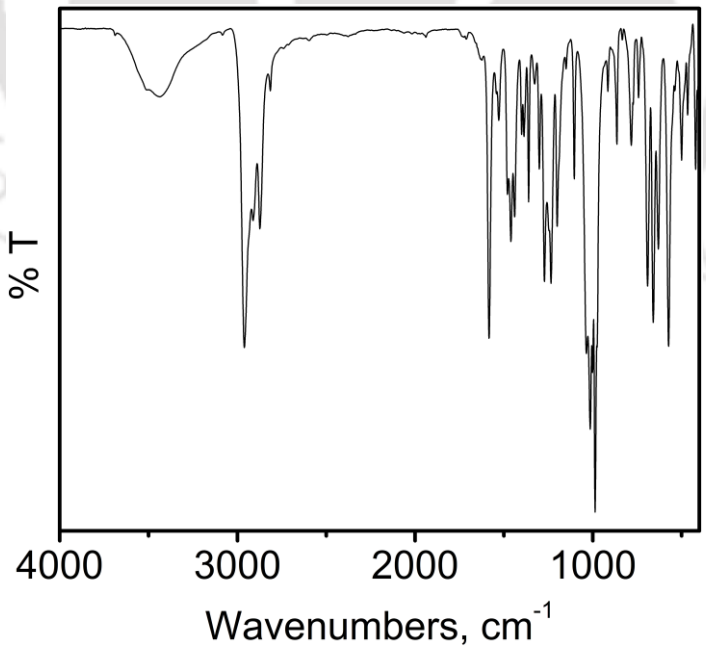

Figure 6.14: *IR spectrum of **2**.*

Synthesis of $[C_{84}H_{96}N_4O_{16}V_4]$; 3:

Equimolar amounts of reaction between $\mathbf{H_3L^{COOH}}$ (0.341 g, 1 mmol) and $VOSO_4 \bullet 5H_2O$ (0.251 g, 1mmol) in methanol in the presence of triethylamine (0.2 mL) under 2 h refluxed and followed by 2 h room temperature stirring provided complex **3**, which was then recrystallized from CH_2Cl_2:CH_3CN:MeOH (3:1:1) solvent mixture.

Yield: 0.211 g, 52%.

FTIR (KBr pellet, cm^{-1}): 2258, 2906, 2869, 1596, 1573, 1520, 1472, 1449, 1408, 1394, 1361, 1010, 829, 747.

^{1}H NMR ($CDCl_3$, 399.85 MHz): δ 1.12 (s, 36 H), 1.55 (s, 36 H), 6.65 (t, J = 7.2 Hz, 4H), 6.86 (s, 4H), 7.18 (d, J = 8.4 Hz, 4H), 7.26 (s, 4H), 7.47 (t, J = 8 Hz, 4H), 7.73 (d, J = 7.6 Hz, 4H) ppm.

ESI–MS (CH_3CN) of $[C_{84}H_{96}N_4O_{16}V_4]$ for $[M + H]^+$: Calcd, 1621.48; Found, 1621.49.

UV–vis/NIR (CH_2Cl_2) λ_{max}, nm (ε, $M^{-1}cm^{-1}$): 794(18200), 388(22800), 310(44600).

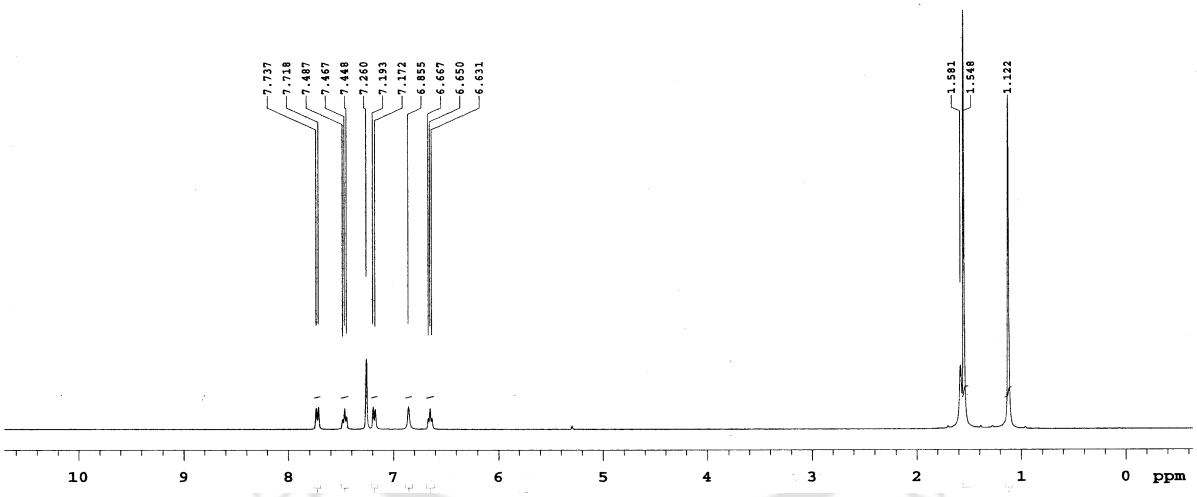

Figure 6.15: *1H NMR spectrum of* ***3•CH_2Cl_2.***

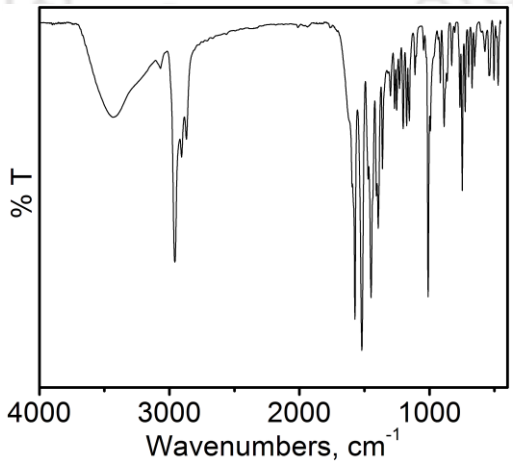

Figure 6.16: *Infrared spectrum of* ***3•CH_2Cl_2.***

Synthesis of Phenoxazine Molecule; 4:

To a stirred solution of $\mathbf{H_2L^{CN}}$ (4, 0.161 g, 0.5 mmol) in CH_3CN (15 mL) was added $MnCl_2 \bullet 4H_2O$ (0.106 g, 0.53 mmol). Addition of Et_3N (0.10 mL), solution color immediately turned to reddish brown. The homogeneous solution was then heated to reflux for 8 h. After filtration at room temperature the filtrate was kept for slow evaporation which provided yellow crystalline solid of desired product **4** suitable for single crystal X–ray crystallography.

Yield: 0.110 g, 69%.

FTIR (KBr pellet, cm^{-1}): 3318, 2961, 2902, 2866, 2226, 1626, 1576, 1484, 1438, 1361, 1319, 1287, 1246, 860, 774, 723.

^{1}H NMR ($CDCl_3$, 399.85 MHz): δ 1.20–1.25 (m, 9H), 1.32–1.37 (m, 9H), 5.82 (s, 1H), 6.42 (d, J = 1.6 Hz, 1H), 6.56–6.64 (t, J = 1.6 Hz, 1H), 6.78–6.83 (t, J = 1.0 Hz, 2H), 6.85–6.92 (m, 1H) ppm.

^{13}C NMR ($CDCl_3$, 100.75 MHz): δ 30.0, 31.5, 34.6, 34.9, 94.8, 110.3, 116.5, 117.8, 119.1, 120.7, 125.8, 129.4, 136.8, 137.1, 139.4, 144.16, 146.5 ppm.

HR–MS (CH_3CN) *m/z* for $[C_{21}H_{24}N_2O]^+$: Calcd, 320.1889; Found, 320.1640.

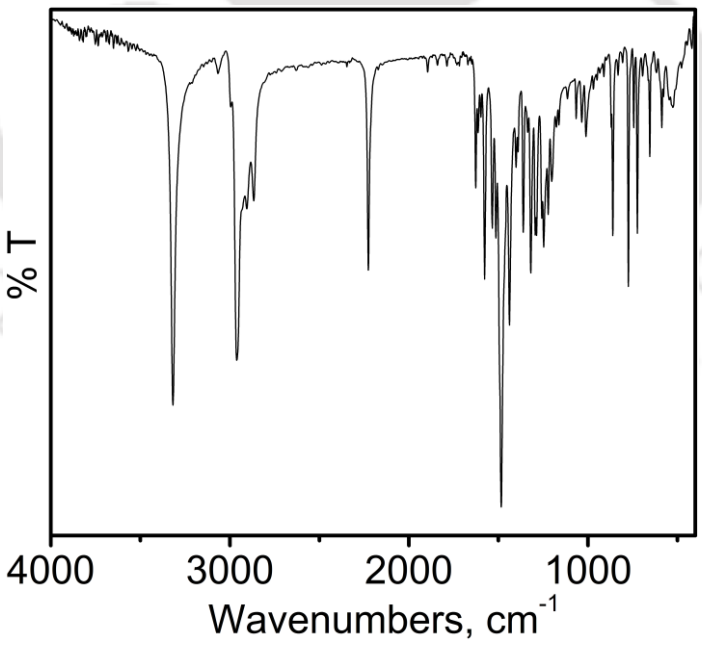

Figure 6.17: *Infrared spectrum of **4**.*

Synthesis of 5:

A recation mixture of $\mathbf{H_2L^{Me}}$ (0.311 g, 1mmol) and $MnCl_2 \bullet 4H_2O$ (0.099 g, 0.5 mmol) and triethylamine (0.2 mL) were refluxed for for 8 h. After cooling to roomtemperature, the resulting reaction mixture was filtered and the residue was washed with acetonitrile. The residue was crystallized from a 3:1 CH_2Cl_2:CH_3CN solvent mixture.

Yield: 0.125 g, 35%.

FTIR (KBr pellet, cm^{-1}): 2955, 2905, 2867, 1576, 1526, 1484, 1459, 1440, 1405, 1363, 1321, 1306, 1251, 1175, 1115, 1031, 891, 720, 610, 544.

ESI–MS (CH_3CN) *m/z* for $[C_{42}H_{54}ClMnN_2O_2]^+$: Calcd, 708.32; Found, 708.48.

ESI–MS (CH_3CN) *m/z* for $[C_{42}H_{54}ClMnN_2O_2 - Cl]^+$: Calcd 673.36; Found, 673.51.

UV–vis/NIR (CH_2Cl_2) λ_{max}, nm (ε, $M^{-1}cm^{-1}$): 820(950); 730(1450); 670(1650); 469(12750); 401(9200); 270(14700).

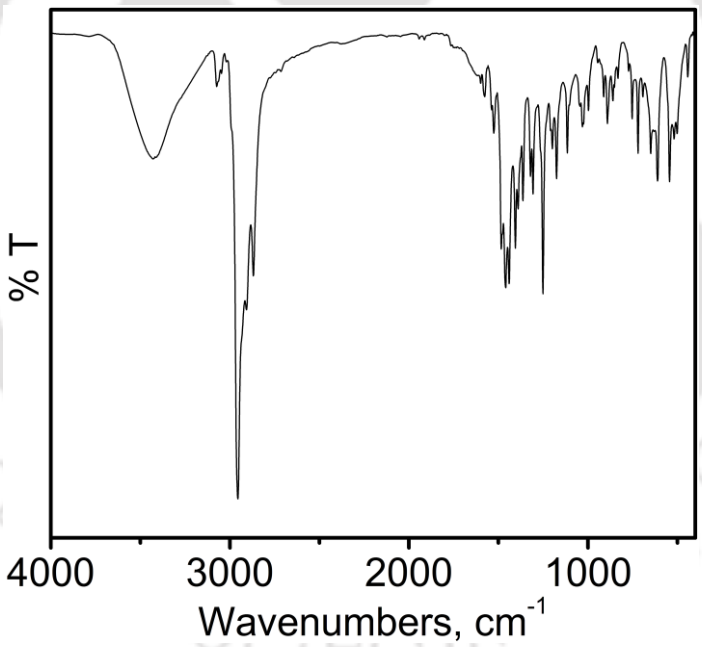

Figure 6.18: *IR spectrum of* ***5****.*

Synthesis of $[Co(L^{CN\bullet})_2Cl]$; 6:

Addition of $CoCl_2 \bullet 6H_2O$ (0.119 g, 0.5 mmol) to a colorless solution of $\mathbf{H_2L^{CN}}$ (0.322 g, 1.0 mmol) in acetonitrile (20 mL) provided a bluish color solution. To it, Et_3N (0.2 mL) was added to the reaction mixture and allowed to stir at room temperature (30 °C) for 2 h. The resulting blue precipitate was then collected through filtration and washed with acetonitrile. The blue solid was recrystallized from 3:1 CH_2Cl_2:CH_3CN solvent mixture by slow solvent evaporation that provided X–ray quality single crystal.

Yield: 0.300 g, 71%.

FTIR (KBr pellet, cm^{-1}): 2957, 2908, 2868, 2228, 1590, 1522, 1479, 1463, 1366, 1310, 1263, 1230, 1203, 1178, 1099, 1025, 996, 912, 856, 758, 735, 650, 616, 538, 510.

^{1}H NMR ($CDCl_3$, 399.85 MHz): δ 1.08 (s, 18H), 1.17 (s, 18H), 7.25 (s, 2H), 7.7 (s, 6H), 8.50–8.56 (m, 4H) ppm.

ESI–MS (CH_3CN) *m/z* for $[C_{42}H_{48}ClCoN_4O_2]^+$: Calcd, 734.28; Found, 734.78;

ESI–MS (CH_3CN) *m/z* for $[C_{42}H_{48}ClCoN_4O_2 - Cl]^+$: Calcd, 699.31; Found, 699.78.

Anal. Calcd for $C_{42}H_{48}ClCoN_4O_2$: C, 68.61; H, 6.58; N, 7.62. Found: C, 68.55; H, 6.38; N, 8.18.

UV–vis/NIR (CH_2Cl_2) λ_{max}, nm (ε, $M^{-1}cm^{-1}$): 892 (12050), 827 (10950), 668 (20500), 510 (5100), 340 (12100).

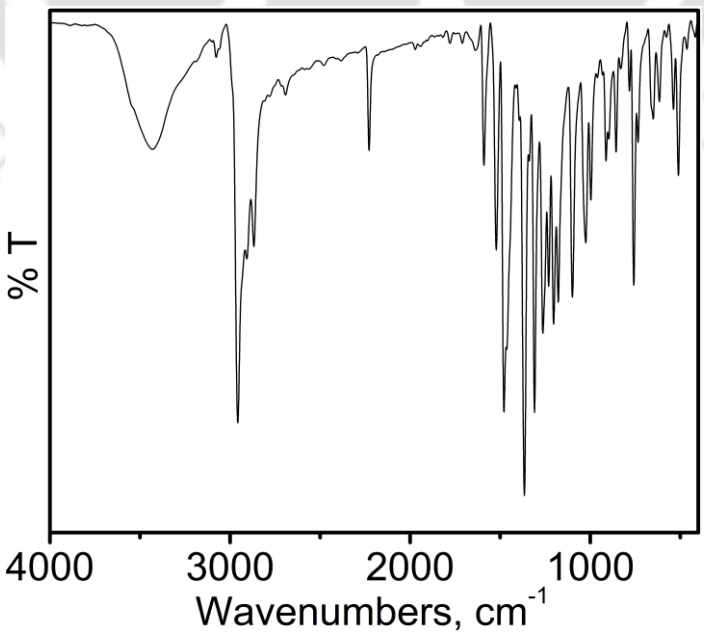

Figure 6.19: *Infrared spectrum of* $[Co(L^{CN\bullet})_2Cl]$*; 6.*

Synthesis of $[Ni(L^{CN\bullet})_2]$; 7:

An acetonitrile solution (15 mL) of $\mathbf{H_2L^{CN}}$ (0.200 g, 0.62mmol), $NiCl_2\bullet 6H_2O$ (0.076 g, 0.32 mmol) and Et_3N (0.2 mL) was heated at reflux for 4 h. After cooling to room temperature (30 °C), it was further stirred at this condition for 1 h, which caused a green precipitation. Then the resulting reaction mixture was filtered and washed with acetonitrile to get a green solid. The green solid was then recrystallized by slow solvent evaporation from CH_2Cl_2:CH_3CN (2:1) solvent mixture that provided microcrystalline compound suitable for single crystal X–ray study.

Yield: 0.072 g, 35%.

FTIR (KBr pellet, cm^{-1}): 2955, 2906, 2867, 2225, 1590, 1526, 1479, 1440, 1382, 1361, 1325, 1291, 1260, 1230, 1201, 1175, 1108, 1030, 1001, 920, 856, 766, 738, 668, 541, 511.

^{1}H NMR ($CDCl_3$, 399.85 MHz): δ 1.02 (s, 18H), 1.09 (s, 18H), 6.22 (s, 2H), 6.91 (s, 2H), 7.53 (t, J = 7.6 Hz, 2H), 7.62–7.71 (m, 2H)), 7.74–7.81 (m, 4H).

ESI–MS (CH_3CN) *m/z* for $[C_{42}H_{48}N_4NiO_2]^+$: Calcd, 698.31; Found, 698.82.

Anal. Calcd for $C_{42}H_{48}N_4NiO_2\bullet 0.5CH_3CN$: C, 71.80; H, 6.93; N, 8.75. Found: C, 72.14; H, 6.37; N, 8.75.

UV–vis/NIR (CH_2Cl_2) λ_{max}, nm (ε, $M^{-1}cm^{-1}$): 906(33350), 593(2100), 376 (6250).

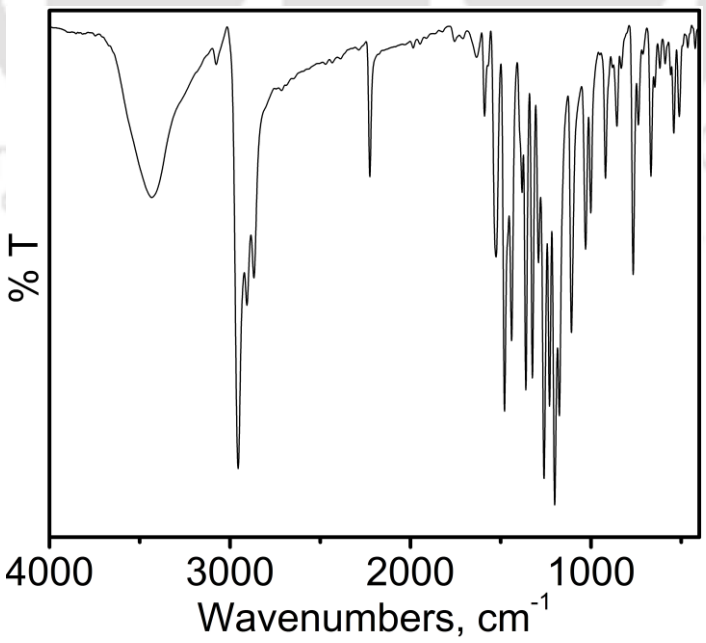

Figure 6.20: *Infrared spectrum of $[Ni(L^{CN\bullet})_2]$; 7.*

Synthesis of $[CuL^{CN\bullet}_2]$; 8:

To a stirred solution of $\mathbf{H_2L^{CN}}$ (0.322 g, 1 mmol), $CuCl_2 \bullet 2H_2O$ (0.086 g, 0.5 mmol) and Et_3N (0.2 mL) were added sequentially. The resulting reaction mixture was stirred at room temperature for 2 h under air. This caused a green precipitation which was collected through filtration. The residue was recrystallized from 3:1 dichloromethane:acetonitrile solvent mixture by slow solvent evaporation that led to the crystalline compound suitable for the single crystal X–ray diffraction study.

Yield: 0.207 g, 58%.

FTIR (KBr pellet, cm^{-1}): 2957, 2907, 2868, 2223, 1584, 1566, 1518, 1479, 1444, 1417, 1386, 1358, 1134, 1272, 1254, 1207, 1176, 1110, 1029, 996, 914, 856, 826, 646, 517.

ESI–MS (CH_3CN) *m/z* for $[C_{42}H_{48}CuN_4O_2]^+$: Calcd, 703.32; Found, 703.12.

Anal. Calcd for $C_{42}H_{48}CuN_4O_2 \bullet 0.4CH_3CN$: C, 71.31; H, 6.88; N, 8.55. Found: C, 71.42; H, 6.71; N, 8.53.

UV–vis/NIR (CH_2Cl_2) λ_{max}, nm (ε, $M^{-1}cm^{-1}$): 1015(3300), 803(8650), 360(14500).

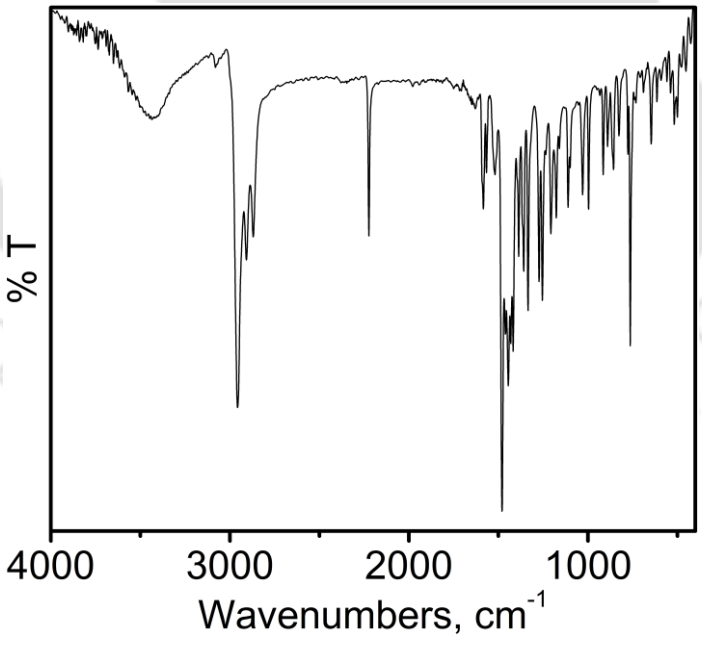

Figure 6.21: *Infrared spectrum of* ***8****.*

Synthesis of [{$C_{42}H_{56}CoN_4O_2$}Cl•H_2O•CH_3CN]; 9•H_2O•CH_3CN:

The ligand $H_4L^{CH_2NH_2}$ (0.163 g, 0.5 mmol) was taken in acetonitrile (15 mL). To this solution $CoCl_2$•$6H_2O$ (0.120 g, 0.5 mmol) and Et_3N (0.2 mL) were added sequentially. The resulting reaction mixture was then stirred for 1.5 h at room temperature (30 °C). During this period a brown color solid was precipitated out. The solid was filtered, washed with acetonitrile and air dried. Single crystals were grown from a dichloromethane:acetonitrile (3:1) solution of the solid by slow solvent evaporation technique.

Yield: 0.125 g, 62%.

FTIR (KBr pellet, cm^{-1}): 3619, 3456, 3399, 3227, 3115, 3066, 2952, 2905, 2867, 1625, 1583, 1569, 1523, 1478, 1462, 1432, 1412, 1385, 1363, 1325, 1258, 1238, 1205, 1179, 1112, 1028, 998, 914, 755.

ESI–MS (CH_3CN) *m/z* for $[C_{42}H_{56}CoN_4O_2]^+$: Calcd, 707.37; Found, 707.80.

Anal. Calcd for $[C_{42}H_{56}CoN_4O_2]Cl$•1.5H_2O: C, 65.48; H, 7.72; N, 7.27. Found: C, 65.21; H, 7.71; N, 7.42.

UV–vis/NIR (CH_2Cl_2) λ_{max}, nm (ε, $M^{-1}cm^{-1}$): 1182(850), 875(1700), 480(8550).

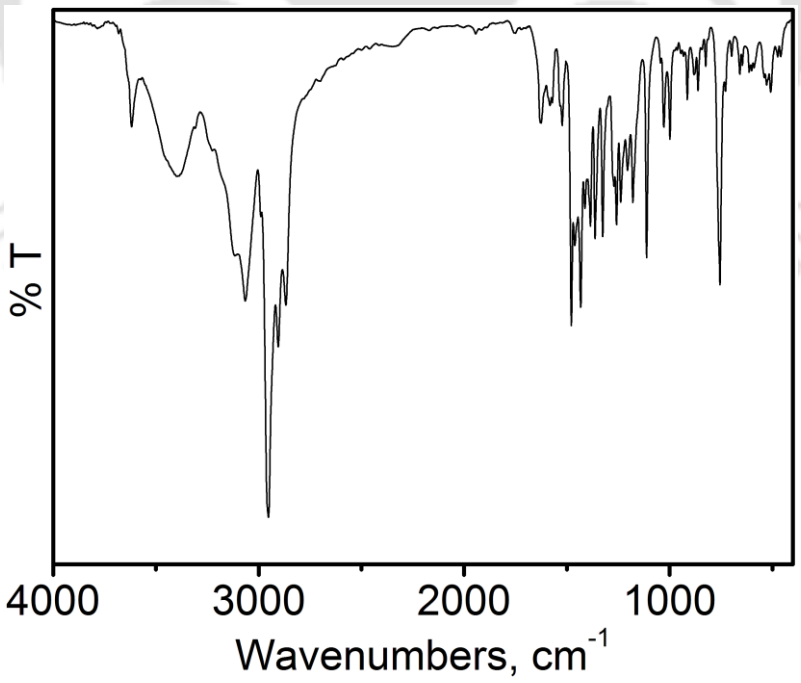

Figure 6.22: *Infrared spectrum of* ***9****.*

Synthesis of $[C_{28}H_{31}N_3NiO]$; 10:

Ligand $\mathbf{H_4L^{CH_2NH_2}}$ (0.326 g, 1.00 mmol) was treated with $NiCl_2 \bullet 6H_2O$ (0.239 g, 1 mmol) in acetonitrile (15 mL) in the presence of triethylamine (0.2 mL). The resulting reaction mixture was allowed to reflux for 3 h. After cooling to room temperature (30 °C), it was further stirred for 1.5 h. After that, the reaction mixture was filtered and washed with acetonitrile to get a red solid. Solid residue was recrystallized from CH_2Cl_2:CH_3CN (3:1) solvent mixture.

Yield: 0.065 g, 27%.

FTIR (KBr pellet, cm^{-1}): 3346, 3056, 2945, 2900, 2860, 1617, 1599, 1560, 1530, 1476, 1446, 1414, 1342, 1326, 1290, 1264, 1221, 1178, 1154, 1121, 850, 834, 746, 730, 677, 538, 457.

^{1}H NMR ($CDCl_3$, 399.85 MHz): δ 1.35 (s, 9H), 1.49 (s, 9H), 5.97 (s, 1H), 6.51 (t, J = 7.2 Hz, 1H), 7.03 (d, J = 8.4 Hz, 1H), 7.15 (t, J = 6.8 Hz, 1H), 7.18 (s, 1H), 7.40 (t, J = 7.6 Hz, 2H), 7.46 (s, 1H), 7.55 (t, J = 7.8 Hz, 1H), 7.69 (d, J = 8.0 Hz, 1H), 7.82 (d, J = 7.6 Hz, 1H), 8.56 (s, 1H), 8.73 (s, 1H) ppm.

ESI–MS (CH_3CN) *m/z* for $[C_{28}H_{31}N_3NiO + H]^+$: Calcd, 484.19; Found, 484.20.

UV–vis/NIR (CH_2Cl_2) λ_{max}, nm (ε, $M^{-1}cm^{-1}$): 518(25100), 390(40200), 326(42050).

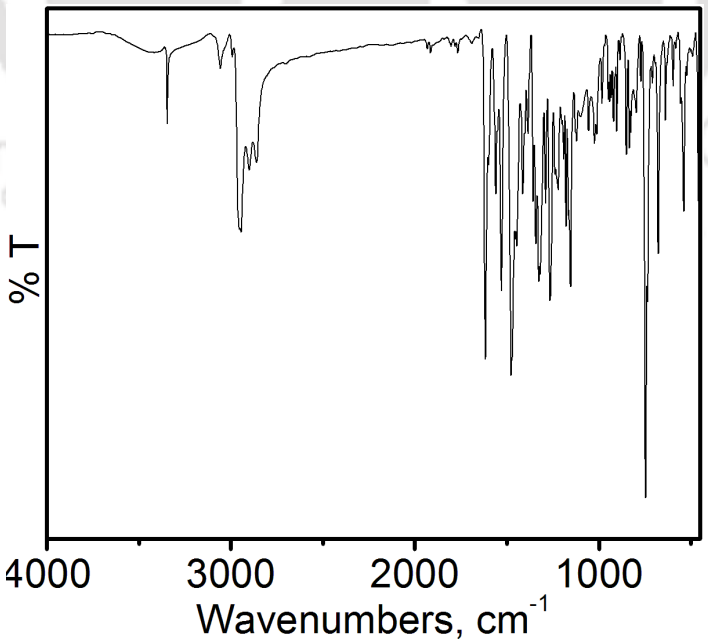

Figure 6.23: *Infrared spectrum of **10**.*

Synthesis of $[C_{28}H_{31}CuN_3O]$; 11:

Upon addition of $CuCl_2 \bullet 2H_2O$ (0.175 g, 1.02 mmol) to an acetonitrile solution (15 mL) of $\mathbf{H_4L^{CH_2NH_2}}$ (0.326 g, 1.00 mmol), the color of the solution immediately turned brown. An addition of Et_3N (0.2 mL) to the solution, a white smoke appeared. The resulting reaction mixture was then heated at reflux for 3 h. After cooling to room temperature, it was further stirred for 1.5 h under air. Then the reaction mixture was filtered and washed with acetonitrile to obtain a red color solid. The red solid was dissolved in a 5:1:1 CH_2Cl_2:CH_3CN:MeOH solvent mixture and by slow solvent evaporation of the mixture needle shaped microcrystalline complex suitable for single crystal X–ray diffraction study precipitated out.

Yield: 0.090 g, 38%.

FTIR (KBr pellet, cm^{-1}): 3350, 3058, 2950, 2902, 2863, 1616, 1571, 1559, 1526, 1474, 1454, 1445, 1414, 1383, 1345, 1311, 1272, 1167, 1156, 854, 829, 777, 747, 679, 534, 515,483, 456.

ESI–MS (CH_3CN) *m/z* for $[C_{28}H_{31}CuN_3O + H]^+$: Calcd, 489.19; Found, 489.17.

Anal. Calcd for $C_{28}H_{31}CuN_3O \bullet 0.25CH_3CN$: C, 68.55; H, 6.41; N, 9.12. Found: C, 69.03; H, 6.21; N, 9.37.

UV–vis/NIR (CH_2Cl_2) λ_{max}, nm (ε, $M^{-1}cm^{-1}$): 662(950), 500(26400), 400(13700), 365(21400).

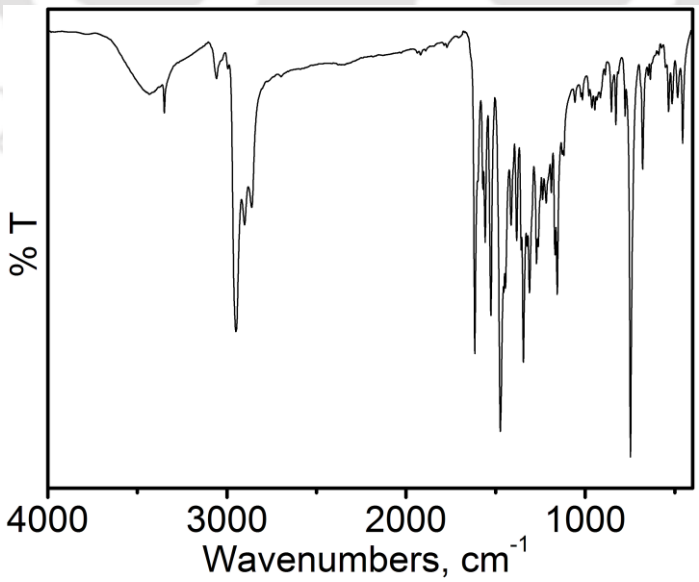

Figure 6.24: *Infrared spectrum of* ***11****.*

Synthesis of $[C_{56}H_{60}N_4O_4Zn_2]$; 12:

Ligand **H_3L1** (0.162 g, 0.5 mmol) and salicylaldehyde (0.061 g, 0.5 mmol) in acetonitrile (10 mL) were stirred at room temperature (30 °C) for 4 h in the presence of $Zn(OAc)_2 \bullet 2H_2O$ (0.110 g, 0.5 mmol) and triethylamine (0.1 mL). This caused precipitation of an orange solid. The resulting solid was filtered and washed with acetonitrile. Recrystallization of the solid from a CH_2Cl_2:CH_3CN (3:1) solvent mixture by slow solvent evaporation technique resulted block shape orange crystals, which were suitable for the single crystal X–ray diffraction analysis.

Yield: 0.147 g, 64%.

FTIR (KBr pellet, cm^{-1}): 2955, 2900, 2862, 1610, 1589, 1566, 1529, 1460, 1440, 1388, 1357, 1276, 1257, 1246, 1218, 1177, 1146, 974, 855, 825, 777, 754.

^{1}H NMR ($CDCl_3$, 399.85 MHz): δ 1.17 (s, 18H), 1.36 (s, 18H), 6.33 (d, *J* = 2 Hz, 2H), 6.46 (t, *J* = 7.4 Hz, 2H), 6.58 (t, *J* = 4.6 Hz, 2H), 6.75 (d, *J* = 8 Hz, 2H), 6.98 (dd, *J* = 8 Hz and 1.6 Hz, 2H), 7.06 (d, *J* = 2.4 Hz, 2H), 7.24 (m, 6H), 7.47 (t, *J* = 4.6 Hz, 2H), 7.82 (s, 2H), 8.04 (s, 2H).

ESI–MS (CH_3CN) *m/z* for $[C_{56}H_{60}N_4O_4Zn_2 + H]^+$: Calcd, 985.33; Found, 985.47.

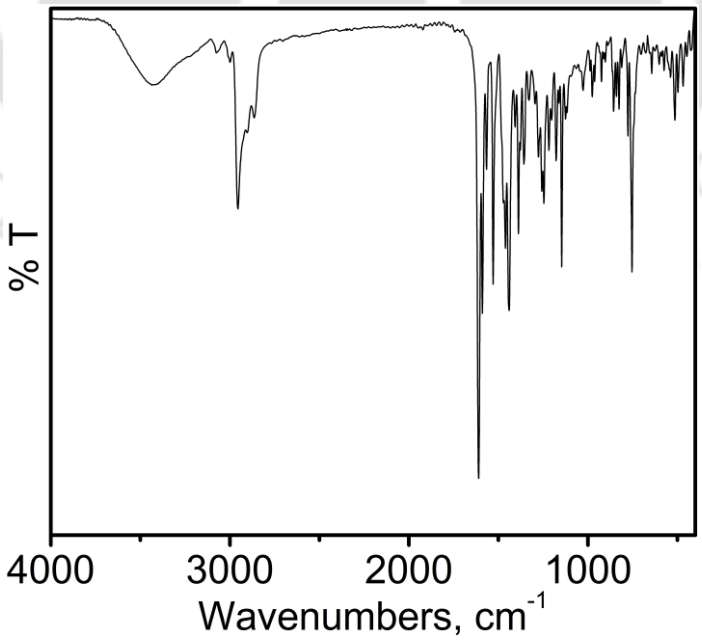

Figure 6.25: *Infrared spectrum of* ***12****.*

Synthesis of $[C_{28}H_{31}ClFeN_2O_2]$; 13:

$H_3L^{Mixed(H)}$ (0.215 g, 0.5 mmol) was treated with $FeCl_3$ (0.082 g, 0.5 mmol) in the presence of triethyamine (0.1 mL) in acetonitrile (10 mL) and stirred for 2 h under air. This caused a green color precipitation. Reaction mixture was then filtered to obtain the solid residues. The residue was recrystallized from a (3:1) CH_2Cl_2:CH_3CN solvent mixture by slow solvent evaporation to get a crystalline complex.

Yield: 0.080 g, 31%.

FTIR (KBr pellet, cm^{-1}): 2955, 2908, 2865, 1612, 1595, 1541, 1481, 1465, 1443, 1394, 1364, 1330, 1303, 1255, 1212, 1177, 1145, 1125, 1024, 994, 904, 858, 813, 765, 758, 619, 605, 491.

ESI–MS (CH_3CN) *m/z* for $[C_{28}H_{31}ClFeN_2O_2]^+$: Calcd, 518.14; Found, 518.52.

ESI–MS (CH_3CN) *m/z* for $[C_{28}H_{31}ClFeN_2O_2 – Cl]^+$: Calcd, 483.17; Found, 483.53.

Anal. Calcd for $C_{28}H_{31}ClFeN_2O_2$: C, 64.82; H, 6.02; N, 5.40. Found: C, 64.51; H, 6.15; N, 5.60.

UV–vis/NIR (CH_2Cl_2) λ_{max}, nm (ε, $M^{-1}cm^{-1}$): 950(2250), 730(6850), 530(5400).

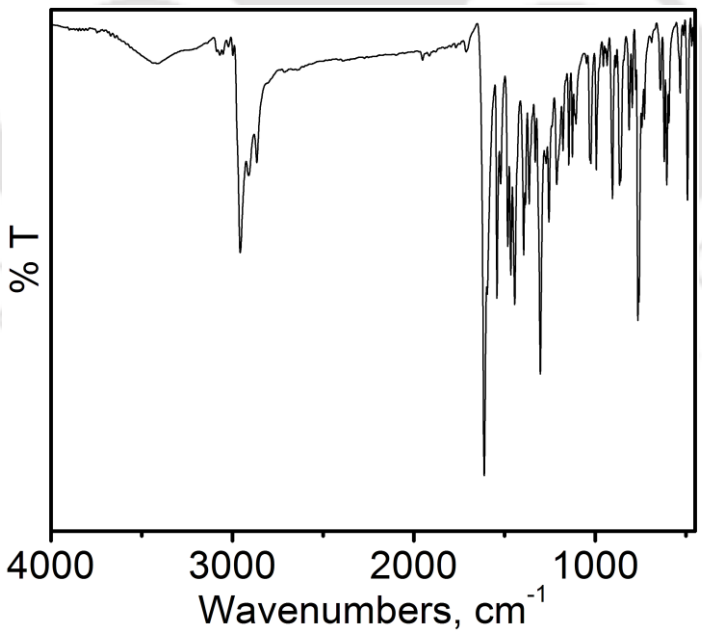

Figure 6.26: *IR spectrum for **13**.*

Synthesise of $[C_{36}H_{47}ClFeN_2O_2]$; 14:

An acetonitrile solution (15 mL) of $\mathbf{H_4L^{CH_2NH_2}}$ (0.326 g, 1 mmol) and 3,5–di–*tert*–butylsalicyaldehyde (0.234 g, 1 mmol) was heated at reflux for 3 h. Then, it was cooled down to room temperature (30 °C), anhydrous $FeCl_3$ (0.163 g, 1 mmol) and Et_3N (0.2 mL) were added sequentially and allowed to stir the resulting mixture for 3 h at room temperature. The resulted green color precipitate was collected through filtration and washed thoroughly with acetonitrile properly. Recrystallization of this green solid from a 4:1 CH_2Cl_2:CH_3CN solvent mixture led to the block shaped crystalline compound suitable for single crystal X–ray analysis was obtained.

Yield: 0.274 g (44%).

FTIR (KBr pellet, cm^{-1}): 2958, 2905, 2866, 1612, 1538, 1482, 1465, 1434, 1406, 1391, 1363, 1309, 1272, 1255, 1199, 1172, 1024, 994, 931, 910, 862, 838, 812, 784, 750, 642,606, 537, 500.

ESI–MS (CH_3CN) *m/z* for $[C_{36}H_{47}ClFeN_2O_2]^+$: Calcd, 630.27; Found, 630.75.

ESI–MS (CH_3CN) *m/z* for $[C_{36}H_{47}ClFeN_2O_2 - Cl]^+$: Calcd, 595.30; Found, 595.74.

Anal. Calcd for $[C_{36}H_{47}ClFeN_2O_2]$: C, 68.52; H, 7.51; N, 4.44. Found: C, 68.76; H, 7.25; N, 4.43.

UV–vis/NIR (CH_2Cl_2) λ_{max}, nm (ε, M^{-1}cm^{-1}): 950(2250), 690(8350), 530(6200).

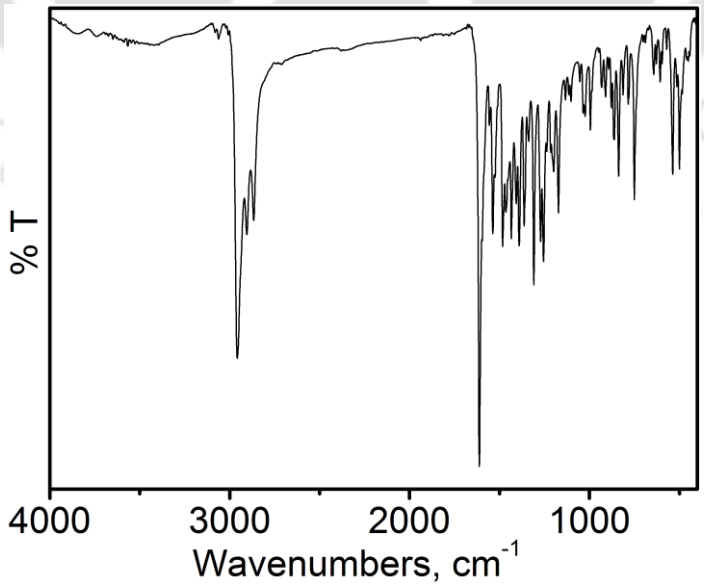

Figure 6.27: *IR spectrum for* ***14****.*

Synthesis of $[C_{28}H_{31}N_2NiO_2]$; 15:

To a methanolic (10 mL) solution of $\mathbf{H_3L^{Mixed(H)}}$ (0.215 g, 0.5 mmol), $NiCl_2 \bullet 6H_2O$ (0.125 g, 0.52 mmol), and Et_3N (0.1 mL) were added, sequentially. The resulting reaction mixture was allowed to reflux for 1 h. After cooling, it was further stirred for 5 h at room temperature (30 °C). This caused precipitation of a green solid. It was filtered and washed with MeOH (15 mL). Recrystallization from a 1:1 CH_2Cl_2:EtOH solvent mixture provided needle shaped microcrystalline compound which was suitable for single crystal X–ray diffraction study.

Yield: 0.125 g, 51%.

FTIR (KBr pellet, cm^{-1}): 3434, 2960, 2944, 2903, 2868, 1612, 1536, 1475, 1452, 1432, 1399, 1385, 1353, 1325, 1257, 1212, 1175, 1148, 1115, 1026, 911, 865, 857, 770, 758, 739, 646, 494.

ESI–MS (CH_3CN) *m/z* for $[C_{28}H_{31}N_2NiO_2]^+$: Calcd, 485.17; Found. 485.10.

Anal. Calcd for $C_{28}H_{31}N_2NiO_2 \bullet 0.6H_2O$: C, 67.74; H, 6.54; N, 5.64. Found: C, 67.59; H, 6.14; N, 5.30.

UV–vis/NIR (CH_2Cl_2) λ_{max}, nm (ε, $M^{-1}cm^{-1}$): 1100(1300), 790(4100), 630(1950), 500(1950), 385(12900), 365(11100)^{sh}, 300(10700).

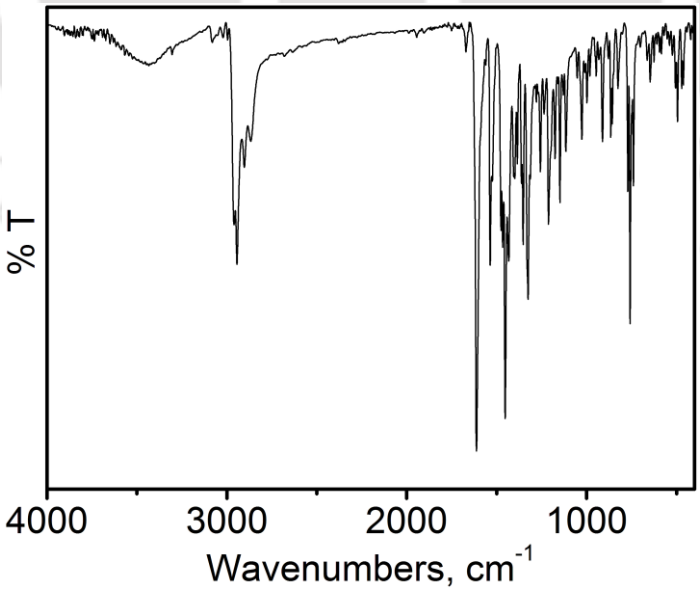

Figure 6.28: *IR spectrum for **15**.*

Synthesis of $[C_{36}H_{47}N_2NiO_2]$; 16:

$H_4L^{CH_2NH_2}$ (0.326 g, 1 mmol) and 3,5–di–*tert*–butylsalicylaldehyde (0.234 g, 1 mmol) were added in CH_3CN (20 mL) and the solution was allowed to reflux for 3 h. $NiCl_2 \bullet 6H_2O$ (0.240 g, 1.01 mmol) and Et_3N (0.3 mL) were added to the solution at room temperature, and the resulting solution was then allowed to reflux for 2 h. After that, 1 h room temperature stirring provided complex **16** as blue green solid. Filtered and washed with CH_3CN. Solid was then dissolved in CH_2Cl_2 (20 mL) and filtered to discard undissolved particles. Solvent was removed. The resulting solid was dried under vacuum and kept under argon. Single crystal suitable for X–ray diffraction study was obtained by recrystallization of the solid in a 2:1 Et_2O:CH_3CN solvent mixture.

Yield: 0.240 g, 40%.

FTIR (KBr pellet, cm^{-1}): 2957, 2946, 2901, 2862, 1611, 1534, 1476, 1451, 1438, 1326, 1257, 1237, 1201, 1176, 753.

ESI–MS (CH_3CN) *m/z* for $[C_{36}H_{47}N_2NiO_2]^+$: Calcd, 597.30; Found, 597.19.

Anal. Calcd for $C_{36}H_{47}N_2NiO_2 \bullet 0.1H_2O$: C, 72.03; H, 7.92; N, 4.66. Found: C, 71.13; H, 7.84; N, 4.64.

UV–vis/NIR (CH_2Cl_2) λ_{max}, nm (ε, $M^{-1}cm^{-1}$): 1180(1800), 835(5500), 625(2550), 520(2150), 385(15450), 365(12000)^{sh}.

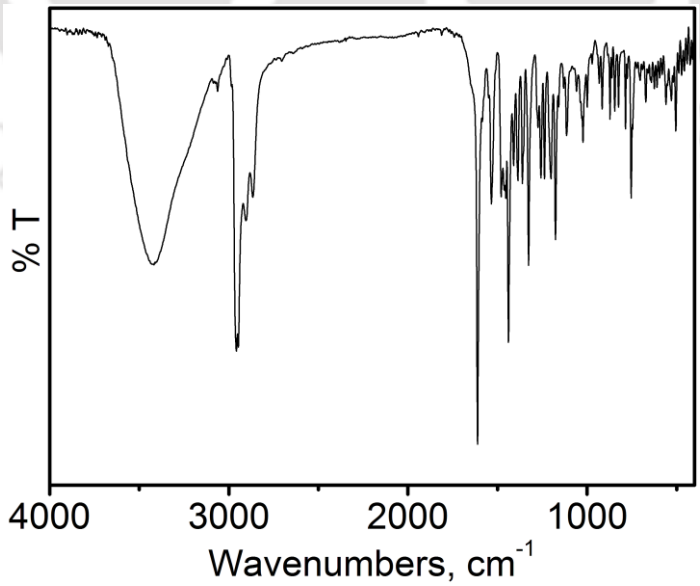

Figure 6.29: *IR spectrum for **16**.*

Synthesis of $[C_{36}H_{45}N_2NiO_3]$; 16a:

Complex **16** (0.100 g, 0.167 mmol) was dissolved in a 5:1:1 CH_2Cl_2:CH_3CN:EtOH solvent mixture and allowed for slow solvent evaporation for three days. During the time brown color crystalline compound, suitable for X–ray diffraction single crystal study, was obtained.

Yield: 0.097 g, 95%.

FTIR (KBr pellet, cm^{-1}): 2959, 2948, 2904, 2866, 1661, 1620, 1560, 1530, 1474, 1431, 1350, 1334, 1292, 1198, 1183, 1112, 1056, 1020, 1003, 915, 753.

ESI–MS (CH_3CN) *m/z* for $[C_{36}H_{45}N_2NiO_3]^+$: Calcd, 611.28; Found, 611.18.

Anal. Calcd for $C_{36}H_{45}N_2NiO_3$: C, 70.60; H, 7.41; N, 4.57. Found: C, 70.42; H, 7.36; N, 4.48.

UV–vis/NIR (CH_2Cl_2) λ_{max}, nm (ε, $M^{-1}cm^{-1}$): 1200(1900), 810(4300), 645(3150), 485(10800), 450(10200)^{sh}, 385(21500), 300(32550).

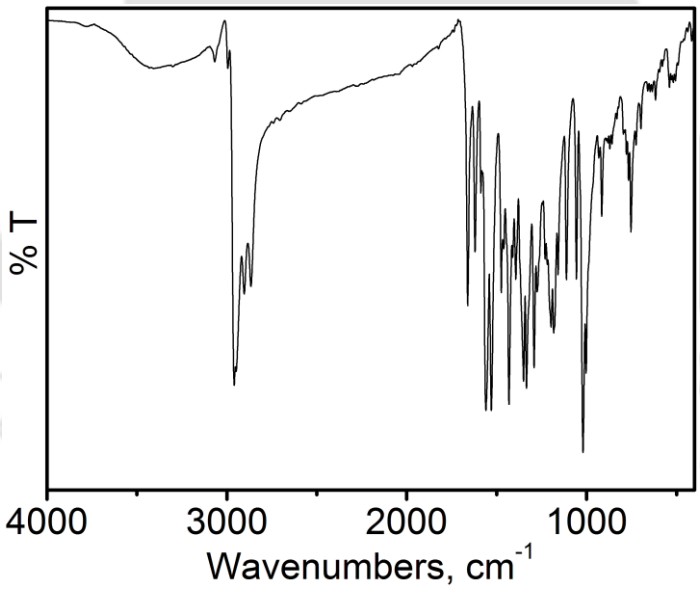

Figure 6.30: *IR spectrum for **16a**.*

Synthesis of $[C_{28}H_{31}CuN_2O_2]$; 17:

$CuCl_2 \bullet 2H_2O$ (0.086 g, 0.5 mmol) was added to an acetonitrile solution (10 mL) of $H_3L^{Mixed(H)}$ (0.215 g, 0.5 mmol). After addition of triethylamine (0.1 mL), the resulting solution was stirred for 2 h at room temperature (30 °C) under air. This led to the formation of a brown color precipitate. The solid was collected by filtration and washed with acetonitrle.

Yield: 0.123 g, 50%.

FTIR (KBr pellet, cm^{-1}): 2955, 2946, 2906, 2868, 1626, 1600, 1534, 1476, 1465, 1450, 1427, 1396, 1349, 1324, 1256, 1195, 1148, 1028, 993, 911, 860, 760, 741.

ESI–MS (CH_3CN) *m/z* for $[C_{28}H_{31}CuN_2O_2]^+$: Calcd, 490.17; Found, 490.36.

Anal. Calcd for $C_{28}H_{31}CuN_2O_2$: C, 68.48; H, 6.36; N, 5.70. Found: C, 68.61; H, 6.30; N, 5.72.

UV–vis/NIR (CH_2Cl_2) λ_{max}, nm (ε, $M^{-1}cm^{-1}$): 970(1800), 845(2900), 540(3400).

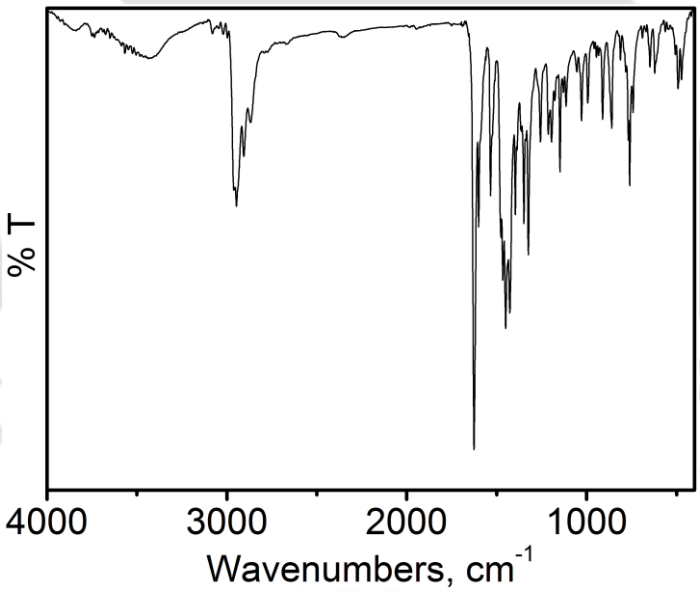

Figure 6.31: *IR spectrum for **17**.*

Synthesis of $[C_{36}H_{47}CuN_2O_2]$; 18:

A solution of $\mathbf{H_4L^{CH_2NH_2}}$ (0.326 g, 1 mmol) and 3,5–di–*tert*–butylsalicyaldehyde (0.234 g, 1 mmol) in CH_3CN (15 mL) was heated at reflux for 3 h. After cooling to room temperature, $CuCl_2 \bullet 2H_2O$ (0.172 g, 1 mmol) and Et_3N (0.2 mL) were added sequentially. Then, the resulting reaction mixture was stirred for 6 h at room temperature (30 °C). A brown precipitate of **18** was appeared. The precipitate was filtered and washed thoroughly with CH_3CN.

Yield: 0.300 g, 50%.

The resulting residue was recrystallized from a (4:1) CH_2Cl_2:CH_3CN solvent mixture by slow solvent evaporation. This provided two distinct kinds of crystalline compounds, those were separated manually. The block shaped crystalline compound was isolated as a major product.

Yield: 0.240 g, 40%.

FTIR (KBr pellet, cm^{-1}): 2959, 2903, 2862, 1619, 1583, 1530, 1479, 1438, 1429, 1390, 1353, 1329, 1256, 1200, 1168, 912, 875, 840, 752, 502.

ESI–MS (CH_3CN) *m/z* for $[C_{36}H_{47}CuN_2O_2]^+$: Calcd, 602.29; Found, 602.53.

Anal. Calcd for $C_{36}H_{47}CuN_2O_2$: C, 71.67; H, 7.85; N, 4.64. Found: C, 71.64; H, 7.65; N, 4.53.

UV–vis/NIR (CH_2Cl_2) λ_{max}, nm (ε, $M^{-1}cm^{-1}$): 970(1800), 845(2900), 540(3050).

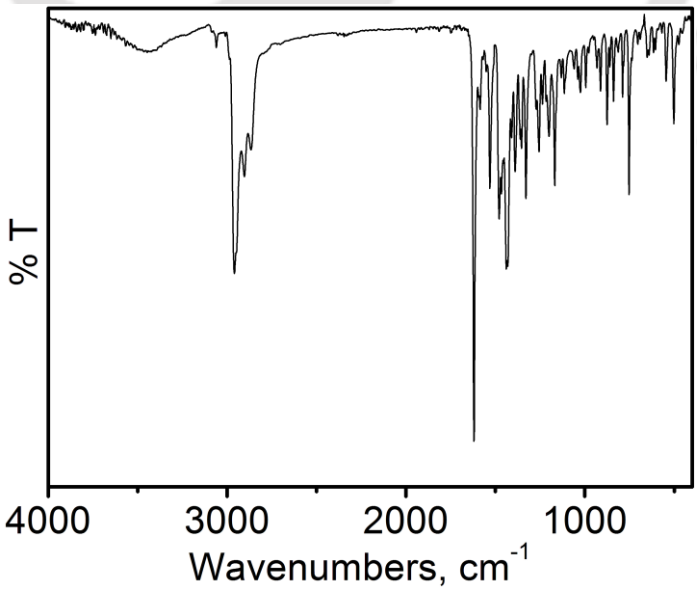

Figure 6.32: *IR spectrum for **18**.*

Synthesis of $[C_{36}H_{45}CuN_2O_3]$; 18a:

The recrystallization of complex **18** (0.300 g, 0.5 mmol) from a (5:1) CH_2Cl_2:CH_3CN solvent mixture provided the complex **18a** as needle shaped microcrystalline solid, suitable for single crystal X–ray diffraction study. The procedure was followed thrice.

Yield: 0.125 g, 40%.

FTIR (KBr pellet, cm^{-1}): 3441, 2960, 2948, 2903, 2863, 1657, 1621, 1557, 1528, 1474, 1438, 1349, 1326, 1288, 1217, 1195, 1173, 1159, 1111, 1024, 1002, 913, 767, 753.

ESI–MS (CH_3CN) *m/z* for $[C_{36}H_{45}CuN_2O_3]$: Calcd, 616.28; Found, 616.54.

Anal. Calcd for $[C_{36}H_{45}CuN_2O_3]$: C, 70.05; H, 7.35; N, 4.54. Found: C, 70.32; H, 7.14; N, 4.34.

UV–vis/NIR (CH_2Cl_2) λ_{max}, nm (ε, $M^{-1}cm^{-1}$): 1100(800), 800(1950), 460(6800).

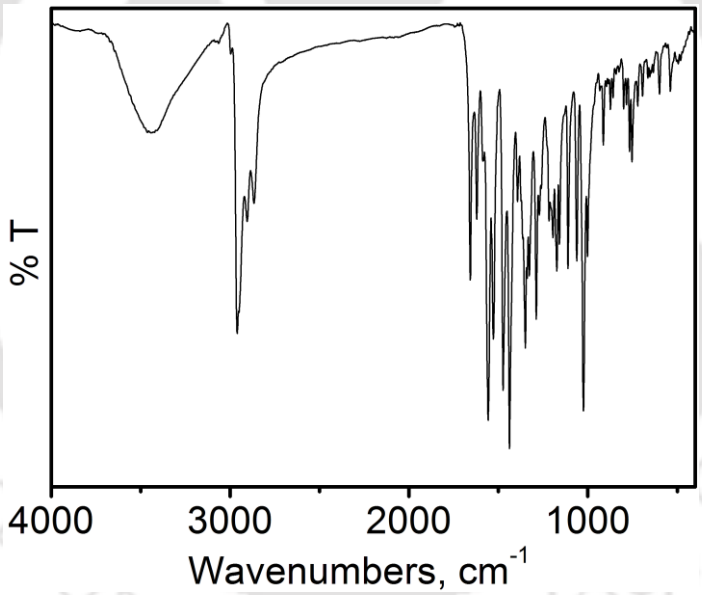

Figure 6.33: *IR spectrum for **18a**.*

Synthesis of $[C_{42}H_{54}CoN_2O_2]$; 19:

Ligand $\mathbf{H_2L^{Me}}$ (0.312 g, 1 mmol) was taken in acetonitrile (10 mL). $CoCl_2 \bullet 6H_2O$ (0.239 g, 1 mmol) and Et_3N (0.2 mL) were added to the solution and allowed to stir for 1 h under air. The resulting reaction mixture was filtered and washed with acetonitrile to obtain green solid. X–ray quality single crystals of the green solid were obtained by slow evaporation of the solid from its 5:1 ether:acetonitrile solvent mixture.

Yield: 0.282 g, 83%.

FTIR (KBr pellet, cm^{-1}): 2954, 2901, 2862, 1537, 1478, 1458, 1358, 1301, 1258, 1181, 1146, 1107, 1026, 912, 896, 856, 754, 738, 658, 517.

ESI–MS (CH_3CN) *m/z* for $[C_{42}H_{54}CoN_2O_2]^+$: Calcd, 677.35; Found, 677.44.

UV–vis/NIR (CH_2Cl_2) λ_{max}, nm (ε, $M^{-1}cm^{-1}$): 1600(2800), 900(22200), 666(15800).

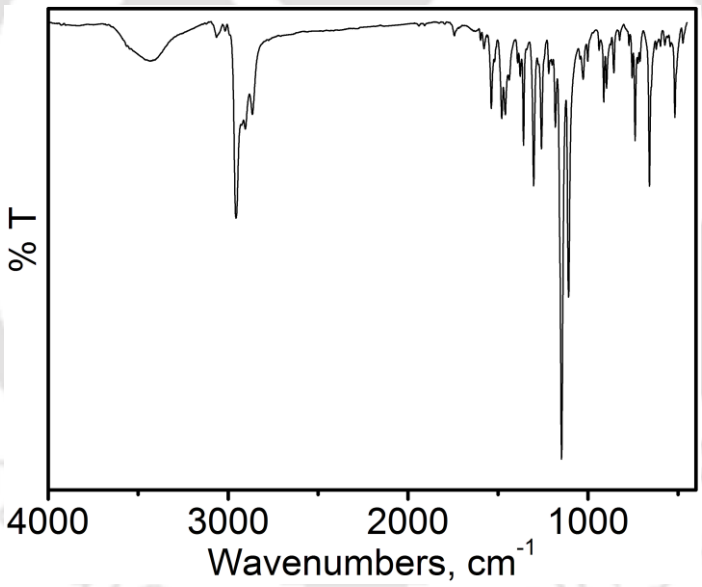

Figure 6.34: *IR spectrum of **19**.*

Synthesis of $[C_{42}H_{54}ClCoN_2O_2]$; 19a:

Complex **19a** was obtained as crystalline compound by recrystallizing the complex **19** (0.138 g, 0.2 mmol) from 5:2 CH_2Cl_2:CH_3CN solvent mixture.

Yield: 0.070 g, 49%.

FTIR (KBr pellet, cm^{-1}): 2955, 2905, 2867, 1586, 1521, 1484, 1460, 1376, 1363, 1308, 1266, 1230, 1206, 1175, 1114, 1096, 1024, 997, 911, 860, 755, 741, 720, 648, 542.

ESI–MS (CH_3CN) *m/z* for $[C_{42}H_{54}ClCoN_2O_2]^+$: Calcd, 712.32; Found, 712.41.

ESI–MS (CH_3CN) *m/z* for $[C_{42}H_{54}ClCoN_2O_2 - Cl]^+$: Calcd, 677.35; Found, 677.44.

UV–vis/NIR (CH_2Cl_2) λ_{max}, nm (ε, $M^{-1}cm^{-1}$): 868(11500); 820(12550); 670(20200).

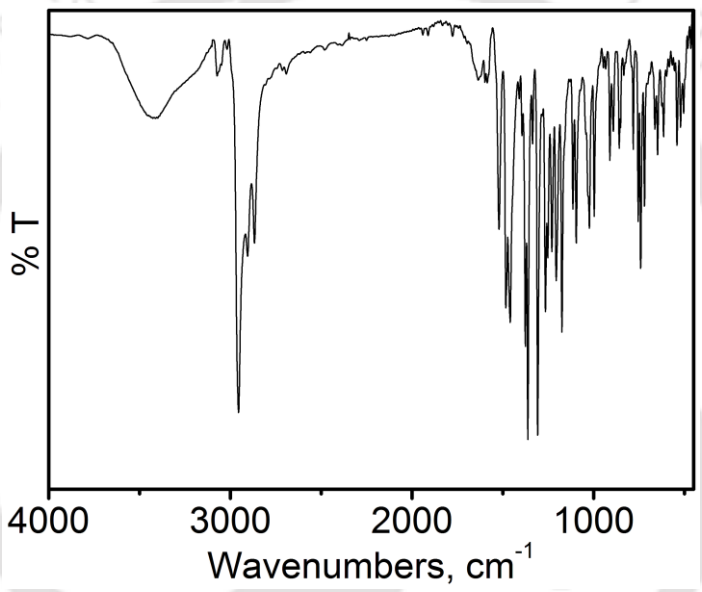

Figure 6.35: *IR spectrum of **19a**.*

Synthesis of $[C_{44}H_{58}CoN_2O_2]$; 20:

The reaction between $\mathbf{H_2L^{Et}}$ (0.326 g, 1 mmol) and $CoCl_2 \bullet 6H_2O$ (0.120 g, 0.5 mmol) in acetonitrile (10 mL) in the presence of triethylamine (0.2 mL) under air for 1 h at room temperature (30 °C) provided a green solid of complex **20**. Slow solvent evaporation of the green solid from a 3:1 ether:acetonitrile solvent mixture provided a microcrystalline solid.

Yield: 0.070 g, 40%.

FTIR (KBr pellet, cm^{-1}): 2956, 2903, 2866, 1579, 1537, 1479, 1460, 1360, 1302, 1259, 1141, 1106, 1028, 1000, 912, 898, 751, 736, 661, 512.

ESI–MS (CH_3CN) *m/z* for $[C_{44}H_{58}CoN_2O_2]^+$: Calcd, 705.38; Found, 705.78.

UV–vis/NIR (CH_2Cl_2) λ_{max}, nm (ε, $M^{-1}cm^{-1}$): 1600(1100); 900(13500); 666(13750).

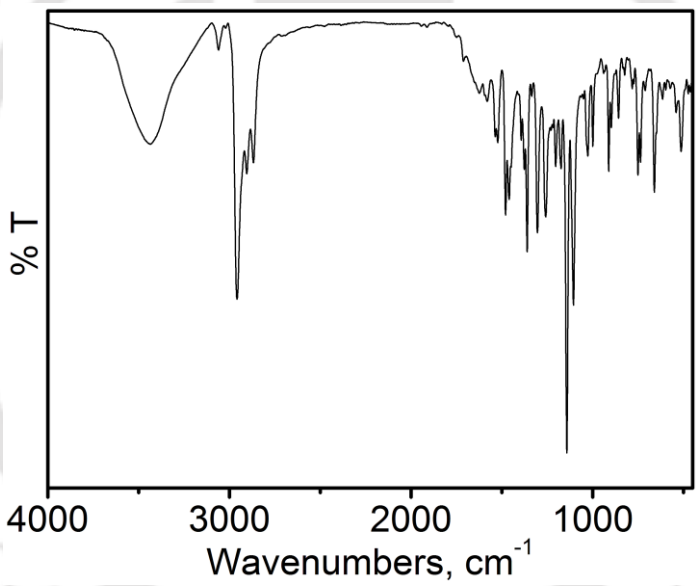

Figure 6.36: *IR spectrum of **20**.*

Synthesis of $[C_{42}H_{58}ClCoN_2O_2]$; 20a:

Complex **20a** was obtained as crystalline compound by recrystallizing the complex **20** from 4:1 CH_2Cl_2:CH_3CN solvent mixture. On the other hand, when the ligand $\mathbf{H_2L^{Et}}$ (0.326 g, 1 mmol) was treated with 1 equivalent of $CoCl_2 \bullet 6H_2O$ (0.239 g, 1 mmol) in acetonitrile (10 mL) in the presence of triethylamine (0.2 mL) under air for 1 h at room temperature (30 °C) provided a green solid of complex **20a**. Complex **20a** was recrystallized from a 4:1 CH_2Cl_2:CH_3CN solvent mixture that led to crystalline compounds suitable for single X–ray diffraction analysis.

Yield: 0.185 g, 50%.

FTIR (KBr pellet, cm^{-1}): 2955, 2904, 2868, 1523, 1482, 1461, 1375, 1362, 1307, 1265, 1230, 1205, 1174, 1117, 1097, 1024, 998, 912, 860, 783, 748,663, 648.

ESI–MS (CH_3CN) *m/z* for $[C_{42}H_{58}ClCoN_2O_2]^+$: Calcd, 740.35; Found, 740.77.

ESI–MS (CH_3CN) *m/z* for $[C_{42}H_{58}ClCoN_2O_2 - Cl]^+$: Calcd, 705.38; Found, 705.78.

UV–vis/NIR (CH_2Cl_2) λ_{max}, nm (ε, $M^{-1}cm^{-1}$): 868(12000); 820(11750); 670(22300).

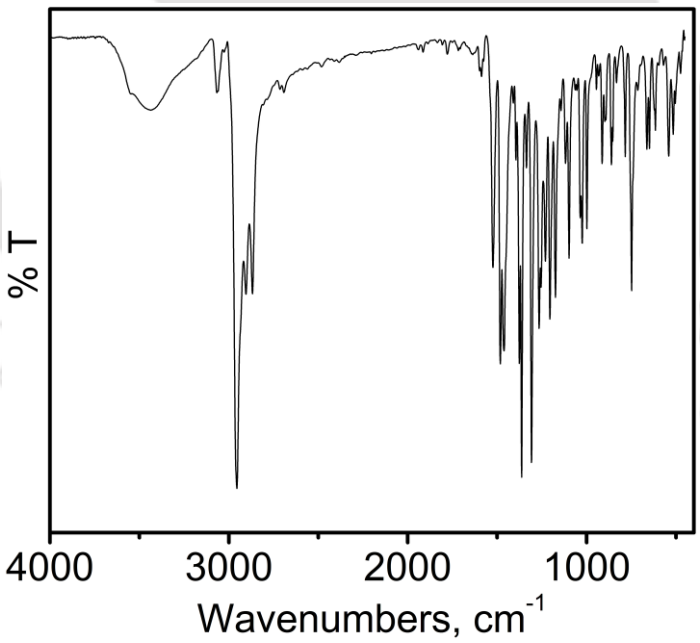

Figure 6.37: *IR spectrum of **20a**.*

Synthesis of $[C_{40}H_{48}CoF_2N_2O_2]$; 21:

Ligand $\mathbf{H_2L^F}$ (0.157 g, 0.5 mmol) was treated with $CoCl_2 \bullet 6H_2O$ (0.060 g, 0.25 mmol) in acetonitrile (5 mL) in the presence of triethylamine (0.1 mL). The resulting reaction mixture was stirred for 5 minutes at room temperature (30 °C). Then the reaction mixture was filtered to obtain a green solid. The resulting green solid was dissolved in THF and filtered through a Whatman filter paper. Evaporation of THF solution, left a green residue of complex **21**.

Yield: 0.105 g, 54%.

FTIR (KBr pellet, cm^{-1}): 2957, 2905, 2867, 1584, 1525, 1490, 1454, 1359, 1307, 1260, 1236, 1179, 1141, 1103, 1024, 1000, 912, 857, 754, 744, 656, 529, 508.

ESI–MS (CH_3CN) *m/z* for $[C_{40}H_{48}CoF_2N_2O_2]^+$: Calcd, 685.30; Found, 685.27.

UV–vis/NIR (CH_2Cl_2) λ_{max}, nm (ε, $M^{-1}cm^{-1}$): 1600(2150); 920(2400); 675(23400).

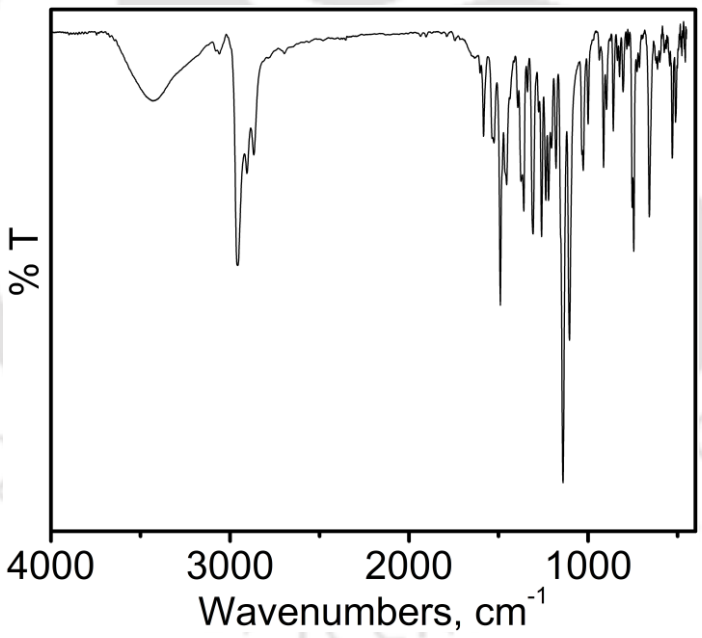

Figure 6.38: *IR spectrum of **21**.*

Synthesis of $[C_{40}H_{48}ClCoF_2N_2O_2]$; 21a:

Treatment of $CoCl_2 \bullet 6H_2O$ (0.060 g, 0.25 mmol) to a stirred solution of $\mathbf{H_2L^F}$ (0.157 g, 0.50 mmol) in acetonitrile (10 mL), a blue color solution was appeared. Et_3N (0.1 mL) was added to it and the resulting reaction mixture was stirred for 40 minutes at room temperature (30 °C). Blue color precipitate was appeared that was filtered and recrystallized from a CH_2Cl_2:CH_3CN (3:1) solvent mixture by slow solvent evaporation technique. This provided crystalline compound within one day.

Yield: 0.125 g, (69%).

FTIR (KBr pellet, cm^{-1}): 2953, 2906, 2868, 1584, 1524, 1491, 1465, 1370, 1338, 1313, 1257, 1236, 1222, 1205, 1177, 1102, 1035, 998, 912, 859, 802, 754, 745, 653, 620, 528, 509.

^{1}H NMR ($CDCl_3$, 399.85 MHz): δ 1.09 (s, 18H), 1.17 (s, 18H), 7.09 (s, 2H), 7.29 (s, 2H), 7.45 (s, 2H), 7.56 (s, 2H), 8.55 (s, 2H), 8.61 (s, 2H) ppm.

ESI–MS (CH_3CN) *m/z* for $[C_{40}H_{48}ClCoF_2N_2O_2]^+$: Calcd, 720.27; Found, 720.26.

ESI–MS (CH_3CN) *m/z* for $[C_{40}H_{48}ClCoF_2N_2O_2 - Cl]^+$: Calcd, 685.30; Found, 685.27.

Anal. Calcd for $C_{40}H_{48}ClCoF_2N_2O_2$: C, 66.64; H, 6.71; N, 3.89. Found: C, 66.02; H, 6.67; N, 3.98.

UV–vis/NIR (CH_2Cl_2) λ_{max}, nm (ε, $M^{-1}cm^{-1}$): 885(11800); 825(11100); 666(21600).

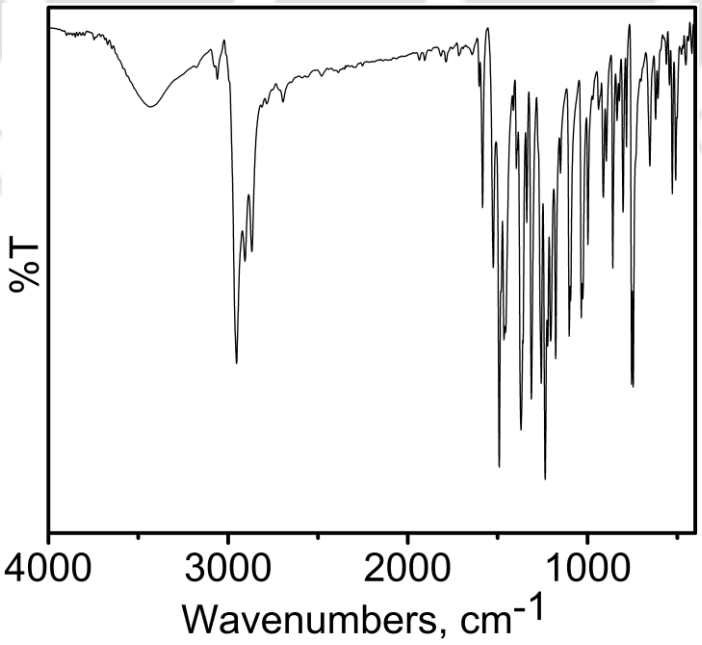

Figure 6.39: *IR spectrum of **21a**.*

Synthesis of $[C_{40}H_{48}Cl_2CoN_2O_2]$; 22:

A reaction mixture containing $\mathbf{H_2L^{Cl}}$ (0.166 g, 0.50 mmol), $CoCl_2 \bullet 6H_2O$ (0.060 g, 0.25 mmol) and Et_3N (0.1 mL) in acetonitrile (10 mL) was stirred for 5 minutes at room temperature (30 °C). A blue color precipitate was appeared that was isolated through filtration and washed one time by acetonitrile (4 mL). Blue solid was then recrystallized from an ether:acetonitrile (4:1) solvent mixture by slow solvent evaporation method that led to the crystalline compound suitable for the single crystal X–ray diffraction study.

Yield: 0.045 g (25%).

FTIR (KBr pellet, cm^{-1}): 2955, 2904, 2867, 1584, 1536, 1465, 1438, 1358, 1305, 1247, 1158, 1144, 1104, 1062, 1026, 913, 853, 742, 654, 514.

ESI–MS (CH_3CN) *m/z* for $[C_{40}H_{48}Cl_2CoN_2O_2]^+$: Calcd, 717.24; Found, 717.52.

Anal. Calcd for $C_{40}H_{48}ClCoN_2O_2$: C, 66.85; H, 6.73; N, 3.90. Found: C, 65.65; H, 6.73; N, 3.81.

UV–vis/NIR (CH_2Cl_2) λ_{max}, nm (ε, $M^{-1}cm^{-1}$): 1600(2800); 920(25100); 675(17700).

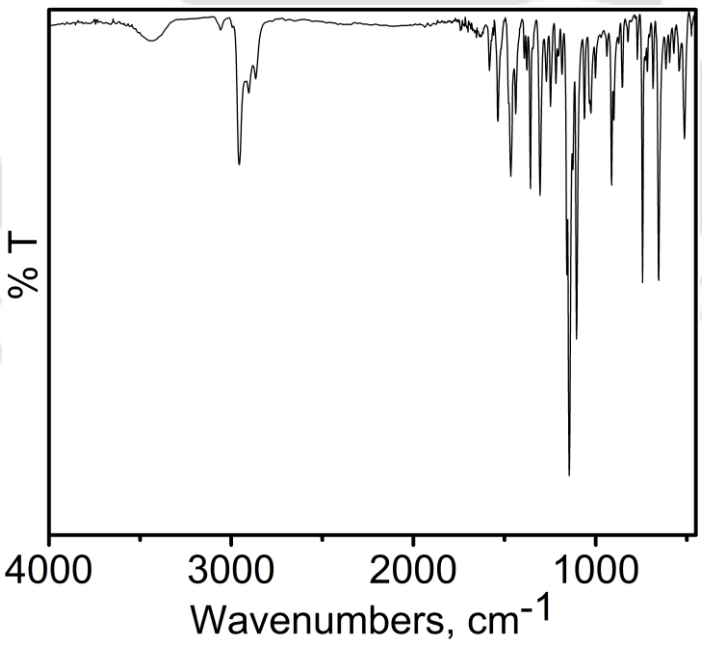

Figure 6.40: *IR spectrum of **22**.*

Synthesis of $[C_{40}H_{48}Cl_3CoN_2O_2]$; 22a:

Equimolar amounts of reaction between ligand $\mathbf{H_2L^{Cl}}$ (0.166 g, 0.5 mmol) and $CoCl_2 \bullet 6H_2O$ (0.120 g, 0.5 mmol) in acetonitrile (10 mL) in the presence of triethylamine (0.1 mL) under air for 5 minutes at room temperature (30 °C) provided a green precipitate that was collected through filtration and washed with acetonitrile.

Yield: 0.147 g, 78%.

FTIR (KBr pellet, cm^{-1}): 3061, 2955, 2905, 2868, 1584, 1523, 1477, 1439, 1376, 1363, 1310, 1260, 1250, 1183, 1098, 1062, 1033, 1023, 998, 914, 856, 748, 700, 649, 542, 514.

^{1}H NMR ($CDCl_3$, 399.85 MHz): δ 1.08 (s, 18H), 1.17 (s, 18H), 7.28 (s, 2H), 7.39 (s, 4H), 7.51 (d, J = 6.8 Hz, 2H), 8.47 (d, J = 10.0 Hz, 4H) ppm.

ESI–MS (CH_3CN) *m/z* for $[C_{40}H_{48}Cl_3CoN_2O_2]^+$: Calcd, 754.21; Found, 754.32.

ESI–MS (CH_3CN) *m/z* for $[C_{40}H_{48}Cl_3CoN_2O_2 - Cl]^+$: Calcd, 717.24; Found, 717.52.

UV–vis/NIR (CH_2Cl_2) λ_{max}, nm (ε, $M^{-1}cm^{-1}$): 885(12550); 825(11450); 666(22500).

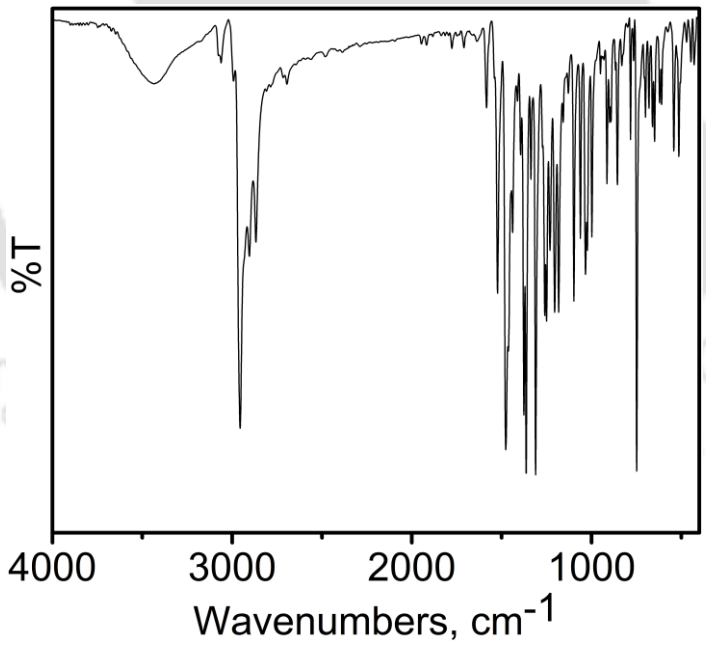

Figure 6.41: *IR spectrum of **22a**.*

Synthesis of $[C_{40}H_{48}Br_2CoN_2O_2]$; 23:

To a stirred acetonitrile solution (10 mL) of $\mathbf{H_2L^{Br}}$ (0.189 g, 0.50 mmol), $CoCl_2 \bullet 6H_2O$ (0.060 g, 0.25 mmol) and Et_3N (0.1 mL) were added sequentially. The resulting reaction mixture was stirred for 5 minutes at room temperature (30 °C) under air. This caused a blue precipitation. The blue precipitate was filtered and washed with acetonitrile (4 mL). Slow solvent evaporation of an ether:acetonitrile (4:1) solution of the blue solid provided X–ray quality single crystal.

Yield: 0.061 g (30%).

FTIR (KBr pellet, cm^{-1}): 2958, 2904, 2866, 1580, 1535, 1510, 1461, 1360, 1348, 1306, 1264, 1247, 1204, 1144, 1100, 1036, 1023, 999, 900, 856, 741, 651, 625, 510.

ESI–MS (CH_3CN) *m/z* for $[C_{40}H_{48}Br_2CoN_2O_2]^+$: Calcd, 807.14; Found, 807.42.

Anal. Calcd for $C_{40}H_{48}Br_2CoN_2O_2$: C, 59.49; H, 5.99; N, 3.47. Found: 60.01; H, 6.10; N, 3.35.

UV–vis/NIR (CH_2Cl_2) λ_{max}, nm (ε, $M^{-1}cm^{-1}$): 1600(2800); 920(26100); 675(17700).

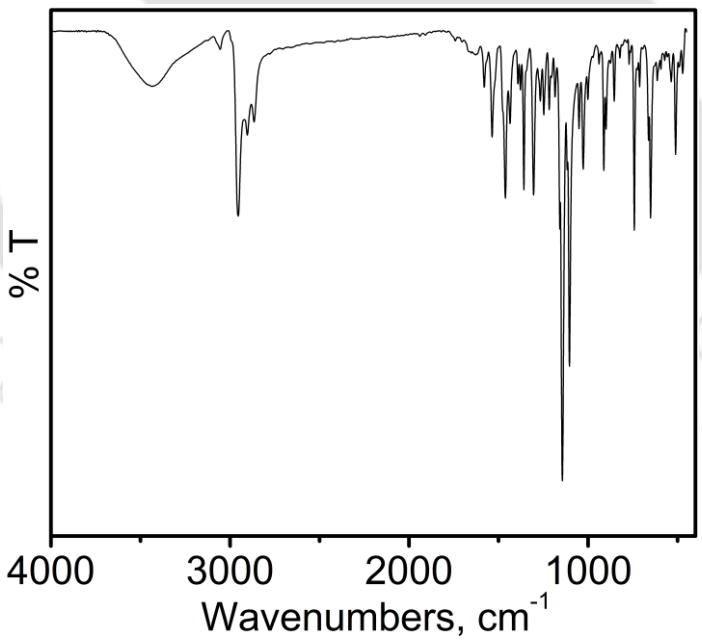

Figure 6.42: *IR spectrum of **23**.*

Synthesis of $[C_{40}H_{48}Br_2CoN_2O_2]$; 23a:

1:1 reaction between ligand $\mathbf{H_2L^{Br}}$ (0.189 g, 0.5 mmol) and $CoCl_2 \bullet 6H_2O$ (0.120 g, 0.5 mmol) in acetonitrile (10 mL) in the presence of triethylamine (0.1 mL) under air for 5 minutes provided the complex **23a**.

Yield: 0.158 g, 75%.

FTIR (KBr pellet, cm^{-1}): 3059, 2955, 2904, 2868, 1580, 1522, 1474, 1462, 1435, 1376, 1363, 1311, 1260, 1250, 1232, 1204, 1182, 1097, 1051, 1027, 998, 913, 898, 856, 782, 747, 665, 650, 541, 511.

^{1}H NMR ($CDCl_3$, 399.85 MHz): δ 1.07 (s, 18H), 1.17 (s, 18H), 7.26 (s, 2H), 7.44 (s, 4H), 7.55 (s, 2H), 8.43 (s, 4H) ppm.

ESI–MS (CH_3CN) *m/z* for $[C_{40}H_{48}Br_2ClCoN_2O_2]^+$: Calcd, 842.11; Found, 842.41.

ESI–MS (CH_3CN) *m/z* for $[C_{40}H_{48}Br_2ClCoN_2O_2 - Cl]^+$: Calcd, 807.14; Found, 807.42.

UV–vis/NIR (CH_2Cl_2) λ_{max}, nm (ε, $M^{-1}cm^{-1}$): 885(11800); 825(11100); 666(20750).

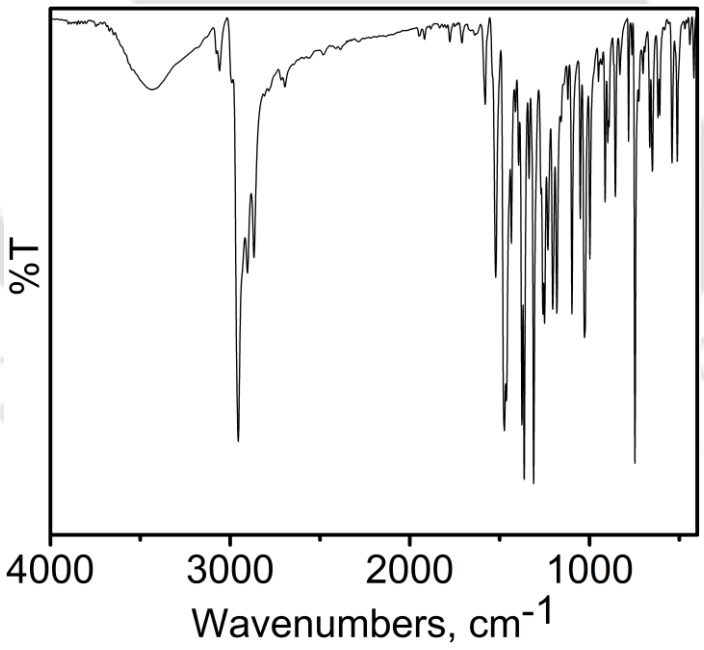

Figure 6.43: *IR spectrum of **23a**.*

Synthesis of $[C_{40}H_{48}ClCoI_2N_2O_2]$; 24:

A stirred solution of $\mathbf{H_2L^I}$ (0.212 g, 0.5 mmol) in acetonitrile (10 mL) was treated with $CoCl_2 \bullet 6H_2O$ (0.060 g, 0.25 mmol), and Et_3N (0.1 mL). After stirring for 5 minutes under air, the resulting reaction mixture was filtered and washed with acetonitrile (10 mL) to get a blue solid. X–ray quality single crystals were grown by the recrystallization of the blue solid from a CH_2Cl_2:CH_3CN (3:1) solvent mixture by slow solvent evaporation method.

Yield: 0.190 g (80%).

FTIR (KBr pellet, cm^{-1}): 3057, 2955, 2904, 2867, 1588, 1522, 1459, 1434, 1377, 1363, 1311, 1251, 1232, 1204, 1182, 1098, 1047, 1021, 998, 913, 897, 855, 782, 745, 648, 616, 541, 513.

^{1}H NMR ($CDCl_3$, 399.85 MHz): δ 1.08 (s, 18H), 1.17 (s, 18H), 7.22 (d, J = 1.6 Hz, 2H), 7.26 (m, 2H), 7.49 (t, J = 7.2 Hz, 2H), 7.8 (d, J = 8.0 Hz, 2H), 8.42 (s, 2H) ppm.

ESI–MS (CH_3CN) *m/z* for $[C_{40}H_{48}ClCoI_2N_2O_2]^+$: Calcd, 936.08; Found, 936.48.

ESI–MS (CH_3CN) *m/z* for $[C_{40}H_{48}ClCoI_2N_2O_2 - Cl]^+$: Calcd, 901.11; Found, 901.48.

Anal. Calcd for $C_{40}H_{48}ClCoI_2N_2O_2$: C, 51.27; H, 5.16; N, 2.99. Found: C, 51.04; H, 5.15; N, 3.80.

UV–vis/NIR (CH_2Cl_2) λ_{max}, nm (ε, $M^{-1}cm^{-1}$): 885(13100); 825(12300); 666(24650).

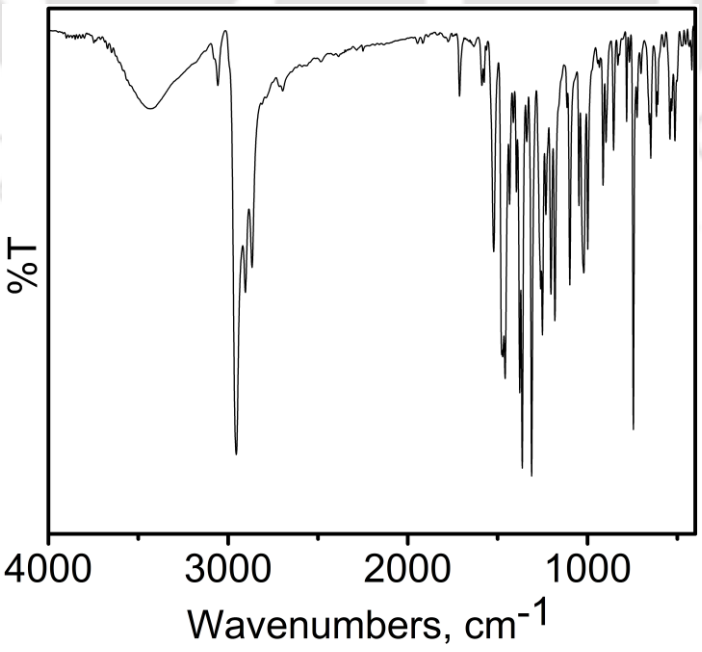

Figure 6.44: *IR spectrum of **24**.*

6.3: Crystallographic data and structure refinement parameters:

Table 6.1:

	1	2	3	4
Empirical formula	$C_{62}H_{105}N_2O_{17}SV_4$	C_{92} H_{164} N_2 O_{32} S_2 V_8	C85 H98 Cl2 N4 O16 V4	$C_{21}H_{24}N_2O$
Formula weight	1386.30	2281.89	1706.33	320.42
Crystal habit, colour	block, blue	block, black	Block, green	block / yellow
Crystal size, mm^3	0.43 X 0.32 X 0.24	0.30 x 0.26 x 0.22	0.42 x 0.32 x 0.28	0.44 X 0.36 X 0.18
Temperature, T /K	296(2)	100(2)	296(2)	296(2)
Wavelength, λ/Å	0.71073	0.71073	0.71073	0.71073
Crystal system	orthorhombic	monoclinic	monoclinic	monoclinic
Space group	'*P* bca'	'*P* 2_1/n'	'*P*12_1/*n*1'	'*C*12/*c*1'
Unit cell dimensions/Å	a = 25.3631(9)	a = 15.1675(12)	a = 18.1390(10)	a = 34.3374(12)
	b = 20.7112(7)	b = 20.323(2)	b = 27.0276(15)	b = 6.0181(2)
	c = 28.6263(9)	c = 20.135(3)	c = 18.7547(11)	c = 18.6307(6)
	$\alpha = \beta = \gamma = 90°$	$\alpha = \gamma = 90°$	$\alpha = \gamma = 90°$	$\alpha = \gamma = 90°$
		$\beta = 111.855(9)°$	$\beta = 93.366(3)°$	$\beta = 104.012(2)°$
Volume, V/$Å^3$	15037.4(9)	5760.5(11)	9178.7(9)	3735.4(2)
Z	8	2	4	8
Calculated density/ $Mg·m^{-3}$	1.225	1.316	1.235	1.140
Absorption coefficient, μ/mm^{-1}	0.569	0.726	0.514	0.070
F(000)	5880	2404	3560	1376
θ range for data collection	1.46 to 25.00°	2.87° to 33.07°	1.32° to 24.22°	1.22 to 25.00°
Limiting indices	$-30 \le h \le 30$, $-24 \le k \le 24$, $-34 \le l \le 34$	$-23 \le h \le 23$, $-31 \le k \le 31$, $-30 \le l \le 30$	$-14 \le h \le 17$, $-30 \le k \le 26$, $-19 \le l \le 19$	$-33 \le h \le 37$, $-7 \le k \le 7$, $-20 \le l \le 22$
Reflection collected / unique	167729 / 13231 [R(int) = 0.0924]	164119 / 21758 [R(int) = 0.0704]	66323 / 10903 [R(int) = 0.0933]	20752 / 3093 [R(int) = 0.0314]
Completeness to θ	99.90% (θ = 25.00°)	99.8 %	73.8 % (θ = 24.22°)	94 % (θ = 25.00°)
Max. and min. transmission	0.872 and 0.804	0.89215 and 0.71712	0.866 and 0.821	0.987 and 0.970
Refinement method	'SHELXL–97 (Sheldrick, 1997)'	Full–matrix least–squares on F^2	'SHELXL–97 (Sheldrick, 1997)'	'SHELXL–97 (Sheldrick, 1997)'
Data / restraints / parameters	13231 / 5 / 799	21758 / 8 / 652	10903 / 0 / 1024	3093 / 0 / 229
Goodness–of–fit on F^2	1.014	1.068	1.030	1.053
Final R indices [I>2sigma(I)]	$R1$ = 0.0605, $wR2$ = 0.1453	$R1$ = 0.0553, $wR2$ = 0.1242	$R1$ = 0.0976, $wR2$ = 0.2871	$R1$ = 0.0856, $wR2$ = 0.2631
R indices (all data)	$R1$ = 0.1065, $wR2$ = 0.1698	$R1$ = 0.0895, $wR2$ = 0.1411	$R1$ = 0.1616, $wR2$ = 0.3185	$R1$ = 0.1038, $wR2$ = 0.2862
Largest diff. peak and hole	0.654 and –0.372 $e·Å^{-3}$	1.898 and –0.767 $e.Å^{-3}$	1.116 and –0.513 $e·Å^{-3}$	0.594 and –0.511 $e·Å^{-3}$

Table 6.2:

	5	6	7	8
Empirical formula	$C_{42}H_{54}ClMnN_2O_2$	$C_{42}H_{48}ClCoN_4O_2$	$C_{42}H_{48}N_4NiO_2$	$C_{42}H_{48}CuN_4O_2$
Formula weight	709.26	735.22	699.53	704.38
Crystal habit / colour	needle / brown	block / blue	needle / green	needle / green
Crystal size, mm^3	0.34 x 0.22 x 0.20	0.44 x 0.34 x 0.28	0.34 x 0.22 x 0.20	0.38 x 0.24 x 0.22
Temperature, T /K	296(2)	296(2)	296(2)	296(2)
Wavelength, λ/Å	0.71073	0.71073	0.71073	0.71073
Crystal system	tetragonal	tetragonal	monoclinic	monoclinic
Space group	'*P* 43'	'*P* 43'	'*P*12_1/*c*1'	'*P*12_1/*c*1'
Unit cell dimensions/Å	a = 15.4181(2)	a = 15.3593(4)	a = 8.4148(4)	a = 8.4682(11)
	b = 15.4181(2)	b = 15.3593(4)	b = 17.4921(7)	b = 17.4855(19)
	c = 16.6835(4)	c = 16.6348(7)	c = 27.8404(11)	c = 28.010(3)
	$\alpha = \beta = \gamma = 90°$	$\alpha = \beta = \gamma = 90°$	$\alpha = \gamma = 90°$	$\alpha = \gamma = 90°$
			$\beta = 106.438(3)$	$\beta = 106.955(7)$
Volume, V/$Å^3$	3965.94(12)	3924.3(2)	3930.4(3)	3967.2(8)
Z	4	4	4	4
Calculated density/ $Mg·m^{-3}$	1.188	1.244	1.182	1.179
Absorption coefficient, μ/mm^{-1}	0.436	0.545	0.532	0.588
F(000)	1512	1552	1488	1492
θ range for data	2.91 to 25.00°	1.33 to 25.00°	1.39 to 25.00°	1.92 to 25.00°

collection				
Limiting indices	$-18 \le h \le 18, -11 \le k \le 17, -19 \le l \le 11$	$-18 \le h \le 18, -18 \le k \le 17, -19 \le l \le 19$	$-9 \le h \le 9, -19 \le k \le 19, -24 \le l \le 33$	$-10 \le h \le 9, -20 \le k \le 20, -33 \le l \le 33$
Reflection collected / unique	8715 / 4698 [*R*(int) = 0.0250]	32758 / 6786 [*R*(int) = 0.0631]	26538 / 6571 [*R*(int) = 0.0513]	41095 / 6836 [*R*(int) = 0.1053]
Completeness to θ	99.8% (θ = 25.00°)	99.7 % (θ = 25.00°)	95.2 % (θ = 25.00°)	98 % (θ = 25.00°)
Max. and min. transmission	0.916 and 0.891	0.858 and 0.801	0.899 and 0.869	0.879 and 0.844
Refinement method	'SHELXL–97 (Sheldrick, 1997)'	'SHELXL–97 (Sheldrick, 1997)'	'SHELXL–97 (Sheldrick, 1997)'	'SHELXL–97 (Sheldrick, 1997)'
Data / restraints / parameters	4698 / 1 / 447	6786 / 1 / 463	6571 / 0 / 454	6836 / 0 / 454
Goodness–of–fit on F^2	1.051	1.043	1.008	1.025
Final *R* indices [*I*>2sigma(*I*)]	*R*1 = 0.0392, *wR*2 = 0.0981	*R*1 = 0.0375, *wR*2 = 0.0864	*R*1 = 0.0663, *wR*2 = 0.1620	*R*1 = 0.0630, *wR*2 = 0.1446
R indices (all data)	*R*1 = 0.0469, *wR*2 = 0.1043	*R*1 = 0.0520, *wR*2 = 0.0988	*R*1 = 0.1617, *wR*2 = 0.2050	*R*1 = 0.1324, *wR*2 = 0.1813
Largest diff. peak and hole	0.247 and –0.199 e·Å^{-3}	0.175 and –0.191 e.Å^{-3}	0.454 and –0.316 e·Å^{-3}	0.507 and –0.434 e·Å^{-3}

Table 6.3:

	9	**10**	**11**	**12**
Empirical formula	$C_{44}H_{61}ClCoN_5O_3$	$C_{28}H_{31}N_3NiO$	$C_{28}H_{31}CuN_3O$	$C_{56}H_{60}N_4O_4Zn_2$
Formula weight	802.36	484.27	489.10	983.82
Crystal habit, colour	block / brown	needle / brown	needle / red	columnar / orange
Crystal size, mm^3	0.38 x 0.27 x 0.12	0.46 x 0.22 x 0.18	0.48 x 0.22 x 0.20	0.34 x 0.20 x 0.18
Temperature, *T* /K	296(2)	296(2)	296(2)	296(2)
Wavelength, λ/Å	0.71073	0.71073	0.71073	0.71073
Crystal system	monoclinic	monoclinic	monoclinic	monoclinic
Space group	'$P2_1/c$'	'$C\,2/c$'	'$C12/c1$'	'$P12_1/n1$'
Unit cell dimensions/Å	a = 11.6089(4)	a = 25.810(2)	a = 25.9067(9)	a = 13.4477(2)
	b = 37.5663(11)	b = 6.9366(6)	b = 6.8845(2)	b = 19.0713(5)
	c = 10.4393(3)	c = 28.778(3)	c = 28.5206(10)	c = 19.6242(4)
	$\alpha = \gamma$ = 90°	$\alpha = \gamma$ = 90°	$\alpha = \gamma$ = 90°	$\alpha = \gamma$ = 90°
	β = 91.379(2)°	β = 96.065(8)	β = 95.595(3)°	β = 91.7956(19)
Volume, *V*/Å^3	4551.3(2)	5123.4(8)	5062.5(3)	5030.44(17)
Z	4	8	8	4
Calculated density/ Mg·m^{-3}	1.171	1.256	1.283	1.299
Absorption coefficient, μ/mm^{-1}	0.477	0.781	0.887	1.003
F(000)	1712	2048	2056	2064
θ range for data collection	1.08 to 22.37°	3.04° to 25.00°	3.06° to 25.00°	3.03 to 25.00°
Limiting indices	$-12 \le h \le 12, -40 \le k \le 40, -10 \le l \le 11$	$-29 \le h \le 30, -8 \le k \le 7, -29 \le l \le 34$	$-22 \le h \le 30, -4 \le k \le 8, -31 \le l \le 33$	$-15 \le h \le 15, -22 \le k \le 22, -21 \le l \le 23$
Reflection collected / unique	39670 / 5824 [*R*(int) = 0.0455]	9287 / 4511 [*R*(int) = 0.0565]	7917/4429[*R*(int) = 0.0211]	22587 / 8829 [*R*(int) = 0.0326]
Completeness to θ	99.5% (θ = 22.37°)	99.9 % (θ = 25.00°)	99.5% (θ = 25.00°)	99.8 % (θ = 25.00°)
Max. and min. transmission	0.944 and 0.857	0.869 and 0.814	0.837 and 0.791	0.835 and 0.786
Refinement method	'SHELXL–97 (Sheldrick, 1997)'	Full–matrix least–squares on F^2	'SHELXL–97 (Sheldrick, 1997)'	'SHELXL–97 (Sheldrick, 1997)'
Data / restraints / parameters	5824 / 0 / 508	4511 / 0 / 304	4429 / 0 / 304	8829 / 0 / 607
Goodness–of–fit on F^2	1.230	1.030	1.221	1.068
Final *R* indices [*I*>2sigma(*I*)]	*R*1 = 0.0468, *wR*2 = 0.1164	*R*1 = 0.0557, *wR*2 = 0.1166	*R*1 = 0.0453, *wR*2 = 0.0787	*R*1 = 0.0443, *wR*2 = 0.1054
R indices (all data)	*R*1 = 0.0686, *wR*2 = 0.1302	*R*1 = 0.0994, *wR*2 = 0.1439	*R*1 = 0.0606, *wR*2 = 0.0841	*R*1 = 0.0667, *wR*2 = 0.1184
Largest diff. peak and hole	0.429 and –0.283 e·Å^{-3}	0.302 and –0.440 e.Å^{-3}	0.292 and –0.396 e·Å^{-3}	0.808 and –0.535 e·Å^{-3}

Table 6.4:

	$H_3L^{Mixed(H)}$	**13**	**14**	**15**

Empirical formula	$C_{28}H_{34}N_2O_2$	$C_{28}H_{31}ClFeN_2O_2$	$C_{36}H_{47}ClFeN_2O_2$	$C_{28}H_{31}N_2NiO_2$
Formula weight	430.57	518.85	631.06	486.26
Crystal habit, colour	block / yellow	needle / brown	block / green	Needle / green
Crystal size, mm^3	0.52 x 0.38 x 0.26	0.52 x 0.34 x 0.28	0.58 x 0.46 x 0.34	0.32 x 0.06 x 0.04
Temperature, *T*/K	296(2)	296(2)	296(2)	296(2)
Wavelength, λ/Å	0.71073	0.71073	0.71073	0.71073
Crystal system	triclinic	monoclinic	triclinic	monoclinic
Space group	'*P* –1'	'$P12_1/n1$'	'*P* –1'	'$P\ 2_1/a$'
Unit cell dimensions	a = 9.5342(8) Å b = 12.0945(10) Å c = 12.3345(11) Å α = 62.280(4)°, γ = 83.074(5)°, β = 81.490(5)°	a = 17.2304(10) Å b = 9.2646(5) Å c = 18.2314(11) Å α = 90.00°, γ = 90.00°, β = 116.090(3)°	a = 10.0516(13) Å b = 13.5590(16) Å c = 14.5359(18) Å α = 112.291(7)°, γ = 91.832(7)°, β = 103.296(7)°	a = 19.4933(18) Å b = 6.1948(6) Å c = 20.415(2) Å α = 90.00°, γ = 90.00°, β = 96.986(9)°
Volume, V/$Å^3$	1243.03(18)	2613.8(3)	1768.2(4)	2447.0(4)
Z	2	4	2	4
Calculated density, $Mg{\cdot}m^{-3}$	1.150	1.319	1.185	1.320
Absorption coefficient, μ/mm^{-1}	0.072	0.706	0.533	0.820
F(000)	464	1088	672	1028
θ range for data collection	1.87 to 25.00°	1.36 to 25.00°	1.57 to 27.45°	3.08 to 26.00°
Limiting indices	$-10 \le h \le 11, -14 \le k \le 13, -14 \le l \le 14$	$-20 \le h \le 18, -10 \le k \le 10, -20 \le l \le 20$	$-13 \le h \le 12, -17 \le k \le 16, 0 \le l \le 18$	$-24 \le h \le 23, -7 \le k \le 6, -25 \le l \le 24$
Reflection collected / unique	13117 / 3931 [*R*(int) = 0.0610]	24729 / 4393 [*R*(int) = 0.0551]	8401 / 8080 [*R*(int) = 0.0050]	10057 / 4806 [*R*(int) = 0.0638]
Completeness to θ	89.9 % (θ = 25.00°)	95.5 % (θ = 25.00°)	100.0 % (θ = 27.45°)	99.8 % (θ = 26.00°)
Max. and min. transmission	0.981 and 0.968	0.821 and 0.750	0.834 and 0.745	0.968 and 0.943
Refinement method	'SHELXL–97 (Sheldrick, 1997)'	'SHELXL–97 (Sheldrick, 1997)'	'SHELXL–97 (Sheldrick, 1997)'	'SHELXL–97 (Sheldrick, 1997)'
Data / restraints / parameters	3931 / 0 / 297	4393 / 0 / 313	8080 / 0 / 391	4806 / 0 / 304
Goodness–of–fit on F^2	1.020	1.073	1.089	1.086
Final *R* indices [*I*>2sigma(*I*)]	*R*1 = 0.0499, *wR*2 = 0.1496	*R*1 = 0.0492, *wR*2 = 0.1119	*R*1 = 0.0830, *wR*2 = 0.1864	*R*1 = 0.0703, *wR*2 = 0.1306
R indices (all data)	*R*1 = 0.0618, *wR*2 = 0.1599	*R*1 = 0.0939, *wR*2 = 0.1381	*R*1 = 0.0830, *wR*2 = 0.1864	*R*1 = 0.1117, *wR*2 = 0.1560
Largest diff. peak and hole	0.325 and –0.372 $e{\cdot}Å^{-3}$	0.494 and –0.266 $e{\cdot}Å^{-3}$	0.772 and –0.643 $e{\cdot}Å^{-3}$	0.932 and –0.818 $e{\cdot}Å^{-3}$

Table 6.5:

	19	**19a**	**20a**	**22**
Empirical formula	$C_{42}H_{54}CoN_2O_2$	$C_{42}H_{54}ClCoN_2O_2$	$C_{44}H_{58}ClCoN_2O_2$	$C_{40}H_{48}Cl_2CoN_2O_2$
Formula weight	677.80	713.25	741.30	718.63
Crystal habit, colour	block / blue	block / blue	block / blue	block / blue
Crystal size, mm^3	0.32 x 0.24 x 0.22	0.36 x 0.30 x 0.28	0.54 x 0.42 x 0.34	0.44 x 0.38 x 0.32
Temperature, *T*/K	296(2)	296(2)	296(2)	296(2)
Wavelength, λ/Å	0.71073	0.71073	0.71073	0.71073
Crystal system	triclinic	tetragonal	tetragonal	triclinic
Space group	'*P*–1'	'*P*43'	'*P*43'	'*P*–1'
Unit cell dimensions	a = 5.9742(3) Å b = 12.7038(11) Å c = 13.2139(7) Å α = 73.037(7)°, γ =83.989(7)°, β = 85.630(4)°	a = 15.3395(2) Å b = 15.3395(2) Å c = 16.7305(6) Å $\alpha = \beta = \gamma$ = 90.00°	a = 15.4294(3) Å b = 15.4294(3) Å c = 17.5250(7) Å $\alpha = \beta = \gamma$ = 90.00°	a = 5.9671(3) Å b = 12.5679(10) Å c = 13.2630(10) Å α = 73.655(7)°, γ = 85.142(5)°, β = 85.587(5)°
Volume, V/$Å^3$	952.87(11)	3936.69(16)	4172.1(2)	949.55(11)
Z	1	4	4	1
Calculated density, $Mg{\cdot}m^{-3}$	1.181	1.203	1.180	1.257
Absorption coefficient, μ/mm^{-1}	0.486	0.539	0.511	0.628
F(000)	363	1520	1584	379
θ range for data collection	3.18 to 25.00°	2.92 to 24.99°	1.76 to 25.00°	3.18 to 25.00°
Limiting indices	$-5 \le h \le 7, -15 \le k \le 15, -15 \le l \le 15$	$-18 \le h \le 14, -17 \le k \le 18, -19 \le l \le 19$	$-18 \le h \le 18, -18 \le k \le 18, -20 \le l \le 20$	$-7 \le h \le 7, -14 \le k \le 14, -15 \le l \le 15$
Reflection collected / unique	6022 / 3346 [*R*(int) = 0.0210]	8776 / 5755 [*R*(int) = 0.0241]	49688 / 7337 [*R*(int) = 0.0399]	6058 / 3329 [*R*(int) = 0.0165]

Completeness to θ	99.9 % (θ = 25.00°)	99.8 % (θ = 24.99°)	100.0 % (θ = 25.00°)	99.9 % (θ = 25.00°)
Max. and min. transmission	0.899 and 0.869	0.860 and 0.824	0.841 and 0.773	0.818 and 0.759
Refinement method	'SHELXL–97 (Sheldrick, 1997)'	'SHELXL–97 (Sheldrick, 1997)'	'SHELXL–97 (Sheldrick, 1997)'	'SHELXL–97 (Sheldrick, 1997)'
Data / restraints / parameters	3346 / 0 / 219	5755 / 0 / 447	7337 / 1 / 466	3329 / 0 / 229
Goodness–of–fit on F^2	0.995	1.043	1.038	1.041
Final R indices [I>2sigma(I)]	$R1$ = 0.0877, $wR2$ = 0.1996	$R1$ = 0.0448, $wR2$ = 0.1046	$R1$ = 0.0348, $wR2$ = 0.0916	$R1$ = 0.0582, $wR2$ = 0.1511
R indices (all data)	$R1$ = 0.1087, $wR2$ = 0.2103	$R1$ = 0.0542, $wR2$ = 0.1135	$R1$ = 0.0424, $wR2$ = 0.0964	$R1$ = 0.0735, $wR2$ = 0.1644
Largest diff. peak and hole	0.808 and –0.548 e·Å^{-3}	0.239 and –0.253 e·Å^{-3}	0.322 and –0.278 e·Å^{-3}	0.557 and –0.314 e·Å^{-3}

Table 6.6:

	22a	**23**	**23a**	**24**
Empirical formula	$C_{40}H_{48}Cl_3CoN_2O_2$	$C_{40}H_{48}Br_2CoN_2O_2$	$C_{40}H_{48}Br_2ClCoN_2O_2$	$C_{40}H_{48}ClCoI_2N_2O_2$
Formula weight	754.08	807.55	843.00	936.98
Crystal habit, colour	block / blue	block / blue	block / blue	block / blue
Crystal size, mm^3	0.42 x 0.34 x 0.30	0.48 x 0.34 x 0.28	0.48 x 0.44 x 0.32	0.54 x 0.44 x 0.38
Temperature, T/K	296(2)	296(2)	296(2)	296(2)
Wavelength, λ/Å	0.71073	0.71073	0.71073	0.71073
Crystal system	tetragonal	triclinic	tetragonal	orthorhombic
Space group	'P43'	'P–1'	'P43'	'$Pca2_1$'
Unit cell dimensions	a = 15.3539(4) Å b = 15.3539(4) Å c = 16.4627(8) Å $\alpha = \beta = \gamma$ = 90.00°	a = 6.0905(6) Å b = 12.3718(6) Å c = 13.3982(8) Å α = 73.762(5)°, β = 84.891(7)°, γ = 85.979(6)°	a = 15.3829(2) Å b = 15.3829(2) Å c = 16.6421(4) Å $\alpha = \beta = \gamma$ = 90.00°	a = 29.2661(7) Å b = 7.8262(2) Å c = 21.2440(5) Å $\alpha = \beta = \gamma$ = 90.00°
Volume, V/Å^3	3880.9(2)	964.36(12)	3938.08(12)	4865.8(2)
Z	4	1	4	4
Calculated density, Mg·m^{-3}	1.291	1.391	1.422	1.279
Absorption coefficient, μ/mm^{-1}	0.684	2.551	2.568	1.705
F(000)	1584	415	1728	1872
θ range for data collection	2.97 to 25.00°	3.17 to 25.00°	2.92 to 24.99°	1.69 to 25.00°
Limiting indices	$-10 \le h \le 18$, $-14 \le k \le 16$, $-19 \le l \le 17$	$-7 \le h \le 7$, $-14 \le k \le 14$, $-12 \le l \le 15$	$-18 \le h \le 12$, $-18 \le k \le 10$, $-13 \le l \le 19$	$-33 \le h \le 32$, $-9 \le k \le 9$, $-21 \le l \le 25$
Reflection collected / unique	7061 / 5077 [R(int) = 0.0238]	6783 / 3382 [R(int) = 0.0344]	8528 / 5358 [R(int) = 0.0188]	44335 / 7903 [R(int) = 0.0408]
Completeness to θ	98.2 % (θ = 25.00°)	99.9 % (θ = 25.00°)	99.8 % (θ = 24.99°)	98.5 % (θ = 25.00°)
Max. and min. transmission	0.814 and 0.756	0.490 and 0.367	0.440 and 0.303	0.523 and 0.423
Refinement method	'SHELXL–97 (Sheldrick, 1997)'	'SHELXL–97 (Sheldrick, 1997)'	'SHELXL–97 (Sheldrick, 1997)'	'SHELXL–97 (Sheldrick, 1997)'
Data / restraints / parameters	5077 / 1 / 445	3382 / 0 / 217	5358 / 1 / 445	7903 / 1 / 445
Goodness–of–fit on F^2	1.094	1.053	0.990	0.974
Final R indices [I>2sigma(I)]	$R1$ = 0.0355, $wR2$ = 0.0888	$R1$ = 0.0736, $wR2$ = 0.1765	$R1$ = 0.0351, $wR2$ = 0.0792	$R1$ = 0.0338, $wR2$ = 0.0683
R indices (all data)	$R1$ = 0.0401, $wR2$ = 0.0929	$R1$ = 0.1255, $wR2$ = 0.2110	$R1$ = 0.0469, $wR2$ = 0.0851	$R1$ = 0.0490, $wR2$ = 0.0726
Largest diff. peak and hole	0.205 and –0.202 e·Å^{-3}	0.761 and –0.608 e·Å^{-3}	0.413 and –0.363 e·Å^{-3}	0.369 and –0.349 e·Å^{-3}

Dalton Transactions

COMMUNICATION

View Article Online
View Journal | View Issue

Effect of ligand substituent on the reactivity of Ni(II) complexes towards oxygen†‡

Cite this: *Dalton Trans.*, 2014, **43**, 394

Received 31st July 2013,
Accepted 26th September 2013

DOI: 10.1039/c3dt52072b

www.rsc.org/dalton

Samir Ghorai and Chandan Mukherjee*

Two radical-containing Ni(II) complexes having either parent salicylidene (complex 1) or 3,5-di-*tert*-butylsalicylidene (complex 2) in the ligand backbone were synthesized. Complex 2 underwent ligand centered C–H activation by aerial oxygen, forming the corresponding amide complex (2a). The UV-Vis/NIR spectral changes upon purging of molecular oxygen to 2 in CH_2Cl_2, along with ESI-MS analysis indicated the generation of Ni–oxygen/dioxygen species as the intermediate(s) for the amide formation. Interestingly, non-participation of the ligand centered π-radical in the oxidation process was observed.

Metal-oxo units have been proposed as active intermediates for several enzymatic and biomimetic C–H bond activation reactions.[1] Since then, transition metal mediated dioxygen activation as well as the characterization of metal-oxo intermediates have drawn considerable attention from both chemists and biologists. Cu-, Co-, and Fe-based metalloenzymes[2] are well known for their oxygen activation, while Ni-based metalloenzymes are very rare.[1a] This could be due to the thermodynamically less favorable oxidation of Ni(II) by molecular oxygen, due to its higher oxidation state.[1a] However, electron rich ligands bound to the Ni(II) centre have been found to favor the Ni center oxidation process by decreasing the oxidation potential, and consequently Ni could be found in its higher oxidation state. For instance, Ni peptide complexes where the Ni center is bound to an amide ligand favor the oxidation of Ni(II) to Ni(III) under air.[3]

In continuation of our ongoing research in understanding the effect of substituents on the reactivity of metal complexes,[4] we have synthesized two new ligands, $H_3Sami^{Mixed(H)}$ and $H_3Sami^{Mixed(tBu)}$, composed of both redox active aminophenol (a change in its oxidation state is favored in the presence of a metal ion and oxygen) and redox inactive (a change in its oxidation state is not favored in the presence of a metal ion and oxygen) salicylidene compartments connected *via* a benzyl linker (Scheme 1). The ligands differ from each other by the presence of *tert*-butyl groups at the 3,5-positions of the salicylidene unit in $[(H_3Sami^{Mixed(tBu)})]$.

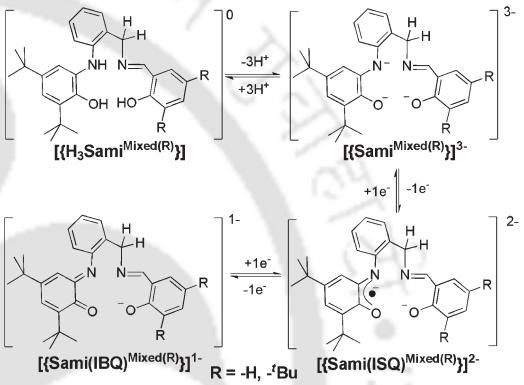

Scheme 1 A schematic representation of the ligands and their different redox states. ISQ and IBQ stand for the iminobenzosemiquinone and iminobenzoquinone forms of the ligand, respectively.

Herein, we report the synthesis of ligands $[(H_3Sami^{Mixed(tBu)})]$ and $[(H_3Sami^{Mixed(H)})]$, and their corresponding Ni(II) complexes. Interestingly, we have observed a remarkable substituent dependent reactivity of the Ni complexes with molecular oxygen. Non-participation of the ligand centered π-radical of the Ni–oxygen/dioxygen intermediate was also observed and reported here.

A schematic diagram for the synthesis of ligands $H_3Sami^{Mixed(H)}$, $H_3Sami^{Mixed(tBu)}$, and the corresponding Ni complexes **1** and **2** is shown in Scheme 2. The reaction between 1 : 1 2-aminobenzonitrile and 3,5-di-*tert*-butylcatechol in the presence of Et_3N provided H_2Sami^{CN} in 72% yield. Further reduction of the bidentate ligand using $LiAlH_4$ gave **A** in 70%

Department of Chemistry, Indian Institute of Technology Guwahati, Guwahati, 781039 Assam, India. E-mail: cmukherjee@iitg.ernet.in; Fax: (+)91-361-258-2349; Tel: (+)91-361-258-2327

† Dedicated to Dr Eckhard Bill on the occasion of his 60th birthday.

‡ Electronic supplementary information (ESI) available: Experimental procedures, characterization data of $H_3Sami^{Mixed(R)}$, **1**, **2**, and **2a**, including IR, mass spectra, ORTEP plots, and X-band EPR spectra. Crystallographic structural parameters, and crystallographic information file of $H_3Sami^{Mixed(H)}$, **1**, **2**, and **2a**. CCDC 951779–951782. For ESI and crystallographic data in CIF or other electronic format, see DOI: 10.1039/c3dt52072b

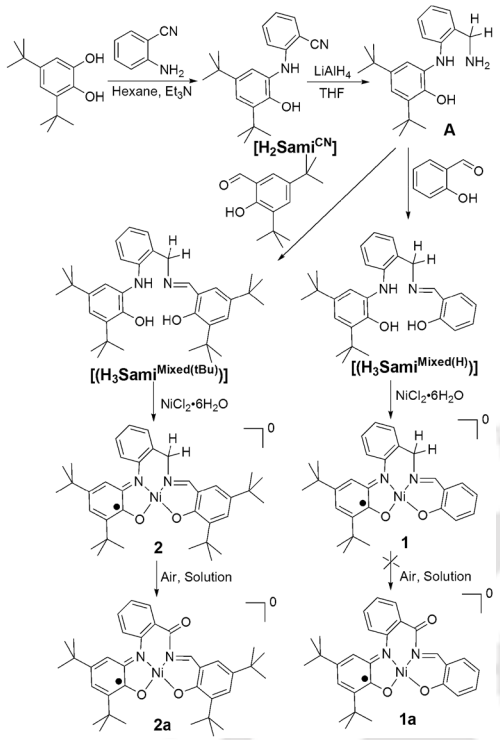

Scheme 2 A schematic representation of the ligands and the formation pathways of the corresponding Ni complexes.

yield. The condensation of equimolar amounts of salicylaldehyde and **A** in ethanol provided ligand $H_3Sami^{Mixed(H)}$ in 70% yield. The ligand $H_3Sami^{Mixed(tBu)}$ was synthesized *in situ* by a 1 : 1 condensation of **A** with 3,5-di-*tert*-butylsalicylaldehyde in CH_3CN under reflux. The addition of $NiCl_2{\cdot}6H_2O$ to $H_3Sami^{Mixed(H)}$ or to the *in situ* generated ligand $H_3Sami^{Mixed(tBu)}$ provided the corresponding complexes **1** and **2** in 51% and 40% yield, respectively. Both complexes were stable under air in the solid state. However, complex **2** changed gradually to complex **2a** when in solution.

Single crystal X-ray diffraction measurements for ligand $H_3Sami^{Mixed(H)}$, complex **1**, complex **2**, and complex **2a** were performed at 296(2) K. Ligand $H_3Sami^{Mixed(H)}$ crystallized in the triclinic space group $P\bar{1}$. The asymmetric ligand was comprised of three different kinds of C_6 aryl ring. The C–C bond distances of the C_6 aryl rings can be taken into consideration when assigning the oxidation state of the ligand. In the fully reduced form, the C–C bond distances in the C_6 aryl ring are all 1.39 ± 0.01 Å.[5,6] In the case of the one-electron oxidized iminobenzosemiquinone (ISQ) or two-electron oxidized iminobenzoquinone (IBQ) forms of the ligand (Scheme 1), discrete alternative short and long C–C bond distances (*i.e.* a quinoid-type distortion) in the C_6 aryl ring are expected.[5] Furthermore, in the ISQ form, the C_{Ph}–N_{Ph} and C_{Ph}–O_{Ph} (C_{Ph}, N_{Ph}, and O_{Ph} stand for the phenyl carbon atom, N, and O atom attached to the phenyl ring, respectively) bond distances are 1.35 ± 01 Å and 1.30 ± 0.01 Å, respectively.[5] These bond distances are in between single bond and double bond character, and correspond to the π-radical form of the organic moiety. In ligand $H_3Sami^{Mixed(H)}$ the C–C bond distances of the 3,5-di-*tert*-butyl-containing aminophenol unit were in range of 1.380(5)–1.400(5) Å (Table 2, S14‡). The C1–N1 = 1.435(5) and C2–O1 = 1.375(5) Å bond distances along with the C–C bond distances indicated the fully reduced form of the aryl ring. The C14–N2 = 1.275(4) Å bond distance indicated its double bond character and the C20–O2 = 1.355(3) Å bond distance was in accord with the phenolic C–O bond distance.[6] The C–C bond distances of the other two C_6 rings were found to be in the range of 1.366(4)–1.402(4) Å with no quinoid-type distortion. Hence, the ligand was in its fully reduced form with the benzyl group bridging between an aminophenol and a salicylidene unit.

All of the complexes were neutral. Complex **1** and complex **2** crystallized in the monoclinic space groups $P2_1/a$ and $C2_1/c1$, respectively, while complex **2a** crystallized in the orthorhombic space group $P2_12_12_1$. The molecular structures are shown in Fig. 1. Selected bond distances and bond angles are given in Table 2 (S14–S15‡).

All of the C–C bond distances of the *tert*-butyl-containing C_6 aryl rings (amidophenolate unit) in the complexes were not within 1.39 ± 01 Å range, rather, a quinoid type distortion was observed (Table 2, S14–S15‡). Furthermore, the C1–N1 = 1.364(6) [**1**], 1.371(4) [**2**], 1.380(5) [**2a**] Å and C2–O1 = 1.293(8) [**1**], 1.310(3) [**2**], 1.305(5) [**2a**] Å (parentheses correspond to the respective complex) bond distances were in between those of their single bond and double bond values. There was shortening in the C20–O2 and C14–C15 bonds, and elongation in the C14–N2 bond, on going from free ligand to **1** or **2** (Table 2, S14–S15‡). These bond distance changes were mainly due to delocalization of the phenolate^{1-} charge over the O2–O20–C15–C14–N2 unit. The shortening and elongation of these bond distances in **2a** were more pronounced due to the increase of delocalization of the charge over the molecule *via* the newly formed amide unit. This type of shortening and elongation is common in salen complexes where the salicylidene unit is in its fully reduced form.[6] Hence, in the complexes, the amidophenolate part of the ligand was found to be in its one-electron oxidized ISQ form and no oxidation in the salen unit was observed.

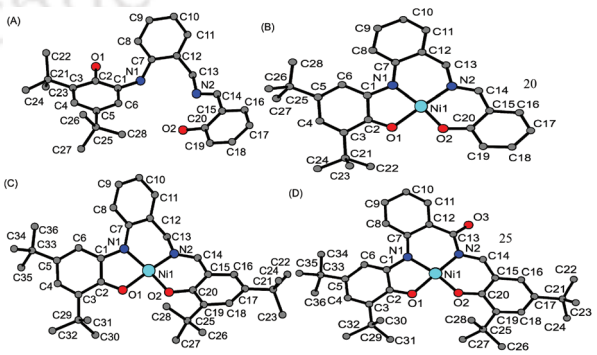

Fig. 1 Ball and stick representation of the (A) $H_3Sami^{Mixed(H)}$, (B) **1**, (C) **2**, and (D) **2a** molecular structures. Hydrogen atoms are omitted for clarity.

In the complexes, the central Ni1 atom was coordinated by two N and two O atoms. The Ni1–O1, Ni1–N1 and Ni1–N2 bond distances were almost equal for both complexes, and found to be within the 1.86 ± 0.01 Å range. These bond distances were in accord with the +II oxidation state of the Ni center.[5b,c,6c,d] Interestingly, the Ni1–O2 bond distance was ~0.02 Å shorter in **2** compared to in **1**, indicating the higher covalency of the bond caused by the presence of the electron donating *tert*-butyl substituent at the 3,5-positions of the parent salicylidene unit. This difference in covalency seemed to be responsible for the observed difference in reactivity under air between **1** and **2**. A higher electron density at the Ni(II) center *via* PhO^- in **2** might facilitate the required stabilization of Ni to its higher oxidation state,[1b,7] and hence the oxygenation reaction.

A detailed solid-state structural comparison was performed and the parameters are given in Table 1 (S13‡). The Ni atom in **1** was observed to be almost planar with respect to both the **P** and **R** planes, while that in **2** was 0.30 Å below and 0.34 Å above the **P** and **R** planes, respectively. Furthermore, it was found that the position of the central Ni atom relative to the plane passing through the salicylidene unit differed remarkably (0.01 Å towards the benzyl carbon atom for **1** and 0.3 Å away from the benzyl carbon atom for **2**). These positional differences of the Ni(II) center seemed to facilitate formation of the oxygen–metal center adduct.

The X-band EPR spectra of **1**, **2**, and **2a** (Fig. 9, S8‡) displayed isotopic resonance signals at g = 2.003 (**1**), g = 2.005 (**2**) and g = 2.002 (**2a**) (parentheses indicate the complex). Thus, the neutral complexes can be best described as Ni(II)-mono (iminobenzosemiquinone) complexes, *i.e.* Ni(II) coordinated to a π-radical anion.

A CH_2Cl_2 solution of **2** was continuously purged with oxygen gas and time-dependent UV-Vis/NIR spectra were simultaneously recorded (Fig. 2). A gradual and regular increase in the absorption band (dotted lines) at ~652 nm was observed until 70 min. Noticeably, the band at ~835 nm, known as a marker of π-radical character,[5c] showed little change in absorption (ε = 5000 M^{-1} cm^{-1}). This confirmed no reaction and/or participation of the ligand centered π-radical [**2**, ~835 nm (ε, 5500 M^{-1} cm^{-1})]. The generation of the band at ~652 nm was related to the formation of diamagnetic species (28%) as evidenced by the decrease of the EPR signal (Fig. 13, S11‡). After 70 min, the band at ~652 nm gradually decreased with

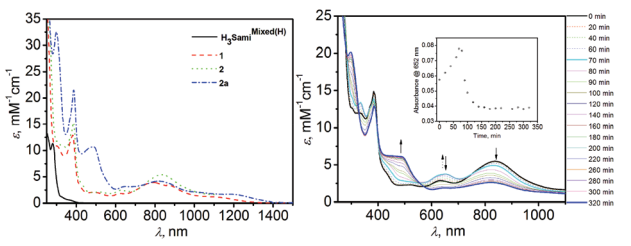

Fig. 2 UV-Vis/NIR spectra of $H_3Sami^{Mixed(H)}$, **1**, **2**, and **2a** (left). Time-dependent UV-vis/NIR spectral changes of **2** at RT in CH_2Cl_2 in the presence of molecular oxygen (right).

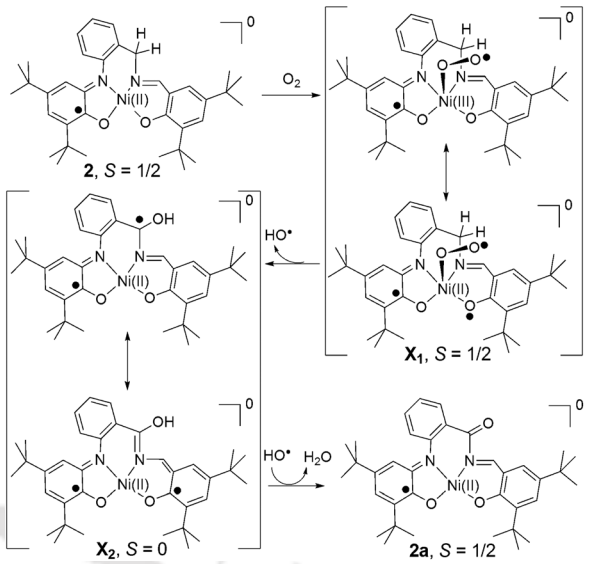

Scheme 3 A mechanistic proposal for the aerial oxidation of **2** to **2a**.

the increase of the product marking band at ~485 nm. This increase was related to the increase of the EPR signal (Fig. 13, S11‡).

Ni(II) or Ni(III)-superoxo, -peroxo, -hydroperoxo, -oxide, and -hydroxo species do not give rise to a strong absorption band at ~652 nm.[8] Moreover, the addition of *m*CPBA (1 equiv.) to the CH_2Cl_2 solution of **2** gave rise to similar changes in the UV-Vis/NIR spectral features (Fig. 14, S12‡) as air did. Therefore, the species showing absorption at ~652 nm were not the corresponding -superoxo, -peroxo, or -hydroperoxo species. Herein, the band at ~652 nm was attributed to the generation of a diamagnetic species $\mathbf{X_2}$, having a delocalizing radical[9] at the benzyl position (Scheme 3).

The ESI (positive mode) mass spectrum of the reaction mixture (**2** + molecular oxygen) at 75 min showed peaks at m/z = 613.30 and m/z = 630.30, in addition to the molecular mass peaks for **2** and **2a** (Fig. 4, S8‡). The m/z = 613.27 peak and its isotope distribution pattern correspond to a $[\{(\mathbf{2} - H) + O\} + H]^+$ species, *i.e.* $[\mathbf{X_2} + H]^+$, while the m/z = 630.26 peak represents a $[\{\mathbf{2} + OO\} + H]^+$ unit, *i.e.* $[\mathbf{X_1} + H]^+$, a dioxygen–**2** adduct (Fig. 15, S12‡). When the reaction was carried out with $^{18}O_2$, the reaction solution exhibited ion peaks at m/z = 615.29 and 613.34. These peaks corresponded to $[\mathbf{2} + {}^{18}O]^+$ and [**2a** (with one ^{18}O)] species with the expected isotope distribution pattern (Fig. 14, S12‡). This labeling experiment confirmed the incorporation of one oxygen atom from molecular oxygen into **2a**, in addition to the transient intermediate (Fig. 15, S12‡). Considering the above experimental (UV-Vis/NIR, X-band EPR, MS) observations, the oxidation process seemed to proceed *via* the route presented in Scheme 3.

Conclusions

To conclude, two asymmetric ligands and their corresponding Ni(II) complexes (**1** and **2**) coordinated to a π-radical anion

were synthesized. Among them, **2** underwent ligand centered C–H bond activation, and consequently a *keto* (C=O) bond formation by reaction with air as the sole oxidant. It was found from X-ray crystallography that the position of the Ni center above the salicylidene plane, and its higher covalency were necessary to activate Ni(II) towards reaction with air. In contrast to **1**, the *tert*-butyl groups present at the salicylidene unit in **2** stabilize the generated radical-containing transient species in its delocalized form, thus favoring the oxidation process.

In general, Ni-oxo, -hydroxo, -peroxo, and -superoxo species are generated either through reaction of oxygen with low-valent Ni(0/I) complexes, or by reaction of Ni(II) complexes with activated oxygen from oxygen releasing sources {*e.g.* hydrogen peroxide (H_2O_2), *meta*-chloroperbenzoic acid (*m*CPBA), *etc.*},[8] whereas complex **2** was converted to its oxygenated product only by reaction with air. This is a very rare example.[8e] Further investigations on the reaction mechanism and the effects of substitution by employing different substituents at the salen unit are ongoing, and our findings might provide Ni(II) complexes as catalysts for aerial oxidation and/or oxygenation *via* C–H activation.

CCDC 951782 [$H_3Sami^{Mixed(H)}$], 951779 [**1**], 951780 [**2**], and 951781 [**2a**] contain the supplementary crystallographic data for this paper.

Acknowledgements

This project was funded by DST (SR/FT/CS-86/2011). SG thanks UGC (India) for doctoral fellowship. Dr T. K. Paine and Dr A. Patra are thankfully acknowledged for their help in general.

Notes and references

1 (*a*) M. T. K. Emmons and C. G. Riordan, *Acc. Chem. Res.*, 2007, **40**, 618; (*b*) S. Yao and M. Driess, *Acc. Chem. Res.*, 2012, **45**, 276.

2 (*a*) E. Y. Tshuva and S. J. Lippard, *Chem. Rev.*, 2004, **104**, 987; (*b*) E. I. Solomon, T. C. Brunold, M. I. Davis, J. N. Kemsley, S.-K. Lee, N. Lehnert, F. Neese, A. J. Skulan, Y.-S. Yang and J. Zhou, *Chem. Rev.*, 2000, **100**, 235; (*c*) M. Akita and S. Hikichi, *Bull. Chem. Soc. Jpn.*, 2002, **75**, 1657; (*d*) N. Kitajima and Y. Moro-oka, *Chem. Rev.*, 1994, **94**, 737; (*e*) M. A. Kopf and K. D. Karlin, in *Biomimetic Oxidations*, ed. B. Muenier, Imperial College Press, London, U.K., 2000, ch. 7; (*f*) L. Q. Hatcher and K. D. Karlin, *J. Biol. Inorg. Chem.*, 2004, **9**, 669.

3 (*a*) W. Bal, M. I. Djuran, D. W. Margerum, T. Edward, J. Gray, M. A. Mazid, R. T. Tom, E. Nieboer and P. J. Sadler, *J. Chem. Soc., Chem. Commun.*, 1994, 1889; (*b*) M. Suzuki, *Acc. Chem. Res.*, 2007, **40**, 609.

4 S. Ghorai and C. Mukherjee, *Chem. Commun.*, 2012, 10180.

5 (*a*) A. L. Smith, K. I. Hardcastle and J. D. Soper, *J. Am. Chem. Soc.*, 2010, **132**, 14358; (*b*) C. Mukherjee, T. Weyhermüller, E. Bothe and P. Chaudhuri, *Inorg. Chem.*, 2008, **47**, 2740; (*c*) C. Mukherjee, T. Weyhermüller, E. Bothe and P. Chaudhuri, *Inorg. Chem.*, 2008, **47**, 11620.

6 (*a*) C. Mukherjee, A. Stmmler, H. Bögge and T. Glaser, *Inorg. Chem.*, 2009, **48**, 9476; (*b*) C. Mukherjee, A. Stmmler, H. Bögge and T. Glaser, *Chem.–Eur. J.*, 2010, 10137; (*c*) T. Glaser, M. Heidemeier, R. Föhlich, P. Hildebrandt, E. Bothe and E. Bill, *Inorg. Chem.*, 2005, **44**, 5467; (*d*) O. Rotthaus, O. Jarjayes, F. Thomas, C. Philouze, C. P. D. Valle, E. S. Aman and J. L. Pierre, *Chem.–Eur. J.*, 2006, **12**, 2293.

7 (*a*) S. Otsuka, A. Nakamura and Y. Tatsuno, *J. Am. Chem. Soc.*, 1969, **91**, 6994; (*b*) S. Sripothongnak, N. Barone and C. J. Ziegler, *Chem. Commun.*, 2009, 4584.

8 (*a*) T. D. Manuel and J.-U. Rohde, *J. Am. Chem. Soc.*, 2009, **131**, 15582; (*b*) F. F. Pfaff, F. Heims, S. Kundu and K. Ray, *Chem. Commun.*, 2012, 3730; (*c*) A. Company, S. Yao, K. Ray and M. Driess, *Chem.–Eur. J.*, 2010, **16**, 9669; (*d*) J. Cho, R. Sarangi, J. Annaraj, S. Y. Kim, M. Kubo, T. Ogura, E. I. Solomon and W. Nam, *Nat. Chem.*, 2009, **1**, 568; (*e*) B. Bag, M. Mondal, G. Rosair and S. Mitra, *Chem. Commun.*, 2000, 1729.

9 (*a*) J. Seth, V. Palaniappan and D. F. Bocian, *Inorg. Chem.*, 1995, **34**, 2201; (*b*) D. Chang, T. Malinski, A. Ulman and K. M. Kadish, *Inorg. Chem.*, 1984, **23**, 817.

RSC Advances

RSC Publishing

COMMUNICATION

View Article Online
View Journal | View Issue

Solvatochromic fluorescent cyanophenoxazine: design, synthesis, photophysical properties and fluorescence light-up sensing of ct-DNA†

Cite this: *RSC Advances*, 2013, **3**, 5374

Received 25th December 2012,
Accepted 25th February 2013

DOI: 10.1039/c3ra23463k

www.rsc.org/advances

Subhendu Sekhar Bag,* Samir Ghorai, Subhashis Jana and Chandan Mukherjee*

We report our new methodology for the Mn^{2+}-catalysed synthesis of donor–acceptor substituted classical fluorescent phenoxazine which showed high solvatochromic emission properties and ct-DNA sensing efficiency *via* a light-up fluorescence response.

The conjugation or complexation of a small organic fluorophore to a biomolecule can extract inner biomolecular information. To investigate chemical and biochemical phenomena, solvatochromic fluorophores are the best suited fluorescent probes because of their ability to sense small variations in dielectric constant within a biomolecular microenvironment.[1] Moreover, for biomolecular applications, long wavelength emission, especially emission in the visible region is highly desirable to discard misleading signals exerted by the auto fluorescence shown by biological macromolecules. In this note, the development of a small organic fluorophore, having strong absorption and long wavelength emission, is described.

Phenoxazines are known for their unexceptional absorbance characteristics that make them non-fluorescent molecules.[2] Fusion of a benzene ring onto the phenoxazine heterocycle does not enhance its fluorescence properties. On the other hand, donor and/or acceptor substituents can give rise to benzophenoxazine fluorophores.[2] Employing this concept, some benzophenoxazines have been generated. Among them very few substituted benzophenoxazines, *e.g.* Meldola's Blue 1, Nile Red 2, Nile Blue 3, are known to show fluorescence properties.[2,3] The available fluorescent benzophenoxazines are mainly based on the benzo[*a*]phenoxazine series and not any other ring fusion series. It is also noticeable that there is no report of simple planar tricyclic classical phenoxazines with fluorescent properties. Furthermore, the synthesis of phenoxazine dyes consists of economically less favorable high temperature condensation methods, and many of them are difficult to carry out in a simple reaction set up.[2e] Therefore, looking at the importance of fluorescent benzophenoxazine-based probes in biological research, there is a need to develop more useful fluorescent phenoxazines/benzophenoxazines which can be utilized as labels/probes of biomolecules *via* a simple but novel synthetic methodology. Hence, in our ongoing research into the design and synthesis of solvatochromic fluorophores,[4] we have considered phenoxazine dyes with donor–acceptor substituents as new potential solvatochromic fluorophores for investigating their possible use in biophysical applications. Herein, we present the synthesis and solvatochromic properties of a phenoxazine derivative, along with its efficient DNA sensing ability *via* a light-up fluorescence response.

Thus, reaction of 1 : 1 3,5-di-*tert*-butylcatechol and 2-aminobenzonitrile in hexane in the presence of Et_3N provided H_2Sami^{CN} (**4**, Scheme 1). When a 1 : 1 acetonitrile solution of H_2Sami^{CN} (**4**) and $MnCl_2{\cdot}4H_2O$ was refluxed in the presence of Et_3N, 69% **1** was isolated.[5] The reaction under room temperature (30 °C) provided **Q** (**5**) in 97% yield. Interestingly, using a catalytic amount of $MnCl_2{\cdot}4H_2O$ (4 mol%), **Q** (**5**) can be obtained in 98% yield. Under reflux, an acetonitrile solution of **Q** provided 96% **1**. It was found that there is no role of the metal salt in the formation of **1** from **Q** (**5**) under the above stated reaction conditions. The final structure of the probe **1** was characterised by NMR, IR, mass spectrometry and X-ray single crystallography.

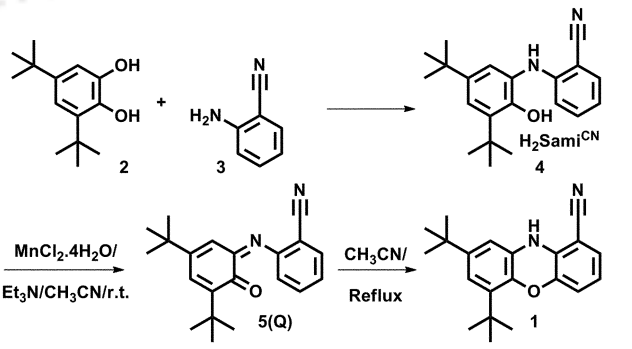

Scheme 1 The synthetic route to **1**.

Department of Chemistry, Indian Institute of Technology Guwahati-781039, Assam, India. E-mail: ssbag75@iitg.ernet.in; cmukherjee@iitg.ernet.in; Fax: +91-361-258-2349; Tel: +91-361-258-2324/2327

† Electronic supplementary information (ESI) available: Experimental details, photophysical spectra and theoretical data. CCDC reference numbers 898030. For ESI and crystallographic data in CIF or other electronic format see DOI: 10.1039/c3ra23463k

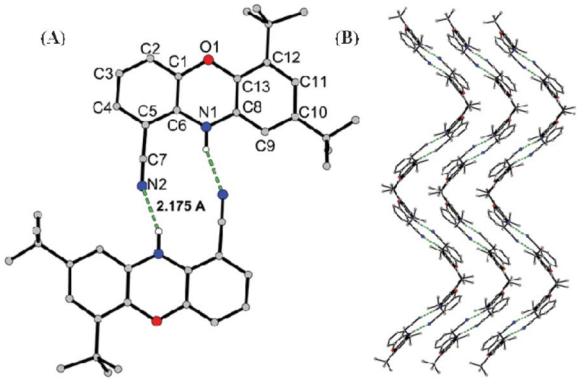

Fig. 1 (A) H-bonding between two individual molecules; (B) H-bonded molecules forming a helical layer (CCDC number for **1**: CCDC 898030).

Crystal structure inspection revealed that two adjacent molecules, connected to each other *via* two strong hydrogen bonds (2.175 Å), form a pair (Fig. 1A). Each pair is almost perpendicular to the previous pair. This results in helical layers with a 2.92 Å interlayer separation (Fig. 1B).

After obtaining the very pure compound in hand we next turned our attention to study its photophysical properties. Thus, the absorption spectra of **1** measured in the 250–700 nm region employing various solvent systems showed two absorption bands at ~309 and ~373 nm. The 373 nm band was assigned as an intramolecular charge transfer (ICT) band owing to the broad shape, intensity, and solvatochromicity (~16 nm) of the band (Fig. 2A).[6] The charge delocalisation from the donor secondary amine (–NH–) to the acceptor cyanide (–CN) substituent is possibly responsible for the polar ground state and ICT nature of the molecule which caused a red shift of the absorption maxima.

A fluorescence photophysical study revealed that the effect of the solvent polarity on the emission maxima is more pronounced than that on the absorption maxima of **1** (Fig. 2B). The fluorescence spectra showed a structureless broad band for the solvents chloroform, ethylacetate, MeOH and CH_3CN, while structured bands were observed for solvents like cyclohexane, toluene, DMSO. An increase in solvent polarity led to a large Stokes shift of the emission maxima for **1**. A simultaneous decrease in both the fluorescence intensity, and the quantum yield (Table 1) was also observed.

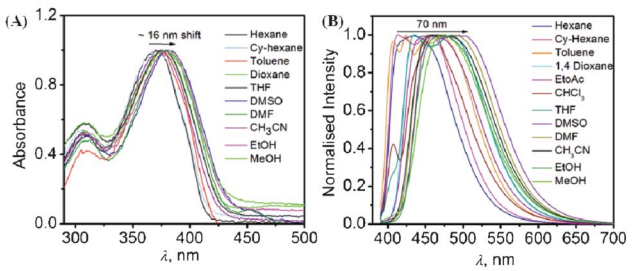

Fig. 2 (A) UV-Vis spectra; (B) normalized emission spectra in various solvents of the donor–acceptor substituted classical phenoxazine **1**.

Table 1 Summary of photophysical properties of **1**

		UV-Vis and fluorescence					
Solvents	Δf	λ_{max}^{abs}(nm)	λ_{max}^{fl}(nm)	Φ_f	τ_1	k_f	k_{nr}
Cyclohexane	0.00	309, 373	415, 457	0.72	—	—	—
Hexane	0.00	308, 373	437	0.78	3.9	1.9	0.5
Toluene	0.01	312, 377	426, 449, 475	0.79	—	—	—
Dioxane	0.02	312, 377	437, 485	0.68	—	—	—
$CHCl_3$	0.15	310, 393	460	0.31	4.6	0.7	1.5
EtOAc	0.20	311, 377	460	0.27	—	—	—
THF	0.21	310, 385	437, 486	0.36	—	—	—
DMSO	0.27	312, 384	460, 503	0.37	6.1	0.6	1.0
DMF	0.28	311, 382	455, 495	0.30	—	—	—
EtOH	0.29	311, 383	474	0.18	—	—	—
ACN	0.31	310, 375	473	0.39	—	—	—
MeOH	0.31	310, 379	477	0.15	3.4	0.4	2.5

τ_1 is in ns; k_f and k_{nr} are $\times 10^{-8}$ s

The fluorophore **1** is solvatochromic as evident by the red shift of the maxima (~40–70 nm) with the increase of solvent polarity ($\lambda_{max,\ cyclohexane}$ 415 nm, and $\lambda_{max,\ DMSO}$ 503 nm). The red shift and signal broadening of the spectra indicated that the conjugation is well extended between the acceptor –CN moiety and the donor –NH– moiety through the internal aromatic benzene ring system. Though the quantum yields decrease gradually as the solvent polarity increases, the intensity of the emission in polar protic solvents is sufficiently high enough for biological applications. Protic solvents, like methanol, are known to induce fluorescence quenching through non-radiative pathways *via* hydrogen bonding.[6] Thus, the fluorescence quantum yield in methanol was low probably because of protic solvent–solute interactions. These properties indicated that **1** has charge transfer (CT) character. The conjugation between the –NH– moiety as an electron donor and the –CN group as an electron acceptor plays an important role in the change in dipole during excitation and makes fluorophore **1** solvatochromic.

A reasonably high slope of $\tilde{\nu}_{max}^{fl}$ *vs.* Δf plot indicated again that the fluorescence states of **1** are of ICT character (ESI†).[7] Time dependent DFT calculations also showed a more significant electron redistribution of the emissive state of **1** and rationalized the explanation of the ICT origin and the solvent polarity dependency of the fluorophores' emission (ESI†).[8] To understand the fluorescence behaviour more precisely, we have measured the fluorescence lifetime in different solvents. It was found that the decay followed a single exponential fitting. Thus, it was clear that the effect of polarity is very similar to what was observed for the fluorescence quantum yield, *i.e.* increasing the polarity of the solvent has led to a shortening of the fluorescence lifetime, and the lifetime is sensitive to H-bonding. In protic polar solvents, like methanol, the fluorescence lifetime of **1** decreases dramatically. A comparison between the decrease in rate constant of the fluorescence emission (k_r) and an increase in rate constant of radiationless deactivation (k_{nr}) points out that the dependence of the fluorescence quantum yield of **1** on the nature of the solvent is mainly dictated by the changes in the rate of radiationless deactivation (ESI†).[6]

The encouraging solvatochromic fluorescence properties shown by **1** and the importance of benzophenoxazine derivatives as labels for several biomolecules has motivated us to examine and explore the possible sensing of biological microenvironments. As an example Nile blue was found to interact with ct-DNA but with a decrease in fluorescence.[2h] Therefore, we have studied the interaction behavior of our probe with calf-thymus DNA (ct-DNA), an easily available biomolecule with wide applications, by spectroscopic means in an aqueous phosphate buffer (pH 7.0).[9] Thus, the gradual addition of ct-DNA showed a negligible effect on the change in absorption maxima and intensity of fluorophore **1** located at 375 nm (ESI†).

The fluorescence titration experiment showed that the emission intensity (λ_{em} = 470 nm) of the probe upon gradual addition of ct-DNA was significantly enhanced upon excitation at 345 nm. The emission reached a maximum at 1 : 1 probe : ct-DNA concentration. This observation clearly indicated the well-defined binding of the probe with ct-DNA (Fig. 3A).[10] Beyond this ratio fluorescence quenching was observed that might be due to the association of more DNA to the probe's surrounding and thus it is likely that the radiationless channel opens up. Further studies of the mechanism of fluorescence quenching are under investigation. The emission response represented the possible binding of the probes along the groove side. The association constant of the probe with ct-DNA was also determined by a Benesi–Hildebrand plot (ESI†) which was found to be 1.4×10^4 M^{-1} with a free energy of binding of -5.6 kcal mol^{-1}.

The thermal melting behavior of ct-DNA in the presence of the probe indicated no destabilization of the ct-DNA, suggesting the probe as a possible groove binder (ESI†).[10] From a dye displacement study we observed no significant change in the fluorescence of an ethidium bromide containing EB–ct-DNA complex upon addition of **1** in different concentrations. This feature indicated that the probe was not interacting with ct-DNA as an intercalator but possibly as a groove binder (ESI†).[11] On the contrary, a decrease in fluorescence intensity of Hoechst 33258 in a Hoechst 33258–ct-DNA complex upon gradual addition of **1** suggested that **1** was most likely a groove binder of ct-DNA.[12] A negligible change in fluorescence anisotropy/polarisation also supported the groove binding of the probe (Fig. 3B).[13] The groove binding of the probe was further supported by the generation of a positive induced CD spectrum appearing at ~305 nm upon the binding of **1** to ct-DNA suggesting a minor groove binding mode which is also supported by macromodel optimized geometry calculations (Fig. 3C and ESI†).[14] Therefore, it is clear from the above facts that **1** senses ct-DNA with a light-up fluorescence response. The low fluorescence intensity of the probes in phosphate buffer in the absence of ct-DNA is not due to the insolubility of the probe but may be attributed to the radiationless channel assisted by the intermolecular hydrogen bonding that is present in aqueous solution.[6c,d] However, as the probe binds more and more along the groove of ct-DNA the nonradiative channels are possibly blocked to a greater extent and are less effective, ultimately leading to an enhancement of the fluorescence signal. Therefore, compared with other phenoxazine dyes such as Nile blue,[2h] our probe has the merit of sensing ct-DNA with a light-up fluorescence response.

In conclusion, we have developed a metal catalysed quinonenamine (**Q**) formation, which subsequently undergoes electrocyclisation followed by aromatization, giving a route to a new classical fluorescent phenoxazine. The phenoxazine showed solvatochromic emission properties. The large to moderate Stokes shift in the emission maxima might make **1** a very effective probe for the analysis of biological microenvironments and labelling of biomolecules utilising the –NH– functionality. We have also shown that the probe **1** is able to sense ct-DNA *via* generation of an enhanced fluorescence signal. The synthesis and exploration of more phenoxazine dyes is our current research focus.

Authors SSB and CM are grateful to DST [SR/SI/OC-69/2008], Govt. of India, and DST [SR/FT/CS-86/2011], respectively, for financial support. Both SG and SJ thank UGC (India) for doctoral fellowships.

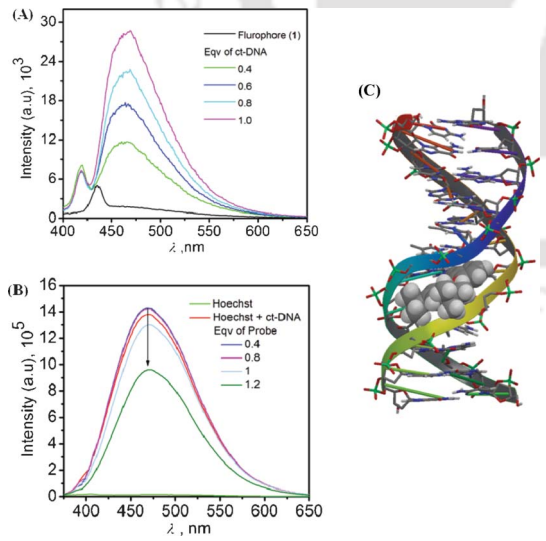

Fig. 3 (A) Fluorescence titration of probe **1** with various concentrations of ct-DNA ([probe] = 50 μM; phosphate buffer, pH 7.0, r.t., λ_{ex} = 345 nm). (B) Emission spectra of Hoechst (light green line at bottom), Hoechst–ct-DNA complex and Hoechst–ct-DNA complex titrated with various concentrations of probe **1**. (C) Amber* energy minimized geometry of the probe with model DNA, showing the minor groove binding of the probe. The DNA sequence was 5′-d(*CP*GP*CP*GP*AP*AP*TP*TP*CP*GP*CP*G)-3′, (PDB Id: 1DNH).

Notes and references

1 (*a*) M. W. Peczuh and A. D. Hamilton, *Chem. Rev.*, 2000, **100**, 2479; (*b*) W. C. Tse and D. L. Boger, *Acc. Chem. Res.*, 2004, **37**, 61; (*c*) J. Wu, W. Liu, J. Ge, H. Zhang and P. Wang, *Chem. Soc. Rev.*, 2011, **40**, 3483; (*d*) L. M. Wysocki and L. D. Lavis, *Curr. Opin. Chem. Biol.*, 2011, **15**, 752.

2 (*a*) S. Rodriguez-Morgade, P. Vfizquez and T. Torres, *Tetrahedron*, 1996, **52**, 6781; (*b*) M. S. J. Briggs, I. Bruce, J. N. Miller, C. J. Moody, A. C. Simmonds and E. Swann, *J. Chem. Soc., Perkin Trans. 1*, 1997, 1051; (*c*) A. Simmonds, J. N. Miller, C. J. Moody, E. Swann, M. S. J. Briggs and I. E. Bruce, *Benzophenoxazine dyes for labeling of biomolecules.*, 19970205; (*d*) C. Sun, J. Yang, L. Li, X. Wu, Y. Liu and S. Liu, *J. Chromatogr., B: Anal. Technol. Biomed. Life Sci.*, 2004, **803**, 173; (*e*) J. Jose and K. Burgess, *Tetrahedron*, 2006, **62**, 11021and references therein;

(*f*) J. Jose and K. Burgess, *J. Org. Chem.*, 2006, **71**, 7835; (*g*) J. Jose, A. Loudet, Y. Ueno, R. Barhoumi, R. C. Burghardt and K. Burgess, *Org. Biomol. Chem.*, 2010, **8**, 2052; (*h*) Q.-y. Chen, D.-h. Li, Y. Zhao, H.-h. Yang, Q.-z. Zhu and J.-g. Xu, *Analyst*, 1999, **124**, 901.

3 (*a*) R. Mohlau and K. Uhlmann, *Justus Liebigs Ann. Chem.*, 1896, **289**, 94; (*b*) C. F. Wichmann, J. M. Liesch and R. E. Schwartz, *J. Antibiot.*, 1989, **42**, 168; (*c*) P. Greenspan and S. D. Fowler, *J. Lipid Res.*, 1985, **26**, 781; (*d*) M. S. J. Briggs, I. Bruce, J. N. Miller, C. J. Moody, A. C. Simmonds and E. Swann, *J. Chem. Soc., Perkin Trans. 1*, 1997, **7**, 1051; (*e*) A. Okamoto, K. Tainaka and Y. Fujiwara, *J. Org. Chem.*, 2006, **71**, 3592; (*f*) K. Kerman, D. Oezkan, P. Kara, H. Karadeniz, Z. Oezkan, A. Erdem, F. Jelen and M. T. Oezsoez, *J. Chem.*, 2004, **28**, 523; (*g*) R. Meldola, *J. Chem. Soc.*, 1879, 2065; (*h*) B. Zinger and P. Shier, *Sens. Actuators, B*, 1999, **56**, 206; (*i*) P. Borowicz, J. Herbich, A. Kapturkiewicz, M. Opallo and J. Nowacki, *Chem. Phys.*, 1999, **249**, 49; (*j*) V. H. J. Frade, M. S. T. Gonçalves and J. C. V. P. Moura, *Tetrahedron Lett.*, 2005, **46**, 4949; (*k*) H. Tanaka, K. Shizu, H. Miyazakia and C. Adachi, *Chem. Commun.*, 2012, **48**, 11392.

4 S. S. Bag and R. Kundu, *J. Org. Chem.*, 2011, **76**, 3348.

5 (*a*) S. Mukherjee, T. Weyhermüller, E. Bothe, K. Wieghardt and P. Chaudhuri, *Dalton Trans.*, 2004, 3842, and references therein; (*b*) C. Mukherjee, T. Weyhermüller, E. Bothe and P. Chaudhuri, *C. R. Chim.*, 2007, **10**, 313, and references therein.

6 (*a*) V. Wintgens, P. Valat, J. Kossanyi, A. Demeter, L. Biczok and T. Berces, *New J. Chem.*, 1996, **20**, 1149; (*b*) B. Ramachandram, G. Saroja, N. B. Sankaran and A. Samanta, *J. Phys. Chem. B*, 2000, **104**, 11824; (*c*) S. Saha and A. Samanta, *J. Phys. Chem. A*, 2002, **106**, 4763; (*d*) B. Ramachandram, G. Saroja, N. B. Sankaran and A. Samanta, *J. Phys. Chem. B*, 2000, **104**, 11824.

7 (*a*) N. Mataga, Y. Kaifu and M. Koizumi, *Bull. Chem. Soc. Jpn.*, 1956, **29**, 465; (*b*) G. M. Badger and I. S. Walker, *J. Chem. Soc.*, 1956, 122; (*c*) J. R. Lakowicz, *Principles of Fluorescence Spectroscopy*, Springer, New York, 3rd edn, 2006; (*d*) M. Shaikh, J. Mohanty, P. K. Singh, A. C. Bhasikuttan, R. N. Rajule, V. S. Satam, S. R. Bendre, V. R. Kanetkar and H. Pal, *J. Phys. Chem. A*, 2010, **114**, 4507.

8 M. J. Frisch *et al.*, *Gaussian 03, revision C.02*; Gaussian, Inc.: Wallingford, CT, 2004.

9 (*a*) A. Granzhan and H. Ihmels, *Org. Lett.*, 2005, **7**, 5119; (*b*) F. Y. Wu, F. Y. Xie, Y. M. Wu and J. I. Hong, *J. Fluoresc.*, 2008, **18**, 175; (*c*) D. Sahoo, P. Bhattacharya and S. J. Chakravorti, *J. Phys. Chem. B*, 2010, **114**, 2044.

10 (*a*) B. F. Ye, Z. J. Zhang and H. X. Ju, *Chin. J. Chem.*, 2005, **23**, 58; (*b*) B. K. Sahoo, K. S. Ghosh, R. Bera and S. Dasgupta, *Chem. Phys.*, 2008, **351**, 163; (*c*) R. Bera, B. K. Sahoo, K. S. Ghosh and S. Dasgupta, *Int. J. Biol. Macromol.*, 2008, **42**, 14; (*d*) R. Ghosh, S. Bhowmik, A. Bagchi, D. Das and S. Ghosh, *Eur. Biophys. J.*, 2010, **39**, 1243.

11 (*a*) J. L. Bresloff and D. M. Crothers, *Biochemistry*, 1981, **20**, 3547; (*b*) H. L. Wu, W. Y. Li, X. W. He, K. Miao and H. Liang, *Anal. Bioanal. Chem.*, 2002, **373**, 163; (*c*) S. Nafisi, M. Bonsaii, P. Maali, M. A. Khalilzadeh and F. Manouchehri, *J. Photochem. Photobiol., B*, 2010, **100**, 84.

12 (*a*) I. Haq, J. E. Ladbury, B. Z. Chowhdry, T. C. Jenkins and J. B. Chaires, *J. Mol. Biol.*, 1997, **271**, 244; (*b*) Y. Guan, R. Shi, X. Li, M. Zhao and Y. Li, *J. Phys. Chem. B*, 2007, **111**, 7336; (*c*) N. Pal, S. D. Verma and S. Sen, *J. Am. Chem. Soc.*, 2010, **132**, 9277.

13 (*a*) C. V. Kumar and E. H. Asuncion, *J. Am. Chem. Soc.*, 1993, **115**, 8547; (*b*) Z. Xu, G. Bai and C. Dong, *Bioorg. Med. Chem.*, 2005, **13**, 5694; (*c*) I. Saha and G. S. Kumar, *J. Fluoresc.*, 2011, **21**, 247.

14 (*a*) A. Rodger and B. Norden, *Circular Dichroism and Linear Dichroism*; Oxford University Press: New York, 1997; (*b*) M. Munde, M. A. Ismail, R. Arafa, P. Peixoto, C. J. Collar, Y. Liu, L. Hu, M.-H. David-Cordonnier, A. Lansiaux, C. Bailly, D. W. Boykin and W. D. Wilson, *J. Am. Chem. Soc.*, 2007, **129**, 13732.

RSC Advances

PAPER

View Article Online
View Journal | View Issue

Synthesis and characterization of a tetraradical-containing octanuclear vanadium cluster formed *via* ligand C–N bond breaking and C–O bond making†

Cite this: *RSC Adv.*, 2014, **4**, 24698

Samir Ghorai and Chandan Mukherjee*

Received 12th March 2014
Accepted 12th May 2014

DOI: 10.1039/c4ra02159b

www.rsc.org/advances

A tetraradical-containing octanuclear vanadium cluster (V_8, complex **2**) was synthesized by reacting *N*(2-methoxyanilino)-3,5-di-*tert*-butylphenol and $VOSO_4 \cdot 5H_2O$ in the presence of Et_3N in MeOH. The reaction proceeded *via* a ligand centre C–N bond cleavage and C–O bond formation. The V_8 cluster was comprised of two identical V_4 clusters where one V_4 cluster was replicated by the other by an inversion centre. A strong antiferromagnetic coupling between the two V_4 clusters, having $S = 1/2$ spin state each, provided a diamagnetic ground state.

Introduction

Polynuclear high-valent vanadium cages have attracted considerable attention due to their immense use in catalysis,[1] intercalated materials,[2] sensor technology,[3] sol–gel chemistry,[3a] and biochemistry.[4] Hence, the synthesis of polynuclear vanadium cages has attracted considerable interests from both chemists and biochemists.

Organic moieties capable of metal ion encapsulation are known as ligands. These ligands can be divided into two groups depending on the change in their oxidation state, which occurs before and after metal ion encapsulation in the presence of oxygen. If there is no change in the ligand oxidation state after metal ion encapsulation, the ligand is called an innocent ligand (IL), while, a change in the ligand oxidation state after metal encapsulation designates the ligand as a non-innocent ligand (NIL). The innocent and non-innocent nature of a ligand depends on the metal ion to which it is coordinated. For example, 2-anilino-4,6-di-*tert*-butylphenol[5] behaves as a non-innocent ligand when it coordinates to copper(II), nickel(II), palladium(II), cobalt(III), iron(III), and manganese(IV) metal ions and provides the corresponding metal–radical complexes. On the contrary, this ligand does not show any change in its oxidation state in its corresponding vanadium(V) complex.[5a] This is possibly because the energy required for the change in the oxidation state of V is lower compared to the energy required for the oxidation of the ligand to its π-radical anion form.[6] This fact holds true for most of the vanadium complexes formed with potential non-innocent ligands. Therefore, radical-containing polynuclear V complexes are very rare in literature.[7,8]

Recently, we have shown that the incorporation of an *-ortho* substituent (–OMe, –CN) with weak coordinating character at the aniline moiety of the ligand 2-anilino-4,6-di-*tert*-butylphenol can provide π-radical-containing tetranuclear V(IV) complex (**1**) *via* ligand centre C–N bond breaking and C–O bond making (Scheme 1).[8a] In complex **1**, three V(IV) centers are anchored by a SO_4^{2-} ion, and the forth one is attached to the cluster mainly by

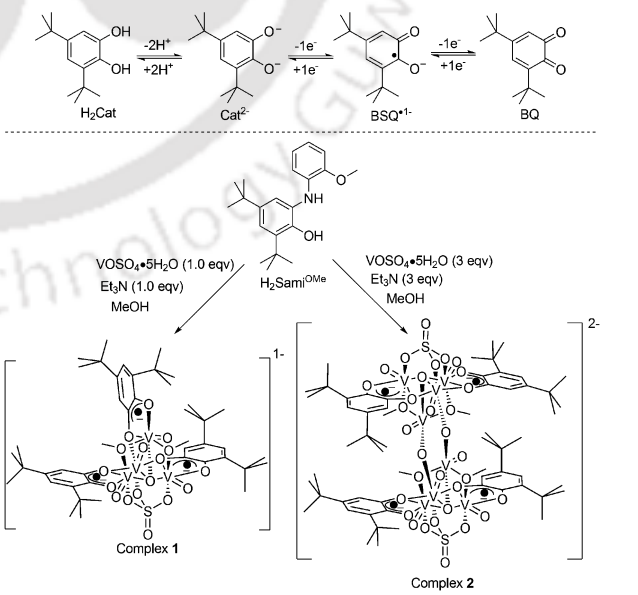

Scheme 1 Top: showing the possible oxidation states that the non-innocent ligand 3,5-di-*tert*-butylcatechol might avail. Bottom: the synthetic routes for complex **1** and complex **2** are presented schematically.

Department of Chemistry, Indian Institute of Technology Guwahati, Guwahati, 781039, Assam, India. E-mail: cmukherjee@iitg.ernet.in; Fax: +91-361-258-2349; Tel: + 91-361-258-2327

† CCDC 981750. For crystallographic data in CIF or other electronic format see DOI: 10.1039/c4ra02159b

two methoxide (–OMe) bridges. Both SO_4^{2-} and –OMe groups are known as labile groups, and therefore, depending on the reaction conditions, *e.g.* vanadium-salt concentration and base concentration, they could be replaced by other oxo-vanadium units formed *in situ* by the aerial oxygenation of the oxophilic vanadium ions supplied by the added vanadium-salt. Moreover, 3,5-di-*tert*-butyl-benzosemioquinone ($BSQ^{\bullet 1-}$) might undergo further oxidation to its two-electron oxidized benzoquinone (BQ^0) form. This form is very labile because of the keto form of its coordination sites, and therefore, could even be replaced easily by the *in situ* formed oxo-vanadium units. Hence, a large polynuclear high-valent vanadium cluster even with coordinated π-radicals could be formed.

Herein, the synthesis and characterization of a tetraradical-containing octanuclear vanadium cluster formed *via* ligand C–N bond breaking and C–O bond making is discussed.

Results and discussion

The ligand H_2Sami^{OMe} was synthesized by reacting equimolar amounts of 2-methoxyaniline and 3,5-di-*tert*-butylcatechol in hexane in the presence of Et_3N under air. The reaction between 1 : 3 : $3H_2Sami^{OMe}$–$VOSO_4 \cdot 5H_2O$–Et_3N in methanol under air provided a deep blue solid. This solid upon recrystallization from a 3 : 1 CH_2Cl_2– MeOH solvent mixture in the presence of $^nBu_4NClO_4$ provided a deep blue crystalline solid suitable for single crystal X-ray diffraction measurement. A detailed synthetic procedure for **2** is given in the Experimental section.

In the infrared (IR) spectrum of H_2Sami^{OMe}, ν(O–H), and ν(N–H) stretching bands appeared at 3425, and 3389 cm^{-1}, respectively. The bending ν(N–H) band appeared at 1600 cm^{-1}. The asymmetric, overtone, and symmetric ν(C–H) stretching bands for *tert*-butyl groups appeared at 2961, 2905, and 2866 cm^{-1}, respectively. Upon complexation, ν(O–H) and ν(N–H) stretching bands disappeared. The asymmetric, overtone, and symmetric ν(C–H) stretching bands for *tert*-butyl groups appeared at 2961, 2912, and 2874 cm^{-1}, respectively. This indicated the presence of 3,5-di-*tert*-butylcatechol moiety in **2**. Strong bands at 978 and 1001 cm^{-1} indicated the presence of a vanadyl (V=O) unit in the complex.[8a] The band at 1014 cm^{-1} appeared because of the coordinated methoxide $\nu(H_3C–O)$ stretching. The ν(S=O) and ν(S–O) stretching bands for the coordinated μ_3–O_3SO units appeared at 1104, 1034, 691, and 660 cm^{-1}.[8a] The ν(V–O) stretching bands appeared in the 573–421 cm^{-1} region. In order to understand the structural difference in terms of bonding-motif between the tetranuclear complex **1** and the octanuclear complex **2**, a comparative IR study was performed (Fig. 1). It was observed that the IR spectra for both complexes were almost similar, except a new band at 783 cm^{-1} was present in the IR spectrum of complex **2** (Fig. 1). This band position was in between ν(V=O) and ν(V–O) stretching values and indicated the presence of a V–O unit with a partial double bond ν(V⋯O) character in **2**. Indeed, bond distance for V–O (1.712 Å) (*vide infra*), which was in between V–O single bond and double band values, was present in **2**.

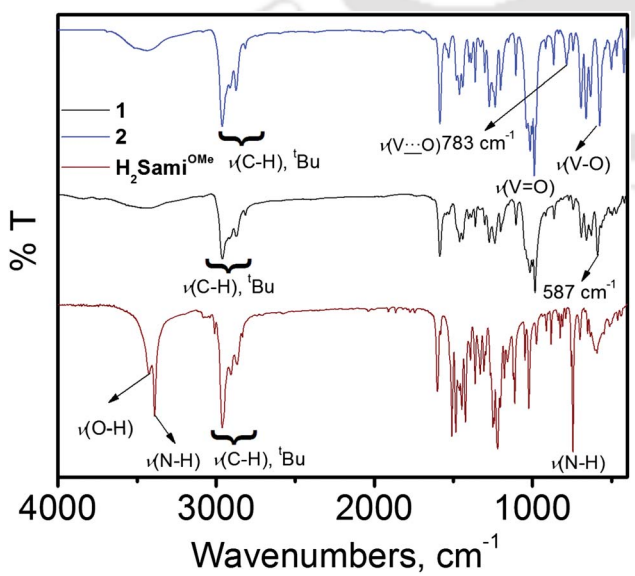

Fig. 1 IR spectra of H_2Sami^{OMe}, **1**, and **2** are presented in 4000–400 cm^{-1} range.

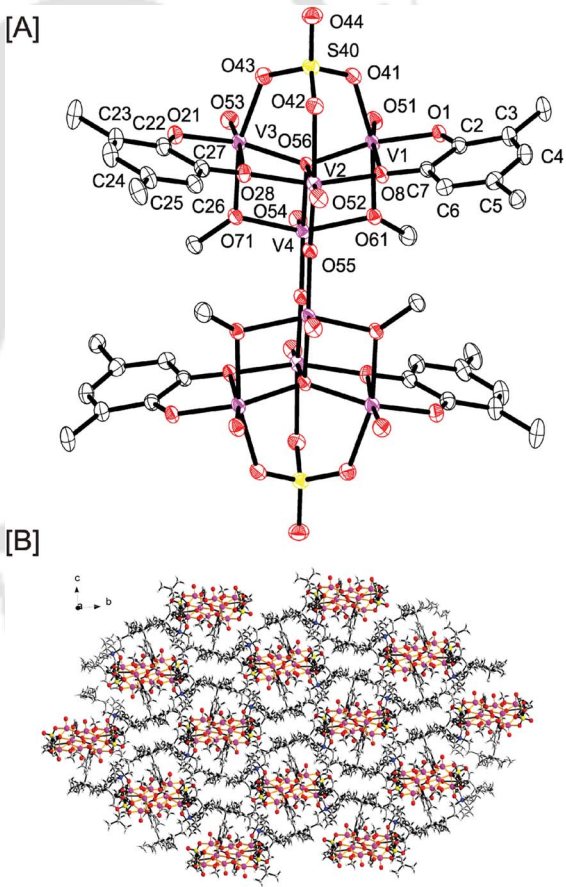

Fig. 2 [A] The dianionic octanuclear V_8 cluster in **2**; thermal ellipsoids are drawn at the 50% probability level. Methyl groups present in the *tert*-butyl groups, and hydrogen atoms are omitted for clarity. [B] Showing discrete V_8 clusters, which are separated from each other and are buried inside a hydrophobic pocket.

Electrospray ionization mass (ESI-MS) in CH_3CN for H_2Sami^{OMe} provided a 100% peak at $m/z = 328.59$. This corresponded to $[M + H]^+$; M is molecular mass. Isotopic pattern distributions confirmed $C_{21}H_{29}NO_2$ as the ligand composition. In the ESI-MS of complex **2** in CH_3CN, a 100% peak in the positive mode appeared at $m/z = 242.25$, showing $C_{12}H_{36}N$ as the composition. This indicated the presence of $^nBu_4N^+$. A 100% mass peak at $m/z = 898.21$ appeared in the negative mode ESI-MS of **2**. Simulated isotopic pattern distribution indicated $C_{60}H_{92}O_{32}S_2V_8$ composition for the observed $m/z = 898.21$ peak and the dianionic character of the V_8 cluster.

Single crystal X-ray diffraction measurement for **2** was performed at 100 K. The complex crystallized in the monoclinic space group $P2_1/n$ (no. 14). The molecular structure is presented in Fig. 2A. Selected bond distances, and bond angles are given in Tables 1 and 2, respectively. Crystallographic data and structure refinement parameters are given in Table 3.

Complex **2** is composed of a dianionic vanadium cluster containing eight vanadium(v) atoms and two $^nBu_4N^+$ ions as counter cations. The eight vanadium centers were distributed equally between the two identical tetranuclear vanadium clusters. Each tetranuclear cluster was reflected by the other using an imaginary point, known as an inversion centre, situated at the middle point of the line connecting two S atoms from the two SO_4^{2-} units. Hence, only one cluster is discussed here.

All four vanadium centers (V1, V2, V3, and V4) in a tetranuclear vanadium cluster were connected by a μ_4–O56 atom in an almost tetrahedron fashion. The V1–O56, V2–O56, V3–O56, and V4–O56 bond distances were 1.9256(15), 2.4001(15), 19402(15), and 2.0234(15) Å, respectively. V1, V2 and V3 were anchored by the μ_3–O_3SO bridging unit and V4 was connected to both V1 and V3 through two individual methoxide (–OMe) bridges. Two tetranuclear vanadium clusters were connected to each other by two oxide (O^{2-}) bridges. The V2–O55 = 1.9362(15) and V4–$O55^i$ = 1.7120(15) Å (i represents the atom obtained by inversion centre operation) bond distances indicated an uneven distribution of O^{2-} charge over the two V–O linkages and emphasized the existence of V2 and V4 in the completely localized + IV and +V oxidation states, respectively.[9]

V1, V2, and V3 atoms were in distorted octahedral geometry, while V4 could be considered to be in square pyramidal geometry due to the long V4–O56 = 2.0234(15) Å bond distance. The V1–O51 = 1.5984(16), V2–O52 = 1.5902(16), V3–O53 = 1.5945(16), and V4–O54 = 1.5944(16) Å bond distances were shorter with respect to other V–O bond distances (Table 1), and represented the vanadyl form of all the vanadium atoms. The coordination site of each V1 and V3 atoms was occupied by a 3,5-di-*tert*-butylcatecholate organic moiety. The V1–O1 = 1.8680(15), V3–O21 = 1.8787(16) Å bond distances were shorter

Table 1 Selected bond distances (Å) for complex **2** are listed below

Bond distance (Å)	**2**
C2–C3	1.420(3)
C3–C4	1.380(3)
C4–C5	1.409(3)
C5–C6	1.391(3)
C6–C7	1.396(3)
C2–C7	1.419(3)
O1–C2	1.328(2)
C7–O8	1.331(2)
V1–O1	1.8680(15)
V1–O51	1.5984(16)
V1–O56	1.9256(15)
V1–O61	1.9879(16)
V1–O41	2.0179(17)
V1–O8	2.2321(15)
V2–O52	1.5902(16)
V2–O28	1.9673(16)
V2–O8	1.9708(15)
V2–O42	2.0504(16)
V2–O56	2.4001(15)
V1–V4	3.0681(5)
V2–V4	3.5996(7)
V2–V1	3.3485(5)
C22–C23	1.423(3)
C23–C24	1.380(4)
C24–C25	1.426(4)
C25–C26	1.386(3)
C26–C27	1.394(3)
C22–C27	1.420(3)
O21–C22	1.322(3)
C27–O28	1.320(3)
V3–O53	1.5945(16)
V3–O21	1.8787(16)
V3–O56	1.9402(15)
V3–O71	1.9745(16)
V3–O43	2.0208(16)
V3–O28	2.2225(16)
V4–O54	1.5944(16)
V4–O71	1.9556(16)
V4–O61	1.9820(15)
V4–O56	2.0234(15)
$V4–V4^i$	3.4533(6)
V3–V4	3.0443(6)
V2–V3	3.3666(7)
V1–V3	3.6496(6)

Table 2 Selected bond angles (°) for complex **2** are given below

O1–V1–O56	153.32(7)
O56–V1–O41	85.49(6)
O51–V1–O8	172.16(7)
O1–V1–O8	75.14(6)
O54–V4–O55	104.68(8)
O71–V3–O43	158.58(7)
O53–V3–O28	174.15(8)
O71–V4–O61	148.96(7)
O56–V3–O21	152.96(7)
O71–V4–O61	148.96(7)
V4–O56–V2	108.63(6)
$V4–O55–V2^i$	149.88(9)
V1–O56–V3	141.50(8)
V1–O56–V4	101.93(7)
V3–O56–V4	100.34(7)
V1–O56–V2	100.88(6)
V3–O56–V2	101.20(6)
O8–V2–O28	144.90(6)
O28–V2–O42	83.42(7)
O52–V2–O56	178.76(7)
$O55^i$–V2–O42	159.89(6)

Table 3 Crystallographic data and structure refinement parameters for **2**

Empirical formula	$C_{92}H_{164}N_2O_{32}S_2V_8$
CCDC number	CCDC 981750
Formula weight	2281.89
Crystal habit, colour	Block, black
Crystal size, mm^3	0.30 × 0.26 × 0.22
Temperature, T	100(2) K
Wavelength, λ	0.71073 Å
Crystal system	Monoclinic
Space group	$P2_1/n$, no. 14
Unit cell dimensions	$a = 15.1675(12)$
	$b = 20.323(2)$ A
	$c = 20.135(3)$ A
	$\alpha = \gamma = 90°$
	$\beta = 111.855(9)°$
Volume, V	5760.5(11) Å^3
Z	2
Calculated density, mg m^{-3}	1.316 mg m^{-3}
Absorption coefficient, μ	0.726 mm^{-1}
$F(000)$	2404
θ range for data collection	2.87° to 33.07°
Limiting indices	$-23 \le h \le 23$, $-31 \le k \le 31$, $-30 \le l \le 30$
Reflection collected/unique	164 119/21 758 [R(int) = 0.0704]
Completeness to θ	99.8%
Max. and min. transmission	0.89215 and 0.71712
Refinement method	Full-matrix least-squares on F^2
Data/restraints/parameters	21758/8/652
Goodness-of-fit on F^2	1.068
Final R indices [$I > 2$sigma(I)]	$R1 = 0.0553$, $wR2 = 0.1242$
R indices (all data)	$R1 = 0.0895$, $wR2 = 0.1411$
Largest diff. peak and hole	1.898 and −0.767 eÅ^{-3}

compared to V1–O8 = 2.2321(15), V3–O28 = 2.2225(16) Å bond distances. This elongation reflected a strong *trans-effect* exerted by both V1–O51 and V3–O53 vanadyl units. The C–C bond distances of the coordinated 3,5-di-*tert*-butyl-containing phenyl rings were not within the 1.390 ± 0.01 Å range as expected for a fully reduced 3,5-di-*tert*-butylcatecholate^{2-} (Cat^{2-}) form.[5,8b] Instead, three long [C22–C27 = 1.420(3), C22–C23 = 1.423(3), and C26–C27 = 1.394(3) Å] and three alternating short and long [C23–C24 = 1.380(4), C24–C25 = 1.426(4), and C25–C26 = 1.386(3) Å] bond distances, as previously reported for benzosemiquinone π-radical (BSQ$^{\bullet 1-}$) systems,[8a] were observed. These indicated a quinoid type distortion in the phenyl ring. In addition, bond distances observed for O21–C22 (1.322(3) Å) and C27–O28 (1.320 (3) Å), which were shorter than that of Cat^{2-} (1.350–1.360 Å)[5a,7f,8b] C–O$_{Ph}$ (O$_{Ph}$ corresponds to oxygen atom attached to phenyl rings) bond distance, emphasized the destruction of the aromaticity of the phenyl rings upon complexation.[8a] Hence, the presence of a π-radical delocalized between two phenolic oxygen atoms could be argued for each of the coordinated 3,5-di-*tert*-butylcatecholate system. In summary, structural analysis indicated that each tetranuclear vanadium cluster was composed of three V(IV) [V1, V2, and V3], and one V(V) [V4] atoms. Among them V1 and V3 each were coordinated to a π-radical.

Further investigation of the crystal structure of **2** revealed that each octanuclear vanadium (V$_8$) cluster was separated from each other and buried inside a hydrophobic pocket. The pockets were made by two chain-like ^{n}Bu$_4$N$^+$ ions and methyl groups from the *tert*-butyl groups, which were attached to 3,5-di-*tert*-butylsemiquinone (BSQ$^{\bullet 1-}$) moieties (Fig. 2B).

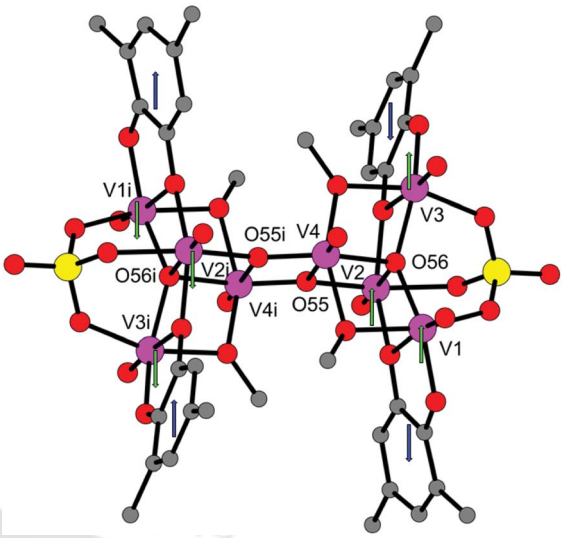

Fig. 3 The dianionic octanuclear V$_8$ cluster with the unpaired-spin alignments.

The V$_8$ cluster was made of two identical V$_4$ clusters, which were connected to each other by two oxide bridges, and one V$_4$ cluster was replicated by the other by an inversion centre (*vide supra*). Each V$_4$ cluster comprised three paramagnetic V(IV) {$3d^1$, $S = 1/2$} centres and one diamagnetic V(V) {$3d^0$, $S = 0$} centre. Among the three V(IV) {V1, V2, and V3} centres, two {V1, and V3} were each coordinated to a π-radical anion ($S = 1/2$) of benzosemiquinone moiety, and the other one {V2} was connected to the diamagnetic V(V) {V4} centre through oxide (O55 and O56) bridges (Fig. 3).

The V$_8$ cluster was X-band EPR inactive at room temperature (25 °C). Variable-temperature magnetic susceptibility measurements indicated that the complex acquired a diamagnetic ground state, and even at 300 K its diamagnetic character was retained. The coupling between a V(IV) {t^1_{2g}} and the corresponding coordinated π-radical (p_z) was expected[10] and known to be antiferromagnetic,[8a] and therefore, a tetranuclear V$_4$ cluster, which contained a localized V(IV) paramagnetic centre, was supposed to have an $S = 1/2$ spin state. The diamagnetic character of the V$_8$ cluster confirmed an antiferromagnetic coupling between the two V$_4$ clusters. Herein, the antiferromagnetic coupling between the two V(IV) {d^1_{xy}} centres, which were separated by 6.23 Å, was anticipated by the presence of an inversion centre. Interestingly, this coupling progressed through two diamagnetic V(V) centres, which were connected to the V(IV) centres by two oxide bridges having coupling favouring ∼150 and ∼109° V4–O55–V2, and V4–O56–V2 bond angles, respectively.

Conclusion

To conclude, a new and scarce tetraradical-containing octanuclear vanadium cluster (V$_8$) has been synthesized by reacting

1 : 3 equivalents of *N*(2-methoxyanilino)-3,5-di-*tert*-butylphenol and $VOSO_4 \cdot 5H_2O$ in the presence of Et_3N in MeOH. The reaction proceeded *via* ligand centre C–N bond breaking and C–O bond making processes. Herein, we found that by changing the concentration of vanadium-salt ($VOSO_4 \cdot 5H_2O$) and base (Et_3N), one of the three 3,5-di-*tert*-butyl benzosemioquinone moieties can be oxidized and removed from the V_4 cluster of complex **1**. Two such generated clusters were then combined with each other by two bridging oxide oxygen atoms to provide the V_8 cluster present in complex **2**. This strategy might open new routes for the rational synthesis of polynuclear vanadium clusters (*e.g.* V_{12}, V_{16}), which could be used as intercalated and magnetic materials.

V_8 cluster in complex **2** comprised of two identical V_4 clusters, which have an $S = 1/2$ spin state each due to the localized V(IV) centers. Herein, we observed a strong antiferromagnetic coupling between two localized V(IV) centers which were separated from each other by 6.23 Å. Interestingly, the coupling proceeded through two diamagnetic V(V) ions and two bridging oxide oxygen atoms.

Experimental section

Materials

All the chemicals and solvents were obtained from commercial sources and were used as supplied, unless mentioned otherwise. 3,5-di-*tert*-butylcatechol, $VOSO_4 \cdot 5H_2O$, and 2-methoxyaniline were purchased from Sigma-Aldrich. Solvents were obtained from Merck (India).

Physical methods

X-ray crystallographic data were collected using a Bruker AXS Enraf-Nonius KappaCCD diffractometer, equipped with a fine focus 1.75 kW sealed tube Mo–Kα radiation ($\lambda = 0.71073$ Å) at 296(2) K with increasing w (width of 0.3° per frame) at a scan speed of 3 s per frame. Structures were solved by direct methods using SHELXS-97 and refined with full-matrix least squares on F^2 using SHELXL-97. All non-hydrogen atoms were refined anisotropically. IR spectra were recorded on a Perkin Elmer Instrument at normal temperature with KBr pellet by grinding the sample with KBr (IR Grade). UV-Vis spectra were recorded on a Perkin Elmer, Lamda 750, UV/VIS/NIR spectrometer by preparing a known concentration of the samples in HPLC Grade CH_2Cl_2 at room temperature using a cuvette of 1 cm width. EPR spectra were measured on X-Band Microwave Unit, JES-FA200 ESR spectrometer. Magnetic measurement using SQUID magnetometer was performed at the Department of Physics, IISc, Bangalore, India.

Synthesis of H_2Sami^{OMe}

The synthetic procedure for H_2Sami^{OMe} was reported previously.[8a]

Synthesis of complex 2

H_2Sami^{OMe} (0.164 g, 0.5 mmol), $VOSO_4 \cdot 5H_2O$ (0.380 g, 1.5 mmol) and Et_3N (0.15 mL) were added sequentially in methanol (7 mL). The reaction mixture was stirred under air at room temperature (30 °C) for 2 h and 40 min. During this period, a blue precipitate appeared. The precipitate was filtered and washed with a minimum volume of methanol (5 mL). This blue precipitate was then recrystallized from a CH_2Cl_2–MeOH (3 : 1) solvent mixture after the addition of tetrabutylammonium perchlorate (0.015 g). A block-shaped crystalline compound appeared in 4 days. The crystalline solid was then thoroughly washed with methanol (20 mL) to obtain complex **2**. Yield: 0.040 g, 15%. FTIR (KBr pellet, cm^{-1}): 2961, 2912, 2874, 1584, 1529, 1480, 1460, 1440, 1400, 1387, 1361, 1301, 1272, 1235, 1200, 1104, 1036, 1014, 1001, 987, 915, 864, 783, 742, 691, 660, 630, 573, 500, 466, 420. ESI-MS (−ve) for $[C_{60}H_{92}O_{32}S_2V_8]^{2-}$: calcd. 898.04; found 898.21. ESI-MS (+ve) for $[C_{16}H_{36}N]^+$: calcd. 242.28; found 242.25.

Acknowledgements

This project is funded by DST (SR/FT/CS-86/2011) and BRNS (2012/37C/28/BRNS/1375). SG thanks UGC (India) for his doctoral fellowship. We thank sincerely Dr Thomas Weyhermüller for the X-ray single crystal measurement and analysis. Prof. P. S. Anil Kumar is thankfully acknowledged for the magnetic moment measurements.

Notes and references

1 (*a*) N. Hall, M. Orio, A. Jorge-Robin, B. Gennaro, C. Marchi-Delapierre and C. Duboc, *Inorg. Chem.*, 2013, **52**, 13424; (*b*) G. Zhang, B. L. Scott, R. Wu, L. A. "Pete" Silks and S. K. Hanson, *Inorg. Chem.*, 2012, **51**, 7354; (*c*) J. Hartung, S. Drees, M. Greb, P. Schmidt, I. Svoboda, H. Fuess, A. Murso and D. Stalke, *Eur. J. Org. Chem.*, 2003, **13**, 2388; (*d*) M. G. Kanatzidis, C.-G. Wu, H. O. Marcy and C. R. Kannewurf, *J. Am. Chem. Soc.*, 1989, **111**, 4139; (*e*) M. Z. A. Munshi, W. H. Smyrl and C. Schmidtke, *Chem. Mater.*, 1990, **2**, 530; (*f*) J.-M. Amarilla, B. Casal, J.-C. Galvan and E. Ruiz-Hitzky, *Chem. Mater.*, 1992, **4**, 62; (*g*) G. Deo, F. D. Hardcastle, M. Richards, A. M. Hirt and I. E. Wachs, in *Novel Materials in Heterogeneous Catalysis*, ed. R. T. K. Baker and L. L. Murrell, American Chemical Society, Washington, D.C., 1990, ch. 29 and references therein; (*h*) R. D. Srivastava, *Heterogeneous Catalytic Science*, CRC Press, Boca Raton, FL, 1988, ch. 3; (*i*) G. Busca and G. Centi, *J. Am. Chem. Soc.*, 1989, **111**, 46; (*j*) F.-L. Wang and W.-S. Lee, *Chem. Commun.*, 1991, 1760 and references therein.

2 (*a*) C. Glynn, D. Thompson, J. Paez, G. Collins, E. Benavente, V. Lavayen, N. Yutronic, J. D. Holmes, G. González and C. O. Dwyer, *J. Mater. Chem. C*, 2013, **1**, 5675; (*b*) Y. Wang and G. Cao, *Chem. Mater.*, 2006, **18**, 2787; (*c*) A. R. Armstrong, C. Lyness, P. M. Panchmatia, M. S. Islam and P. G. Bruce, *Nat. Mater.*, 2011, **10**, 223.

3 (*a*) J. Livage, *Chem. Mater.*, 1991, **3**, 579; (*b*) A. R. Raju and C. N. R. Rao, *Chem. Commun.*, 1991, 1260.

4 (*a*) D. W. Boyd, K. Kustin and M. Niwa, *Biochim. Biophys. Acta*, 1985, **827**, 472; (*b*) P. Csermely, A. Martonosi, G. C. Levy and A. J. Ejchart, *Biochem. J.*, 1985, **230**, 807; (*c*) D. C. Crans and

S. M. Schelble, *Biochemistry*, 1990, **29**, 6697; (*d*) D. C. Crans and C. M. Simone, *Biochemistry*, 1991, **30**, 6734; (*e*) D. C. Crans, E. M. Willging and S. R. Butler, *J. Am. Chem. Soc.*, 1990, **112**, 427; (*f*) D. Rehder, *Angew. Chem., Int. Ed.*, 1991, **30**, 148.

5 (*a*) H. Chun, C. N. Verani, P. Chaudhuri, E. Bothe, E. Bill, T. Weyhermüller and K. Wieghardt, *Inorg. Chem.*, 2001, **40**, 4157; (*b*) P. Chaudhuri, C. N. Verani, E. Bill, E. Bothe, T. Weyhermüller and K. Wieghardt, *J. Am. Chem. Soc.*, 2001, **123**, 2213; (*c*) H. Chun, E. Bill, T. Weyhermueller and K. Wieghardt, *Inorg. Chem.*, 2003, **42**, 5612; (*d*) H. Chun, P. Chaudhuri, T. Weyhermueller and K. Wieghardt, *Inorg. Chem.*, 2002, **41**, 790.

6 P. J. Chirik and K. Wieghardt, *Science*, 2010, **327**, 794.

7 (*a*) A. M. Morris, C. G. Pierpont and R. G. Finke, *Inorg. Chem.*, 2009, **48**, 3496; (*b*) S. Bruni, A. Canneschi, F. Cariati, C. Delfs, A. Dei and D. Gatteschi, *J. Am. Chem. Soc.*, 1994, **116**, 1388; (*c*) Y.-H. Chang, C.-L. Su, R.-R. Wu, J.-H. Liao, Y.-H. Liu and H.-F. Hsu, *J. Am. Chem. Soc.*, 2011, **133**, 5708; (*d*) M. E. Cass, D. L. Greene, R. M. Buchanan and C. G. Pierpont, *J. Am. Chem. Soc.*, 1983, **105**, 2680; (*e*) M. E. Cass, N. R. Gordon and C. G. Pierpont, *Inorg. Chem.*, 1986, **25**, 3962; (*f*) To review: S. N. Brown, *Inorg. Chem.*, 2012, **51**, 1251.

8 (*a*) S. Ghorai and C. Mukherjee, *Chem. Commun.*, 2012, **48**, 10180; (*b*) S. Ghorai and C. Mukherjee, *Dalton Trans.*, 2014, **43**, 394.

9 A. Müller, M. Penk and J. Döring, *Inorg. Chem.*, 1991, **30**, 4935.

10 O. Khan, in *Molecular Magnetism*, VCH, New York, 1993, pp. 199–200.

ChemComm

Dynamic Article Links

Cite this: *Chem. Commun.*, 2012, **48**, 10180–10182

www.rsc.org/chemcomm

COMMUNICATION

Ortho-substituent induced triradical-containing tetranuclear oxo-vanadium(IV) cluster formation *via* ligand C–N bond breaking and C–O bond making†‡

Samir Ghorai and Chandan Mukherjee*

Received 6th June 2012, Accepted 29th August 2012
DOI: 10.1039/c2cc35963d

Substituent having weak-coordination character, and attached at the *ortho*-carbon atom to the aniline moiety of 2-anilino-4,6-di-*tert*-butylphenol, provided a triradical-containing tetranuclear vanadium(IV) complex *via* ligand C–N bond breaking and C–O bond making.

Since the discovery of radical-containing intermediates for various metalloenzymatic transformations,[1] transition-metal complexes where the metal center is coordinated to π-radical(s) have drawn considerable attention. In this regard, several redox-active organic compounds, known as non-innocent ligands, and their corresponding metal complexes have been synthesized.[2] The complexes have been studied by X-ray crystallography and various other spectroscopic techniques towards better understanding of the metal–radical interactions, and consequently, the intermediates involved in various enzymatic transformations.[2]

2-Anilino-4,6-di-*tert*-butylphenol {$H_2[AP^H]$} (Scheme 1) is a non-innocent ligand and stabilizes several radical-containing transition-metal complexes, *e.g.*, Cu(II), Ni(II), Co(III), Cr(III), Fe(III), *etc.*[3] However, its corresponding vanadium(V) complex is a mononuclear non-oxo V(V) with no coordinated π-radical anion. This could be because of the energy required for the change in oxidation state of V is lower compared to the energy required for the oxidation of the non-innocent ligand to its radical form.[4]

Copper(II) complexes derived from 2-[3,5-di-substituted(X)-anilino]-4,6-di-*tert*-butylphenol ($H_2[AP^X]$, Scheme 1) ligands show a clear trend in the ligand-based oxidation potentials with the electron-donating and -withdrawing capability of the attached *meta*-substituent.[5] In this case, the geometric and electronic structural modulations of the corresponding Cu(II) complexes operate *via* σ-bonding (σ-effect).

Knowing that (a) the π-effect is more pronounced compared to σ-effect, and (b) substituents have an effect on both electronic and geometric structure of the corresponding complexes, we have made a modification to the non-innocent ligand {$H_2[AP^H]$} by substituting a cyanide group (H_2Sami^{CN}, Scheme 1) at the *ortho*-carbon atom to the aniline unit. The aim is an understanding of the effect of *ortho*-substituent to the geometric and electronic structure of the corresponding transition-metal complexes. As a priority, we chose vanadium (V) as metal because; (i) radical-containing vanadium complexes are rare and have remained elusive till now,[6] and (ii) substitution effect could lower the ligand center oxidation potential compared to the metal center, hence a radical-containing V complex might be achieved.

Herein, we report the synthesis and characterization of the ligand H_2Sami^{CN} and the corresponding V complex, which has been found as a triradical-containing tetranuclear oxo-V(IV) cluster.

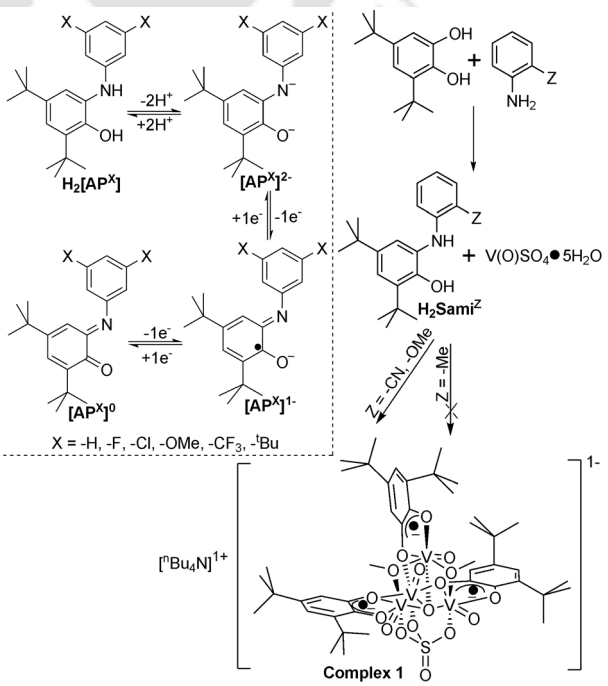

Scheme 1

Department of Chemistry, Indian Institute of Technology, Guwahati, 781039, Assam, India. E-mail: cmukherjee@iitg.ernet.in; Fax: +91-361-258-2349; Tel: +91-361-258-2327

† Dedicated to Dr Thomas Weyhermüller on the occasion of his 50th birthday.

‡ Electronic supplementary information (ESI) available: Experimental procedures and characterization data; mass, EPR,UV-vis. X-ray structural parmeters and bond distances and angles for **1**. CCDC 883669. For ESI and crystallographic data in CIF or other electronic format see DOI: 10.1039/c2cc35963d

H_2Sami^{CN} was synthesized by reacting equimolar amounts of 2-aminobenzontrile and 3,5-di-*tert*-butylcatechol in hexane in the presence of triethyl amine (Et_3N) under air (Scheme 1). Reaction between 1 : 1 $VO(SO_4)\cdot 5H_2O$ and H_2Sami^{CN} in MeOH in the presence of Et_3N provided the corresponding vanadium complex as a deep blue solid. Addition of $^nBu_4NClO_4$ to a 3 : 1 : 1 CH_2Cl_2–CH_3CN–CH_3OH solution of the blue solid, and finally, slow evaporation of the resulting solution provided a crystalline solid suitable for X-ray diffraction studies (Scheme 1).

In the IR spectrum of H_2Sami^{CN}, ν(O–H), ν(N–H) and ν(C–H) [^{t}Bu] stretching bands appeared at 3421, 3355, and 2950, 2904, 2864 cm^{-1}, respectively. The band at 2221 cm^{-1} confirmed the presence of –CN group. Upon complex formation, the ν(O–H) and ν(N–H) stretching bands vanished, indicating deprotonation of the groups. Interestingly, no band corresponding to ν(C≡N) stretch appeared in the IR spectrum of **1**. This implied ligand C–N bond cleavage. Furthermore, the presence of 2960, 2905, 2873 cm^{-1} bands emphasized the coordination of the 3,5-di-*tert*-butylcatecholate moiety to the metal ion. Strong bands at 982 and 999 cm^{-1} indicated the presence of vanadyl (V=O) units in different coordination environments. A sharp band at 1015 cm^{-1} appeared due to coordinated methoxy groups [$\nu(H_3C–O)$ stretch]. Bands at 1103, 1030, 689 and 657 cm^{-1} bands are attributed to ν(S=O) and ν(S–O) stretching of the coordinated μ_3-O_3SO unit.[7] The ν(V–O) stretching bands appeared in the 587–496 cm^{-1} region.[8]

Electrospray ionization mass (ESI-MS) in CH_3CN for H_2Sami^{CN} provided a 100% peak at m/z = 323.56, corresponding to $[M + H]^+$; M = molecular mass, and confirmed the composition $C_{21}H_{26}N_2O$ for the ligand (Fig. S1‡). In the ESI-MS mass spectrum of complex **1** in CH_3CN a 100% peak at m/z = 242.25 arose in the positive mode, while, in the negative mode, a 100% peak at 1101.92 was observed. The peak at m/z = 242.25 confirmed the presence of $^nBu_4N^+$ in the complex. Simulated isotope pattern distributions indicated a $C_{44}H_{66}O_{17}S_1V_4$ composition for the observed peak at m/z = 1101.92 (Fig. S2 and S3‡).

Single-crystal X-ray diffraction measurement for **1**·CH_3CN was performed at 296(2) K‡. It crystallized in the orthorhombic space group *Pbca* (no. 61) and the molecular structure is presented in Fig. S4‡with selected bond distances and angles given in Tables S2 and S3‡, respectively.

Complex **1** is composed of a monoanionic cluster containing four vanadium atoms (Fig. 1) and a $^nBu_4N^+$ counter cation. All the four vanadium (V1, V2, V3 and V4) atoms are in a distorted octahedral coordination environment ligated by six oxygen donors, and are connected to each other *via* a μ_4-O7 atom in almost tetrahedral fashion (Fig. 1). The V1–O7, V2–O7, V3–O7 and V4–O7 bond distances are 1.937(3), 1.964(3), 1.946(3) and 2.408(3) Å, respectively. The V1–O13 = 1.583(3); V2–O14 = 1.584(3), V3–O15 = 1.584(3) and V4–O16 = 1.577(3) Å bond distances are shorter compared to other V–O bonds and are in accord with previously reported V(IV)=O units.[9] The shortest V4–O16 bond distance was because of the lowest *trans* effect as reflected by the highest V4–O7 bond distance compared to other V–O7 bonds. This feature allows the V4 center to be also considered as in a square-pyramidal geometry.

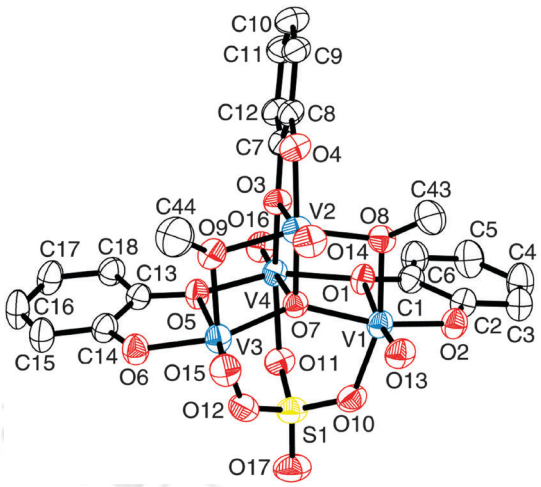

Fig. 1 The monoanionic tetranuclear V_4 cluster present in **1**; thermal ellipsoids are drawn at the 50% probability level. The *tert*-butyl groups at C3, C5, C9, C11, C15 and C17 together with hydrogen atoms are omitted for clarity.

The V2 atom is connected to each V1 and V3 *via* two methoxy (–OMe) groups while a SO_4^{2-} group anchors V1, V3 and V4 centers as a μ_3-O_3SO bridging unit. V1, V2 and V3 atoms are each connected to a 3,5-di-*tert*-butylcatecholate moiety *via* O1 and O2; O3 and O4; O5 and O6 atoms, respectively. The V4 atom shares one oxygen atom (O1, O3 and O5) from each of the three 3,5-di-*tert*-butylcatecholate moieties as its coordinating sites. The C–C bond distances of the phenyl rings were not all within the 1.400 ± 0.010 Å range as observed for catecholate (Cat^{2-})[3,10] systems. Rather alternate short and long C–C bond distances [*e.g.* C3–C4 = 1.371(6); C4–C5 = 1.421(6), C5–C6 = 1.381(7) Å], as previously reported for semiquinone π-radical (SQ^{-})[5,6d,f,10] systems, are observed. Additionally, the observed C–O_{Ph} (O_{Ph} corresponds to oxygen atom attached to phenyl rings) bond distances [C1–O1 = 1.316(5), C2–O2 = 1.322(5), C7–O3 = 1.333(5), C8–O4 = 1.346(5), C13–O5 = 1.329(5), C14–O6 = 1.331(5) Å], which were found in between that of Cat^{2-} (1.350–1.360 Å)[6c,d,f,9b,10] and SQ^{1-} (1.298–1.326 Å)[6a,d,f] C–O_{Ph} bond distances, indicate the destruction of the aromaticity of the phenyl rings upon complexation. Hence, the presence of a π-radical delocalized between two phenolic oxygen atoms could be argued for the each 3,5-di-*tert*-butylcatecholate system.

The inconsistent V–O_{Ph} bond distances could not be considered for the assignment of the oxidation state of the V atoms [*e.g.* V1–O1 = 2.242(3) and V1–O2 = 1.862(3) Å]. However, the presence of three π-radical-containing catecholate moieties, almost same vanadyl bond distances, and the mononegative character of the V_4-cluster invoke the +IV oxidation state for all the V atoms (*vide infra*). Therefore, the monoanionic part of the complex is best described as a triradical-containing tetranuclear oxo-V(IV) cluster.

Temperature-dependent magnetic susceptibility measurements showed μ_{eff} = 1.70 μ_B at 5 K. The value increased with increase in temperature and reached at 3.77 μ_B at 300 K (Fig. S5‡). This feature indicated the existence of multiparamagnetic centers in **1**. V1, V2 and V3 were each coordinated

to ligand centered π-radical anions. The antiferromagnetic coupling between the paramagnetic V(IV) and π-radical provided a diamagnetic environment around the vanadium centers. V4, which was not coordinated to a π-radical anion, was then the paramagnetic center and carried the residual electron density at 5 K.

Complex **1** was EPR active and showed an eight-line X-band EPR spectrum (^{51}V; I = 7/2). The best fit to the experimental data provided the parameters; g_{av} = 1.978; A_{av} = 72 × 10^{-4} cm^{-1} (Fig. S6‡).

To understand the role of the substituent and the probable mechanism for the C–N bond breaking, C–O bond making and consequently, the triradical-containing tetranuclear oxo-V(IV) cluster formation, we have synthesized another ligand by replacing –CN with –OMe. Here, we chose –OMe as a π-electron donor, in contrast to –CN, so as study the electronic effect. Furthermore, both groups are moderately bulky and can also undergo a weak-interaction to metal ion, consequently, geometrical (steric and/or coordination) effects can also be studied.

Interestingly, under the same reaction conditions, the –OMe substituent-containing ligand also provided complex **1**.[11] This implied that the formation of complex **1** progressed *via* the same geometrical intermediate(s), and it can also be argued that the geometrical effect predominated over the electronic effect (little or no effect) for the complex formation. To understand the geometrical effect (steric and/or coordination), ligand H_2Sami^{CH3}, where a moderately bulky and non-coordinating $–CH_3$ group was attached at the *ortho*-position, was also synthesized. Employing this ligand, complex **1** could not be isolated under the same reaction condition. This indicated a weak interaction (coordination effect) between the substituent and metal center was essential for the radical-containing vanadium complex formation.

ESI-MS of the reaction solution after 2 h reflux and 15 min air-stirring showed a peak corresponding to a vanadyl moiety ligated to a deprotonated ligand $[Sami^{Z}]^{n-}$, and a SO_4^{2-} ion. Though the actual mechanism for the cluster formation is not understood yet, herein, we propose that at the initial stage both ligands form an identical SO_4^{2-}-ligated vanadyl complex (Fig. S11‡). The substituent might then undergo a weak-interaction with the vanadium center of another molecule owing their ambidentate (–CN)/bridging (–OMe) character, and consequently, favors cluster formation *via* C–N bond cleavage and C–O bond formation.

To conclude, we have synthesized two new ligands, H_2Sami^{CN} and H_2Sami^{OMe}. Both ligands reacted with $VO(SO_4)\cdot 5H_2O$ and provided the same paramagnetic oxo-vanadium complex, *i.e.* a triradical-containing oxo-V(IV) complex, under the same reaction conditions. It seems that the coordination of *ortho*-substituent is the key for the ligand centered π-radical formation. Though it is to early to generalize, our study shows that the presence of a substituent, having weak-coordination character, at the *ortho*-carbon atom to the aniline part of a 2-anilino-4,6-di-*tert*-butylphenol ligand, will provide the triradical-containing oxo-V(IV) complex.[12] In our laboratory, the newly discovered phenomenon is under further investigation by employing various types of *ortho*-substituent. Furthermore, our attempts towards the understanding of the mechanism will illuminate small molecule (*e.g.* O_2, N_2) activation by vanadium and vanadium-radical complex formation.

This project is funded by IITG (SG/CHM/P/CM/1). S. G. thanks UGC (India) for a doctoral fellowship. Dr T. K. Paine, Dr S. S. Bag, Prof. M. Ray, Dr P.S. Anil Kumar and Prof. G. K. Lahiri are thankfully acknowledged for their immense support in general.

Notes and references

1 (*a*) J. Stubbe and W. A. van der Donk, *Chem. Rev.*, 1998, **98**, 705; (*b*) R. H. Holm, P. Kennepohl and E. I. Solomon, *Chem. Rev.*, 1996, **96**, 2239; (*c*) J. W. Whittaker, *Chem. Rev.*, 2003, **103**, 2347; (*d*) R. Banerjee, *Chem. Rev.*, 2003, **103**, 2081.

2 (*a*) P. Chaudhuri and K. Wieghardt, *Prog. Inorg. Chem.*, 2001, **50**, 151; (*b*) R. H. Holm and E. I. Solomon, *Chem. Rev.*, 2004, **104**, 347; (*c*) B. A. Jazdzewski and W. B. Tolman, *Coord. Chem. Rev.*, 2000, **633**, 200; (*d*) F. Thomas, G. Gellon, I. Gautier-Luneau, E. Saint-Aman and J.-L. Pierre, *Angew. Chem., Int. Ed.*, 2002, **41**, 3047; (*e*) A. Sokolowski, H. Leutbecher, T. Weyhermüller, R. Schnepf, E. Bothe, E. Bill, P. Hildebrandt and K. Wieghardt, *JBIC, J. Biol. Inorg. Chem.*, 1997, **2**, 444; (*f*) L. Benisvy, A. J. Blake, D. Collison, E. S. Davies, C. D. Garner, E. J. L. McInnes, J. McMaster, G. Whittacker and C. Wilson, *Chem. Commun.*, 2001, 1824; (*g*) P. Chaudhuri, K. Wieghardt, T. Weyhermüller, T. K. Paine, S. Mukherjee and C. Mukherjee, *Biol. Chem.*, 2005, **386**, 1023.

3 H. Chun, C. N. Verani, P. Chaudhuri, E. Bothe, E. Bill, T. Weyhermüller and K. Wieghardt, *Inorg. Chem.*, 2001, **40**, 4157.

4 P. J. Chirik and K. Wieghardt, *Science*, 2010, **327**, 794.

5 C. Mukherjee, U. Pieper, E. Bothe, V. Bachler, E. Bill, T. Weyhermüller and P. Chaudhuri, *Inorg. Chem.*, 2008, **47**, 8943.

6 (*a*) A. M. Morris, C. G. Pierpont and R. G. Finke, *Inorg. Chem.*, 2009, **48**, 3496; (*b*) S. Bruni, A. Canneschi, F. Cariati, C. Delfs, A. Dei and D. Gatteschi, *J. Am. Chem. Soc.*, 1994, **116**, 1388; (*c*) Y. H-. Chang, C. L-. Su, R. R-. Wu, J. H-. Liao, Y. H-. Liu and H. F-. Hsu, *J. Am. Chem. Soc.*, 2011, **133**, 5708; (*d*) M. E. Cass, Greene, D. L. Greene, R. M. Buchanan and C. G. Pierpont, *J. Am. Chem. Soc.*, 1983, **105**, 2680; (*e*) M. E. Cass, N. R. Gordon and C. G. Pierpont, *Inorg. Chem.*, 1986, **25**, 3962; (*f*) To review: S. N. Brown, *Inorg. Chem.*, 2012, **51**, 1251.

7 (*a*) R. Farrmann, S. Boghosian, G. N. Papatheodorou, K. Nielsen, R. W. Berg and N. J. Bjerrum, *Inorg. Chem.*, 1989, **28**, 1849; (*b*) M. N. Bhattacharjee, M. K. Chaudhuri and N. S. Islam, *Inorg. Chem.*, 1989, **28**, 2420.

8 (*a*) C. Daniel and H. Hartl, *J. Am. Chem. Soc.*, 2005, **127**, 13978; (*b*) C. Rocchiccioli-Deltcheff, R. Thouvenot and M. Fouassier, *Inorg. Chem.*, 1982, **21**, 30.

9 (*a*) E. Carolina Sañudo, A. A. Smith, P. V. Mason, M. Helliwell, G. Arom and R. E. P. Winpenny, *Dalton Trans.*, 2006, 1981; (*b*) S. R. Cooper, Y. B. Koh and K. N. Raymond, *J. Am. Chem. Soc.*, 1982, **104**, 5092; (*c*) J. Selbin, *Chem. Rev.*, 1965, **65**, 153; (*d*) J. Selbin, *Coord. Chem. Rev.*, 1966, **1**, 293.

10 (*a*) H. Chun, P. Chaudhuri, T. Weyhermüller and K. Wieghardt, *Inorg. Chem.*, 2002, **41**, 790; (*b*) C. Mukherjee. T. Weyhermüller, E. Bother and P. Chaudhuri, *Inorg. Chem.*, 2008, **47**, 11620.

11 A comparison study has been performed between complex **1** (formed with ligand H_2Sami^{CN}) and complex **2** (formed with ligand H_2Sami^{OMe}) to show they were the same vanadium complex. See Fig. S8 (IR spectra), Fig. S9 (X-band EPR spectra), and Fig. S10 (UV-vis/NIR spectra) in ESI‡ (S7–S8). X-ray diffraction parameters **1 [2]**: a = 25.3631(9) [25.3663(8)], b = 20.7112(7) [20.7183(7)], c = 28.6263 [28.5477(9)], $\alpha = \beta = \gamma$ = 90°; V = 15037.4(9) [15003.3(8)] $Å^3$.

12 Strong interaction causes oxo-substitution of vanadyl moiety and results in non-oxo vanadium complex; see refs. 3, 10*b*.

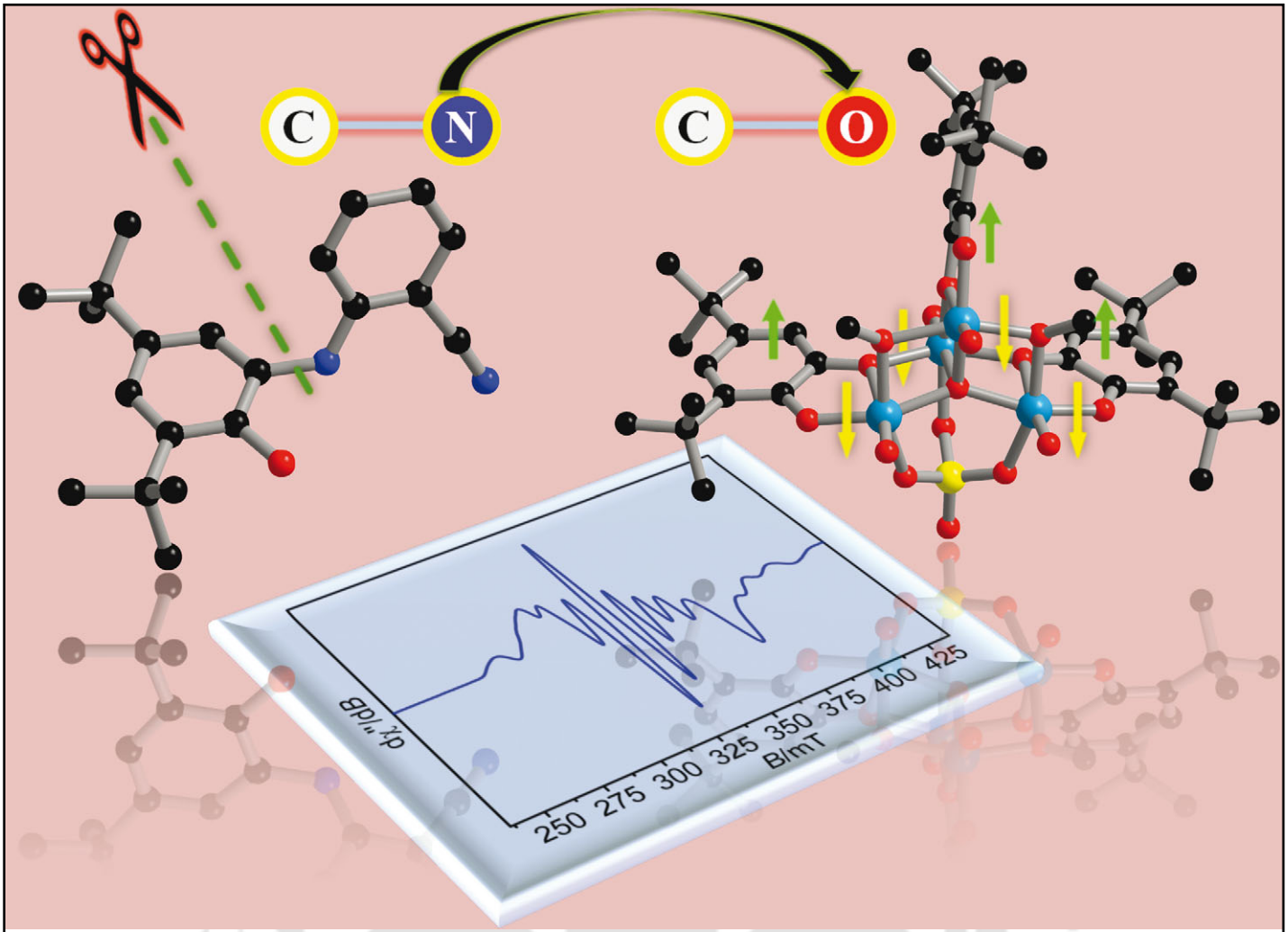

Showcasing research from The Mukherjee Group (Synthetic Inorganic Laboratory), Department of Chemistry, Indian Institute of Technology Guwahati, India

***Ortho*-substituent induced triradical-containing tetranuclear oxo-vanadium(IV) cluster formation *via* ligand C–N bond breaking and C–O bond making**

C–N bond breaking and C–O bond making: Substituents acquiring ambidentate or weak coordination character and residing at the *ortho*-position to the *N*-phenyl ring causes C–N bond breaking and C–O bond making *via* vanadium centre activation. This leads to a tetraradical-containing tetranuclear vanadium(IV) cluster formation.

As featured in:

See Samir Ghorai and Chandan Mukherjee, *Chem. Commun.*, 2012, **48**, 10180.

RSC Publishing

www.rsc.org/chemcomm

Registered Charity Number 207890

TH-1360_11612213

Inorganic Chemistry

Article

pubs.acs.org/IC

Effect of Ligand Substituent Coordination on the Geometry and the Electronic Structure of Cu(II)-Diradical Complexes[§]

Richa Rakshit,[†,⊥] Samir Ghorai,[†,⊥] Soumava Biswas,[‡] and Chandan Mukherjee*[,†]

[†]Department of Chemistry, Indian Institute of Technology, Guwahati 781039, Assam, India

[‡]Indian Institute of Science Education and Research Bhopal, Bhopal 462023, Madhya Pradesh, India

Supporting Information

ABSTRACT: Two organic moieties, known as ligands, having −OMe and −SePh as the ortho substituent attached to the aniline moiety of the parent 2-anilino-4,6-di-*tert*-butylphenol ligand, were synthesized. The ligands reacted with $CuCl_2·2H_2O$ in a 2:1 ratio in CH_3CN in the presence of Et_3N and provided the corresponding mononuclear Cu(II)-diradical complexes **1** (−OMe) and **2** (−SePh). Complex **1** was square planar, while complex **2** was in distorted square planar geometry due to the secondary coordination between the Se atom and the central Cu(II) center. Both complexes were comprised of multi-paramagnetic centers and exhibited an S_t = 1/2 ground state as established by variable-temperature magnetic susceptibility measurements. X-band electron paramagnetic resonance measurements indicated the presence of an unpaired electron at the Cu(II) center in complex **1** and at the ligand center (π-radical) in complex **2**. The extent of the secondary interaction was found to be dependent on the "softness" of the donor atom belonging to the ortho substituent.

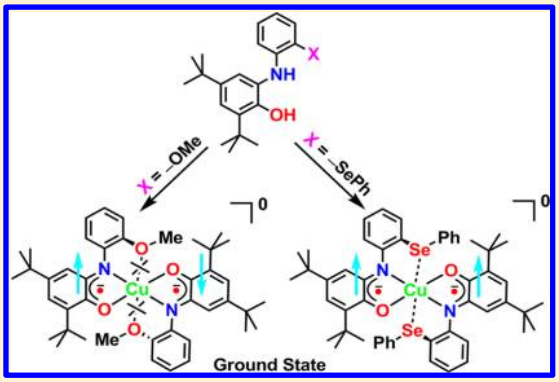

INTRODUCTION

Mononuclear Cu(II) ion containing metalloenzyme galastose oxidase (GOase) selectively catalyzes aerial oxidation of primary alcohols to their corresponding aldehydes, with concomitant reduction of molecular oxygen to H_2O_2.[1] Because of the structural simplicity and high utility as oxidation catalyst, synthesis of radical(s)-containing Cu(II) complexes as structural and/or functional models of GOase has drawn considerable attention.[2] In this regard, several Cu(II)-diradical complexes were synthesized.[2a,g,i−k] In those complexes the ground state is predominated by a Cu(II)-centered unpaired electron, which was caused by the stronger antiferromagnetic coupling between the two radical centers than that between the Cu(II) and a radical center. Although incorporation of different functional groups or steric crowding at the ligand backbone changes the dihedral angle (i.e., the angle between two ligating O−Cu−N planes, and will be noted here as distortion) around the Cu(II) center up to 35.5°,[2i,j] no alteration in the coupling fashion between the radicals and the Cu(II) and a radical centers are known.

In contrast to the conventional coupling fashion, in 2005 Kaim and coworkers[2k] showed that the presence of a −SMe substituent at the ligand backbone (at the ortho position of the aniline moiety, Scheme 1) in a Cu(II)-diradical complex (**3**) can alter the coupling fashion; that is, antiferromagnetic coupling between the two radicals is less than that of the Cu(II) and a radical. It is proposed that the change in the coupling fashion is due to the 32.2° dihedral angle between two ligating O−Cu−N planes, caused by the weak secondary

Scheme 1. Schematic Representations of (a) the Ligand and the Corresponding Cu(II) Complex Reported by Kaim and Coworkers, (b) Synthetic Route for H_2L^{OMe} and H_2L^{SePh} and Their Corresponding Cu(II)-Diradical Complexes, and (c) the Possible Different Redox-States of the Ligands

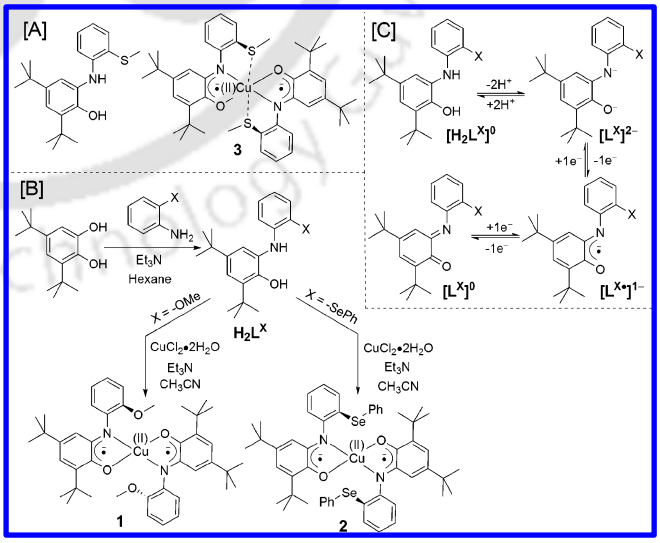

Received: October 16, 2013
Published: March 21, 2014

interaction between the Cu(II) center and the S atom from the −SMe substituent. However, it is known that Cu(II)-diradical complex having 35.5° dihedral angle around the Cu(II) center with no secondary interaction does not alter the coupling fashion.[2j] This acute observation indicates that the alteration in the coupling fashion might not be solely because of the distortion around the Cu(II) center but is rather possibly due to the secondary interaction that promotes a geometrical change in the complex. Because of this change the couplings fashion, and the coupling magnitude between the paramagnetic centers might change over. To find out the actual fact, we have employed two ligands by placing −OMe and −SePh at the ortho position of the aniline moiety (Scheme 1). We chose −OMe and −SePh substituted ligand because both of them could interact with the Cu(II) center. Additionally, on going from O to Se the "hardness" of the donor atom will decrease and consequently the Cu−substituent interaction (secondary coordination) should increase. Hence, the extent of interaction and its effect on the geometry as well as electronic structure of the corresponding Cu(II)-diradical complexes can be evaluated. Herein, we report the synthesis and characterization of ligand H_2L^{OMe}, H_2L^{SePh}, and their corresponding Cu(II)-diradical complexes (Scheme 1). The effect of secondary coordination on the geometry and the electronic structure of the Cu(II) complexes are presented.

RESULTS AND DISCUSSION

Ligands H_2L^X (X = −OMe and −SePh) were synthesized by reacting equimolar amounts of 3,5-di-*tert*-butylcatechol and the corresponding amine in the presence of Et_3N in hexane (Scheme 1). Reaction of the individual ligand (H_2L^{OMe} or H_2L^{SePh}) with $CuCl_2{\cdot}2H_2O$ in a 2:1 ratio in CH_3CN in the presence of Et_3N provided the corresponding Cu(II)-diradical complexes **1** and **2**, respectively (Scheme 1). Single crystals for **1** [$\{Cu^{II}(L^{OMe\cdot})_2\}{\cdot}H_2O$] and **2** [$\{Cu^{II}(L^{SePh\cdot})_2\}$] were obtained by recrystallizing the corresponding complex from a 5:2 CH_2Cl_2/CH_3CN solvent mixture. The molecular structures are presented in Figure 1. Selected bond distances and bond angles are given in Table 1.

In both neutral complexes (**1** and **2**) the central copper atom was coordinated by two ligand-centered N as well as O atoms. Although the Cu(1)−N(1) = 1.935(3) [**1**], 1.940(3) Å [**2**] (brackets indicate the complex) bond distance was almost same for both complexes and was in accord with the +II oxidation state of the copper center,[2i−l] a remarkable elongation (0.055 Å) in Cu−O bond distance {Cu(1)−O(1) = 1.908(3) [**1**], 1.963(2) Å [**2**]} due to secondary coordination, Cu(1)−Se(1) = 3.076(1) Å, was observed in **2**. Furthermore, the secondary coordination caused a large deviation in the O1−Cu(1)−O(1i) bond angle {180.00(11) [**1**], 143.79(5)° [**2**]}. The geometry around the copper center in **1** was square planar (τ = 0.0°) with no Cu−O_{Me} (O_{Me} indicates O atom from the −OMe group), 3.513(4) Å, interaction from the two oppositely (trans) oriented −OMe groups attached at the ortho position of the aniline moiety (Figure 1). On the contrary, a distorted square planar geometry (τ = 26.2°), which can also be considered as pseudo-octahedron, with a large dihedral angle (36.6°) between the two N(1)−Cu(1)−O(1) planes was observed in **2**. Interestingly, in complex **2**, two −SePh groups were situated cis to each other.

The C−C bond distances of the *tert*-butyl-containing C_6 rings in both **1** and **2** were not equal and were falling within the 1.39 ± 0.01 Å range. This indicated that the rings were not

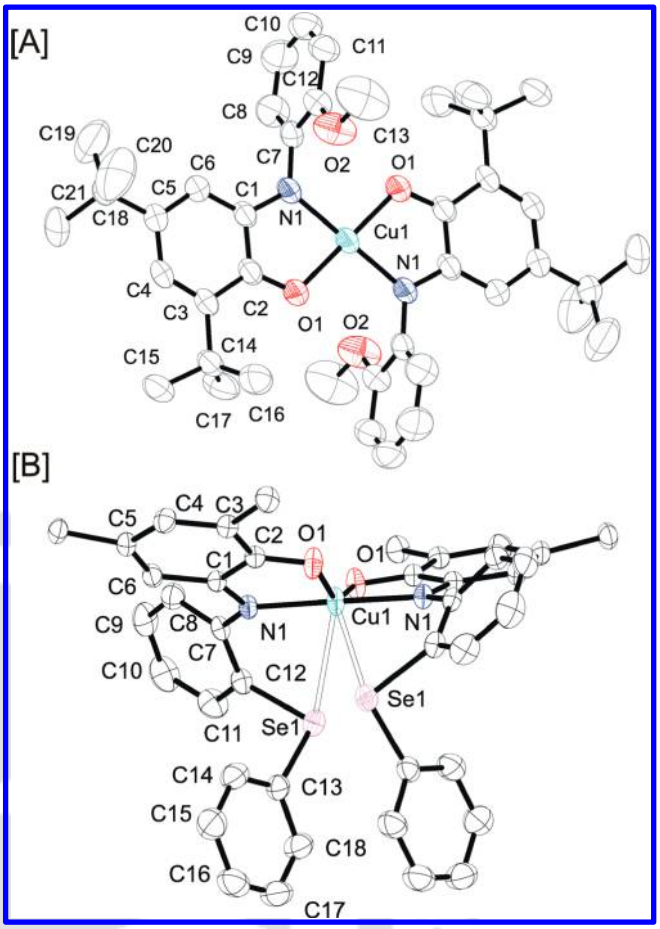

Figure 1. Molecular structure of (a) complex **1** and (b) complex **2**; thermal ellipsoids were drawn at 50% probability. Hydrogen atoms, solvent molecules, and methyl group attached to the *tert*-butyl groups (only in **2**) were omitted for clarity.

actual phenyl rings. An alternating short and long C−C bond distance showed a quinoid-type distortion. This type of distortion was expected for phenyl ring with its oxidized form(s) (Scheme 1). Additionally, the C(1)−N(1) = 1.341(4) [**1**], 1.349(2) Å [**2**] and C(2)−O(1) = 1.294(4) [**1**], 1.293(3) Å [**2**] bond distances, which were between their single bond and double bond character, confirmed one-electron oxidized iminobenzosemiquinone form {$[L^{X\cdot}]^-$, Scheme 1} of the coordinating ligands in **1** and **2**.[2i−l] Therefore, from the X-ray single-crystal analysis, both complexes can be described as Cu(II)-diradical.

Variable-temperature magnetic susceptibility measurements for both **1** and **2** are shown in Figure 2 as a plot of μ_{eff} versus T. Both complexes were composed of three paramagnetic centers with one unpaired electron on each (vide supra). At 10 K, μ_{eff} = 1.82 μ_B (**1**) and μ_{eff} = 1.73 μ_B (**2**) were observed (parentheses indicates the complex). These values were in accord with an S = 1/2 ground state for both complexes and discarded the possible ferromagnetic coupling among the three paramagnetic centers. A higher μ_{eff} value (>1.73 μ_B) in **1** was related to the higher g value (g > 2.00) and indicated that the unpaired electron was residing on Cu(II) center. The μ_{eff} = 1.73 μ_B value in **2** arose due to the presence of radical-centered unpaired electron (g = 2.00). In **1**, the μ_{eff} value remained almost constant up to 150 K, then increased slightly and gradually with the increase in temperature, and reached at 2.06 μ_B at 300 K. This feature

Table 1. Selected Bond Distances (Å) and Angles (deg) for Complexes 1 and 2

	1	2
Cu1−N1	1.935(3)	1.940(3)
Cu1−O1	1.908(3)	1.963(2)
C1−N1	1.341(4)	1.349(2)
N1−C7	1.421(4)	1.411(3)
C2−O1	1.294(4)	1.293(3)
C1−C2	1.449(4)	1.453(3)
C2−C3	1.424(4)	1.439(3)
C3−C4	1.363(4)	1.374(3)
C4−C5	1.418(4)	1.430(3)
C5−C6	1.371(4)	1.366(3)
C6−C1	1.409(4)	1.421(3)
C7−C8	1.381(6)	1.404(3)
C8−C9	1.375(6)	1.385(3)
C9−C10	1.372(7)	1.381(4)
C10−C11	1.341(6)	1.368(3)
C11−C12	1.390(5)	1.386(3)
C12−C7		1.405(3)
C13−C14		1.383(3)
C14−C15		1.383(4)
C15−C16		1.388(4)
C16−C17		1.356(4)
C17−C18		1.391(4)
C18−C13		1.381(3)
O2−C12	1.346(5)	
O2−C13	1.436(6)	
Se1−C12		1.922(2)
Se1−C13		1.923(2)
N1−Cu1−N1i	180.00(11)	179.30(6)
O1−Cu1−O1i	180.00(11)	143.79(5)
N1−Cu1−O1	83.84(11)	83.29(6)
N1−Cu1−O1i	96.16(11)	96.93(6)
Cu1−N1−C1	112.6(2)	113.10(12)
Cu1−O1−C2	113.20(21)	112.24(12)
N1−C1−C2	113.20(28)	113.54(16)
O1−C2−C1	117.09(26)	117.68(16)
C12−O2−C13	117.28(31)	
C12−Se1−C13		99.78(9)

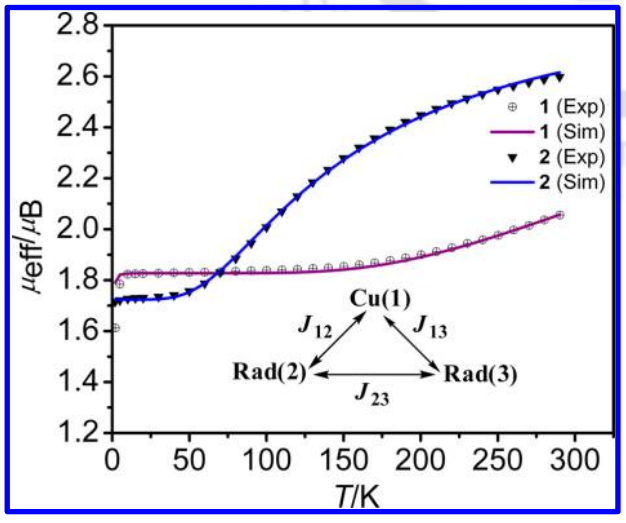

Figure 2. Showing μ_{eff} vs T plots for **1** and **2**.

consolidated the presence of multi-paramagnetic centers, and indicated the energy difference between the ground state (S = 1/2) and the higher spin state (S = 3/2) as high (>105 cm^{-1}, as 1 K ≈ 0.7 cm^{-1}). In the case of **2**, the μ_{eff} value started increasing gradually at 45 K and reached almost to a plateau at 300 K (μ_{eff} = 2.62 μ_B). This feature showed the existence of energetically low-lying S = 3/2 spin state (~32 cm^{-1}, as 1 K ≈ 0.7 cm^{-1}). The experimental results were simulated (Figure 2) using the following parameters: [**1**], $g_{Cu(II)}$ = 2.10, g_R = 2.00, J_{12} = J_{13} = 0.0 cm^{-1}, J_{23} = −342.0 cm^{-1}, and [**2**], $g_{Cu(II)}$ = 2.03, g_R = 2.00, J_{12} = J_{13} = −64.0 cm^{-1}, J_{23} = −23.0 cm^{-1}.[3]

The interactions between the three unpaired electrons will provide electronic spin states (S_t, S^*) = (3/2, 1), (1/2, 1), and (1/2, 0), where S_t = S_{Cu} + S_{rad1} + S_{rad2} and S^* = S_{rad1} + S_{rad2}. These electronic spin states can be symbolically represented as (↑↑↑), (↑↓↑), and (↑↑↓), respectively. The observed S = 1/2 ground state for both complexes indicated that the electronic spin state (3/2, 1) was higher in energy compared to the others. The S = 1/2 ground state could appear due to the presence of an unpaired electron either on a Cu(II) center or on a radical center. The ground state electronic configuration (↑↑↓) would provide Cu(II)-centered electron paramagnetic resonance (EPR) spectrum, while (↑↓↑) would provide a radical-centered EPR spectrum. Therefore, to define the exact location of unpaired electron and ground state electronic configuration, X-band EPR measurements were performed for both complexes at 77 K in a 1:1 CH_2Cl_2/toluene solvent mixture and depicted in Figure 3.

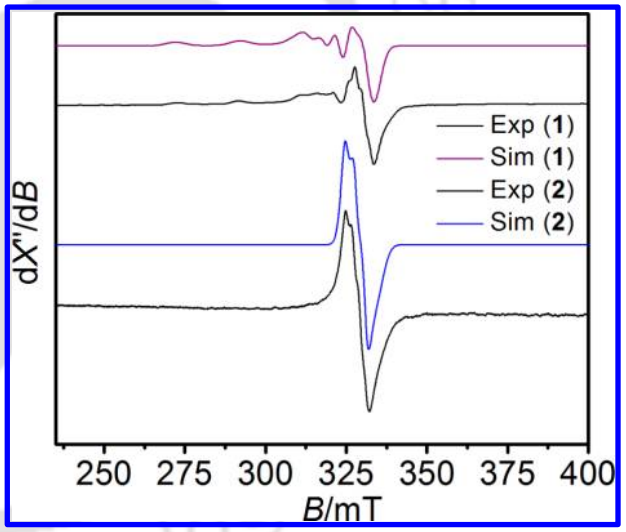

Figure 3. Experimental (Exp) X-band EPR spectrum for **1** and **2** presented with simulation (Sim). X-band microwave frequency (GHz): 9.125 [**1**], 9.145 [**2**]; modulation frequency (kHz): 100 [**1**, **2**].

Simulation of the experimental results provided the following parameters: [**1**], (g_1, g_2, g_3) = 2.000, 2.025, 2.170, g_{av} = 2.065; Cu(A_1, A_2, A_3) = (33, 43, 173) × 10^{-4} cm^{-1}, N(A_1, A_2, A_3) = (6, 7, 2) × 10^{-4} cm^{-1}, and [**2**], (g_1, g_2, g_3) = 1.964, 1.992, 1.992, g_{av} = 1.983; (A_1, A_2, A_3) = (13, 30, 30) × 10^{-4} cm^{-1}, Cu(A_1, A_2, A_3) = (10, 10, 8) × 10^{-4} cm^{-1}. Complex **1** exhibited a slight rhombic signal with $g_{||} > g\perp$ and g_{av} = 2.065. This type of signal is common for square planar Cu(II) complexes with $(d_x^2-_y^2)^1$ magnetic orbital.[2i,j,l] Hence, the (↑↑↓) ground state prevailed in **1** with dominating antiferromagnetic coupling between the radicals. Unlike complex **1**, an axial signal at g_{av} = 1.983 was observed in complex **2**. This indicated a radical-centered unpaired electron and (↑↓↑) as the ground-state electronic configuration owning stronger antiferromagnetic coupling

between the Cu(II) and a radical center.[2k] These results agreed well with the variable-temperature magnetic susceptibility measurements. The lower g_{av} value [<2.0023 (free radical)] in **2** emphasized the fact that spin state with nonzero orbital angular momentum situated at low energy.[4] Herein, it is important to note that g_{av} = 1.983 in **2** was much lower than that of g_{av} = 2.0006 observed for the Cu(II)-diradical complex with −SMe as the ortho substituent (**3**). This higher g_{av} deviation from 2.0023 in **2** than in **3** implicated a greater extent of interaction, due to low energy difference, between the ground state and the excited state with nonzero orbital angular momentum. This was possible due to the higher "softness" of the donor Se atom compared to the donor S atom.

CONCLUSIONS

To conclude, two Cu(II)-diradical complexes were synthesized by placing −OMe and −SePh as the ortho substituents. Hard donor O atom did not undergo secondary coordination with the Cu(II) center, while soft donor Se atom did. Because there was no secondary coordination, complex **1** was square planar. A distorted square planar or a pseudo-octahedral geometry was found in **2** because of the secondary coordination. It was observed that the higher softness of the donor atom caused (i) higher secondary coordination [Cu−S = 3.336(av), Cu−Se = 3.076 Å], (ii) more distortion [τ(**1**, **3**, **2**) = (0, 32.2,[2k] 36.6)°], and (iii) elongation in the Cu−O bond distance with higher deviation in the O−Cu−O bond angle [{**1**} = 1.908, 180.0; {**3**} = 1.923 (av), 149.7; {**2**} = 1.963 Å, 143.8°]. Interestingly, no significant deviation was caused by the secondary coordination in the N−Cu−N bond angle [{**1**} = 180.0; {**3**} = 172.0; {**2**} = 179.3°].

In the square planar complex **1** (τ = 0.0°), the radical-centered magnetic orbitals (p_z orbitals) were orthogonal to the Cu(II) {$d_{x^2-y^2}$} orbital. The two radicals were coupling to each other through the Cu(II)-centered t_{2g} orbital. This coupling is strongly antiferromagnetic in nature[2f] and dominated over the Cu(II) and a radical center coupling magnitude and provided (↑↑↓) as the ground state. On the contrary, because of the secondary interaction a remarkable deviation from the linearity in the O−Cu−O bond angle occurred in **2** (Table 1). Because of this deviation, the orthgonality between the radical-centered and the Cu(II)-centered magnetic orbitals was lost. Thus, an antiferromagnetic coupling between the magnetic orbitals appeared. Furthermore, the extent of antiferromagnetic interaction between the two radical centers was diminished due to the deviation in the O−Cu−O bond angle. In complex **2** (∠ O−Cu−Oi = 149.7°), the ligand-centered radicals interacted strongly with the Cu(II)-centered magnetic orbital and underwent a higher extent of coupling (antiferromagnetic) than did the two radicals. This caused (↑↓↑) to be the ground state. Herein, it is important to note that the previously reported Cu(II)-diradical complex[2j] having (i) 35.5° dihedral angle, (ii) no secondary interaction, and (iii) (↑↑↓) as the ground state shows two cross angles (cross angle = the two largest angles around the central metal atom in a square planar complex) as 155.1 and 157.4°. These indicate an almost same deviation from the linearity in both cross angles, while we observed almost linearity in one of the two cross angles (Table 1); the other was <150°, to have (↑↓↑) as the ground state. Hence, it is evident now that the dihedral angle is not the factor that alters the couplings fashion. It is mainly the secondary coordination that causes a geometrical change in terms of the deviation only in one of the two cross angles, and consequently promotes an alteration in the couplings fashion and their magnitudes between magnetic orbitals.

EXPERIMENTAL SECTION

General Considerations. All the chemicals and solvents were obtained from commercial sources and were used as supplied, unless noted otherwise. The 3,5-di-*tert*-butylcatechol, *o*-anisidine, diphenyl diselenide, and 2-fluoronitrobenzene were purchased from Sigma-Aldrich. Solvents were obtained from Merck (India). Air-sensitive reaction was performed under Ar atmosphere using proper glass apparatus.

Physical Methods. X-ray crystallographic data were collected using a Bruker SMART APEX-II CCD diffractometer, equipped with a fine focus 1.75 kW sealed tube Mo Kα radiation (λ = 0.71073 Å) at 296(2) K, with increasing w (width of 0.3° per frame) at a scan speed of 3 s/frame. Structures were solved by direct methods using SHELXS-97 and refined with full-matrix least-squares on F^2 using SHELXL-97.[5] All the non-hydrogen atoms were refined anisotropically.

IR spectra were recorded on Perkin-Elmer instrument at normal temperature with KBr pellet by grinding the sample with KBr (IR grade). UV−visible spectra were recorded on Perkin-Elmer, Lamda 750, UV−vis−near-IR spectrometer by preparing a known concentration of the samples in high-performance liquid chromatography (HPLC) grade CH_2Cl_2 at room temperature using a cuvette of 1 cm width. EPR spectra were measured on X-Band Microwave unit, JES-FA200 ESR spectrometer. Mass spectral (MS) data were obtained from quadrupole time-of-flight (QTOF)-MS spectrometer. Variable-temperature magnetic susceptibility measurements were performed using superconducting quantum interference device (SQUID) magnetometer at 1 T (**1**) and 0.1 T (**2**).

Synthesis of $[C_{21}H_{29}NO_2]$, H_2L^{OMe}. Synthesis of this ligand was reported previously.[6]

Synthesis of $[C_{26}H_{31}NOSe]$, H_2L^{SePh}. To a solution of 3,5-di-*tert*-butylcatechol (2.54 g, 11.47 mmol) and 2-(phenylselanyl)aniline (2.85 g, 11.47 mmol) in hexane (25 mL), Et_3N (0.05 mL) was added. The resulting solution was stirred for 48 h at room temperature (30 °C). A dark brown solution was obtained with an orange precipitate. The mixture was filtered and washed with hexane (10 mL). The brown filtrate was evaporated in vacuo to give a viscous brown liquid as crude product. The crude product was purified by column chromatography on silica gel (60−120 mesh) with ethyl acetate−hexane (1:9) as the eluent. The product was afforded as yellow viscous liquid. Yield: 2.78 g, 54%. Fourier transform infrared (FTIR) (KBr pellet cm^{-1}): 3433, 3322, 2956, 2905, 2867, 1583, 1476, 1362, 1309, 1021, 734, 689. ^{1}H NMR ($CDCl_3$, 399.85 MHz): δ 1.21 (s, 9H), 1.39 (s, 9H), 6.04 (s, 1H), 6.06 (s, 1H), 6.48 (dd, J = 8.4, 0.8 Hz, 1H), 6.77 (d, J = 2 Hz, 1H), 6.81 (dt, J = 7.2, 1.2 Hz, 1H), 7.19−7.30 (m, 7H), 7.71 (dd, J = 7.6, 1.6 Hz, 1H) ppm. ^{13}C NMR ($CDCl_3$, 75.47 MHz): δ 29.5, 31.6, 34.4, 35.0, 109.8, 114.0, 114.7, 119.8, 122.1, 122.5, 126.7, 127.1, 129.3, 129.5, 129.6, 131.3, 131.1, 135.3, 138.4, 142.3, 148.5, 149.7 ppm. ESI-MS (+) m/z for $[C_{26}H_{31}NOSe + H]^+$: Calcd, 454.1703; found, 454.1679. Anal. Calcd for $C_{26}H_{31}NOSe$: C, 68.85; H, 6.89; N, 3.10. Found: C, 68.66; H, 7.09; N, 3.20%.

Synthesis of $[C_{42}H_{54}CuN_2O_4{\cdot}H_2O]$, **1**. To a stirred solution of H_2L^{OMe} (0.328 g, 1.00 mmol) in CH_3CN (20 mL), $CuCl_2{\cdot}2H_2O$ (0.090 g, 0.53 mmol) and Et_3N (0.2 mL) were added sequentially. The reaction mixture was stirred for 2.5 h at room temperature. This caused a brown-black precipitation. The precipitate was filtered and washed with CH_3CN. Recrystallization of the solid from a CH_2Cl_2/CH_3CN (5:2) solvent mixture provided a crystalline compound suitable for single-crystal X-ray diffraction study. Yield: 0.204 g, 56%. FTIR (KBr pellet, cm^{-1}): 3434, 3071, 2956, 2906, 2867, 2853, 1580, 1508, 1490, 1463, 1435, 1422, 1387, 1360, 1333, 1301, 1256, 1244, 1204, 1174, 1113, 1043, 1025, 996, 926, 911, 881, 787, 775, 746, 693, 644, 604, 500. ESI-MS (+) m/z for $[C_{42}H_{54}CuN_2O_4]^+$: Calcd, 713.35; found, 713.37. UV−vis−NIR (CH_2Cl_2) λ_{max}, nm (ε, M^{-1} cm^{-1}): 1030(2600), 780(6750), 472(5600), 340(17 200), 305(20 050). Anal.

Calcd for $C_{42}H_{54}CuN_2O_4{\cdot}0.7H_2O$: C, 69.43; H, 7.69; N, 3.86. Found: C, 69.84; H, 7.47; N, 3.89%.

Synthesis of $[C_{52}H_{58}CuN_2O_2Se_2]$, 2. To a solution of H_2L^{SePh} (0.305 g, 0.67 mmol) in CH_3CN (10 mL), $CuCl_2{\cdot}2H_2O$ (0.062 g, 0.35 mmol) was added followed by addition of Et_3N (0.1 mL). The reaction solution was then stirred for 16 h. This caused precipitation of a black solid. The solid was washed with CH_3CN and then dried under air. The solid was then recrystallized from a 5:1 CH_2Cl_2/CH_3CN solvent mixture. A brown-black crystalline solid suitable for single-crystal X-ray study appeared in 2 d. Yield: 0.200 g, 55%. FTIR (KBr pellet, cm^{-1}): 3429, 2949, 2904, 2866, 1462, 1424, 1250, 1022, 739, 687. ESI-MS (+) m/z for $[C_{52}H_{58}CuN_2O_2Se_2]^+$: Calcd, 965.23; found, 965.23. UV−vis−NIR (CH_2Cl_2) λ_{max}, nm (ε, M^{-1} cm^{-1}): 1036(2900), 806(6050), 460(5850), 342(18 250), 294(23 650). Anal. Calcd for $C_{52}H_{58}CuN_2O_2Se_2$: C, 64.65; H, 6.06; N, 2.90. Found: C, 64.28; H, 6.14; N, 2.73%.

■ ASSOCIATED CONTENT

Supporting Information

Details of crystallographic structural parameters for **1** and **2**. This material is available free of charge via the Internet at http://pubs.acs.org. CCDC 935848 ($1{\cdot}1H_2O$) and CCDC 926557 (**2**) contain the supplementary crystallographic data for this Paper. These data can be obtained free of charge from The Cambridge Crystallographic Data Centre via www.ccdc.cam.ac.uk/data_request/cif.

■ AUTHOR INFORMATION

Corresponding Author

*E−mail: cmukherjee@iitg.ernet.in.

Author Contributions

⊥R.R. and S.G. contributed equally.

Notes

The authors declare no competing financial interest.

■ ACKNOWLEDGMENTS

This project is funded by DST (SR/FT/CS−86/2011) and BRNS (2012/37C/28/BRNS/1375). R.R. thanks IIT Guwahati and S.G. thanks UGC (India) for doctoral fellowship.

■ DEDICATION

§Dedicated to Prof. Dr. Phalguni Chaudhuri on the occasion of his 70th birthday.

■ REFERENCES

(1) (a) Ito, N.; Phillips, S. E. V.; Stevens, C.; Ogel, Z. B.; Mcpherson, M. J.; Keen, J. N.; Yadav, K. D. S. P.; Knowles, F. *Nature* **1991**, *350*, 87. (b) Ito, N.; Phillips, S. E. V.; Yadav, K. D. S.; Knowles, P. F. *J. Mol. Biol.* **1994**, *238*, 794. (c) Stubbe, J.; van der Donk, W. A. *Chem. Rev.* **1998**, *98*, 705. (d) Holm, R. H.; Kennepohl, P.; Solomon, E. I. *Chem. Rev.* **1996**, *96*, 2239. (e) Whittaker, J. W. *Chem. Rev.* **2003**, *103*, 2347. (f) Banerjee, R. *Chem. Rev.* **2003**, *103*, 2081.

(2) For some examples: (a) Chaudhuri, P.; Wieghardt, K. *Prog. Inorg. Chem.* **2001**, *50*, 151. (b) Que, L., Jr.; Tolman, W. B. *Nature* **2008**, *455*, 333. (c) Jazdzewski, B. A.; Tolman, W. B. *Coord. Chem. Rev.* **2000**, *200*, 633. (d) Thomas, F.; Gellon, G.; Gautier−Luneau, I.; Saint−Aman, E.; Pierre, J.−L. *Angew. Chem., Int. Ed.* **2002**, *41*, 3047. (e) Sokolowski, A.; Leutbecher, H.; Weyhermüller, T.; Schnepf, R.; Bothe, E.; Bill, E.; Hildebrandt, P.; Wieghardt, K. *J. Biol. Inorg. Chem.* **1997**, *2*, 444. (f) Benisvy, L.; Blake, A. J.; Collison, D.; Davies, E. S.; Garner, C. D.; McInnes, E. J. L.; McMaster, J.; Whittacker, G.; Wilson, C. *Chem. Commun.* **2001**, 1824. (g) Chaudhuri, P.; Wieghardt, K.; Weyhermüller, T.; Paine, T. K.; Mukherjee, S.; Mukherjee, C. *Biol. Chem.* **2005**, *386*, 1023. (h) Wang, Y.; Dubois, J. L.; Hedman, B.; Hodgson, K. O.; Stack, T. D. P. *Science* **1998**, *279*, 537. (i) Mukherjee, C.; Pieper, U.; Bothe, E.; Bachler, V.; Bill, E.; Weyhermüller, T.; Chaudhuri, P. *Inorg. Chem.* **2008**, *47*, 8943. (j) Mukherjee, C.; Weyhermüller, T.; Bothe, E.; Chaudhuri, P. *Inorg. Chem.* **2008**, *47*, 11620. (k) Ye, S.; Sarkar, B.; Lissner, F.; Schleid, T.; van Slageren, J.; Fiedler, J.; Kaim, W. *Angew. Chem., Int. Ed.* **2005**, *44*, 2103. (l) Chaudhuri, P.; Verani, C. N.; Bill, E.; Bothe, E.; Weyhermüller, T.; Wieghardt, K. *J. Am. Chem. Soc.* **2001**, *123*, 2213. (m) Schnepf, R.; Sokolowski, A.; Müller, J.; Bachler, V.; Wieghardt, K.; Hildebrandt, P. *J. Am. Chem. Soc.* **1998**, *120*, 2352. (n) Pierpont, C. G.; Lange, C. W. *Prog. Inorg. Chem.* **1994**, *41*, 331. (o) Ward, M. D.; McCleverty, J. A. *J. Chem. Soc., Dalton Trans.* **2002**, 275. (p) Razuvaev, G. A.; Cherkasov, V. K.; Abakumov, G. A. *J. Organomet. Chem.* **1978**, *160*, 361. (q) Buchanan, R. M.; Wilson-Blumberg, C.; Trapp, C.; Larsen, S. K.; Greene, D. L.; Pierpont, C. G. *Inorg. Chem.* **1986**, *25*, 3070. (r) Benelli, C.; Dei, A.; Gatteschi, D.; Pardi, L. *Inorg. Chem.* **1990**, *29*, 3409. (s) Speier, G.; Tisza, S.; Tyeklár, Z.; Lange, C. W.; Pierpont, C. G. *Inorg. Chem.* **1994**, *33*, 2041. (t) Pierpont, C. G. *Coord. Chem. Rev.* **2001**, *99*, 216. (u) Abakumov, G. A.; Cherkasov, V. K.; Nevodchikov, V. I.; Kuropatov, V. A.; Yee, G. T.; Pierpont, C. G. *Inorg. Chem.* **2001**, *40*, 2434. (v) Blackmore, K. J.; Ziller, J. W.; Heyduk, A. F. *Inorg. Chem.* **2005**, *44*, 5559. (w) Mukherjee, C.; Weyhermüller, T.; Bothe, E.; Chaudhuri, P. *C. R. Chim.* **2007**, *10*, 313. (x) Mukherjee, C.; Weyhermüller, T.; Wieghardt, K.; Chaudhuri, P. *Dalton Trans.* **2006**, 2169. (y) Ghorai, S.; Mukherjee, C. *Dalton Trans.* **2014**, *43*, 2169.

(3) The simulations of the experimental results indicated that a unique value for coupling constant J_{12}, J_{13}, and J_{23} (Figure 2, inset) cannot be achieved; that is, J_{12}, J_{13}, and J_{23} can be varied to reproduce the experimental result. In the case of **1** we observed Cu(II)-centered ground state, and that is why we chose antiferromagnetic coupling (J_{23} = −342.0 cm^{-1}) between two radical centers keeping J_{12} = J_{13} = 0.0 cm^{-1}. Because we had a radical-centered ground state we kept antiferromagnetic coupling between Cu and radicals higher than that of radicals.

(4) Kaim, W. *Coord. Chem. Rev.* **1987**, *76*, 187.

(5) Sheldrick, G. M. *SHELXL−97*;University of Göttingen: Göttingen, Germany, 1997.

(6) Ghorai, S.; Mukherjee, C. *Chem. Commun.* **2012**, *48*, 10180.

View Letter

Close

Date: 18 Aug 2014
To: "Chandan Mukherjee" cmukherjee@iitg.ernet.in
From: "ChemAsianJ" chemasianj@wiley-vch.de
Subject: Decision on your Manuscript asia.201402868R1 for Chemistry - An Asian Journal

Title: "Cu(II)-Mediated Transformation of a Tridentate Non-Innocent Ligand to a Tetradentate Salen-Type Innocent Ligand"

DOI: 10.1002/asia.201402868R1
for citing the article before publication in an issue, please use this DOI number.

Dear Dr. Mukherjee,

Thank you for your submission of 23 Jul 2014. We are pleased to inform you that the revised version of the above-mentioned manuscript has now been accepted for publication in Chemistry - An Asian Journal.

Thank you for sending the production material with the revised version of the manuscript. Should anything be missing or unclear we will contact you shortly.

Yours sincerely,

Dr. Theresa Kueckmann
Editor
Chemistry - An Asian Journal

WILEY-VCH
Boschstrasse 12, 69469 Weinheim, Germany
phone: +49-6201-606-129 fax: +49-6201-606-331 /-328
e-mail: chemasianj@WILEY-VCH.de www.chemasianj.org

A journal of the Asian Chemical Editorial Society (ACES). Supported by GDCh, ChemPubSoc Europe, and FACS. Published by Wiley-VCH: www.wiley-vch.de

Close

TH-1360_11612213